Geophysical Monograph Series

Including

IUGG Volumes
Maurice Ewing Volumes
Mineral Physics Volumes

Volcanism and the Earth's Atmosphere

Alan Robock
Clive Oppenheimer
Editors

Published under the aegis of the AGU Books Board

Front cover: Gunung Bromo (left, steaming), Gunung Batok (closest), and Gunung Semuru (on horizon, erupting), eastern Java, Indonesia. Photo was taken at sunrise on July 24, 2000 during a field trip after the IAVCEI General Assembly in Bali. Bromo was continuously emitting water, sulfur gases, and other material, which filled the larger, older crater, trapped by the crater walls and an atmospheric inversion. Within this layer, the smell of sulfur was very strong. Semeru was erupting every 5-10 minutes. Very sadly, three days later, as another field trip was visiting the rim on the summit of Semeru, an unexpectedly large eruption killed two volcanologists, Wildan and Mukti, and injured six others, including Kris, Amit Mushkin, Mike Ramsey, Lee Siebert, and Paul Kimberly. Photograph copyright by Alan Robock, taken on July 24, 2000.

Back cover: Lava from the Kilauea volcano on the island of Hawaii burning its way to the sea. This eruption has been nearly continuous for 20 years, producing massive sulfate emissions and contributing to local pollution called "vog." Photograph copyright by Alan Robock, taken on July 27, 2002.

Printed in the United States of America.

CONTENTS

CONTENTS

PREFACE

Volcanic activity can have a profound effect on the Earth's atmosphere and environment across many spatial and temporal scales. From being the source of most gases in the atmosphere over geologic time scales, to producing climate change, to threatening aviation, volcanic eruptions as well as non-eruptive volcanic gas and particle emissions provide a strong link between the lithosphere and the impact of the atmosphere on human activities. Since the massive 1991 Mt. Pinatubo eruption we have gained—and continue to gain—greater understanding of the impacts of volcanic eruptions on the atmosphere and climate. Among other things, we have learned about the winter warming effect on Northern Hemisphere continents, about effects on ozone chemistry, and about the impacts of volcanic radiative forcing on the carbon cycle. The importance of quantifying the effects of volcanic eruptions on interdecadal climate change has become more apparent in the context of anthropogenic global warming. New instruments and techniques have strengthened our ability to measure volcanic gas and aerosol concentrations, fluxes, and chemistry in the atmosphere. And new ice cores have allowed us to significantly improve the record of past volcanism.

This book is designed for climatologists, volcanologists, atmospheric scientists, environmental scientists, anthropologists, archeologists, geologists, glaciologists, dendrochronologists, those working on ground-based and satellite remote sensing, atmospheric hazards forecasters, and others interested in the connection between the solid Earth and the atmosphere. Observations of volcanic gas and particle emissions, reconstruction of past emission histories, and quantification of the effects on the biosphere and the climate system bridge a large number of disciplines. Never before has a monograph from so many disciplines been assembled to address the effects of volcanic eruptions on the atmosphere, and this once again emphasizes the value of interdisciplinary work in modern science research.

While this book presents our current understanding of volcanic emissions to the atmosphere, remote sensing of volcanic emissions, ice core records of past volcanism, tree ring records of the climate change following volcanic eruptions, effects of volcanic eruptions on ozone depletion and

recovery, volcanic aerosols in the atmosphere, and even taking volcanic eruptions into account when making seasonal forecasts, there remain a number of outstanding scientific issues to be addressed. These include:

• What exactly goes into the atmosphere during an explosive eruption, and where does it go?
• How do quiescent emissions change over time?
• How can we better quantify the record of past climatically significant volcanism?
• Can we design an improved system for measuring and monitoring the atmospheric gases and aerosols resulting from future eruptions—are we ready for the next Pinatubo?
• How can we better model the climatic impact of eruptions, incorporating microphysics, chemistry, transport, radiation, and dynamical responses?
• How do high-latitude eruptions affect climate?
• How much do season, atmospheric dynamics, and other non-volcanic "environmental" factors affect the climatic forcing of an eruption?
• How important are indirect effects of volcanic emissions on clouds?
• Where are the important potential sites for future eruptions?

The chapters in this book serve as an excellent basis for continued work on these topics.

To improve understanding of these phenomena, the International Association of Volcanism and Chemistry of the Earth's Interior (IAVCEI) and the International Association for Meteorology and Atmospheric Sciences (IAMAS) formed the Commission on Volcanism and the Earth's Atmosphere at the AGU Chapman Conference on "Climate, Volcanism and Global Change" in 1992 following one of the largest eruptions of the 20th century, that of Mt. Pinatubo in 1991. To review the progress since then and stimulate new work, the Commission sponsored a 10th anniversary Chapman Conference on the site of one of the most important past volcanic eruptions that profoundly affected civilization, the "Minoan" eruption of Santorini in

Introduction: Mount Pinatubo as a Test of Climate Feedback Mechanisms

Alan Robock

Department of Environmental Sciences, Rutgers University, New Brunswick, New Jersey

The June 15, 1991 Mount Pinatubo eruption was a large but relatively short-lived shock to the Earth's atmosphere. It thus provided an excellent opportunity to study the workings of the climate system, to test climate models, and to examine the impacts of climate change on life. The largest eruption of the 20th Century inspired a large amount of research on the connection between volcanic eruptions and the Earth's atmosphere in the 12 years since that eruption, as exemplified by the chapters in this book. Here several additional examples of our new understanding of these connections are presented. While the global cooling after Pinatubo was not surprising, the observed winter warming over Northern Hemisphere continents in the two winters following the eruption is now understood as a dynamic response to volcanically produced temperature gradients in the lower stratosphere from aerosol heating and ozone depletion, and to reduced tropospheric storminess. Interactions of the Quasi-Biennial Oscillation of tropical stratospheric winds with the climate system are also now better understood by examining their role in the Pinatubo response. We have more confidence in the sensitivity of climate models used for attribution and projection of anthropogenic effects on climate because the strength of the water vapor feedback has been validated with Pinatubo simulations. The response of the biosphere to the Pinatubo eruption also illustrates its sensitivity to climate change and clarifies portions of the carbon cycle. Death of coral in the Red Sea in the winter of 1991–1992 and an unusually large number of polar bear cubs born in the summer of 1992 were two responses to the characteristic winter and summer temperature responses of the climate system. This strengthens our concern about negative impacts of global warming on polar bears and other wildlife. Enhanced vegetation growth from more diffuse and less direct solar radiation took more carbon dioxide out of the atmosphere than normal, temporarily reducing the observed long-term increase in carbon dioxide. Continued research on the Pinatubo eruption and its aftermath will undoubtedly enhance our understanding of the climate system.

1. INTRODUCTION

Volcanic eruptions have been an important cause of weather and climate change on timescales ranging from hours [*Robock and Mass*, 1982] to centuries [*Humphreys*, 1913]. Their atmospheric aerosol and gas inputs, in addition to being potentially very dangerous to people nearby and to

aircraft during explosive eruptions, produce local air pollution and haze that not only can have a strong atmospheric impact while being erupted, but also when concentrated in peat that is much later dried and burned [*Langmann and Graf*, 2003]. Major eruptions, such as the Santorini blast in the 17th Century BCE, have had major impacts on civilization and changed history.

For 51 years before the 1963 Gunung Agung eruption in Bali, Indonesia, there had not been a major volcanic eruption on Earth. Starting then, Agung and the 1980 Mt. St. Helens, 1982 El Chichón and 1991 Mount Pinatubo eruptions have stimulated research on the impacts of volcanic eruptions on the atmosphere. The 12 years since the June 15, 1991 Mount Pinatubo eruption in the Philippines have been particularly productive, and the chapters in this book, based on presentations at the Chapman Conference on Volcanism and the Earth's Atmosphere in Thera, Greece, June 17–21, 2002, give many examples of this excellent work. Here I present examples of additional recent research to paint a broader picture of the new understanding we have gained.

A comprehensive survey of the effects of volcanic eruptions on climate was presented by *Robock* [2000], updated by *Robock* [2002a, 2003]. While we have gained much new understanding, the work presented in this book and at the Chapman Conference raises more sophisticated questions that will inspire continued work on the subject [*Robock*, 2002b].

2. VOLCANIC ERUPTIONS AND CLIMATE

Most causes of climate change are gradual shifts in atmospheric composition or land surface characteristics. Volcanic eruptions, however, can produce a very large, but short-lived, perturbation to the Earth's radiative balance. While we cannot use these perturbations to test long-term processes, such as changes in the thermohaline circulation, we can take advantage of them to examine some short time-scale feedback processes and impacts.

Plates 1 and 2 show the lower tropospheric temperature anomalies for the Northern Hemisphere winters of 1991/92 and 1992/93. Before the Pinatubo eruption, cooling was the only well-understood response of climate to volcanic eruptions. The large continental warming seen in this plate was not predicted, but we now understand it as a dynamical response to the radiative perturbation from the volcanic aerosols and ozone depletion from the eruption. *Stenchikov et al.* [2002] recently presented atmospheric general circulation model simulations which illustrate that this winter warming phenomenon, a positive mode of the Arctic

Oscillation [*Thompson and Wallace*, 1998], can be produced by the enhanced temperature gradient in the lower stratosphere from aerosol heating in the tropics, or from aerosol-induced ozone depletion in the higher latitudes, or by reduced winter synoptic wave activity (storminess) in the troposphere caused by reduced latitudinal temperature gradients (Figure 1). The Arctic Oscillation is the dominant mode of interannual variability of Northern Hemisphere atmospheric circulation, and a positive mode corresponds to a stronger than normal polar vortex, with strong westerly winds in the midlatitudes in the lower stratosphere and upper troposphere. The references in that paper and in *Robock* [2000] provide a detailed description of other observational and modeling studies that support this conclusion. We might expect similar Arctic Oscillation responses to long-term ozone depletion and increases in greenhouse gases, a mechanism now better understood by examining the response of the climate system to the Pinatubo eruption. *Stenchikov et al.* [2003] have shown that the Quasi-Biennial Oscillation of tropical lower stratospheric winds [*Angell and Korshover*, 1964] significantly modifies the response of stratospheric winds to the volcanic aerosols, making the polar vortex stronger in the second winter following the eruption, amplifying the response to a diminished aerosol loading and producing winter warming for the second winter, too. Thus, our understanding of stratospheric dynamics has also been enhanced by studying the reaction to an explosive volcanic eruption.

Plate 3 shows the lower troposphere temperature anomalies for the Northern Hemisphere summer of 1992, one year after the Pinatubo eruption. Virtually the entire planet was cooler than normal, as expected. But the amount of
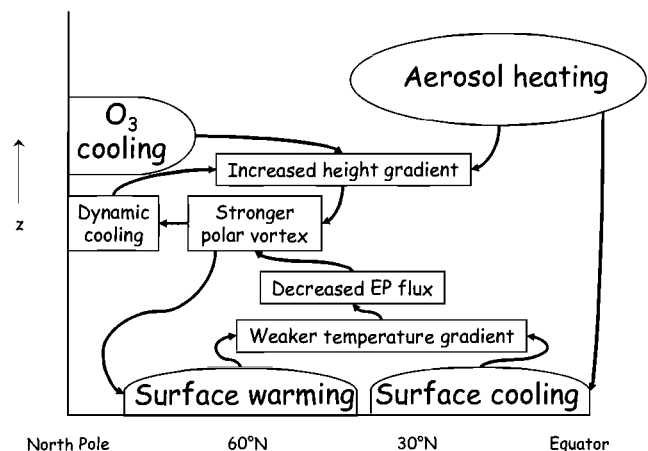
Figure 1. Ways volcanic eruptions cause a positive mode of the Arctic Oscillation. (Figure 13 from *Stenchikov et al.* [2002].)

Plate 1. Winter (DJF) lower tropospheric temperature anomalies [...] with the non-volcanic period of 1958-1960 used to calculate the means for the 1991-92 Northern Hemisphere winters. [...] illustrating the 1991-92 Pinatubo warming. This pattern is typical of that following all large volcanic eruptions, with warming over North America, Europe, and Siberia, and cooling over Alaska, Greenland, the Middle East, and China. Data from Microwave Sounding Unit Channel 2R [...] are standardized [...] Anomalies greater than [...] the color version of this plate at the back of this volume. [...] general courtesy of J. Christy and type credit [...]

4. CARBON CYCLE

The carbon dioxide concentration has been measured at the Mauna Loa observatory since 1958 [*Keeling and Whorf*, 2002], and is representative of global trends since CO_2 has such a long atmospheric lifetime (~100 years). Figure 3 shows that the Mauna Loa CO_2 concentration has a large upward trend superimposed on the terrestrial biologically induced seasonal cycle. This trend is not uniform however (Figure 4), and changes in emissions and El Niño and La Niña episodes explain part, but not all, of these interannual variations.

The tropical ocean warming associated with El Niño results in enhanced emissions from the ocean. The terrestrial component of the carbon cycle, however, is less well understood, and the Pinatubo eruption has provided another opportunity to learn about a part of the climate system that increases our understanding of the global warming problem. Enhanced forward scattering of incoming solar radiation caused by the Pinatubo aerosols increased the diffuse radiation reaching the surface and decreased the direct flux [*Robock*, 2000]. This allowed plants to photosynthesize more of the time, increasing the CO_2 sink [*Gu et al.*, 2002, 2003; *Farquhar and Roderick*, 2003]. *Jones and Cox* [2001] model experiments showed that the cool temperatures over land following volcanic eruptions produced reduced soil and plant respiration globally and enhanced gross primary productivity in the tropics, both of which would also reduce atmospheric CO_2 concentrations. These effects can be seen in the reduced rate of increase of CO_2 following each large volcanic eruption (Figure 4). This reponse somewhat mimics the effect of tropospheric clouds, and illustrates a biospheric climate feedback.
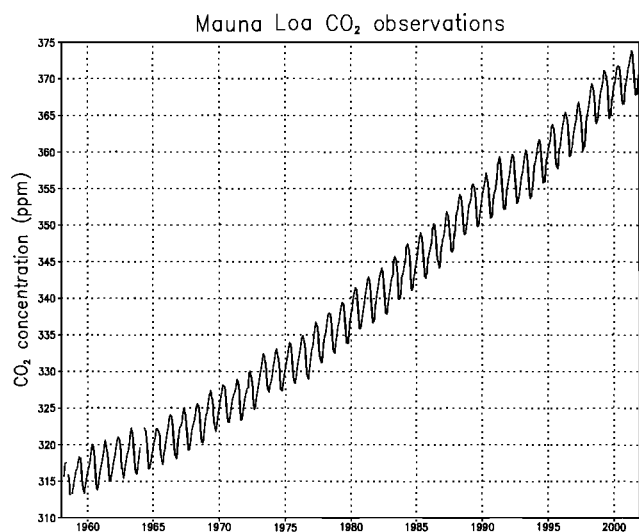
Figure 3. Record of CO_2 concentration at the Mauna Loa Observatory. Data are from *Keeling and Whorf* [2002].
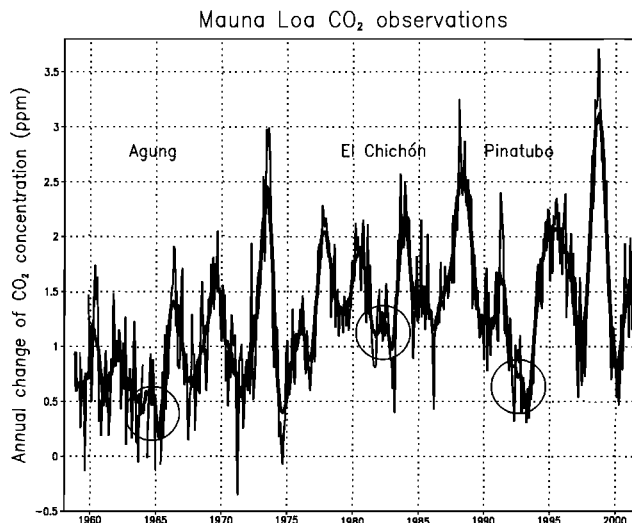
Figure 4. Annual rate of increase of CO_2 in the atmosphere. Data are from *Keeling and Whorf* [2002]. Thin line is monthly values and thick line is 9-month running mean. Minima following the largest volcanic eruptions of the period are indicated. Other interannual variations are partially due to El Niños, La Niñas, and emission variations.

5. SUMMARY

This brief introduction presents just a few examples of how studies of the responses to a large, recent volcanic eruption have deepened our understanding of the climate system. As a result, our confidence in our projections of the carbon cycle, the climatic response to anthropogenic greenhouse gases and land surface changes, and the biological response to the predicted warming has increased. Future studies, addressing outstanding issues in the impacts of volcanic eruptions on the atmosphere [Preface; *Robock*, 2002b], will surely add to this understanding.

REFERENCES

Angell, J. K., and J. Korshover, Quasi-biennial variations in temperature, total ozone, and tropopause height, *J. Atmos. Sci.*, *21*, 479-492, 1964.

Farquhar, G. D., and M. L. Roderick, Pinatubo, diffuse light, and the carbon cycle, *Science*, *209*, 1997-1998, 2003.

Genin, A., B. Lazar, and S. Brenner, Vertical mixing and coral death in the Red Sea following the eruption of Mount Pinatubo, *Nature*, *377*, 507-510, 1995.

Gu, L., D. Baldocchi, S. B. Verma, T. A. Black, T. Vesala, E. M. Falge, and P. R. Dowty, Advantages of diffuse radiation for terrestrial ecosystem productivity, *J. Geophys. Res.*, *107(D6)*, 10.1029/2001JD001242, 2002.

Gu, L., D. D. Baldocchi, S. C. Wofsy, J. W. Munger, J. J. Michalsky, S. P. Urbanski, and T. A. Boden, Response of a deciduous forest to the Mount Pinatubo eruption: Enhanced photosynthesis, *Science*, *299*, 2035-2038, 2003.

Humphreys, W. J., Volcanic dust and other factors in the production of climatic changes, and their possible relation to ice ages, *J. Franklin Institute, August*, 131-172, 1913.

Jones, C. D., and P. M. Cox, Modeling the volcanic signal in the atmospheric CO_2 record, *Glob. Biogeochem. Cycles*, *15*, 453-465, 2001.

Keeling, C. D., and T. P. Whorf, Atmospheric CO_2 records from sites in the SIO air sampling network. In *Trends: A Compendium of Data on Global Change* (Carbon Dioxide Information Analysis Center, Oak Ridge National Laboratory, U.S. Department of Energy, Oak Ridge, Tenn., U.S.A.), 2002.

Langmann, B., and H. F. Graf, Indonesian smoke aerosols from peat fires and the contribution from volcanic sulfur emissions, *Geophys. Res. Lett.*, *30(11)*, 1547, doi: 10.1029/2002 GL016646, 2003.

Robock, A., Volcanic eruptions and climate, *Rev. Geophys.*, *38*, 191-219, 2000.

Robock, A., Pinatubo eruption: The climatic aftermath, *Science*, *295*, 1242-1244, 2002a.

Robock, A., Blowin' in the wind: Research priorities for climate effects of volcanic eruptions. *EOS*, *83*, 472, 2002b.

Robock, A., Volcanoes: Role in climate, in *Encyclopedia of Atmospheric Sciences*, J. Holton, J. A. Curry, and J. Pyle, Eds., (Academic Press, London), 10.1006/rwas.2002.0169, 2494-2500, 2003.

Robock, A., and C. Mass, The Mount St. Helens volcanic eruption of 18 May 1980: Large short-term surface temperature effects, *Science*, *216*, 628-630, 1982.

Schneider, S. H., and R. E. Dickinson, Climate modeling, *Rev. Geophys. Space Phys.*, *12*, 447-493, 1974.

Soden, B. J., R. T. Wetherald, G. L. Stenchikov, and A. Robock, Global cooling following the eruption of Mt. Pinatubo: A test of climate feedback by water vapor, *Science*, *296*, 727-730, 2002.

Spencer, R. W., J. R. Christy, and N. C. Grody, Global atmospheric temperature monitoring with satellite microwave measurements: Method and results 1979-1984, *J. Climate*, *3*, 1111-1128, 1990.

Stenchikov, G., A. Robock, V. Ramaswamy, M. D. Schwarzkopf, K. Hamilton, and S. Ramachandran, Arctic Oscillation response to the 1991 Mount Pinatubo eruption: Effects of volcanic aerosols and ozone depletion, *J. Geophys. Res.*, *107 (D24)*, 4803, doi:10.1029/2002JD002090, 2002.

Stenchikov, G., K. Hamilton, A. Robock, V. Ramaswamy, and M. D. Schwarzkopf, Arctic Oscillation response to the 1991 Pinatubo eruption in the SKYHI GCM with a realistic Quasi-Biennial Oscillation, Submitted to *J. Geophys. Res.*, 2003.

Stirling, I., The importance of polynyas, ice edges, and leads to marine mammals and birds, *J. Marine Systems*, *10*, 9-21, 1997.

Thompson, D. W. J., and J. M. Wallace, The Arctic Oscillation signature in the wintertime geopotential height and temperature fields, *Geophys. Res. Lett.*, *25*, 1297-1300, 1998.

Alan Robock, Department of Environmental Sciences, Rutgers University, 14 College Farm Road, New Brunswick, NJ 08901
E-mail: robock@envsci.rutgers.edu

Petrological and Volcanological Constraints on Volcanic Sulfur Emissions to the Atmosphere

Bruno Scaillet

ISTO-CNRS, UMR 6113, Orléans, France

James F. Luhr

Department of Mineral Sciences, Smithsonian Institution, Washington, D.C., U.S.A.

Michael R. Carroll

Dipartimento di Scienze della Terra, Universita' di Camerino, Camerino, Italy

A review of current knowledge about the physics of volcanic eruptions and the experimental constraints on sulfur behavior in *magmas* is presented with the aim of evaluating the range of sulfur yields from major explosive eruptions based on petrological and volcanological data. The so-called *petrologic method*, used to evaluate syn-eruptive *melt* degassing, is expanded by also considering the role of a pre-eruptive gas *phase*. It is shown that more than 90% of the atmospheric sulfur loading may come from release of the pre-eruptive gas *phase* during eruptions of *intermediate* to *silicic magmas* at subduction-related volcanoes. In contrast, the role of a pre-eruptive gas *phase* may be much less important in more *mafic magmas* erupted in other tectonic settings. Bulk sulfur contents are weakly (*spreading-ridges* and *hot spots*) to non-correlated (*subduction-zones*) with *bulk-rock composition*. With the exception of some persistently active volcanoes, bulk sulfur contents generally do not exceed 0.5 wt %. The sulfur yields are positively correlated with mass of erupted *magma*, but the dispersion in sulfur emission for a given erupted mass increases progressively as the erupted mass decreases. The sulfur yields of single eruptive events retrieved from this *improved petrologic method* are shown to closely agree with independent estimates obtained from analysis of ice cores, optical-depth measurements, and remote-sensing spectroscopic techniques (*TOMS* and *COSPEC*).

INTRODUCTION

Sulfur injected into the atmosphere during volcanic eruptions can affect Earth's climate on regional to global scales [*Graf et al.*, 1998; *Robock*, 2000]. Although the sulfur emitted by numerous eruptions within the past 30 years has been directly monitored by either ground- or satellite-based tools

[e.g., *Krueger*, 1983; *Krueger et al.*, 1990; *Bluth et al.*, 1993; 1994], direct evidence for sulfur injection associated with older eruptions is lacking. Yet, volcanic activity and related sulfur emissions comprise one of the main forcing factors affecting short-term climate variability. Several climate models have shown that before the onset of clear anthropogenic influence on the climate system, which started 50–60 years ago, volcanic and astronomical factors were the two main forces affecting climate variability on a decadal time scale [*Crowley*, 2000]. A major advance in establishing the impact of volcanism on climate came with the recognition that ice cores preserve records of atmospheric sulfur loading from eruptions, through the presence of acidity peaks of non-marine origin in discrete ice layers, sometimes associated with shards of volcanic *glass* [e.g., *Hammer et al.*, 1980; *Legrand and Delmas*, 1987; *Zielinski et al.*, 1994; *De Silva and Zielinski*, 1998]. Early work [*Hammer et al.*, 1980] showed that for the past few millenia, such acidity peaks (H_2SO_4) could be correlated with known volcanic eruptions, and these correlations have now been extended over a much longer time interval [e.g., *Zielinski et al.*, 1996a]. The ice-core record, however, currently spans less than 500,000 years. No recognised proxies allow specific volcanic eruptions and their atmospheric sulfur loading to be evaluated at greater ages. In addition, because of compaction processes the temporal resolution of ice cores decreases significantly at deeper levels [e.g., *Zielinski et al.*, 1996b], and the assignment of acidity peaks to specific eruptions becomes difficult, thus obscuring the volcano-climate link in the remote past. Even for recent eruptions, large uncertainties may surround the attribution of a volcanic source to a given acidity peak, which complicates the estimation of the stratospheric aerosol mass responsible for the observed acidity peaks. The above reasons highlight the need for a reliable petrological and volcanogical approach to the evaluation of volcanic forcing on climate. If such an approach produces results that compare favorably with those from direct atmospheric measurements (*TOMS*, *COSPEC*) or established climate proxies, such as ice-core and tree-ring data, confidence can be gained for application to the older geological record.

The *petrologic method*, as originally devised by *Devine et al.* [1984], sought to constrain the extent of syn-eruptive *melt* degassing. *Devine et al.* [1984] and *Palais and Sigurdsson* [1989] used the *petrologic method* to evaluate the sulfur yields of several eruptions. For eruptions involving *mafic magmas*, they found good agreement compared with sulfur yields estimated from ice-core data or optical-depth measurements. However, several studies have since shown that the *petrologic method* significantly underesti-

mates sulfur yields for some eruptions of *subduction-zone* volcanoes [e.g., *Luhr et al.*, 1984; *Westrich and Gerlach*, 1992; *Wallace and Gerlach*, 1994; *Gerlach and McGee*, 1994; *Gerlach et al.*, 1994]. The case has been made clear for *silicic magmas* but also suggested for a number of *basaltic* eruptions [*Andres et al.*, 1991; *Allard et al.*, 1994; *Symmonds et al.*, 1994]. This deficiency in sulfur yield based on the *petrologic method* has been ascribed to the degassing of unerupted *magmas* [*Devine et al*, 1984, *Andres et al.*, 1991], to the breakdown of sulfur-bearing *phases* during eruption such as *sulfide* or *sulfate* minerals [*Devine et al*, 1984], to mixing between *oxidized* and *reduced magmas* [*Kress*, 1997], or to the presence of a separate gas *phase* in which most of the sulfur is stored prior to eruption [e.g., *Luhr et al.*, 1984, *Westrich and Gerlach*, 1992; *Wallace and Gerlach*, 1994]. Critical examination of each of the above hypotheses led *Wallace* [2001] to favour the existence of a separate gas *phase* in the *magma reservoir* as the most probable source for the excess sulfur.

It is the purpose of this paper to review recent advances in the fields of *petrology* and volcanology that are relevant to the evalution of sulfur yields from eruptions. The paper is aimed at non-geologists interested in the volcano-climate problem. Physical and chemical aspects of erupted *magmas* are treated in greater detail in *Sigurdsson et al.* [2000], whereas the physics and dynamics of volcanic eruptions are thoroughly presented and discussed by *Sparks et al* [1997]. We discuss an *improved petrologic method*, one that includes an estimate of the contribution from the pre-eruptive gas *phase*, and emphasize the uncertainties associated with this approach. We start by reviewing basic concepts necessary to understand the factors controlling the behavior and abundance of sulfur in *magmas* and its injection into the atmosphere during eruptions. We end by comparing sulfur yields based on the *improved petrologic method* with independent estimates. Because volcanic sulfur plays a key role in climate forcing, we focus primarily on this *volatile* element. Technical terms are italicized and defined in the glossary.

MAGMAS ON EARTH

Figure 1 shows a hypothetical box of *magma* sitting in a *reservoir* beneath a volcano prior to eruption. This model *magma* contains crystals of three different minerals surrounded by liquid silicate *melt*. Upon explosive eruption into the atmosphere, or eruption into cold seawater, the *melt* will cool rapidly and freeze to *glass* and fragment into *pyroclasts*. In more slowly cooled *lava* flows, the *melt* will instead crystallize to form an interlocking *matrix* of fine-

Figure 1. A hypothetical box of vapor-saturated *magma* showing the key *phases*, including *melt*, minerals A, B, and C, and gas bubbles. Note that some crystals contain trapped *melt inclusions*.

grained crystals. Several of the crystals in Figure 1 contain small *melt inclusions*. If this box of *magma* were to crack its way to the surface and erupt, virtually all of the gaseous species (H_2O, CO_2, H_2S, SO_2) in the main body of the *melt* would bubble out and provide the propellant for the eruption through their expansion. The *melt inclusions*, however, are protected from this process of eruptive decompression and degassing through the strength of the host crystal, and quench to *glass inclusions*. The remaining *phase* in this model *magma* system, represented by the white circles, is *vapor* or gas. Much of the analysis in this paper concerns

this separate gas *phase*, its abundance in the *magma*, and its role in the sulfur budget, because sulfur strongly partitions into the gas *phase*. This model *magma* is said to be gas-saturated.

Although exceptions do exist, the vast majority of Earth's *magmas* are produced within three main types of tectonic settings: *spreading ridges*, *subduction zones*, and *hot spots* (Figure 2). The volumes of *magma* produced in these three tectonic settings are given in Table 1, after *McBirney* [1989].

The dominant type of *magma* erupted at oceanic *spreading ridges* is *basalt* (SiO_2 < 52 wt%), commonly termed *MORB* with low *volatile* contents, especially H_2O and Cl. Because *MORB* eruptions typically take place at water depths of 2.5–4 km, equivalent to pressures of 250–400 bars, extensive degassing is inhibited and *glassy* rims on *pillow basalts* can provide valuable information on pre-eruption magmatic *volatile* contents, comparable to data from trapped *glass inclusions* (however, CO_2-rich gas bubbles must be considered for both types of *glass*). Although oceanic

Table 1. Global rate of *magma* production ($km^3 y^{-1}$) in *spreading-ridge*, *hot-spot*, and *subduction-zone* settings [*McBirney*, 1984].

setting	spreading	hot spot	subduction
volcanic	3	0.3–0.5	0.4–0.6
plutonic	18	1.6–3.5	2.5–8
Total (average)	21	3	6
Percent (average)	71	10	19
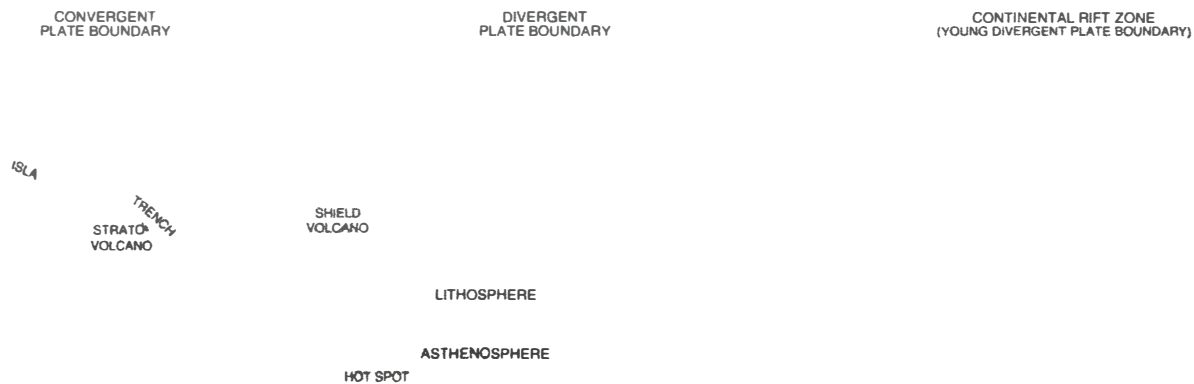
Figure 2. Tectonic settings of *magma* production shown in cross section. Taken from the wallmap This Dynamic Planet [*Simkin et al.*, 1994].

spreading-ridge basalts represent the volumetrically dominant type of magmatism at Earth's surface (Table 1), *MORB* activity has little direct impact on climate, except in areas where the ridge crest rises above sea level such as in Iceland. At Iceland and similar islands atop *spreading ridges*, *intermediate* and *silicic magmas* also erupt, sometimes explosively.

At *subduction zones*, the chemical variability of erupted *magmas* is typically large, ranging from *basalt* to *rhyolite* depending on the degree of *differentiation* (Figure 3). Although the type of *magma* erupted may differ between *subduction zones*, in many cases *intermediate* compositions, *andesite-dacite* (57–67 wt% SiO_2), represent the common surficial expression of magmatic activity in this setting.

Oceanic *hot-spot magmas*, like those from oceanic *spreading ridges*, are also mainly *basaltic* in composition. *Hot-spot* activity is associated with some of the most massive outpourings of *magma* in Earth's history, with volumes often in excess of 10^6 km³ erupted during relatively short periods of times, and thus with potentially global environmental consequences [see *Eldholm and Coffin*, 2000]. These include the Deccan Plateau eruption (western India), which correlates in time with the end-Cretaceous mass extinction, and the Siberian Traps eruption (Russia), which correlates in time with the end-Permian mass extinction and represents one of the largest known events of this type [see *Coffin and Eldholm*, 1994; *Eldholm and Coffin*, 2000; *Wignall*, 2001]. Some of these massive *basaltic* outpourings are accompanied by emission of *silicic magmas*, whose volumes may be equally impressive [see *Ayalew et al.*, 2002; *Bryan et al.*, 2002].

In all tectonic settings, *basalt* originates by partial melting of *peridotite*, the dominant rock type of Earth's *mantle*. Beneath *spreading ridges* and *hot spots*, however, the melting process occurs under H_2O-poor and *reduced* conditions, and the resulting *basalts* are H_2O-poor and *reduced*. In contrast, magmatism in *subduction zones* is triggered by release of water from subducted hydrothermally altered oceanic crust, with the released water acting as a flux that lowers the melting temperature of the overlying *mantle wedge* (Figure 2). The *basalts* so produced are thus comparatively richer in water than *MORBs* and *hot-spot basalts* and are also more *oxidized*. Their richness in water drives the derivative compositions to be richer in silica and poorer in iron: *andesite*, *dacite*, and *rhyolite* (Figure 3). Because water concentrates preferentially into the residual liquid, such derivatives are also enriched in water. Thus, *subduction-zone magmas* are water rich and their eruptions can be violently explosive.
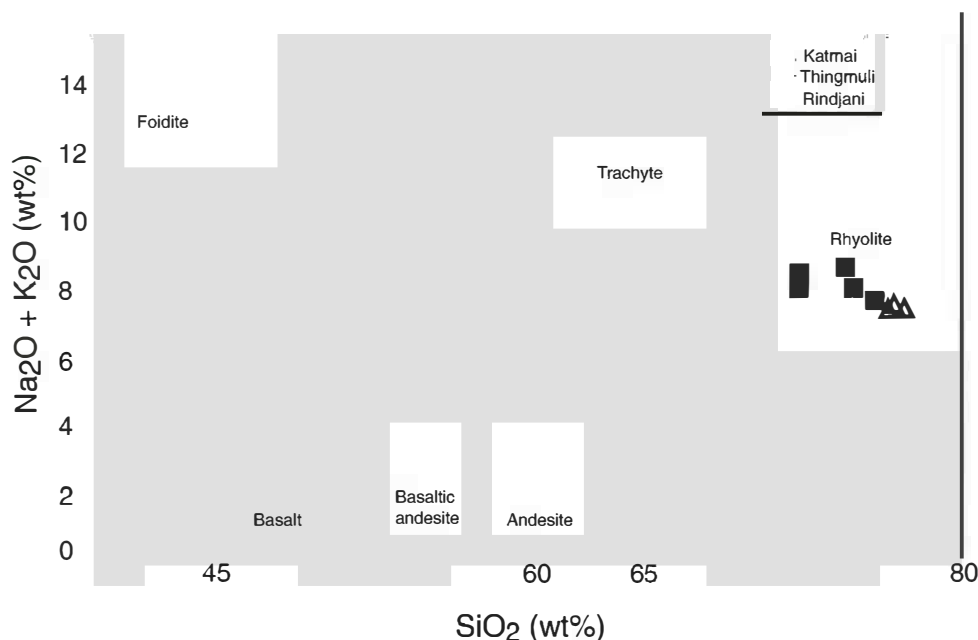
Figure 3. Total *Alkalies* versus *Silica* (TAS) diagram after *Le Bas et al.* [1986] for the classification of volcanic rocks showing the *differentiation* trends of Katmai (*subduction*, [*Hildreth*, 1983]), Rindjani (*subduction*, [*Foden*, 1982]), Tenerife (*hot-spot*, [*Ablay et al.*, 1998]), Thingmuli (*spreading-ridge*, [*Carmichael*, 1964]).

Regardless of the tectonic setting, in addition to the process of *basalt* crystallisation that produces *silicic* derivatives, minor to voluminous amounts of *silicic magma* can be generated by the thermal effects of *basaltic* intrusion into continental crust [*Huppert and Sparks*, 1988] and resultant widespread and sustained partial melting of crustal rocks [see *Bryan et al.*, 2002]. These crustal *melts* can subsequently mix with new *mafic* injections on coarse to fine scales, contributing to the chemical diversity observed in erupted *magmas*.

Volatiles in Magmas

For the most abundant magmatic *volatile* species, H_2O and CO_2, pressure is the major variable controlling *melt* *volatile* contents, and other variables such as *melt* composition, temperature, and *redox state* are of secondary importance. The effect of pressure on sulfur, chlorine, and fluorine solubilities is variable and, for sulfur, still debated (see below). Laboratory experiments have shown that pressure increases the *solubility* of both H_2O and CO_2 (Figure 4, see *Carroll and Holloway* [1994]). At Earth's surface (~1 bar), natural silicate *melts* cannot hold much more than 0.1 wt% H_2O in solution.

General and detailed accounts of *volatiles* in *magmas* are given in *Carroll and Holloway* [1994], *Scaillet et al.* [1998a], *Scaillet and Pichavant* [2003], and *Wallace and Anderson* [2000]. Important species of these elements in both *melt* and gas *phases* are given in Table 2. Pre-eruptive *melt* concentrations of H_2O, Cl, and S, based on analyses of *glass inclusions* or quenched submarine *glass* rims from different tectonic settings are shown in Figure 5. The plot of H_2O versus Cl indicates that submarine *spreading-ridge glasses* (squares) have the lowest concentrations of both components. The 1783–84 Laki *glass* is the square that falls in with the *hot-spot* Hawaii and Reunion *glasses* (open circles), which is appropriate because Iceland is thought to be a hybrid between a *spreading ridge* and a *hot spot*. The triangles (*subduction zone*) indicate higher Cl, and range to much higher water contents, as might be expected from *magmas* whose melting is triggered by release of subducted Cl-rich seawater. Sulfur contents vary widely and overlap for *glasses* from all three tectonic settings. As a dissolved species, CO_2 (not plotted on Figure 5) dominates the *volatile* budget in *MORB*, is equal in importance to H_2O in *hot-spot basalts* (up to 0.7 wt%), but is generally found in low abundances in *intermediate* to *silicic subduction*-related *glasses*. However, CO_2 concentration can reach 1000 ppm in some *basaltic subduction-zone glasses* [e.g., *Roggensack*, 2001; *Luhr*, 2001].

Subduction zone magmas commonly contain 4–7 wt% dissolved H_2O, which is the *solubility* of H_2O in most silicate liquids in the pressure range 1000–2000 bars (Figure 4), the pressure at which most *reservoirs* feeding active volcanoes lie (4–8 km depth). Because under ambient atmospheric conditions the H_2O *solubility* is very low (Figure 4), this implies that during ascent towards the surface *magmas* must exsolve nearly all of the water that they contained at depth. The extent to which this exsolved water is degassed and lost from the *magma* during ascent dictates in large part the eruption regime (*effusive* or explosive) as explained below.
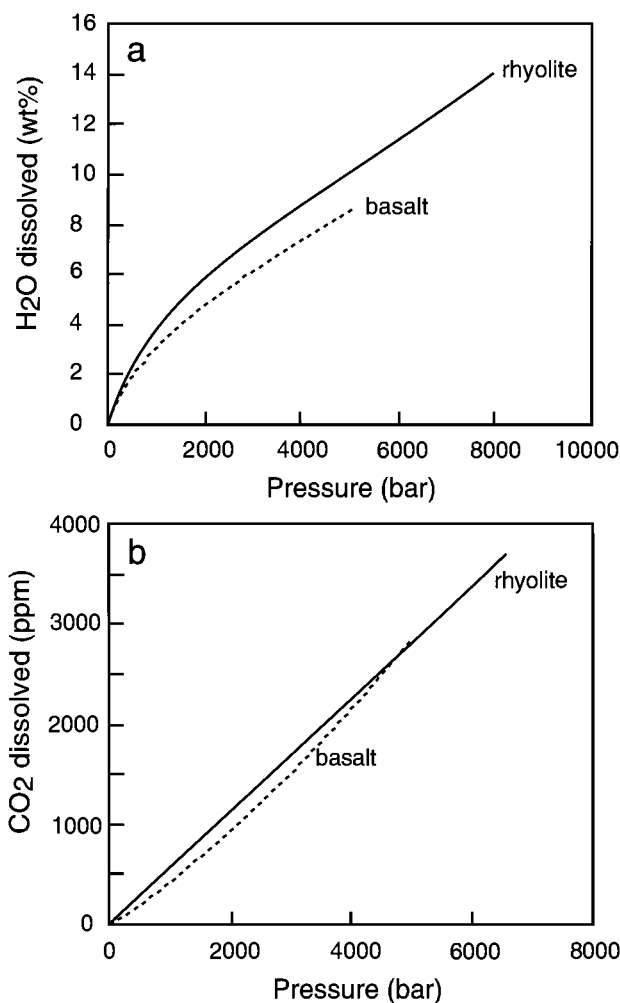
Figure 4. *Solubility* of (a) H_2O and (b) CO_2 in *basalt* [*Dixon et al.*, 1995] and *rhyolite* [*Fogel and Rutherford*, 1990; *Holtz et al.*, 1992; 1995] *melts* as a function of pressure. Temperature is 1200°C for *basalt*, 800°C for H_2O in *rhyolite*, and 1000°C for CO_2 in *rhyolite*.

ERUPTION OF MAGMAS AND VOLCANIC PLUMES

Effusive and Explosive Eruptions

Volcanic eruptions may be either *effusive* or explosive, depending on (1) the ability of the *magma* to exsolve its *volatiles*, which itself depends on *magma viscosity* and ascent velocity, (2) the ability of those *volatiles* to escape the *magma* body toward fractured country rocks [e.g., *Eichelberger et al.,* 1986; *Jaupart and Allègre,* 1991] and/or rise ahead of it toward the surface, likely feeding the persistent vapor plumes observed at many active volcanoes, and (3) the special case when *magma* interacts with external water in a *phreatomagmatic* eruption.

In the case of *basaltic magmas,* low *melt viscosity* allows rapid and efficient *volatile* escape during ascent in the *conduit* owing to the contrasting buoyancy between gas bubbles and the silicate *melt.* Bubbles rise faster than the surrounding *melt* and reach the surface first where they expand and equilibrate at atmospheric pressure, producing bursting bubbles in *lava* lakes, and feeding persistent vapor plumes that trail downwind from the active vent. This process of degassing may be accelerated by convective motions driven by thermal gradients accross the *magma* column [e.g., *Kazahaya et al.* 1994]. When *basalts* finally erupt they can be extensively degassed and emerge in a nearly non-explosive fashion to feed *lava* flows. *Basaltic magmas* in *hot-spot* settings commonly ascend rapidly enough to retain more of their primary *volatiles* and erupt in impressive fire fountains, feeding extensive *lava* flows. Along *oceanic spreading ridges,* the pressure of the overlying water column is sufficient to keep most *volatiles* in solution in the *melt,* although CO_2-rich bubbles are common and their abundance may vary with eruption depth.

In contrast to *effusive* eruptions of low-*viscosity basalts* are eruptions involving *magmas* with highly viscous *melts* (i.e., silicic magmas, sensu lato), which inhibit efficient *volatile* exsolution and separation. In such cases, the silicate *melt*+crystals+bubble mixtures may reach near-surface conditions largely unequilibrated with much of the water still in solution in the silicate liquid where bubbles cannot expand

Table 2. Important *volatile* species in the *melt* and gas *phases*

Element	Dominant *melt* species	Dominant gas species
H	H_2O, OH^-	H_2O, H_2
C	CO_2, CO_3^{2-}	CO_2, CH_4, CO
S	SO_4^{2-}, S^{2-}	SO_2, H_2S
Cl	Cl^-	HCl
F	F^-	HF
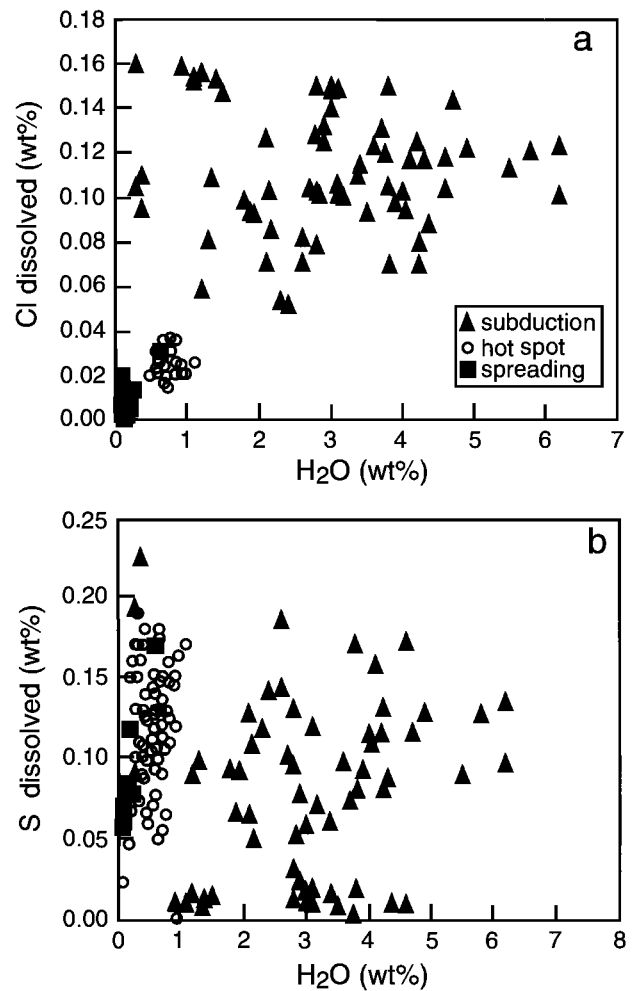
Figure 5. *Volatile* contents in natural volcanic *glasses*: H_2O versus (a) Cl and (b) S for *glassy pillow rims* and trapped *glass inclusions,* with symbols distinguishing tectonic setting: *spreading ridges* shown as solid squares (MORBs [*Byers et al.,* 1986]; Laki [*Thordarson et al.,* 1996]), *hot spots* shown as open circles (Hawaii [*Dixon et al.,* 1991; *Anderson and Brown,* 1993]; Piton de la Fournaise [*Bureau et al.,* 1998]; Etna [*Metrich et al.,* 1993]), and *subduction-zones* shown as triangles (Cerro Negro [*Roggensack et al.,* 1997]; Pinatubo [*Gerlach et al.,* 1996]; Fuego [*Sisson and Layne,* 1993]; Galunggung [*Sisson and Bronto,* 1998]; Parícutin [*Luhr,* 2001]; Satsuma-Iwojima [*Saito et al.,* 2001]).

easily because they are restrained by viscous resistance to deformation of the surrounding *melt.* Ultimately bubble overpressure may exceed the strength of the surrounding *magma* and resulting failure followed by rapid decompression and gas expansion provides the PDV work needed to power an explosive volcanic eruption. For instance, 1 m³ of a rhyolitic *melt* at 900°C with 5 wt% dissolved H_2O (= x ~5 km depth)

eruption, and thus the *magma* discharge rate increases too, the eruption can reach a point beyond which the ejected mixture cannot efficiently mix with air and thus loses the ability to become less dense than the ambient air: as a consequence, the fountain collapses and generates *pyroclastic flows* (Figure 6b). These give rise to *pyroclastic-flow* or *ignimbrite* deposits. Field observations combined with analog and numerical modelling have shown that the height of the fountain before collapse is only a few kilometers, which would imply that such an eruptive regime cannot inject material high into the stratosphere. However, *pyroclastic flows* may give rise to secondary columns or plumes (*co-ignimbrite plumes*) that can rise above them to heights in excess of 40 km. Figure 6b shows an example from Redoubt volcano. Most of the *ash-fall* deposits associated with the 1991 Pinatubo eruptions are also thought to have derived from *co-ignimbrite plumes* [*Scott et al.*, 1996; *Holasek et al.*, 1996]. The discrimination between *co-ignimbrite* and *Plinian fall* deposits is not straightforward and requires detailed field and laboratory studies of the deposits. A fundamental difference between the two deposits is that *Plinian fall* deposits originate from a point source injection into the atmosphere, whereas the *co-ignimbrite plumes* originate from extensive surfaces, up to 10^6 km^2 in area, basically from most of the area covered by the *pyroclastic flows*. Another difference is that *volatiles* in *Plinian* columns are a combination of *juvenile* (magmatic) and ambient air, whereas in *co-ignimbrite plumes*, part of *volatiles* may originate in the various terrains traversed by the *pyroclastic flow*, such as rivers, lakes, seawater, or from combustion of entrained vegetation. The possibility of multiple sources of *volatiles* in *co-ignimbrite plumes* makes it more difficult to evaluate the *volatile* budget associated with such eruptions.

Column Heights

The height of the eruption column is critical for evaluating *tephra* dispersal and the extent to which stratospheric injection of aerosols occurs. For historical eruptions, eyewitness accounts can provide estimates of eruption column height, although reliable data are not abundant. For past eruptions, the measurement of maximum *clast* sizes at various places is commonly used [*Sparks et al.*, 1997]. Theoretical modelling allows calculation of transport paths for particles of various sizes and densities in sustained *Plinian*-type eruptions [*Carey and Sparks*, 1986; *Wilson and Walker*, 1987]. These modelling results combined with direct observation have been used by *Carey and Sigurdsson* [1989] to show that the peak column height of a *Plinian* eruption is closely correlated with the total mass of *magma*

discharged. They derived the following simple relationships:

$$H = 7.2 \ (\log_{10} M) - 60.5 \qquad (1)$$

where H is the height in kilometers, and M the mass of *magma* in kilograms.

Fire fountains associated with voluminous *basalt* outflows represent a special case of *effusive* activity that generally has only a local to regional impact when issued from a point source of emission (a single volcano). When sustained *effusive* eruptions occur along fractures several kilometers long, the amount of *magma* ejected is so high that it may generate convective plumes above the line source. These plumes can transport gas (e.g., SO_2) and entrained *ash* into the upper troposphere or even into the lower stratosphere. In such cases, *effusive* eruptions may produce global atmospheric effects, as hypothesized for the 1783 Laki event in Iceland [*Thordarson et al.*, 1996]

Volumes of Erupted Magmas

Besides the eruption style, the mass of erupted material is obviously a key parameter for evaluating the atmospheric impact. Estimation of ejecta volumes associated with modern explosive eruptions benefits from air-borne or satellite observations [e.g., *Holaseck et al.*, 1996] as well as detailed field observations before erosional processes remove part of the *tephra* blanket. For *effusive* events, the volumes of *lava* flows are relatively easy to measure, and because *lavas* are much more resistant to erosion than loose *pyroclastic* material from explosive events, *lava* volumes are much better constrained than volumes of *pyroclastic* deposits. In the latter case, various empirical methods have been developed to estimate *tephra* volumes from the study of volcanic deposits [e.g., *Fierstein and Nathensen*, 1992; *Pyle*, 1989, 1995]. Volumes are calculated from a map of deposit thickness (*isopach map*) and some method of extrapolating out to the distal, commonly unmapped, portions of the deposit. This may involve mathematical extrapolation or calculations based on mineral/*glass* ratios, which are affected by transport mechanisms and distance from the vent [*Walker*, 1980]. It is usually observed that the deposit thickness decreases exponentially away from the vent and can be fitted to the following equation [*Pyle*, 1989]:

$$E = E_{max} \ \exp(-kA^{0.5}) \qquad (2)$$

where A is the area enclosed by the *isopach* contour of thickness E, E_{max} the maximum thickness of the deposit,

and k a decay constant. For deposits fitting the above empirical law, the volume V can be calculated from [*Pyle*, 1995]:

$$V = 13.08 \ E_{max}b_t^2 \qquad (3)$$

where b_t is the distance over which the thickness halves. It is apparent from equation (3) that volumes calculated this way for older eruptions are most probably minimum estimates since erosion will tend to decrease both E_{max} and b_t. A single tropical rainy season can remove most of the distal fines. The volume obtained from equation 3, corresponds to the deposit volume and should not be confused with the volume of *magma* erupted. The deposit includes *juvenile* fragments of *pumice* or *scoria* displaying a range in vesicularity and *density*, *ash* made of *glass* shards and minerals fragments, and accidental *lithic* fragments (which, being non-*juvenile*, should be excluded from estimates of equivalent *magma* volume). Because the degree of compaction may vary across the deposit, the bulk *density* may also vary. Measurements show that typical bulk *densities* of *Plinian* deposits vary between 300 and 1500 kg/m³, as compared to average magmatic *densities* before degassing of 2300–2700 kg/m³. For *pyroclastic-flow* deposits, compaction soon after emplacement while the deposit is still hot, may lead to partial or complete sintering and welding, which gives the rocks a massive or *lava*-like appearance *density*. Thus, to convert a volcanic deposit volume into an equivalent *magma* volume (*DRE* volume), a knowledge of the average deposit *density* is needed, which requires extensive field investigation. The uncertainty attached to the deposit *density* may thus significantly affect the estimate of erupted *magma* volume. Overall, the uncertainty on the estimated *magma* volumes of older eruptions can be as large as 100% (see below the case for the Huaynaputina eruption).

Volumes of erupted *magmas* are generally stated in units of cubic kilometers. Estimated volumes for single eruptive events range from 0 km³, in the case of purely *phreatic* eruptions (no *magma* erupted), to as high as 5000 km³ for the largest *ignimbrite* deposits, the latter being comparable to the volume of water stored in the Great Lakes of North America. For large eruptions, the mass of *magma* ejected is so large that the roof of the *reservoir* may collapse inward to form a large *caldera*, such as the 6-km-wide *caldera* left after the 1815 Tambora eruption in Indonesia. When the *caldera* morphology is well preserved, its volume gives a minimum estimate of the amount of *magma* involved in the eruption.

One important aspect for modelling purposes is the duration of an eruption. Despite the impressive volumes involved in large explosive events, eruption durations are commonly estimated as only several days to weeks. This is not the case for *basaltic* fissure eruptions, such as the 1783 Laki or 934 A.D. Eldgja events in Iceland, which lasted, respectively 8 months and perhaps 3–8 years [e.g., *Thordarson et al.* 1996; 2001]. Although both types of events can be considered as geologically instantaneous, their climatic impacts may differ, at least on short timescales.

In summary, the study of volcanic deposits allows an estimate of the erupted *magma* volume, but erosion of unconsolidated *pyroclastic* deposits means that estimated volumes for ancient events are almost certainly minima. Only eruptions of very high magnitude will survive the erosional filter. Any systematic study aimed at restoring volcanic sulfur yield in the remote past will face a strong bias toward large-scale events.

SULFUR BEHAVIOR IN MAGMAS

Solubility in Melts

As illustrated in Figures 4 and 5, silicate *melts* can dissolve several wt % of water at crustal pressures. In contrast, the concentration of sulfur (expressed as S) in natural silicate *melts* under conditions relevant to *magma* genesis and eruption is largely below 1 wt% (Figure 7). Various experimental studies [see *Carroll and Webster*, 1994] have shown that the concentration of sulfur depends on silicate *melt* composition, temperature, pressure, *redox state* (reflected in the *oxygen fugacity*, fO_2), and sulfur *fugacity* (fS_2).

Sulfur dissolves as two different species at least, whose relative abundances are determined by the prevailing fO_2 [e.g., *Carroll and Rutherford*, 1988; *Wallace and Carmichael*, 1994]. Under *reduced* conditions sulfur has a charge of –2 and dissolves as *sulfide*. Under *oxidized* conditions, sulfur has a charge of +6 and occurs in the *melt* in *sulfate* groups. Below *NNO*–1, almost all sulfur occurs as *sulfide*, whereas above *NNO*+2, almost all sulfur dissolves as *sulfate*. From *NNO*–1 to *NNO*+2, the abundance of *sulfide* gradually decreases as *sulfate* increases. Under *reduced* conditions, there is a close correlation between the *saturation* limit for *sulfide* and the abundance of FeO in both experimental and natural silicate *melts* [e.g., *Haughton et al.*, 1974; *Wallace and Carmichael*, 1992], which suggests that Fe^{2+} is preferentially complexed with S^{2-}. As a result, all other factors being equal, silicate *melts* with higher FeO contents can have higher sulfur concentrations than those with low FeO content. Under oxidizing conditions, the situation is less clear, but available evi-
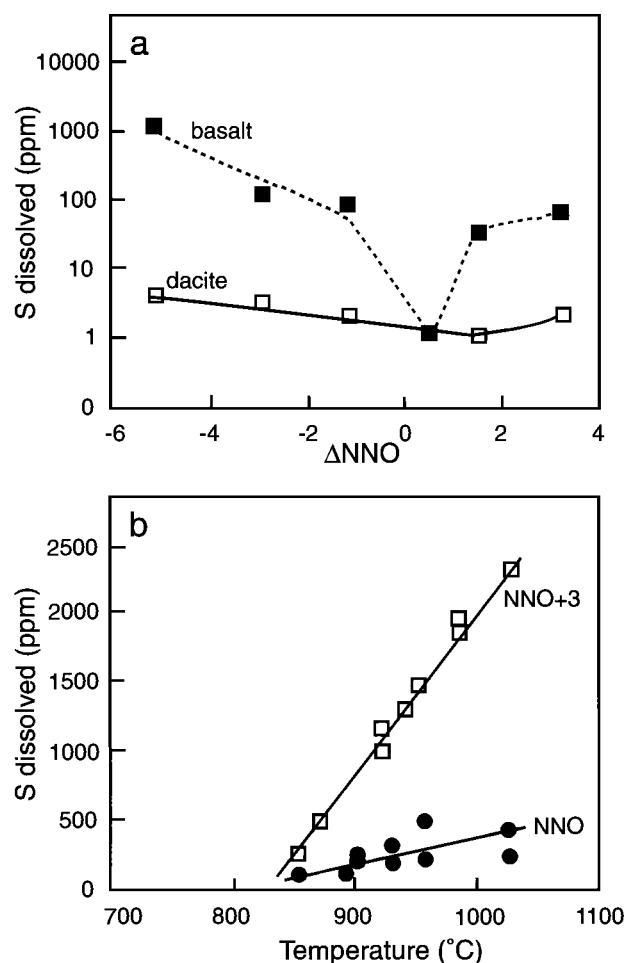
Figure 7. *Solubility* of sulfur in silicate *melts* as functions of: (a) fO_2 (expressed as DNNO) [*Nagashima and Katsura*, 1974; *Katsura and Nagashima*, 1974] and (b) temperature [*Carroll and Rutherford*, 1987]. Data from Nagashima and Katsura are for one-bar experiments on dry *basaltic* and *dacitic melts* under fixed fSO_2 and T = 1250°C. Data from *Carroll and Rutherford* [1987] are for *anhydrite-saturated dacitic* to *rhyolitic melt* compositions at 2000 bars, and H_2O *saturation* (6–7 wt% dissolved H_2O) at two fO_2 values that broadly bracket the fO_2 of *subduction*-related *magmas*. Note that the temperature dependence of sulfur *solubility* increases with fO_2, but that in any case, *solubility* below 800°C is at most 100 *ppm*.

dence suggest that sulfur complexes preferentially with Ca or alkalies. An important aspect of sulfur behavior in silicate *melts* is the dependence of its *solubility* on fO_2. Whatever the silicate *melt* composition and P-T conditions of equilibration, numerous experimental studies have demonstrated that there exists a minimum in sulfur *solubility* in the range *NNO* to *NNO*+1, with higher solubilities

observed at both more *reducing* and more *oxidizing* conditions (Figure 7a). Although the importance of this behavior in natural *magmas* is still debated, the existence of this *solubility* minimum has been called upon by *Kress* [1997] as the driving mechanism leading to the sulfur excess observed during the 1991 Pinatubo eruption. According to thermodynamical calculations performed by this author, mixing between a *reduced basaltic magma* and an *oxidized silicic* one could give rise to a hybrid *intermediate magma* (*andesite*) having an fO_2 lying near the minimum in S *solubility*. In this scenario, the sulfur dissolved in the *melt phase* of two *magmas* before their interaction is transferred to the gas *phase* upon mixing, thereby producing a sulfur-enriched gas *phase*.

The effects of temperature on *magma* sulfur content are not well understood but available data suggest that higher temperatures are typically associated with higher *melt* sulfur contents: silicate *melts* equilibrated at temperatures below 800°C have sulfur concentrations barely exceeding 100 *ppm*, whereas *oxidized melts* above 1000°C can reach sulfur concentrations of 2000 *ppm* (Figure 7b). The sulfur *fugacity* may play a critical role: an increase in fS_2 increases the silicate *melt* sulfur content, all other factors being constant. However, the magnitude of fS_2 control on sulfur concentration is only well established at low-pressure [e.g., *Haughton et al.*, 1974], near-anhydrous conditions. Its role at high pressure is still under investigation.

Pressure exerts a significant, but variable, control on sulfur *solubility*. In dry silicate *melts* saturated with an *immiscible sulfide melt*, recent data have shown that *solubility* decreases as pressure increases [*Mavrogenes and O'Neill*, 1999]. In contrast, in H_2O-bearing silicate *melts*, the opposite behaviour is observed [*Carroll and Rutherford*, 1987; *Luhr*, 1990]. The extensive degassing of *basaltic melts* upon eruption can be explained by considering that the driving force for degassing is the difference of *volatile* chemical potential (or *fugacity*) between the silicate *melt* and the gas *phase* (bubble or atmosphere). Silicate *melts* reaching the open surface, enter a medium (the atmosphere) with an extremely low fS_2, and in response S will be exsolved from the *magma* in an attempt to equilibrate with the new surroundings; this proceeds until *magma* has cooled sufficiently to kinetically inhibit further degassing (i.e., it is 'frozen'). The higher temperature of *basalts* allows them to degas sulfur much more efficiently than do *rhyolites* ; in other words, on the time-scale of eruption, S diffusion in *rhyolitic melts* is too slow to result in significant transfer of S from *melt* to gas (see *Watson* [1994] and *Baker and Rutherford* [1996] for additional details on sulfur diffusion in silicate *melts*).

Sulfur in Solids or Immiscible Liquids

Relative to other *volatile* species occurring in *magmas*, the behavior of sulfur is complicated by the fact that it not only exists in the silicate *melt* and gas *phases*, but it may also comprise a significant component of some minerals (*pyrrhotite, anhydrite*) and under some circumstances an *immiscible sulfide melt phase*. Under *reduced* conditions, and depending on temperature, *sulfide* ions can partition either into the mineral *pyrrhotite* ($Fe_{1-x}S$: ~39 wt% S) or into a liquid that is immiscible with the silicate *melt* (with Fe, S, and O in varying proportions depending on fO_2, fS_2 and T; this liquid quenches to a solid referred to as intermediate *sulfide* solid solution [*Craig and Scott*, 1976]). Under *oxidized* conditions, *pyrrhotite* can be joined by the mineral *anhydrite* ($CaSO_4$: ~24 wt% S). In addition, the common phosphate mineral apatite can lock up to 1 wt.% S [*Peng et al.*, 1997]. Because sulfur enters *pyrrhotite, immiscible sulfide melts,* and *anhydrite* at the level of several tens of wt%, compared to its *solubility* in silicate *melts* of only a few 1000 *ppm* at most, their presence and propensity to sink gravitationally because all three *phases* are relatively dense, can significantly reduce the amount of sulfur left to partition among the silicate *melt* and a gas *phase*.

Sulfur in Gas

In addition to the *partitioning* of sulfur among minerals, silicate *melt*, and possible *immiscible sulfide melt* discussed above, if the *magma* is gas saturated sulfur also partitions into the gas *phase*. Here again, experimental constraints are few but they indicate that under certain conditions, sulfur may be strongly partitioned into the gas *phase* relative to the silicate *melt* [*Scaillet et al.*, 1998b; *Keppler*, 1999]. In low-temperature (<900°C) *intermediate magmas* such as the 1991 Pinatubo *dacite*, the *partitioning* depends strongly on *redox conditions* (Figure 8a). Under low fO_2 conditions, almost all the sulfur is locked up in the stable sulfur-bearing solid *phase*, either *pyrrhotite* or *immiscible sulfide-rich liquid*, and sulfur contents of both the gas *phase* and coexisting silicate *melt* are low. In contrast, under high fO_2, where *anhydrite* crystallizes, a substantial amount of sulfur partitions into the gas *phase* because thermodynamic *equilibrium* requires significant *fugacities* of S-bearing species (mainly SO_2, H_2S) under these conditions.

At around 800°C, a typical temperature for many *silicic magmas*, and for fO_2 higher than *NNO*+0.5, sulfur concentration in the gas is *ca.* 1000 times that of the coexisting *rhyolitic melt*. For instance, the 1991 Pinatubo *dacite* had a residual *rhyolitic melt* with 70 *ppm* dissolved sulfur before
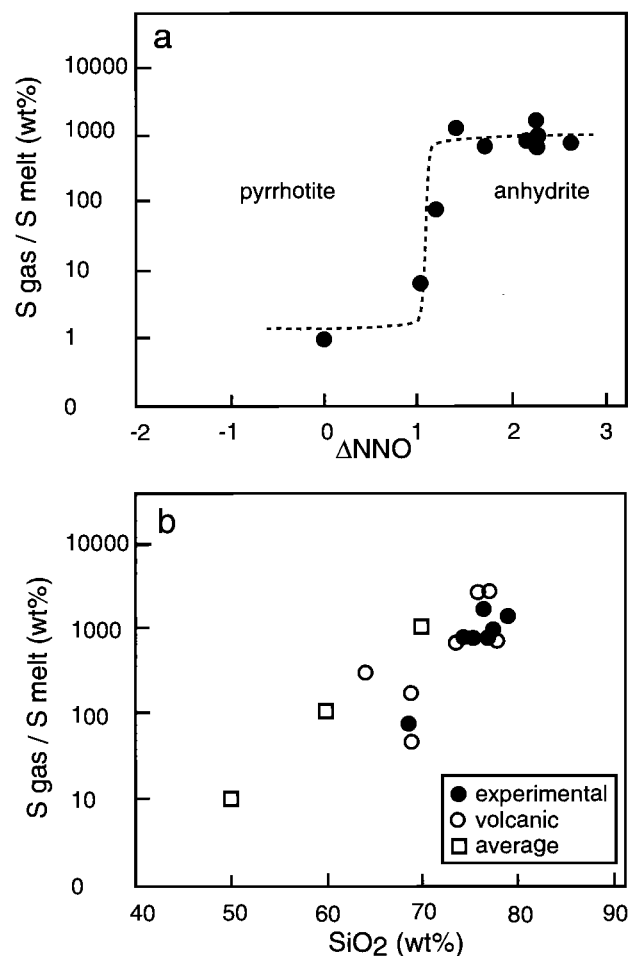
Figure 8. *Partition coefficient* of sulfur between gas and silicate *melt* as functions of: (a) fO_2 and (b) *melt* SiO_2 content [*Scaillet et al.*, 1998b]. In the lower panel, in addition to experimental data (symbols termed experimental) obtained on the Pinatubo *dacite*, the *partition coefficients* obtained using *COSPEC* and *TOMS* data available for several explosive *subduction-zone* eruptions (symbols termed volcanic, which include Pinatubo, St Helens, Redoubt, El Chichón and Nevado del Ruiz eruptions, see *Scaillet et al.* [1998b]) are shown together with the average values used in this paper (symbols termed average) when the gas *phase* composition cannot be calculated using thermodynamic constraints. See text for additional details.

the onset of eruption [*Westrich and Gerlach*, 1992]. According to the experimental studies of *Scaillet et al.* [1998b] and *Keppler* [1999], a coexisting gas *phase* in the *magma reservoir* would have contained about 7 wt% sulfur (70,000 *ppm*). Available data suggest that the preferential enrichment of sulfur in the gas *phase* decreases as the *melt* becomes less *silicic*, probably down to around 100 times that in the *melt* for *dacitic* liquids (Figure 8b). The *parti-*

tioning behavior of sulfur between high-temperature *basaltic melt* and a coexisting gas *phase* still awaits experimental investigation, but thermodynamic calculations suggest S_{melt}/S_{gas} values in the range 10–20 [*Scaillet and Pichavant*, 2003]. For *melt* compositions other than *rhyolites*, the fO_2 control on *melt*-vapor *partitioning* of sulfur is still unknown.

Sulfur Behavior in Eruption Clouds

During an eruption not all the *melt*- or vapor-hosted sulfur in the *magma reservoir* necessarily reaches the stratosphere, which is the condition for global dispersion and detection by remote sensing or in ice cores. Several studies have shown that *volatile* scavenging by adsorption on *ash* particles in the eruption cloud can remove a significant fraction of the emitted *volatiles* [e.g., *Taylor and Stoiber*, 1973; *Rose*, 1977; *Rose et al.*, 1982; *Varekamp et al.*, 1984]. This is particularly true for sulfur, which because of its oxidation during transport, ends up becoming highly soluble in water, the main binding agent of particle aggregation. Observational evidence demonstrating the importance of such a process is particularly clear in the recent eruptions of *mafic* to *intermediate magmas* at Fuego, Mount St. Helens, El Chichón, and Nevado del Ruiz [*Rose et al.*, 1982; *Smith et al.*, 1983; *Varekamp et al.*, 1984; *Sigurdsson et al.*, 1990; *Gerlach and McGee*, 1994]. In these cases, *ash-leachate studies* have shown that *ash* deposited on land adsorbed from 7 to 62% of the sulfur injected into the atmosphere (Table 3). Although the figures retrieved for *silicic* eruptions are similar, there are no reasons to believe that they represent threshold or average values of general use. Aerosol adsorption is closely related to particle-aggregation mechanisms in volcanic plumes [see *Sparks et al.*, 1997]. Laboratory experiments have shown that particle aggregation to form *accretionary lapilli*, and thus aerosol adsorption, are largely controlled by the humidity prevailing in the eruptive column [*Gilbert and Lane*, 1994], which itself depends on the atmospheric conditions at the time of the eruption (excluding *phreatomagmatic* eruptions where abundant water may produce more *accretionary lapilli*). An eruption in a dry atmosphere may not give rise to particle aggregation, whereas under humid conditions accretion and accelerated fallout of particles will take place. In some cases the volcanic plume can be affected by rainfall, which may wash out a significant proportion of solid or gaseous components. Once deposited or during transport, the *ash* particles lose their water by evaporation leading to precipitation of *sulfate* condensates. It is important to understand that *ash-leachate* studies need to be performed immediately after *ash* deposition, and prior to rainfall (which will

wash away adsorbed *sulfate*). Such data cannot therefore be obtained on older deposits, or even on recent ones after rainfall. Unfortunately, no reliable leachate data are available for the 1991 Pinatubo eruption, owing to a typhoon that passed over Luzon at the time of the eruption. On the basis of the above evidence, it is clear that *TOMS*, optical-depth, and ice-core estimates may under-evaluate by up to 60 % or more the actual amount of sulfur released during volcanic eruptions.

Another important factor that may affect volcanic sulfur emission to the atmosphere involves changes in eruptive style as an eruption proceeds, such as a shift from a sustained *Plinian* column to dominance by *pyroclastic flows*, which may or may not generate *co-ignimbrite plumes*. A *co-ignimbrite plume* may carry non-*juvenile volatiles* in significant proportions, but a quantitative evaluation of this process remains to be done. In particular, *pyroclastic flows* entering the open sea may lead to significantly different *volatile* yields compared to those flowing on land (see *Sansone et al.* [2002] for a related topic). The above factors, *ash* adsorption and change in eruption style, are two reasons for observing a mismatch between sulfur yields derived from the petrologic approach and those from optical depth, ice core or remote-sensing methods (see also the case for Cl, *Tabazadeh and Turco*, [1993]). However, both of these factors would cause the S yield from the *petrologic method* to exceed the observed value, opposite the pattern found for many *subduction-zone* eruptions.

AN IMPROVED PETROLOGIC METHOD FOR ESTIMATION OF SULFUR EMISSIONS

A major goal of this paper is to build on the *petrologic method* for the estimation of *volatile* releases from major eruptions devised by *Devine et al.* [1984], by adding what

Table 3. Mass of sulfur adsorbed on *ash* relative to the amount of sulfur released to the atmosphere measured by *TOMS* or *COSPEC* (10^{12}g)

eruption	Fuego 1974[a]	St Helens 1980[b]	El Chichón 1982[c]	Ruiz 1985[d]
S yield[e]	1.5	0.74	3.5	0.33
S on *ash*	0.1	0.24	5.8	0.14
S total	1.6	0.98	9.3	0.47
% S on *ash*	7	25	62	30

[a] from *Rose et al.* [1982]
[b] from *Gerlach and McGee* [1994]
[c] from *Varekamp et al.* [1984] and *Luhr and Logan* [2002]
[d] from *Sigurdsson et al.* [1990]
[e] sulfur measured by *TOMS* and *COSPEC* [*Rose et al.*, 1982; *Gerlach and McGee*, 1994; *Krueger*, 1983; *Krueger et al.*, 1990]

we believe to be a missing component for many explosive eruptions of *intermediate* to *silicic magma*: a separate gas *phase* [e.g., *Luhr et al.*, 1984; *Gerlach et al.*, 1996]. In this view, many *magmas* prior to eruption, consist of *melt* + crystals + bubbles in variable proportions, even at depths of 4–8 km in the crust. The main contribution of this paper, following *Scaillet and Pichavant* [2003], is to present a method for quantifying the sulfur contribution from the gas *phase* to estimates of total sulfur yield from single volcanic eruptions.

A thermodynamic approach can be applied to estimate the sulfur content of the magmatic gas *phase* [*Scaillet and Pichavant*, 2003]. In this approach, chemical *equilibrium* between minerals, *melt*, and gas in the *magma reservoir* is assumed, at least just prior to the onset of eruption. The basic tenet of this approach is that the *fugacities* of *volatile* species dissolved in the *melt* are equal to those in the gas, as thermodynamic *equilibrium* demands. Calculation of the gas *phase* composition is done at the pre-eruptive P and T conditions of the *magma reservoir*. These can be assessed using a variety of methods, but the most reliable approach involves *phase-equilibrium experiments* conducted in a pressurized furnace using representative erupted products, usually *pumice clasts* from *pyroclastic* deposits. The Mt. Pelée (1902), Mount St. Helens (1980), El Chichón (1982), and Mount Pinatubo (1991) pre-eruptive P-T conditions have been estimated in this manner [*Rutherford et al.*, 1985; *Carroll and Rutherford*, 1987; *Luhr*, 1990; *Rutherford and Devine*, 1996; *Martel et al.*, 1998; *Scaillet and Evans*, 1999]. Calculation of the gas-*phase* composition is done in the C-O-H-S system, neglecting the role of F and Cl, which still lack critical thermodynamic data regarding their activity-composition relationships in silicate *melts*. In most cases, however, the C-O-H-S system allows us to consider more than 95% of the gas species and their relative abundances.

To constrain the C-O-H-S system, three *intensive* parameters need to be fixed in addition to P and T. These are usually the *fugacities* of water, oxygen, and sulfur: fH_2O, fO_2, and fS_2. In some cases, carbon dioxide *fugacity* (fCO_2) can be used in lieu of one of the above. The fH_2O is calculated using appropriate thermodynamical models of water *solubility* in silicate *melts* [*Dixon et al.*, 1995; *Moore et al.*, 1998; *Zhang*, 1999; *Newman and Lowenstern*, 2002], which relate water concentration in the *melt* to water *fugacity* (that is the activity-composition relationship is known). The *melt* water content is estimated by laboratory *phase-equilibrium experiments* that constrain the stability of minerals growing in the *magma* relative to the *melt* water content, or by *infra-red spectroscopic* or ion microprobe analysis of *glass inclusions* [*Ihinger et al.*, 1994] The fO_2 is best constrained using

mineral-mineral equilibria such as Fe-Ti oxides (magnetite and ilmenite), whose compositions are sensitive to both fO_2 and T. The common occurrence of both oxide minerals in many *intermediate* to *silicic magmas* has led to widespread use of this approach. For fS_2, the composition of the solid-solution mineral *pyrrhotite*, which is sensitive to fS_2 [*Toulmin and Barton*, 1964], is commonly used when this *phase* is stable [*Whitney*, 1984]. Empirical models relating fS_2 to *melt* sulfur content also exist, but only for dry *basaltic* and moderately *reduced melts* [*Wallace and Carmichael*, 1992] or for hydrous *rhyolitic* ones [see *Scaillet and Pichavant*, 2003]. Much remains to be done regarding the thermodynamic behavior of sulfur in silicate *melts*, and fS_2 remains one of the most weakly constrained intensive parameters in magmatic systems. For the time being the thermodynamic approach explained above is the only one that allows us to calculate the gas-*phase* composition coexisting with hydrous, *oxidized basaltic melts*.

We make the following key assumptions in application of the *improved petrologic method*, following *Scaillet and Pichavant* [2003]. For all *subduction-related* non-*basaltic* eruptions we have assumed that the *magma* had 5 wt% gas at depth, in keeping with the available evidence summarised below. Similarly, for *subduction-related basaltic* eruptions, we have assumed that the *magma* had 1 wt% gas at depth. When the necessary information required to perform the thermodynamic calculation is lacking, we use gas/*melt partition coefficients* for sulfur of 1000 for *rhyolite*, 100 for *dacite-andesite*, and 10 for *basaltic melt* compositions, in keeping with available data suggesting that sulfur partitions less strongly into the gas as the *silica* content of the *melt* decreases (Figure 8b, *Scaillet et al.* [1998b]; *Scaillet and Pichavant*, [2003]).

Errors in Petrologic Sulfur Yield Estimates

There are various sources of error embodied in the petrological approach when used to test the volcano-climate link. The first obviously concerns volume estimates, which are strongly hampered by erosion of volcanic deposits. This problem is roughly a function of latitude, with highest erosion rates in the tropics [*Walker*, 1981]. For example, volume estimates (*DRE*) for the relatively recent (1600 AD) eruption of Huaynaputina, Peru (16.61°S) vary by a factor of 2, between slightly less than 5 km³ [*Thouret et al.*, 2002] to over 10 km³ [*De Silva and Zielinski*, 1998]. The reasons of disagreement are multiple, but lie in the study and interpretation of the deposits. The uncertainty attached to volume estimates is likely to vary between different eruptive events depending on age, the conditions of deposit preser-

vation (latitude) and quality of field work. The Huaynaputina eruption illustrates, however, that volumes of erupted *magma*, even for recent events lacking remote sensing control, can be subject to 50 % error. The problem can be further exascerbated when large fractions of *tephra fall* at sea.

Another major source of error is the estimate of *magma* sulfur content, whether dissolved in the silicate *melt* or in a separate gas *phase*. Use of the electron microprobe has allowed important advances in this regard, yet this tool has a detection limit of 50 *ppm*. For large eruptions with low *melt* sulfur contents, this can translate into significant errors on sulfur yield due to *melt* degassing. The 181 AD Taupo eruption, which produced more than 35 km^3 (*DRE*) of *magma* [*Walker*, 1980], illustrates well this point. Analyses of *glass inclusions* and *matrix glass* from the *Plinian* phase gave sulfur contents of 46 and 38 *ppm*, respectively [*Palais and Sigurdsson*, 1989], the difference being statistically insignificant given that both values fall below the detection limit of 50 *ppm*. Depending on whether full (50 *ppm* sulfur lost) or no degassing (0 *ppm* sulfur lost) is assumed, the sulfur yield for this particular eruption may range between 3.3 10^{12} g (i.e. similar to El Chichón sulfur release) and zero. Use of alternative and more precise analytical tools such as the ion microprobe [*Hauri et al.*, 2002] are thus needed to improve the quantitative evaluation of *melt* degassing in eruptions involving sulfur-poor *melts*.

The amount of sulfur in the gas and the amount of gas are next in the list of major sources of error. Although the amount of gas at depth is difficult to quantify, geochemical modelling, remote-sensing data on volcanic gases, experimental constraints, and theoretical considerations all suggest that the amount of gas present in the upper reaches of *silicic magma reservoirs* feeding eruptions lies in the range 0 to 6 wt% [see *Wallace*, 2001]. We accept that this range is not presently well constrained. *Mafic* systems are more poorly constrained, but simple simulations of degassing during ascent suggest that the gas fraction present at any given time in *mafic magmas* is no higher than 1 wt% [*Scaillet and Pichavant*, 2003], because the low *viscosity* of *mafic melts* allows efficient segregation of bubbles from *magma* [e.g., *Vergniolle and Jaupart*, 1986]. In contrast, in more viscous *silica*-rich *melts*, bubble segregation is kinetically inhibited (slow bubble rise velocities) and the *magma* retains gas bubbles. This accumulation proceeds until the percolation threshold is attained and gas advection through an interconnected bubble network starts [*Candela*, 1991; *Wallace*, 2001]. Thus, whatever the ultimate mechanism of gas *saturation* in the storage region, a maximum of 5–6 wt% of gas in *magma reservoirs* (or *ca.* 20–30% in volume at the

pressure of *magma* storage) seems reasonable. In addition, because gas *saturation* and accumulation in the apical portion of a *magma reservoir* is one likely mechanism of eruption triggering [*Blake*, 1984; *Tait et al.*, 1989], values falling at the upper end of the 0–6 wt% range are probably representative of the amount of gas in most *silicic* to *intermediate arc magmas* prior to eruption.

The error associated with the estimate of gas sulfur content is more complex to evaluate, especially when the gas *phase* composition is calculated using a thermodynamic approach, which requires various input parameters. Table 4 lists the pre-eruption conditions estimated for the 1600 AD eruption of Huaynaputina, using a combination of experimental and analytical data [*Costa et al.*, 2003], which were used to calculate the *equilibrium* gas composition in the *magma reservoir*. Also given is the effect produced by varying each input parameter while holding the others constant, to help appreciate their individual influences on sulfur content of the gas *phase*. The variations imposed by each input parameter correspond to the uncertainty expected in the most thoroughly documented and constrained eruptive events, such as Mt. Pelée (1902), Mount St. Helens (1980), El Chichón (1982), or Mount Pinatubo (1991) (T, ± 20°C; P, ± 500 bars; fO$_2$, ± 0.2 log unit; H$_2$O dissolved in the *melt*, ± 0.5 wt%; and fS$_2$, ± 0.2 log units). Variations within the quoted ranges induce either an increase or a decrease, generally within a factor of 2, in the sulfur content of the gas relative to that obtained with the average input value. Thus,

Table 4. Variation on the calculated gas sulfur content of the Huaynaputina 1600 AD eruption arising from variations of pre-eruption P, T, fO$_2$, S$_{melt}$ and H$_2$O$_{melt}$.

parameter	variation	new S content of gas (wt%)	average S content of gas (wt%)
T (°C)	+20	5.7	4.2
log fO$_2$	+0.2	3.4	4.2
H$_2$O$_{melt}$ (wt%)	−0.5	4.4	4.2
S$_{melt}$ (ppm)	+ 50	5.9	4.2
P (bar)	+500	3.0	4.2

The average pre-eruption conditions of Huaynaputina are [*Costa et al.*, 2003]: T = 850°C; fO$_2$ = *NNO*+1.2; H$_2$O in *melt* = 6.1 wt%; S content of *melt* = 264 *ppm*; P = 2400 bars. In each line, the new S$_{gas}$ gives the sulfur content of the gas obtained when changing the corresponding parameter (i.e., 870°C instead of 850°C). Variations are positive (except for water), but could be negative as well, in which case the error on S content would be broadly similar although not strictly identical in magnitude.

for well known eruptions, the sulfur content of the gas can be constrained via thermodynamic calculations to within about a factor of 2.

In summary, large uncertainties may surround the estimation of sulfur yield using petrological constraints, even following the *improved petrologic method* discussed in this paper. This is especially true when detailed petrological knowledge of the eruption is lacking. The input parameters needed to perform the calculation, i.e. volume of erupted *magma*, percent of gas in pre-eruptive *magma*, sulfur content of gas and *melt*, all scale linearly with sulfur yield estimates: an uncertainty of a factor of 2 in the sulfur content for any of these parameters translates into a two-fold variation of sulfur yield. In the best known events, minimum uncertainties on sulfur yields are on the order of a factor of 2.

Applications

The *improved petrologic method* has been applied to 46 different eruptions from Earth's major tectonic settings (Table 5). Most eruptions (38) are from the past 2,000 years, but we also include some older examples of large-magnitude eruptions, e.g., Campanian Ignimbrite, Toba Tuff, Bishop Tuff, and Fish Canyon Tuff. In Table 5, basic data for these eruptions are listed along with the sulfur contents of *matrix glasses* and *glass inclusions*, and the estimated sulfur content of the pre-eruptive gas *phase*.

As in many previous studies aimed at constraining volcanic sulfur yields [e.g., *Stoiber et al.*, 1987; *Bluth et al.*, 1993; *Schneztler et al.*, 1997], the eruptions are divided in two main categories: *subduction*-related and others (mostly *spreading ridge* and *hot spot*: note that Etna has been included in the latter category, although its exact geodynamic setting is debated). Given the limited data set a more complex discrimination is not warranted. Also listed are sulfur yields obtained from a number of persistently active volcanoes such as Stromboli, Pacaya, and Fuego [*Stoiber et al.*, 1987; *Andres et al.*, 1991; 1993; *Allard et al.*, 1991, 1994]. These, although not giving rise to major explosive eruptions, have well constrained erupted volumes and sulfur budgets, the latter from remote-sensing measurements performed over several decades, which give time-averaged sulfur emissions that are useful to compare to those associated with single explosive events.

For non-*subduction*-related eruptions no attempt was made to estimate their pre-eruptive gas composition (excepting Etna) because we lack sufficient data on pre-eruptive conditions. We note however that for *magmas* rich in CO_2 (*spreading-ridge* and *hot-spot* settings), gas *saturation* may be a contributing factor to sulfur release. For *sub*-

duction-related eruptions, the gas composition for many examples has been calculated by *Scaillet and Pichavant* [2003] and only the sulfur content is repeated here. For other eruptions (in bold in Table 5), the sulfur content of the gas *phase* has been calculated using the estimated gas/*melt* partition coefficients discussed above (with the exception of Tambora, whose alkali-rich phonolitic composition makes it difficult to estimate the coexisting gas composition : *Scaillet et al.* [1998b]).

The restored gas-*phase* sulfur contents for *subduction*-related *magmas* range from 0.12 up to 8.7 wt%, with an average of 3.6 ± 2.3 wt% (1s) for 31 eruptions. In *silicic* to *intermediate magmas*, the sulfur in the gas represents more than 90 wt% of the *melt*+gas sulfur budget (Figure 9). This shows that if *intermediate* to *silicic subduction*-related *magmas* contain 5 wt% gas in the *magma reservoir*, gas release is the dominant source of sulfur input to the atmosphere (ignoring the still poorly constrained possibility of breakdown of *sulfide* or *sulfate phases* during eruption). In contrast, if *basaltic subduction*-related *magmas* contain ~1% gas in their reservoir, the *melt* and gas contribution are approximately equal, although the *melt* contribution may dominate in some cases (e.g., Fuego, Pacaya, Tarawera). Unlike previous studies [*Devine et al.,* 1984; *Palais and Sigurdsson,* 1989], we observe no clear correlation between *bulk-rock composition* and gas+*melt* sulfur content (Figure 10). Only in non-*subduction magmas* does there appear to be a general decrease in sulfur content as SiO_2 increases. Such a trend, however, is not apparent for *subduction*-related *magmas*, let alone the extraordinary high apparent bulk sulfur concentrations obtained for the small-volume eruptions of Lascar, Lonquimay, and Stromboli volcanoes, the latter reaching an apparent S concentration of 37 wt% of erupted *magma* (not shown on Figure 10 to preserve the scale, but see Table 5). Excluding these three 'anomalous' small-volume eruptions, for which degassing of unerupted *magma* is suspected, maximum bulk sulfur contents for *subduction* related *magmas* are close to 0.5 wt %, being reached in *intermediate* rather than in *rhyolitic magmas*.

There is, in contrast, a general broad positive correlation between the volume of erupted *magma* and the sulfur yield (*melt*+gas). *Subduction-zone magmas* have on average higher sulfur yields than non-*subduction* ones (Figure 11), but we stress that for the latter, our sulfur estimates should be considered as minima because of the possible involvement of a gas *phase*. As the volume of *magma* erupted increases, the erupted volume-sulfur yield correlation tends to improve, but at low erupted volumes a large dispersion in sulfur output is observed. For instance, eruptions discharging ~1 km^3 of *magma* have sulfur yields that spread over ~2

Table 5. Petrologic estimates of sulfur yield for some historical and pre-historical eruptions, compared to ice core, optical depth, COSPEC and/or TOMS estimates

Eruption	age	volume (DRE) (km³)	rock name	SiO₂ bulk (wt%)	SiO₂ in matrix glass (wt%)	S in matrix glass (ppm)	S in glass inclusions (ppm)	S in gas (ppm)	mass magma (10^{12} g)	mass S gas (10^{12} g)	mass S melt (10^{12} g)	mass S m+g (10^{12} g)	IC/OD TOMS COSPEC (10^{12} g)	S content (wt%)
Non-subduction zone magmas														
Baitoushan	969 AD	24	rhyolite	72	72–76	600	1000	–	55200	–	1	1	13.1	1.8×10^{-3}
Bishop Tuff	700000	700	rhyolite	72–77	77	<100	<100	17000	1610000	1369	0.01	1369	–	8.5×10^{-2}
Eldgja	934 AD	19.6	basalt	47–50	46	100–1110	2150	–	52920	–	110	110	170	0.21
Etna*	1975	1.5×10^{-5}	basalt	45	49–53	170	300–3380	**33800**	0.04	6.8×10^{-5}	1.2×10^{-4}	1.9×10^{-4}	75×10^{-3}	15.79
Fish Canyon T.	28.9 Ma	5000	trachyte	66	77	<100	100	18300	12500000	11438	250	11688	–	9.3×10^{-2}
Heimaey	1973	0.13	basalt	46	48	337	734–773	–	351	–	0.15	0.15	–	4.4×10^{-2}
Hekla-1	1104 AD	0.5	dacite	64(?)	74	10	71	–	1250	–	0.07	0.07	10.1	5.6×10^{-3}
Hekla-2	2800 BP	2.2	dacite	64(?)	73	50	80	–	5500	–	0.16	0.16	–	2.9×10^{-3}
Katla	1357	0.15	basalt	47(?)	48	776	1358	–	405	–	0.24	0.24	–	5.8×10^{-2}
Krafla	1981	2×10^{-2}	basalt	50(?)	50	126	693–738	–	54	–	0.03	0.03	–	6.1×10^{-2}
Laacher See	12900 BP	6.3	phonolite	59	56–60	150–820	150–1490	–	15750	–	1.9	1.9	–	1.2×10^{-2}
Laki	1783	12.6	basalt	49	49	195–490	1675	–	34020	–	61	61	100	0.18
Oraefajokull	1362 AD	2	rhyolite	72 (?)	73	50	77	–	4600	–	0.12	0.12	–	2.6×10^{-3}
Mauna Loa*	1984	0.216	basalt	50	50	700	1300	–	583.2	–	0.58	0.58	0.12	9.9×10^{-2}
Surtsey	1963	1	basalt	46	47	577	961–1003	–	2700	–	1.15	1.15	–	4.3×10^{-2}
Subduction-zone magmas														
Agung	1963	0.95	bas-and	54–58	60–65	70	650	**6500**	2375	0.77	1.25	2.02	3.5	8.5×10^{-2}
Bezymianny	1956	1	andesite	59	66	47	514	**51400**	2500	6.43	1.20	7.63	3.6	0.30
Campanian	37000 BP	150	trachyte	58–63	62	380	313–565	56500	375000	1059	117	1176	–	0.31
Coseguina	1835 AD	10	andesite	58(?)	62	357	355	35500	25000	44	1.25	46	23	0.18
El Chichon	1982	1	trach-and	59	69	200	150	18300	2500	2.29	0.02	2.31	3.5	9.2×10^{-2}
Fuego	1974	8.2×10^{-2}	basalt	51	51	1300	1700–5200	**52000**	220.05	0.11	0.88	0.99	1.6	0.45
Huaynaputina	1600 AD	5	dacite	65	73	80	264	42000	12500	26	3	29	50	0.23
Katmai	1912	8	rhyolite	77	77	19–68	65–170	14500	18400	13	1	14	10	7.8×10^{-2}
Krakatau	1885	12.5	rhyodacite	69	72		200	52100	31250	81	3	84	18	0.27
Lascar	1989	1.5×10^{-3}	andesite	59–67	55–76	300	<150–4400	**44000**	3.7	0.008	1×10^{-3}	0.009	0.27	6.80
Lonquimay	1989	4.4×10^{-5}	andesite	60(?)	65(?)	?	?	–	0.11	–	–	–	3.5×10^{-3}	3.08
Minoan	3650	32	rhyodacite	71	72	53	74	14500	80000	58	5.5	63.5	65.3	7.9×10^{-2}
Montserrat	1995	0.4	andesite	60	76	<100	<100	46700	1000	2.335	2.5×10^{-3}	2.3375	–	0.23
Mt Pelée	1902	0.1	andesite	60	75	150	150	26800	250	0.335	0	0.335	–	0.13
Mt St Helens	1980	0.25	dacite	63	73	68	25	21700	625	0.68	0.04	0.72	1	0.11
Mt St Helens	1800 AD	0.25	dacite	63	70	46	48	**48000**	625	1.50	0.00	1.50	–	0.24
Mt St Helens	1480 AD	1	dacite	67	75	38	71	**71000**	2500	8.88	0.08	8.96	6.53	0.36
Pacaya	1972	9.6×10^{-6}	basalt	50	51(?)	1300	1700–5200	**52000**	0.026	1.3×10^{-5}	1×10^{-4}	1.2×10^{-4}	1.3×10^{-4}	0.50
Pinatubo	1991	5	dacite	65	77	60	80	13800	12500	8.63	0.11	8.74	10	6.9×10^{-2}
Rabaul	1400 BP	4.1	dacite	65	68	279	314–615	61500	9430	29.00	0.48	29.48	45	0.47
Redoubt	1989–1990	0.105	andesite	58–63	69–78	60–360	60–870	87000	262.5	1.14	1.15	1.16	0.5	0.44

Table 5.(continued)

Eruption	age	volume (DRE) (km³)	rock name	SiO₂ bulk (wt%)	SiO₂ in matrix glass (wt%)	S in matrix glass (ppm)	S in glass inclusions (ppm)	S in gas (ppm)	mass magma (10^12 g)	mass S gas (10^12 g)	mass S melt (10^12 g)	mass S m+g (10^12 g)	IC/OD TOMS COSPEC (10^12 g)	S content (wt%)
Roseau Tuff	28000	30	rhyolite	75(?)	77	47	47	**47000**	75000	176	4	180	–	0.24
Ruiz	1985	2.8x10⁻²	andesite	59–64	65–75	39–386	91–589	**58900**	70	0.21	0.05	0.26	0.47	0.36
Santa Maria	1902	8.5	dacite	65	74	108	198	63500	22950	73	2	75	22	0.32
Soufrière	1979	0.05	bas-and	55	68	28	148–610	**61000**	125	0.38	0.08	0.46	–	0.37
Stromboli	1980-1993	7.1x10⁻⁵	basalt	50	51–53	<100	880–1000	10000	0.19	1.9x10⁻⁵	1.9x10⁻³	2.0x10⁻³	0.11	36.67
Tambora	1815	50	phonolite	57	59	309	381	381	125000	2.38	9.8	12.5	28-65	0.20
Tarawera	1886 AD	0.35	basalt	50(?)	52	47–74	801–1888	**18880**	945	0.18	1.50	1.68	–	0.18
Taupo	181 AD	35	rhyolite	72	75	38	46	1200	80500	4.83	0.10	4.93	6.5	6.1x10⁻³
Toba	71000 BP	2800	rhyolite	75	77	<100	<100	4000	6440000	1288	129	1417	1468	2.2x10⁻²
Unzen	1991	0.1	dacite	66	77	50	50	19900	250	0.25	0.00	0.25	–	0.10

Question marks are given when information about the given parameter is not available or is estimated. The sulfur (S) content of degassed melt (S in *matrix glass*), non-degassed melt (S in *glass inclusions*), and gas (S in gas) are given in ppm. *Magma* masses are calculated from published *DRE* volumes using a *density* of 2700 kgm⁻³for *basalt* and *basaltic andesite*, 2500 kgm⁻³ for *andesite-dacite*, and 2300 kgm⁻³ for *rhyolite*. The columns "mass S gas" and "mass S melt" refer to the amount of S released by melt and gas respectively, whose sum gives the total S released (mass S m+g). IC and OD are for ice core and optical depth estimates of sulfur, in addition to *TOMS* and *COSPEC* (for Toba only the upper IC estimate of sulfur yield is given, the lower being 733x10¹²g). The column "S content" gives the S content of the *magma* (S total/(S total + mass *magma*), not taking into account sulfur in either solid *sulfide* or *sulfate phases*, including both magmatic crystals and sulfur adsorbed onto the *ash*. Stars indicate volcanoes belonging to *hot spot* settings. The sulfur content of the gas phase is derived from thermodynamical calculations except for numbers in bold for which the following *partition* coefficients were used, S$_{gas}$/S$_{melt}$ = 1000 for *rhyolite*, 100 for *dacite-andesite*, and 10 for *basalt melt* compositions, using the sulfur content of *glass inclusions*. When a range of sulfur content in *glass inclusions* is given, the maximum has been used to derive the sulfur in gas.

Eruptions for which the sulfur degassed from *melt* has been calculated in the present study assume the following sulfur loss (i.e., *glass inclusion* minus *matrix glass*): Etna, 3000 ppm ; Fish Canyon, 20 ppm ; Mauna Loa, 1000 ppm, Fuego and Pacaya, 4000 ppm ; Montserrat, 50 ppm ; Roseau Tuff, 50 ppm ; Stromboli 1000 ppm ; Toba, 20 ppm.

Sources of petrological and volcanological data : Baitoushan : *Horn and Schmincke* [2000], *Zielinski* [1995] ; Bishop Tuff : *Anderson et al.* [1989] ; Eldgja : *Thordarson et al.* [2001] ; Etna : *Allard et al.* [1991], *Métrich et al.* [1990] ; Fish Canyon T. : *Scaillet et al.* [1998b] ; Heimaey : *Devine et al.* [1984] ; Hekla-1 : *Devine et al.* [1984], *Zielinski* [1995] ; Hekla-2 : *Devine et al.* [1984] ; Katla : *Devine et al.* [1984] ; Krafla : *Devine et al.* [1984] ; Laacher See : *Harms and Schmincke* [2000] ; Laki : *Thordarson et al.* [1996] ; Oraefajokull : *Palais and Sigurdsson* [1989] ; Mauna Loa : *Andres et al.* [1991], *Gerlach* [1986] ; Surtsey : *Devine et al.* [1984] ; Agung : *Self and King* [1996] ; Bezymianny : *Palais and Sigurdsson* [1989], *Zielinski* [1995] ; Campanian : *Palais and Sigurdsson* [1989], *Civetta et al.* [1997] ; Coseguina : *Palais and Sigurdsson* [1989] ; El Chichon : *Devine et al.* [1984], *Carey and Sigurdsson* [1986], *Krueger et al.* [1995], *Luhr and Logan* [2002] ; Fuego : *Rose et al.* [1984], Roggensack [2001] ; Huaynaputina : *Costa et al.* [2003] ; Katmai : *Westrich et al.* [1991] ; Krakatau : *Mandeville et al.* [1998] ; Lascar : *Andres et al.* [1991], *Matthews et al.* [1999] ; Lonquimay : *Andres et al.* [1991] ; Minoan : *Devine et al.* [1984], *Sigurdsson et al.* [1990a] ; Montserrat : *Scaillet and Pichavant* [2003] ; Mt Pelée : *Scaillet et al.* [2002] ; Mt St Helens-1980 : *Devine et al.* [1984], *Gerlach and MacGee* [1994] ; Mt St Helens-1800 : *Palais and Sigurdsson* [1989] ; Mt St Helens-1480 : *Palais and Sigurdsson*, [1989], *Zielinski* [1995] ; Pacaya : *Andres et al.* [1991], *Bardindtzeff and Deniel* [1992] ; Pinatubo : *Westrich and Gerlach* [1992], *Bluth et al.* [1993] ; Rabaul : *Palais and Sigurdsson* [1989], *Redoubt* : *Gerlach et al.* [1994], *Nye et al.* [1994] ; Roseau Tuff : *Devine et al.* [1984] ; Ruiz : *Sigurdsson et al.* [1990b], *Krueger et al.* [1990] ; Santa Maria : *Palais and Sigurdsson* [1989], *Rose* [1987] ; Soufrière : *Devine et al.* [1984], *Devine and Sigurdsson* [1983] ; Stromboli : *Allard et al.* [1994] ; Tambora : *Devine et al.* [1984], *Scaillet et al.* [1998b] ; Tarawera : *Palais and Sigurdsson* [1989] ; Taupo : *Palais and Sigurdsson* [1989] ; Toba : *Scaillet et al.* [1998b], *Zielinski et al.* [1996b] ; Unzen : *Scaillet and Pichavant* [2003].
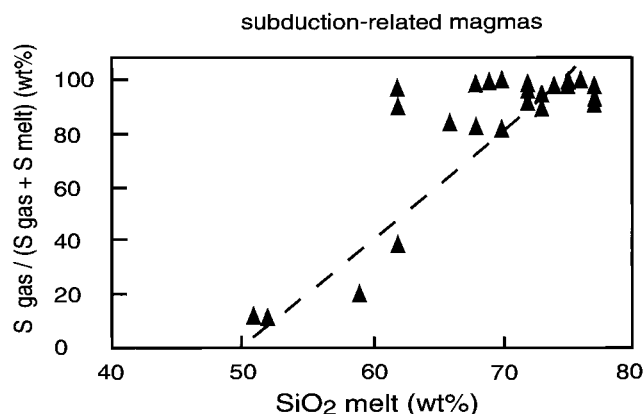
Figure 9. Proportion of S in gas relative to *melt* + gas, versus *melt* SiO_2 for *subduction-related magmas*. The dashed line is a visual estimate best-fit.

orders of magnitude, while the sulfur yield associated with ~100 km³ events ranges over less than 1 order of magnitude. Although some of the dispersion corresponds to errors associated with the method of calculation, part of the observed scatter reflects the variability in bulk sulfur contents of *magmas*, even when considering a specific tectonic environment (see *Wallace* [2001] for additional considerations on sources and long-term outgassing of sulfur).

The *improved petrologic method* for eruptions of hydrous, *subduction*-related *basaltic magmas* gives sulfur yields that are close to those derived from *COSPEC* measurements for the Pacaya and Fuego eruptions, for which the sulfur budget was dominated by the *melt*. In contrast, the same approach falls short in retrieving remote sensed measurements for Stromboli, Lascar, Lonquimay, and Etna volcanoes (Table 5). These four volcanoes fall above the upper envelope drawn from all other eruptions for which gas *saturation* and the improved petrological method can adequately explain sulfur behavior (Figure 11). A possible explanation is that for these *magmas* the gas *phase* abundance actually exceeded 5 wt.%, although for the cases of Stromboli and Etna even scaling up the amount of gas by a factor of 10 still does not reproduce the remotely sensed sulfur yields. In these cases, alternative explanations for the source of excess sulfur may involve degassing of larger volumes of *magma* than are actually erupted, a process that may be particularily important for volcanoes characterized by open-vent conditions [e.g., *Kazahaya et al.*, 1994; *Allard et al.*, 1994].

The highest sulfur yields calculated in this study are close to 10^{16} g, and correspond to super-eruptions such as the Fish Canyon and Toba events, which ejected over 1000 km³ of *magma*. The significance of the Toba estimate is discussed

below in more detail but the data presented in Table 5 clearly show that large *silicic* eruptions, provided that they are gas-saturated prior to eruption, can release enormous quantities of sulfur, with potentially severe worldwide climatic impacts [*Rampino et al.*, 1988; *Rampino and Self*, 1992].

The emblematic nature of the Toba super-eruption in volcano-climate studies warrants special attention. To this event has been ascribed a sulfur loading of 10^{15}–10^{16}g, based on scaling up the sulfur yields of smaller eruptions [*Rampino and Self*, 1992], using ice-core data [*Zielinski et al.*, 1996b], and through thermodynamic considerations [*Chesner et al.*, 1991]. In contrast, *Scaillet et al.* [1998b] used experimental data on sulfur *partitioning* between *melt* and gas to argue that the Toba sulfur yield could have been much lower (circa 3 x 10^{13}g, or only three times that of the Pinatubo event), basically because the *reduced* character of the *magma* (ΔNNO = 0) implies a sulfur-poor gas *phase* with only a few hundred *ppm* sulfur (Figure 8). However, the thermodynamic calculations of *Scaillet and Pichavant* [2003], assuming that the magmatic mineral assemblage represents *equilibrium*, suggest that the sulfur content of the gas was ~4000 *ppm*, which is the value used in Table 5: this implies a sulfur yield close to the upper ice-core-based estimate of *Zielinski et al* [1996a]. Still, recent *phase-equilibrium experiments* carried out by *Gardner et al.* [2002] indi-
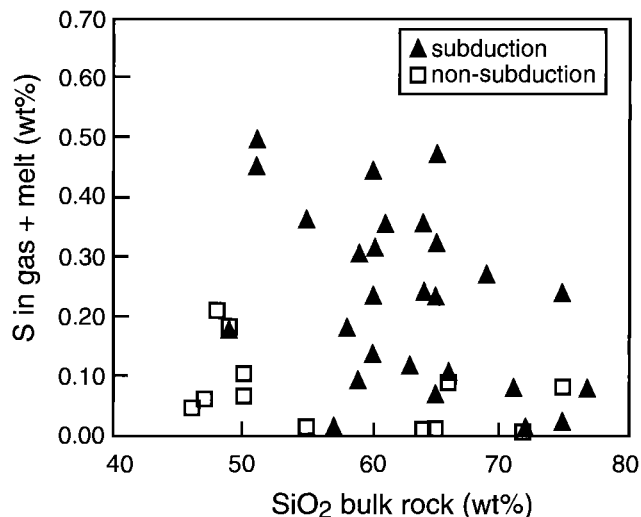
Figure 10. *Bulk-rock* SiO_2 content versus gas+*melt* sulfur content. For eruptions spanning a range in bulk *silica* content an average value of SiO_2 has been used. Note that the sulfur stored in the minerals *anhydrite* and *pyrrhotite* is not taken into account, and thus the bulk sulfur contents are likely to be higher. The sulfur values for Stromboli (S = 36.7 wt%), Etna (S = 15.8 wt%), Lascar (S = 6.8 wt%), and Lonquimay (S = 3.1 wt%) are not shown to preserve the scale.

cate that part of the mineral assemblage (hornblende) is not in *equilibrium* with the host *magma*, which virtually invalidates the thermodynamic calculations. At present, the petrologic estimate of sulfur yield for the Toba event is poorly constrained as 10^{13} to 10^{16} g. While there is little doubt that super-eruptions have the potential to strongly impact climate, the atmospheric sulfur yield of the Toba event remains uncertain. Because of the low pre-eruption temperature of the Toba *magma* (~800°C), diffusive loss of sulfur from the sulfur-poor *melt* during eruption was probably a minor source of sulfur output [*Scaillet et al.*, 1998b]. The Toba figures of Table 5 show that *melt* degassing may account for less than 10% of the total amount of sulfur released. Therefore, the presence and composition of a gas *phase* at Toba is the vital issue to be settled for a proper petrologic estimate of sulfur-yield. The disagreement found between various studies of this eruption serves to illustrate that a detailed petrological knowledge is essential for a correct assessment of sulfur yield in past eruptions.

Comparison Between Petrologic and Independent Estimates

The sulfur yields obtained using the *improved petrologic method* are compared against those derived from ice-core, optical-depth, and remote-sensing methods (*COSPEC, TOMS*) in Table 5 and Figure 12 for non-*subduction* and *subduction magmas* (including the anomalous Lascar, Stromboli, and Etna volcanoes) For non-*subduction magmas*, the limited data set precludes any definitive statement but we note that the difference between the approaches is
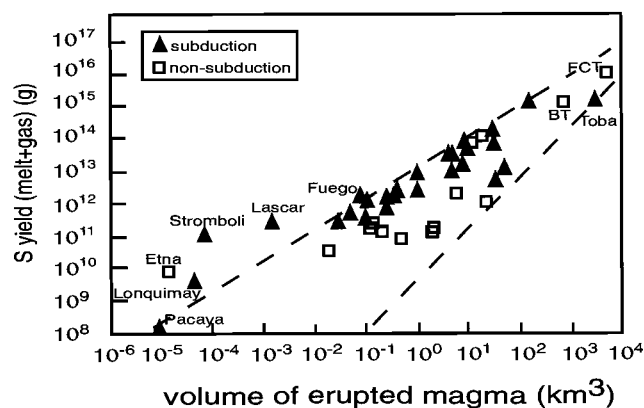
Figure 11. Correlation between the volume of erupted *magma* and the sulfur yield (*melt* + gas). Eruptions plotting above the bounded field are those that degassed more sulfur than was stored either in the *melt* prior to eruption or within the assumed volume of coexisting gas *phase*. FCT is for Fish Canyon Tuff, BT for Bishop Tuff.
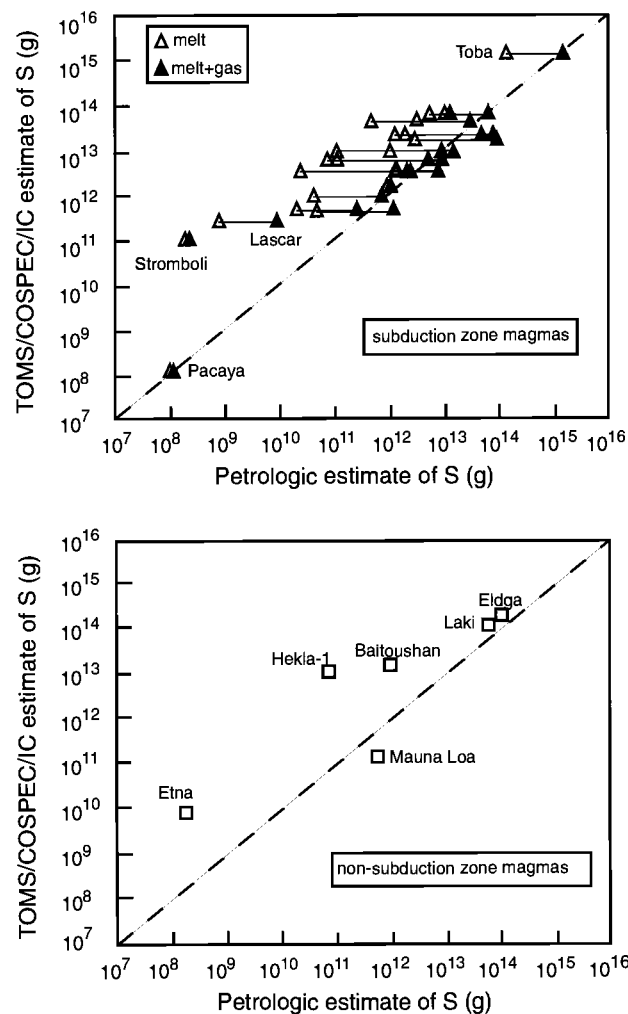
Figure 12. Comparison between petrologic and independent estimates of sulfur yield for: (a) *subduction*-related, and (b) non-*subduction*-related *magmas*. In (a), the open triangles represent the sulfur contribution arising from *melt* degassing only. For eruptions having a range of independent estimates (Toba, Tambora), the maximum was used.

largest with *evolved magmas* (*rhyolite* of Baitoushan or *dacite* of Hekla-1). Several studies on *evolved magmas* in extensional settings have also emphasized their H_2O-rich nature [e.g., *Kovalenko et al.*, 1988; *Lowenstern and Mahood*, 1991; *Barclay et al.*, 1996; *Horn and Schmincke*, 1999; *Harms and Schmincke*, 2000; *Scaillet and Macdonald*, 2001], which suggests that the condition of gas *saturation* might also have been attained in *fractionated magmas* produced in such settings [see *Barclay et al.*, 1996]. Therefore, we argue that the discrepancy observed between independent and petrologic approaches for these

non-*arc evolved magmas* is also likely due to the existence of a separate gas *phase*.

Although our current understanding of sulfur emissions in extensional settings might seem satisfactory, in particular with respect to Laki-type events, the discrepancy noted above regarding Figure 12 illustrates the need for additional work concerning sulfur in *alkalic magmas*. Recent *TOMS* studies of eruptions from volcanoes in the East Africa Rift valley have indeed shown that considerable amounts of sulfur can be released by *alkali-basalts* at Nyamuragira in a few days [*Krueger et al.*, 1996]. Similarly, more *evolved alkali*-rich *magmas* are potentially important magmatic carriers of sulfur into the atmosphere, as illustrated by the 1815 AD Tambora eruption as well as the Laacher See and Vesuvius 79 AD eruptions, all of which can be correlated to large acidity peaks in ice cores [*Zielinski*, 1995; *Zielinski et al.*, 1996b]. However, the quantification of the potential climatic effects of eruptions of such alkaline *magma*s using an improved petrological method is limited by the lack of experimental data on the sulfur *solubility* and *partitioning* in alkali-rich silicate *melts*.

For *subduction-zone magmas*, sulfur yields derived from considering only *melt* release (original *petrologic method*) and *melt*+gas release (*improved petrologic method*) are shown separately in Figure 12 to illustrate the importance of the gas *phase* in controlling the total sulfur yield of explosive eruptions from *subduction-zone* volcanoes. Clearly, consideration of the gas-*phase* sulfur helps remove much of the apparent disagreement between the original *petrologic method* and independent sulfur-yield estimates, notably for *silicic magmas* (excluding Lascar and Stromboli). The fact that the difference between *melt* degassing alone and estimates based on ice-core or optical-depth methods increases as the sulfur yield decreases primarily reflects the low sulfur contents of *melts* in low-T *silicic magmas*, for which *melt* degassing contributes little to the bulk sulfur emitted. Overall, the good agreement between independent estimates of sulfur yield and those derived from the *improved petrologic method* shown in Figure 12 suggests that both methods retrieve the correct order of magnitude of atmospheric sulfur loading associated with major eruptive events. Furthermore, this suggests that the *improved petrologic method* can be used for eruptions lacking independent constraints from remote sensing or ice core data.

Comparisons of sulfur yields by different methods should therefore be considered in the light of volcanological factors on a case by case basis. If all parameters needed to calculate the bulk sulfur yield have been correctly evaluated, then all petrologic estimates shown on Figure 12, should fall on or slightly to the right of (depending on *ash* adsorption effects or troposphere/stratosphere aerosol partitioning) the 1/1 correlation line, a trend that is apparent for the largest sulfur yields. The fact that some of the data fall left of the line may indicate that one or more of the factors controlling sulfur yield in the calculation procedure has been underestimated (e.g., *DRE* volume, sulfur *fugacity*, amount of gas present in the *reservoir*) or, alternatively, that an additional source of *volatiles* exists (vaporisation of seawater?).

CONCLUSIONS

Provided that a given eruption has benefited from detailed field and laboratory studies, the *improved petrologic method*, including thermodynamic estimation of the gas-*phase* composition, can give reasonable results for atmospheric sulfur loading from past volcanic eruptions. For cases in which a significant level of uncertainty exists, in particular as to what mass of *magma* has been erupted or its *redox state*, the present study gives general guidelines to be used for roughly estimating sulfur yields. For *intermediate* to *silicic* eruptions from subduction-related volcanoes, gas/*melt* sulfur *partition coefficients* of 100 (*intermediate*) or 1000 (*silicic*) can be used as first-order approximations or, alternatively, an average sulfur content of 3 wt% for the gas *phase* whose amount can be taken as 5 wt% of the erupted mass. For more *mafic* compositions erupted from subduction-related volcanoes a gas/*melt* sulfur ratio of 10 can be used together with an assumed 1 wt% of gas. With respect to erupted masses, provided that some field constraints exist, possible effects of erosion on deposit volume estimates can be approximated by scaling up the estimated deposit mass by a factor of two, which is a typical uncertainty; this will provide an upper possible limit for the mass of erupted *magma*. Altogether, these approximations should give maximum sulfur yields for the purposes of modelling the impact of volcanic activity in the past.

Finally, we have deliberately ignored the role of Cl and F, basically because these cannot yet be incorporated in the thermodynamic approach applied to calculate the gas composition. This is an important future target to be addressed by experimental petrologists for a fuller characterisation of *volatile* contributions to the atmosphere by volcanic eruptions.

GLOSSARY

accretionary lapilli - aggregates of fine *ash*, commonly having a concentric structure and formed by accretion of damp *ash* in eruption clouds.

airfall or **fall** - an adjective that usually precedes *ash*, *pumice*, or deposit, and indicates that the *pyroclasts* fell from the air as opposed to flowing along the ground in a *pyroclastic flow*.

alkalic - said of a *magma* that is rich in the alkaline-earth metals Na and K. Because these two elements tend to concentrate in the *melt* relative to the crystals, *alkali*-rich *melts* usually signal a low *melt* fraction in the parent *magma* or solid rock. *Magmas* rich in *alkalies* are therefore indicative of either extreme crystallisation or an incipient stage of melting.

andesite - a volcanic rock with 57–63 wt.% SiO_2. *Andesite* is one of the most common rock types found at continental *subduction-related* volcanoes, such as in the Andes.

anhydrite - the mineral $CaSO_4$ was once thought to form only in sedimentary environments by the evaporation of seawater, or in hydrothermal deposits, but since the 1982 eruption of El Chichón (México) is now also known to precipitate from silicate *melts* at high oxygen *fugacities*.

arc magmas: see *subduction zone*.

ash - *pyroclasts* smaller than 2 mm in diameter.

ash flows: see *ignimbrites*.

ash-leachate studies: investigations designed to extract and measure the water-soluble components adsorbed onto fresh volcanic ash. A known quantity of ash is placed in a known volume of distilled water. The water is later passed through a filter to extract all solid components and the dissolved components are analyzed.

basalt - a volcanic rock with <52 wt.% SiO_2. *Basalt* is the most common volcanic rock on Earth. Virtually all oceanic crust is *basaltic*, and huge volumes of *basalt* erupt on land as well.

bomb: see *pyroclast*.

bulk-rock composition - The chemical composition obtained by crushing up a large representative rock sample and analyzing the powder. For volcanic rocks it is taken to represent the composition of the corresponding *magma*.

caldera - crater-like depression, generally >1km in diameter, formed by collapse of a volcanic edifice, commonly into

an underlying *magma reservoir* that was emptied by a major eruption.

clast - piece of rock. See *pyroclast*.

co-ignimbrite ash and plume - *ash* ellutriated from the surface of a *pyroclastic flow* is entrained by heated convecting air and thereby buoyantly rises into the atmosphere forming *co-ignimbrite plumes* that, in some cases, reach the stratosphere. The *ash* ultimately falls back to Earth.

conduit - a pipe-like pathway for the transport of *magma*.

COSPEC - a ground-based or aircraft-based, remote sensing, ultraviolet correlation spectrometer that measures the flux of sulfur dioxide gas from volcanoes.

dacite - a volcanic rock with 63–67 wt.% SiO_2. Like *andesite, dacite* is a common rock type found at continental *subduction-related* volcanoes.

dense rock equivalent (DRE) - *pyroclastic* eruptions typically produce *pumice-* and *scoria*-rich deposits with bulk *densities* between 300 and 1500 kg/m^3, much less than typical *lava densities* of 2300–2700 kg/m^3. For comparison purposes, estimated deposit volumes are converted to *DRE* values at typical *lava densities*..

density - for small substances, such as minerals, *densities* are typically given in g/cm^3. Common rock-forming minerals range from ~2.6 g/cm^3 (quartz, feldspars) to 3.2–4.0 g/cm^3 (pyroxenes, olivine). Silicate *melts* and *glasses* lie at the low end of this range. *Density* units of kg/m^3 are typically used for larger-scale domains, such as *lava* flows and *magmas* (2300–2700 kg/m^3), and *pyroclastic* deposits (300–1500 kg/m^3). The two *density* units are easily converted multiplying by 1000.

differentiation - this term includes various processes by which a higher temperature, lower SiO_2 *magma* (the parent) changes composition, evolving to a lower temperature, higher SiO_2 *magma* (the daughter). Commonly invoked processes are *fractional crystallization* (in which sidewall crystallization or gravitational settling of early formed crystals that are denser than the *melt*, such as pyroxenes and olivine, accompanies heat loss and cooling) and digestion (assimilation) of *silica*-rich crustal rocks by the parent *magma*.

effusive - non-explosive eruptions of *lava*.

equilibrium - the stable thermodynamic condition in which the activities or *fugacities* of all components are equal in all *phases*.

evolved - a *magma* produced by *differentiation* of a more *mafic* parent *magma*. Compared to the parent, the *evolved magma* is generally richer in SiO_2, lower in MgO, and has a lower temperature.

felsic - a general term that refers to SiO_2-rich *magmas* and igneous rocks. It reflects the feldspar-rich nature of these rocks. For volcanic rocks it includes the terms rhyodacite (SiO_2 >67 wt.% and *rhyolite* SiO_2 >73 wt.%). Part of a three-fold hierarchy: *mafic* <57 wt.% SiO_2 < *intermediate* < 67% SiO_2 < *felsic*.

fractional crystallization - as a *magma* cools and crystals grow in response, the residual *melt* becomes depleted in elements that preferentially enter the crystals and thereby changes composition. If the crystals and *melt* get physically segregated, perhaps by gravitational settling of the crystals, the *magma* is said to be *fractionated* to a new composition, typically richer in *silica*.

fugacity - a gas is considered to be perfect if its behavior can be described by the ideal gas law: $PV = nRT$, where P is pressure, V is volume, n is the number of moles, R is the ideal gas content, and T is temperature. Most gases are not perfect, especially at high pressures or low temperatures. The *fugacity* is a kind of equivalent pressure that accounts for the deviation of a real gas from ideal gas bahavior.

glass - a silicate *melt* that is cooled very rapidly, as in many volcanic eruptions, can quench to form a *glass*, rather than crystallizing.

glass inclusions - see *melt inclusions*. When *magmas* containing *melt inclusions* are rapidly quenched against either air or water, the *melt inclusions* freeze to *glass inclusions*.

hot spot - places where a plume of hot solid rock rises through Earth's *mantle*, partially melts, and generates *magma*. As an overlying plate travels across a *hot spot*, a chain of volcanoes forms (ie the Hawaian-Emperor chain). The ages and orientation of the volcanoes record the plate's past motion.

ignimbrite - a ground-hugging, fluidized density current of *pumice*, *ash*, and gas that moves laterally away from a volcanic vent at high velocity following topographic lows: also

called *pyroclastic flows*. *Ignimbrite* is also the name of the deposit produced by these flows.

immiscible sulfide melt - at relatively low oxygen *fugacities* sulfur in excess of the *solubility* limit in the silicate *melt* can form a separate liquid *phase* that is also rich in iron. The *sulfide* liquid is usually present as tiny spherules scattered through the silicate *melt*. The two *melts* are immiscible, like oil and water.

improved petrologic method - as discussed in this paper, the improved version of the *petrologic method* includes an estimate of the sulfur release from a separate gas *phase* in the pre-eruptive *magma*.

infrared spectroscopy - an instrumental method based on absorption of infrared radiation used to determine concentrations of hydrogen and carbon species in glasses. Time intensity data are Fourier transformed to yield frequency-intensity spectra, hence the common name Fourier-transform *infrared spectroscopy* (FTIR). Species that can be analyzed include molecular H_2O and hydroxyl (OH^-), their summation as total H_2O, molecular CO_2 and carbonate (CO_3^{2+}).

intermediate - a general term that refers to *magmas* and igneous rocks with *intermediate* SiO_2 contents of 57-67 wt.%. For volcanic rocks it includes the terms *andesite* (57-63 wt.% SiO_2) and *dacite* (63-67 wt.% SiO_2). Part of a three-fold hierarchy: *mafic* <57 wt.% SiO_2 < *intermediate* < 67% SiO_2 < *felsic*.

isopach map - a map for a *pyroclastic* deposit that shows contour lines for the deposit thickness at various field stations.

juvenile – parts of a volcanic deposit that represent portions of the erupted *magma*, as opposed to accidental fragments of old rock that were ejected in the same eruption, which are termed *lithics*.

lapilli - *pyroclasts* between 2 and 64 mm in diameter, including *pumice* and *scoria*.

lava - *magma* with relatively low residual gas content that erupts and flows as a fluid on Earth's surface. Also the name of the solidified rock.

lithic - an accidental fragment of pre-existing rock expelled in an explosive eruption.

mafic - a general term that refers to *magmas* and igneous rocks with low SiO_2 contents <57 wt.%. For volcanic rocks it includes the terms *basalt* (SiO_2 <52 wt.%) and *basaltic andesite* SiO_2 52–57 wt.%). Part of a three-fold hierarchy: *mafic* <57 wt.% SiO_2 < *intermediate* < 67% SiO_2 < *felsic*.

magma - partially to completely molten rock. Common *magmas* contain a silicate *melt* ± crystals of various minerals ± *gas* bubbles. Some *magmas* contain a separate, *immiscible sulfide melt*.

magma reservoir - the volume occupied by *magma* prior to eruption; equivalent to *magma* chamber but with no connotation about the shape of the volume.

mantle - middle, silicate layer of the Earth, between the thin silicate crust and the molten iron-nickel outer core. The *mantle* accounts for 84% of Earth's volume. It begins 10–70 km beneath the surface and extends to a depth of 2990 km. Earth's center is at 6370 km depth. *Peridotite* xenoliths brought to the surface by some deep-seated volcanic eruptions are thought to represent the rocks of the upper *mantle*. Deeper *mantle* rocks are probably compositionally similar but formed from mineral assemblages stable at higher pressures and temperatures.

mantle wedge - portion of the convecting *mantle* that lies above *subducting* oceanic plates. Petrologists believe that fluids/*melts* released from the *subducting* plates rise into the overlying *mantle wedge* and trigger partial melting events that feed *magmas* to *subduction-zone* volcanoes. The phenomenon is not unlike the process of throwing salt on an icy sidewalk to melt the ice. The temperature of the *mantle wedge* (or icy sidewalk) stays the same, but the melting temperature of the wet *mantle wedge* (or ice-salt mixture) is decreased until melting ensues.

matrix - when a *magma* erupts, the former silicate *melt* either forms *glass* (if quickly quenched against air or water) or a fine-grained felt-like aggregate of tiny crystals (if more slowly cooled, such as in the interior of a *lava* flow). These two materials are referred to as *matrix glass* and microcrystalline *matrix*. *Matrix* is the glassy to fine-grained material that surrounds the larger crystals in a volcanic rock.

melt - the liquid portion of a *magma*.

melt inclusions - small parcels of the silicate *melt* that were accidentally engulfed by the crystals as they grew from the *melt*. *Melt inclusions* can preserve, through the strength of the host crystal, the composition of the *melt*, including its *volatiles*, prior to eruptive degassing. Upon eruption and rapid cooling, *melt inclusions* freeze to form *glass inclusions*.

MORB - acronym for Mid-Ocean Ridge *Basalt*. See *basalt*.

NNO - a synthetic oxygen buffer used by experimental petrologists to control *oxygen fugacity*. It consists of mixing nickel metal with the mineral bunsenite (NiO). As long as both remain they fix the *oxygen fugacity* according to the reaction: $Ni + 1/2O_2 = NiO$. Although neither solid is present in natural *magmas*, many *magmas* have oxygen fugacities close to that defined by the *NNO* buffer, which is used as a convenient reference for natural *magmas*. Variations in magmatic fO_2 span several orders of magnitude and are thus commonly expressed in log units [*Carmichael*, 1991; *Ghiorso and Sack*, 1991]. A *magma* having an fO_2 10 times lower than the *NNO* buffer at the same P and T, is said to have an fO_2 of *NNO*-1, or 1 log unit below *NNO* (also expressed as DNNO=-1). Conversely, a *magma* with an fO_2 ten times higher has an fO_2 of *NNO*+1 (ΔNNO=+1). *Reduced magmas* are those with an fO_2 below *NNO*, whereas *oxidized magmas* lie above *NNO*. *Basalts* erupted at *spreading ridges* and *hot spots* are relatively *reduced* and have fO_2 in the range *NNO*-3 to *NNO*-1; *magmas* erupted from *subduction-zone* volcanoes are generally more *oxidized*, with fO_2 in the range *NNO* up to *NNO*+2. This increase in oxidation accompanies, and perhaps results from, an increase in magmatic water content.

oxidized - said of a *magma* that has a high *oxygen fugacity* (above *NNO*). This is reflected by elevated ferric to ferrous iron ratios (Fe^{3+}/Fe^{2+}) in the *melt* or *glass*, some iron-bearing minerals, and the whole-rock composition, unless obscured by post-eruptive alteration.

oxygen fugacity - a thermodynamic parameter related to the partial pressure of oxygen (pO_2), which accounts for the fact that O_2 is not an ideal gas. *Oxygen fugacity* (fO_2) equals pO_2 times the *fugacity* coefficient of oxygen (gO_2).

partition coefficient - the ratio of a particular element between two *phases*. Common *phase* ratios are mineral/*melt* and gas/*melt*.

partitioning – the distribution of a chemical component among the *phases* present (*melt*, minerals, gas).

parts per million (ppm) - a unit of concentration by weight commonly used by petrologists and geochemists for

trace elements, those present at levels below 0.1 wt.% (=1000 *ppm*).

peridotite - the common rock of Earth's *mantle*. It consists of olivine, orthopyroxene, clinopyroxene, plus an aluminum-rich mineral that shifts with increasing pressure from plagioclase, to spinel, to garnet.

petrologic method - as originally defined by *Devine et al.* [1984], the S (or Cl) content of *matrix glass* was subtracted from the S content in *glass inclusio*ns, and the difference was scaled to the volume of the deposit to estimate the S (or Cl) yield to the atmosphere from an eruption.

petrology - the study of rocks (from the Greek «petros» meaning «rocks»).

phase - a compositionally and structurally homogeneous material, such as a mineral, *melt*, or gas.

phase-equilibrium experiment - laboratory-based experimental study using a pressurized furnace designed to recreate a magmatic condition of *equilibrium* among *phases* at high temperature and pressure.

phreatomagmatic - said of an eruption produced by the interaction beween *magma* and external water (oceans, lakes, aquifers).

pillow basalt/lava - submarine *lava* characterized by rounded and tubular shapes with striated outer glassy surfaces, the result of hot *magma* quenching against cold seawater.

Plinian - violently explosive eruptions of *pumice* and *ash* that generate powerful convecting columns extending into the stratosphere. The term honors Pliny the Younger, who vividly described the towering eruption column from the 79 AD eruption of Vesuvius, in which his uncle, the famous Roman naturalist Pliny the Elder, lost his life.

plutonic - a *magma* that crystallizes at depth in the Earth without erupting at the surface. Named for Pluto, the Greek god of the underworld, *plutonic* rocks are characterized by the absence of *glass*, and larger crystals than common volcanic rocks (a result of slow cooling).

pumice - see *pyroclast*.

pyroclast - all solid fragments of *magma* ejected from volcanoes (from the Greek meaning «fire-broken»). Size is used to distinguish between *ash* < 2 mm < *lapilli* < 64 mm < *bombs*. *Lapilli* and *bombs* that are *mafic* to *intermediate* in composition, darker in color, and can't be broken by hand are typically called *scoria* (plural scoriae), whereas the same size fragments of *felsic* composition, which are typically lighter in color and can be broken by hand, are called *pumice*. *Scoria* and *pumice* fragments are generally thought to closely approach the bulk composition of *magma* before eruption (apart from the lost *volatiles*), and accordingly are referred to as *juvenile*.

pyroclastic fall - the rainout of *bombs*, *lapilli*, and *ash* through the atmosphere from an explosive eruption plume or jet.

pyroclastic flow - a ground-hugging, fluidized density current of *pumice*, *ash*, and gas that moves laterally away from a volcanic vent at high velocity following topographic lows: also called *ignimbrite*.

pyrrhotite - a fairly common *sulfide* mineral in volcanic rocks. It is a solid-solution mineral whose composition, expressed as $Fe_{1-x}S$, is a function of sulfur *fugacity* (fS_2).

redox state - a qualitative term that refers to the relative degree of oxidation in a system; the *oxygen fugacity* of the system is the quantitative equivalent.

reduced - said of a material, *magma* in the present case, that has a low *oxygen fugacity* (below *NNO*). Usually this is reflected by low ferric to ferrous iron ratios of the rock (Fe^{3+}/Fe^{2+}).

rhyolite - a volcanic rock with at least 69 wt.% SiO_2. *Rhyolite* lies at the opposite end of the *magma* spectrum from *basalt*, having low magmatic temperature (generally < 900°C) and high *viscosity*. Primarily erupted from continental volcanoes, where contributions from melting of SiO_2-rich crustal rocks are important.

saturation - Suppose an experiment where H_2O is progressively added to a silicate *melt* at high P and T. The system silicate *melt* - H_2O, is said to be saturated with a gas *phase* when bubbles of nearly pure H_2O nucleate in the *melt*. Any further addition of H_2O just increases the amount of gas relative to *melt*. Addition of CO_2 to this system will produce *saturation* of a gas *phase* at lower amounts of H_2O added, because CO_2 has a lower *solubility* than H_2O. In this case the gas *phase* will be a mixture of H_2O and CO_2. In this paper, *saturation* mainly refers to P-T conditions under

which a gas *phase* exists. Yet *saturation* can be employed for other *phases* such as solid or liquid. For example, a *melt* can be saturated with sulfur in three ways: formation of sulfur-bearing gas bubbles, precipitation of a sulfur-bearing mineral like *anhydrite* or *pyrrhotite*, or formation of an *immiscible sulfide melt*. Common mechanisms by which a *magma* may reach gas *saturation* include the following: (1) continuous crystallisation of anhydrous minerals, which enriches water in the residual *melt* until *saturation* is reached; (2) decompression, which lowers *solubility* of all volatile species; and (3) upward release of gas from deeper *magmas* that are cooling, crystallizing, and degassing.

scoria - see *pyroclast*.

silica - SiO_2 is the most abundant component of most *magmas* on Earth. The *silica* content largely dictates the *viscosity* of *magmas* and is the primary variable used in the classification of *magmas* and rocks.

silicic - characterized by having a high SiO_2 content.

solubility - the maximum amount of a *volatile* species or other component that can be dissolved in a silicate *melt* at a given pressure, temperature, and *melt* composition (see *saturation*).

spreading-ridge - a major class of tectonic plate boundary where new oceanic crust is formed by *magmas* rising from partially molten *mantle* beneath the ridge. Two oceanic plates move away from one another like two opposed conveyor belts. Oceanic *spreading ridges* form a globe-encircling system of sea-floor mountain ranges with a total length of ~65,000 km. It is estimated that *spreading ridges* account for more than 60% of the *magma* erupted on Earth (see Table 1).

subduction-zone - a major class of tectonic plate boundary where an oceanic lithospheric plate descends into the *mantle* beneath either another oceanic lithospheric plate (island arc) or a continental lithospheric plate (continental arc). The very high geothermal gradients beneath *spreading ridges* drive hydrothermal circulation of seawater through newly formed oceanic crust, which soaks up seawater like a sponge. Water is incorporated both in pores and in the structures of clays and other alteration minerals. After lateral journeys of tens to hundreds of millions of years the oceanic crust may reach a trench and descend, or subduct, into the *mantle*. Melting in *subduction zones* is triggered by release of water-rich fluids or *melts* from the subducted slab, which

accounts for the water-rich nature of *subduction-zone magmas* and their explosive eruptive styles. Note that *subduction* is synonymous to *arc*, a term used to reflect the arcuate shape in map view of many *subduction-related* volcanic chains (i.e. Aleutians, Lesser Antilles, and Marianas).

sulfate – the ionic group SO_4^{2-} in which the S atom has a +6 charge.

sulfide - the *reduced* form of sulfur (S^{2-}) dissolved in silicate *melts*, *immiscible sulfide melts*, and gases, as well as in the mineral *pyrrhotite* ($Fe_{1-x}S$).

tephra - all *pyroclasts* that fall to the ground during an explosive eruption (from the Greek meaning «*ashes*»).

TOMS - the Total Ozone Mapping Spectrometer, a satellite-based sensor that is also used to monitor volcanic SO_2.

viscosity - a measure of the resistance of a material to flow in response to stress; opposite of fluidity.

volatiles - all those chemical species that are lost upon cooling, crystallisation, or eruption toward the gas *phase* (see Table 2 for those common in Earth's *magmas*).

REFERENCES

Ablay, GJ, M.R. Carroll, M.R. Palmer, J. Marti, R.J.S. Sparks, Basanite-phonolite lineages of the Teide-Pico Vielo volcanic complex, Tenerife, Canary Islands. *J. Petrol.*, *39*, 905-936, 1998.

Allard, P., J. Carbonnelle, D. Dajlevic, J. Le Bronec, P. Morel, M.C. Robe, J.M. Maurenas, R. Faivre-Pierre, D. Martin, J.C. Sabroux, P. Zettwoog, Eruptive and diffuse emissions of CO_2 from Mount Etna, *Nature, 351*, 387-391, 1991.

Allard, P., J. Carbonnelle, N. Métrich, H. Loyer, and P. Zettwoog. Sulphur output and magma degassing budget of Stromboli volcano. *Nature, 368*, 326-330, 1994.

Anderson, A.T., and G.G. Brown, CO_2 and formation pressures of some Kilauean melt inclusions, *Am. Mineral.*, *78*, 794-803, 1993.

Anderson, A. T., S. Newman, S.N. Williams, T.H. Druitt, C. Skirius, and E. Stolper, H_2O, CO_2, Cl, and gas in Plinian and ash-flow Bishop rhyolite, *Geology, 17*, 221-225, 1989.

Andres, R.J., W.I. Rose, P.R. Kyle, S. DeSilva, P. Francis, M. Gardeweg, and H. Moreno Roa, Excessive sulfur dioxide emissions from Chilean volcanoes, *J. Volcanol. Geotherm. Res., 46*, 323-329, 1991.

Andres, R.J., W.I. Rose, R.E. Stoiber, S.N. Williams, O. Matias, and R. Morales. A summary of sulfur dioxide emission rate measurements from Guatemalan volcanoes. *Bull. Volcanol., 55*, 379-388, 1993.

Ayalew, D., P. Barbey, B. Marty, L. Reisberg, G. Yirgu, and R. Pik, Source, genesis, and timing of giant ignimbrite deposits associated with Ethiopian continental flood basalts, *Geochim. Cosmochim. Acta, 66*, 1429-1448, 2002.

Baker, L.L., and M.J. Rutherford, Sulfur diffusion in rhyolitic melts, *Contrib. Mineral. Petrol., 123*, 335-344, 1996.

Barclay, J., M.R. Carroll, B.F. Houghton, and C.J.N. Wilson, Pre-eruptive volatile content and degassing history of an evolving peralkaline volcano, *J. Volcanol. Geotherm. Res., 74*, 75-87, 1996;

Bardintzeff, J.M. and C. Deniel. Magmatic evolution of Pacaya and Cerro Chiquito volcanological complex, Guatemala. *Bull. Volcanol., 54*, 267-283, 1992.

Blake, S. Volatile oversaturation during the evolution of silicic magma chambers as an eruption trigger. *J. Geophys. Res., 89*, 8237-8244, 1984

Bluth, G.J.S., C.C. Schnetzer, A.J. Krueger, and L.S. Walter, The contribution of explosive volcanism to global atmospheric sulphur dioxide concentrations, *Nature, 366*, 327-329, 1993.

Bluth, G.J.S., S.D. Doiron, A.J. Krueger, L.S. Walter, and C.C. Schnetzer, Global tracking of the SO_2 clouds from the June, 1991 Mount Pinatubo eruptions, *Geophys. Res. Lett., 21*, 2833-2836, 1994.

Bureau, H., F. Pineau, N. Métrich, M. Semet, and M. Javoy, A melt and fluid inclusion study of the gas phase at Piton de la Fournaise volcano (Réunion Island), *Chem. Geol., 147*, 115-130, 1998.

Byers, C.D., M.O. Garcia, and D.W. Muenow, Volatiles in basaltic glasses from the East Pacific Rise at 21°N: implications for MORB sources and submarine lava flow morphology, *Earth Planet. Sci. Lett., 79*, 9-20, 1986.

Bryan, E.S., Riley, T.R., Jerram, D.A., Stephens, C.J., and Leat, P.L. Silicic volcanism: an undervaluated component of large igneous provinces and volcanic rifted margins, In : Menzies, M.A., Klemperer, S.L., Ebinger, C.J., and Baker, J. (eds.) Volcanic rifted margins, *Geol. Soc. Am. Spec. Pap. 362*, 97-118, 2002.

Candela, P.A. Physics of aqueous phase evolution in plutonic environments. *Am. Mineral., 76*, 1081-1091, 1991.

Carey, S.N., and H. Sigurdsson, The intensity of plinian eruptions. *Bull. Volcanol., 51*, 28-40, 1989.

Carey, S.N., and H. Sigurdsson, The 1982 eruptions of El Chichón Volcano, México (2): Observations and numerical modelling of tephra-fall distribution. *Bull. Volcanol., 48*, 127-141, 1986.

Carey, S.N., and R.J.S. Sparks, Quantitative models of the fallout and dispersal of tephra from volcanic eruption columns. *Bull. Volcanol., 48*, 109-125, 1986.

Carmichael, I.S.E. The petrology of Thingmuli, a Tertiary volcano in eastern Iceland. *J. Petrol., 5*, 435-460, 1964.

Carmichael, I.S.E., The redox states of basic and silicic magmas: a reflection of their source region. *Contrib. Mineral. Petrol., 106*, 129-141, 1991.

Carroll, M.R., and J.R. Holloway, Volatiles in Magmas, *Rev. Mineral., 30*, pp. 500, Am. Mineral. Soc., Washington, D.C., 1994.

Carroll, M.R., and M.J. Rutherford, The stability of igneous anhydrite: Experimental results and implications for sulfur behavior in the 1982 El Chichón trachyandesite and other evolved magmas, *J. Petrol., 28*, 781-801, 1987.

Carroll, M.R., and M.J. Rutherford, Sulfur speciation in hydrous experimental glasses of varying oxidation states: Results from measured wavelength shifts of sulfur x-rays, *Am. Mineral., 73*, 845-849, 1988.

Carroll, M.R., and J. Webster, Solubilities of sulfur, noble gases, nitrogen, chlorine, and fluorine in magmas, In M.R. Carroll and J.R. Holloway (eds.), *Volatiles in Magmas*, Rev. Mineral., vol. 30, pp. 231-280, Am. Mineral. Soc., Washington, D.C., 1994.

Chesner, C.A., Petrogenesis of the Toba Tuffs, Sumatra, Indonesia, *J. Petrol., 39*, 397-438, 1998.

Chesner, C. A., W.I. Rose, A. Deino, R. Drake, and J.A. Westgate, Eruptive history of Earth's largest Quaternary caldera (Toba, Indonesia) clarified, *Geology, 19*, 200-203, 1991.

Christie, D.M., I.S.E. Carmichael, and C.H. Langmuir. Oxidation states of mid-ocean ridge basalt glasses. *Earth Planet. Sci. Lett., 79*, 397-411, 1986.

Civetta, L., G. Orsi, L. Pappalardo, R.V. Fisher, G. Heiken, and M. Ort., Geochemical zoning, mingling, eruptive dynamics and depositional processes. The Campanian Ignimbrite, Campi Flegrei caldera, Italy. *J. Volcanol. Geotherm. Res., 75*, 183-219, 1997.

Coffin, M.F., and O. Eldholm, Large igneous provinces: crustal structure, dimensions, and external consequences, *Rev. Geophys., 32*, 1-36, 1994.

Costa, F., B. Scaillet, and A. Gourgaud, Massive atmospheric sulfur loading of the AD 1600 Huaynaputina eruption, *GRL* vol. 30, no. 2, 1068, doi:10.1029/2002GL0164602, 2003.

Cottrell, E., J. Gardner, and M.J. Rutherford, Petrologic and experimental evidence for the movement and heating of the pre-eruptive Minoan rhyodacite (Santorini, Greece). *Contrib. Mineral. Petrol. 135*, 315-331, 1999.

Craig, J.R. and S.D. Scott, Sulfide phase equilibria. In P.H. Ribbe (ed.) *Sulfide Mineralogy*, pp. CS1-110, Rev. Mineral., 1, Mineral. Soc. Am., Washington D.C., 1976.

Crowley, T.J. Causes of climate change over the past 1000 years. *Science, 289*, 270-277, 2000.

Devine, J.D., and H. Sigurdsson. The liquid composition and crystallisation history of the 1979 Soufrière magma, St Vincent, W.I. *J. Volcanol. Geotherm. Res., 16*, 1-31, 1983.

Devine, J.D., H. Sigurdsson, A.N. Davis, and S. Self. Estimates of sulfur and chlorine yield to the atmosphere from volcanic eruptions and potential climatic effects, *J. Geophys. Res., 89*, 6309-6325, 1984.

De Silva, S., and G. Zielinski, Global influence of the AD1600 eruption of Huaynaputina, Peru, *Nature, 393*, 455-457, 1998.

Dixon, J.E., D.A. Clague, and E.M. Stolper, Degassing history of water, sulfur, and carbon in submarine lavas from Kilauea volcano, Hawaii, *J. Geol., 99*, 371-394, 1991.

Dixon, J.E., E.M. Stolper, and J.R. Holloway, An experimental study of water and carbon dioxide solubilities in Mid-Ocean Ridge basaltic liquids. Part I. Calibration and solubility models, *J. Petrol., 36*, 1607-1631, 1995.

Eichelberger, J.C., C.R. Carrigan, H. Westrich, and R.H. Price, Non-explosive silicic volcanism, *Nature, 323*, 598-602, 1986.

Eldholm, O., and M.F. Coffin, Large igneous provinces and plate tectonics, In M.A. Richards, R.G. Gordon, and R.D. Van der Hilst (eds.) *The history and dynamics of global plate motions*, pp 309-326, *Geophys. Monogr. 21*, 2000.

Fierstein, J., and M. Nathensen, Another look at the calculation of fallout tephra volumes, *Bull. Volcanol., 54*, 156-167, 1992.

Foden, J.D., The petrology of the calcalkaline lavas of Rindjani Volcano, East Sunda arc: a model for island arc petrogenesis. *J. Petrol. 24*, 98-130, 1982.

Fogel, R.A., and M.J. Rutherford, The solubility of carbon dioxide in rhyolitic melts: a quantitative FTIR study. *Am. Mineral., 75*, 1311-1326, 1990.

Gardner, J.E., P.W. Layer, and M.J. Rutherford. Phenocrysts versus xenocrysts in the youngest Toba tuff: implications for the petrogenesis of 2800 km^3 of magma. *Geology, 30*, 347-350, 2002.

Gerlach, T.M. Oxygen buffering of Kilauea volcanic gases and the oxygen fugacity of Kilauea basalt. *Geochim. Cosmochim. Acta, 57*, 795-814, 1993.

Gerlach, T.M., Exsolution of H_2O, CO_2, and S during eruptive episodes at Kilauea volcano, Hawaii, *J. Geophys. Res., 91*, 12177-12185, 1986.

Gerlach, T.M., and K.A. McGee, Total sulfur dioxide emissions and pre-eruption vapor-saturated magma at Mount St. Helens, 1980-88, *Geophys. Res. Lett., 21*, 2833-2836, 1994.

Gerlach, T.M., H.R. Westrich, T.J. Casadevall, and D.L. Finnegan, Vapor saturation and accumulation in magmas of the 1989-1990 eruption of Redoubt volcano, Alaska, *J. Volcanol. Geotherm., Res. 62*, 317-337, 1994.

Gerlach, T.M., H.R. Westrich, and R.B Symonds, Pre-eruption vapor in magma of the climactic Mount Pinatubo eruption: Source of the giant stratospheric sulfur dioxide cloud, in C.G. Newhall and R. Punongbayan (eds.) *Fire and Mud: Eruptions and Lahars of Mount Pinatubo*, pp. 415-434, Univ. of Wash. Press, Seattle, 1996.

Ghiorso, M.S., and R.O. Sack, Fe-Ti oxide geothermometry: Thermodynamic formulation and the estimation of intensive variables in silicic magmas, *Contrib. Mineral. Petrol., 108*, 485-510, 1991.

Gilbert, J.S. and S.J. Lane, The origin of accretionary lapilli, *Bull. Volcanol., 56*, 398-411, 1994.

Graf, H.F., B., Langmann, and J. Feitcher, The contribution of Earth degassing to the atmospheric sulfur budget, *Chem. Geol., 147*, 131-145, 1998.

Hammer, C.U., H.B. Clausen, and W. Dansgaard, Greenland ice sheet evidence of post-glacial volcanism and its climatic impact, *Nature, 288*, 230-235, 1980.

Hansen, J., A. Lacis, R. Ruedy, and M. Sato, Global surface temperature in 1995: Return to pre-Pinatubo level, *Geophys. Res. Lett., 23*, 1665-1668, 1996.

Harms, E., and H.U. Schmincke, Volatile composition of the phonolitic Laacher See magma (12,900 yr BP): implications for syn-eruptive degassing of S, F, Cl and H_2O. *Contrib. Mineral. Petrol., 138*, 84-98, 2000.

Haughton, D.R., P.L. Roeder, and B.J. Skinner, Solubility of sulfur in mafic magmas, *Econ. Geol., 69*, 451-467, 1974.

Hauri, E.H., J.Wang, J.E. Dixon, P.L. King, C. Mandeville, S. Newman. SIMS analysis of volatiles in silicate glasses; 1, Calibration, matrix effects and comparisons with FTIR. In, E.H. Hauri, A.J.R. Adam, and N. Arndt (eds.) Melt inclusions at the millennium; toward a deeper understanding of magmatic processes, *Chem. Geol., 183*, 99114, 2002.

Hildreth, W., The compositionally zoned eruption of 1912 in the Valley of Ten Thousand Smokes, Katmai National Park, Alaska, *J. Volcanol. Geotherm. Res., 18*, 1-56, 1983.

Hildreth, W., R.B. Christiansen, and J.R. O'Neil. Catastrophic modification of rhyolitic magma at time of caldera subsidence, Yellowstone plateau volcanic field, *J. Geophys. Res. 89*, 8339-8369, 1984.

Holaseck, R.E., S. Self, A.W. Woods, Satellite observations and interpretation of the 1991 Mount Pinatubo eruption plumes. *J. Geophys. Res., 101*, 27635-27655, 1996.

Holtz, F., H. Behrens, D.B. Dingwell, and R.P. Taylor, Water solubility in aluminosilicate melts of haplogranite composition at 2 kbar, *Chem. Geol., 96*, 289-302, 1992.

Holtz, F., H. Behrens, D.B. Dingwell, and W. Johannes, H_2O solubility in haplogranitic melts: compositional, pressure, and temperature dependence, *Am. Mineral., 80*, 94-108, 1995.

Horn, S., and H.U. Schmincke, Volatile emission during the eruption of Baitoushan volcano (China/North Korea) ca. 969 AD. *Bull. Volcanol., 61*, 537-555, 2000.

Huebner, J.S. and M. Sato. The oxygen fugacity-temperature relationships of manganese oxide and nickel oxide buffers. *Am. Mineral., 55*, 934-952, 1970.

Huppert, H.E., and R.J.S. Sparks. The generation of granitic magmas by intrusion of basalt into continental crust. *J. Petrol. 29*, 599-624, 1988.

Ihinger, P.D, R.L. Hervig, and P.F. McMillan. Analytical methods for volatiles in glasses. In: Carroll MR, Holloway JR (eds) *Volatiles in magmas*, vol 30, Min. Soc. Am, Rev. Mineral., pp 67-121, 1994.

Katsura, T., and S. Nagashima, Solubility of sulfur in some magmas at 1 atmosphere. *Geochim. Cosmochim. Acta, 38*, 517-531, 1974.

Jaupart, C. and C.J. Allègre. Gas content, eruption rate and instabilities of eruption regime in silicic volcanoes. *Earth Planet. Sci. Lett.*, 102, 413-429, 1991.

Kazahaya, K. H. Shinohara and G. Saito. Excessive degassing of Izu-Oshima Volcano; magma convection in a conduit. *Bull. Volcanol., 56*, 207-216. 1994.

Keppler, H., Experimental evidence for the source of excess sulfur in explosive volcanic eruptions, *Science, 284,* 1652-1654, 1999.

Kovalenko, V.I., R.L. Hervig, and M.F. Sheridan. Ion-probe analyses of trace elements in anorthoclase, hedenbergite, aenigmatite, quartz, apatite and glass in pantellerite: evidence for high water content in pantellerite melts. *Am. Miner., 73,* 1038-1045, 1988.

Kress, V., Magma mixing as a source for Pinatubo sulfur, *Nature, 389,* 591-593, 1997.

Krueger, A.J., Sighting of El Chichón sulfur dioxide clouds with the Nimbus 7 total ozone mapping spectrometer, *Science, 220,* 1377-1378, 1983.

Krueger, A.J., L.S. Walter, P.K. Bhartia, C.C. Schnetzler, N.A. Krotkov, I. Sprod, and G.J.S. Bluth, Volcanic sulfur dioxide measurements from the total ozone mapping spectrometer instruments, *J. Geophys. Res., 100,* 14057-14076, 1995.

Krueger, A.J., C.C. Schnetzler, and L.S. Walter, The December 1981 eruption of Nyamuragira volcano (Zaire), and the origin of the "mystery cloud" of early 1982, *J. Geophys. Res., 101,* 15191-15196, 1996.

Krueger, A.J., C.C. Schnetzler, L.S. Walter, and S. D. Doiron, TOMS measurement of the sulfur dioxide emitted during the 1985 Nevado del Ruiz eruptions, *J. Volcano. Geotherm. Res., 41,* 7-15, 1990.

Le Bas, M.J., R.W. Le Maitre, A. Streckeisen, and B. Zanettin, A chemical classification of volcanic rocks based on the total alkali-silica diagram. *J. Petrol., 27,* 745-750, 1986.

Legrand, M., and R.J. Delmas, A 220-year continuous record of volcanic H_2SO_4 in the Antarctic ice sheet, *Nature, 327,* 671-676, 1987.

Lowenstern, J. and G. Mahood. New data on magmatic H_2O contents of pantellerites, with implications for petrogenesis and eruptive dynamics at Pantelleria. *Bull. Volc., 38,* 498-505, 1991.

Luhr, J.F., Experimental phase relations of water- and sulfur-saturated arc magmas and the 1982 eruptions of El Chichón volcano, *J. Petrol., 31,* 1071-1114, 1990.

Luhr, J.F., Volcanic shade causes cooling, *Nature, 354,* 104-105, 1991.

Luhr, J.F., Glass inclusions and melt volatile contents at Paricutin volcano, Mexico. *Contrib. Mineral. Petrol., 142,* 261-283, 2001.

Luhr, J.F., I.S.E. Carmichael, and J.C. Varekamp, The 1982 eruptions of El Chichón volcano, Chiapas, Mexico: Mineralogy and petrology of the anhydrite-bearing pumices, *J. Volcanol. Geotherm. Res., 23,* 69-108, 1984.

Luhr, J.F. and Logan, M.A.V., Sulfur isotope systematics of the 1982 El Chichón trachyandesite: An ion microprobe study. *Geochim. Cosmochim. Acta, 66,* 3303-3316, 2002.

Mandeville, C.W., S. Carey, and H. Sigurdsson, Magma mixing, fractional crystallization and volatile degassing during the 1883 eruption of Krakatau volcano, Indonesia, *J. Volcanol. Geotherm. Res., 74,* 243-274, 1996.

Marsh, B.D., On the crystallinity, probability of occurrence, and rheology of lava and magma, *Contrib. Mineral. Petrol., 78,* 85-98, 1981.

Martel, C., Pichavant, M., Bourdier, J.L, Traineau, H., Holtz, F. & Scaillet, B. Magma storage conditions and control of eruption

regime in silicic volcanoes: experimental evidence from Mt. Pelée, *Earth Planet. Sci. Lett. 156,* 89-99, 1998

Matthews, S.J., R.S.J. Sparks, and M.C. Gardeweg, The Piedras Grandes-Soncor eruptions, Lascar volcano, Chile; evolution of a zoned magma chamber in the Central Andean upper crust, *J. Petrol., 40,* 1891-1919, 1999.

Mavrogenes, J.A., and H.St.C. O'Neil, The relative effects of pressure, temperature and oxygen fugacity on the solubility of sulfide in mafic magmas. *Geochim. Cosmochim. Acta, 63,* 1173-1180, 1999.

McBirney, A.R., Igneous petrology, San Fransisco, Freeman, Cooper, 504 pp., 1984.

Métrich, N., and R. Clocchiatti, Sulfur abundance and its speciation in oxidized alkaline melts, *Geochim. Cosmochim. Acta, 60,* 4151-4160, 1996.

Métrich, N., R. Clocchiatti, M. Mosbah, and M. Chaussidon, The 1989-1990 activity of Etna: magma mingling and ascent of H_2O-Cl-S rich basaltic magma. Evidence from melt inclusions. *J. Volcanol. Geotherm. Res., 59,* 131-144, 1993.

Métrich, N., H. Sigurdsson, P.S. Meyer, and J. Devine, The 1783 Lakagigar eruption in Iceland: geochemistry, CO_2 and sulfur degassing, *Contrib. Mineral. Petrol., 107,* 435-447 1991.

Michaud, V., R. Clocchiatti, and S. Sbrana. The Minoan and post-Minoan eruptions, Santorini (Greece), in the light of melt inclusions: chlorine and sulphur behaviour. *J. Volcanol. Geotherm. Res., 99,* 195-214, 2000.

Moore G.M., T. Vennemann, and I.S.E. Carmichael. An empirical model for the solubility of water in magmas to 3 kilobars, *Am. Min., 83,* 36-42, 1998.

Nagashima, S., and T. Katsura. The solubility of sulfur in Na_2O-SiO_2 melts under various oxygen partial pressures. *Chem. Soc. Jap. Bull., 46,* 3099-3103, 1973.

Newman, S. and J.B. Lowenstern. VOLATILECALC : a silicate-melt-H_2O-CO_2 solution model written in Visual Basic for excel. *Comp. Geosci., 28,* 597-604, 2002.

Nye, C.J., S.E. Swanson, V.F. Avery, and T.P. Miller, Geochemistry of the 1989-1990 eruption of Redoubt volcano: Part I. Whole-rock major and trace-element chemistry. *J. Volcanol. Geotherm. Res., 62,* 429-452, 1994.

Palais, J. M., and H. Sigurdsson, Petrologic evidence of volatile emissions from major historic and pre-historic volcanic eruptions, in A.L. Berger, R.E. Dickinson, and J. Kidson (eds.) *Understanding Climate Change, Geophys. Monog. Ser.* vol. 52, pp. 31-53, AGU, Washington, D.C., 1989.

Peng, G., J.F. Luhr, and J.J. McGee, Factors controlling sulfur concentrations in volcanic apatite. *Am. Mineral.* 82: 1210-1224, 1997.

Pyle, D.M., The thickness, volume and grainsize of tephra fall deposits, *Bull. Volcanol., 51,* 1-15, 1989.

Pyle, D.M., Assessment of the minimum volume of tephra fall deposits. *J. Volcanol. Geotherm. Res. 69,* 379-382, 1995.

Rampino, M. R., and S. Self, Volcanic winter and accelerated glaciation following the Toba super-eruption, *Nature, 359,* 50-52, 1992.

Rampino, M.R., S. Self, and R.B. Stothers, Volcanic winters, *Ann. Rev. Earth Planet. Sci., 16,* 73-99, 1988.

Robock, A. Volcanic eruptions and climate. *Rev. Geophys., 38*, 191-219, 2000.

Roggensack, K, Unraveling the 1974 eruption of Fuego volcano (Guatemala) with small crystals and their young melt inclusions. *Geology, 29*, 911-914, 2001.

Roggensack, K., R.L. Hervig, S.B. McKnight, and S.N. Williams, Explosive basaltic volcanims from Cerro Negro volcano: influence of volatiles on eruptive style, *Science, 277*, 1639-1642, 1997.

Rose, W.I. Scavenging of volcanic aerosol by ash: atmospheric and volcanological implications. *Geology, 5*, 621-624, 1977.

Rose, W. I., Santa María, Guatemala: Bimodal, soda-rich calc-alkalic stratovolcano, *J. Volcanol. Geotherm. Res., 33*, 109-129, 1987.

Rose, W. I., R.E. Stoiber, and L.L. Malinconico. Eruptive gas compositions and fluxes of explosive volcanoes: budget of S and Cl emitted from Fuego volcano, Guatemala. In R.S. Thorpe (ed.), *Andesites*, pp 669-676, Wiley, 1982.

Rutherford, M. J., H. Sigurdsson, and S. Carey, The May 18, 1980, eruption of Mount St. Helens, 1. Melt compositions and experimental phase equilibria, *J. Geophys. Res., 90*, 2929-2947, 1985.

Rutherford, M.J., and J. Devine, Pre-eruption pressure-temperature conditions and volatiles in the 1991 dacitic magma of Mount Pinatubo, in C. Newhall and R. Punongbayan (eds.) *Fire and Mud: Eruptions and Lahars of Mount Pinatubo*, pp.751-766, Univ. of Wash. Press, Seattle, 1996.

Saito, G., K. Kazahaya, H. Shinohara, J. Stimac, and Y Kawanabe, Variation of volatile concentration in a magma system of Satsuma-Iwojima volcano deduced from melt inclusion analyses. *J. Volcanol. Geotherm. Res., 108*, 11-31, 2001.

Sansone, F.J., C.R. Benitez-Nelson, E.H. DeCarlo, S.M. Vink, J.A. Heath, B.J. Huebert, and J.A. Resing, Geochemistry of atmospheric aerosols generated from lava-seawater interactions, *Geophys. Res. Lett., 29*, 49, 2002.

Scaillet, B., F. Holtz, and M. Pichavant, Phase equilibrium constraints on the viscosity of silicic magmas 1. Volcanic-plutonic comparison, *J. Geophys. Res., 103*, 27257-27266, 1998a.

Scaillet, B., B. Clemente, B.W. Evans, and M. Pichavant. Redox control of sulfur degassing in silicic magmas. *J. Geophys. Res., 103*, 23937-23949, 1998b.

Scaillet, B., and B.W. Evans, The June 15, 1991 eruption of Mount Pinatubo, I, Phase equilibria and pre-eruption P-T-fO$_2$-fH$_2$O conditions of the dacite magma, *J. Petrol., 40*, 381-411, 1999.

Scaillet, B., and R. Macdonald, Phase relations of peralkaline silicic magmas and petrogenetic implications, *J. Petrol., 42*, 825-845, 2001.

Scaillet, B., Pichavant, M. and Clemente, B. A general model of sulfur solubility in silicate melts, basaltic to silicic, dry to wet: application to degassing processes of Lesser Antilles arc magmas. Mount Pelée 1902-2002. *Explosive volcanism in subduction zones, 47*, 2002.

Scaillet, B., and M. Pichavant. Experimental constraints on volatile abundances in arc magmas and their implications for degassing processes, in C. Oppenheimer, D.M. Pyle, and J. Barclay, (eds.) *Volcanic Degassing, Geol. Soc. Spec. Pub., 213*, 23-52, 2003.

Schnetzler, C.C., G.J.S. Bluth, A.J. Krueger, and L.S. Walter, A proposed volcanic sulfur index (VSI), *J. Geophys. Res., 102*, 20087-20091, 1997.

Schmidt, M., and S. Poli, Experimentally based water budget for dehydration slabs and consequences for arc magma generation. *Earth Planet. Sci. Lett., 161*, 361-379, 1998.

Scott, W.E., R.P. Hoblitt, R.C. Torres, S. Self, M.L. Martinez, and T. Nillos Jr., Pyroclastic flows of the June 15, 1991, climactic eruption of Mount Pinatubo, in C.G. Newhall and R.S. Punongbayan (eds.) *Fire and Mud: Eruptions and Lahars of Mount Pinatubo, Philippines*, pp 545-570, Univ. of Wash. Press, Seattle, 1996.

Self, S., and A.J. King, Petrology and sulfur and chlorine emissions of the 1963 eruption of Gunung Agung, Bali, Indonesia, *Bull. Volcanol., 58*, 263-285, 1996.

Shaw, H., Viscosities of magmatic silicate liquids: an emprirical method of prediction, *Am. J. Sci., 272*, 870-893, 1972.

Sigurdsson, H., *Encyclopedia of Volcanoes*, Academic Press, 1417 pp., 2000

Sigurdsson, H., S. Carey, and J. Devine, Assessment of the mass, dynamics, and environmental effects of the Minoan eruption of Santorinin volcano. In Hardy, D.A. (ed.) *Thera and the Agean world II*. The Thera Foundation, London, 101-108, 1990a.

Sigurdsson, H., S. Carey, J.M. Palais, and J. Devine, Pre-eruption compositional gradients and mixing of andesite and dacite erupted from Nevado del Ruiz volcano, Colombia in 1985, *J. Volcanol. Geotherm. Res., 42*, 127-151, 1990b.

Simkin, T., R.I. Tilling, J.N. Taggart, W.J. Jones, and H. Spall, This Dynamic Planet, 1 x 1.5 m wall map, 2nd edition, *SI and USGS*, 1994.

Sisson, T.W., and G.D. Layne, H$_2$O in basalt and basaltic andesite glass inclusions from four subduction-related volcanoes, *Earth Planet. Sci. Lett., 117*, 619-635, 1993.

Sisson, T.W., and S. Bronto, Evidence for pressure-release melting beneath magmatic arcs from basalt at Galunggung, Indonesia, *Nature, 391*, 883-886, 1998.

Smith, D.B., R.A. Zielinski, H.E. Taylor, M.B. Sawyer. Leaching characteristics of ash from the May 18, 1980, eruption of Mount St. Helens volcano, Washington. *Bull. Volcanol., 46*, 103-124, 1983.

Sparks, R.J.S., Bursik, M.I., Carey, S.N., Gilbert, J.S., Glaze, L.S., Sigurdsson, H. and Woods, A.W., *Volcanic plumes*, Wiley, 574 pp, 1997.

Stoiber, R.E., S.N. Williams, Huebert, B., Annual contribution of sulfur dioxide to the atmosphere by volcanoes, *J. Volcanol. Geotherm. Res., 33*, 1-8, 1987.

Symmonds, R.B., W.I. Rose, G.J.S. Bluth, and T.M. Gerlach, Volcanic-gas studies: Methods, results, and applications, in M.R. Carroll and J.R. Holloway (eds.), *Volatiles in Magmas, Rev. Mineral.*, vol. 30, pp. 1-66, Am. Mineral. Soc., Washington, D.C., 1994.

Tabazadeh, A., and R.P. Turco, Stratospheric injection by volcanic eruptions: HCl scavenging and implications for ozone, *Science, 260*, 1082-1086, 1993.

Tait, S., C. Jaupart, and S. Vergniolle, Pressure, gas content and eruption periodicity of a shallow crystallizing magma chamber. *Earth Planet. Sci. Lett., 92*, 107-123, 1989.

Taylor, P.S., and R.E. Stoiber, Soluble material on ash from active Central American volcanoes, *Geol. Soc. Am. Bull., 84*, 1031-1042, 1973.

Thordarson, Th., S. Self, N. Oskarsson, T. Hulsebosch, Sulfur, chlorine, and fluorine degassing and atmospheric loading by the 1783-1784 AD Laki (Skaftar fires) eruption in Iceland. *Bull. Volcanol., 58*, 205-225, 1996.

Thordarson, Th., D.J. Miller, G. Larsen, S. Self, and H. Sigurdsson, New estimates of sulfur degassing and atmospheric mass-loading by the 934 AD Eldgja eruption, Iceland. *J. Volcanol. Geotherm. Res., 108*, 33-54, 2001.

Thouret, J.C., Juvigné, E., A. Gourgaud, P. Boivin, and J. Davila. Reconstruction of the AD 1600 Huaynaputina eruption based on the correlation of geologic evidence with early Spanish chronicles, *J. Volcanol. Geotherm. Res., 243*, 1-43, 2002.

Toulmin, P., III, and P.R. Barton, Jr., A thermodynamic study of pyrite and pyrrhotite. *Geochim. Cosmochim. Acta, 28*, 641-671, 1964.

Varekamp, J.C., J.F. Luhr, and K.L. Prestegaard, The 1982 eruptions of El Chichón volcano (Chiapas, Mexico): Character of the eruptions, ash-fall deposits, and gasphase, *J. Volcanol. Geotherm. Res., 23*, 39-68, 1984.

Vergniolle, S., and C. Jaupart, Separated two-phase flow in basaltic eruptions. *J. Geophys. Res., 91*, 12840-12860, 1986.

Walker, G.P.L., The Taupo pumice: product of the most powerful known (Ultraplinian) eruption?, *J. Volcanol. Geotherm. Res., 8*, 69-94, 1980.

Walker, G.P.L., Plinian eruptions and their products, *Bull. Volcanol, 44*, 223-240, 1981.

Wallace, P.J., Volcanic SO$_2$ emissions and the abundance and distribution of exsolved gas in magma bodies. *J. Volcanol. Geotherm. Res., 108*, 85-106, 2001.

Wallace, P.J., and A.T. Anderson, Volatiles in magmas, in H. Sigurdsson (ed.), *Encyclopedia of Volcanoes*, pp, 149-170, Academic Press, 2000.

Wallace, P.J., and I.S.E. Carmichael, Sulfur in basaltic magmas. *Geochim. Cosmochim. Acta, 56*, 1863-1874, 1992

Wallace, P.J., and I.S.E. Carmichael, S speciation in submarine basaltic glasses as determined by measurements of SKa X-ray wavelength shifts, *Am. Mineral., 79*, 161-167, 1994.

Wallace, P.J., and T.M. Gerlach, Magmatic vapor source for sulfur dioxide released during volcanic eruptions: Evidence from Mount Pinatubo, *Science, 265*, 497-499, 1994.

Wallace, P.J., A.T. Anderson, and A.M. Davis, Quantification of pre-eruptive exsolved gas contents in silicic magmas, *Nature, 377*, 612-615, 1995.

Watson, E.B., Diffusion in volatile-bearing magmas, in M.R. Carroll and J.R. Holloway (eds.) *Volatiles in Magmas, Rev. Mineral.*, vol. 30, pp. 371-411, Am. Mineral. Soc., Washington, D.C., 1994.

Westrich, H.R., and T.M. Gerlach, Magmatic gas source for the stratospheric SO$_2$ cloud from the June 15, 1991, eruption of Mount Pinatubo, *Geology , 20*, 867-870, 1992.

Westrich, H.R., J.C. Eichelberger, and R.L. Hervig, Degassing of the 1912 Katmai magmas, *Geophys. Res. Lett., 18*, 1561-1564, 1991.

Whitney, J.A., Fugacities of sulphurous gases in pyrrhotite-bearing silicic magmas, *Am. Mineral., 69*, 69-78, 1984

Wignall, P.B. Large igneous provinces and mass extinctions. *Earth Sci. Rev.*, 53, 1-33, 2001.

Williams, S.T., N.C. Sturchio, M.L. Calvache, F. Ricardo Mendez, C. Adela Londoño, and P. Nestor Garcia, Sulfur dioxide from Nevado del Ruiz volcano, Colombia: Total flux and isotopic constraints on its origin, *J. Volcanol. Geotherm. Res., 42*, 53-68, 1990.

Wilson, L., and G.P.L. Walker, Explosive volcanic eruptions - VI. Ejecta dispersal in Plinian eruptions: the control of eruption conditions and atmospheric properties. *Geophys. J. Roy. Astron. Soc., 89*, 657-679, 1987.

Woods, A.W. Moist convection and the injection of volcanic ash into the atmosphere. *J. Geophys. Res.* 98, 17627-17636, 1993.

Woods, A. W. The dynamics of explosive eruptions. *Rev. Geophys.* 33, 495-530, 1995.

Zielinski, G. A., Stratospheric loading and optical depth estimates of explosive volcanism over the last 2100 years derived from the Greenland Ice Sheet Project 2 ice core, *J. Geophy. Res., 100*, 20937-20955, 1995.

Zielinski, G. A., P.A. Mayewski, L.D. Meeker, S. Whitlow, M.S. Twickler, M. Morrison, D.A. Meese, A.J. Gow, and R.B. Alley, Record of volcanism since 7000 B.C. from the GISP2 Greenland Ice Core and implications for the volcano-climate system, *Science, 264*, 948-952, 1994.

Zielinski, G.A., P.A. Mayewski, L.D. Meeker, S. Whitlow, M.S. Twickler, and K. Taylor, Potential atmospheric impact of the Toba mega-eruption 71,000 years ago, *Geophys. Res. Lett., 23*, 837-840, 1996a.

Zielinski, G.A., P.A. Mayewski, L.D. Meeker, S. Whitlow, and M.S. Twickler, A 110000-yr record of explosive volcanism from the GISP2 (Greenland) ice core, *Quat. Res., 45*, 109-118, 1996b.

Zhang, Y. H$_2$O in rhyolitic glasses and melts: measurement, speciation, solubility, and diffusion, *Rev. Geophys., 37*, 493-516, 1999.

B. Scaillet, ISTO-CNRS, UMR 6113, 1a rue de la Férollerie, 45071, Orléans cedex 2, France (email : bscaille@cnrs-orleans.fr)

J.F. Luhr, Department of Mineral Sciences, NHB-119, Smithsonian Institution, Washington, D.C. 20560, U.S.A. (email : luhr@volcano.si.edu)

M.C. Carroll, Dipartimento di Scienze della Terra, Via Gentile III da Varano, Universita' di Camerino, 62032, Camerino, Italy (email : michael.carroll@unicam.it)

Degassing of Trace Volatile Metals During the 2001 Eruption of Etna

Alessandro Aiuppa, Gaetano Dongarrà, and Mariano Valenza

Dipartimento CFTA, Università di Palermo, Italy

Cinzia Federico and Giovannella Pecoraino

Istituto Nazionale di Geofisica e Vulcanologia-Sezione di Palermo, Italy

This paper provides new data on sulfur, halogens, and minor and trace metal contents in airborne particulate matter from the Mt. Etna volcanic plume. Aerosol samples were collected by conventional filtration techniques before and during the summer 2001 eruption, in order to investigate relations between plume chemistry and volcano dynamics. Data analysis reveals that abundances of trace metals in the plume result from mixing of erosive and volatile components. The former is responsible for the contents of rare earth elements (REE), Ca, Ba, Sr, Ti, Sc, Y, Hf and Th; the latter contributes significantly to the abundance of Cs, Rb, Na and K, probably transported in the plume as metal halides, and Cd, Pb, Zn, Ge, Te, Mo, Re, Se, Sb, Sn, In, Bi, Tl, Cu and Au, associated with sulfur in plume particles. Enrichment factors show that plume particulate matter from the Monti Carcarazzi vent, which opened on the southern flank of the volcano in July 2001, is typically depleted in volatile trace elements with respect to the output from the summit crater, suggesting the "secondary" nature of the outpouring lavas. The decreasing trend observed throughout the eruption in the enrichment factors of most trace metals probably indicates a small-volume batch of magma with limited feed from depth.

1. INTRODUCTION

Increasing evidence has been given for the significant contribution of volcanic emissions to the natural atmospheric cycling of trace elements. Pioneering studies on condensates [*Stoiber and Rose*, 1970; *Menyailov and Nikitina*, 1980; *Gemmel*, 1987], incrustations and sublimates [*Stoiber and Rose*, 1974; *Oskarsson*, 1981; *Le Guern and Bernard*, 1982] and aerosols [*Cadle et al.*, 1973; *Mroz and Zoeller*, 1975; *Lepel et al.*, 1978; *Buat-Ménard and Arnold*, 1978]

have revealed the significant transport of volatile trace elements in the volcanic environment. Experimental works [*Webster and Halloway*, 1980; *Shinohara et al.*, 1989; *Webster et al.*, 1989] and thermodynamic modeling have suggested that the formation of stable complexes with the hard ligands Cl, F and S may be responsible for the high concentrations of volatile trace metals observed in volcanic plumes [*Symonds et al.*, 1987, 1992; *Quisefit et al.*, 1989; *Symonds and Reed*, 1993]. Upon cooling at surface conditions, trace metals are partly deposited as sublimates and incrustations [*Le Guern*, 1988; *Quisefit et al.*, 1989] or dispersed in the atmosphere as sub-micron sized aerosols in volcanic plumes [*Mroz and Zoeller*, 1975; *Buat-Ménard and Arnold*, 1978; *Lepel et al.*, 1978; *Phelan-Kotra et al.*, 1982, 1983; *Olmez et al.*, 1986; *Rose et al.*, 1986; *Crowe et*

al., 1987; Le Cloarec et al., 1992; Zreda-Gostynska et al., 1997; Gauthier and Le Cloarec, 1998; Hinkley et al., 1999; Allard et al., 2000].

Many studies have been carried out on Mount Etna because of the persistent activity of this volcano, characterized by voluminous release of magmatic volatiles, during both quiescent and eruptive phases. Persistent plume emissions at the summit craters are due to open conduit degassing of alkali basalt-hawaiite rising from a shallow mantle diapir [Sharp et al., 1980; Hirn et al., 1997]. This makes Etna the strongest volcanic emitter on Earth [Buat-Ménard and Arnold, 1978; Allard et al., 1991, 1997; Francis et al., 1995; Gauthier and Le Cloarec, 1998].

Concentrations and fluxes of trace metals from the Etna plume were first documented by Buat-Ménard and Arnold [1978]. Since then, several investigations have been carried out [Quisefit et al., 1982, 1983, 1988; Vié Le Sage, 1983; Bergametti et al., 1984; Varekamp et al., 1986; Pennisi et al., 1988; Andres et al., 1993; Toutain et al., 1995; Gauthier and Le Cloarec, 1998]. Quisefit et al. [1983] and Vié Le Sage [1983] examined the partitioning of metal-rich particles among differing granulometric classes, and concluded that volatile metals are preferentially enriched in the finest ($d<0.5$ μm) size fractions. Quisefit et al. [1988] emphasized that the relative abundances of K and Zn in the plume may be accurately described by two-component mixing between wall rock erosion and gaseous sources. They also showed that the proportion of the two contributions is highly variable in time and closely related to volcanic activity. Varekamp et al. [1986], Andres et al. [1993] and Toutain et al. [1995] provided insights on the mineralogical composition of airborne particles and volatile transport mechanisms. Several studies regarding the content of radionuclides in Etna's plume emissions [Lambert et al., 1986; Le Cloarec et al., 1988, Pennisi et al., 1988] allowed the construction of a degassing model, according to which gases released at the summit craters are exsolved from a shallow, small-volume magma chamber, periodically replenished by batches of non-degassed melts. A comprehensive characterization of trace metal emissions from Etna has recently been furnished by Gauthier and Le Cloarec [1998]. These authors estimated mean emission rates of metals for the period 1991–95, and also ranked trace metals according to their mean volatility using emanation coefficients. Their results indicate that chalcophile elements (elements with strong affinity for reduced sulfur; Se, Tl, Bi, Cd, Sn, Cu and many other) are the most enriched in Etna's plume.

Despite this huge mass of information, very few effort [Le Cloarec et al., 1988] has been spent in trying to establish the relationship, if any, between trace metal abundance in the plume and volcanic activity. This paper deals with the changes in trace element compositions occurring during the 2001 eruption of Etna. The peculiar dynamics and timing of this eruption allowed us to collect aerosol samples both at the summit craters (before the eruption) and at the eruptive fracture which opened on July 18 at an altitude of 2100 m on the southern flank of the volcano. Here, we discuss some of the main chemical processes controlling trace metal abundances in the plume, in order to relate the variations observed with the mechanisms of volcano dynamics and degassing.

2. MATERIALS AND METHODS

2.1. Study Area

Mt. Etna (Figure 1), on the eastern coast of Sicily, is a large (elevation, 3350 m a.s.l.; area, 1150 km^2) highly active alkali-basaltic volcano, which formed on tensional lithospheric faults cutting the eastern margin of the Apennine-Magrehebide chain [Barberi et al., 1974; Hirn et al., 1997; Monaco et al., 1997; Gvirtzman and Nur, 1999]. The volcano has been growing for 0.6 million years and consists of a lower shield unit overlain by a strato-volcano [Chester et al., 1985; Tanguy et al., 1997].

Etna is best known for its endless open-conduit activity [Allard et al., 1991]. Since the huge 1991–93 flank eruption [Villari, 1994], persistent activity has been confined to the summit craters, ranging from open-conduit passive degassing to sub-terminal lava effusions, strombolian and lava-fountain phases [La Volpe et al., 1999]. A progressive increase in activity occurred from late 1998 to 1999, with frequent paroxysmal episodes at the South-East Crater (SEC), often giving rise to lava flows [La Delfa et al., 2001].

The summer 2001 eruption of Mount Etna started on July 13, with the opening of a N-S trending 7-km long fracture field on the southern flank of the volcano (Figure 1). Lava started to pour out on July 17 from the uppermost sector of the fracture system and, later (July 18), from a fissure which opened at 2100 m between La Montagnola and Monti Silvestri (Monti Carcarazzi vent, MCV) (Figure 1). The lava emission rate from MCV underwent a significant increase after the opening, on July 19, of a new crater at Pian del Lago, 2550 m (Pian Del Lago vent, PLV) (Figure 1). Explosive activity at this newly formed vent produced considerable ashfallout on the eastern Sicilian coast; at the same time, lava issuing from MCV had reached an elevation of 1035 m by the end of July and threatened the village of Nicolosi on the upper southern slope of the volcano. After this, the eruption declined, ending on August 9. Based on

holder containing a Poelmann-Schneider cellulose filter (diameter 11 mm, porosity 0.2 μm) [*Le Cloarec et al.,* 1992]. The sampling device consisted of a battery-powered (12V) portable pump, connected in series with a flowmeter and a filter holder. Air was pumped at a controlled flow rate (80–140 l·min^{-1}) for 60 min, air volumes typically ranging from 6.0 to 8.1 m^3. Repeated measurements showed good reproducibility ($\pm$ 5%) of element ratios determined by filtration techniques, at least for sulfur and halogens [*Aiuppa et al.,* 2002]. Five samples were collected at Bocca Nuova (BNC) summit crater between May 2 and July 12. After the onset of the eruption, three samples were collected at MCV on July 19, July 25 and August 1. The BNC samples were collected at the inner crater rim; at MCV, sampling was carried out about 100 m downwind from the main effusive vent. On July 19, one aerosol sample from the degassed lava flow, at about 1 km from the eruptive vent, was also collected (site LF, sample ET 7; see Table 1 and Figure 1).

Absolute elemental concentrations were determined, after appropriate chemical preparation, by ion chromatography (S, Cl, F), instrumental neutron activation (INAA) and inductively coupled plasma mass spectrometry (ICP-MS). Particulate S, Cl and F deposited on the filter surface were eluted in a beaker containing 20 mL of double-distilled water and H_2O_2, and stirred for 24 hours. By the use of this procedure, only soluble phases (i.e., sulfates, halides) were leached, whereas S and halogens tied up on silicates were probably retained on the insoluble solid residua. Leacheates were analyzed for F$^-$, Cl$^-$ and SO$_4^{2-}$ by Ion Chromatography ($\pm$5%). INAA and ICP-MS analyses were performed at the Activation Laboratories Ltd. (Ontario, Canada). Prior to analysis by ICP-MS, particles deposited on filters were totally dissolved by HNO_3-HF-$HCLO_4$ acid mixture in a microwave oven. The quality assurance of measurements was tested by analyzing three reference materials (NIST 1547, NIST 1632B, LKSD-1); precision was estimated at $\pm$10% for most trace elements. The complete analytical results are listed in Table 1.

3. RESULTS

The sulfur, halide and trace metal contents in the sampled volcanic aerosols show great variability, with percentile variation coefficients (100·standard deviation/mean) ranging from 35% to 210%. This broad range of compositions is due to the erratic density of the plume, which in turn depended on distance from emission source, meteorological conditions (wind speed and direction, relative humidity) and erosive and volatile output at the craters. Total abundances in aerosols are also controlled by intensity and characteris-

tics of volcanic activity. For instance, one sampling survey was carried out on July 12, when a dark ash-laden plume rich in angular-shaped lithic fragments was emitted at the craters. This event, probably due to collapse of the magma column inside the summit conduits, accompanied dyke intrusion below the southern flank of the volcano and preluded the imminent onset of the eruption. The filter collected at BNC on that day (sample ET 5) was particularly burdened in silicate ash particles (visual observations showed it had a dark brown color), and displayed the highest contents of lithophile elements (i.e., Al, Ba, Ca, Mg, Ti, etc.; see below) upon later chemical analysis in the lab.

The most abundant species in particulate matter from the Etna plume were S, Cl, F and rock-forming elements such as Al, K, Na, Ca, Fe, Mg and Ti. Despite variability, the analyzed elements showed a fairly constant sequence when ranked according to their absolute concentrations.

The recovery of sulfur and halogens in aerosols stands for the general occurrence of homogeneous and heterogeneous chemical reactions taking place upon cooling in air of volatiles vented at the craters, including gas-to-particle conversion, HCl scavenging by liquid droplets and sulfur oxidation (e.g., from S(IV) in SO$_{2(g)}$ to S(VI) in SO$_4^{2-}$$_{(s)}$). Comparing the data reported in Table 1 with the sulfur and halide abundances in the gaseous phase [*Aiuppa et al.,* 2002], we infer that, on average, 6%, 4% and 7% of total S, Cl and F were transported in the particulate phase. Bromine was exclusively detected as particulate Br. S/Cl and Cl/F molar ratios in aerosols ranged from 0.9–2.7 and 0.9–2.8, respectively, and were consistent with S/Cl and Cl/F molar ratios in the gas phase (0.1–2.0 and 1.3–4.4; [*Aiuppa et al.,* 2002]), though exhibiting some preferential partitioning of S and F (with respect to Cl) in the condensed phase. It is also interesting to note that MCV and BNC samples have distinct geochemical signatures, the former displaying sulfur to chlorine (0.9–1.2) ratios systematically lower than those characteristic of crater emissions (2.0–2.7). Again, this is consistent with data on acidic gases [*Aiuppa et al.,* 2002]. The most noteworthy sulfur depletion (S/Cl = 0.09) was observed in the July 19 sample collected from the degassed lava flow (sample ET 7 in Table 1).

Previous investigations (e.g., *Gauthier and Le Cloarec,* [1998], and references therein) have shown that Si, Al, K, Na, Ca, Fe, Mg, Mn and Ti are the most abundant metals in the plume air. These elements, being in the range 1–600 μg·m^{-3}, are also the main constituents of Etna's volcanics (Table 1). Their abundances on filters is indicative of a significant contribution from fragments of volcanic glass and silicate minerals derived from the ash ejected during strombolian explosions and/or entrained by winds. It must be

Table 1. Concentration of S, Cl, F and trace elements in airborne particulate matter from Etna's summit and eruptive plumes. The mean metal abundances in lavas, computed from a compilation of literature and unpublished compositional data on recent Etna's volcanics [*Aiuppa, 1999*], are also listed, as long as the mean element weight ash fractions (WAF).

	ET 1	ET 2	ET 3	ET 4	ET 5	ET 6	ET 7	ET 8	ET 9	Mean lavas	WAF
sampling site	BNC	BNC	BNC	BNC	BNC	MCV	LF	MCV	MCV		
date	5/3	5/18	6/5	6/29	7/12	7/19	7/19	7/25	8/1		
time (m)	72	65	65	60	60	60	60	65	50		
flow rate ($l \cdot m^{-1}$)	150-40	132	150-8	150-94	130	130	130	130	130		
volume (m^3)	7.9	8.1	6	7.7	7.7	7.7	7.7	7.7	7.7		
	$\mu g \cdot m^{-3}$	$\mu g \cdot m^{-3}$	$\mu g \cdot m^{-3}$	$\mu g \cdot m^{-3}$	$\mu g \cdot m^{-3}$	$\mu g \cdot m^{-3}$	$\mu g \cdot m^{-3}$	$\mu g \cdot m^{-3}$	$\mu g \cdot m^{-3}$	$mg \cdot kg^{-1}$	%
F	24	29	113	41	23	77	95	41	9	700	4
Cl	67	144	373	161	114	226	219	66	22	2300	3
S	181	274	669	309	291	267	20	60	21	2800	3
Ag	0.0025	0.0083	0.0082	0.0038	0.0058	0.0092	0.0158	0.0030	0.0013	0.9	31
Al	274	253	364	384	593	285	306	228	250	96000	38
As	0.37	0.15	0.33	0.24	0.21	0.09	0.01	0.20	0.03	1	2
A u	0.00051	0.00156	0.00150	0.00195	0.00065	0.00117	0.00117	0.00062	0.00013	0.1	22
Ba	0.20	0.07	0.45	0.35	1.60	0.18	0.15	0.16	0.07	680	100
Bi	0.04	0.10	0.11	0.08	0.04	0.08	0.002	0.02	0.01	0.02	0.1
Br	11.04	3.48	3.33	3.29	1.35	2.60	1.77	0.62	0.32	4.5	0.4
Ca	48.7	32.1	84.5	52.3	177.9	49.0	39.0	36.2	35.6	74200	100
Cd	0.09	0.14	0.26	0.15	0.10	0.09	0.004	0.06	0.01	0.85	3
Ce	0.05	0.01	0.12	0.13	0.34	0.04	0.04	0.05	0.02	105	100
Co	0.29	0.13	0.20	0.21	0.23	0.12	0.14	0.10	0.12	29.5	23
Cr	0.27	0.14	0.12	<0.06	0.17	<0.06	<0.06	0.11	<0.06	32	36
Cs	0.01	0.03	0.04	0.02	0.02	0.03	0.03	0.01	0.003	0.8	8
Cu	1.53	8.6	4.1	2.3	2.4	8.9	5.3	1.4	0.78	90	6
Dy	0.00197	0.00046	0.00397	0.00519	0.01338	0.00140	0.00126	0.00070	0.00059	9	100
Er	0.00097	0.00026	0.00208	0.00262	0.00705	0.00076	0.00069	0.00031	0.00033	2.4	100
Eu	0.00119	0.00031	0.00265	0.00300	0.00935	0.00093	0.00079	0.00041	0.00038	2.4	100
Fe	17.4	4.6	21.3	51.0	102	11.3	8.9	6.8	4.7	77200	100
Ga	0.04	0.04	0.06	0.04	0.09	0.04	0.04	0.03	0.04	16	48
Gd	0.0044	0.0011	0.0091	0.0109	0.0305	0.0034	0.0029	0.0015	0.001	6.5	100
Ge	0.0025	0.0015	0.0070	0.0042	0.0034	0.0011	0.0004	0.0014	0.0003	1.6	100
Hf	0.0013	0.0004	0.0023	0.0025	0.0074	0.0008	0.0002	0.0003	0.0002	4.3	100
Hg	0.008	0.004	0.007	0.001	0.009	0.004	0.003	0.006	0.0032	0.04	3
Ho	0.00036	0.00009	0.00069	0.00088	0.0024	0.00027	0.00023	0.00012	0.00011	0.91	100
I	0.14	0.17	<0.08	0.08	0.18	<0.06	0.06	0.09	<0.06	0.8	0.43
In	0.006	0.021	0.027	0.028	0.018	0.012	<0.001	0.010	0.003	0.08	0.05
K	46.3	119.2	154.8	89.6	96.4	109.7	101.5	35.9	11.1	15400	35
La	0.03	0.01	0.06	0.07	0.19	0.02	0.02	0.01	0.01	72.5	100
Li	0.02	0.03	0.03	0.02	0.04	0.04	0.07	0.02	0.01	52.5	100
Lu	0.00013	0.00003	0.00023	0.00030	0.00085	0.00010	0.00007	0.00004	0.00004	0.31	100
Mg	16.4	8.6	23	24	64	13.3	11.5	10	10.2	30700	100
Mn	1.75	0.49	2.53	4.34	6.77	1.30	0.79	1.10	0.82	1000	74
Mo	0.03	0.02	0.06	0.08	0.03	0.01	0.005	0.01	0.00	3.7	33
Na	38.4	83	109.6	63.3	102.7	87.2	95.9	28.0	14.9	27100	67
Nb	0.012	0.003	0.026	0.029	0.108	0.010	0.008	0.003	0.003	60	100
Nd	0.020	0.005	0.048	0.055	0.153	0.017	0.015	0.007	0.007	50.7	100
Ni	0.087	0.011	0.054	0.068	0.184	0.036	0.017	0.044	0.011	54	100
Pb	0.39	0.44	0.80	0.58	0.40	0.46	0.26	0.29	0.10	8	3
Pr	0.0058	0.0014	0.0135	0.0149	0.0425	0.0045	0.0042	0.0020	0.0019	13.3	100
Pt	0.00003	0.00003	0.00004	0.00003	0.00017	0.00006	0.00003	0.00003	0.00003	0.0004	1
Rb	0.20	0.57	0.78	0.43	0.44	0.55	0.51	0.18	0.06	40.3	19
Re	0.0009	0.0022	0.0030	0.0068	0.0012	0.0016	0.0004	0.0007	0.0002	0.0004	0.1

Table 1. *(Continued)*

	ET 1	ET 2	ET 3	ET 4	ET 5	ET 6	ET 7	ET 8	ET 9	Mean lavas	WAF
	$\mu g \cdot m^{-3}$	$\mu g \cdot m^{-3}$	$\mu g \cdot m^{-3}$	$\mu g \cdot m^{-3}$	$\mu g \cdot m^{-3}$	$\mu g \cdot m^{-3}$	$\mu g \cdot m^{-3}$	$\mu g \cdot m^{-3}$	$\mu g \cdot m^{-3}$	$mg \cdot kg^{-1}$	%
Sb	3.32	0.35	0.48	11.04	1.47	0.08	0.01	0.05	0.01	0.12	0.2
Sc	0.03	0.01	0.03	0.05	0.09	0.01	0.01	0.01	0.01	20	100
Se	0.33	0.23	0.62	1.57	0.17	0.03	0.03	0.12	0.03	0.05	0.1
Si	45.9	32.2	78.3	35.4	42.0	31.4	20.5	26.6	18.3	490000	100
Sm	0.0047	0.0012	0.0102	0.0118	0.0331	0.0035	0.0031	0.0016	0.0015	9.2	100
Sn	0.0014	0.0013	0.0008	0.0100	0.0006	0.0006	0.0006	0.0006	0.0006	1.5	100
Sr	0.37	0.13	0.82	0.66	3.29	0.31	0.28	0.17	0.19	1270	100
Tb	0.0005	0.0001	0.0010	0.0012	0.0033	0.0004	0.0003	0.0002	0.0001	1	100
Te	0.0371	0.0089	0.0890	0.0655	0.0296	0.0053	0.0004	0.0104	0.0010	1.9	59
Th	0.0039	0.0013	0.0081	0.0096	0.0244	0.0030	0.0018	0.0015	0.0008	8.6	100
Ti	8.73	0.43	3.10	22.86	45.32	5.32	1.05	2.84	0.43	6300	100
Tl	0.18	0.63	0.49	0.43	0.20	0.56	0.27	0.14	0.07	0.09	0.1
Tm	0.0001	0.0001	0.0002	0.0003	0.0008	0.0001	0.0001	0.00001	0.00001	0.33	100
U	0.0038	0.0030	0.0059	0.0044	0.0102	0.0040	0.0035	0.0031	0.0031	2.5	73
V	0.16	0.02	0.28	0.91	0.99	0.05	0.13	0.01	0.06	305	100
W	0.0013	0.0009	0.0028	0.0023	0.0027	0.0009	0.0001	0.0009	0.0017	1	100
Y	0.0107	0.0029	0.0215	0.0291	0.0713	0.0084	0.0070	0.0039	0.0036	27.6	100
Yb	0.0008	0.0002	0.0017	0.0022	0.0060	0.0006	0.0005	0.0003	0.0003	1.3	100
Zn	0.62	0.83	1.19	0.72	0.99	0.91	0.27	0.43	0.30	110	23
Zr	0.07	0.02	0.12	0.14	0.44	0.05	0.01	0.02	0.01	210	100

noted, however, that elements like Se, Sb and Cd, present in magma as ultra-trace constituents (<0.1 mg·kg^{-1}), in volcanic aerosols exhibit absolute concentrations (~ 0.1–10 $\mu g \cdot m^{-3}$) which are considerably higher than those observed for minor crustal elements (i.e., Sc, Th and U: 2–20 mg·kg^{-1} in the magma; <0.01 $\mu g \cdot m^{-3}$ in particulate matter). This is a convincing indication that significant chemical fractionation between volatile and non-volatile (lithophile) elements takes place during magmatic degassing.

Multivariate statistical (cluster) analysis, performed in order to highlight similarities between individual elements, evidenced the existence of three distinct groups of clustering elements, likely sharing a similar geochemical behavior during processes of aerosol formation. One cluster (L in Figure 2) is characterized by the high correlations displayed by elements such as REE (rare earth elements), alkaline-earth elements (Ca, Ba, Sr), Al, Ti, Sc, Mn, U and Th. Due to lithophile nature of these elements—i.e., their tendency to concentrate in the rock phase rather than on fluid phases during shallow geochemical processes—this cluster likely represents suspended particles forming as a result of erosive processes. This is supported by the chondrite-normalized REE patterns shown in Figure 3a. REE, due to their coherent geochemical behavior (i.e., the fact they do not fractionate during most geological processes), are widely applied in geo-

chemistry as tracers of rock-forming processes and as provenance markers. It is common practice in geochemistry, in order to compare graphically REE abundances for different natural media, to normalize the concentration of individual REE in a sample to their abundance in chondritic meteorites, assumed to be primitive solar system material parental to the Earth (e.g., *Nakamura*, [1974]). The REE patterns for mean Etna hawaiite and aerosols are markedly parallel (Figure 3a), pointing to: i) the crustal derivation of REE, and ii) the lack of fractionations among REE during magmatic degassing. This is probably true for all the elements in cluster L.

Cluster H (halide-forming elements) includes Cl, F, Cs, Rb, Na and K. The significant correlations between alkalis and chlorine (Figure 2) suggest that the former are primarily non-crustal in origin and are transported in the plume as halides. This is further demonstrated in Figure 3b, showing chondrite-normalized abundances for some rock-forming elements. The aerosol samples exhibit a spike-shaped pattern, which indicates that alkalis are preferentially enriched in the plume with respect to low-volatile elements from cluster L (i.e., Th, Ba, Nb, Sr, Hf, Y). Clearly, an additional contribution, i.e., a gas-to-particle conversion process, is added to the ash component, to account for alkali contents in aerosols. This should also be partially true for aluminum (Figure 3b), which is also highly correlated with lithophile elements.
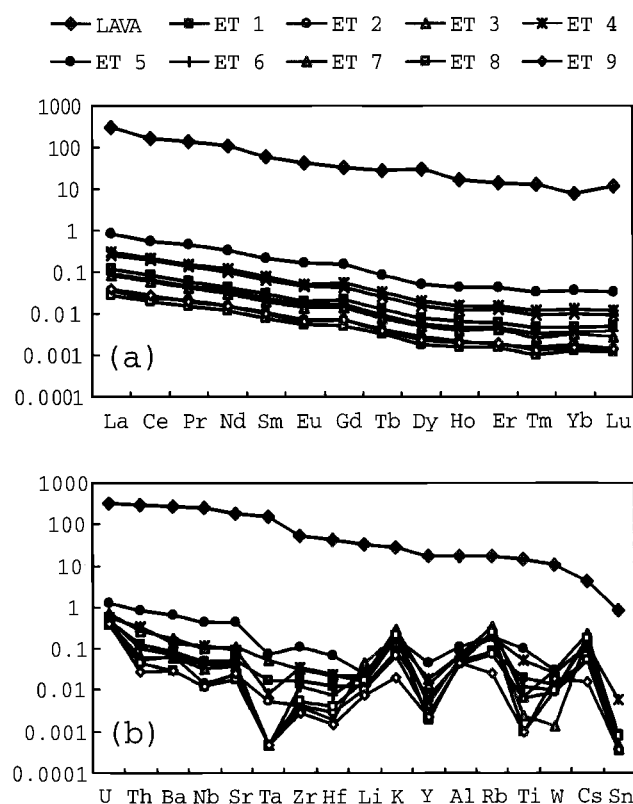
100

1

1

Figure 3. (a) REE chondrite-normalized patterns for mean Etna hawaiites and aerosol samples from this study. The chemical trends for lavas and airborne plume particles are markedly parallel, pointing to an erosive origin of REE and the lack of fractionations among REE during magmatic degassing; (b) chondrite-normalized abundances for some rock-forming elements. The aerosol samples exhibit a spike-shaped pattern, highlighting that alkalis are preferentially enriched in the plume with respect to low-volatile elements from cluster L (i.e., Th, Ba, Nb, Sr, Hf and Y).

is a main determining factor, so that even mildly volatile elements such as K and Zn may have EFs close to 1 during ashfall events [*Quisefit et al.*, 1988]. To avoid the influence of variable ash contribution, several authors [*Crowe et al.*, 1987; *Zreda-Gostynska et al.*, 1997] have computed EFs with reference to the concentration of bromine, which is a minor constituent of volcanic ash and is also one of the most volatile elements at magmatic conditions.

If one is chiefly interested in gaining insights into trace metal degassing mechanisms, ash contribution is a "noise" to be subtracted from total element content. This erosive contribution, expressed by the weight ash fraction (WAF in Table 1), may be evaluated for each X element from the equation:

$$WAF\% = (100 \cdot X_{er})/X_t = [100 \cdot (REE_T)_a \cdot (X/REE_T)_r]/X_t \quad (2)$$

where X_{er} is the erosive contribution to X_t, the total amount of each X element in aerosols (in $\mu g \cdot m^{-3}$); $(REE_T)_a$ is the total rare earth element content (Σ rare earths) in aerosols; and $(X/REE_T)_r$ is the average element/(Σ rare earths) ratio in the parent rocks. When using equation 2, it is implicitly assumed that REE are purely erosive in origin, which is consistent with multivariate statistical analysis (Figure 2) and chondrite-normalized patterns (Figure 3a). It is also presumed that trace element abundances in the magma involved in the 2001 Etna activity do not diverge greatly from the mean compositions of historical volcanics (Table 1), which appears reasonable in the light of petrological data [*Pompilio et al.*, 2001].

The calculated WAF range is 0.1–100% (Table 1). There is a clear separation between volatile and lithophile elements, the former having WAF<5% and the latter about 100%. It is worth noting that some elements (Ag, Al, Au, Co, Cr, Ga, K, Mn, Mo, Na, Rb, Te, U, Zn) display WAFs of 20–70%, which presumably indicates intermediate
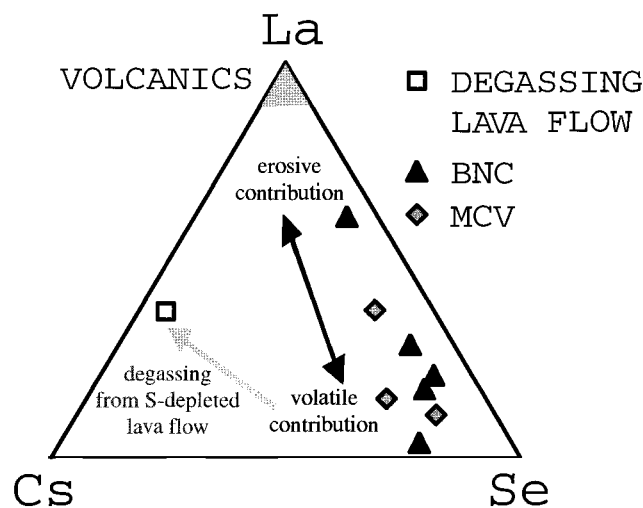
Figure 4. La, Se, Cs triangular plot for Etna's plume aerosol samples from May-August 2001. Compositions range from lanthanum-rich to selenium-rich, the former element having an erosive origin (see Fig. 3a) and the latter deriving from a non-crustal volatile source (see WAFs in Table 1). This suggests that the chemical composition of plume aerosols can be best interpreted in terms of mixing between erosive and volatile components. Cesium, as other alkaline elements, display mixed behavior (mean WAF = 8; Table 1). The departure from the main trend of sample ET 7, collected on the plume of the degassed the lava flow, is probably related to the exhaustion of chalcophile elements (like Se; see Fig. 5 and related discussion).
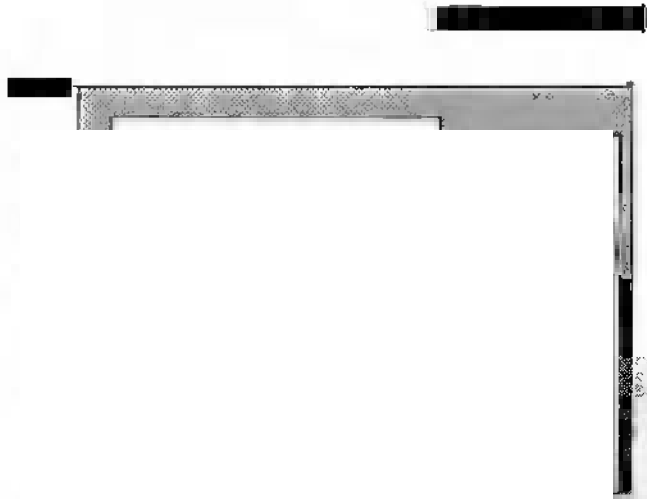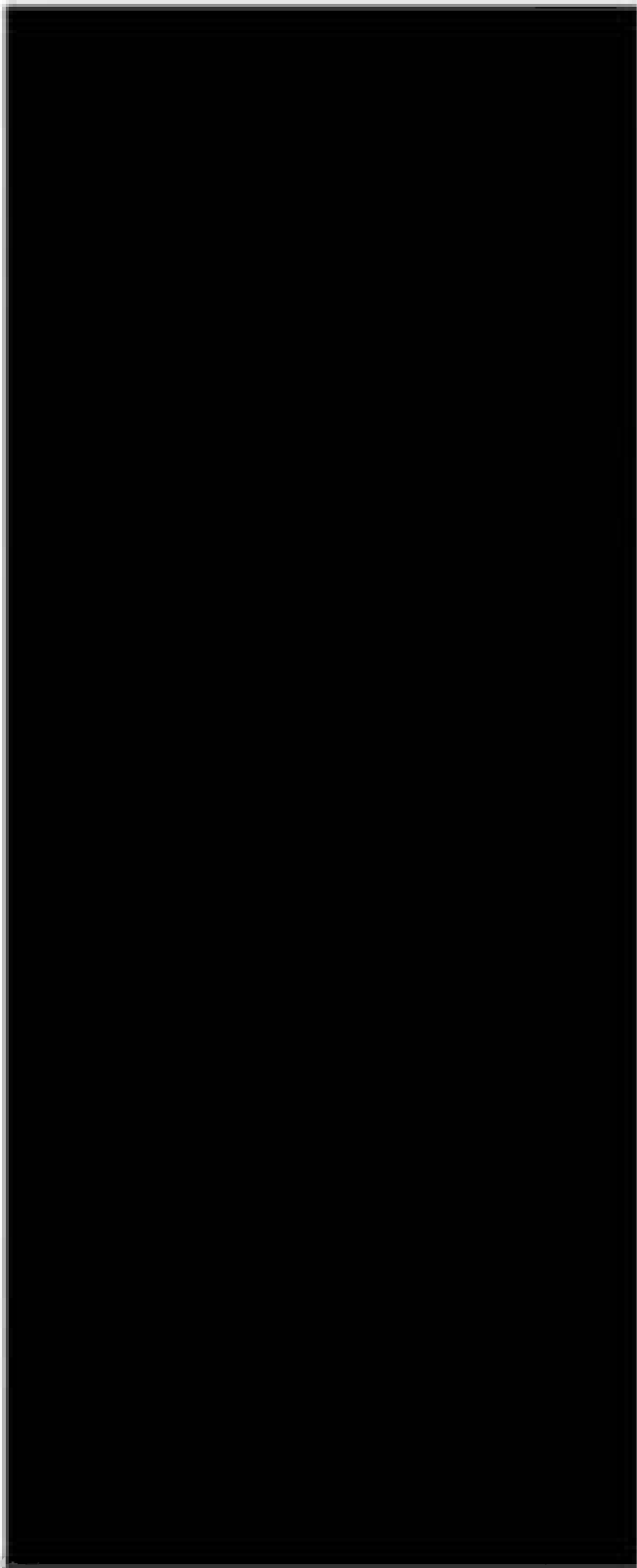
U   Mn   K   Zn   Mo   Te   Cu   Hg   Cd   As   Bi   Re   Sb

V. Activity

April
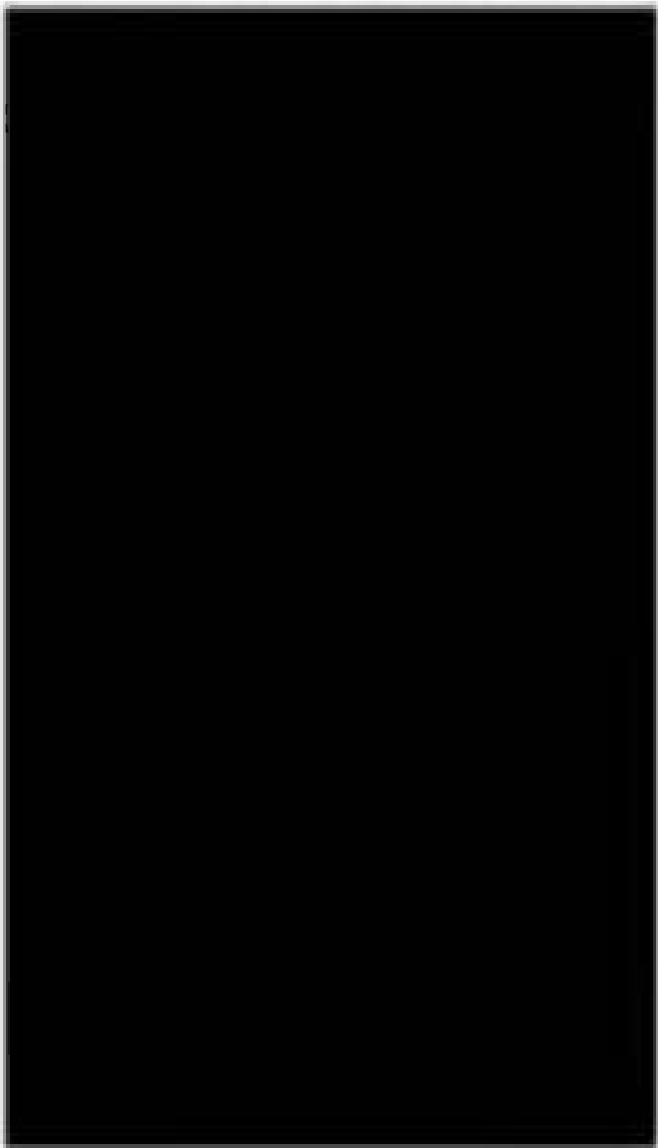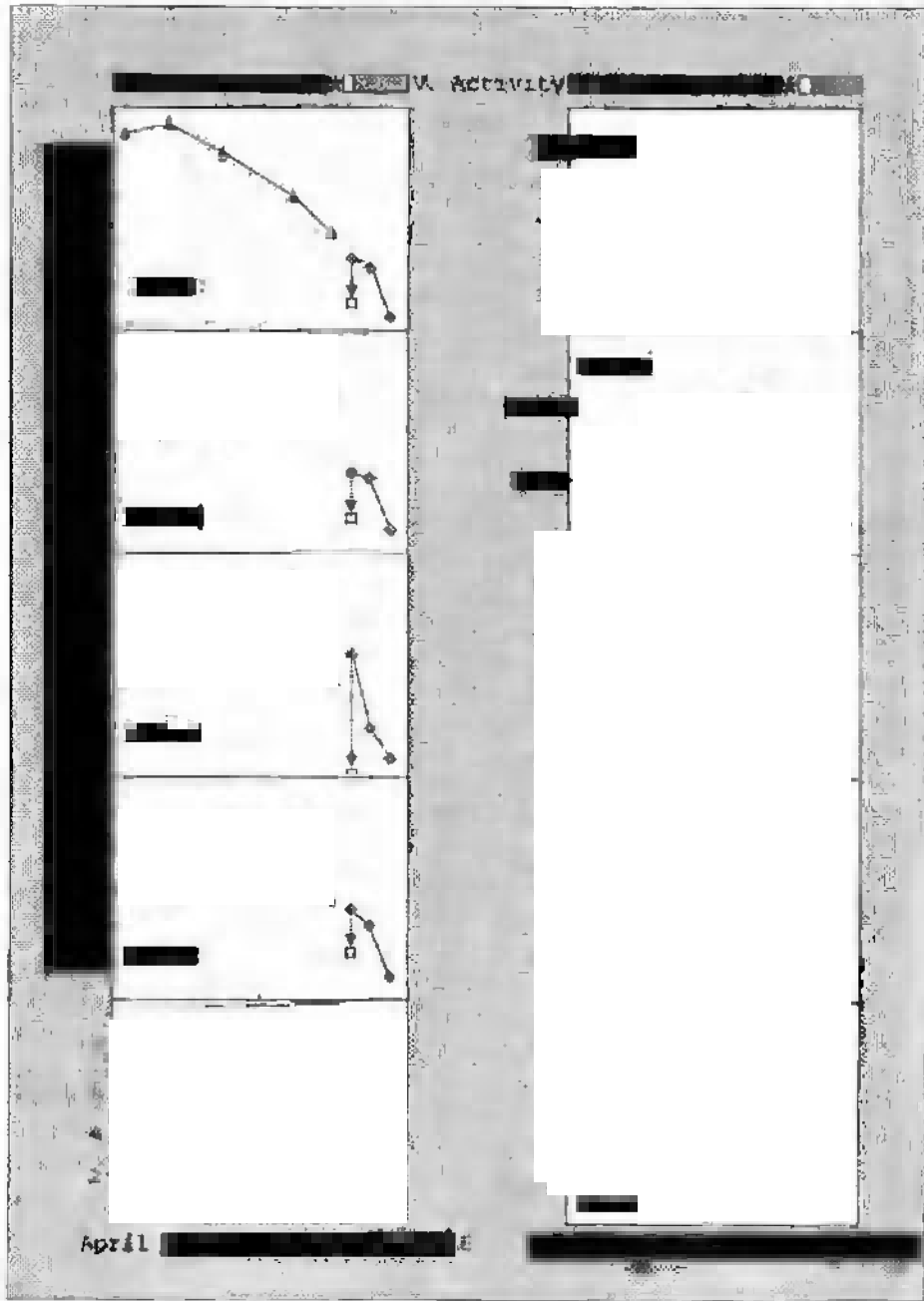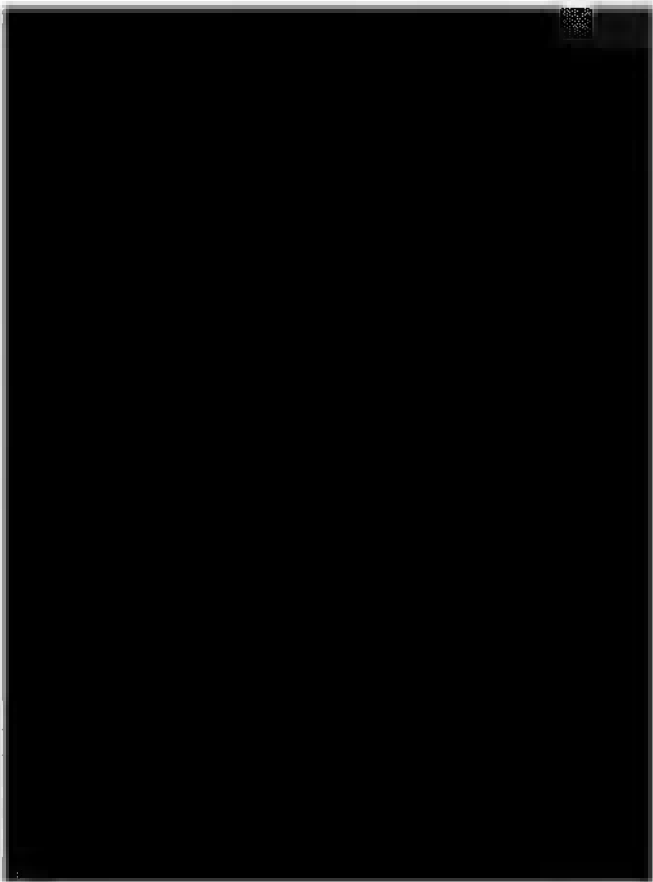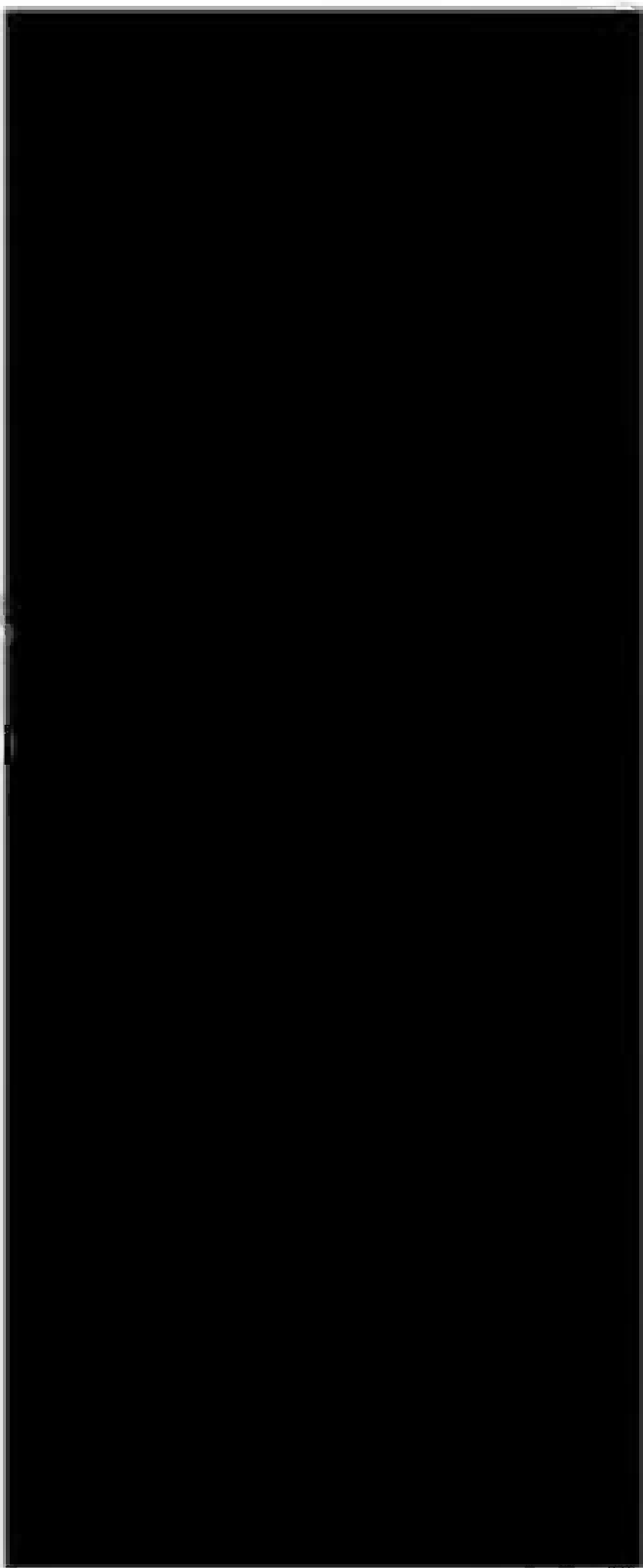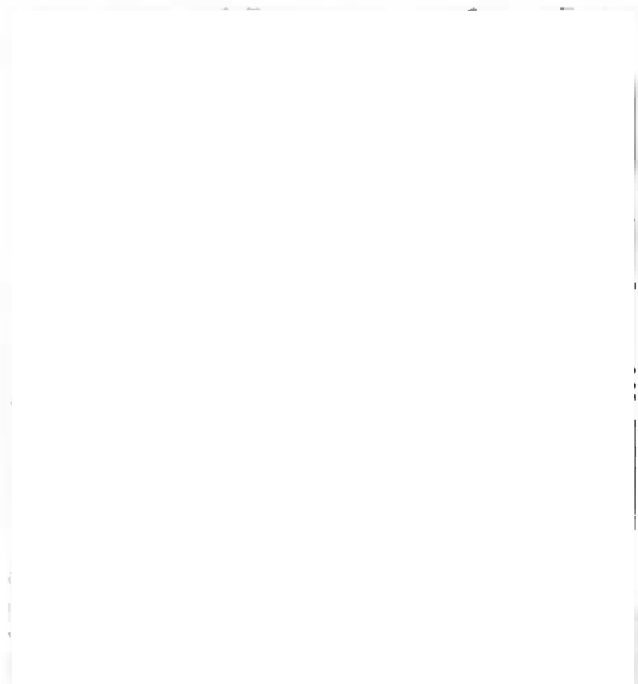
rapid depletion of the most volatile species (S, Cl, chal-
cophile trace metals) during the three-week eruption.

The main implication of the results presented in this paper
is the fact that changeable trace metal abundances in vol-
canic plumes may provide insight into the dynamics of
magmatic degassing. The wide range of trace element
behavior during vapor-melt separation processes and chem-
ical reactions in the plume atmosphere provides evidence
for their usefulness in tracking changes in the activity state
of a volcano. Also, the significant time variability in trace
element composition of volcanic plumes, evidenced here,
implies that much caution should be paid when estimating
the volcanic contribution to the Earth's atmosphere.

REFERENCES

Aiuppa, A., Trace element geochemistry of volcanic fluids
released by eastern Sicilian volcanoes, PhD thesis, University of
Palermo, Italy, 1999.

Aiuppa, A., C. Federico, A. Paonita, G. Pecoraino, and M. Valenza,
S, Cl and F degassing as an indicator of volcanic dynamics: the
2001 eruption of Mount Etna, Geophys. Res. Lett., 29-11,
10.1029/2002GL015032, 2002.

Allard, P., J. Carbonelle, D. Dajlevic, J. Le Bronec, P. Morel, J. M.
Maurenas, M. C. Robe, R. Faivre-Pierret, J. C. Sabroux, and P.
Zettwoog, Eruptive and diffuse emissions of carbon dioxide
from Etna volcano, Nature, 351, 387-391, 1991.

Allard, P., Endogenous magma degassing and storage at Mt. Etna,
Geophys. Res. Lett., 24, 2219-2222, 1997.

Allard, P., A. Aiuppa, H. Loyer, F. Carrot, A. Gaudry, G. Pinte, and
G. Dongarrà, Acid gases and metal emission rates during long-
lived basalt degassing at Stromboli volcano, Geophys. Res.
Lett., 27, 1207-1210, 2000.

Allard, P., N. Bruno, M. Burton, T. Caltabiano, D. Condarelli, V.
Longo, and F. Muré, Remote sensing gas measurements during
Etna's July-August 2001 eruption, paper presented at Assemblea
Annuale GNV-INGV, Rome, Italy, 2001.

Andres, R.J., P.R. Kyle, and R.L. Chuan, Sulphur dioxide, particle
and elemental emissions from Mount Etna, Italy during July
1987, Geol. Rundsch., 82, 687-695, 1993.

Barberi, F., F. Innocenti, G. Ferrara, J. Keller, and L. Villari,
Evolution of Aeolian arc volcanism (southern Tyrrhenian sea),
Earth Planet. Sci. Lett., 21, 269-276, 1974.

Bergametti, G., D. Martin, J. Carbonelle, R. Faivre Pierret, and R.
Vié Le Sage, A mesoscale study of the elemental aerosol com-
position emitted from Mount Etna volcano, Bull. Volcanol., 47,
1107-1114, 1984.

Buat-Ménard, P., and M. Arnold, The heavy metal chemistry of
atmospheric particulate matter emitted by Mount Etna volcano,
Geophys. Res. Lett., 5-4, 245-248, 1978.

Cadle, R.D., A.F. Wartburg, W.H. Pollak, B.W. Gandrup, and J.P.
Shedlovsilk, Trace constituents emitted to atmosphere by
Hawaiian volcanoes, Chemosphere, 6, 231-234, 1973.

Chester, D.K., A.M. Duncan, J.E. Guest, and C.R.J. Kilburn,
Mount Etna: The Anatomy of a Volcano, Chapman & Hall,
London, 404 pp, 1985.

Crowe, B.M., D.L. Finnegan, W.H. Zoller, and W.V. Boynton,
Trace element geochemistry of volcanic gases and particles
from 1983-1984 eruptive episodes of Kilauea volcano, J.
Geophys. Res., 92, 13708-13714, 1987.

Francis, P, A. Maciejewski, C. Oppenheimer, C. Chaffin, and T.
Caltabiano, SO_2:HCl ratios in the plumes from Mt. Etna and
Vulcano determined by Fourier transform spectroscopy,
Geophys. Res. Lett., 22, 1717-1720, 1995.

Gauthier, P.J., and M.F. Le Cloarec, Variability of alkali and heavy
metal fluxes released by Mt. Etna volcano, Sicily, between 1991
and 1995, J. Volcanol. Geotherm. Res., 81, 311-326, 1998.

Gemmel, J. B., Geochemistry of metallic trace elements in
fumarolic condensates from Nicaraguan and Costa Rica volca-
noes, J. Volcanol. Geotherm. Res., 33, 161-181, 1987.

Gerlach, T.M., and E.J. Graeber, Volatile budget of Kilauea vol-
cano, Nature, 313, 273-277, 1985.

Goff, F., C.J. Janik, , H. Delgado, C. Werner, D. Counce, J.A.
Stimac, C. Ciebe, S.P. Love, S.N. Williams, T. Fischer, and L.
Johnson, Geochemical surveillance of magmatic volatiles at
Popocatépetl volcano, Mexico, GSA Bulletin, 110, 695-710, 1998.

Gvirtzman, Z., and A. Nur, The formation of Mount Etna as the
consequence of slab rollback, Nature, 401, 782-785, 1999.

Hinkley, T.K., M-F. Le Cloarec, and G. Lambert, Fractionation of
families of major, minor and trace metals across the melt-vapor
interface in volcanic exhalations, Geochim. Cosmochim. Acta,
58, 3255-3263, 1994.

Hinkley, T.K., P.J. Lamothe, S.A. Wilson, D.L. Finnegan, and T.M.
Gerlach, Metal emissions from Kilauea, and a suggested revision
of the estimated worldwide metal output by quiescent degassing
of volcanoes, Earth Planet. Sci. Lett., 170, 315-325, 1999.

Hirn, A., R. Nicolich, J. Gallart, M. Laigle, and L. Cernobori,
ETNASEIS Scientific Group Roots of Etna volcano in faults
of great earthquakes, Earth Planet. Sci. Lett., 148, 171-191,
1997.

INGV-CT, Multidisciplinary approach yields insights into Mt.
Etna eruption, EOS Transactions, AGU, 82, 655-657, 2001.

La Delfa, S., G. Patanè, R. Clocchiatti, J.-L. Joron, and J.-C. Tanguy,
Activity of Mount Etna preceding the February 1999 fissure erup-
tion: inferred mechanism from seismological and geochemical
data, J. Volcanol. Geotherm. Res., 105, 121-139, 2001.

Lambert, G., M.F. Le Cloarec, B. Ardouin, and J.C. Le Roulley,
Volcanic emissions of radionuclides and magma dynamics,
Earth Planet. Sci. Lett., 76, 185-192, 1986.

La Volpe, L., P. Manetti, R. Trigila, and L. Villari, Volcanology and
chemistry of the Earth's interior, Boll. Geof. Teor. Appl., 40,
163-298, 1999.

Le Cloarec, M.F., M. Pennisi, B. Ardouin, J.-C. Le Roulley, and G.
Lambert, Relationship between gases and volcanic activity of
Mount Etna in 1986, J. Geophys. Res., 93, 4477-4484, 1988.

Le Cloarec, M.F., P. Allard, B. Ardouin, W.F. Giggengach, and
D.S. Sheppard, Radioactive isotopes and trace elements in

gaseous emissions from White Islands, New Zeland, *Earth Planet. Sci. Lett.,* 108, 19-28, 1992.

Le Guern, F., Ecoulements gazeux réactifs à hautes températures, mésures et modélisation, Thèse Doct. Etat, Université Paris VII, France, 1988.

Le Guern, F., and A. Bernard, A new method for sampling and analyzing volcanic sublimates—Application to Merapi volcano, Java, *J. Volcanol. Geotherm. Res.,* 12, 133-146, 1982.

Lepel, E.A., K.M. Stefansson, and W.H. Zoeller, The enrichment of volatile elements in the atmosphere by volcanic activity: Augustine volcano, 1976, *J. Geophys. Res.,* 83, 6213-6220, 1978.

Menyailov, I.A., and L.P. Nikitina, Chemistry and metal contents of magmatic gases, the Tolbachik volcanoes gas (Kamchatka), *Bull. Volcanol.,* 43, 197-207, 1980.

Miller, T.H., Zoeller, W.H., Crowe, B.M., and D. Finnegan, Variations in trace metal and halogen ratios in magmatic gases through an eruptive cycle of the Pu'u O'o vent, Kilauea, Hawaii: July–August 1985, *J. Geophys. Res.,* 95, 12607-12615, 1990.

Monaco, C., P. Tapponier, L. Tortorici, and P.Y. Gillot, Late quaternary slip rates on the Acireale-Piedimonte normal faults and tectonic origin of Mt. Etna (Sicily), *Earth Planet. Sci. Lett.,* 147, 125-139, 1997.

Mroz, E.J., and W.H. Zoeller, Composition of atmospheric particulate matter from the eruption of Heimaey, Iceland, *Science,* 180, 461-464, 1975.

Nakamura, N., Determination of REE, Ba, Fe, Mg, Na and K in carbonaceous and ordinary chondrites, *Geochim. Cosmochim. Acta,* 38, 753-773, 1974.

Olmez, I., D.L. Finnegan, and W.H. Zoeller, Iridium emissions from Kilauea volcano, *J. Geophys. Res.,* 91, 653-663, 1986.

Oskarsson, N., The chemistry of Icelandic incrustations and the latest stages of degassing, *J. Volcanol. Geotherm. Res.,* 12, 93-111, 1981.

Pennisi, M., M-F. Le Cloarec, G. Lambert, and J-C. Le Roulley, Fractionation of trace metals in volcanic emissions, *Earth Planet. Sci. Lett.,* 88, 284-288, 1988.

Phelan-Kotra, J.M., D.L. Finnegan, D.S. Ballantine, W.H. Zoeller, M.A. Hart, and J.L. Moyers, Airborne aerosol measurements in the quiescent plume of Mount St. Helens: September, 1980, *Geophys. Res. Lett.,* 9, 1093-1096, 1982.

Phelan-Kotra, J., D.L. Finnegan, W.H. Zoeller, M.A. Hart, and J.L. Moyers, El Chichon: compqsition of plume gases and particles, *Science,* 232, 1018-1021, 1983.

Pompilio, M., R.A. Corsaro, C. Freda, L. Miraglia, P. Scarlato, and J. Taddeucci, Petrological evidences of a complex plumbing system feeding the July-August 2001 eruption of Mt. Etna. *EOS,* American Geophysical Union Transactions - Fall Meeting Suppl. Abstract 82(47), F1412, 2001.

Quisefit, J.P., G. Bergametti, R. Vié Le Sage, D. Martin, P. Zettwoog, J. Carbonelle, and R. Faivre-Pierret, Nouvelle évaluation des flux particulaires de l'Etna—1980, *C.R. Acad. Sci.,* 295, 943-945, 1982.

Quisefit, J.P., G. Bergametti, and R. Vié le Sage, Mécanismes physico-chimique de génération des aérosols d'origine d'haute

température. Exemple des aérosols volcaniques. *Pollut. Atmos.,* 98, 133-141, 1983.

Quisefit, J.P., G. Bergametti, D. Tedesco, J. Pinart, and J.L. Colin, Origin of particulate potassium in Mt. Etna emissions before and during the 1983 eruption, *J. Volcanol. Geotherm. Res.,* 35, 111-119, 1988.

Quisefit, J.P., J.P. Toutain, G. Bergametti, M. Javoy, B. Cheynet, and A. Person, Evolution versus cooling of gaseous volcanic emissions from Momotombo Volcano, Nicaragua: Thermochemical model and observations. *Geochim. Cosmochim. Acta,* 53, 2591-2602, 1989.

Rose, W.I., C.L. Raymond, W.F. Giggenbach, P.R. Kyle, and R.B. Symonds, Rates of sulphur dioxide and particle emissions from White Island volcano, New Zealand and estimate of the total flux of major gaseous species, *Bull. Volcanol.,* 48, 181-188, 1986.

Sharp, A.D.L., P.M. Davis, and F. Gray, A low velocity zone beneath Mt. Etna and magma storage, *Nature,* 287, 587-591, 1980.

Shinohara, H., J.T. Iiyama, and S. Matsuo, Partitioning of chlorine compounds between silicate melt and hydrothermal solutions, *Geochim. Cosmochim. Acta,* 53, 2617-2630, 1989.

Stoiber, R.E., and W.I. Rose, The geochemistry of Central American volcanic gas condensates, *Geol. Soc. Am. Bull.,* 81, 2891-2912, 1970.

Stoiber, R.E., and W.I. Rose, Fumarole incrustations at active central America volcanoes. *Geochim. Cosmochim. Acta,* 38, 495-516, 1974.

Symonds, R.B., W.I. Rose, M.K. Reed, F.E. Lichte, and D.L. Finnegan, Volatilization, transport and sublimation of metallic and non-metallic elements in high temperature gases at Merapi Volcano, Indonesia, *Geochim. Cosmochim. Acta,* 51, 2083-2101, 1987.

Symonds, R.B., M.K. Reed, and W.I. Rose, Origin, speciation and fluxes of trace-element gases at Augustine Volcano, Alaska: Insights into magma degassing and fumarolic processes, *Geochim. Cosmochim. Acta,* 56, 633-657, 1992.

Symonds, R.B., and M.K. Reed, Calculation of multicomponent chemical equilibria in gas-solid-liquid system: Part II. Thermochemical data and application to studies of high-temperature volcanic gases with examples from St. Helens, *Amer. J. Sci.,* 293, 758-864, 1993.

Tanguy, J.C., M. Condomines, and G. Kieffer, Evolution of the Mount Etna magma: Constraints on the present feeding system and eruptive mechanism, *J. Volcanol. Geotherm. Res.,* 75, 221-250, 1997.

Toutain, J.P., J.P. Quisefit, P. Briole, P. Aloupogiannis, P. Blanc, and G. Robaye, Mineralogy and chemistry of solid aerosols emitted from Mount Etna, *Geochem. J.,* 29, 163-173, 1995.

Varekamp, J.C., E. Thomas, M. Germani, and P.R. Busek, Particle geochemistry of volcanic plumes of Etna and Mount St, Helens, *J. Geophys. Res.,* 91, 12233-12248, 1986.

Vié Le Sage, R., Chemistry of the volcanic aerosols, *In Forecasting volcanic events,* edited by H. Tazieff and J.C. Sabroux, pp. 445-474, Elsevier, Amsterdam, 1983.

Villari, L., (Editor), The 1991-93 Etna eruption, *Acta Vulcanologica*, 4, 1994.

Webster, E.A., and J.R. Holloway, The partitioning of REEs, Sc, Rb, and Cs between a silicate melt and a Cl fluid, *EOS*, 61, 46, 1152, 1980.

Webster, J.D., J.R. Halloway, and R.L. Herving, Partitioning of lithophile trace elements between H_2O and H_2O+CO_2 fluids and topaz rhyolite melt, Econ. *Geol.*, 84, 116-134, 1989.

Zreda-Gostynska, G., P.R. Kyle, D. Finnegan, and M.K. Prestbo, Volcanic gas emissions from Mt. Erebus and their impact on the Antarctic environment. *J. Geophys. Res.*, 102, 15039-15055, 1997.

Alessandro Aiuppa, Gaetano Dongarrà and Mariano Valenza, Dipartimento CFTA, Università di Palermo, via Archirafi 36, 90123, Palermo, Italy. (aiuppa@unipa.it)

Cinzia Federico and Giovannella Pecoraino, INGV—Sezione di Palermo, Via La Malfa 153, 90146, Palermo, Italy.

Surface-Based Observations of Volcanic Emissions to the Stratosphere

Dave Hofmann[1], John Barnes[1], Ellsworth Dutton[1], Terry Deshler[2],
Horst Jäger[3], Richard Keen[4], and Mary Osborn[5]

Long-term, surface-based observations of the stratospheric aerosol layer are presented and compared. These include three LIDAR aerosol backscatter measurements, at Mauna Loa Observatory (Hawaii), Langley Research Center (Virginia), and Garmisch-Partenkirchen (Germany); balloonborne in situ particle concentration measurements at Laramie, Wyoming, solar visible transmission measurements at Mauna Loa Observatory; aerosol optical depth measurements at South Pole Station and Mauna Loa Observatory; and lunar eclipse optical depth determinations, which is a globally integrating technique. Surface-based measurements have provided a useful historical record of volcanic effects on the stratospheric aerosol and the agreement between the various techniques is very good. However, some uncertainties exist when the stratosphere is relatively free of volcanic aerosol and some of the techniques are not able to easily resolve the very small amount of aerosol from natural and/or anthropogenic sources. The lunar eclipse data, which go back to the late 1800s, suggest that the Pinatubo eruption in 1991 probably perturbed the stratospheric aerosol layer at least as much as that of Krakatau in 1883. This is an important observation as it is one of the few ways to accurately compare the stratospheric effects of eruptions prior to modern measurements that began in the late 1950s. At the time of this writing (September 2002) the stratosphere appears to be at background with the lowest level of aerosol observed since the layer was discovered in 1959.

[1]Climate Monitoring & Diagnostics Laboratory, NOAA, Boulder, Colorado
[2]University of Wyoming, Laramie, Wyoming
[3]Forschungszentrum Karlsruhe, IMK-IFU, Garmisch-Partenkirchen, Germany
[4]University of Colorado, Boulder, Colorado
[5]Langley Research Center (SAIC), NASA, Hampton, Virginia

1. INTRODUCTION

Enhanced twilights following major volcanic eruptions have been the historical indicators of the sudden injection of particulate matter into the stratosphere. Thus parameters such as the "Dust Veil Index" [Lamb, 1970, 1977], to gauge the severity of the atmospheric effects of eruptions, came into existence. In situ measurements of the nature of stratospheric particulate material in the late 1950s by Junge et al. [1961] revealed that sulfur was the main particle composition. They postulated that the source of this "sulfate layer," during a period when the stratospheric aerosol content was very low due to a dearth of volcanic injections for the previous 25 years, was sulfurous gases of Earthly origin. Thus, the stratospheric particle layer is often referred to as the "Junge Layer." There is also a small micro-meteoritic com-

ponent of the background aerosol related to the ablation of meteors in the stratosphere. However, the episodic injection into the stratosphere of material from major volcanic eruptions is the main source of stratospheric aerosol. The importance of the aerosol layer becomes obvious following these eruptions as an initial stratospheric heating, due to radiation absorption by the aerosol, followed by a global tropospheric cooling, related to aerosol backscatter of solar radiation, results [*Hansen et al.*, 1978; *Dutton and Christy*, 1992]. In addition, the added surface area of the volcanic aerosol particles enhances heterogeneous chemical reactions which affect stratospheric ozone [*Solomon*, 1999].

Utilizing particle vaporization techniques with balloon-borne particle counters, *Rosen* [1971] showed that the stratospheric particles consisted of a solution having an approximately 75% sulfuric acid, 25% water composition, or a "stratospheric sulfuric acid aerosol" as it became known. Following the eruption of Fuego (Guatemala) in 1974, *Hofmann and Rosen*, [1977] used balloonborne optical particle counters to show that particles from the eruption were also made up of this sulfuric acid-water mixture and that only a very small fraction was in the form of non-volatile material, i.e., silicate or other crustal material. Condensation nuclei detectors flown on balloons after the Mt. St. Helens (Washington state, USA) eruption in 1980 [*Hofmann and Rosen*, 1982] showed that new sulfuric acid aerosol was formed from the gas phase following the eruption. It was thus postulated that the main, lasting effect on the stratosphere was volcanic injection of sulfur dioxide which chemically converted to sulfuric acid vapor followed by condensation into sulfuric acid droplets. The "dust" or "ash" particles, being of larger size, apparently fall out of the stratosphere within a few months during the early eruption decay phase. Further study of the chemical conversion both theoretically [*McKeen et al.*, 1984] and from satellite data [*Bluth et al.*, 1992] indicate that the characteristic time of conversion of sulfur dioxide into sulfuric acid vapor is about 1 month. Growth of new and pre-existing droplets by vapor accretion follows, increasing droplet size and total mass by an order of magnitude or more. The sulfuric acid-water aerosol which forms, decays with an e-folding time of about 1 year.

It has now been over 30 years since more or less continuous measurements of the stratospheric aerosol layer began from surface-based sites. In what follows we review some of the longer records obtained by laser radar (LIDAR), balloonborne optical particle counters, solar atmospheric transmission measurements, solar optical depth and lunar eclipse optical depth. We apologize for not being able to include all records that may exist but chose those that have the longest continuous records and are readily available.

2. LIDAR OBSERVATIONS

The first application of a "ruby optical maser," later to become LIDAR, an acronym for "LIght Detection And Ranging," to particle detection was made by *Smullin and Fiocco* [1962]. The "particle" was the Moon and optical echoes of 50 joule pulses of 694 nm ruby laser radiation were detected at Lexington, Massachusetts, in May of 1962. Following the eruption of the volcano Agung on Bali in 1963, *Grams and Fiocco* [1967] applied an "optical radar" (pulsed ruby laser) to detect backscatter from volcanic particles in the stratosphere. This was the forerunner of many LIDAR measurement programs operating today, three of the longest records being those from Garmisch-Partenkirchen (GAP), Germany (47.5°N) which began in 1976; Langley (LRC), Virginia (37.1°N); and Mauna Loa Observatory (MLO), Hawaii (19.5°N) both of which began in 1974.

Method

The ground-based atmospheric aerosol LIDAR systems included in this paper employ either a ruby or Nd:YAG pulsed laser transmitter and an optical receiver in parallel or collinear arrangement. The system transmits intense, short duration light pulses of linear polarization at a high repetition rate into the receiver field of view. The intensity of the light elastically backscattered by atmospheric molecules and particles is measured versus time, or equivalently altitude, through the telescope receiver, collimating optics, and an appropriate detector. The signal profile is stored by a fast analog-to-digital converter or by a photon counting device. Relative intensity data are accumulated separately from all altitude intervals for a selected averaging period, which may include thousands of individual laser shots.

This provides a high-resolution vertical profile of the optical scattering characteristics of aerosols, clouds, and the background molecular atmosphere. Typically the profiles obtained from many laser shots are averaged together to reduce noise. Raw data products are profiles of total backscatter, i.e., molecular plus particle backscatter signals. The particle backscatter signal must be separated from the molecular signal by suitable algorithms. Primary data products are then profiles of aerosol backscatter or scattering ratio. Secondary products are aerosol extinction profiles and aerosol optical depth.

The LIDAR scattering ratio, a primary parameter derived from the analysis of LIDAR data, is defined as

$$R(z) = \frac{b_a(z) + b_m(z)}{b_m(z)} \tag{1}$$

where b_a (z) is the aerosol backscatter and b_m (z) is the molecular backscatter, both in units of 1/(km-sr) and both at altitude z. The molecular backscatter is calculated from a temperature-pressure profile obtained by a nearby radiosonde launch, just prior to or just after the LIDAR data are collected. The scattering ratio is calculated by evaluating

$$R(z) = \frac{CS(z)z^2}{b_m(z)T^2(z)} \tag{2}$$

where S (z) is the LIDAR signal received from altitude z, T^2 (z) is the two-way atmospheric transmittance, and C is a system constant determined by normalizing the right-hand side of the equation to an expected minimum value of R over a specified altitude range. The transmittance is calculated from a combination of radiosonde-derived molecular extinction model or LIDAR-derived aerosol extinction, and model ozone absorption. During periods of moderate to heavy aerosol loading, aerosol extinction must be scaled to the aerosol backscatter using a model extinction-to-backscatter ratio [*Jäger and Hofmann*, 1991]. The LIDAR equation (2) is then solved several times using an updated value of aerosol extinction for each iteration.

The integrated stratospheric aerosol backscatter is defined as

$$\int_{h_t}^{30km} b_a(z)dz \tag{3}$$

where h_t is the height of the tropopause. b_a (z) can be easily obtained from $R(z)$ and b_m (z) using equation (1). Integrated aerosol backscatter is a good measure of the stratospheric column loading, and can be converted to optical depth using an appropriate extinction-to-backscatter ratio.

Results

All three LIDAR records investigated here began with ruby lasers as used by *Grams and Fiocco* [1967] in the early work. However, as the ruby lasers aged and advances in laser technology made high pulse repetition rate, multiple wavelength lasers available, two of the three ruby lasers (GAP and MLO) were replaced in the 1990s with Nd:YAG lasers which have a primary wavelength of 1064 nm and a double-frequency wavelength of 532 nm. Because of its ease of detection, the latter wavelength has become a standard for stratospheric aerosol work.

To extend the ruby record at GAP and MLO, the backscatter at the ruby wavelength (694 nm) was calculated from the measured backscatter of the Nd:YAG laser. At GAP, the 532 nm laser measured backscatter was used along with a model of the wavelength dependence of aerosol backscatter using balloonborne aerosol size distribution measurements [*Jäger and Hofmann*, 1991; *Jäger et al.*, 1995, *Jäger and Deshler*, 2002]. At MLO, both the 532 nm and the 1064 nm backscatter were measured and the value at 694 nm was determined by simple interpolation. In the latter case, an overlap period of the ruby and Nd:YAG lasers indicated that the interpolation technique produced a similar result as the ruby LIDAR itself, in fact, due to the higher repetition rate of the Nd:YAG laser (30 Hz as compared to 0.1 Hz), the statistics of the latter were considerably better.

A distinct advantage of LIDAR measurements is the ability to obtain a vertical profile of aerosol backscatter. In this sense they provide additional information compared to column measurements such as optical depth and solar transmission. In Plate 1 we compare vertical profiles of the LIDAR backscatter ratio at three locations during a period of high volcanic aerosol loading (July 1992, about a year after the eruption of Pinatubo) and a background period (June-July, 1999). In situ measurements of particle mixing ratio (particles per milligram of air) from Laramie, Wyoming, for the same periods are also shown.

The time history of integrated backscatter coefficient from three LIDARs is compared in Plate 2. The integral in all cases includes the entire stratosphere. Although the agreement between the three LIDARs is generally good, there are several noticable differences. The onset of the El Chichón and Pinatubo events at MLO is more abrupt. This is related to the fact that both were low-latitude eruptions and the volcanic aerosol enhancement was observed more promptly at the lower latitude MLO site than at the other two midlatitude sites. The early decay phases, especially after the Pinatubo eruption, also occur more promptly at MLO, possibly for the same reasons. While MLO indicates a uniform annual variation after about 1996, which has been interpreted as indicating the background, non-volcanic level of stratospheric aerosol [*Barnes and Hofmann*, 2001], the midlatitude sites suggest a continuing decline although the measurement statistics are not very good at these sites after about 1999.

Vertical profiles of scattering ratio at 694 nm from three LIDARs during the background period (July 1999) are compared in Plate 3. The stratospheric aerosol layer resides at higher altitudes (lower air densities) at lower latitudes because of the increase in tropopause height from pole to equator. The increase in altitude of the aerosol layer will in turn increase the scattering ratio, which is scaled to air den-

10^{-1}

10

10

10

10

394 nm Integrated Aerosol Backscatter (sr^{-1})
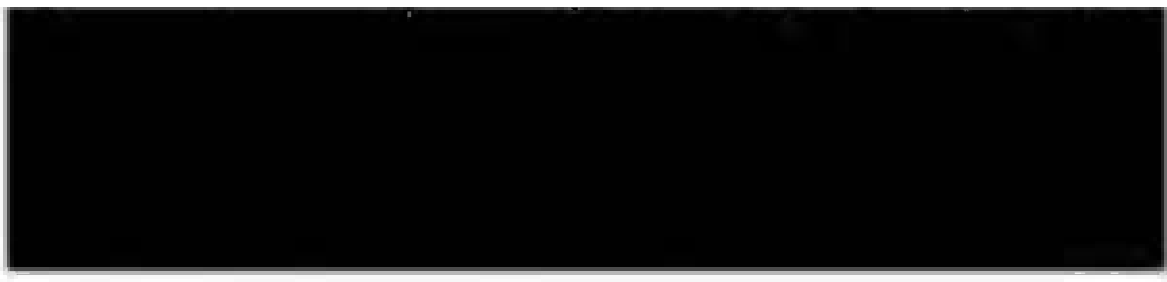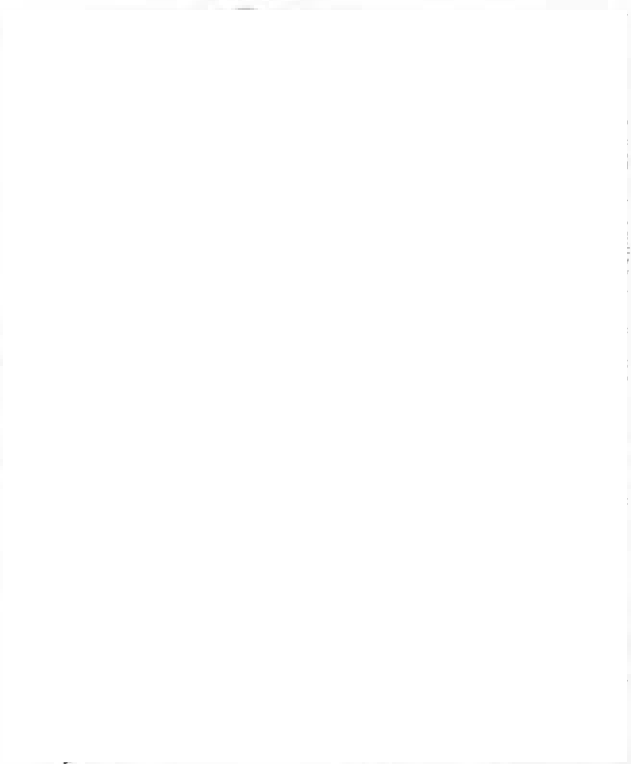
sity through the dependence on molecular backscatter, for the same total aerosol scatter, i.e., scattering ratio is an atmospheric mixing ratio. This is clearly observed in the MLO measurements.

The data in Plate 2 suggest that the peak aerosol effects on the stratosphere after the El Chichón and Pinatubo eruptions were of similar magnitude, yet it was observed by satellite that Pinatubo injected about three times as much sulfur dioxide [about 20 megatons—*Bluth et al.*, 1992] as El Chichón. This is related to the fact that the initial El Chichón eruption cloud came directly from Mexico to the Hawaiian Islands and caused the largest integrated backscatter ever observed (see the narrow spike in Plate 2 with an integrated backscattering coefficient of about 1.2 × 10^{-2} sr^{-1}, 200 times the pre-eruption level.) In general, measurements from a few discrete sites are not adequate to judge the relative intensity of eruptions prior to a time when more or less global uniformity in the stratospheric aerosol distribution has been achieved.

The rate of sulfuric acid aerosol droplet growth following an equatorial eruption depends, among other factors, on the density of the reacting/condensing sulfurous gases in the equatorial reservoir. The latter is a region equator-ward of about 20° [*Grant et al.*, 1996]. Some factors that affect the density of sulfuric acid that can form, in addition to the amount of sulfur dioxide injected, is the rate of oxidation of the parent volcanic gas, which can be reduced if the reactant hydroxyl radical concentration is depleted by excessive sulfur dioxide, thus causing self-limiting growth [*Pinto et al.*, 1989]. The sulfuric acid growth rate also depends on the altitude of the injection through aerosol size-dependent growth variations [*Hamill et al.*, 1977]. Another factor that can affect growth through reducing the gas density is dispersion related to transport to higher latitudes [*Hofmann*, 1987]. Meridional transport from the equatorial region occurs primarily in winter and is enhanced with westerly stratospheric winds. Since transport depends on season, aerosol particle size will depend to some degree on the season of the eruption and the phase of the quasi-biennial oscillation (QBO) in the direction of stratospheric equatorial winds.

The eruption of El Chichón (17.4°N, April 4, 1982) occurred in the southern hemisphere fall and that of Pinatubo (15.1°N, June 15, 1991) in the southern hemisphere winter. Both occurred during the easterly phase of the QBO, but the vertical wind structure was different with strong easterlies above 21 km for El Chichón, but above 25 km for Pinatubo. Since easterlies generally inhibit poleward dispersal of equatorial stratospheric air toward the winter hemisphere, the sulfurous gases from El Chichón were initially confined to the equatorial region and northern

hemisphere compared to Pinatubo when large transport of material into the southern hemisphere was observed [*Trepte et al.*, 1993]. The El Chichón eruption occurred two months earlier than Pinatubo, and thus before southern hemisphere winter. This suggests that considerably more particle growth could occur prior to transport out of the equatorial reservoir region for El Chichón, while transport south and possibly the self-limiting affect of large amounts of sulfur dioxide, probably resulted in less relative growth for Pinatubo, even though more sulfur dioxide was injected. Satellite data show the large increase in aerosol extinction following the Pinatubo eruption in the southern hemisphere early in the event [*McCormick and Veiga*, 1992], and the optical depth data at the south pole (to be shown later) showed the Pinatubo event to be much larger than the El Chichón event at this remote site. MLO is situated near the equatorial reservoir northern boundary and likely did not sample the Pinatubo aerosol at its most concentrated state as it apparently did for El Chichón.

Relatively minor aerosol backscatter increases were observed after the eruptions of Mt. St. Helens, Alaid and Ruiz, in 1980, 1981 and 1986, respectively. In addition, the eruption of Nyamuragira early in 1982, caused an observable stratospheric aerosol increase just prior to the major eruption of El Chichón. These eruptions were either too weak (e.g., Alaid, Ruiz, Nyamuragira, Kelut) or contained too little sulfur (e.g., Mt. St. Helens) to cause significant perturbations to the stratospheric aerosol. The high latitude of some of these eruptions (e.g., Alaid, Mt. St. Helens) also limits their global impact.

3. BALLOONBORNE PARTICLE COUNTERS

One of the longest records of stratospheric aerosol measurement has been produced by the University of Wyoming's balloonborne optical particle counter program. Approximately monthly in situ measurements of the vertical profile of stratospheric aerosol size distributions and number concentrations have been maintained since 1971. Several different particle counters have been utilized but two size ranges have been preserved throughout the period, particles having radii greater than 0.15 μm and greater than 0.25 μm [*Deshler et al.*, 2003]. These data will be presented here and compared with other techniques, in particular LIDAR instruments which also give vertical profile information.

Method

The University of Wyoming optical particle counter, initially developed by *Rosen* [1964], is a white light counter

measuring aerosol scattering in the forward direction and using Mie theory to determine aerosol size. Light scattered from particles passing through the light beam is collected over a 30° half-angle cone and focused onto a photomultiplier tube for pulse height discrimination. Two symmetrical independent photon paths are used to limit noise, and the influence of cosmic rays in the stratosphere, by coincidence counting. These instruments are sensitive to optically detectable aerosol as small as 0.15 μm in radius. Initial observations in the 1970s consisted of measurements of particles $\geq$ 0.15 and 0.25 μm at a sample flow rate of 1 liter min^{-1}. Current measurement capabilities consist of condensation nuclei (r > 0.01 μm) and optically detectable aerosol, r $\geq$ 0.15–2.0 μm in twelve size ranges at a flow rate of 10 liters min^{-1} [*Deshler et al.*, 2003]. These instruments are flown on balloons to obtain aerosol profiles from the surface to altitudes of over 30 km.

Results

The particle concentrations in two size ranges, as measured in balloon flights at Laramie, Wyoming, since 1971, have been integrated between altitudes of 15 and 25 km and are shown in Plate 4. All major volcanic eruptions, which occurred during this period, show up clearly in the record. As in the LIDAR record, the magnitude of the El Chichón and Pinatubo events are similar for reasons discussed earlier. The value of the optical particle counter data is in their size-selective properties which indicate that the size distribution is dominated by larger particles after a major volcanic eruption. This is related to the excessive growth of sulfuric acid droplets at this time. The in situ data at Laramie indicate that the stratospheric aerosol at northern mid latitudes likely reached a minimum in 1997–1998 at a value similar to that in 1979 and 1990 for the smaller particle size range (r $\geq$ 0.15 μm) but slightly lower for the larger particle size range (r $\geq$ 0.25 μm). On a mass basis, this would suggest that the stratosphere is probably in its cleanest state since at least about 1959 when the sulfate layer was discovered by *Junge* [1961] following a long volcanically quiescent period. This would also agree with the midlatitude LIDAR data at LRC and GAP, the LIDAR backscatter being closely related to the mass present in the stratosphere [*Hofmann and Barnes*, 2002].

In Plate 5 we compare the LIDAR and balloon data which confirm that the LIDAR backscatter variations follow those of the larger particle size range closely.

4. SOLAR VISIBLE TRANSMISSION

Accurate measurements of the broadband solar transmission of the atmosphere from a clean, high altitude site is a relatively inexpensive way to monitor aerosol levels in the stratosphere. The apparent transmission technique was first used at Mauna Loa Observatory by *Ellis and Pueschel* [1971] and showed that there were no significant trends related to air pollution for the 1958–1970 period. These data have been extended and reported by *Dutton and Bodhaine* [2001] and are updated here.

Method

The apparent transmission method uses ratios of the total direct solar irradiance measured at different fixed solar elevation angles during the course of a clear morning or afternoon. A daily average of three such ratios is taken as the day's apparent transmission, which is insensitive to instrument calibration uncertainties due to the cancellation of the linear instrument calibration factor in the ratio. It has been shown that variations in the apparent transmission are due primarily to aerosols whereas water vapor sensitivity is muted due to line saturation. Monthly averages of apparent transmission have been used to reduce some local variability and develop a long time series of the MLO apparent transmission. For further explanation of the apparent transmission method and past analysis of the record see *Dutton and Bodhaine* [2001] and references therein.

Results

The broadband visible solar radiation transmission data at MLO as measured since 1958, are shown in Plate 6. Most notable are the decreases in transmission associated with major volcanic eruptions that occurred during this period. They include Agung in 1963, Fuego in 1974, El Chichón in 1982, and Pinatubo in 1991. Here also the El Chichón eruption caused a large initial spike that decayed rapidly in 1982. Perhaps a better comparison of the severity of the El Chichón and Pinatubo eruptions as observed at MLO would be the area under the transmission curves in Plate 6. Springtime pollution events, related to the long-range transport of Asian desert dust, have been observed at Mauna Loa Observatory for many years [*Bodhaine et al.*, 1981]. These events are clearly observed in the Mauna Loa solar transmission record in Plate 6.

Integrated Particle Number (cm^{-2} column)

10^{10}

10^{9}

10^{8}

10^{7}

10^{6}

10^{4}
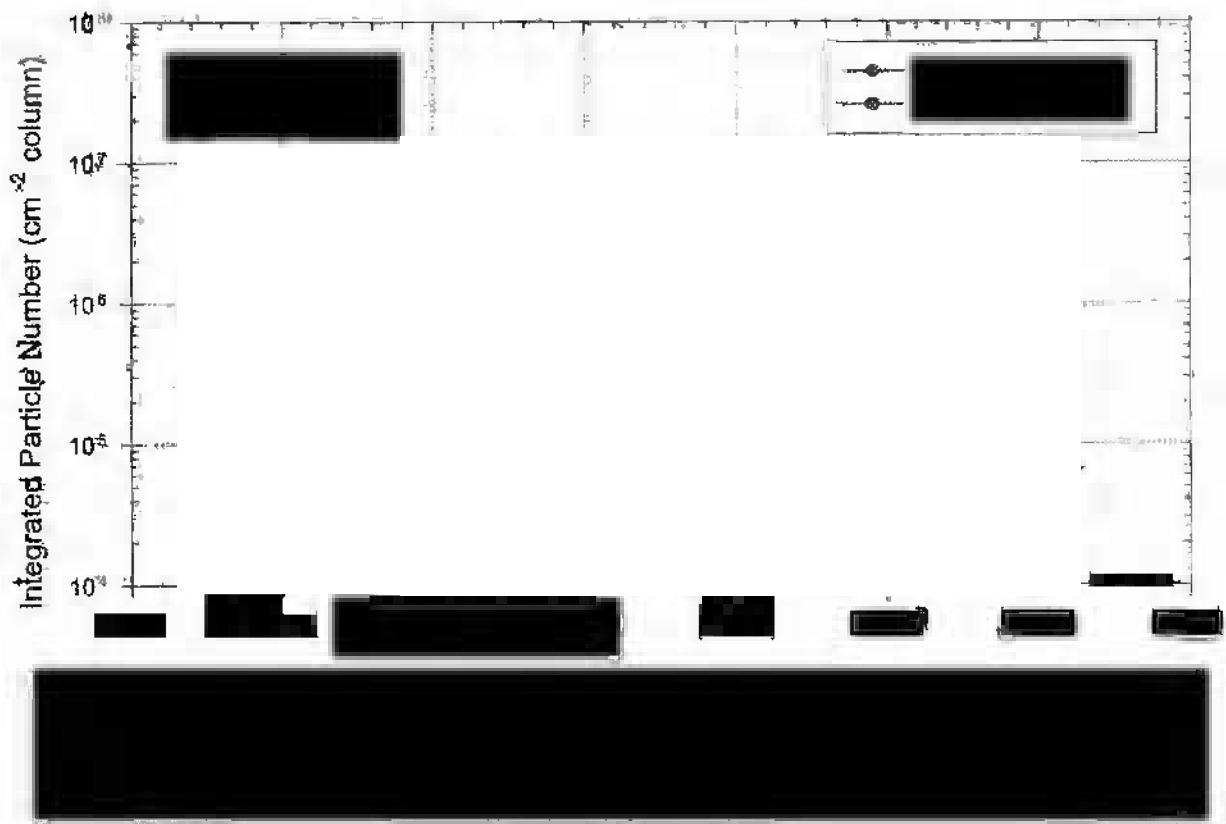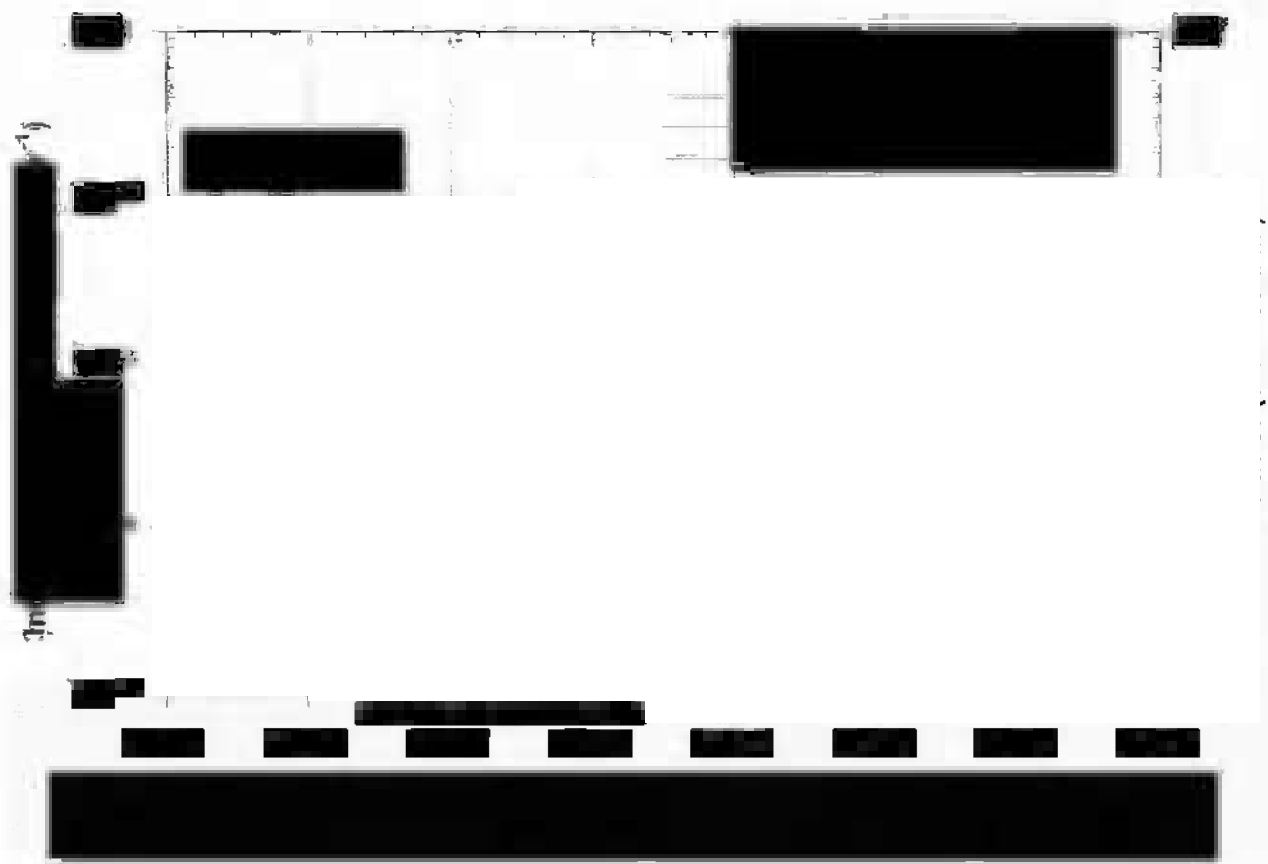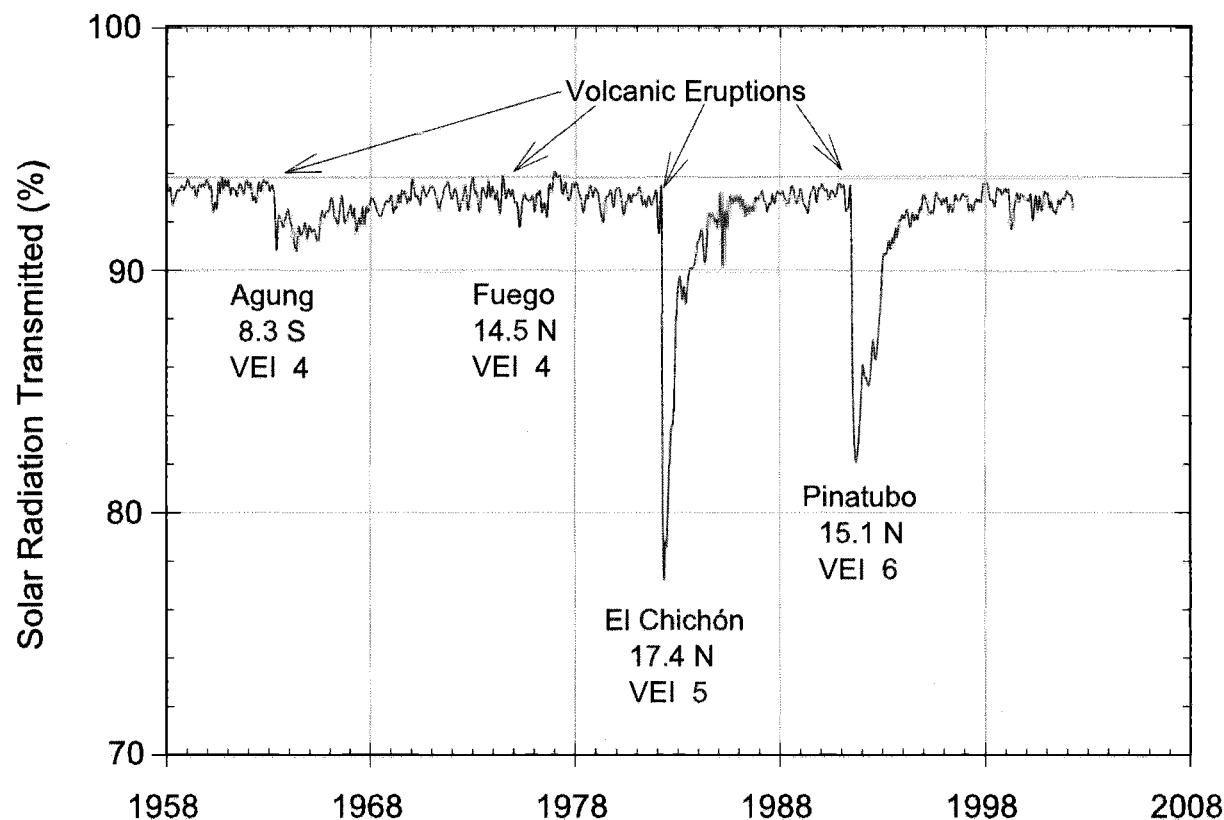
Plate 6. Transmission of solar radiation through the clean Mauna Loa Observatory atmosphere at an elevation of 3.4 km as determined since 1958. The names, latitudes and volcanic explosive index of eruptions that perturbed the stratosphere during this period are indicated in the Plate. The light blue line is the estimated transmission for an aerosol-free atmosphere. The small annual decreases in transmission are real and are associated with enhanced springtime transport of Asian effluents to the site. (See the color version of this plate at the back of this volume.)

5. AEROSOL OPTICAL DEPTH

The aerosol optical depth or thickness (τ) of the atmosphere is defined as the negative of the natural logarithm of the ratio of intensity of direct solar radiation of a particular wavelength at the top of the atmosphere to that at the surface, and is thus an absolute measure of the transmission of the atmosphere. The average value of τ at solar visible wavelengths for a volcanically unperturbed stratospheric aerosol is about 0.02, which includes the upper troposphere. The maximum value that has been observed following major volcanic eruptions is about 0.3, or a reduction of the direct solar intensity by about 25%.

There have been a number of attempts to establish global stratospheric aerosol optical depth climatologies [*Sato et al.*, 1993; *Stothers*, 1996]. Varying techniques used to estimate optical depth after volcanic eruptions range, for example, from early dust veil indices to pyrheliometry to satellite measurements of aerosol extinction. Because the data quality has increased over time, the uncertainties in the records decline with time as well. However, these analyses provide useful databases for the history of volcanic eruptions which perturbed the stratosphere and thus for long-term climate simulations.

Method

Aerosol optical depths at NOAA Climate Monitoring and Diagnostics Laboratory observatories have been deduced under clear skies over the past three decades using a low accuracy but relatively stable method of comparing wideband filtered (Schott glass) pyrheliometer measurements to simple spectral radiative transfer calculations. Progressively larger aerosol optical depths are introduced into the model until the best agreement with the observations is achieved. While the absolute accuracy of the resulting optical depth when compared to modern sunphotometer measurements is on the order of 0.04 optical depth units, the long-term precision of the measurements appears to be close to 0.01, which rivals the best results achieved to date from sunphotometers. Some previous results of these observations at the four main CMDL observatories are given by *Dutton and Christy* [1992].

Results

Aerosol optical depth observations at the U.S. South Pole Station in Antarctica were chosen for this analysis because it is remote from the sites of the eruptions and is relatively free of obscuring tropospheric aerosol. In Plate 7 these data are compared to aerosol optical depth measurements using the same technique at Mauna Loa Observatory to place the overall observations in perspective. Since the sun cannot be observed at the south pole in winter, the South Pole Station record has breaks in it. The large optical depth at Mauna Loa immediately after the El Chichón eruption is again related to the transport of the Mexican eruption cloud directly over the Hawaiian Islands early in the event. At south pole, Pinatubo caused a larger optical depth than El Chichón; however, the El Chichón peak was expected in southern winter 1983 when the sun was not present for observations. The Pinatubo event as observed at the south pole would be expected to be much larger than the El Chichón event, both because more sulfur dioxide was involved in the Pinatubo event and because the initial transport was to the south, arriving in summer rather than in winter as was the case for El Chichón.

It is interesting to note the springtime minima in the south pole optical depth record that occurred each year following the Pinatubo eruption. These minima are believed to be related to the large-scale subsidence that occurs within the antarctic vortex during winter and to the fallout from the stratosphere of ice crystals and nitric acid hydrate particles (polar stratospheric cloud particles) that form around sulfuric acid droplets in the austral winter resulting in the now familiar drying and denitrification of the antarctic winter stratosphere. These processes are prerequisites for the springtime ozone hole chemistry to take place when the sun appears.

6. LUNAR ECLIPSE OPTICAL DEPTH

About once per year, on average, the Moon is eclipsed as it passes into the Earth's shadow; at these times the Moon is visible due to sunlight refracted (and to a much lesser extent, scattered) into the shadow by the Earth's atmosphere. *Kepler* [1604] attributed the near disappearance of the Moon during an eclipse in 1588 to "mists and smoke" in the atmosphere, and the volcanic nature of these atmospheric aerosols became apparent when a dark eclipse followed the 1883 eruption of Krakatau [*Flammarion*, 1884]. Comparing *Link's* [1956] theory with photometric observations of three eclipses following the 1963 eruption of Agung, *Hansen and Matsuhima* [1966] derived quantitative values for aerosol optical depth. Thus, our satellite can be used as a remote sensor of the globally averaged optical depth of stratospheric aerosols of volcanic origin.

Conceptually, the linkage between volcanic aerosols and lunar eclipses is as follows. Most of the refracted sunlight that illuminates the eclipsed Moon passes through the stratosphere. Stratospheric aerosols reduce the transmission

of sunlight into the umbra. The path length of sunlight through a stratospheric aerosol layer is about 40 times the vertical thickness of the layer (this factor is for a layer concentrated between heights of 15 and 20 kilometers, but the factor can range between 25 and 50 for other layer heights and depths and various eclipse geometries). Therefore, the brightness of the eclipsed Moon is extremely sensitive to the amount of aerosols in the stratosphere.

Method

Aerosol optical depths can be calculated for the date of an eclipse from the difference between the observed brightness of the eclipse and a modeled brightness computed for an aerosol-free standard atmosphere, modified by assumed distributions of ozone and cloud. Details of this technique, applied to observations during 1960 through 1982, appear in *Keen* [1983]. Using this technique, optical depths have been derived from observations of all 38 total lunar eclipses between 1960 and 2001. In addition, results from all eight total eclipses during the period 1880-1888 have been included to allow comparison with the effects of the Krakatau eruption in 1883. In all, six distinct increases, believed to be associated with volcanic eruptions, were identified in the derived optical depth data. The probable identities of the eruptions are given in Table 1.

During any total lunar eclipse, the Moon is illuminated by sunlight passing through every latitudinal segment of the Earth's limb; hence, the brightness of the Moon is affected by volcanic aerosols at all latitudes, and the derived optical depths may be considered a global average. This interpretation is particularly true for those eclipses (about one-third of all total lunar eclipses) for which the Moon's disk passes across the center of the Earth's shadow. However, during some eclipses, the Moon may pass north or south of the Earth's shadow axis, and the derived optical thickness is weighted toward aerosols in the respective hemisphere of
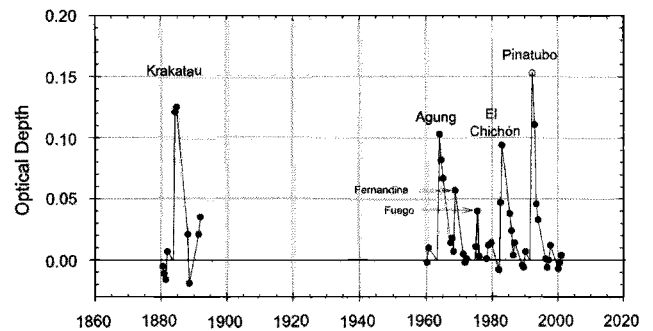

Figure 1. Optical depth following major volcanic eruptions as determined by the lunar eclipse technique for the periods 1880-1888 and 1960-2000. Zero points prior to the eruptions of Krakatau, Agung, Fuego, and Pinatubo are estimated. The peak value following the Pinatubo eruption (open circle in graph) is estimated (see text).

the Earth. This sampling bias was particularly apparent during the first year or so following the eruptions of Agung and El Chichón, when higher concentrations of aerosols occurred in the southern and northern hemisphere, respectively, and eclipses crossing the same (or opposite) hemisphere produced systematically higher (or lower) optical depths (relative to an exponential decay curve). An empirical correction factor of 0.8 removed most of these systematic differences (if the Moon passed south of the Earth's shadow axis during an eclipse following Agung, the derived optical thickness was multiplied by 0.8, while the derived value was divided by 0.8 if the Moon passed north of the axis). As indicated later, the derived optical depth following major eruptions is of the order 0.1 ±0.01. Since the empirical correction factor of 0.8 is derived from these observations, the uncertainty in the factor is of the same relative magnitude, i.e., ±0.1. The correction factor was applied to the optical depths following the eruptions of Agung, Fuego, and El Chichón. Although the Pinatubo eruption occurred in

Table 1. Volcanic Eruption Data and Lunar Eclipse Derived Maximum Optical Depth

Volcano Name	Latitude	Longitude	Major Eruption Date	Volcanic Explosive Index[a]	Maximum Optical Depth
Krakatau	6.10°S	105.43°E	1883-08-27	6	0.13
Agung	8.34°S	115.51°E	1963-03-17	4	0.10
Fernandina	0.37°S	91.55°W	1968-06-11	4	0.06
Fuego	14.47°N	90.88°W	1974-10-10	4	0.04
El Chichón	17.36°N	93.23°W	1982-04-03	5	0.09
Pinatubo	15.13°N	120.35°W	1991-05-15	6	0.15

[a]*Simkin and Siebert* [1994]
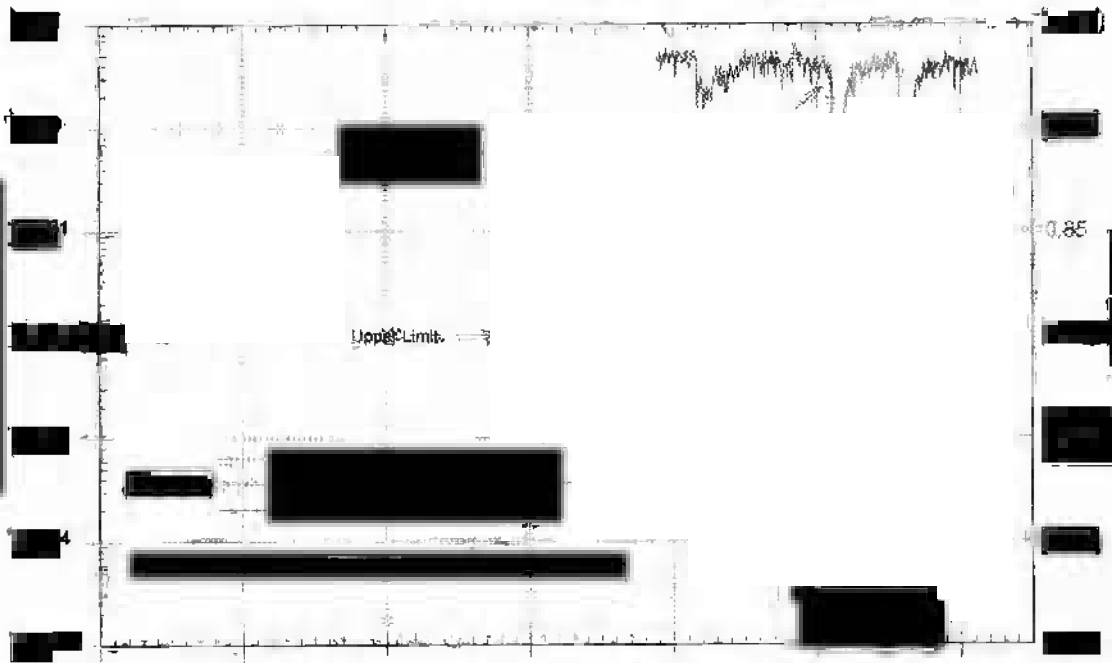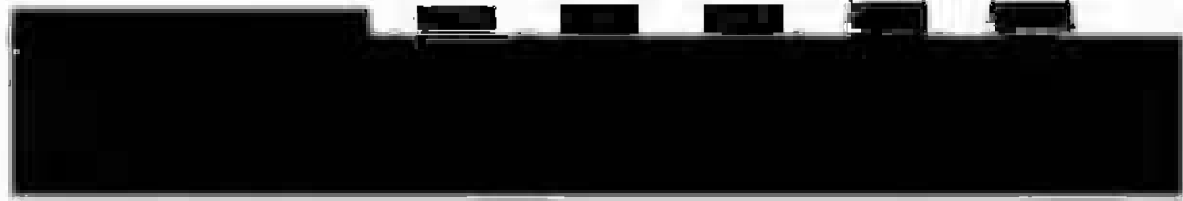
the northern hemisphere, it was near the meteorological equator at the time of the eruption, so no corrections were applied. The four eclipses following the Krakatau eruption were all central eclipses (the Moon crossed the Earth's shadow axis), so no corrections were applied to that event.

Optical depths were set to zero on the dates of the eruptions of Krakatau, Agung, Fuego, and Pinatubo; observed values were near zero for eclipses close to the dates of the eruptions of Fernandina and El Chichón. No lunar eclipses occurred until 18 months following the Pinatubo eruption in June 1991, while results from Agung and El Chichón indicate that peak optical depths occurred about 9 months after those eruptions. Therefore, the time series of optical depths following Pinatubo was extrapolated backwards to a date 9 months after the eruption using a composite decay curve (with a time constant of 1.92 years) derived from the Agung and El Chichón eclipse data.

Results

Of the 46 eclipses for which optical depths were derived, 15 have elevated values apparently due to volcanic eruptions. The mean optical depth derived from the other 31 eclipses is 0.002, with a standard deviation of 0.009. This indicates that the probable error of each derived optical depth is about ±0.01. Occurrences of maximum global optical depths substantially larger than 0.01 are listed in Table 1 with probable volcanic eruption identification. The identification of Fernandina with the 1968 peak is uncertain. Increases of observed values to slightly above the 0.01 uncertainty level occurred in 1979 and in late 1997. If real, these slightly elevated values could indicate aerosols from the eruptions of Soufriere on St. Vincent (1979) and Soufriere Hills on Montserrat (1997). All optical depth determinations are plotted in Figure 1.

Maximum observed values of 0.13 for Krakatau occurred for eclipses 8 and 14 months after the eruption, and the actual maximum could be slightly greater. For Pinatubo, the maximum value of 0.15 is extrapolated from an observed value of 0.11 for an eclipse 18 months after the eruption. Furthermore, if the aerosol layer height for either event was higher than the 15 to 20 kilometer height assumed for these calculations, the optical depth could be as much as 30% greater. It is, therefore, within the range of error that the two events produced approximately the same maximum optical depth.

7. SUMMARY AND CONCLUSIONS

Plate 8 compares most of the long-term records presented here. We conclude that the agreement is remarkable, in par-

ticular, between the optical depth measurements at the south pole and by the lunar eclipse technique following the El Chichón and Pinatubo eruptions.

Because of its global stratospheric integrating properties, the lunar eclipse technique is perhaps the most definitive for defining the global effect of volcanic eruptions on the stratospheric aerosol. The results suggest that not only did the Pinatubo eruption have a larger effect on the stratosphere than the El Chichón event, but that it is likely that it was at least as large as the Krakatau event. At this time, lunar eclipses which occurred after other volcanic events between the period 1888 and 1960 have not been analyzed. This period includes about 30 eruptions which had Volcanic Explosive Indices (VEI) of 4 or greater, including three with VEI's of 5 and two with 6 [*Simkin and Siebert*, 1994]. Included in the latter is the 1902 eruption of Santa Maria (14.75°N) in Guatemala which, occurring at low latitude, likely had a global effect on the stratosphere. In addition, observations for most eclipses exist back to about 1800. Completing this unique record of the effects of volcanic eruptions on the global stratosphere over a 200-year period is a goal worth pursuing.

REFERENCES

Barnes, J. E., and D. J. Hofmann, Variability in the stratospheric background aerosol over Mauna Loa Observatory, *Geophys. Res. Lett., 28*, 2895-2898, 2001.

Bodhaine, B. A., B. G. Mendonca, J. M. Harris, and J. M. Miller, Seasonal variations in aerosols and atmospheric transmission at Mauna Loa Observatory, *J. Geophys. Res., 86*, 7395-7398, 1981.

Bluth, G. J. S., S. D. Doiron, C. S. Schnetzler, A. J. Krueger, and L. S. Walter, Global tracking of the SO_2 clouds from the June 1991 Mount Pinatubo eruptions, *Geophys. Res. Lett., 19*, 151-154, 1992.

Deshler, T. M., E. Hervig, C. Kröger, D. J. Hofmann, J. M. Rosen, and J. B. Liley, Thirty years of in situ stratospheric aerosol size distribution measurements from Laramie, Wyoming (41°N), using balloonborne instruments, *J. Geophys. Res.,108*, 4167.doi:10.1029/2002JD002514, 2003.

Dutton, E. G., and B. A. Bodhaine, Solar irradiance anomalies caused by clear-sky transmission variations above Mauna Loa: 1958-1999, *J. Climate, 14*, 3255-3262, 2001.

Dutton, E. G., and J. R. Christy, Solar radiative forcing at selected locations and evidence for global lower tropospheric cooling following the eruptions of El Chichón and Pinatubo, *Geophys. Res. Lett., 19*, 2313-2316, 1992.

Ellis H. T., and R. F. Pueschel, Solar radiation: Absence of air pollution trends at Mauna Loa, *Science, 172*, 845-846, 1971.

Flammarion, C., L'eclipse totale de lune du 4 Octobre, *L'Astronomie 3*, 401- 408, 1884.

Grams, G., and G. Fiocco, Stratospheric aerosol layer during 1964 and 1965, *J. Geophys. Res., 14*, 3523-3542, 1967.

Grant, W. B., E. V. Browell, C. S. Long, L. L. Stowe, R. G. Grainger, and A. Lambert, Use of volcanic aerosols to study the tropical stratospheric reservoir, *J. Geophys. Res., 101*, 3973-3988, 1996.

Hamill, P., O. B. Toon, and C. S. Kiang, Microphysical processes affecting stratospheric aerosol particles, *J. Atmos. Sci., 34*, 1104-1119, 1977.

Hansen, J. E., and S. Matsushima, Light illuminance and color in the Earth's shadow, *J. Geophys. Res. 71*, 1073-1081, 1966.

Hansen, J. E., W.–C. Wang, and A. A. Lacis, Mount Agung eruption provides test of a global climatic perturbation, *Science, 199*, 1065-1068, 1978.

Hofmann, D. J., Perturbations to the global atmosphere associated with the El Chichón volcanic eruption of 1982, *Rev. Geophys., 25*, 743-759, 1987.

Hofmann, D. J., and J. E. Barnes, Interannual variability in the background stratospheric aerosol over Mauna Loa Observatory and the effects of the quasi-biennial oscillation, *Network for the Detection of Stratospheric Change 2001 Symposium*, Archachon, France, 24-27 Sept., p. 131, 2002.

Hofmann, D. J., and J. M. Rosen, Balloon observations of the time development of the stratospheric aerosol event of 1974-75, *J. Geophys. Res., 82*, 1435, 1977.

Hofmann, D. J., and J. M. Rosen, Balloonborne observations of stratospheric aerosol and condensation nuclei during the year following the Mt. St. Helens eruption, *J. Geophys. Res., 87*, 11,039-11, 061, 1982.

Jäger, H., and T. Deshler, Lidar backscatter to extinction mass and area conversions for stratospheric aerosols based on midlatitude balloonborne size distribution measurements, *Geophys.Res. Lett., 29*, doi:10.1029/2002GL015609, 2002.

Jäger, H., and D. Hofmann, Midlatitude lidar backscatter to mass, area, and extinction conversion model based on in situ aerosol measurements from 1980 to 1987, *Appl. Opt., 30*, 127-138, 1991.

Jäger, H., T. Deshler, and D. J. Hofmann, Midlatitude lidar backscatter conversions based on balloonborne aerosol measurements, *Geophys. Res. Lett., 22*, 1729-1732, 1995.

Junge, C. E., C. W. Chagnon, and J. E. Manson, Stratospheric aerosols, *J. Meteorol., 18*, 81-108, 1961.

Keen, R., Volcanic aerosols and lunar eclipses, *Science, 222*, 1011-1013, 1983.

Kepler, J., *Astronomiae Pars Optica,* Marnium and Aubrii, Frankfurt, pp. 267-284, 1604.

Lamb, H. H., Volcanic dust in the atmosphere, with a chronology and assessment of its meteorological significance, *Phil. Trans. Royal Soc. London, Series A, 266*, 425-533, 1970.

Lamb. H. H., Supplemental dust veil index assessments, *Climate Monitor, 6*, 57-67, 1977.

Link, F., *Die Mondfinsternisse*, Akademische Verlagsgesel-lschaft, Leipzig, 127 pp., 1956.

McCormick, M. P., and R. E. Veiga, SAGE II measurements of early Pinatubo aerosols, *Geophys. Res. Lett., 19*, 155-158, 1992.

McKeen, S. A., S. C. Liu, and C. S. Kiang, On the chemistry of stratospheric SO_2 from volcanic eruptions, *J. Geophys. Res., 92*, 4873-4881, 1984.

Pinto, J. P., R. P. Turco, and O. B. Toon, Self-limiting physical and chemical effects in volcanic eruption clouds, *J. Geophys. Res., 94*, 11,165-11,174, 1989.

Rosen, J. M., The vertical distribution of dust to 30 km, *J. Geophys. Res., 69*, 4673-4676, 1964.

Rosen, J. M., The boiling point of stratospheric aerosols, *J. Appl. Meteorol.* 10, 1044, 1971.

Sato, M., J. E. Hansen, M. P. McCormick, and J. B. Pollack, Stratospheric aerosol optical depths, 1850-1990, *J. Geophys. Res., 98*, 22,987-22,994, 1993.

Simkin, T., and L. Siebert, *Volcanoes of the World*, 349 pp., Geoscience Press, Inc., Tucson, 1994.

Smullin, L. D., and G. Fiocco, Optical echoes from the Moon, *Nature, 194*, 1267, 1962.

Solomon, S., Stratospheric ozone depletion: A review of concepts and theory, *Rev. Geophys., 37*, 275-316, 1999.

Stothers. R. B., Major optical perturbations to the stratosphere from volcanic eruptions: Pyrheliometric period, 1881-1960, *J. Geophys. Res., 101*, 3901-3920, 1996.

Trepte, C. R., R. E. Veiga, and M. P. McCormick, The poleward dispersal of Mount Pinatubo volcanic aerosol, *J. Geophys. Res., 98*, 18,563-18,573, 1993.

J. Barnes, Mauna Loa Observatory, Rm. 202, NOAA, P.O. Box 275, Hilo, HI 96721

T. Deshler, Dept. of Atmospheric Science, University of Wyoming, Laramie, Wyoming 82071

E. Dutton and D. Hofmann, Climate Monitoring and Diagnostics Laboratory, NOAA, 325 Broadway, Boulder, CO 80305-3328

H. Jäger, Forschungszentrum Karlsruhe, IMK-IFU, Kruezech-bahnstr. 19, 8100 Garmisch-Partenkirchen, Germany

R. Keen, PAOS-UCB 311, University of Colorado, Boulder, CO 80309

M. Osborn, Code 475, NASA Langley Research Center (SAIC), Hampton, VA 23665

Global, Long-Term Sulphur Dioxide Measurements From TOVS Data: A New Tool for Studying Explosive Volcanism and Climate

A. J. Prata[1], W. I. Rose[2], S. Self[3], and D. M. O'Brien[1]

A new technique for retrieving sulphur dioxide concentrations from TIROS Operational Vertical Sounder (TOVS) data is described. The retrieval technique relies on absorption of infrared radiation by the anti-symmetric stretch of the sulphur dioxide (SO_2) molecule centred around 7.3 μm. The High-resolution infrared radiation sounder (HIRS/2) is part of the TOVS package and has a channel that covers this absorption region. The HIRS/2 data are global, span almost 24 years, have a sub-satellite spatial resolution of about 18 km and can be used both day and night. The retrieval method is described and its accuracy and sources of error discussed. Case studies for the June 1991 Pinatubo eruptions, for the August 1991 eruptions of Cerro Hudson and for several eruptions of Hekla volcano, are used to illustrate the retrievals and the results are compared with independent SO_2 retrievals from the TOMS instrument. These new SO_2 data provide a potentially valuable tool for studying the climatic effects of explosive eruptions. Because the satellite measurements are global, long-term and can simultaneously provide other climate parameters (e.g. surface temperatures, temperature profiles, humidity profiles, cloudiness, ozone amount and long- and short-wave radiation) they can be used to test and validate volcanically-induced effects in global climate simulations.

1. INTRODUCTION

The global atmospheric budget of sulphur is important to climate [*Seinfeld and Pandis*, 1998]. Knowledge of the SO_2 component in the atmosphere has come from a variety of sources including ground-based, airborne and more recently satellite-based measurements [*Stoiber and Jepsen*, 1973; *Allard et al.*, 1994; *Pyle et al.*, 1996; *Bluth et al.*, 1993; *Bluth et al.*, 1997]. Estimates of the SO_2 budget provide lim-

[1]CSIRO Atmospheric Research, Victoria, Australia.
[2]Geological Engineering and Sciences, Michigan Technological University, Houghton, Michigan, USA.
[3]Department of Earth Sciences, The Open University, Milton Keynes, United Kingdom.

its on the amount of H_2SO_4 aerosol in the stratosphere [*Hofmann and Rosen*, 1981], which in turn can be used to evaluate the radiative effects on climate [*Kiehl and Briegleb*, 1993; *Mass and Portman*, 1989; *Robock*, 2000]. Stratospheric sulfuric acid aerosol derives principally from SO_2 injected by volcanic eruptions and these aerosols are important in the chemistry of the stratosphere by providing surfaces for chemical reactions. The current estimate of the stratospheric portion of the flux of SO_2 ranges from ~0.3 Tg a^{-1} to ~3 Tg a^{-1}, with a mean of ~1 Tg a^{-1} [*Pyle et al.*, 1996]. Indirect measurements of this flux have been made from the Total Ozone Mapping Spectrometer (TOMS) satellite [*Bluth et al.*, 1997; *Krueger et al.*, 1995], and more recently from the Global Ozone Monitoring Experiment (GOME)—see for example *Eisinger and Burrows* [1998]. *Rose et al.* [2000] have shown the usefulness of combining different satellite measurements of SO_2 to improve estimates of the atmospheric emission of this gas from volcanic eruptions. Given the importance of the stratospheric budget of SO_2 to climate and the sporadic and global nature of vol-

canic eruptions, it is useful to have other independent satellite measurements of SO_2. The purpose of our work here is to document a source of satellite SO_2 measurements that complement existing measurements and provide a valuable data-set for intercomparison with TOMS and GOME.

The NOAA series of satellites carry the TIROS Operational Vertical Sounder (TOVS) instrument package which includes the High-resolution Infrared Radiation Sounder (HIRS/2–see *Smith et al.*, [1979]). This instrument measures infrared radiation in nineteen narrow channels (bandwidths $\approx 0.5–1$ μm) with the purpose of retrieving atmospheric temperature and moisture profiles. One channel (channel 11) completely covers the strong, anti-symmetric stretch vibration (v_3-band) of SO_2 situated near 7.34 μm (see Figure 1). This channel is used for tropospheric water vapour sounding, but it is shown here that provided the water vapour lies below the SO_2, the channel can also be used to measure SO_2 column abundance.

Figure 1 shows the vertical transmittance, in the wavelength range 6–13 μm, for a cloud layer containing 100 m atm-cm (dashed line) and 1000 m atm-cm (solid line) of SO_2, with a width of 2 km, placed at 25 km in an otherwise absorber-free atmosphere.

The main absorption features are the v_1 and v_3 bands, centred near 8.55 μm and 7.34 μm, respectively. Both of these bands can be used to retrieve SO_2 column amounts.[1] The v_1 feature looks particularly interesting because it lies within the 'window' where absorption due to water vapour is smaller. Indeed *Realmuto et al.*, [1994] and *Realmuto* [1996] have developed methods for retrieving SO_2 using this feature from airborne and spaceborne sensors (e.g. MASTER, ASTER and MODIS). Ground-based interferometric measurements have also been made using this band

Figure 1. Positions of HIRS/2 filter functions and vertical atmospheric transmittance (100 m atm-cm and 1000 m atm-cm) for the v_1 and v_3 SO_2 bands.

[*Francis et al.*, 1995; *Love et al.*, 1998; *McGee and Gerlach*, 1998]. Use of the v_3-band can be traced to work first published by *Mankin et al.* [1992] and *Goldman et al.* [1992] who used a high spectral resolution instrument (an interferometer) to exploit the 'micro-windows' around 7.3 μm. *Crisp* [1995] was first to suggest that the 7.3 μm band on MODIS could be used to provide an SO_2 alert, but she did not develop a quantitative retrieval procedure. *Ackerman and Strabala* [1994] used HIRS/2 data to study H_2SO_4 aerosols by utilising information in the 8- to 12-μm region. *Baran and Foot* [1994] demonstrated the use of HIRS/2 data and radiative transfer modelling to derive quantitative estimates of H_2SO_4 aerosols. Our work is the first to attempt a quantitative retrieval based on broadband (bandwidths $>\sim 0.4$ μm) infrared measurements of the v_3 absorption feature of SO_2. In essence the retrieval from satellite-based broadband measurements is possible whenever the SO_2 is well-separated from H_2O and above it. Thus the method is ideally suited to studies of SO_2 that affect the climate, that is, quantitative studies of large volcanic emissions of SO_2 that have been injected into the upper troposphere/lower stratosphere.

In this paper we describe the principle of the retrieval method and suggest a model and methodology for use with HIRS/2 data. Next we discuss the practical implementation of the algorithm and provide a thorough error analysis. Examples of retrievals for several well-studied eruptions are given together with results for the 1996 Mt Ruapehu eruptions–for which no TOMS data were available. Two appendices are provided—Appendix 1 contains a list of the acronyms used throughput the paper, and Appendix 2 contains some of the mathematical detail. Finally, we suggest ways these new data can be used to study the atmospheric effects of explosive volcanism on climate.

2. SO₂ RETRIEVAL FROM INFRARED MEASUREMENTS

2.1 The HIRS/2 Instrument

The first TOVS package was launched on board the TIROS-N satellite in 1978 and the latest is on the NOAA-17 platform-providing 24 years of continuous global measurements. The HIRS/2 instrument includes measurements in 20 channels (19 in the infrared and 1 visible channel)—giving estimates of surface temperature, atmospheric profiles of temperature and moisture, cloudiness and column ozone abundance. These data are used operationally to provide meteorological data for numerical weather forecasting.
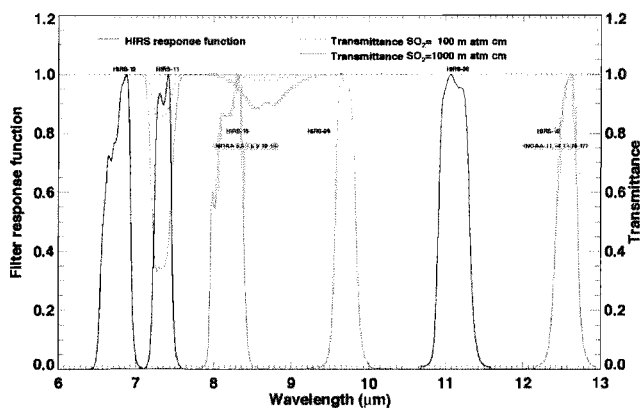
Table 1. Characteristics of the HIRS/2 channels relevant to SO_2 retrieval

Channel No.	Central wavelength (μm)	Half-power bandwidth (μm)	Purpose	Weighting function peak (hPa); (km in brackets)
8	11.11	0.45	Surface/clouds	Surface (0–2 km)
9	9.71	0.48	Ozone	25 (25–35 km)
10	8.16/12.47[a]	0.42/0.46[b]	Surface/cloud	900 (1–2 km)
11	7.33	0.44	Water vapour	700 (3–4 km)
12	6.72/6.52[a]	0.37/0.37[b]	Water vapour	500 (5–6 km)

[a] New central wavelength on HIRS/3.
[b] New half-power bandwidth on HIRS/3.

The channels were chosen to maximize information retrieved from radiances sampling different vertical layers of the atmosphere several kilometres thick. Most of the channels lie near strong absorption features (e.g. near to CO_2 or H_2O absorption features), while some channels are located in atmospheric window regions where information about the surface and lower atmosphere can be retrieved. Table 1 provides information about the channels of relevance to this study. Table 2 provides information on the HIRS/2 instrument—more comprehensive information may be found in *Smith et al.* [1979], *Planet* [1988], and *Kidwell* [1991].

The filter functions of the HIRS/2 instrument are also shown in Figure 1, together with SO_2 transmittance of the v_1 and v_3 SO_2 bands. Only the channels at 6.7, 7.3, 8.2, 9.7, 11 and 12 μm are shown—the channels used in the retrieval are plotted using thick lines. Note that the SO_2 v_3 feature is almost entirely covered by HIRS/2 channel 11, while only a small part of the SO_2 v_1 band is covered by channel 10. The HIRS/2 instrument has undergone some changes over its 24 year history; there are in fact three versions of the instrument—HIRS (originally flown on Nimbus-6), HIRS/2 (NOAA-satellite series) and the present HIRS/3. Table 3 provides a chronology of the instruments' service record, spacecraft, launch date, and the node crossing times.

2.2 Transmittance Model

To exploit the SO_2 information contained in the HIRS/2 measurements we employ an accurate transmittance model that relates the absorption in HIRS/2 channel 11 to SO_2 absorber amount. The anti-symmetric stretch of the SO_2 molecule is situated around 7.34 μm and the transmittance of this feature has been modelled using a double-exponential model by *Pierluissi and Tomiyama* [1980] and *Pierluissi et al.* [1984]. We validated this model against line-by-line calculations and found the results to be accurate below about 200 m atm-cm[(2)]. Above this value the model diverged from the line-by-line results. Based on this assess-

ment we decided to use an exponential sum-fitting procedure (ESFT, see *Wiscombe and Evans* [1977]) to the band transmittance. The ESFT model has the form,

$$t_s = \sum_{i=1}^{n} a_i \exp(-k_i u), \qquad (1)$$

where t_s is the transmittance (see Appendix 2 for a definition), u is absorber amount, and a_i, k_i are coefficients. This model is accurate over a wide range of absorber amounts and is very fast for use operationally because a table of coefficients can be generated off-line for each assumed absorber layer (characterized by its atmospheric layer pressure and temperature) and for all the satellite filter response functions. Since HIRS/2 channel 11 has a finite bandpass, the coefficients for the band model account for the variation of the absorption across the channel 11 filter function. In practice the absorber amounts are pre-computed for 26 different atmospheric layers, and each HIRS/2 channel 11 on each satellite, in 0.001 transmittance steps. This provides a large look-up table which can be efficiently searched to provide excellent processing

Table 2. Characteristics of the HIRS/2 instruments.

Parameter	Value
Field-of-view	21.8 mrad
Ground field-of-view	
Nadir	18.5 km circular
End of scan	31.8 km × 62.8 km
Scan line	
Scan time	6.4 s
Scan angle	±49.5°
Swath width	±1115 km
Number of spots per scan line	56
Distance between spots	
Cross-track	26.4 km
Along-track	41.8 km
Gap between consecutive passes at the equator	540 km

Table 3. Chronology of the NOAA meteorological satellite series.

Space-craft	Launch date	Ascending node	Descending node	Service period
TIROS-N	Oct-13-1978	15:00	03:00	Oct-19-1978-Jan-30-1980
NOAA-6	Jun-27-1979	19:30	07:30	Jun-27-1979-Nov-16-1986
NOAA-7	Jun-23-1981	14:30	02:30	Aug-24-1981-Jun07-1986
NOAA-8	Mar-28-1983	19:30	07:30	May03-1983-Oct-31-1985
NOAA-9	Dec-12-1984	14:20	02:20	Feb-25-1985-Aug-03-1995
NOAA-10	Sep-17-1986	19:30	07:30	Nov-17-1986-March-1995
NOAA-11	Sep-24-1988	13:30	01:40	Nov-08-1988-Sep-09-1994
NOAA-12	May-14-1991	19:30	07:30	May-14-1991-present
NOAA-13	Aug-09-1993		Power failure 12 days after launch	
NOAA-14	Dec-300-1994	13:40	01:40	Dec-30-01994-present
NOAA-15	May-13-1998	19:26	07:26	Dec-15-1998-present
NOAA-16	Sep-21-2000	14:00	02:00	Sep-21-2000-present
NOAA-17	Jun-24-2002	22:00	10:00	Jun-24-2002-present

speed for global retrievals. The precise look-up tables used are available from the authors on request.

A simplified radiative transfer model is proposed for deriving SO₂ transmittance from the HIRS/2 temperature measurements. The details of the derivation are given in Appendix 2—the main result is given here. As noted in Appendix 2, Eq. (16) may be written in the form:

$$I - I_a = (1 - t_s)(B_s - I_a),$$ (2)

where I is the measured radiance at 7.3 μm, I_a is the radiance at 7.3 μm for an atmosphere free of SO₂, t_s is the SO₂ transmittance and B_s is the Planck radiance for the SO₂ cloud layer at temperature T_S This equation suggests that,

$$\Delta T = \alpha + \beta(1 - t_s).$$ (3)

where ΔT is the temperature difference corresponding to the difference between the measured radiance and the SO₂-free radiance, obtained using the inverse Planck function. α and β are parameters to be estimated. From analysis of data and from Modtran [*Berk et al.*, 1989] modelling it has been found that,

$$\alpha \approx -8K,$$
$$\beta \approx -32K.$$

In practice α and β are functions of the atmospheric state and, in particular the temperature of the SO₂ cloud. Since the SO₂ cloud temperature is unknown we have used data and modelling to estimate these parameters, but the algorithm still requires an independent estimate of the height of the SO₂ cloud in order to generate the appropriate look-up table.

3. PRACTICAL CONSIDERATIONS

The simple model presented here permits the evaluation of t_S from a measurement of ΔT. For HIRS/2 data, the evaluation of ΔT is made by estimating I_a through a linear interpolation of a radiance measurement at 6.7 μm (HIRS/2 channel 12) and a radiance measurement at 11.1 μm (HIRS/2 channel 8). The use of the 11.1 μm channel is made in preference to a channel at 8.2 μm because this channel is also affected by SO₂ absorption and so cannot give a reliable estimate of the unperturbed atmospheric state. Thus,

$$I_a = I_a^{lin} = a + b\lambda_{7.3}$$
$$b = \frac{B[T, \lambda_{6.7}] - B[T, \lambda_{12}]}{\lambda_{6.7} - \lambda_{12}}$$ (4)
$$a = B[T, \lambda_{6.7}] - b\lambda_{6.7}.$$

Here all λ subscripts refer to central wavelengths (in μm). Finally,

$$\Delta I_a^{lin} = B[T, \lambda_{7.3}] - I_a^{lin}.$$ (5)

It should be noted that, in general, $\Delta I_a^{lin} < 0$. The HIRS/2 data processing proceeds on a pixel-by-pixel basis.

3.1 Estimating the Background Radiance

The scheme outlined above relies on an estimate of the background (unperturbed) radiance at 7.3 μm, which has been obtained using a linear interpolation (Eq. 5). The accuracy of the linear interpolation of radiance as a function of wavelength has been gauged by studying large amounts of HIRS/2 data for cases where there are no SO₂ clouds present. In most situations this appears to be accurate (within ±2

K in 95% of cases studied). There is however a notable bias with the interpolated value usually higher than the actual value. In some cases, with no SO_2 present, it was found that the linear interpolation was a poor estimate of the observed radiance. Presumably, this is due to the effects of clouds within the HIRS/2 field-of-view. With just a small addition in complexity, a significant improvement to the scheme was made in the following manner:

(1) Blackbody radiance curves are generated using the observed radiances at 6.7 and 11.1 μm, and 'pseudo' radiances ($I^*(T_{\lambda 1}, \lambda_2)$) are calculated at all three wavelengths:

$$I^*(T_{11.1}, 6.7) = B(T_{11.1}, 6.7),$$

$$I^*(T_{6.7}, 7.3) = B(T_{6.7}, 7.3),$$

$$I^*(T_{11.1}, 7.3) = B(T_{11.1}, 7.3),$$

$$I^*(T_{6.7}, 11.1) = B(T_{6.7}, 11.1),$$

The blackbody radiance curves bracket the range of possible observed radiances at 7.3 μm. (See Figure 2.)

(2) An estimate of the observed radiance is obtained from:

$$\hat{I}_a = 0.5\left[I^*(T_{6.7}, 7.3) + I^*(T_{11.1}, 7.3)\right].$$

(3) An adjustment to the linearly interpolated 7.3 μm radiance is obtained from:

$$I_a^{adj} = 2.0\left[I^*(T_{11.1}, 7.3) - I^*(T_{6.7}, 7.3)\right].$$

(4) If the brightness temperature at 11.1 μm is above a certain threshold (270 K is used), then the 7.3 μm radiance estimate is obtained from the adjusted linearly interpolated value; otherwise the average of the 'pseudo' radiances is used:

$$\hat{I}_{a7.3} = I^{lin} - I_a^{adj} \qquad T_{11.1} > T_{thresh},$$

$$\hat{I}_a = 0.5\left[I^*(T_{6.7}, 7.3) + I^*(T_{11.1}, 7.3)\right] \quad \text{otherwise}$$

The scheme attempts to account for the effects of multiple layer clouds within the pixel, whilst also remaining relatively simple to implement. Figure 2 provides a graphical illustration of the interpolation scheme for a pixel containing SO_2.

The difficulty in estimating the background radiance lies in the non-linear temperature response from a pixel of mixed composition (i.e. clear-sky and clouds at multiple levels). Ideally the scheme should be designed to first estimate the fractional coverage of cloud within the pixel, together with an estimate of the clouds' height or radiating

temperature. Then, under less restrictive assumptions the radiance at 7.3 μm is estimated from clear and cloud-sky radiances separately and combined by weighting the radiances with the fractional cover estimate. Further accuracy could be gained by employing a radiative transfer model with forward calculations and utilising the full suite of HIRS/2 channels. Such improvements are beyond the scope of this paper, and we readily concede that this retrieval scheme suffers limitations.

3.2 The Effects of the HIRS Filter Function

The HIRS filter functions cover approximately 0.44 μm and the response is not constant across the band. *Pierluisi*
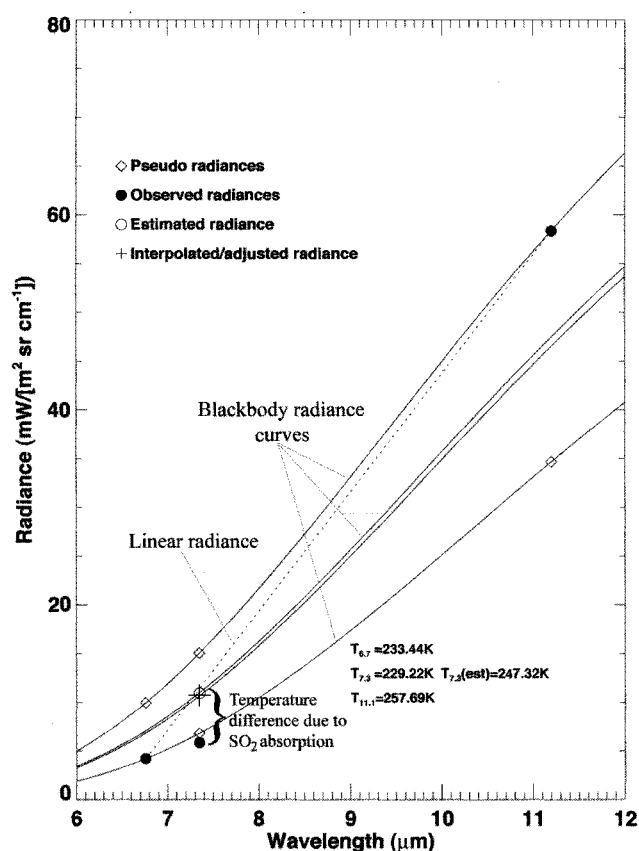
Figure 2. Radiance *vs.* Wavelength for a pixel which contains SO_2. The curves are blackbody radiances at the temperatures found by inverting the Planck function at 6.7 μm and 11.1 μm. The + shows the adjusted linearly interpolated radiance at 7.3 μm, the open circle shows radiance at 7.3 μm derived from Eq. 5, and the solid circles show the measured radiances. The difference between the observed 7.3 μm temperature and the estimated 7.3 μm temperature is the temperature anomaly.

et al. [1984] provide spectral band parameters for SO$_2$ that can be used to assess the effect of the HIRS filter response on the transmittance. The analysis indicates that the effect is small but important. The difference between assuming a monochromatic transmittance function and doing an integration across the HIRS filter function varies with absorber amount and with the height of the SO$_2$ cloud. The transmittance difference was found to be less than 0.05 over the whole parameter range and peaked between 10–20 m atm-cm. Above 50 m atm-cm the transmittance difference was less than 0.02. The ESFT scheme employed here accounts for the effects of the HIRS filter functions.

3.3 The Effects of the Surface

The analysis indicates that the surface radiance has only a small effect on the retrieval. This lack of dependence arises through the use of radiances from different channels for the same pixel when estimating the unperturbed radiance at 7.3 μm, and from the fact that this channel is almost opaque, except for very dry atmospheres. For optically thin veils of SO$_2$[3], the sensitivity of the scheme will prohibit accurate retrievals. A test is used to limit the retrieval to cases where,

$$T_{11.1} < 295K,$$

where T$_{11.1}$ is the (Planck) brightness temperature sensed in the 11.1 μm channel at the top of the atmosphere.

3.4 The Effects of Water Vapour

Residual water vapour absorption may cause anomalies in the retrieval. If there is significant water vapour absorption within the SO$_2$ cloud then this will also show up as extra absorption in the 6.7 μm channel. This channel is used in the linear interpolation scheme so the algorithm will compensate for the effect of in-cloud water vapour. For cases where there are very high water vapour amounts lying just below the SO$_2$ cloud it is possible that the retrieval will produce anomalous results. The effect will be worse if the SO$_2$ cloud is thin—this sets a limit on the lowest SO$_2$ amount that can be retrieved. There may also be situations where the vertical water vapour distribution causes the linear interpolation scheme to break-down, however these are unlikely to be common situations as they require unusual atmospheric conditions. Finally, SO$_2$ lying below significant water vapour will not produce a useful signal because the 7.3 μm channel is sensitive to water vapour. This puts a constraint on the lowest level in the atmosphere for which SO$_2$ can be measured. A rule-of-

thumb estimate for this is 3 km, which is the mean water vapour scale height [*Randel et al.*, 1996]. A test is employed to eliminate water vapour anomalies. To pass the test, pixels must satisfy the condition:

$$T_{11.1} > T_{6.7}. \qquad (6)$$

Essentially this test regards the brightness temperature in the window channel (11.1 μm) as *always* being *larger* than the brightness temperature in the water vapour channel (6.7 μm). There are occasions when this may not be true (e.g. strong inversions). The test eliminates very few pixels from the retrieval process.

A further test checks that the brightness temperature at 8.2 μm (or 12.5 μm for NOAA-11 and beyond) is larger than the brightness temperature at 11.1 μm, when the 11.1 μm brightness temperature is low (250 K is used). This eliminates some volcanic ash signals and abnormal water vapour and cloud signals. The test is conservative.

3.5 The Effects of Clouds

Water/ice clouds lying above the SO$_2$ cloud will mask SO$_2$ absorption and consequently the scheme will not 'see' the SO$_2$. This can occur for very high, thick (cold) cloud, particularly in the tropics. A test has been devised to limit the retrieval to cases where,

$$T_{11.1} > 200K.$$

This test also doubles to eliminate problems arising from thin SO$_2$ veils overlying very cold surfaces (e.g. ice covered surfaces in winter), which suffer from the same constraints as described in 3.3.

A second test is employed to remove the effects of poor calibration, pixel misalignment and some abnormal conditions, notably very high water vapour loadings and strong cirrus cloud signals. The test is:

$$T_{8.2} - T_{11.1} < -10K. \qquad (7)$$

For satellites after NOAA-10 the test is:

$$T_{12.5} - T_{11.1} < -10K. \qquad (8)$$

The thresholds used in these tests were determined through extensive data analysis and trial-and-error. A better approach would be to use an objective cloud detection scheme, such as *English et al.* [1999]. Work is in progress to

include such a scheme. The current tests are preliminary and need refinement.

3.6 Data Integrity Tests

The TOVS data processing is complex and occasionally suspect data are delivered into the processed HIRS/2 data files. There appears to be no systematic problem with the data processing, rather anomalies appear to occur in an unpredictable, almost random manner. To eliminate spurious data a simple spike test has been employed. This takes the form of calculating the mean of 8 neighbouring pixels and testing the pixel being processed against the mean. If the pixel value lies well outside the mean the retrieval halts for this pixel. There is a small cost of losing valid data. That is, having a valid pixel with an anomalously high valid value in the neighbourhood of low values, being eliminated in the process.

3.7 Sensitivity to Cloud Height

The conversion of ΔT measurements into transmittance is relatively straightforward via (3), and the transmittance model (1) allows an estimate of the absorber amount u. However, this conversion has a dependence on pressure and temperature of the absorber (through the pressure and temperature dependence of the ESFT coefficients a_i and k_i); in other words it depends on the location of the SO_2 in the vertical. The dependence on pressure is stronger than that on temperature. Thus, the retrieval requires a height estimate for the SO_2. Figure 3 illustrates the variation of SO_2 absorber amount (u) with temperature anomaly (ΔT) for different cloud heights.

4. ERROR ANALYSIS

Several sources of error have been identified in the retrieval of SO_2 from HIRS/2 infrared measurements. We class these errors into two types: those that contribute to the accuracy of the retrieval and those that limit the operation of the retrieval. The first type of errors (Type I) include as major sources:

- Inherent accuracy of the measurements–the NEΔT,
- Errors in estimating the background radiance,
- Transmittance modelling errors,
- Error in SO_2 cloud height and temperature estimation.

The Noise Equivalent Temperature Difference (NEΔT) of HIRS/2 channels 8, 11 and 12 are ~0.5 K. The background
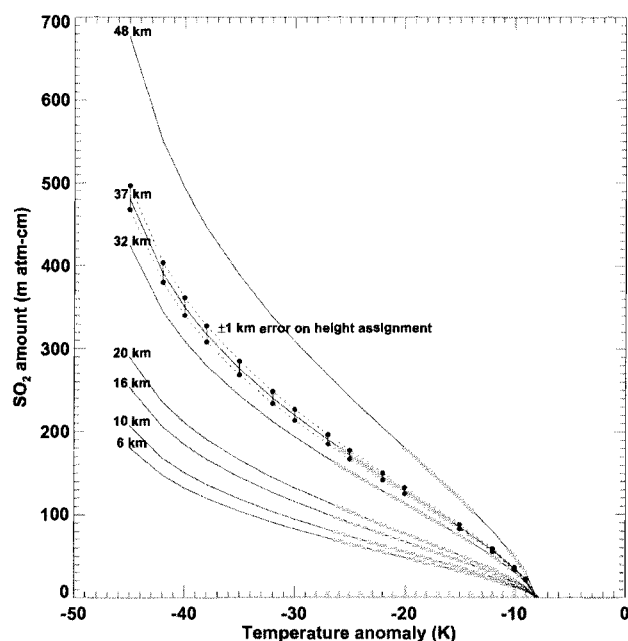

Figure 3. Variation of SO_2 amount with temperature anomaly (ΔT). Each curve shows the variation of the temperature anomaly (ΔT) with absorber amount for a particular SO_2 cloud-top height. An indication of the error resulting from a ±1 km error in the height assignment is also shown.

radiance errors are difficult to estimate theoretically, but can be estimated by analysis of large amounts of HIRS/2 data when no SO_2 clouds are present. These analyses suggest an rms error of ±1 K. Transmittance modelling errors include SO_2 band parameter errors, errors due to misfit in the ESFT procedure, errors in the filter response specification, and errors in the relation between SO_2 transmittance and 7.3 μm temperature differences. The largest of these four sources of error is the latter and we have estimated this to be ±1 K, based on radiative transfer simulations. Combining these errors and assuming that they are independent, the Type I error is:

$$\delta T_i \approx \pm 1.5K.$$

This can be easily assessed by conversion into an error in SO_2 amount by using the sensitivity of the double-exponential model [*Pierluisi et al.*, 1984]. Figure 4 illustrates Type I error in retrieved SO_2 for measurement and modelling errors and two cloud heights.

For relatively low clouds, SO_2 amounts of < 5 D.U. (1 D.U.=1 m atm-cm) are subject to large error and are probably indistinguishable from the noise (unless spatial coherence is evident). For higher clouds this lower thresh-

ous problem will need to wait until routine high spectral resolution data are available across the 7.3 μm band (e.g. from AIRS data–see *Chahine et al.*, [2003]).

5. EXAMPLES

5.1 Pinatubo

Quantitative use of HIRS/2 data to estimate SO_2 has not been made previously and it is therefore necessary to demonstrate what is possible using examples from well-known cases of volcanic SO_2 clouds. One such case is that of the June 1991 Pinatubo eruptions which are generally regarded to have injected ~15–19 Tg of SO_2 into the stratosphere [*Self et al.*, 1996]. Such a large SO_2 anomaly should be readily detectable in the HIRS/2 data.

The Pinatubo SO_2 cloud was measured by the TOMS instrument and also by several other airborne and satellite-borne sensors [*McCormick et al.*, 1995; *Self et al.*, 1996]. During 1991 three HIRS/2 instruments were flying (see Table 2)–on NOAA-10, NOAA-11 and NOAA-12. These satellites had different node crossing times and, since HIRS/2 is an infrared sensor both day and night coverage was possible. Plate 1 shows a time sequence of SO_2 retrievals made from the three HIRS/2 instruments and Table 4 provides a comparison of total masses (determined in the same way as in *Krueger et al.*, 1995, Eq. 15) retrieved from combined HIRS/2 measurements (3 instruments) with TOMS for several days. Generally, the agreement is good: HIRS/2-TOMS=+1.0 Tg, σ = ±1.2 Tg.

5.2 Cerro Hudson

In August 1991, Cerro Hudson erupted sending a large amount (> 1 Tg) of SO_2 into the upper troposphere and lower stratosphere. HIRS/2 retrievals have successfully tracked the SO_2 cloud for nearly 3 weeks as it circled the southern hemisphere at latitudes south of 30 °S. Plate 2 shows a montage of SO_2 retrievals obtained over a 9-day period as the cloud encircled the hemisphere. Numerical modelling of the cloud transport and TOMS data verify that the cloud passed over southern Australia and the Tasman sea, causing several aviation encounters [*Doiron et al.*, 1991; *Barton et al.*, 1992].

The HIRS/2 retrievals gave very similar results to those obtained from TOMS and because of the greater temporal sampling offer new opportunities to estimate the decay rate of stratospheric SO_2 and permit new studies of the conversion rate of SO_2 to H_2SO_4. Both of these parameters are important to the chemistry of atmospheric SO_2 [*McKeen*

et al., 1984]. Diurnal effects on SO_2 and the relation between SO_2, H_2SO_4 and O_3 (using the HIRS/2 9.7, μm channel) are also possible.

5.3 Ruapehu

The examples given so far can be readily verified against the TOMS data. During 1996 no TOMS instruments were flying and consequently little is known about the SO_2 stratospheric loading during that year. However, there were several volcanic eruptions reported, some of which are likely to have injected SO_2 into the upper troposphere/lower stratosphere.

Between June and August 1996, Mt Ruapehu on the North island of New Zealand erupted several times injecting ash and SO_2 into the atmosphere. Satellite tracking of the Ruapehu plumes using AVHRR data suggested that the ash content of the eruption clouds was significant [*Prata and Grant*, 2001]. Ground-based monitoring of the emissions also suggested that there was significant SO_2 degassing. The first satellite measurements of the SO_2 emissions from Ruapehu are presented here. Results are shown in Plate 3 for retrievals from the NOAA-12 and NOAA-14 HIRS/2 instruments. Maximum SO_2 amounts did not exceed 100 D.U.; the average amounts were ~20–30 D.U. The total mass loadings were less than 0.05 Tg-values of 0.03, 0.02, 0.02, and 0.01 Tg were found for the 17 June, 1996 eruption.

5.4 Hekla–Trajectories

A fourth example of detection and monitoring of relatively small (~< 1 Tg), stratospheric SO_2 clouds from eruptions

Table 4. SO_2 column abundances (Tg) retrieved from HIRS/2 infrared measurements and TOMS ultraviolet measurements [*Bluth et al.*, 1992] for several days after the Pinatubo eruptions of 15 June, 1991. The HIRS/2 means (μ) and standard deviations (σ) are obtained by combining measurements from all three HIRS/2 instruments.

Date	HIRS/2		TOMS
	μ	σ	μ
16-June-1991	15.2	±1.8	15.5
17-June-1991	18.7	±2.2	18.5
18-June-1991	16.5	±1.2	16.0
19-June-1991	15.9	±1.1	14.0
20-June-1991	17.4	±1.1	14.5
21-June-1991	16.3	±0.9	–
22-June-1991	16.9	±1.6	–
23-June-1991	15.0	±1.8	14.0
24-June-1991	12.9	±1.7	–
25-June-1991	11.5	±1.7	–

SO₂ absorber amount (m atm-cm)
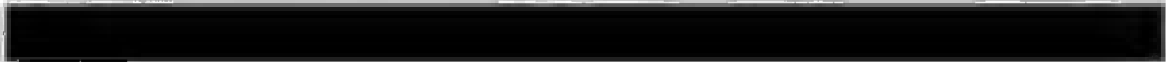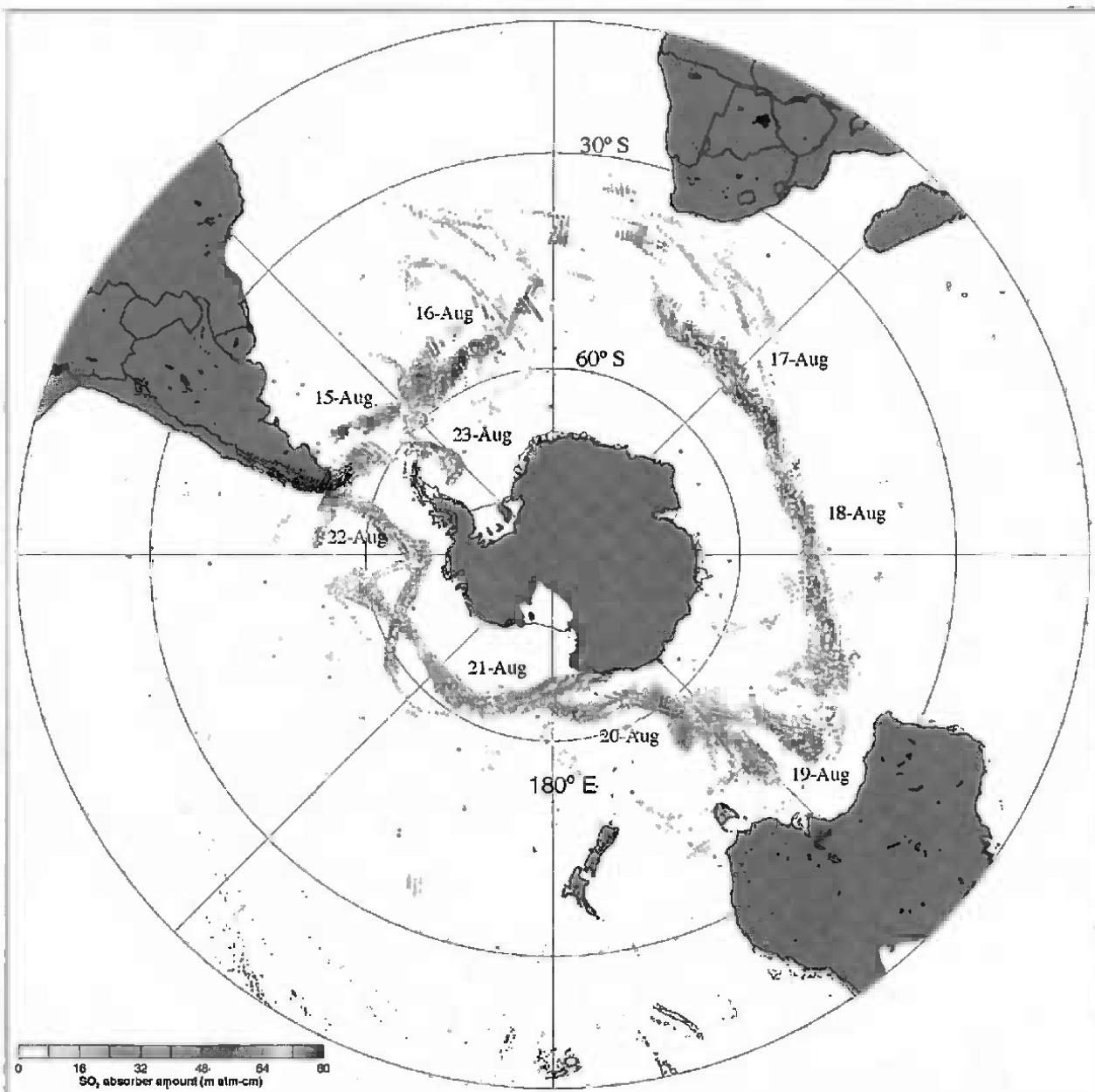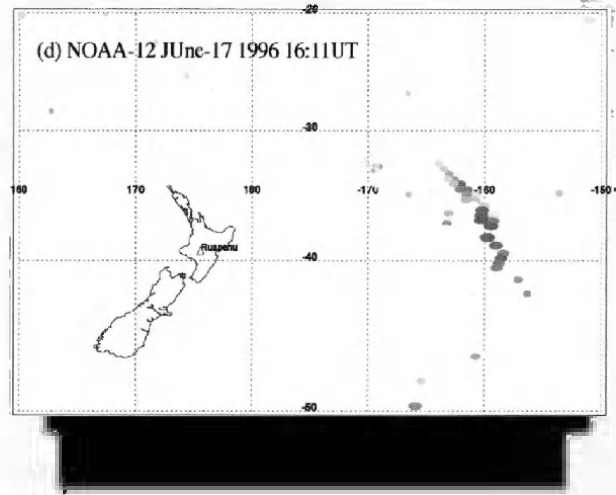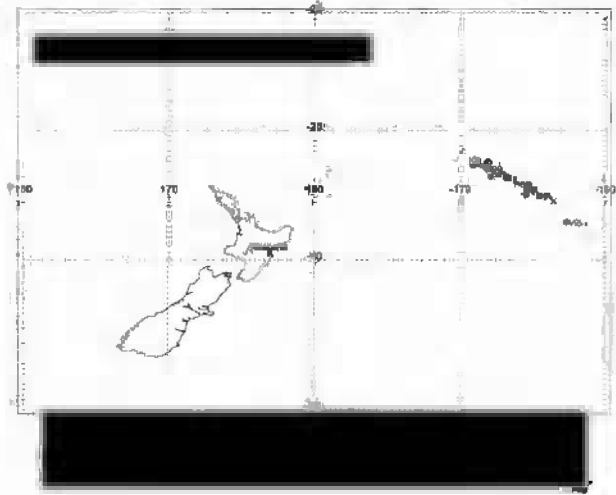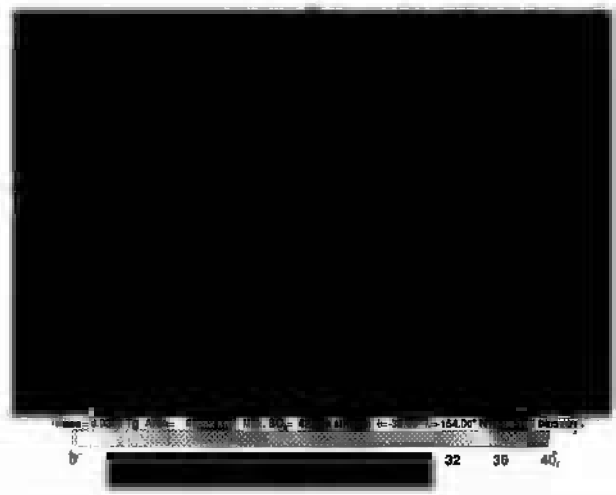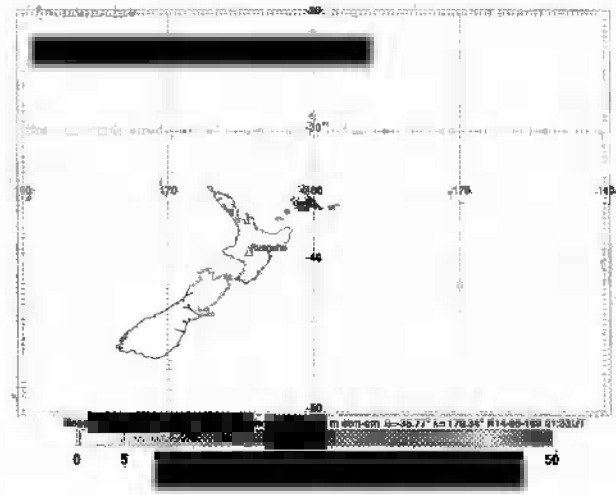
(d) NOAA-12 JUne-17 1996 16:11UT

Hekla Eruption August 1980. TOVS SO₂ analysis NOAA 6

(a)

(b)

radiative transfer modelling, an improved cloud detection scheme, and better use of the multispectral measurements available with the HIRS/2 instrument. The scheme presented here is fast and ideally suited to operational processing of global data in near real-time.

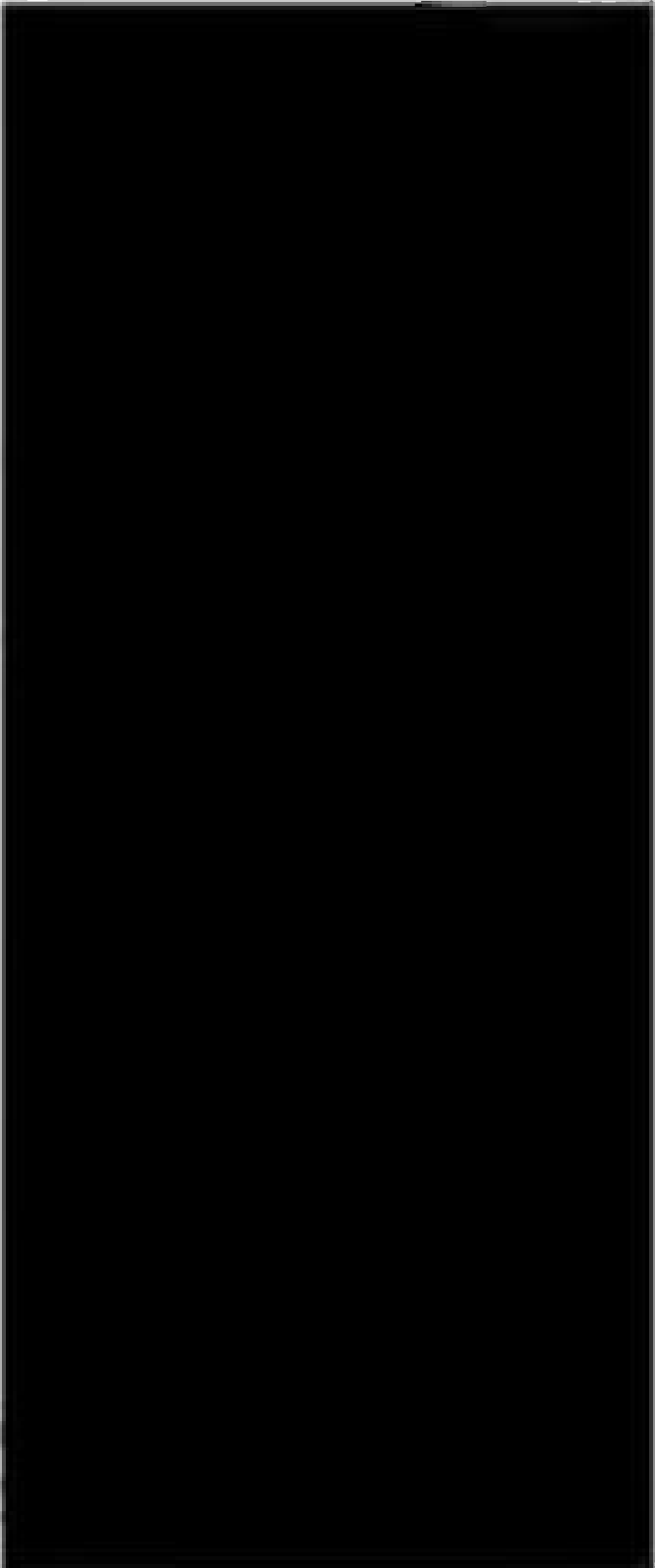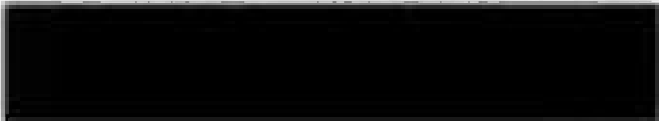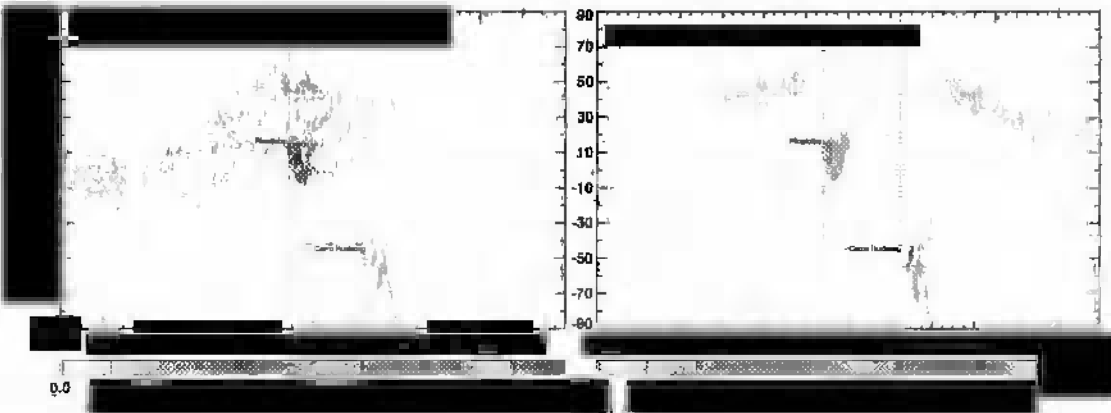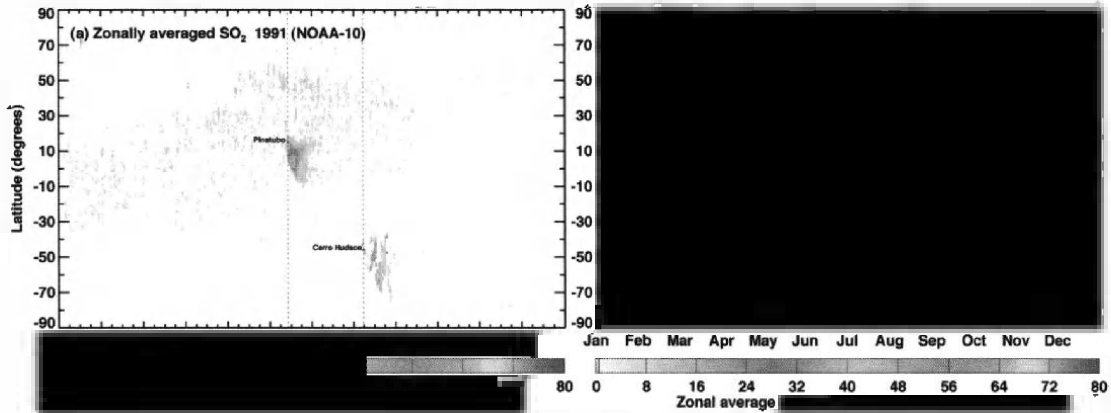Further analysis of the HIRS/2 data will permit retrieval of volcanic ash, H_2SO_4 (cf. *Ackerman and Strabala* [1996] and *Baran and Foot* [1994]) as well as SO_2, providing a more comprehensive set of data for understanding the climatic influence of volcanic eruptions. Use of the 9.7 μm HIRS/2 channel in combination with the SO_2 retrievals may also provide new information on the effects of volcanic aerosols on ozone depletion.

The retrieval scheme is not restricted to HIRS/2 data-any instrument with channels near 6.7, 7.3 and 11 μm is amenable to this technique. The MODIS instruments on board Terra and Aqua can be used to derive SO_2 [see Rose et al:, 2003 this volume] as can the new multispectral imager-SEVIRI, on board the Meteosat Second Generation platform. Currently the AIRS instrument on board the Aqua platform can be used to derive SO_2 by exploiting the 7.3 μm feature, with the strong possibility of using the high-spectral content and the narrow channels (up to 2378) to probe the lower troposphere and derive vertical profile information. Perhaps more exciting is the possibility of using the high-spectral resolution data from the Geostationary Infrared Fourier-Transform Spectrometer (GIFTS), which will provide high spatial, temporal and spectral resolution data capable, in principle, of giving SO_2 concentrations at several levels in the upper troposphere/lower stratosphere. To date we have processed only a small part of the considerable global archive of HIRS/2 data. In due course we hope to complete the processing back to the TIROS-N HIRS/2 (1978) and provide a real-time processor for users with access to direct broadcast NOAA data. An operational HIRS/2 SO_2 product would be useful for aviation hazard warning as well as for studying local and global effects of SO_2 on climate.

APPENDIX 1: LIST OF ACRONYMS

AIRS–*Atmospheric InfraRed Sounder*
ASTER–*Advanced Spacebourne Thermal Emission and Reflection radiometer*
AVHRR–*Advanced Very High Resolution Radiometer*
HIRS–*High-resolution InfraRed Sounder*
GIFTS–*Geostationary Infrared Fourier-Transform Spectrometer*
GOME–*Global Ozone Monitoring Experiment*
MASTER–*MODIS/ASTER Airborne Simulator*
MODIS–*Moderate-resolution Imaging Spectroradiometer*
NOAA–*National Oceanographic and Atmospheric Administration*
SEVIRI–*Spinning Enhanced Visible amd Infrared Imager*
TIROS–*Television and InfraRed Orbiting Satellite*
TOMS–*Total Ozone Monitoring Spectrometer*
TOVS–*TIROS Operational Vertical Sounder*

APPENDIX 2: RADIATIVE TRANSFER MODEL

The model assumed for analysis of HIRS data has a layer of SO_2 embedded in an otherwise clear atmosphere between heights $z = a$ and $z = b$. Variations in the density of SO_2 and its specific absorption coefficient are assumed to be negligible throughout the layer. The optical thickness from height z to space along a vertical ray is

$$l(z) = \begin{cases} l_a(z) & \text{if } b \le z \\ l_a(z) + \alpha_s(b-z) & \text{if } a \le z \le b. \\ l_a(z) + \alpha_s(b-a) & \text{if } z \le a \end{cases}$$

Here $l_a(z)$ is the optical path from height z to space of an atmosphere without SO_2, and α_s is the volume absorption coefficient of SO_2. The corresponding transmittances from height z to space are

$$t(z) = \begin{cases} t_a(z) & \text{if } b \le z \\ t_a(z) \exp(-\alpha_s(b-z)) & \text{if } a \le z \le b, \\ t_a(z) \exp(-\alpha_s(b-a)) & \text{if } z \le a \end{cases}$$

where $t_a(z)$ is the transmittance of an atmosphere without SO_2. We let τ_s and t_s denote the optical thickness and transmittance of the SO_2 column, defined by

$$\tau_s = \alpha_s(b-a) \quad \text{and} \quad t_s = \exp(-\tau_s). \tag{9}$$

The SO_2 layer attenuates the radiance emitted by the atmosphere below, while within the SO_2 layer, where both the atmosphere and SO_2 are active, absorption by each gas modifies the radiance emitted by the other. The radiance I emitted to space consists of four terms,

$$I = t_s I_a + (1-t_s) I_a^+ + I_{as} + I_{sa}. \tag{10}$$

The first represents the radiance I_a emitted to space by a atmosphere free of SO$_2$,

$$I_a = B_0 t_a(0) + \int_0^\infty dz \, \alpha_a(z) B(z) t_a(z), \qquad (11)$$

attenuated by the transmittance t_s of the SO$_2$ column. Here $\alpha_a(z)$ is the volume absorption coefficient of the atmosphere at height z, B_0 is the Planck emission by the surface, and $B(z)$ is the Planck emission from the atmosphere at height z where the temperature is $T(z)$. The second term is the radiance I_a^+ emitted by the atmosphere above the SO$_2$ layer,

$$I_a^+ = \int_b^\infty dz \, \alpha_a(z) B(z) t_a(z), \qquad (12)$$

in this case modified by $(1 - t_s)$. The third term represents radiance emitted by the atmosphere within the SO$_2$ layer and modified there by absorption by SO$_2$,

$$I_{as} = \int_a^b dz \, \alpha_a B(z) t_a(z) t_s \left[e^{\tau s(z-a)/(b-a)} - 1 \right]. \qquad (13)$$

The final term represents radiance emitted by SO$_2$ and subsequently attenuated by absorption in the atmosphere above the point of emission,

$$I_{sa} = \int_a^b dz \, \alpha_s B(z) t_a(z) e^{-\tau_s(b-z)/(b-a)}. \qquad (14)$$

Our analysis of HIRS data is based on two additional assumptions that simplify these equations.

1. We assume that the SO$_2$ layer lies above the peak of the weighting function for H$_2$O in the 7.3 μm channel, so that the absorption coefficient $\alpha_a(z)$ is zero for $z > a$. This is a significant assumption, because H$_2$O absorbs strongly at 7.3 μm and the weighting function peaks relatively high in the atmosphere.
2. The SO$_2$ layer is assumed to be isothermal, and therefore may be characterized by a single temperature T_s. Clearly, this assumption is questionable when the SO$_2$ layer is very deep.

Justification for these assumptions is pragmatic, in the sense that the technique appears to track SO$_2$ plumes from major volcanic eruptions, even though we know that frequently the emission of SO$_2$ is accompanied by large emissions of H$_2$O.

With these assumptions, the formulae simplify. Because $\alpha_a(z)$ is zero for $z > a$, the second and third terms in equation (10) are zero, while the fourth term reduces to

$$I_{sa} = \alpha_s B_s \int_a^b dz \, e^{-\tau_s(b-z)/(b-a)} = (1 - t_s) B_s, \qquad (15)$$

where B_s denotes the Planck function at the temperature T_s of the SO$_2$ cloud. Thus,

$$I = t_s I_a + (1 - t_s) B_s, \qquad (16)$$

which we also write in the forms

$$I - I_a = (1 - t_s)(B_s - I_a) \quad \text{and} \quad e^{-\tau_s} = \frac{B_s - I}{B_s - I_a}.$$

Our aim is to estimate τ_s. The data will be observations of the radiance I emitted to space in the HIRS 7.3 μm channel and estimates of B_s and I_a derived from other HIRS/2 channels insensitive to SO$_2$.

NOTES

1. Profiles can also be retrieved but this requires much higher spectral resolution.
2. In keeping with previous practice (e.g. *Krueger et al.* [1995]), we use the units miili atmosphere centimetre (m atm-cm) for absorber amount. 1 m atm-cm =1 D.U. (Dobson Unit) or in S.I. units 1 atm-cm =0.446157 mol m^{-2}
3. An infrared (7.3 μm) optical depth of less than 0.05 is equivalent to $\approx$2 K difference between the background atmosphere and the SO$_2$ layer

REFERENCES

Ackerman, S. A., and Strabala, K. I., Satellite remote sensing of H$_2$ SO$_4$ aerosol using the 8- to 12- μm window region: Application to Mount Pinatubo, *J. Geophys. Res.*, *99*(D9), 18,639-18,649, 1994.

Allard, P., Carbonnelle, J., Métrich, Loyer, H., and Zettwoog, P., Sulphur output and magma degassing budget of Stromboli volcano, *Nature*, *368*, 326-330, 1994.

Baran, A., J. and Foot, J., S., A new application of the operational sounder HIRS in determining a climatology of sulphuric acid aerosol from the Pinatubo eruption, *J. Geophys. Res.*, *99*(D12), 25,673-25,679, 1994.

Barton, I. J., Prata, A. J., Watterson, I. G and Young, S. A., Identification of the Mt. Hudson volcanic cloud over SE Australia, *Geophys. Res. Lett.*, *19*, 1211-1214, 1992.

Berk, A., Bernstein, L. S., and Robertson, D. C., MODTRAN: A moderate resolution model for LOWTRAN 7, U. S., Air Force Phillips Laboratory, Nascom Air Force Base, MA, U. S. A., AFGL-TR-89-0122, 1989.

Bluth, G J. S., Rose, W. I., Sprod, I. E., and Krueger, A. J., Stratospheric loading of sulfur from explosive volcanic eruptions, *J. Geol. 105*, 671-683, 1997.

Bluth, G. J. S., Schnetzler, C. C., Krueger, A. J., and Walter, L. S., The contribution of explosive volcanism to global atmospheric sulphur dioxide concentrations, *Nature, 366*, 327-329, 1993.

Chahine, M., Gunson, M., Syvertston, M., and Parkinson, C., AIRS/AMSU/HSB, *NASA Publication*, NP-2001-5-248-GSFC, 21 pp.

Crisp, J., Volcanic SO_2 alert-Version 3, *EOS IDS Volcanology Team Data Product Document-Product #3288*, 13pp, 1995.

Doiron, S. D., Bluth, G. J. S., Schnetzler, C. C., Krueger, A. J., and Walter, L. S., Transport of Cerro Hudson SO_2 clouds, *EOS Trans AGU, 72*, 489-498, 1991.

Eisinger, M., and Burrows, J. P., Tropospheric sulfur dioxide observed by the ERS-2 DOME instrument, *Geophys. Res. Lett., 25*(22), 4177-4180, 1998.

Francis, P., Maciejewski, Oppenheimer, C., Chafes n, C., and Caltabiano, T., SO_2:HCl ratios in the plumes from Mt Etna determined by Fourier transform spectroscopy, *Geophys. Res. Lett., 22*(13), 1717-1720, 1995.

Gerstell, M. F, Crisp, J., and Crisp, D., Radiative forcing of the stratosphere by SO_2 gas, silicate ash, and H_2SO_4 aerosols shortly after the 1982 eruptions of El Chichón, *J. Clim., 8*, 1060-1070, 1995.

Goldman, A., Murcray, F. J., Rinsland, C. E, Blatherwick, R. D., David, S. J., Murcray, F. H., and Murcray, D. G., Mt Pinatubo SO_2 column measurements from Mauna Loa, *Geophys. Res. Lett., 19*(2), 183-186, 1992.

Hofmann, D. J., and Rosen, J. M., On the background stratospheric layer, *J. Atmos. Sci., 38*, 168-181, 1981.

Kidwell, K. B., NOAA polar orbiter user's guide-December 1991, *National Oceanic and Atmospheric Administration-NESDIS*, U. S. Department of Commerce, NOAA, Washington D. C., 1991.

Kiehl, J. T., and Briegleb, B. P., The relative roles of sulfate aerosols and greenhouse gases in climate forcing, *Science, 260*, 311-314, 1983.

Krueger, A. J., Walter, L. S., Bhartia, P. K., Schnetzler, C. C., Kmtkov, N. A., Sprod, I., and Bluth, G. J. S., Volcanic sulphur dioxide measurements from the total ozone mapping spectrometer instruments, *J. Geophys. Res., 100*, 14,057-14,076, 1995.

Love, S. P., Goff, F., Counce, D., Siebe, C., and Delgado, H., Passive infrared spectroscopy of the eruption plume at Popocatepétl volcano, *Nature, 396*, 563-567, 1998.

Mankin, W. G., Coffey, M. T., & Goldman, A., Airborne observations of SO_2, HCl, and O_3, in the stratospheric plume of the Pinatubo volcano in July 1991, *Geophys. Res. Lett., 19*(2), 179-182, 1992.

Mass, C. F., and Portman, D. A., Major volcanic eruptions and climate: A critical evaluation, *J. Climate, 2*, 566-583, 1989.

McCormick, M. P., Thomason, L. W., and Trepte, C. R., Atmospheric effects of the Mt. Pinatubo eruption, *Nature, 373*, 399-404, 1995.

McGee, K. A., & Gerlach, T. M., Airborne volcanic plume measurements using a FTIR spectrometer, Kilauea volcano, Hawaii, *Geophys. Res. Lett., 25* (5), 615-618, 1998.

McKeen, S. A., Liu, S. C., and Kiang, C. S., On the chemistry of stratospheric SO_2 from volcanic eruptions, *J. Geophys. Res., 89*(D3), 4873-4881, 1984.

Pierluissi, J. H., and Tomiyama, K., Numerical methods for the generation of empirical and analytical transmittance functions with applications to trace gases, *Appl. Optics, 19*(14), 2298-2309, 1980.

Pierluissi, J. H., Jarem, J. M., and Maragoudakis, C., Validated transmittance band model for SO_2 in the infrared, *Appl.Optics, 23*(19), 3325-3330, 1984.

Planet, W. G., Data extraction and calibration of TIROS-N/NOAA radiometers, *NOAA Tech. Rep. NESS 107-Rev. 1*, Natl. Environ. Satell. Data and Inf. Serv., Washington, D.C., 1988.

Prata, A. J., and Grant, I. F, Retrieval of microphysical and morphological properties of volcanic ash plumes from satellite data: Application to Mt Ruapehu, New Zealand, *Quart. J. Roy. Meteorol. Soc., 127*, 2153-2179, 2001.

Pndykiewicz, J. A., and Dastoor, A. P., On numerical simulation of the global distribution of sulfate aerosol produced by a large volcanic eruption, *J. Clim., 8*, 464-473, 1995.

Pyle, D. M., Beanie, P. D., and Bluth, G. J. S., Sulphur emissions to the stratosphere from explosive volcanic eruptions, *Bull. Volcanol., 57*, 663-671, 1996.

Rampino, M. R., and Self, S., Sulphur-rich volcanic eruptions and stratospheric aerosols, *Nature, 310*, 677-679, 1984.

Randel, D. L., Vonder Haar T. H., Ringerud, M. A., Stephens, G. L., Greenwald, T. J., and C. L. Combs, A new global water vapor dataset, *Bull. Amer. Meteorol. Soc., 77*(6), 1233-1246, 1996.

Realmuto, V. J., Abrams, M. J., Buongiorno, M. F., and Pieri, D. C., The use multispectral thermal infrared image data to estimate sulfur dioxide fhx from volcanoes: A case study from Mount Etna, Sicily, July 29, 1986, *J. Geophys. Res., 99*, 481-488, 1994.

Realmuto, V. J., Volcanic SO_2—High and moderate spatial resolution, Version 3, *EOS IDS Volcanology Team Data Product Document-Product #3289*, 20pp, 1995.

Robock, A., Volcanic eruptions and climate, *Rev. Geophys., 38*(2), 191-219, 2000.

Rose, W. I., Bluth, G. J. S., and Ernst, G. G. J., Integrating retrievals of volcanic cloud characteristics from satellite remote sensors: a summary, *Phil. Trans. R. Soc. London A., 358*, 1585-1606, 2000.

Rose, W. I., Gu, Y., Watson, I. M., Yu, T., Bluth, G. J. S., Prata, A. J., Krueger, A. J., Krotkov, N., Carn, S., Fromm, M. D., Hunton, D., Viggiano, A. A., Miller, T. M., Ballentin, J. O., Ernst, G. G. J., Reeves, J. M., Wilson, C., and Anderson, B. E., The February-March 2000 eruption of Hekla, Iceland from a satellite perspective, *This volume*, 2003.

Self, S., Zhao, J-X, Holasek, R. E., Torres, R. C., and King, A. J., The atmospheric impact of the 1991 Mount Pinatubo eruption, *In Fire and Mud: Eruptions and Lahars of Mount Pinatubo, Philippines, C. G. Newhall and R. S. Punongbayan, eds., Philippine Institute of Volcanology and Seismology, Queen City, and University of Washington Press, Seattle*, 1089-1115, 1996.

Seinfeld, J. H., and Pandis, S. N., Atmospheric chemistry and physics. From air pollution to climate change. *John Wiley and Sons, New York,* 1326 pp, 1998.

Smith, W. L., Woolf, H. M, Hayden, C. M., Wark, D., and McMillin, L. M., The TIROS-N operational vertical sounder, *Bull. Amer. Meteorol. Soc., 60,* 1177-1187, 1979.

Stoiber, R., and Jepsen, A., Sulfur dioxide contributions to the atmosphere by volcanoes, *Science, 182,* 577-578, 1973.

Wiscombe, W. J., and Evans, J. W., Exponential-sum fitting of radiative transmission functions, *J. Comp. Phys., 24,* 416-444, 1977.

D. M. O'Brien, CSIRO Atmospheric Research, PB1, Aspendale, Victoria 3195, Australia, Email: Denis.O'Brien@csiro.au

A. J. Prata, CSIRO Atmospheric Research, PB1, Aspendale, Victoria 3195, Australia, Email: Fred.Prata@csiro.au

W. I. Rose, Geological Engineering and Sciences, Michigan Technological University, Houghton, Michigan, USA, Email: raman@mtu.edu

S. Self, Department of Earth Sciences, The Open University, Walton Hall, Milton Keynes, MK7 6 AASA, United Kingdom, Email:Stephen.Self@open.ac.uk.

Characterization of Stratospheric Aerosol Distribution for Volcanic and Non-Volcanic Aerosols Observed Through 16 Years of SAGE II Data (1984–2000)

Christine Bingen, Didier Fussen and Filip Vanhellemont

Belgian Institute for Space Aeronomy, Brussels, Belgium

The particle number density and particle size distribution of stratospheric aerosols have been derived from aerosol extinction profiles provided by the Stratospheric Aerosol and Gas Experiment II (SAGE II), using a regularized optical inversion method. We present here a global climatology derived from those profiles, and describe the spatiotemporal evolution of stratospheric aerosols through the three following aerosol parameters: particle number density, modal radius and modal width of the size distribution that is supposed to be lognormal. We illustrate the evolution of all those parameters, especially in the case of high and very low volcanism. We put emphasis on the latter case, which already could be studied during previous periods of quiet volcanic activity. We present profiles of aerosol parameters that reflect a possible situation of "background aerosol", and compare them with previously published works.

1. INTRODUCTION

Aerosols are known to play a very important role in the physical chemistry and in the radiative properties of the stratosphere [*McCormick al.*, 1995; *Russell et al.*, 1996]. Therefore, the determination of aerosol microphysical characteristics (such as particle number density, modal radius and width of the particle size distribution, effective radius, surface area density or volume density) is a crucial point: reliable data are necessary if we want to be able to build realistic atmospheric models taking into account heterogeneous chemistry processes. It is also a difficult problem, due to the great variability of the composition and size with time, latitude and altitude. For instance, a major volcanic eruption such as the Pinatubo eruption in June 1991 is able to increase the quantity of aerosol in the stratosphere up to more than two orders of magnitude. Moreover, the retrieval

of aerosol parameters by optical inversion of aerosol extinction profiles, is an ill-conditioned problem [*Echle et al.*, 1998], leading to unstable solutions and to strongly correlated parameters. For this reason, most of the results published so far concern integrated parameters such as the surface area density, volume density and effective radius, for which extended results have been published [*Thomason et al.*, 1997a; *Anderson and Saxena*, 1996; *Hervig and Deshler*, 2002]. Very few data are available for the aerosol parameters that we consider in this work. A noticeable exception concerns the parameter profiles supplied in the version 6.1 of the SAGE II package. Unfortunately, no publication is available at this time concerning the retrieval of those profiles.

Recently, we presented a regularized inversion method in order to improve the stability of the solution [*Fussen et al.*, 2001a], and we applied it to SAGE II extinction profiles [*Bingen et al.*, 2002]. The corresponding data set is characterized by a large temporal and latitudinal coverage in the stratosphere, between 1984 and 2000, and from 80°S to 80°N. Thanks to this, we dispose on a wide range of volcanic levels, from a very low volcanism possibly close to

a "background aerosol" as observed during the latest period, to the very high volcanism found after the Pinatubo eruption. Several major eruptions occurred during the SAGE II mission, like those of the Mt Ruiz (5°N, 75°W) in November 1985, Kelut (8°S, 112°E) in February 1990, and Pinatubo (15°N, 120°E) in June 1991. Also, a part of the aerosol decay after the eruption of El Chichon (17°N, 93°W) in November 1982 was observed. Therefore, the SAGE II experiment is a very rich and useful data source for the study of many aspects of aerosol physics: transport, formation and removal mechanisms such as nucleation, coagulation and sedimentation, latitudinal and vertical distribution, etc.

We present here a climatology of stratospheric aerosols derived from the whole SAGE II mission, as a function of the altitude, latitude and time. We consider three parameters in this study: the particle number density, and the modal radius and width of the particle size distribution that we will assume to be lognormal. We first present the inversion method we used for the retrieval of those parameters. Further, we present various profiles in the case of high and low volcanism level, and we describe the general features of the aerosol distribution in the stratosphere. Finally, we discuss the case of very low level of volcanism in some more details, and compare the aerosol features we found with other results retrieved during previous periods of very low volcanic activity.

2. DATA SET

The Stratospheric Aerosol and Gas Experiment II (SAGE II) was launched in October 1984 [*Chu et al.*, 1989] and has been extensively used for the study of stratospheric aerosols [*Brogniez et al.*, 1996; *Hitchman et al.*, 1994; *Thomason et al.*, 1997a; *Thomason et al.*, 1997b; *Trepte et al.*, 1994]. Four spectral channels are available for the aerosol study, at 1.020, 0.525, 0.453 and 0.385 μm.

In this work, we used the version 6.0 of the extinction profiles, given with a vertical resolution of 0.5 km from October 1984 to March 2000. In this version, the altitudes were reprocessed and the estimation of the uncertainties was refined. These changes resulted in significant improvements of the aerosol parameters that we retrieved with the inversion process, leading to much more reliable values of the profiles above 25 km altitude.

3. THEORETICAL BACKGROUND

The microphysical characteristics of aerosols are well described by the particle number density N, expressed in particle number per volume unit, and by a particle size distribution $f(r)$. A very commonly used function for the definition of a particle mode is the lognormal distribution defined as

$$f(r) = \frac{1}{\sqrt{2\pi}r\sigma}\exp\left(-\frac{\ln^2(r/\rho)}{2\sigma^2}\right) \quad (1)$$

where ρ and σ represent respectively the modal radius and width of the size distribution. A great advantage of this formulation is to allow the description of the whole distribution by using only positive defined values for the particle size r. This type of distribution is found to be usually satisfactory for describing the aerosol size distribution, except during periods following major volcanic eruptions. In that case, two or even three modes are observed, due to the coexistence of aerosol particles with different features: very thin condensation nuclei from fresh aerosols with a typical size of about 0.05 to 0.15 μm, aerosols growing on preexisting droplets with sizes ranging around 0.3 to 0.5 μm, and ashes characterized by a large radius ($\sim$ 0.8 μm) [*Deshler et al.*, 1992; *Deshler et al.*, 1993; *Deshler*, 1994; *Pueschel et al.*, 1994; *Thomason*, 1992]. Although such a situation has been encountered within the period we consider here, we are not able to use multimodal size distributions, due to the small number of SAGE II channels and the impossibility to extract valuable information for particles whose size lies outside the optical range of the instrument.

From the knowledge of N, ρ and σ, it is possible to retrieve all the other aerosol parameters of interest for aerosol description or modeling purpose, such as the surface area density S, the volume density V or the effective radius ρ_{eff}, which are, in the case of a lognormal size distribution, given by

$$S(\rho, \sigma, N) = 4\pi N\rho^2 \exp\left[2\sigma^2\right] \quad (2)$$

$$V(\rho, \sigma, N) = \frac{4\pi}{3} N\rho^3 \exp\left[\frac{9}{2}\sigma^2\right] \quad (3)$$

$$\rho_{eff}(\rho, \sigma) = \rho \exp\left[\frac{5}{2}\sigma^2\right] \quad (4)$$

The aerosol parameters N, ρ and σ can be retrieved from radiative measurements by inversion of the extinction coefficient β. This coefficient describes the radiative response of a population of atmospheric particles (i.e. the combination of light scattering and absorption caused by the particles) through the expression

$$\beta(z;\lambda) = \int_0^\infty N(z) f(r) Q(r;\lambda) \, dr \qquad (5)$$

where $Q(r;\lambda)$ is the extinction cross section, r is the particle radius and λ is the wavelength. The extinction coefficient is usually expressed in km^{-1}.

Since N only depends on the altitude z, the problem can be simplified by elimination of N through a proper normalization. We defined the reduced extinction β_n as

$$\beta_n = \frac{\beta(z;\lambda)}{\beta(z;\lambda_r)} \qquad (6)$$

and chose the 1.020 μm SAGE II channel as reference wavelength λ_r. The inverse problem then comes down to the inversion of

$$\beta_n(z;\lambda) = \frac{\int_0^{+\infty} f(r) Q(r;\lambda) \, dr}{\int_0^{+\infty} f(r) Q(r;\lambda_r) \, dr} \qquad (7)$$

at each altitude z, i.e. the retrieval of ρ and σ from Eqns. (1, 7) and from available data for $\beta_n(z;\lambda)$. We can derive $\beta_n(z;\lambda)$ values from the SAGE II extinctions at the four wavelengths using (6), leading to three normalized experimental values $\beta_n^e(z;\lambda_i)$ at $\lambda_i = 0.525$, 0.453 and 0.385 μm.

A common way to solve this problem is to build up a look-up table of theoretical values $\beta_n^t(\rho, \sigma, \lambda_i)$. These are chosen within the working ranges $[\rho_{min}, \rho_{max}]$ and $[\sigma_{min}, \sigma_{max}]$ respectively, that have to be large enough to include the solution of the problem. The extinction cross section $Q(r;\lambda)$ can be computed from the Mie theory [van de Hulst, 1957], which describes the extinction of light by spherical particles. When the particle size is on the same order of magnitude as the wavelength, $Q(r;\lambda)$ is an oscillating function due to the effect of diffraction, and depends on the refractive index, the particle size and the wavelength. Replaced in (7), this factor supplies the useful information allowing the retrieval of the particle signature in the inversion scheme. When the particle size is very small compared to the wavelength, the expression of $Q(r;\lambda)$ simplifies, tending toward a form which still depends on λ, but no more on r. This is the well-known Rayleigh limit for scattering of punctual particles. Consequently, all techniques based on the particle size retrieval from scattering measurements appear to be usable only if the wavelength is on the same order of magnitude as the particle size.

For the calculation of $Q(r;\lambda)$, we considered, following a commonly accepted hypothesis, that stratospheric aerosols are a mixture of about 75% H_2SO_4 and 25% H_2O by weight, and show an index of refraction of 1.43 in the visible range. There is no absorption observed in this wavelength range.

From the reference profiles $\beta_n^t(\rho, \sigma, \lambda_i)$ calculated in this way, the solution in ρ and σ of the inversion problem (7) at altitude z can be derived by comparison of the normalized experimental values $\beta_n^e(z;\lambda_i)$ with corresponding theoretical values $\beta_n^t(\rho, \sigma, \lambda_i)$, through the minimization of the merit function

$$M(\rho,\sigma;z) = \sum_{i=1}^4 \left[\frac{\beta_n^e(z;\lambda_i) - \beta_n^t(\rho,\sigma;\lambda_i)}{\Delta\beta_n^e(z;\lambda_i)} \right]^2 \qquad (8)$$

The experimental uncertainty $\Delta\beta_n^e(z;\lambda_i)$ on β_n^e is used to weigh the contribution of each SAGE II channel in function of its estimated accuracy. Due to its non-linear character, the optimization problem has to be processed by an iterative search algorithm. We used a Levenberg-Marquardt routine at this end.

The inverse problem of retrieving ρ and σ values that minimize Eq. (8) is an ill-conditioned problem. A study of the behavior of the merit function M in the $\{\rho, \sigma\}$ space shows [Echle et al., 1998; Fussen et al., 2001a] that this function takes its minimum in a valley with sharp edges but a rather flat bottom. Therefore, the minimization leads to unstable solutions, especially in the modal width σ, and the different retrieved aerosol parameters show correlations between each other.

One can greatly improve the solution by imposing a constraint on the inversion problem. We chose to apply a continuity constraint on the vertical dependence of each aerosol parameter, by forcing ρ and σ to be in the form

$$\rho(z) = \rho_{min} + (\bar{\rho} - \rho_{min}) \exp\left[-\left(\sum_{i=0}^{n-1} a_i z^i \right)^2 \right] \qquad (9)$$

$$\sigma(z) = \sigma_{min} + (\bar{\sigma} - \sigma_{min}) \exp\left[-\left(\sum_{i=0}^{n-1} b_i z^i \right)^2 \right] \qquad (10)$$

where, $\bar{\rho}$, $\bar{\sigma}$ are imposed to remain within the working ranges $[\rho_{min}, \rho_{max}]$ and $[\sigma_{min}, \sigma_{max}]$ respectively. The choice of this working range insures to remain within realistic values of the parameters and the use of an exponential guarantees the positive defined character of $\rho(z)$ and $\sigma(z)$. Finally, the continuity condition obtained by the use of a polynomial as argument of the exponential avoids possible jumps to unrealistic values of $\rho(z)$ and $\sigma(z)$ owing to local fails of the search algorithm.

The optimization problem then comes down to the minimization of the merit function of the constrained problem

$$M^c\left(\bar{\rho},\bar{\sigma};a_i,b_i\right)=\sum_z M\big(\rho\big(z;\bar{\rho};a_i\big),\sigma\big(z;\bar{\sigma};b_i\big);z\big) \quad (11)$$

Replacing the solutions $\bar{\rho}$, $\bar{\sigma}$; a_i, b_i into Eqns. (9, 10) leads to the solutions in ρ and σ for the vertical extinction profile $\beta_n(z)$. The corresponding particle density profiles $N(z)$ can be retrieved from Eqns. (5), (6) and from the theoretical values $\beta_n^t(\rho(z)$, $\sigma(z)$; $\lambda)$.

4. CLIMATOLOGICAL DATA

After inversion of all the SAGE II events, binned profiles were processed using latitude intervals of 10 degrees, a 1 km increment for the vertical resolution and periods of 1 month. Notice that a bin corresponding to the latitude interval $[\phi$, $\phi + 10°]$ will be referenced in the following by the value ϕ.

As explained in the previous section, main limitations of the inversion scheme concern the inability to discriminate thin particles in the Rayleigh limit of scattering, and to describe multimodal size distribution, what essentially concerns transient periods following volcanic eruptions. We compared the resulting climatological data with other data sets from both remote sounding and *in situ* experiments. We found a satisfactory agreement as far as the modal radius is larger than the Rayleigh limit of diffraction (about 0.2 μm) [*Bingen et al.*, 2002].

Plates 1, 2 and 3 show typical aerosol parameter isopleths during a period of high volcanic loading (15 months after the Pinatubo eruption). At this time, the stratosphere contains a large amount of volcanic aerosols, covering the whole latitude range.

Plates 4, 5 and 6 illustrate the same aerosol parameter isopleths, 7 years after the Pinatubo eruption. At this stage, the volcanism level has become particularly low and reaches a quite stable state, possibly related to a "background" level.

A comparison between both sets of Plates (1–3) and (4–6) shows the dramatic incidence of a major event such as the Pinatubo eruption on the stratospheric aerosol content. Mass injection can reach altitudes higher than 30 km and the particle number density can increase by two orders of magnitude.

In all cases, the particle density is maximal in the so-called Junge layer, whose altitude and thickness depend on the latitude, season and the proximity of a volcanic eruption, but which roughly extends from the lowermost stratosphere up to about 22 to 27 km. Within this layer, the particle size distribution shows an enhanced modal radius and width.

The general shape also reveals the transport features of the global circulation, with a strong upwards air mass elevation above the central latitudes giving rise to vertical transport of aerosol from a tropical reservoir, and a poleward transport which roughly follows the isentropics in the extratropical regions [*Trepte et al.*, 1994].

In this general pattern, the strength of the vertical transport between the tropics and the meridional transport are affected by the quasi-biennial oscillation (QBO), which consists in an alternation of westerly and easterly wind regimes, with a periodicity of about two years, above the equator up to 20–25° of latitude. The change in the wind direction appears at 30 km altitude, and gradually propagates downwards to about 23 km altitude, with a speed of about 1 km per month [*Baldwin et al.*, 2001; *Holton*, 1992].

During the easterly shear of the QBO, the strong gradient between the easterly wind and the westerly wind characterizing the winter hemisphere prevents meridional air motions, and favors the upwards transport of aerosol from the tropical reservoir. The poleward transport out of the tropics occurs in the middle stratosphere, making possible an equatorward transport in the lower stratosphere (*upper regime*). On the contrary, the westerly shear of the QBO reduces drastically the velocity gradient between air masses above the tropics and in the winter hemisphere, making meridional transport possible. This results in a subsidence of the tropical reservoir and in a poleward transport in the lower stratosphere (*lower regime*). This structure and the presence of those two transport modes have been observed and discussed into detail by [*Hitchman et al.*, 1994], and extensively described in the literature [*Choi et al.*, 1998; *Jones et al.*, 1998; *McCormick al.*, 1995; *Trepte et al.*, 1992]. The influence on N of the enhanced elevation of aerosols during the easterly shear, and of the subsidence during the westerly shear is illustrated in Figure 1.

Plates 7, 8 and 9, show the evolution in time and latitude of the three aerosol parameters N, ρ, σ during the time interval 1984–2000 at 22.5 km altitude. At all latitudes, this altitude lies within the aerosol layer, so that the figures are representative for the region of the stratosphere where the amount of aerosol is high. Missing data correspond to regions not covered by the satellite, except the wide gap at central latitudes during 1991 and 1992. In this case, the signal was below the sensitivity range of the instrument, due to the huge aerosol loading consecutive to the Pinatubo eruption.

The influence of the main volcanic eruptions (El Chichon, Ruiz, Kelut, Pinatubo) is visible on all parameter profiles: increase of the particle number density, up to several orders of magnitude in the case of the Pinatubo eruption, significant growth of the modal radius and higher dispersion of the size distribution. A poleward dispersal of the aerosol mass loading is very well observed during the first months following the eruption (lasting about two years in the case of Pinatubo, the volcanic cloud reaching the poles after one

97

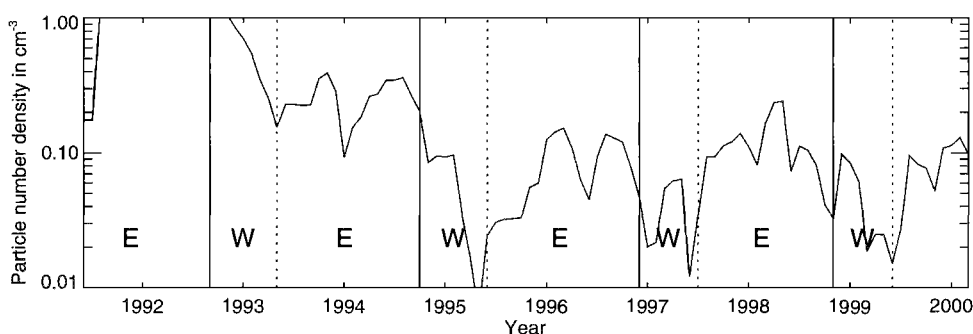log$_{10}$(Number density in cm^{-3}) - September 1999
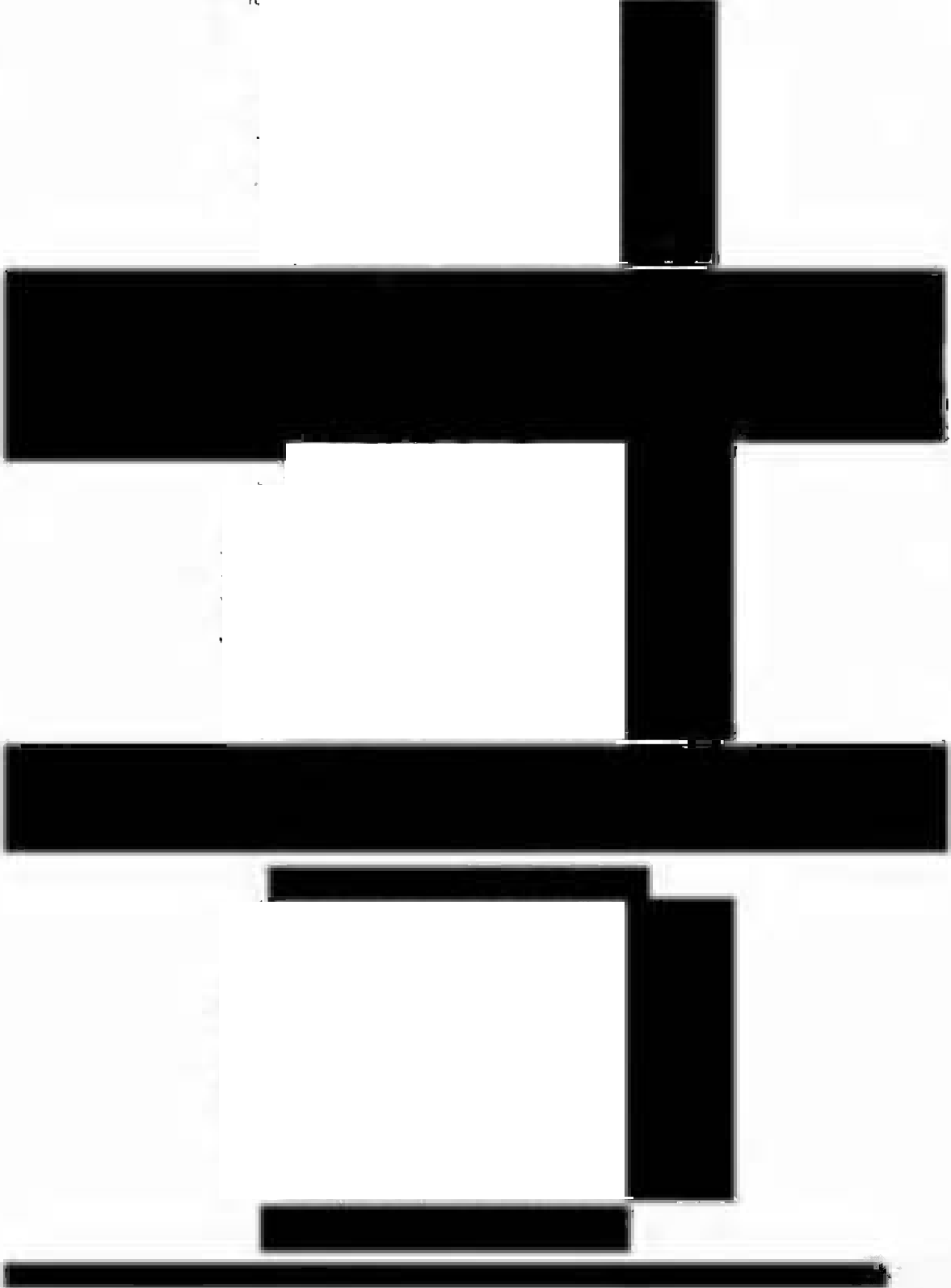
Figure 1. Influence of the QBO on the particle number density at $z=26.5$ km and $10°N$, derived from SAGE II extinction profiles for the post-Pinatubo period. The solid and dotted vertical lines show the beginning of the westerly and easterly shear respectively. The particle number density N is expressed *in* cm^{-3}.

year). Beyond the phase of the QBO observed at the moment of the eruption, which favors either the *upper* or the *lower* transport regime, the time of the year at which the eruption occurs also plays an important role on the efficiency of poleward dispersal. The presence of the polar night jets at high latitudes, with easterly winds in the summer hemisphere and westerly winds in the winter hemisphere, influences the poleward air mass propagation [*Holton*, 1992]. More particularly, the strong polar night jet in the winter hemisphere provides a guide for vertical transport, and forms an efficient barrier inhibiting further transport to the poles. It results in a subsidence of the air mass and an accumulation of aerosol loading at mid-latitude. At the beginning of the spring, the vortex breaks up, allowing aerosol transport to the pole. An illustration of this seasonal effect is given in figure 2. As a consequence of this, the climatic impact of a volcanic eruption depends not only on the amount of material injected into the stratosphere, but also on the phase of the QBO and on the period of the year at the moment of the eruption. A comparison of the impact of several past eruptions with respect to those factors has been proposed by Hofmann [*Hofmann*, 1988], whereas [*McCormick al.*, 1995] investigated the particular case of the Pinatubo eruption in 1991.

While the particle number density is found to decrease in a monotonic way after the eruption, the time evolution of the modal radius and width appears to be more complex. In the first instance, a fast release of ashes and thick volcanic particles by transport and by direct sedimentation results in a rapid decay of ρ and σ. Afterward, both parameters increase again at the central latitudes around 18 months (Ruiz) to two years (Pinatubo) after the eruption, due to coagulation processes. The effect of an eruption as strong as this of Pinatubo, is seen to remain visible in the stratosphere until at least six years after the eruption.

5. BACKGROUND AEROSOL

Volcanism is known as the most important source of stratospheric aerosols. However, other sources have been identified, contributing in a significant way to the aerosol loading out of highly volcanic periods, and resulting in the so-called "background" aerosol level. An important source of aerosol is carbonyl sulfide OCS, whose contribution to stratospheric aerosols has been investigated by several authors [*Crutzen*, 1976; *Turco et al.*, 1979; *Chin and Davis*, 1995; *Koziol and Pudykiewicz*, 1998].

With the long period of low volcanic activity that followed the eruption of Pinatubo in 1991, the mean aerosol content tends to stabilize, so that investigations around background aerosol again becomes a topic of great interest. Several fundamental questions arise. One of them concerns the reality of a background level: due to the continuous injection of volcanic aerosol from minor eruptions, it is not sure that the *actual non volcanic background aerosol level* is ever reached, so that the exact contribution of non volcanic sources will possibly never be known exactly [*Hofmann*, 1988; *Hitchman et al.*, 1994]. Moreover, seasonal effects also have an impact on the stratospheric aerosol content, as already seen, and can mislead about the outcome of a steady state during a particular period [*Thomason et al.*, 1997b].

Another question of interest concerns the long time evolution of the background aerosol level, and the impact of anthropogenic activities on it. Several studies have attempted to identify both natural and anthropogenic sources of aerosol and to quantify their impact on the stratosphere [*Hofmann*, 1991; *Chin and Davis*, 1995; *Pitari et al.*, 1993]. However, the lack of measurements due to the rare occurrence of representative periods for this study, and to the relatively recent development of reliable experimental techniques (about four decades), make any conclusions temporary and uncertain.
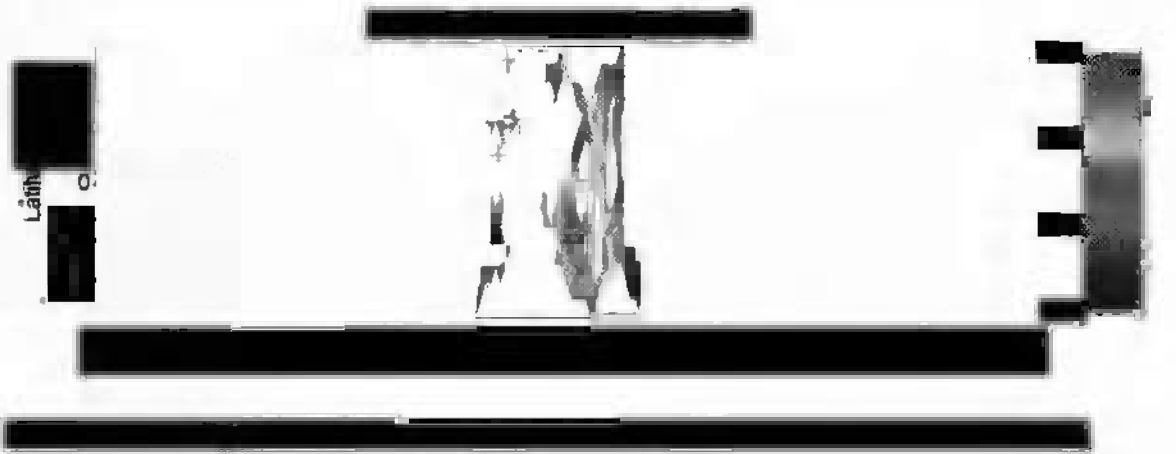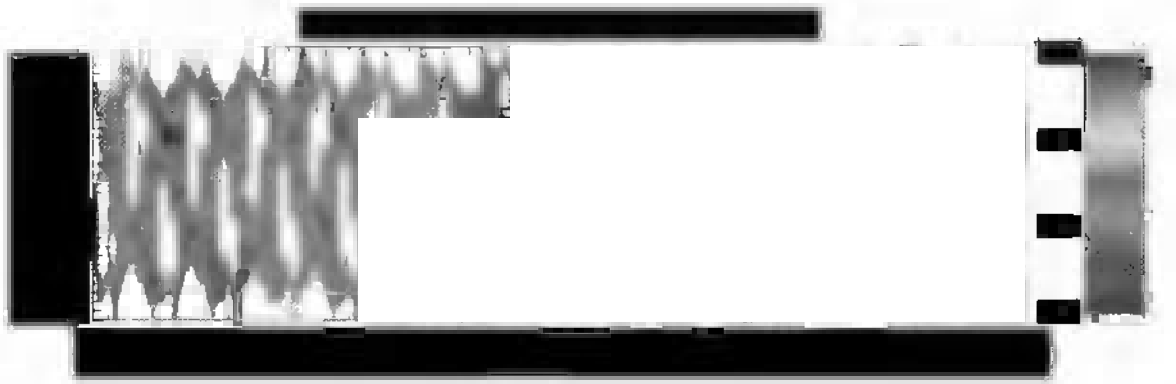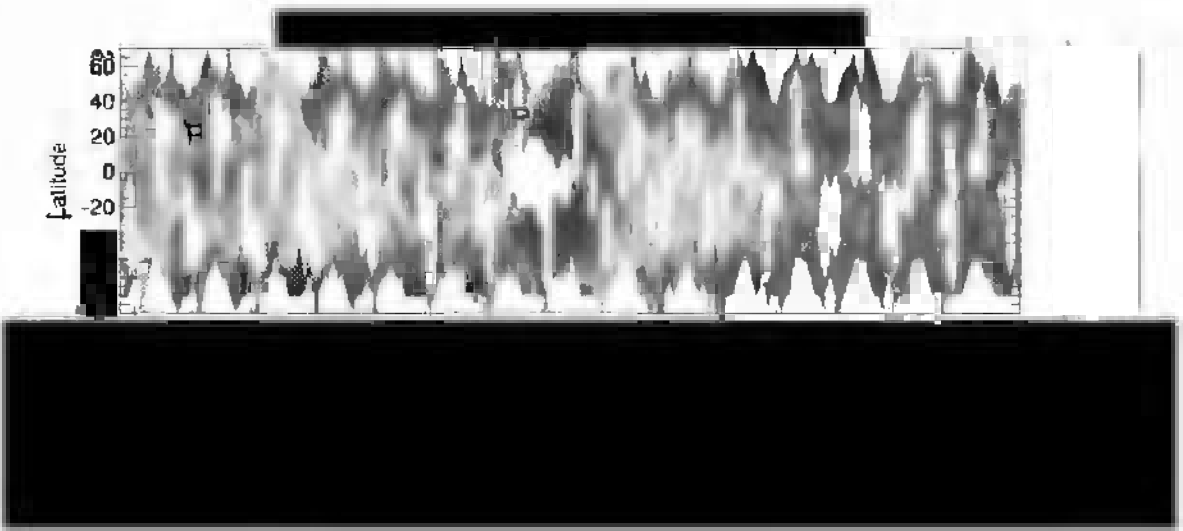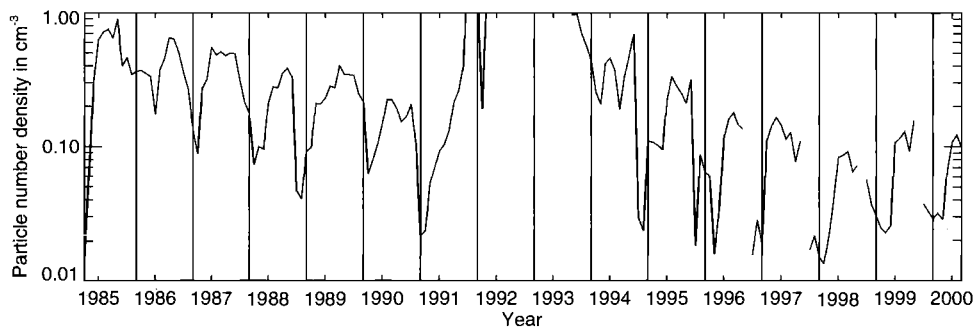
Figure 2. Influence of the polar night jet on the poleward transport and effect on the particle number density at $z=20.5$ km and 60°S, derived from SAGE II extinction profiles for the whole SAGE II flight period. The vertical lines indicate the position of the month of September. The particle number density N is expressed in cm^{-3}.

The periods of low volcanism which could be studied are the period 1957–1960, with the first investigations of Junge [*Junge*, 1961] using *in situ* measurements of the aerosol layer, the period 1972–1973, investigated by means of balloon-borne counting experiments at various latitudes [*Hofmann et al.*, 1975; *Hofmann et al.*, 1976; *Toon et al.*, 1979], and the period 1977–1979, the first one to have been extensively studied by lidar, *in situ* and remote sensing measurements through the SAM and SAGE experiments [*Yue and Deepak*, 1983; *Kent et al.*, 1985; *McCormick et al.*, 1987; *Kent et al.*, 1991; *Hitchman et al.*, 1994; *Thomason et al.*, 1997b]. Finally, the end of the nineties shows again a very low and quite stable aerosol content.

In this context, the present climatology offers a useful tool to distinguish trends in the evolution of a possible "background" aerosol. The global coverage supplied by SAGE II also allows the study the latitudinal dependence of the aerosol profile and the comparison with various existing data sets. However, we have to keep in mind that the results obtained from SAGE II measurements are unable to describe very thin particles in a reliable way, due to already cited theoretical limitations of Mie scattering.

In order to evaluate the present aerosol loading with respect to previous periods of very low aerosol loading, we compared our results with data obtained by Hofmann and Rosen in Laramie (41°N, 106°W) during the period 1978–1979 [*Hofmann and Rosen*, 1981]. These authors studied the temporal evolution and vertical profiles of aerosols through the aerosol mixing ratio Q, expressed in number of particles by mg air mass, and given by

$$Q = \frac{N}{\mu} \tag{12}$$

where the air mass density μ expressed in mg/cm^{-3} is defined as

$$\mu = m_{air}^{molec} \frac{P}{RT} \tag{13}$$

R is the molar gas constant, T is the temperature expressed in K, P is the pressure, and the mean molecular air mass m_{air}^{molec} is equal to 28.97 g/mole for dry air. The advantage of using the aerosol mixing ratio instead of the particle number density is to get rid of the influence of seasonal variations of the tropopause height, and perturbations due to eddy-mixing processes. Using this parameter for two cumulated particle classes corresponding to particle sizes ≥ 0.15 and 0.25 μm respectively, the authors showed their observations to be in good agreement with aerosol features during the previous period of very low volcanism around March 1975 and December 1976.

From the aerosol parameters N, ρ and σ, it can be easily shown that for a lognormal size distribution (1), the partial particle number density corresponding to the particle size class $r \geq r^*$ is given by

$$N_{[r \geq r^*]}(z) = \frac{1}{2} N(z) \left[1 - \mathrm{erf}\left(\frac{\ln\left(r^*/\rho(z)\right)}{\sqrt{2}\sigma(z)} \right) \right] \tag{14}$$

Figure 3 shows the post-Pinatubo decay period of aerosol mixing ratio for the particle class $r \geq 0.25\mu m$ from 1992. We do not consider the particle class $r \geq 0.15\mu m$ because, as already discussed, we cannot expect particle as thin as $0.15\mu m$ to be correctly described by the SAGE II derived data. The solid line corresponds to aerosol mixing ratio representative for the latitude range [40°N, 50°N]. These values were calculated using the binned values of our SAGE II derived climatology. The air mass density values in (12) were processed from climatological data supplied by the United Kingdom Meteorological Office (UKMO). The plotted values correspond to the peak value of Q for the region
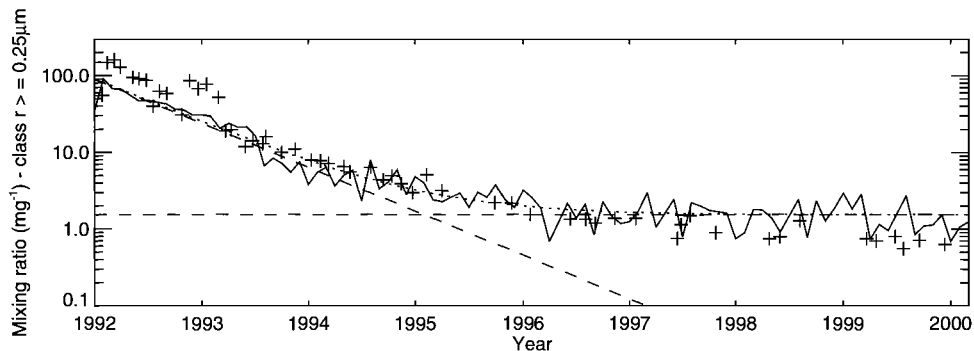
Figure 3. Time evolution of the peak value of the aerosol mixing ratio profile during the post-Pinatubo period. Two data sets are considered: SAGE II derived data (solid lines) and *in situ* derived data (crosses) from the Wyoming time series [*Deshler et al.*, 2002]. The fit of those curves by the sum of a possible constant "background" aerosol Q_{backg} and an exponential decay is represented by the dotted lines for the case of the SAGE II derived time series.

situated above the tropopause. In order to check the validity of the data, the same quantities have been derived from the time series supplied by the University of Wyoming, Laramie [*Deshler et al.*, 2003]. In this case, the data source consists of 0.5 km averaged vertical profiles of the particle number density, modal radius and width of the size distribution, measured by balloonborne optical particle counter (OPC). Depending on the particle population, either monomodal or bimodal lognormal distributions are used. Notice that one profile set corresponds to one flight, and hence reflects the local particle distribution at the time of the measurement. The corresponding values are also reported on Fig. 3 for comparison. The agreement between both data set is quite good, at least when the use of a monomodal size distribution can be considered as rather satisfactory. For both data sets, the time evolution shows an exponential decay, tending to stabilize after about 5 years.

Although the mixing ratio possibly further decreases in a much slower way after this time, we can model this time evolution on a simple way using the function

$$Q_{fit} = Q_{backg} + Q_1 . \exp^{-\frac{t}{\tau}} \qquad (15)$$

in order to evaluate the relaxation time τ and to compare typical value of an hypothetical "background" aerosol mixing ratio Q_{backg} with values previously found by Hofmann and Rosen. Such a fit was processed on data from January 1992 to March 2000 for both data sets. The fit values are reported in Table 1 for the SAGE II derived data set, the OPC time series corresponding to the same period, and values derived by Hofmann and Rosen for the period 1978–1979. The mixing ratio values of 1.1 particles per mg found in the latest case corresponds to a concentration 0.1 cm-3 at 20 km [*Hofmann and Rosen*, 1981].

Intercomparison and deduction of general trends for the aerosol content of the atmosphere must be considered very cautiously due to the random error induced by the optimization algorithm (especially for τ for which a great uncertainty is found; the random error on Q_{backg} is less than 1%), and by the error on N (about 30% for the estimations from SAGE II, unknown in the case of OPC values). Keeping in mind this fact, the comparison of those results shows an overestimation of SAGE II derived Q_{backg} with respect to OPC derived values for the same period.

Further, the value of Q_{backg} derived by Hofmann and Rosen is situated between both other values so that, at this stage, we cannot deduce any clear long term trend to increase in the evolution of the aerosol "background" level. Moreover, the fact that OPC values reached in 2000 are lower than those obtained in the period 1978–1979 leads us at this stage to consider cautiously the hypothesis that aerosol really reaches the background level during these periods. Further observations and a correct estimation of the error should learn us more about that point.

Plate 10 shows vertical profiles corresponding to the tropical region in May and June 1997. For this choice of latitude

Table 1. Comparison between the features of the aerosol mixing ratio decay found in this work, and corresponding OPC data published by Hofmann and Rosen for the period 1978–1979 in Laramie, Wyoming. Q_{backg} and τ are respectively the asymptotic value and the relaxation time of the aerosol mixing ratio. These values concern the particle class $\rho \geq 0.25$ μm.

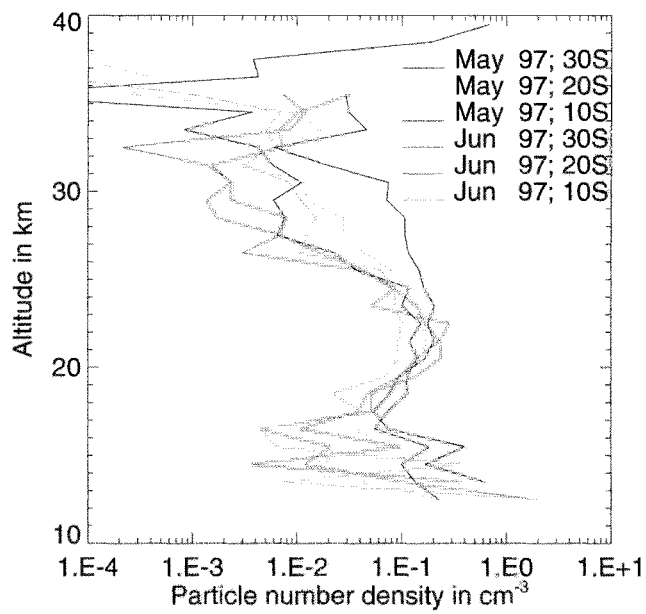| Data source	Q_{backg} (mg-1)	τ
SAGE II data (1992–2000)	1.5	9.1
OPC data (1992–2000)	0.9	9.2
Hofmann & Rosen (1978–1979)	1.1	8.1

Plate 10. Mean vertical profiles of particle number density at various latitudes, during the months May and June 1997. (See the color version of this plate at the back of this volume.)

and time, the tropopause height is quite constant, around 14.6 to 15.3 km. On the other side, June 1997 marks the very beginning of the easterly shear of the QBO, at about 30 km, the westerly wind being still dominating elsewhere. Therefore, no significant difference due to seasonal influences is expected between the various curves, making the comparison meaningful. The peak value of N at the level of the aerosol layer is found to be in agreement with already cited data reported by Hofmann and Rosen for the periods 1974–1975 and 1978–1979.

All those results seem to indicate that the concentration of "background" aerosols, if they are really observed, has not sensibly increased since the previous periods of very low volcanism. This observation is at least valid for particles of the class $r \geq 0.25$ μm, well detected by SAGE II.

6. CONCLUSIONS

We present a climatology of stratospheric aerosols based on the particle number density, and the modal radius and width of the particle size distribution supposed to be log-normal. The three parameters were derived from a regularized inversion method which allowed to partly get rid of the ill-posedness inherent to the optical inversion problem. However, fundamental limitations of scattering measurements in the limit of Rayleigh scattering cannot be avoided, so that the description of very thin particles (smaller than 0.2 μm) has to be considered cautiously. Taking this limitation into account, the climatology still appears to be a very promising tool for the study of aerosol distribution, transport and microphysics. Several illustrations were presented, concerning the influence of the QBO and of the annual variations of the polar night jet on them. We also put special emphasis on the cases of high and very low volcanic situations. In the latter case, we derived the aerosol mass loading, and showed from the study of its time evolution that the stratosphere reached a new period of low and quite stable aerosol level at the end of the nineties, after the long relaxation which followed the Pinatubo eruption. This period can be thought to be representative of a possible "background" aerosol situation. However, in the expectation of new observations, we cannot exclude the possibility of a further slow decay of the aerosol level, and the inability to really observe the aerosol background level. A comparison of aerosol profiles with values derived from *in situ* measurements and with already published data related to prior times of very low aerosol level do not reveal a clear increase of the quantity of "background" aerosol per mg air for particles within the size range correctly detected by a radiative measurement technique such as SAGE II.

REFERENCES

Anderson, J. and Saxena V. K., Temporal changes of Mount Pinatubo aerosol characteristics over northern midlatitudes derived from SAGE II extinction measurements, *J. Geophys. Res., 101*, 19455-19463, 1996

Baldwin, M. P., L. J. Gray, T. J. Dunkerton, K. Hamilton, P. H. Haynes, W. J. Randel, J. R. Holton, M. J. Alexander, I. Hirota, T. Horinouchi, D. B. A. Jones, J. S. Kinnersley, C. Marquardt, K. Sato and M. Takahashi, The quasi-biennial oscillation, *Rev. Geophys., 39*, 179-229, 2001.

Bingen, C., F. Vanhellemont and D. Fussen, A new regularized inversion method for the retrieval of stratospheric aerosol size distributions applied to 16 year SAGE II data (1984–2000): method, results and validation, *Ann. Geophys., 21*, 797-804, 2003.

Brogniez, C., J. Lenoble, M.Herman, P. Lecomte and C. Verwaerde, Analysis of two balloon experiments in coincidence with SAGE II in case of large stratospheric aerosol amount: Post-Pinatubo period, *J. Geophys. Res., 101*, 1541-1552, 1996.

Chin, M. and D. D. Davis, A reanalysis of carbonyl sulfide as a source of stratospheric background sulfur aerosol, *J. Geophys. Res., 100*, 8993-9005, 1995.

Choi, W., W. B. Grant, J. H. Park, K.-M. Lee, H. Lee, J. M. Russell III, Role of the quasi-biennial oscillation in the transport of aerosols from the tropical stratospheric reservoir to midlatitudes, *J. Geophys. Res., 103*, 6033-6042, 1998.

Chu, W. P., M. P. McCormick, J. Lenoble, C. Brogniez and P. Pruvost, SAGE II Inversion Algorithm, *J. Geophys. Res., 94*, 8839-8351, 1989.

Crutzen P. J., The possible importance of CSO for the sulfate layer of the stratosphere, *Geophys. Res. Lett., 3*, 73-76, 1976.

Deshler, T., D. J. Hofmann, B. J. Johnson and W. R. Rozier, Balloonborne measurements of the Pinatubo aerosol size distribution and volatility at Laramie, Wyoming during the summer of 1991, *Geophys. Res. Lett., 19*, 199-202, 1992.

Deshler, T., B. J. Johnson and W. R. Rozier, Balloonborne measurements of the Pinatubo aerosol during 1991 and 1992 at 41°N : vertical profiles, size distribution, and volatility, *Geophys. Res. Lett., 20*, 1435-1438, 1993.

Deshler, T., In situ measurements of Pinatubo aerosol over Kiruna on four days between 18 January and 13 February 1992, *Geophys. Res. Lett., 21*, 1323-1326, 1994.

Deshler, T., M. E. Hervig, D. J. Hofmann, J. M. Rosen and J. B. Liley, Thirty years of in situ stratospheric aerosol size distribution measurements from Laramie, Wyoming (41°N), using balloonborne instruments, *J. Geophys. Res., 108(D5)*, 4167, doi:10.1029/2002JD002514, 2003.

Echle, G., T. von Clarmann, and H. Oelhaf, Optical and microphysical parameters of the Mt. Pinatubo aerosol as determined

from MIPAS-B mid-IR limb emission spectra, *J. Geophys. Res., 103,* 19193-19211, 1998.

Fussen, D., F. Vanhellemont and C. Bingen, Evolution of stratospheric aerosols in the post-Pinatubo period measured by solar occultation, *Atmospheric Environment, 35,* 5067-5078, 2001a.

Fussen, D., F. Vanhellemont and C. Bingen, Evidence of transport, sedimentation and coagulation mechanisms in the relaxation of post-volcanic stratospheric aerosols, *Annales Geophysicae, 19,* 1157-1162, 2001b.

Hervig, M., and T. Deshler, Evaluation of aerosol measurements from SAGE II, HALOE and balloonborne optical particle counters, *J. Geophys. Res., 107(D3),* 10.1029/2001JD000703, 2002.

Hitchman, M. H., M. McKay and C. R. Trepte, A climatology of stratospheric aerosol, *J. Geophys. Res., 99,* 20689-20700, 1994.

Hofmann, D. J., J. M. Rosen, T. J. Pepin and R. G. Pinnick, Stratospheric aerosol measurements I: Time variations at northern midlatitudes, *J. Atmos. Sci, 32,* 1446-1456, 1975.

Hofmann, D. J., J. M. Rosen, J. M. Kiernan and J. Laby, Stratospheric aerosol measurements IV: Global time variations of the aerosol burden and source considerations, *J. Atmos. Sci, 33,* 1782-1788, 1976.

Hofmann, D. J. and J. M. Rosen, On the Background Stratospheric Aerosol Layer, *J. Atmos. Sci, 38,* 168-181, 1981.

Hofmann, D. J., Aerosols from past and present volcanic emissions, in *Aerosols and Climate,* edited by P. V. Hobbs and M. P. McCormick, pp. 195-214, Deepak Publishing, Hampton, Virginia, 1988.

Hofmann, D. J., Increase in the Stratospheric Background Sulfuric Acid Aerosol Mass in the Past 10 Years, *Science, 248,* 996-1000, 1990.

Hofmann, D. J., Aircraft sulphur emissions, *Nature, 349,* 659, 1991.

Holton, J. R., *An Introduction to Dynamic Meteorology,* Academic Press, International geophysics series, Vol. 48, third edition, 1992.

Jones, D. B. A., H. R. Schneider and M. B. McElroy, Effects of the quasi-biennial oscillation on the zonally averaged transport of tracers, *J. Geophys. Res., 103,* 11235-11249, 1998.

Junge, C. E., C. W. Chagnon and J. E. Manson, Stratospheric aerosols, *J. Meteor, 18,* 81-108, 1961.

Kent, G. S., C. R. Trepte, U. O. Farrukh and M. P. McCormick, Variation in the stratospheric aerosol associated with the north cyclonic polar vortex as measured by the SAM II satellite sensor, *J. Atm. Sci., 42,* 1536-1551, 1985.

Kent, G. S., M. P. McCormick and S. K. Shaffner, Global optical climatology of the free tropospheric aerosol from 1.0-μm satellite occultation measurements, *J. Geophys. Res., 96,* 5249-5267, 1991.

Koziol A. S. and J. Pudykiewicz, High-Resolution Modeling of Size-Resolved Stratospheric Aerosol, *J. Atmos. Sci., 55,* 3127-3147, 1998.

McCormick, M., P. and C. R. Trepte, Polar stratospheric optical depth observed between 1978 and 1985, *J. Geophys. Res., 92,* 4297-4306, 1987.

McCormick M. P., L. W. Thomason and C. R. Trepte, Atmospheric effects of the Mt Pinatubo eruption, *Nature, 373,* 399-404, 1995.

McCormick, M., P., P.-H. Wang and M. C. Pitts, Background stratospheric aerosol and polar stratospheric cloud reference models, *Adv. Space Res., 18,* 155-177, 1996.

Osborn, M., T., R. J. DeCoursey, C. R. Trepte, D. M. Winker and D. C. Woods, Evolution of the Pinatubo volcanic cloud over Hampton, Virginia, *Geophys. Res. Lett., 22,* 1101-1104, 1995.

Pitari G., V. Rizi, L. Ricciardulli and G. Visconti, HighSpeed Civil Transport Impact: Role of Sulfate, Nitric Acid Trihydrate, and Ice Aerosols Studied With a Two-Dimensional Model Including Aerosol Physics, *J. Geophys. Res., 98,* 23141-23164, 1993.

Pueschel, R. F., P. B. Russell, D. A. Allen, G. V. Ferry, K. G. Snetsinger, J. M. Livingston and S. Verma, Physical and optical properties of the Pinatubo volcanic aerosol: Aircraft observations with impactors and a Sun-tracking photometer, *J. Geophys. Res., 99,* 12915-12922, 1994.

Russell, P., B., J. M. Livingston, R. F. Pueschel, J. J. Hughes, J. B. Pollack, S. L. Brooks, P. Hamill, L. W. Thomason, L. L. Stowe, T. Deshler, E. G. Dutton and R. W. Bergstrom, Global to microscale evolution of the Pinatubo volcanic aerosol, derived from diverse measurements and analyses, *J. Geophys. Res., 101,* 18745-18763, 1996.

Thomason, L. W., Observations of a new SAGE II aerosol extinction mode following the eruption of Mt Pinatubo, *Geophys. Res. Lett., 19,* 2179-2182, 1992.

Thomason, L. W., L. R. Poole and T. Deshler, A global climatology of stratospheric aerosol surface area density deduced from Stratospheric Aerosol and Gas Experiment II measurements: 1984–1994, *J. Geophys. Res., 102,* 8967-8976, 1997a.

Thomason, L. W., G. S. Kent and C. R. Trepte and L. R. Poole, A comparison of the stratospheric aerosol background periods of 1979 and 1989-1991, *J. Geophys. Res., 102,* 3611-3616, 1997b.

Toon, O. B., Turco, R. P., P. Hamill, C. S. Kiang and R. C. Whitten, A One-Dimensional Model Describing Aerosol Formation and Evolution in the Stratosphere : II. Sensitivity studies and comparison with observation, *J. Atmos. Sci., 36,* 718-736, 1979.

Trepte, C. R. and M. H. Hitchman, Tropical stratospheric circulation deduced from satellite aerosol data, *Nature, 355,* 626-628, 1992.

Trepte, C. R., L. W. Thomason, and G. S. Kent, Banded structures in stratospheric aerosol distributions, *Geophys. Res. Lett., 21,* 2397-2400, 1994.

Turco, R. P., P. Hamill, O. B. Toon, *R.* C. Whitten and C. S. Kiang, A One-Dimensional Model Describing Aerosol Formation and Evolution in the Stratosphere : I. Physical Processes and Mathematical Analogs, *J. Atmos. Sci., 36,* 699-717, 1979.

van de Hulst, H. C., *Light Scattering by Small Particles,* Dover Publications, Inc., New York, 1957.

Yue G. K. and A. Deepak, Retrieval of stratospheric aerosol size distribution from atmospheric extinction of solar radiation at two wavelengths, *Appl. Opt., 22,* 1639-1645, 1983.

C. Bingen, D. Fussen and F. Vanhellemont, Belgian Institute for Space Aeronomy (IASB-BIRA), 3, Avenue Circulaire, B-1180, Brussels, Belgium. (e-mail:Christine.Bingen@oma.be,Didier.Fussen@oma.be and Filip.Vanhellemont@oma.be)

The February–March 2000 Eruption of Hekla, Iceland from a Satellite Perspective

W. I. Rose[1], Y. Gu[1], I. M. Watson[1], T. Yu[1], G. J. S. Bluth[1], A. J. Prata[2], A. J. Krueger[3], N. Krotkov[3], S. Carn[3],
M. D. Fromm[4], D. E. Hunton[5], G. G. J. Ernst[6], A. A. Viggiano[5], T. M. Miller[5], J. O. Ballenthin[5],
J. M. Reeves[7], J. C. Wilson[7], B. E. Anderson[8], D. E. Flittner[9]

An 80,000 km^2 stratospheric volcanic cloud formed from the 26 February 2000 eruption of Hekla (63.98° N, 19.70° W). POAM-III profiles showed the cloud was 9–12 km asl. During 3 days this cloud drifted north. Three remote sensing algorithms (TOMS SO_2, MODIS & TOVS 7.3 μm IR and MODIS 8.6 μm IR) estimated ~0.2 Tg SO_2. Sulfate aerosol in the cloud was 0.003–0.008 Tg, from MODIS IR data. MODIS and AVHRR show that cloud particles were ice. The ice mass peaked at ~1 Tg ~10 hours after eruption onset. A ~0.1 Tg mass of ash was detected in the early plume. Repetitive TOVS data showed a decrease of SO_2 in the cloud from 0.2 Tg to below TOVS detection (i.e.<0.01 Tg) in ~3.5 days. The stratospheric height of the cloud may result from a large release of magmatic water vapor early (1819 UT on 26 February) leading to the ice-rich volcanic cloud. The optical depth of the cloud peaked early on 27 February and faded with time, apparently as ice fell out. A research aircraft encounter with the top of the cloud at 0514 UT on 28 February, 35 hours after eruption onset, provided validation of algorithms. The aircraft's instruments measured ~0.5–1 ppmv SO_2 and ~35–70 ppb sulfate aerosol in the cloud, 10–30% lower than concentrations from retrievals a few hours later. Different SO_2 algorithms illuminate environmental variables which affect the quality of results. Overall this is the most robust data set ever analyzed from the first few days of stratospheric residence of a volcanic cloud.

[1]Geological Engineering & Sciences, Michigan Technological University, Houghton, MI
[2]CSIRO, Atmospheric Research, Aspendale, Victoria, Australia
[3]JCET/UMBC, Baltimore, MD
[4]Computational Physics, Inc; Springfield, VA
[5]Air Force Research Laboratory, Space Vehicles Directorate, Hanscom AFB, MA
[6]CEGF, Earth Sciences, University of Bristol, UK
[7]Engineering Dept., University of Denver, CO
[8]NASA Langley Research Center, Hampton, VA
[9]University of Arizona, Tucson, AZ 85721

INTRODUCTION

This is a study of satellite remote sensing of a small stratospheric eruption using thermal infrared and ultraviolet sensors. The focus is the Hekla February 2000 eruption, the first explosive event studied with the MODIS instrument (http://modis.gsfc.nasa.gov/index.html). MODIS (Moderate Resolution Imaging Spectroradiometer) is a key instrument aboard the Terra (EOS AM) and Aqua (EOS PM) satellites. Other instruments used in this study include meteorological polar-orbiting multispectral IR sensors Advanced Very High Resolution Radiometer (AVHRR; http://www.ngdc.noaa.gov/seg/globsys/avhrr2.shtml) and High Resolution Infrared Radiation Sounder/ TIROS Operational Vertical Sounder (HIRS-2/TOVS). AVHRR and HIRS/2 are carried on the same platforms and are favorably positioned for frequent imagery of polar

regions such as Iceland. We also used the Total Ozone Mapping Spectrometer (TOMS, http://skye.gsfc.nasa.gov/) which has already been shown to be sensitive to volcanic SO_2 (*Krueger et al.,* 1995), as well as data from the Polar Ozone Aerosol Measurement (POAM-III) instrument on the SPOT 4 spacecraft to constrain the height and width of the Hekla cloud. We have done this study to investigate MODIS' robust potential for volcanic cloud measurements and to compare its results with other sensors. The data from all sensors represent a comprehensive set of scientific data for an eruption, taking advantage of the synoptic satellite view. We also present some data collected in situ, following an accidental encounter with this volcanic cloud by a NASA research aircraft on February 28, 2000. These latter data represent a serendipitous chance for validating data for the various algorithms used in remote sensing of volcanic clouds.

Details of the Eruption and Hekla's Past

On 26 February 2000 at 1819 UT, an eruption of Hekla began, its 18th since European settlement about 876 AD [*Haraldsson et al.,* 2002]. The eruption had an early energetic subplinian phase, which produced a dominantly white plume [*Good,* 2001]. At 1825 UT, radar observations show the eruption column reached 11 km asl and was carried north by light winds [*R Stefansson, GVN* 25/2]. Clear observations from the ground were prevented beyond the first 60 minutes of eruption due to severe blizzard conditions and rapidly settling darkness. Snow flakes falling at 2000 UT encased ash particles [*H Mattson, pers commun,* 2002]. Pilot reports to the Icelandic CAA [*S Kristjansson, pers comm,* 2002], real time seismic data and weather radar imagery [*S Karlsdóttir, pers comm,* 2002] indicate that the most intense explosive activity lasted several hours until about 2200 UT, after which the summit activity decreased to a level of intense fire fountaining and phreatomagmatic explosions in the summit area. At about 2200 UT the explosive activity stabilized to a low intensity and explosive activity ended entirely by 0500 UT on 27 February. Following this, a 4.5 km long fissure which opened on Hekla's ridge early in the eruption extruded lava flows until March 8, 2000 [*Ólafsdóttir et al.,* 2002; *Hoskuldsson, pers comm,* 2001]. In all a total volume of about 0.17 km³ of magma was erupted [*Ólafsdóttir et al.,* 2002]. The explosive phase produced a tephra fallout deposit covering roughly 18,000 km² in a N direction with total volume estimated at 0.01 km³ [*Haraldsson et al.,* 2002]. By the morning of 27 February, the explosive phase had waned and effusive fissure activity dominated. The lava and ashfall composition

was mainly basaltic andesite with an SiO_2 content of 54% (by weight). There was a small amount of dacite in the ashfall materials [*Hoskuldsson and Ólafsdóttir,* 2002].

The dynamics of Hekla's 2000 eruption qualitatively resembled 4 previous events in 1947–48 [*Thorarinsson,* 1967], 1970 [*Thorarinsson & Sigvaldason,* 1972], 1980–1 [*Gronvold et al.,* 1983] and 1991 [*Gudmundsson et al.,* 1992]. Each started with a prominent explosive phase which resulted in stratospheric venting of erupted materials and a tephra fallout deposit, followed by a more extended effusive period with fissure lavas, generally of basaltic andesite composition. The silicic Hekla dacite and rhyolite which occurs in Hekla's early plinian phases has been interpreted as being due to the partial melting of the Icelandic metabasic crustal materials by rising mantle-derived basalt which itself differentiates to produce basaltic andesite before eruption [*Sigmarsson et al.,* 1992].

Hekla's plinian volcanic cloud of 1947–48 was described in detail by *Thorarinsson* [1967] as being mainly gas-rich and ash-poor based on photographs taken at that time, showing a white uppermost part of the plinian cloud. The 1970 Hekla volcanic cloud was actively sampled by aircraft [*Cadle & Blifford,* 1971] and it contained silicate glass shards with 55% SiO_2 and an abundance of sulfates and sulfuric acid. *Oskarsson* [1980] studied fluorine adsorption on Hekla's 1970 tephra, which poisoned surface water, and *Frogner et al.* [2001] studied the reactions between the 2000 ashfall and ocean water.

Data and Methods Used

The satellite data sets we examined are listed in Table 1. We used those data to map the position of the volcanic clouds at successive times and to make estimates of the various components (ash, ice, sulfate and SO_2). Various IR bands of interest in our studies are listed in Table 5. We used 11 and 12 µm wavelength IR data from AVHRR and MODIS to retrieve information about the optical depth of the volcanic cloud, the effective radius of ash or ice particles visible by the sensor [*Rose et al.,* 2000] and the mass of fine ash or ice following the methods of *Wen & Rose* [1994] and *Rose et al.* [1995].

Three different methods are used to measure volcanic cloud SO_2. We used 7.3 µm wavelength IR data from MODIS and HIRS/2-TOVS [*Smith et al.,* 1979] for SO_2 burden determinations using the scheme of *Prata et al.* [2003]. With the 8.6 µm wavelength IR data available on MODIS, we used a scheme first developed by *Realmuto et al.* [1997] and employing atmospheric corrections applied via the MODTRAN radiative transfer code [*Berk et al.*

Table 1. Eruption details, satellite and aircraft data of this study.

Date	UT	sensors	retrievals, comments
2/26/00	**1819**		**onset of eruption**
"	**1828**	**ground based radar**	**Top at 11 km asl**
"	1945	AVHRR, TOVS	ash, ice, SO_2
"	~2000	**pilot report to CAA**	**Cloud top at 10-12 km asl**
"	2100	MODIS	ice
"	2135	AVHRR	ice
"	**2200**		**Decrease in eruption intensity**
2/27/00	0359	AVHRR	ice
"	0547	AVHRR, TOVS	ice, SO_2
"	**~0600**		**End of explosive activity**
"	0737	AVHRR, TOVS	ice, SO_2
"	0918	AVHRR,TOVS	ice, SO_2
"	1108	AVHRR,TOVS	ice, SO_2
"	1139	TOMS	SO_2, AI
"	1236	AVHRR, TOVS	ice, SO_2
"	1350	MODIS	ice, SO_2 (7.3, 8.6), sulfate
"	1417	AVHRR, TOVS	ice, SO_2
"	1557	AVHRR, TOVS	ice, SO_2
"	1616	AVHRR, TOVS	ice, SO_2
"	1740	AVHRR, TOVS	ice, SO_2
"	2015	MODIS	ice, SO_2 (7.3, 8.6), sulfate
"	2155	MODIS	ice, SO_2 (7.3, 8.6), sulfate
"	2335	MODIS	ice, SO_2 (7.3, 8.6), sulfate
2/28/00	0359	AVHRR, TOVS	ice, SO_2
"	**0508**	**DC8 encounter**	**CIMS data**
"	0536	AVHRR, TOVS	ice, SO_2
"	0706	AVHRR, TOVS	ice, SO_2
"	1041	AVHRR, TOVS	ice, SO_2
"	1115	MODIS	ice, SO_2 (7.3, 8.6), sulfate
"	1200	TOMS	SO_2, AI
"	1407	TOVS	SO_2
"	1559	TOVS	SO_2

also see listing of TOVS data collected on 29 Feb and 1 Mar in Table 6.

1989] to estimate SO_2 burdens. We also estimated SO_2 burdens using the UV TOMS sensor, following the methods explained by *Krueger et al.* [1995].

For retrievals of the effective radius and masses of sulfate aerosols and ice, we used a multispectral IR scheme which is based on 7 MODIS thermal IR channels (27-33) and the method of *Yu & Rose* [2000], using the MODTRAN code and a lookup table for mixtures of ice and sulfate particles. Validation of all of these methods is sparse, and the Hekla data set represents the very first opportunity to compare and evaluate independent SO_2 retrievals on a given volcanic cloud. Moreover, there is independent validation information in this case because of the research aircraft encounter discussed hereafter.

The NASA DC-8 aircraft's great circle route from Edwards AFB, California USA, to Kiruna, Sweden, inter-cepted the Hekla volcanic cloud at an altitude of 11.3 km at about 75°N and 5°W between 0508 and 0518 UT on 28 February (Figure 1) about 1300 km NNE of Hekla. The position of the airplane at these times is shown as the thick line segment along the flight path. Before and after encountering the volcanic cloud trace gas and aerosol measurements were unperturbed. The intercept occurred 35 hours after the start of the eruption and its time with respect to all our measurements is given in Table 1. The volcanic cloud moved considerably between the time of the TOVS image and the DC-8 encounter, as our remote sensing data shows. The calculated plume crossing position matches our observations.

The DC-8 payload for the SOLVE (SAGE III Ozone Loss and Validation Experiment) mission consisted of 17 scientific instruments or suites of instruments [*Newman, 1999*]. Three
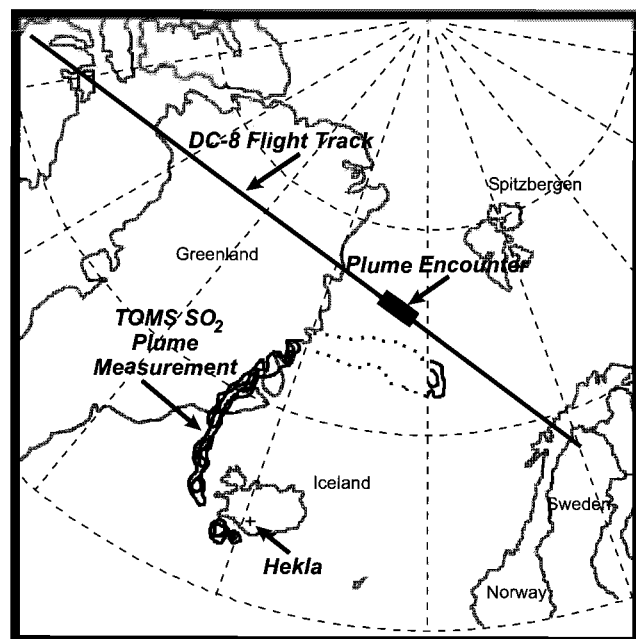
Figure 1. Map showing Hekla Volcano, the volcanic cloud as detected by TOMS on Feb. 27th, and the flight track of the NASA DC-8 aircraft on Feb. 28th.

of these are particularly important for the present comparison to remote sensing data. The Air Force Research Laboratory chemical ionization mass spectrometer (CIMS) [*Hunton et al., 2000; Talbot et al., 1999; Viggiano & Hunton, 1999; Miller et al., 2000*] was optimized to measure *in-situ* mixing ratios of HNO_3, SO_2, and HCN. The details of the operation of this instrument are reported elsewhere. For these gases, the instrument attained 20% accuracy, better than 10% precision, response times faster than 1 second, and detection sensitivities approaching 10 pptv. Concentrations of H_2SO_4, HCl, HF, and H_2S were obtained from less frequent full mass scans. The ion chemistry and instrument sensitivity for these gases were confirmed during post-mission laboratory calibrations. Here, only data on SO_2 and a limit on the amount of gas phase H_2SO_4 are reported since those species are important for comparison with the remote sensing data. Only a limit can be placed on gas phase H_2SO_4 due to the possibility of evaporation of aerosol H_2SO_4 in the inlet line.

Aerosol size measurements were made by the University of Denver Focused Cavity Aerosol Spectrometer (FCAS II) [*Jonsson et al., 1995*] and Nuclei-Mode Aerosol Size Spectrometer (N-MASS). The N-MASS detects particles in the diameter range 4 to 100 nm, while the FCAS II covers 90 to 2000 nm. Corrections were made for diffusion loss, instrument efficiencies, and departures from isokinetic sampling at the inlet. The combined measurements were then

inverted to obtain the full aerosol size distribution from 4 to 2000 nm. The volatile and nonvolatile fractions of aerosol concentrations in various size bins were measured by the NASA Langley Particle Measurement System (PMS).

POAM III made observations of the Hekla volcanic cloud on February 29 and March 1, 2000. POAM measures solar extinction by the atmosphere using the solar occultation technique: the sun is observed through the Earth's atmosphere as it rises and sets as viewed from the satellite. POAM data have been applied to the study of Polar Mesospheric Clouds [*Debrestian et al., 1997*], and the study of Polar Stratospheric Clouds and stratospheric clouds of smoke traceable to boreal forest fires [*Fromm et al., 1997, 1999, 2000*]. In this paper the POAM cloud height determinations were especially important.

SATELLITE SENSING OF VOLCANIC CLOUD ICE

Thermal infrared sensors are routinely used to map clouds. At 10 μm wavelength cloud outlines are well-detected day and night. If they are optically thick and in the troposphere, their radiances and temperatures correlate inversely with cloud height. Thus cloud patterns may be mapped and the heights of clouds estimated. Meteorological clouds with temperatures less than −15°C usually contain appreciable numbers of ice crystals, while supercooled liquid water cannot exist in clouds below −40°C [*Rogers & Yau, 1989*]. In the earliest images of the Hekla eruption (Figure 2) the Hekla volcanic cloud spreads as a partially bifurcating plume and wind blown cloud [*Ernst et al., 1994*]. It extends from the volcano, spreading laterally under gravity while being advected downwind to the NE and drifting N. Brightness temperatures of this plume were −55° to −70°C which matches the temperature values of 7–13 km asl that day (tropopause temperatures were −60 to −65 °C at 9.5–10 km) as measured by radiosonde (from stations at Keflavik, and in Greenland and Jan Mayan).

Many eruption clouds have been mapped and discriminated using brightness temperature differencing (BTD) methods [*Prata, 1989a, b*], where volcanic ash absorbs and scatters upwelling infrared energy from under the volcanic cloud differently than water droplets or ice. Silicate particles absorb and scatter more strongly than water or ice at 10 μm while ice and water absorb and scatter more at 11 μm. Thus in a dry atmosphere BTD differencing shows clouds dominantly laden with ash with BTD < 0 while clouds dominantly laden with with liquid water or ice particles have BTD > 0 [*e.g. Wen & Rose, 1994*]. Apart from the first image at 1945 UT, which shows some regions with weakly negative BTD, the 2000 Hekla volcanic clouds show nearly always BTD > 0, and

Figure 3. MODIS imagery of Hekla's volcanic cloud acquired at 1115 UT on 28 February. The upper left panel shows MODIS band 28 (7.3 μm) data with the volcanic cloud showing brightly—this is likely due to SO_2 absorption effects which lower the BT. The lower left panel shows band 31 (10.7 μm) BT data, with the volcanic cloud practically invisible. The upper right panel is band 31–32 BTD, showing the volcanic cloud as similar to other high clouds. The example shows that to discriminate and map ice-rich and/or ash-poor volcanic clouds, SO_2 detection may be very useful.

then declined by a factor of three in 12 hours (Table 3; Figure 6). The Hekla clouds moved gradually to the north, being deformed by storm systems. By the 28th of February, ~36 hours after eruption, the Hekla cloud no longer stands out in a BTD image (Figures 5 and 6) but the cloud is prominent in MODIS band 28 BT (at ~7.3 μm, Figure 6a), suggesting that it was by then dominated by SO_2.

SATELLITE SO_2 MEASUREMENTS

We were able to map the Hekla cloud clearly with 3 independent satellite SO_2 detection schemes: 8.6 μm SO_2 (Plate 4), 7.3 μm SO_2 (Plate 5) and Earth Probe TOMS SO_2 (Plate 6). We also were able to compare mass estimates of SO_2 from the various methods for the first time (Tables 2, 4). The mapped results show that SO_2 sensing was an excellent way to track the Hekla cloud, especially as ash particles were either hidden by ice or had already fallen from the cloud. The analysis also shows that the positions mapped by each method matched very closely with each other and with the position of the stratospheric cirrus cloud mapped with BTD and already discussed.

The SO_2 mass for the entire Hekla cloud retrieved by the various algorithms (Tables 2, 4) give values in the range of
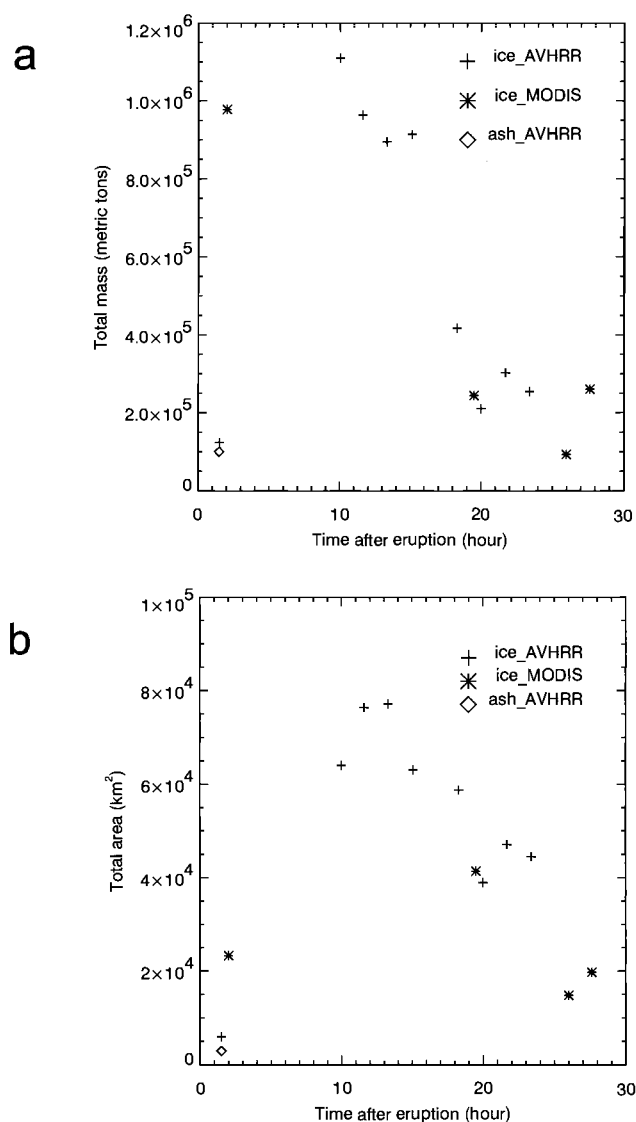
Figure 4. Fine Particle Mass and Cloud Area for Hekla Volcanic Cloud (Table 3) plotted against time after the onset of eruption. The plots crudely depict three evolutionary stages: 1. the first few hours after eruption onset when the volcanic cloud increased rapidly in size and ice mass; 2. a poorly defined intermediate stage about 10–15 hours after eruption when the cloud reached maximum area and began to decline in ice mass. At this point it was possible to track the cloud using BTD (Figure 3; Plates 1 and 2) and 3. a third stage beginning about 16 hours after eruption onset where the ice signal has faded markedly and the cloud can be better tracked by SO_2 (Plate 3, Fig 3).

0.13 to 0.37 Tg, except for the values determined on 26 February, which were much lower. We attribute the low values on the first day as being due to the very high optical depth of the volcanic cloud at that time, during the explo-

sive venting phase of the eruption (Figures 2; Plates 4a and 5a). With a high optical depth the transmission of energy from beneath the volcanic cloud is greatly limited, and SO_2 detection is inhibited or amounts to a partial detection. This is the first time that MODIS-based determinations have been made for SO_2 so that we can compare independent results. Table 2 shows that agreement of the three methods is imperfect, yet encouraging, considering the non-optimum viewing conditions. On February 27 and 28 all estimates of SO_2 mass range from 0.1-0.3 Tg.

On Feb. 27, 2000, the Earth Probe TOMS (11:54 UT, Orbit 19683) found a very long and unusually narrow arc of sulfur dioxide extending west from southern Iceland, then north across Greenland, and finally east toward Norway (Plate 6a). The TOMS aerosol index signal on the same orbit showed no evidence of ash, but instead indicated the presence of sulfate in this very fresh cloud (~18 hrs of atmospheric residence). TOMS observed sections of the SO_2 cloud on the following two days as the cloud drifted east across the Barents Sea and south into northern Russia as shown in Plate 6b. The mass of sulfur dioxide can be determined in the more southerly portions of the cloud but retrievals near the northern terminator are very noisy because of low radiances. Thus, it is not possible to determine the total SO_2 eruption tonnage for this cloud from TOMS. We estimate that the section of the cloud shown in Plate 6a from Iceland to 74° N contained about 60 +/– 20 kt of SO_2. The analysis includes estimates from different combinations of TOMS wavelength bands.

The complete cloud found in the MODIS data of 27 February (Plates 4b and 5b) includes more SO_2 than observed with TOMS. The probable reason for the discrepancy between TOMS and MODIS is mainly due to the fact that MODIS sensed more of the cloud than TOMS. MODIS data close to the time of the TOMS overpass (see MODIS images above) indicate that a relatively large portion of the cloud was too far north and east for TOMS to measure. On the other hand MODIS appears to lose the SO_2 signal for the southern part of the plume, south of Iceland and over the Greenland ice sheet (compare TOMS images above). Thus, TOMS UV and MODIS IR data are highly complementary in unambiguous detection of plumes. There is no consistent relationship between the 7.3 and 8.6 μm retrievals, and because of the high latitude we cannot compare TOMS estimates with the others. TOMS values, which are based on scattering of solar uv radiation, are adversely affected by low solar energy of the high latitude winter season, which makes it difficult to distinguish the SO_2 signal from background noise. This problem worsened after the first day, as the cloud was located near the light terminator. MODIS values are evidently affected by cold underlying temperatures
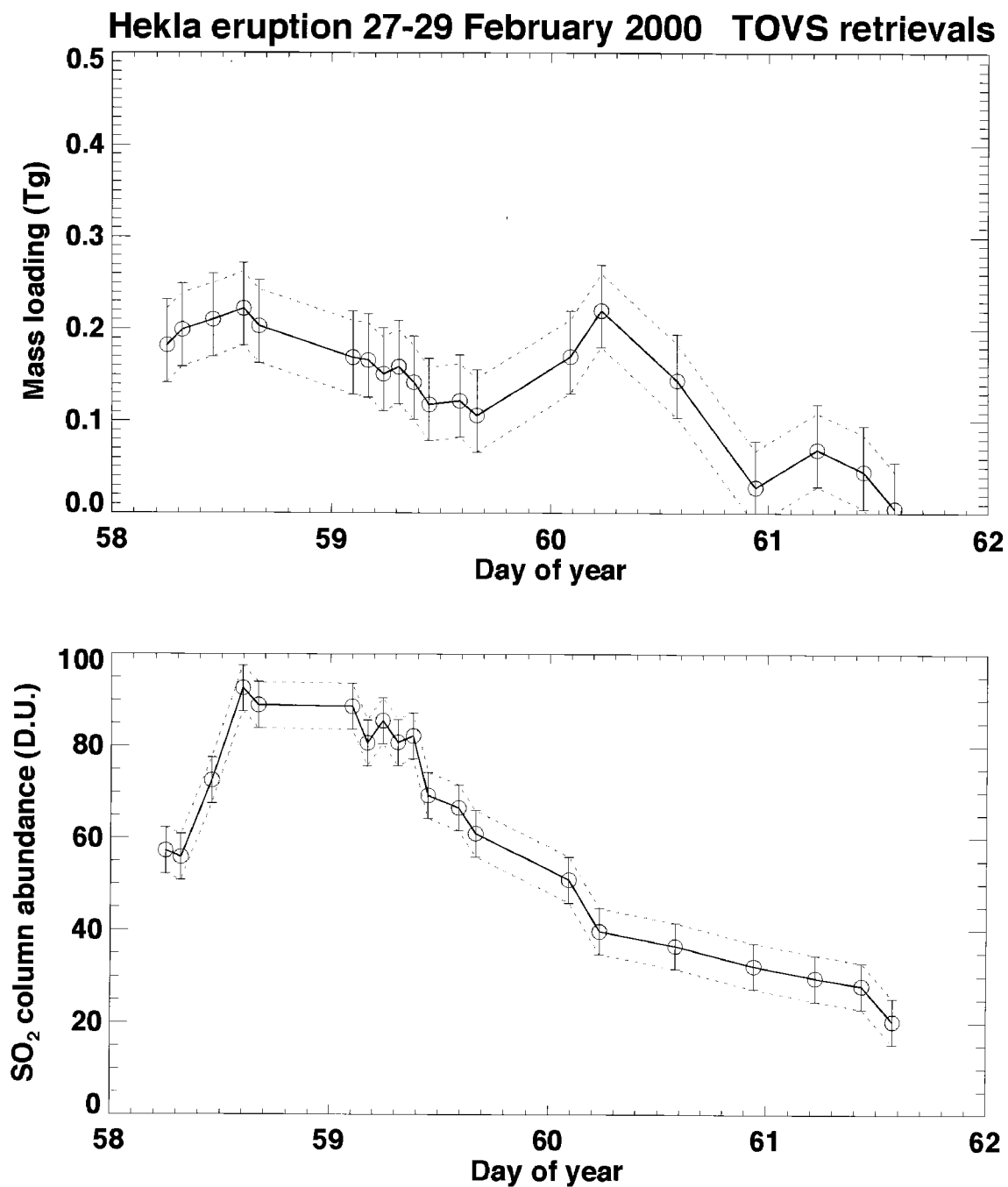
Figure 5. Plots of TOVS SO_2 retrieval data from Table 4, showing decay of mass loading of SO_2 and maximum column abundance with time (Day 58=February 27; Day 59=February 28, etc). The TOVS data on SO_2 shown extends the time of observation of the Hekla cloud beyond the data listed in Table 1, into February 29 and March 1. One interesting (and so far unexplained) feature of the data is an apparent increase in SO_2 mass on February 29.
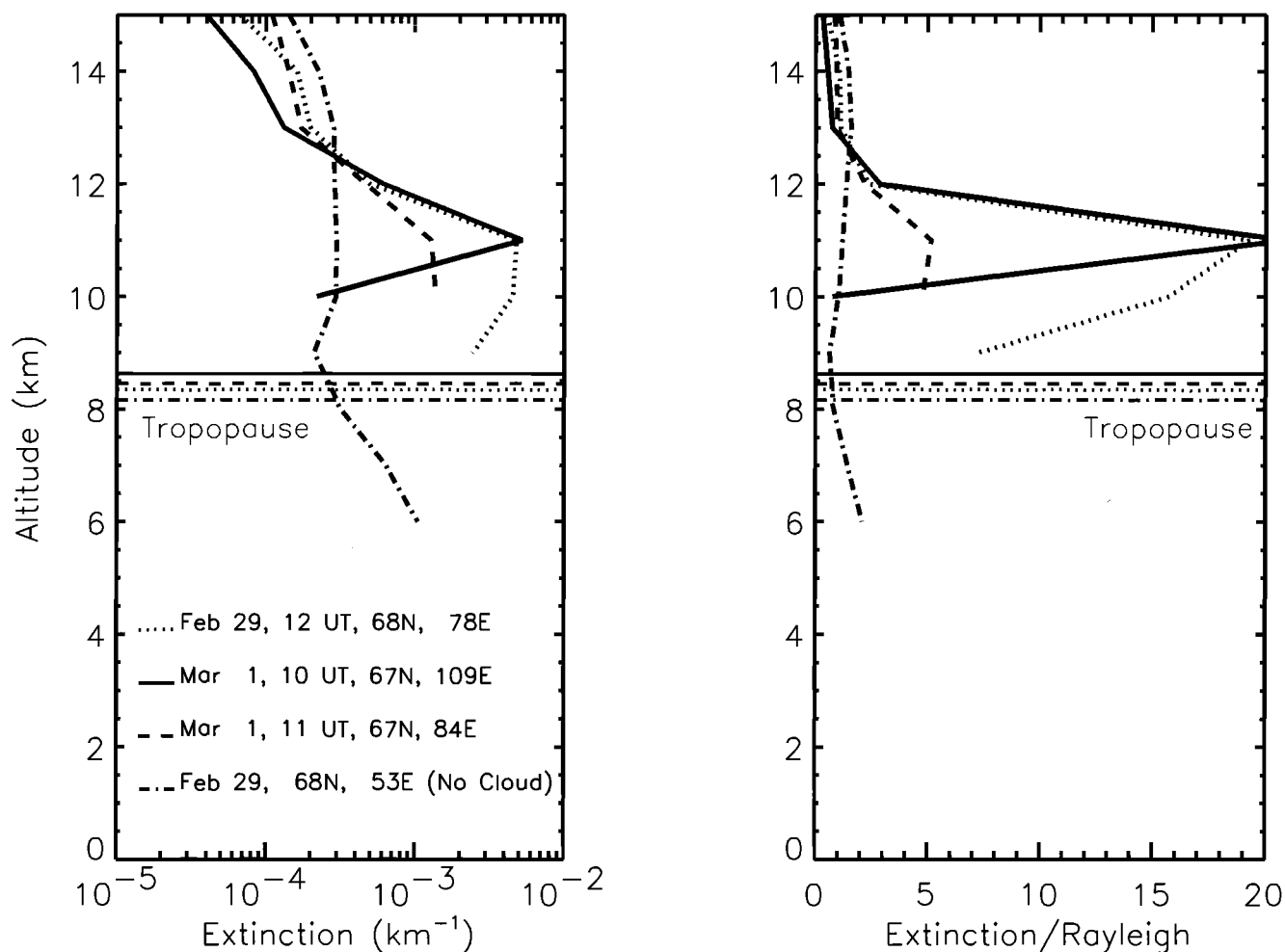
Figure 6. POAM III 1020 nm aerosol extinction and extinction ratio (Total/Rayleigh) by altitude for 29 February and 1 March 2000. These data are used to constrain the volcanic cloud height and thickness. See text for explanation.

and underestimate in these conditions, particularly when the volcanic cloud travels over Greenland (early on 27 February). It is likely that there are effects of ice on the SO_2 retrievals for both the 7.3 and 8.6 μm cases. Based on the IR transmission spectrum of ice [*Watson et al., in review*], it is

likely that the 7.3 μm channel will be more strongly affected by ice, but it does not give consistently lower SO_2 as would be expected if this were the only significant environmental factor. We are only beginning to investigate the differences shown by detectors (see discussion also).

Table 2. SO_2 and sulfate mass estimates from MODIS IR and TOMS, Hekla 2000 eruption. All values in Tg.

MODIS date, time	7.3 μm SO_2	8.6 μm SO_2	TOMS SO_2	Sulfate	Revised Ice mass
26 Feb 2110	0.08	0.034	na	0.003	0.83
27 Feb 1350	0.20	0.13	0.06*	0.004	0.40
27 Feb 2155	0.17	0.37	na	0.008	0.91
28 Feb 1115	0.16	0.16-0.24		0.005	0.05

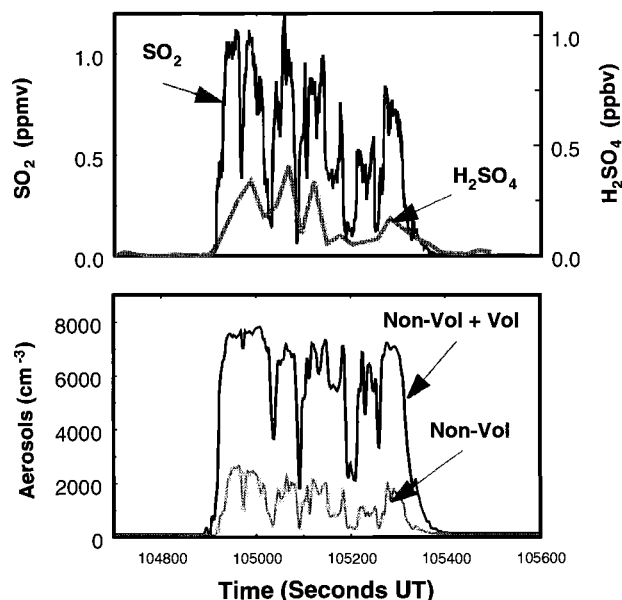* 1139 UT; only part of the cloud sensed—<74°N portion only.

Figure 7. In-situ measurement of plume properties during the Feb. 28 DC 8 encounter at 11. 3 km altitude. The top panel shows CIMS measurements of SO_2 and H_2SO_4 and the bottom panel shows aerosol number densities in the 12–1000 nm diameter range. Both the unheated inlet (volatile plus non-volatile) and the heated inlet (non-volatile) channels are shown. The times given in the plots are in seconds starting at 0000 UT on 27 February, and amount to about 0510 UT on February 28, 2000. See text for discussion.

We used the HIRS-2/TOVS data from the same polar orbiting platform as AVHRR to retrieve the 7.3 μm data for SO_2, using the methodology of *Prata et al.,* [2003] and assuming a constant cloud height of 11 km (Table 4). These

results are plotted in figure 5, and generally show agreement with the MODIS results and a gradual but not continuous decrease in SO_2 mass from just above 0.2 Tg (teragram = 10^{12} g) to 0 in about 3.5 days. The error bounds shown are determined as +/– 5 Dobson Units (milli atm cm) based on modeling errors and measurement errors. This translates into about +/– 36 kt (kiloton = 10^9 g) for a nadir pixel. The lower plot in figure 5 shows peak column abundance data, which shows a steady decline after 1400 UT on 27 February, about 7 hours after the peak in ice mass (Fig 4a). There is an increase in SO_2 mass early on 29 February, but not an increase in column abundance. We are unsure of the reason for this.

SATELLITE SULFATE AND AEROSOL DATA

A negative TOMS Aerosol Index (AI) anomaly (up to -5) was observed along the SO_2 trail on February 27 (Plate 7). This is inconsistent with volcanic ash, which would have produced a positive AI, but could have been produced by an unexpected sulfate component. This aerosol index anomaly continued on February 28 and on February 29. Non-absorbing aerosols, such as sulfate, can produce a negative AI.

Table 2 also lists the results of sulfate retrievals done with a multispectral algorithm which assumes a mixture of ice and sulfate aerosol [*Yu & Rose, 2000*]. These show aerosol sulfate masses that amount to about 2–5% of the SO_2 masses in the same cloud. Gas phase conversion to sulfate at high solar zenith angle conditions have e-folding times of ~35 days (Bluth *et al.*, 1997, p 674). Thus the results are similar to those shown for the 1982 El Chichón clouds by *Yu &*

Table 3. Ice retrievals, Hekla Volcanic Clouds of Feb 2000.

Date; time, UT	Eff Radius, μm	mean OD, unitless	Mean Burden, T/ km²	Ice Mass, Tg	Cloud area, km²
2/26/00; 1945	27.3	1.3	20.7	0.12	5800
2/26/00; 2100	**38.1**	**1.7**	**41.9**	**0.98**	**23000**
2/27/00; 0413	14.7	1.8	17.3	1.11	64000
2/27/00; 0554	16.7	1.1	12.6	0.96	77000
2/27/00; 0737	15.9	1.1	11.6	0.89	77000
2/27/00; 0923	18.6	1.1	14.5	0.91	63000
2/27/00; 1236	13.8	0.7	7.1	0.42	59000
2/27/00; 1350	**12.9**	**0.6**	**5.9**	**0.24**	**41000**
2/27/00; 1417	10.4	0.7	5.4	0.21	39000
2/27/00; 1557	9.3	0.9	6.4	0.30	47000
2/27/00; 1740	11.5	0.6	5.7	0.25	45000
2/27/00; 2020	**13.4**	**0.6**	**6.3**	**0.09**	**15000**
2/27/00; 2155	**20.6**	**0.9**	**13.2**	**0.26**	**20000**

Rows in **Bold type are MODIS data**; others are AVHRR, see Table 1 also.

02/26/2000
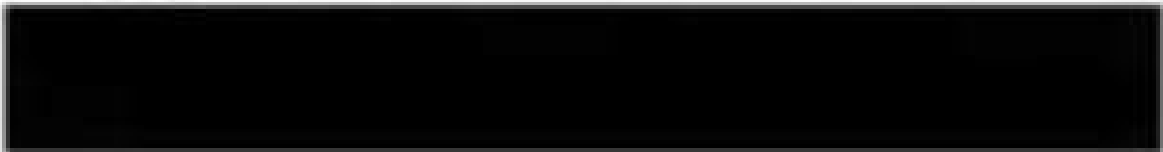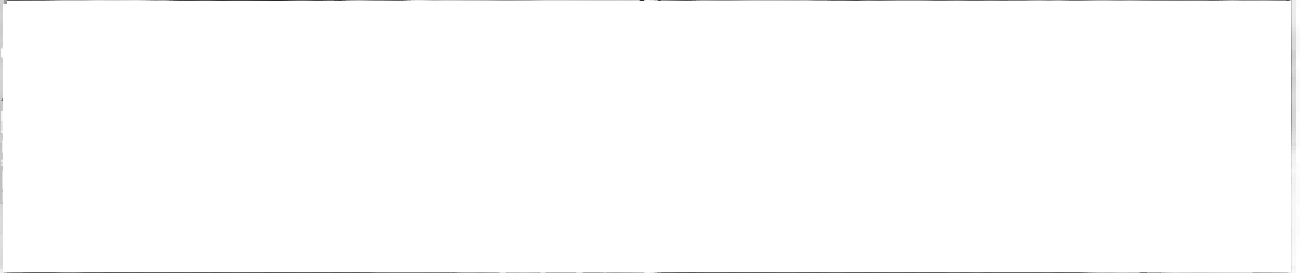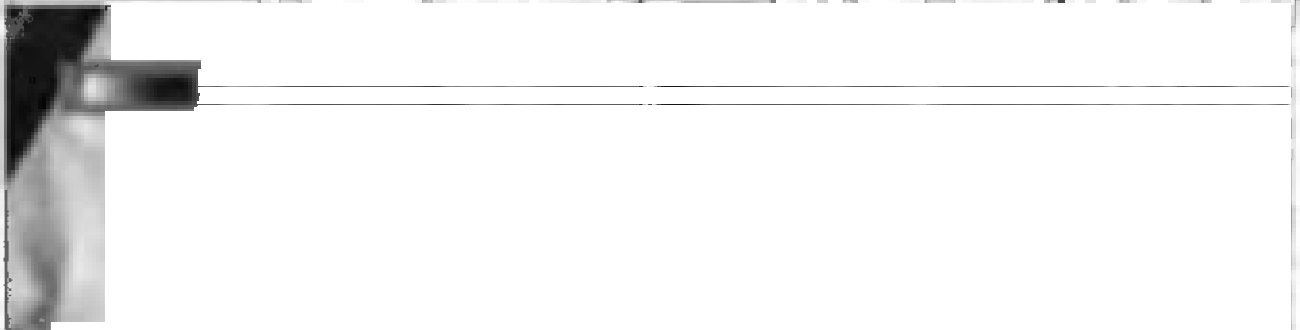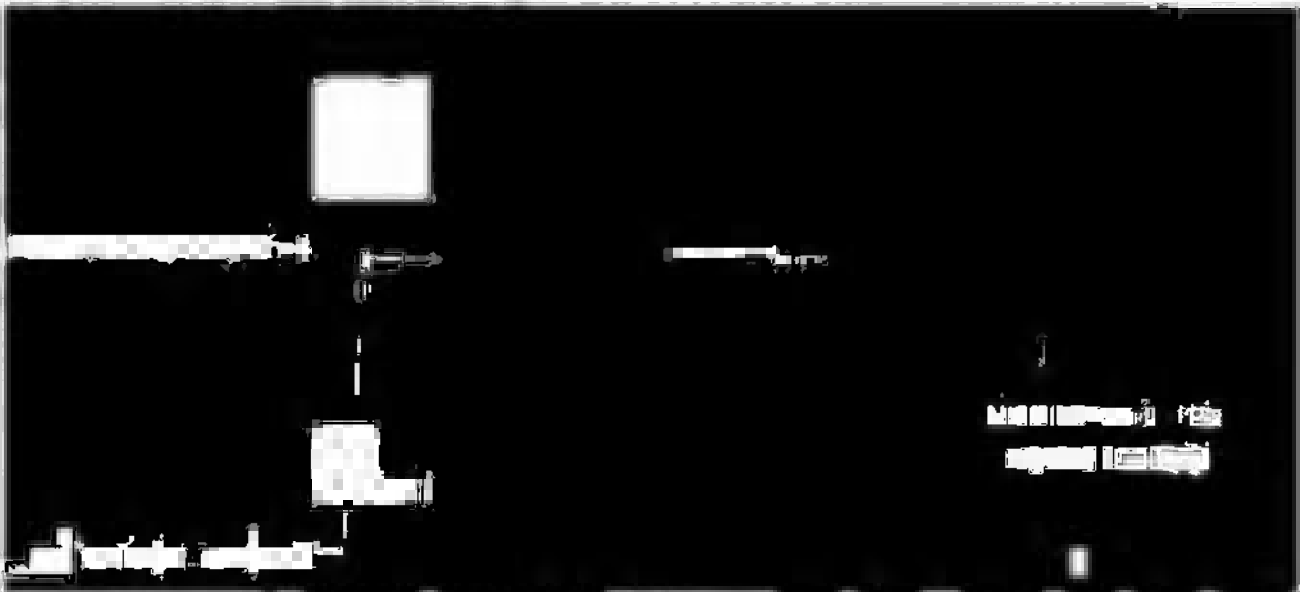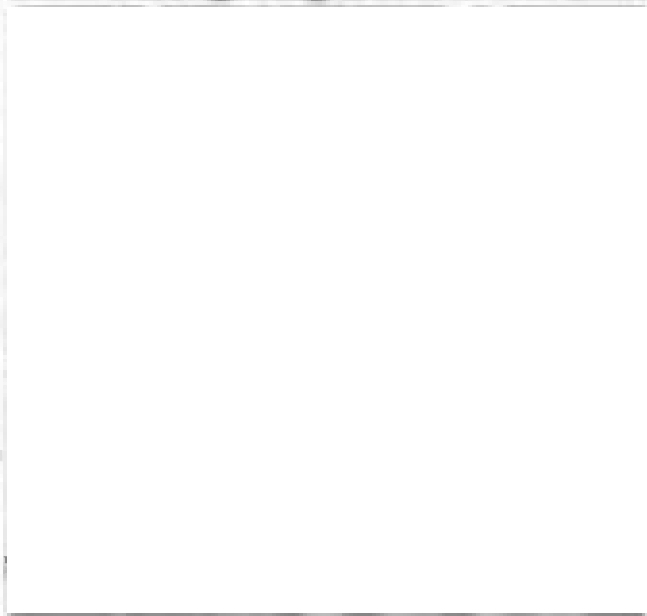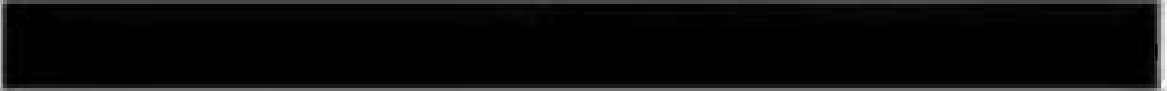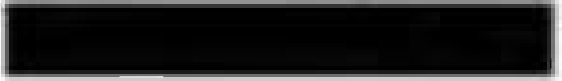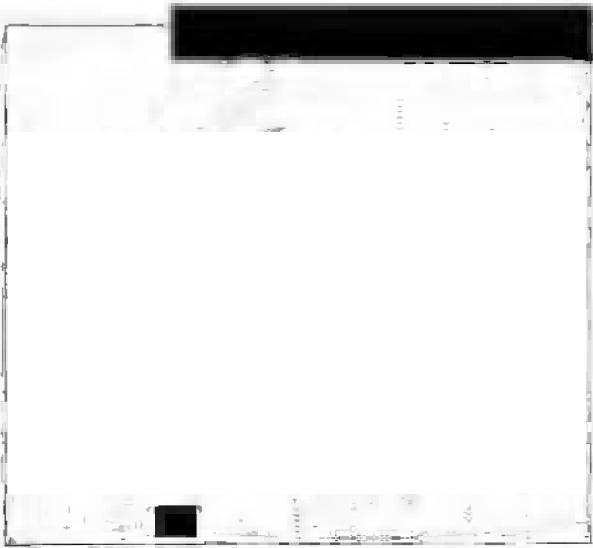
Table 4. Hekla mass loadings from TOVS data.

Day	UT	Max DU	SO$_2$ Tg
27 Feb	05:58	57.3	0.182
"	07:38	55.9	0.199
"	10:58	72.9	0.210
"	14:19	92.6	0.222
"	16:01	88.9	0.203
28 Feb	02:22	88.6	0.169
"	04:03	80.7	0.166
"	05:44	85.5	0.151
"	07:25	80.8	0.159
"	09:05	82.2	0.142
"	10:45	69.3	0.118
"	14:07	66.6	0.122
"	15:59	61.0	0.106
29 Feb	02:10	51.0	0.170
"	05:34	39.8	0.220
"	13:55	36.6	0.144
"	22:35	32.2	0.028
1 Mar	05:17	29.6	0.069
"	10:20	27.9	0.045
"	13:43	20.2	0.01

Cloud height assumed to be 11 km; time listed is time for pixel with largest SO$_2$ abundance. Areas calculated for mass loadings are equivalent space filling rectangles as projected onto earth. Error bounds are +/– % –5 DU and +/– 40 kT as shown in Fig 5.

Rose [2000] and indicate either that sulfate was formed prior to eruption or there is some (aqueous phase?) conversion of volcanic SO$_2$ to sulfate in the first hours to days of atmospheric residence.

POAM RESULTS

On February 29 and March 1, 2000 POAM detected enhancements of 1 μm aerosol extinction above the tropopause (Figure 6). The POAM measurements were made inside the polar vortex air mass so it is important to differentiate these aerosol clouds from polar stratospheric clouds, which POAM also detected inside the vortex near these dates. At this time the location of PSC sightings was generally near the Greenwich meridian. PSC-formation temperatures were not found near the longitudes of the POAM observations in Figure 6, which are located over far northern Siberia. To investigate the possible link with the Hekla eruption, we calculated isentropic back trajectories (not shown) from the level of the peak aerosol enhancement, which in these three cases was approximately 335 K. We found excellent corroboration between the trajectories and the location/time of the volcanic injection, thus we conclude that these aerosols were part of the Hekla plume.

The POAM data can be used to make some inferences about the spread, top, composition and thickness of the volcanic cloud. The February 29 profile was the only one that day indicating any stratospheric enhancement. POAM's coarse longitudinal sampling (roughly 25 degrees) allows us only to make the crude conclusion that the volcanic cloud had spread no further than about 50 degrees in longitude at POAM's measurement latitude (68°N) on that date. This is consistent with Defense Meteorological Satellite Program (DMSP) imagery which reveals the Hekla volcanic cloud as a narrow filament stretching from north of Scandinavia southeastward to Siberia, almost precisely to the POAM location. (DMSP shows a distinct cloud in visible imagery, but no signal in the IR. The visible cloud has impressively long shadows, confirming a very high cloud. The fact that it is invisible in the IR strongly suggests the cloud is composed of very small, hence IR-transparent, particles.) On March 1, two neighboring POAM profiles measured an aerosol layer at 11 km. These two are at 84 and 110 degrees E. Thus it appears the Hekla cloud spread out or became aligned in a meridional direction at the POAM latitude by March 1.

The POAM data, with 1-km vertical resolution, indicate

Table 5. Some infrared channels of interest on various sensors used in this study. Channels of approximately equivalent wavelength are positioned in the same row.

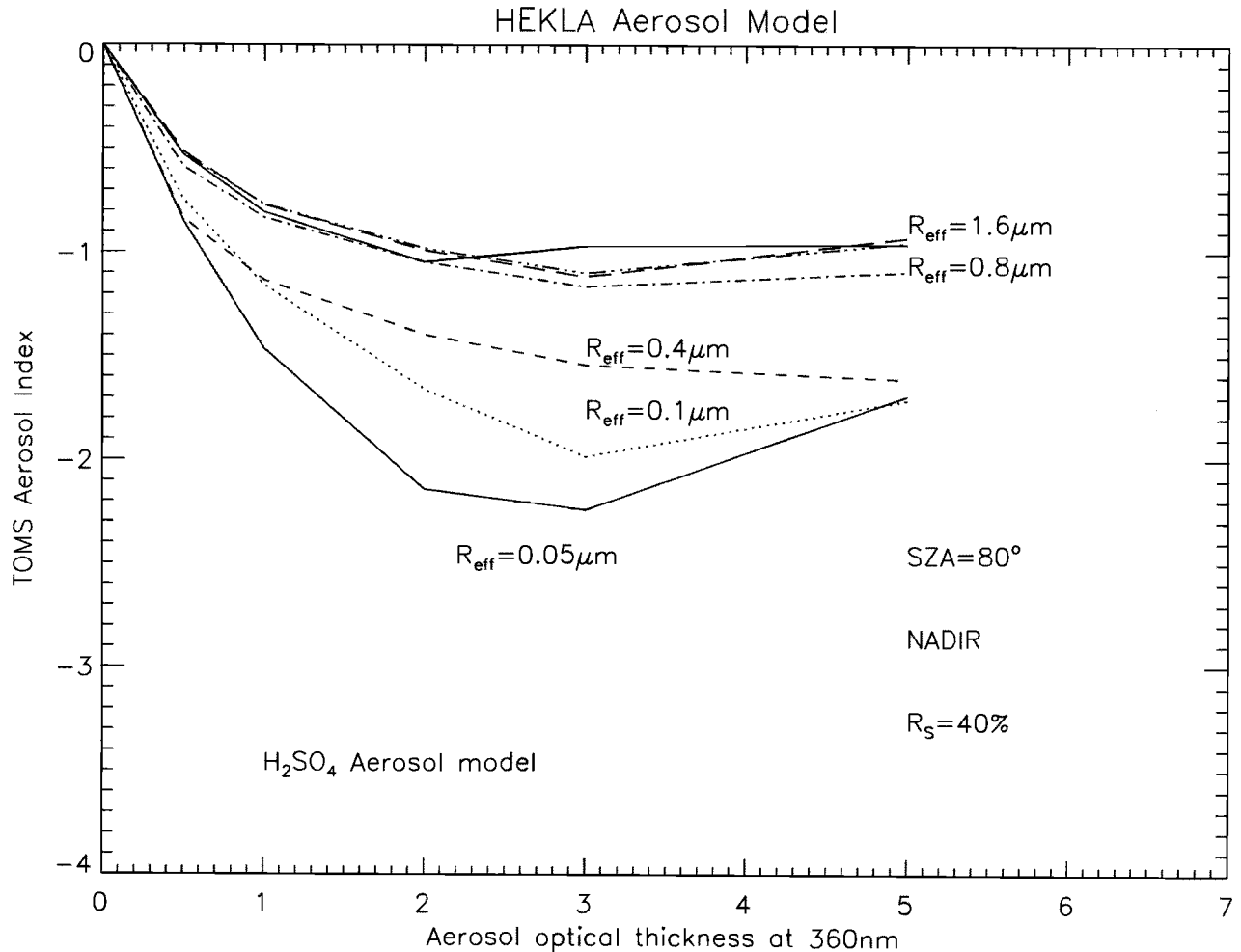| AVHRR		MODIS		TOVS HIRS/2	
Ch. No	center •, μm	Ch. No	center •, μm	Ch. No	center •, μm
		27	6.72	12	6.72
		28	7.33	11	7.33
				10	8.16
		29	8.55		
		30	9.73	9	9.71
4	10.7	31	11.03	8	11.11
5	12	32	12.02		
		33	13.34	7	13.35

HEKLA Aerosol Model

Figure 8. TOMS Aerosol Index vs. non-absorbing aerosol optical thickness at high solar zenith angles. The effect of effective radius of the particles is illustrated by the different curves. Only particles smaller than 0.05 μm will produce very negative AI values.

that the top of the plume was between 11 and 12 km. It is not possible to determine how well POAM sampled the highest portion of the cloud, but all three measurements of the Hekla cloud have the aerosol returning to "background" at 12 km. The thickness of the volcanic cloud above the tropopause may be estimated by considering that the enhanced aerosol extinction resides at all altitudes between 11 km and the tropopause (here the tropopause altitude is determined with the dynamic definition-the level at which the potential vorticity equals 3 PV Units.) The tropopause height in the three POAM cloud profiles is roughly 8.5 km. Thus the thickness of the plume in the lowermost stratosphere is on the order of 2–3 km. It is likely that the POAM profiles indicate that the depth of the cloud extends below the tropopause. Under normal

background conditions, POAM can make measurements well into the troposphere (until clouds obscure the sun from the sun tracker). Figure 6 gives an example from a neighboring profile on February 29. The 3 cloud profiles all "cut off" at or above the tropopause, which indicates the presence of a cloud on the limb that is opaque to POAM. This might be cirrus or a lower portion of the Hekla cloud.

NASA DC8 ENCOUNTER

On February 28, 2000 at 0510 UT 75°N and 1°W (figure 1, Plate 3d) a NASA DC8 flying from California to Sweden crossed through the Hekla volcanic cloud [*Grindle & Burcham, 2002*]. This encounter occurred some 700 nauti-
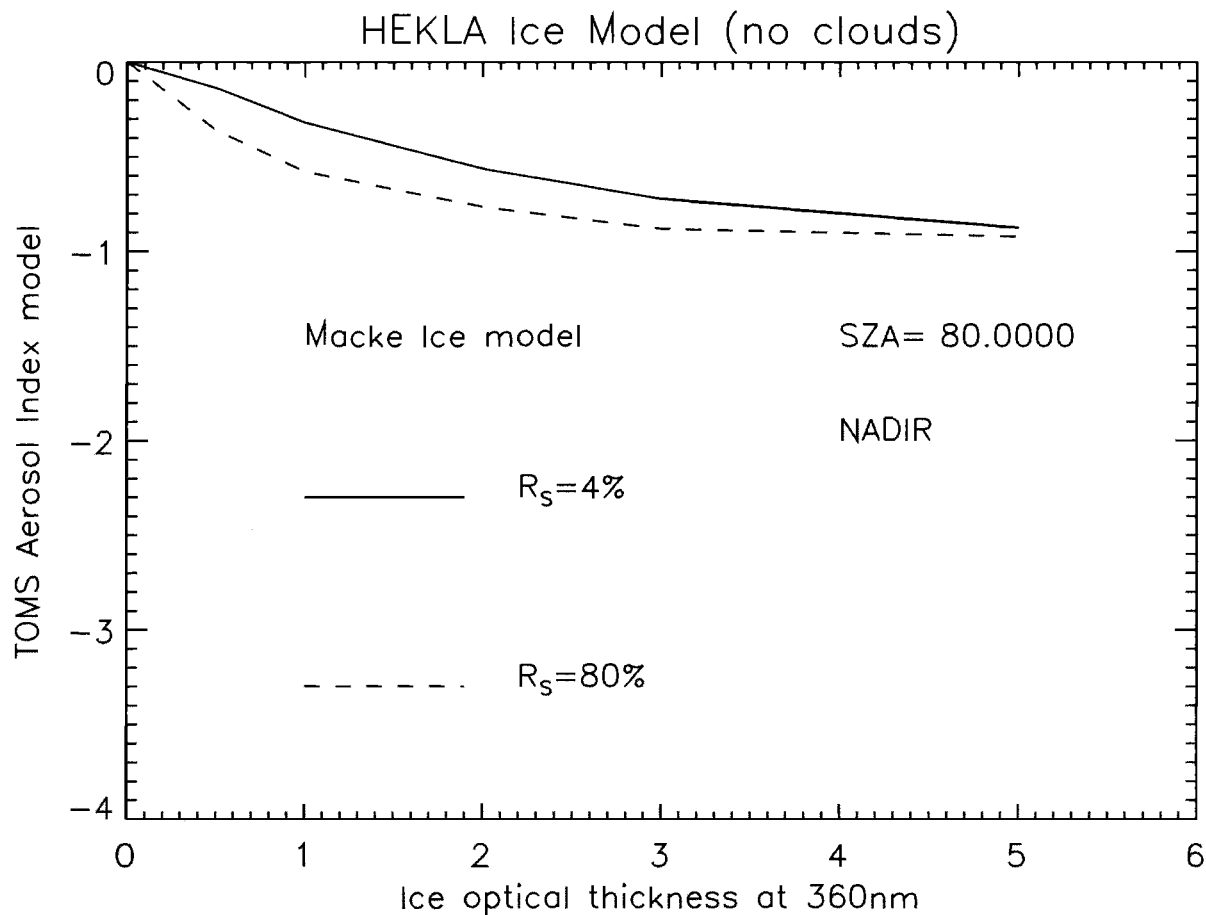
HEKLA Ice Model (no clouds)

Figure 9. TOMS Aerosol Index vs. ice optical thickness for two different surface reflectivity conditions at a high solar zenith angle. No realistic amount of ice can produce the observed negative AI values.

cal miles N of the northernmost predicted position of the volcanic cloud [*Grindle & Burcham, 2002; Pieri et al., 2002*]. It was very close in time to the MODIS images shown in Plates 3c, 3d, Fig. 3, Plate 4d and 5d, and the instruments on this research aircraft collected data which are important for validation. Note that the altitude of the encounter was 11.3 km (37,000 ft.) which is near the top of the volcanic cloud, according to POAM results (see above), thus the aircraft may not have encountered the highest cloud concentrations.

SO$_2$, H$_2$SO$_4$ and aerosol concentrations from the 28 February cloud crossing are plotted in Figure 7. The H$_2$SO$_4$ values are upper limits to the amount in the gas phase. The timescale for each panel is seconds in Universal Time counting from 0:00 hours on 27 February; the day the flight began. The top panel shows Chemical Ionization Mass Spectrometry (CIMS) measurements of SO$_2$ and H$_2$SO$_4$ volume mixing ratios (VMRs). As the aircraft entered the

plume the SO$_2$ concentration increased abruptly from the ambient level of approximately 10 pptv to 1 ppmv, an increase of approximately 5 orders of magnitude. During the 10 minutes that the DC-8 spent in the plume, numerous concentration peaks were encountered with maximum concentrations on the order of 0.5–1 ppmv, with the latter ones lower. Higher frequency, i.e. smaller spatial fluctuations, are also evident, consistent with a non-Gaussian "lumpiness" of the cloud.

SO$_2$ is oxidized in the atmosphere by OH forming H$_2$SO$_4$. H$_2$SO$_4$ then condenses with H$_2$O to form aerosols. Data from the CIMS and aerosol instruments can address the amount of oxidation. The CIMS instrument provides an upper limit to the amount of H$_2$SO$_4$ in the gas phase since aerosols can evaporate in the inlet system. The CIMS H$_2$SO$_4$ data was taken only occasionally during full mass scans of the instrument since ambient H$_2$SO$_4$ concentrations are too low to measure and the encounter with the volcanic

Brightness Temperature
Band 4 - Band 5 = Positive
Band 4 > Band 5

Band 4
Refractive Index
Water* 1.153+0.097i
Ice*   1.091+0.168i

Band 5
Refractive Index
Water* 1.111+0.199i
1.258+0.409i

▲
: Absorption :
: B4 < B5 :

*Hale and Querry (1973)
** Warren et al.. (1983)

Band 4
(10.3 - 11.3 µm)

Band 5
(11.5 - 12.5 µm)

Emitted Thermal Radiation From Underlying Surface

Volcanic Cloud

Brightness Temperature
Band 4 - Band 5 = Negative
Band 4 < Band 5

Band 4
Refractive Index
Andesite***
2.053+0.610i

Band 4
Refractive Index
Andesite**
1.839+0.138i

▲
: Absorption :
: B4 > B5 :

***Pollack et al.. 1973

Band 4
(10.3 - 11.3 µm)

Band 5
(11.5 - 12.5 µm)

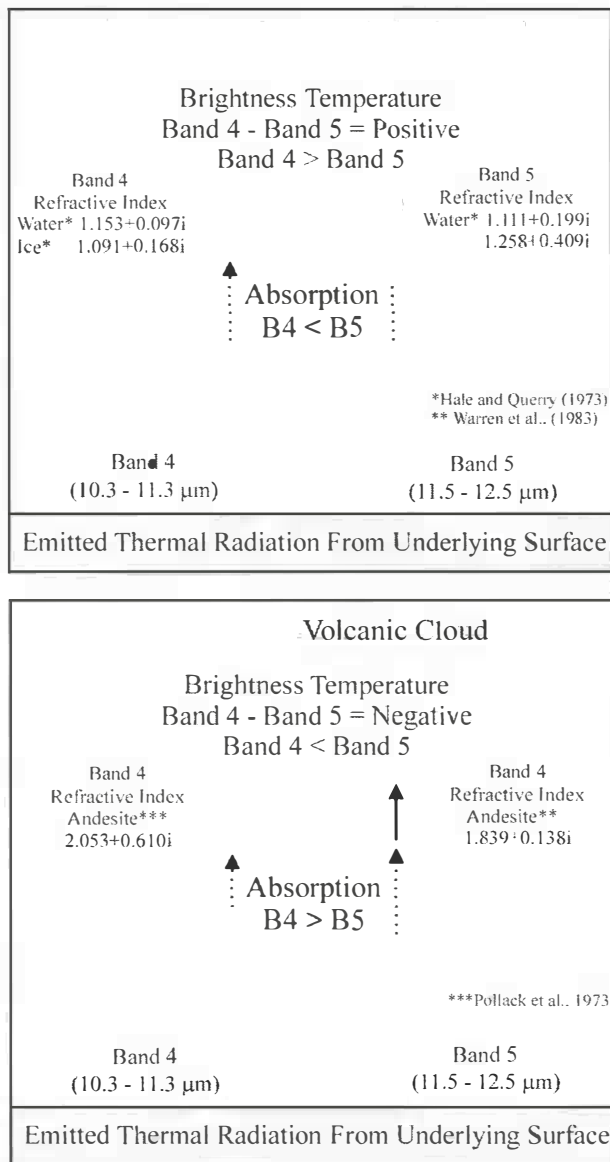Emitted Thermal Radiation From Underlying Surface

Figure 10. Schematic diagram showing how two band thermal IR transmission through meteorological and ash laden volcanic clouds is different. Bands 4 and 5 refer to AVHRR or Geostationary Operational Environmental Satellite (GOES) detectors, the equivalent bands for MODIS are 31 and 32 respectively. In the case of the Hekla volcanic clouds, which have a predominance of ice particles over volcanic ash, the response of the sensors is like a meteorological cloud.

cloud was unexpected. The peak values are on the order of 0.4 ppbv or 0.04% of the SO_2 values, indicating that little or none of the volcanic sulfur is gas phase H_2SO_4.

The bottom panel (Figure 7) shows aerosol number density data from the Langley instrument suite for aerosol particles between 12 and 1000 nm in diameter. The top trace (labeled "volatile plus non-volatile") derives from an unheated inlet line in which all aerosol particles were counted. The bottom trace (non-volatile) comes from the heated inlet in which all volatile components of the aerosol were evaporated. This portion of the measured aerosol concentration is most likely due to volcanic ash particles. A quick glance at the figure immediately shows that most of the particles were volatile. The volatile aerosols are assumed to be made of H_2O and H_2SO_4.

The amount of aerosol H_2SO_4 is derived as follows. The total aerosol volume for particles between 4 and 2000 nm diameter is calculated from the measured size distributions of the aerosol particles. Aerosol volume was converted to the mass of S in the aerosol phase using an average density for the sulfate aerosol particles of 1.68 g/cm^3 and an average bulk composition of 96% H_2SO_4 by weight (the aerosols are dehydrated in the sampling process). This calculation indicates the aerosol H_2SO_4 was 7% of the SO_2 value. This may come from atmospheric oxidation or can be viewed as an upper limit to how much is injected directly from the volcano. Note this value is at least a factor of 175 times the gas phase value. With the cold temperatures and the large surface area it is expected that any H_2SO_4 formed would condense rapidly.

Comparison of Aircraft and Satellite SO_2 and Sulfate Measurements

The concentrations of SO_2 inside the Hekla cloud were 0.5 to 1 ppmv, based on CIMS measurements (Figure 7). The burdens of the same cloud determined across transects similar to the aircraft trajectory had peak values of 100 DU and a mean of about 20 DU for the two IR algorithms. The TOMS peak values were lower (~40 DU), as would be expected from its poorer spatial resolution, but the mean was also near 20 DU. 20 DU would be equivalent to about 1 ppmv if we assume that the cloud is 2.5 km thick, consistent with the POAM results already discussed. We consider this remarkably good agreement given the fact that the aircraft crossed the cloud at an altitude near the upper limit of the cloud. The sulfate mixing ratio estimates obtained from the aircraft data (35–70 ppbv) also agree with the sulfate mixing ratio implied by the aerosol retrieval (Table 2) which is equivalent to 20–75 ppbv.

Notes on Ash and Aircraft Damages

The aircraft engines sustained significant damage from the encounter (they were all replaced), which is likely to reflect abrasive and other effects of volcanic ash [*Grindle*

& Burcham, 2002] and almost certainly corrosion by acid sulfates. We obtained samples of particles in the aircraft engines and air filters to look for ash particles. We found metallic particles and potassic feldspar fragments but no obvious volcanic ash. Another research group [*Pieri et al., 2002*] reported finding some fine ash in the air filters. This observational data is consistent with minor perhaps very fine ash being in the cloud, perhaps acting as ice nuclei, as has been the case in other eruption clouds [*Rose et al., 1995*].

DISCUSSION

We interpret the changes in ice mass in the Hekla volcanic cloud (Figure 4) to be due to the growth of ice, perhaps on ash nuclei, followed by fallout from the lower part of the cloud. The intensity of the explosive phase had strongly declined after 3–4 hours, and after 0500 UT on 27 February larger (diameter ~30 μm) ice particles were being rapidly removed from the volcanic cloud leading to the drop of retrieved ice mass beginning by about 0500 to 0900 UT on 27 February (Figure 4a, Table 3). The size of ice particles we retrieve are too small to fall to the ground in a few hours. Their effective size seems to rapidly decrease together with ice mass, so that this is also consistent with a convective instability in which the volcanic cloud separates into a gas-rich upper part and an ice-rich lower part must have occurred [*Holasek et al., 1996*] and led to fingering convection and enhanced turbulence underneath the cloud and to rapid removal of the ice [*Hoyal et al., 1999*]. Sublimation of sinking ice would liberate SO_2 contained/trapped in ice particles and lead to enhanced column OH. This idea is consistent with observed second day increase in SO_2 (Tables 2 and 4).

Our results give us an opportunity to compare three different algorithms for SO_2 retrieval (Table 2). The masses calculated agree fairly well. TOMS results are limited and cannot be rigorously compared with the IR results: 1. TOMS missed part of the Hekla cloud outside the edge of its scan line and 2. The high latitude and winter season restricted the solar scattering, causing a high background noise. We note some differences in the three algorithms: 1. TOMS produces better results than the IR when the volcanic cloud is above Greenland, which has an unusually cold background for IR., 2. The 7.3 μm IR algorithm, seems to be affected less than the 8.6 μm by the high particle concentrations in the early Hekla cloud. Based on our testing to date we think that the 7.3 μm scheme might be more adversely affected by ice and the 8.6 μm scheme by ash. 3. The two MODIS based algorithms (7.3 μm, 8.6 μm) also deal differently with atmospheric effects. The 7.3 μm method takes advantage of the fact that atmospheric water

vapor beneath the volcanic cloud is emitting IR radiation that is subsequently absorbed by SO_2 in the volcanic cloud, i.e. that it can see little of the tropospheric water vapor column. In contrast the 8.6 μm scheme sees radiation from earth's surface and must consider MODTRAN based calculations of radiative transfer through radiosonde profiles of the whole atmospheric profile. The 7.3 μm retrievals might be more accurate in high, large volcanic clouds while the 8.6 μm will do better in smaller and especially lower clouds particularly if they are ash-poor and/or water/ice rich. There are also some interesting differences, such as the much higher masses of SO_2 which are calculated from the later retrieval on 27 February (Table 2) which are of unknown cause, but possibly could be influenced by ice fallout processes which release SO_2 as suggested above. The TOVS data set (Fig 5) shows a small increase on Feb 27 (day 58) and a larger increase on 29 February (day 60), which is unexplained.

High solar zenith angle geometry cases were modeled to determine the sensitivity of the TOMS Aerosol Index (AI) to sulfate aerosols. Different conditions, such as surface reflectivity and particle size were considered. A radiative transfer model of the Hekla plume, containing small sulfate aerosols, was able to produce a negative AI signature, although not as strong as in the TOMS data.

The model shows sulfate particles smaller than 0.5 μm in radius are needed to produce a large, negative AI (Fig 8). The measured Aerosol Index (AI) is more negative than possible for larger particles. This suggests that very small aerosols were produced within the 1st day of the Hekla cloud residence or erupted with the SO_2. Ash is ruled out because it would produce a positive AI. The remaining differences are under investigation and can be associated with complex background (underlying clouds, ice surfaces, large solar zenith angles) and with the presence of ice particles in the Hekla cloud. According to the model (Fig 9) ice particles alone cannot produce the observed AI anomaly.

Our results pose questions about the relative proportions of ash, ice and gas in explosive eruptions. Ice and volcanic ash have opposing effects on upwelling thermal IR radiation (Fig 10). In other examples of recent eruptions, such as the 3 eruptions of Crater Peak, Mount Spurr, Alaska in 1992 [*Schneider et al., 1995; Rose et al., 2001*] there is an apparent dominance of ash particles as reflected by the remote sensing which features negative BTD of 10 and 11 μm IR data. Hekla's volcanic cloud is quite unlike the Spurr clouds, because it shows negative BTD only briefly and at very high optical depth (see Figure 2). We interpret this difference as being the result of abundant ice—so much ice that any ash that is present has little influence on the remote sensor. Either there are more ice particles or perhaps ice

coats ash particles, having acted as a nucleus for condensed water vapor.

We have observed other examples of ice-rich volcanic clouds: at Rabaul in 1994 [*Rose et al., 1995*] and at Soufriere Hills, Montserrat on 26 December 1997 [*Mayberry et al., 2002*]. There have been many more examples of ash-rich volcanic clouds [*Rose et al., 2000*]. In the cases of Rabaul and Soufriere Hills, it was suggested that much of the H_2O which was in the rising eruption columns came from the ocean, which evaporated extensively from contact with very hot magma. The ocean cannot have contributed to Hekla's eruption, as the volcano is miles inland and far above sea level. There is ice and snow on the volcano and some of this could have melted, but we do not judge this to have been a major source. Magmatic H_2O, which was dissolved in the magma and exsolves during magma ascent normally is released wholly or in part during eruption. In many eruptions such as the Spurr examples discussed above, the amounts of H_2O are insufficient to have produced enough ice to overwhelm the volcanic ash signal in IR sensing. Given these points, what can explain the abundance of ice in the Hekla volcanic cloud?

The mass of fine ash may have been quite limited in the Hekla volcanic cloud. We know that there was an ashfall on land in the first 3–4 hours after the eruption onset, and at least some fine ash was detected by the satellite and in aircraft filters. *Thorarinsson's* [1967] careful study of the 1947–8 Hekla eruption also described evidence for a gas-rich and ash-poor initial explosive phase. Based on the other descriptions of the Hekla activity it appears that Hekla's recent eruptions, although smaller in scale, may have started with similar early gas-rich and later gas-poor explosive phases and then evolved to effusive fissure eruptions. It is possible that degassing of magma at Hekla could have been extensive in the first 3–4 hours of activity, perhaps resulting in the loss of much of the magmatic gas from the magma erupted over the next 9 days. If gas was coming from magma staying in the system after eruption, it could be coming from a much larger volume, as much as 10 km^3 or more. We estimate, using model calculations of column dynamics after *Sparks et al.* [1997, fig 7.23, p. 206] that a 10–11 km high column could arise from about 10 Tg of H_2O at 1200°C erupted in the first hour. The total mass of magma erupted in the 9 days was about 300 Tg (0.11 km^3 dense rock equivalent volume), thus the H_2O proportion needed to degas is equivalent to about 3% of the total mass erupted.

CONCLUSIONS

SO_2 from the February–March 2000 Hekla eruption was detected by TOMS, the HIRS-2/ TOVS sensor and by two different MODIS IR algorithms, and was also measured by a NASA research aircraft. Thus we had an unusual opportunity to compare various methods. Overall the various detectors demonstrate that UV solar scattered data was affected by low sunlight of the polar winter and the IR data was affected by cold subsurfaces, particularly the Greenland icecap. Having multiple methods of SO_2 retrieval is highly advantageous because the methods each have environmental advantages under different conditions.

Hekla's eruption produced a lower stratospheric cloud to 11–12 km asl height, with up to 0.3–0.4 Tg of SO_2, up to 0.008 Tg of sulfate aerosol, >0.1 Tg of ash and >1 Tg of H_2O. The cloud resembled a high cirrus cloud. This cloud drifted north, passing over Greenland then toward Svalbard and then passing Karelia and on to Siberia in a few days. The cloud increased in ice mass throughout the explosive phase for ~10 hours and then declined after that, corresponding to migration of large ice particles to the cloud base and fallout from it after that by a convective instability of the cloud base generating rapidly sinking ice laden plumes, which may have led to ice sublimation and release of trapped SO_2. SO_2 column abundance increased in the second day and then declined after about 24 hours and was nearly undetectable after 3.5 days. With an apparent paucity of ash, the source of the cloud's buoyancy may have come from an early magmatic degassing of H_2O and other gases from magma in an explosive but ash poor phase which preceded an effusive fissure eruption of degassed magma over the ensuing 9 days.

The damage done to the NASA aircraft in spite of the paucity of ash indicates that even very small masses of airborne ash in an old and much diluted volcanic cloud more than 1000 km from its source are hazardous and should be avoided. Our data shows that such clouds can be tracked using IR data, because high cirrus cloud BTD (brightness temperature difference) detection, especially if verified with IR or UV SO_2 detection can track volcanic clouds readily, even though they show no ash signal by IR or UV. It was possible to track the Hekla cloud using AVHRR and MODIS, and new sensors such as SEVIRI (first data expected, October 2003) should have ideal capabilities [e.g. *Watkin & Ringer, 2000*].

MODIS is shown to be a robust IR sensor for volcanic clouds which can readily track the clouds progress in spite of its low ash concentration. As such the MODIS results show that new geostationary sensors which have multiple thermal IR bands, such as SEVIRI and the GOES ABI will be powerful for tracking volcanic clouds.

The Hekla example shows the value of multiple methods to monitor volcanic clouds effectively even when they are ash-poor and to advance understanding of incompletely

understood processes such as the link between fluid dynamical and microphysical processes and atmospheric chemistry modifications. The variability of volcanic clouds means that their detection must use a variety of principles and should consider that they can contain a predominance of ice over ash (or vice versa), and that they can be found in a variety of environmental conditions. The detection of SO_2, ash and ice should all be attempted and this information allows a fuller interpretation. In this case detection of ash was barely possible at all, but the tracking of the cloud using other techniques was straightforward.

REFERENCES

Berk, A., L. S. Bernstein, and D. C. Robertson, *MODTRAN: A Moderate Resolution Model for LOWTRAN 7, AFGL_TR-89-0122,* U. S. Air Force Geophysics Laboratory, Hanscom Air Force Base, MA, 1989.

Bluth, G. J. S., W. I. Rose, I. E. Sprod and A. J. Krueger, Stratospheric loading from explosive volcanic eruptions, *J Geology,* 105: 671-683, 1997.

Cadle, R D and I H Blifford, Hekla eruption clouds, *Nature* 230: 573-574, 1971.

Constantine, E K, G J S Bluth and W I Rose, TOMS and AVHRR sensors applied to drifting volcanic clouds from the August 1991 eruptions of Cerro Hudson, A*GU Monograph 116— Remote Sensing of Active Volcanism,* ed by P Mouginis-Mark, J Crisp and J Fink, pp. 45-64, 2000.

Debrestian, D.J., J.D.Lumpe, E.P.Shettle, R.M.Bevilacqua, J.J.Olivero, J.S.Hornstein, W.Glaccum, D.W.Rusch, & M.D.Fromm, Preliminary Analysis of Southern Hemisphere POAM II Observations of Polar Mesospheric Clouds, *J. Geophys. Res.,* 102, 1971-1981, 1997

Ernst, G G J, J P Davis and R S J Sparks, Bifurcation of volcanic plumes in a crosswind. *Bull Volcanol* 56: 159-169, 1994.

Foster, T C and Hallett Ice crystal orientation in cirrus: Secondary torque on plate crystals in diverging electrical fields, *EOS Trans A G U* 83 Suppl: F 99, 2002.

Frogner P., S R Gislason and N Oskarsson, Fertilizing potential of volcanic ash in ocean surface water, *Geology* 29: 487-490, 2001.

Fromm, MD, R.M.Bevilacqua, J. Hornstein, E. Shettle, K. Hoppel, & J.D. Lumpe, An analysis of POAM II Arctic polar stratospheric cloud observations, 1993-1996, *J. Geophys. Res.,* 104, 24,341-24,357, 1999.

Fromm, M.D., R.M.Bevilacqua, J.D. Lumpe, E.P.Shettle, J.S. Hornstein, S.T. Massie, and K.H. Fricke, Observations of Antarctic Polar Stratospheric Clouds by POAM II in 1994 and 1995, *J. Geophys. Res.,* 102,23,659-23,672, 1997.

Fromm, M., J. Alfred, K. Hoppel, J. Hornstein, R. Bevilacqua, E. Shettle, R. Servranckx, Z. Li, and B. Stocks, Observations of boreal forest fire smoke in the stratosphere by POAM III, SAGE II, and lidar in 1998, *Geophys. Res. Lett.,* 27, 1407-1410, 2000.

Good, M Y, Cover Photo of Hekla eruption, *Geology* 29, no 6, 2001.

Grindle, T J and F. W Burcham, Jr., Even minor ash encounters can cause major damage to aircraft, *ICAO Journal,* 57: 12-30, 2002.

Grönvold, K., G Larsen, P Einarsson, S Thorarinsson and K Saemundsson, The Hekla eruption 1980-81, *Bull Volcanol* 46:349-363 1983.

Gudmundsson, A., N Oskarsson, K Grönvold, K Saemundsson, O Sigurdsson, R Stefansson, S R Gislason, P Einarsson, B Bransdottir, G Larsen, H Johannesson and T Thordarson, The 1991 eruption of Hekla, Iceland. *Bull Volcanol* 54: 238-246, 1992.

Haraldsson, K O, S G Arnason, G Larsen and J Einarsson, The Hekla eruption of 2000: The tephra fall (abstract), *25th Nordic Geological Winter Meeting,* Jan 6-9, 2000; Reykjavik, 2002.

Holasek, R E, A W Woods, and S Self, Experiments on gas-ash separation processes in volcanic umbrella clouds. J Volcanol Geoth. Res 70: 169-181, 1996.

Höskuldsson, A. and R. Ólafsdóttir. Pyroclastic flows formed in the eruption of Hekla 2000. 25th Nordic geological winter meeting, Reykjavik, 86, 2002

Hoyal D, M I Bursik, J F Atkinson, Settling-driven convection: a mechanism of sedimentation from stratified fluids, *J Geophys Res* 104: 7953-7966, 1999.

Hunton, D. E.; Ballentin, J. O.; Borghetti, J. F.; Federico, G. S.; Miller, T. M.; Thorn, W. F.; Viggiano, A. A. Anderson, B. E.; Cofer, W. R., III; McDougal, D. S.; Wey, C. C. Chemical ionization mass spectrometric measurements of SO_2 emissions from jet engines in flight and test chamber operations, *J. Geophys. Res.* 105, 26841-26856 (2000).

Jonsson, H. H. et al., *J. Ocean. Atmos. Technol.* 12, 115-129 (1995)

Krotkov, N A, O Torres, C Seftor, A J Krueger, A Kostinski, W I Rose, G J S Bluth, D J Schneider and S J Shaefer, Comparison of TOMS and AVHRR volcanic ash retrievals from the August 1992 eruption of Mount Spurr, *Geophys Res Lett.,* 26: 455-458, 1999a.

Krotkov, N.A., D.E. Flittner, A.J. Krueger, A. Kostinski, C. Riley and W. Rose, O. Torres, Effect of particle non-sphericity on satellite monitoring of drifting volcanic ash clouds, *JQSRT,* 63, 613-630, 1999b.

Krueger A J, L S Walter, P K Bhartia, C C Schnetzler, N A Krotkov, I Sprod and G J S Bluth, Volcanic sulfur dioxide measurements from the Total Ozone Mapping Spectrometer (TOMS) instruments. *J Geophys Res* 100: 14057-14076, 1995.

Mayberry, G C, W I Rose and G J S Bluth, Dynamics of the Volcanic and Meteorological Clouds Produced by the December 26, 1997 Eruption of Soufrière Hills volcano, Montserrat, W.I., in The Eruption of Soufrière Hills Volcano, Montserrat, 1995-99, ed by T Druitt and P Kokelaar, *Geological Society of London, Memoir* 21: 539-555, 2002.

Miller, T. M.; Ballenthin, J. O.; Meads, R. F.; Hunton, D. E.; Thorn, W. F.; Viggiano, A. A.; Kondo, Y.; Koike, M.; Zhao, Y. Chemical ionization mass spectrometer technique for the measurement of HNO_3 in air traffic corridors in the upper troposphere during the SONEX campaign *J. Geophys. Res.* 105, 3701-3707, 2000.

Newman, P. A. SAGE III Ozone Loss and Validation Experiment, SOLVE, A NASA DC-8, ER-2 and High Altitude Balloon Mission, http://cloud1.arc.nasa.gov/solve/; 1999.

Ólafsdóttir, R., A. Höskuldsson and K. Grönvold. The evolution of the lava flow from Hekla eruption 2000. *25th Nordic geological winter meeting,* Reykjavik, 149, 2002.

Oskarsson, N The interaction between volcanic gases and tephra: Fluorine adhering to tephra of the 1970 Hekla eruption, *J Volcanol Geoth Res* 8: 251-266, 1980.

Pieri, D., C Ma, J J Simpson, G L Hufford, T Grindle and C Grove, Analysis of in situ airborne volcanic ash from the February 2000 eruption of Hekla, *Geophys Res Lett,* 29, no 16 10.1029/2001GL013688, 2002.

Prata, A. J., Observations of volcanic ash clouds using AVHRR-2 radiances. *Int. J. Remote Sensing,* 10(4-5), 751-761, 1989a.

Prata, A. J., Radiative transfer calculations for volcanic ash clouds, *Geophys. Res. Lett.,* 16(11), 1293-1296, 1989b.

Prata, A. J., S Self, W I Rose, D M O'Brien, Global, long term sulphur dioxide measurements from TOVS data: A new tool for studying explosive volcanism and climate, EOS Trans *A G U Abstracts with Program, Spring 2002 meeting,* 2002.

Realmuto, VJ, AJ Sutton and T Elias, Multispectral thermal infrared mapping of sulfur dioxide plumes - a case study from the East Rift Zone of Kilauea volcano, Hawaii, *Jour. Geophys. Res.,* 102: 15057-15072, 1997.

Rogers R R and M K Yau, *A short course in cloud physics,* Pergamon 293 pp, 1989.

Rose, W I and G C Mayberry, Use of GOES thermal infrared imagery for eruption scale measurements, Soufrière Hills, Montserrat, *Geophys Res Lett,* 27: 3097-3100, 2000.

Rose, W I, G J S Bluth and G G J Ernst, Integrating retrievals of volcanic cloud characteristics from satellite remote sensors—a summary, *Philosophical Transactions of Royal Society, Series A,* vol. 358, pp. 1585-1606, 2000.

Rose, W. I., D. J. Delene, D. J. Schneider, G. J. S. Bluth, A. J. Krueger, I. Sprod, C. McKee, H. L. Davies and G. G. J. Ernst, Ice in the 1994 Rabaul eruption cloud: implications for volcano hazard and atmospheric effects, *Nature,* 375: 477-479, 1995.

Rose, W I, G J S Bluth, D J Schneider, G G J Ernst, C M Riley and R G McGimsey, Observations of 1992 Crater Peak/Spurr Volcanic Clouds in their first few days of atmospheric residence, *J Geology,* 109: 677-694, 2001.

Schneider, D. J., W. I. Rose and L. Kelley, Tracking of 1992 eruption clouds from Crater Peak vent of Mount Spurr volcano, Alaska, using AVHRR, in the 1992 eruptions of Crater Peak vent, Mount Spurr Volcano, Alaska, Keith, T. E. C. (Ed.), *U.S. Geological Survey Bulletin,* 2139, 220 p., 1995.

Schneider, D. J., W. I. Rose, L. R. Coke, G. J. S. Bluth, I. Sprod and A. J. Krueger, Early Evolution of a stratospheric volcanic erup-

tion cloud as observed with TOMS and AVHRR, *J. Geophys. Res.,* 104; 4037-4050, 1999.

Seftor, C. J., N. C. Hsu, J. R. Herman, P. K. Bhartia, O. Torres, W. I. Rose, D. J. Schneider and N. Krotkov, Detection of volcanic ash clouds from Nimbus-7/TOMS, *J. Geophys. Res.,* 102: 16749-16760, 1997.

Sigmarsson, O; M Condomines and S Fourcade, A detailed Th, Sr and O isotope study of Hekla: differentiation processes in an Icelandic Volcano, *Contr Mineral Petrol* 112: 20-34, 1992.

Smith, W. L., Woolf, H. M, Hayden, C. M., Wark, D., and McMillin, L. M., The TIROS-N operational vertical sounder, *Bull. Amer. Meteorol. Soc.,* 60, 1177-1187, 1979.

Sparks R S JM I Bursik, S N Carey, J S Gilbert, L S Glaze, H Sigurdsson and A W Woods, *Volcanic Plumes,* J Wiley & Sons, 574 pp, 1997.

Talbot, R. W.; Dibb, J. E.; Scheuer, E. M.; Kondo, Y.; Koike, M.; Singh, H. B.; Salas, L. B.; Fukui, Y.; Ballenthin, J. O.; Meads, R. F.; Miller, T. M.; Hunton, D. E.; Viggiano, A. A.; Blake, D. R.; Blake, N. J.; Atlas, E.; Flocke, F.; Jacobs, D. J.; Jaegle, L. Reactive Nitrogen Budget During the NASA SONEX Mission *Geophys. Res. Lett.* 26, 3057-3060 (1999).

Thorarinsson, S, *Surtsey: a new island in the North Atlantic.* Reyjavik Almenna Bokafelagid, 1966.

Thorarinsson, S, *The eruption of Hekla 1947-1948,* Visindafelag Islendinga, Reyjavik 1967.

Thorarinsson, S., and G E Sigvaldason, The Hekla eruption of 1970, *Bull Volcanol* 36: 269-288, 1972.

Viggiano, A. A. D. E. Hunton, Airborne Mass Spectrometers: Four Decades of Atmospheric and Space Research at the Air Force Research Laboratory, *J. Mass Spectrom.* 34, 1107-1129 (1999).

Wallace, J M and P V Hobbs, *Atmospheric Science: An introductory Survey,* Academic Press, 1977.

Watkin, S and M A Ringer, Investigation into the use of SEVIRI imagery for the automatic detection of volcanic ash clouds. UK Met Office *NWP Forecasting Res Tech Rep No* 297, 2000.

Watson, I. M., V. J. Realmuto, W. I. Rose, A. J. Prata, G. J. S. Bluth, Y. Gu and T. Yu, Thermal infrared Remote Sensing of Volcanic Emissions using the Moderate Resolution Imaging Spectrometer (MODIS), *J. Volcanol Geoth. Res.* in press.

Wen, S and W I Rose, Retrieval of Particle sizes and masses in volcanic clouds using AVHRR bands 4 and 5, *J. Geophys. Res.,* 99:5421-5431, 1994.

Yu, T and W I Rose, Retrieval of sulfate and silicate ash masses in young (1-4 days old) eruption clouds using multiband infrared HIRS/2 data, *AGU Monograph 116 —Remote Sensing of Active Volcanism,* ed by P Mouginis-Mark, J Crisp and J Fink, pp. 87-100, 2000.

William I. Rose Geological Engineering & Sciences, Michigan Technological University, Houghton, MI 49931 USA raman@mtu.edu

Yingxin Gu Geological Engineering & Sciences, Michigan Technological University, Houghton, MI 49931 USA yigu@mtu.edu

I. Matthew Watson Geological Engineering & Sciences, Michigan Technological University, Houghton, MI 49931 USA watson@mtu.edu

Gregg J. S. Bluth Geological Engineering & Sciences, Michigan Technological University, Houghton, MI 49931 USA gbluth@mtu.edu

A. J. Prata CSIRO, Atmospheric Research, Aspendale, Victoria, Australia Fred.Prata@csiro.au

Arlin J. Krueger JCET/UMBC 1000 Hilltop Circle Baltimore, MD 21250

Nikolai A. Krotkov krotkov@chescat.gsfc.nasa.gov

Simon Carn JCET/UMBC 1000 Hilltop Circle Baltimore, MD 21250 scarn@umbc.edu

Michael D. Fromm Computational Physics, Inc; 8001 Braddock Road Suite 210 Springfield, VA 22151 mike.fromm@nrl.navy.mil

Donald E. Hunton Air Force Research Laboratory, Space Vehicles Directorate, Hanscom AFB, MA Donald.Hunton@hanscom.af.mil

Gerald G. J. Ernst, CEGF, Earth Sciences, University of Bristol, UK, gerald.j.ernst@bristol.ac.uk

A. A. Viggiano, Air Force Research Laboratory, Space Vehicles Directorate, Hanscom AFB, MA 01731 USA Albert.Viggiano@hanscom.af.mil

T. M. Miller, Air Force Research Laboratory, Space Vehicles Directorate, Hanscom AFB, MA 01731 USA Thomas.Miller@hanscom.af.mil

J. O. Ballenthin, Air Force Research Laboratory, Space Vehicles Directorate, Hanscom AFB, MA 01731 USA balleuthin@plh.af.mil

J. M. Reeves, Engineering Department, University of Denver, Denver CO 80208, jreeves@du.edu

J. C. Wilson, Engineering Department, University of Denver, Denver CO 80208, jwilson@du.edu

B. E. Anderson, NASA Langley Research Center, Hampton, VA b.e.anderson@larc.nasa.gov

D. E. Flittner, Atmospheric Sciences, University of Arizona, Tucson, AZ 85721 flittner@atmo.arizona.edu

Real-Time AVHRR Thermal Monitoring and Ash Detection: The Case of Colima Volcano (Mexico)

Ignacio Galindo and [2]Tonatiuh Domínguez

Centro Universitario de Investigaciones en Ciencias del Ambiente and [2]Observatorio Vulcanológico, Universidad de Colima. Colima, Mexico

In this report we examine the application of the Advanced Very High Resolution Radiometer (AVHRR) data for real-time surveillance of volcanic thermal phenomena and eruption plumes. The 14 active volcanoes of Mexico are monitored in real-time, additionally a further 18 volcanoes across Central America. This paper concentrates on the thermal monitoring and ash plume detection at Volcán de Colima, considered one of Mexico's most active volcanoes. The results reported here were selected from 296 nocturnal satellite passes acquired during 18:00 and 8:00 hours (local time). Ash clouds were detected in forty-seven (16%) passes. Frequent thermal anomalies were observed in sequential satellite passes together with ash emission. These were correlated with explosion-related waveforms apparent in seismic data. Two time periods are identified: the first period (March to May 2002) was characterized by very strong thermal anomalies with thermal pulses lasting 5 to 7 days. These anomalies were associated with incandescent pyroclastic and lava flows on the flanks of the volcano. During the second period (June to August 2002) the thermal anomalies had a much lower magnitude, with minor ash emission observed only on 19 July. During the middle of August 2002 a slight increase in the magnitude of the thermal anomalies was observed, with ash emission only on 21 August. Although there were no observations of ash fall in the city of Colima, or damage to human health, infrastructure or economic activities during this period, such real-time satellite monitoring may prove to be a very useful tool for volcano surveillance.

1. INTRODUCTION

There is no doubt that in a more crowded world as it is observed particularly in the emergent countries located along the well-known circum-Pacific "Ring of fire", the potential risk from any volcanic eruption increases.

Fortunately, rapid developments in remote sensing science in recent years, across the entire electromagnetic spec-

trum, has vastly expanded, the monitoring capabilities for volcanoes [*Dean* et al., 2002; *Francis and Rothery*, 2000; *Francis* et al., 1996; *Harris* et al, 2000, 2002; *Oppenheimer*, 1998; *Sparks* et al., 1997]. The synoptic coverage of meteorological satellites and the relative low cost (see Table 1) of satellite ground receiving stations [*Harris* et al., 1977] provides a unique opportunity even for emergent countries for monitoring active volcanoes. The Advanced Very High Resolution Radiometer (AVHRR) flown on board the National Oceanic and Atmospheric Administration (NOAA) satellites provides multispectral data that provide (1) high temporal resolution, (2) wavebands suitable for hot spot detection, and (3) data which are directly available to the

Table 1. Costs of a high resolution picture transmission station (HRPT)

A. Initial investment	$34,822
Antenna, controller, down converter One Work Station One PC for parallel processing	
B. Monthly operational costs	$5,100
Personnel	$4,600
Materials	$500
Total	$39,922

user [*Harris* et al, 1997]. Using such data, heat sources, such as fires, lavas, lava lakes and lava flows can be detected and measured [e.g. *Galindo and Domínguez*, 2002; *Galindo* et al., 2003; *Harris* et al., 1995a, 1997; *Higgins and Harris*, 1997; *Oppenheimer,* 1993; *Oppenheimer* et al. 1993; *Pereira and Setzer* 1993; *Schneider and Rose*, 1995; *Rothery*, 1992; *Rothery* et al. 1988; *Wooster*, 2001; *Wooster and Rothery*, 1997; *Wooster and Kaneko*, 1998; *Wooster* et al. 2000; *Wright* et al. 2002]. The most important feature for thermal observations of volcanic hotspots made with satellites is that shortwave and mid-infrared sensors respond strongly to thermal emission from surfaces at magmatic temperatures even when those surfaces occupy a very small fraction of the sensor's instantaneous field of view (IFOV) [*Harris* et al. 1997; *Oppenheimer*, 1998].

Real-time satellite volcano monitoring can contribute to civil protection, research regarding the potential risks of volcano reactivation, or for tracking the development of an on-going eruption. In addition space-based monitoring is particularly applicable and relevant to volcanoes where traditional monitoring methods are not available or not deployed. This may be the result of inaccessibility or lack of adequate and consistent funding. [*Harris* et al. 1995, 1996; *Oppenheimer*, 1998]. Examples of cases where satellite-based data have been used in an operational monitoring role include the Alaska Volcano Observatory, where AVHRR, Geostationary Operational Environmental Satellites (GOES) and the Geostationary Meteorological Satellite (GMS) data are used to routinely monitor thermal features and ash plume detection several times a day at over 100 active volcanoes across the North Pacific region. This region includes Alaska, the Kamchatka Peninsula and the northern Kuril Islands [*Dean* et al. 2002]. In addition, the

University of Hawaii also performs real-time GOES satellite monitoring of volcanic hot spots of the Pacific region of North as well as North, Central and South America, and their results are provided via the Internet [*Harris* et al. 2000, 2002]. In Asia and Australia, the Japanese Meteorological Institute and the Australian Bureau of Meteorology routinely use AVHRR for ash tracking, and the use of satellite-data for ash tracking and communications to the Volcanology Ash Advisory Center (VAAC).

In the case of Mexico, systematic ground-based monitoring is in operation at Popocatépetl by the Centro Nacional de Prevención de Desastres (CENAPRED) and the Colima Volcano by the Universidad de Colima. However, 12 other active Mexican volcanoes are not regularly monitored. In Central America there are at least 18 active volcanoes in the same situation. Thus using our NOAA satellite ground receiving station, and methods published in the literature [e,g, *Rothery*, 1992; *Langaas,* 1993; *Pereira and Setzer* 1993; *Harris* et al., 1995b; *Prata* 1989; *Holasek and Rose*, 1991] we have improved multispectral methods to allow near real-time thermal monitoring and ash detection of all these volcanoes (Figure 1). Popocatépetl and Colima's volcanoes are at present the most active volcanoes in Mexico. Continuous thermal monitoring and plume detection are required due to the large population around Popocatépetl. In addition both volcanoes are located within the flight paths of commercial jets [*Galindo*, 1996; *Galindo and Domínguez*, 2002; *Galindo* et al. 1998, 1999; *Zobin* et al. 2002a]. As a result, daily reports on thermal activity and ash emission are delivered by email to the Mexican Civil Protection and Civil Aviation Authorities and the Volcanic Ash Advisory Center (VAAC) in Washington, D.C.

Actually there is an interesting research line that consists of the use of satellite (AVHRR or GOES) data together with ancillary geophysical data: seismic data and AVHRR time series have been reported both for the 1996 Pavlov eruption [*Roach* et al. 2001] and Colima's eruption [*Galindo and Domínguez*, 2002]. Whereas statistical analyses/correlations have been carried out between gas, RSAM and GOES time series for the Popocatépetl process [*Wright* et al, 2002]. In this report AVHRR time series alongside seismic data are used to analyze aspects of the present activity of Volcán de Colima.

The purpose of this paper is to present one methodology that we apply using AVHRR multispectral data in order to achieve near real-time volcano monitoring. The results provide basic and complementary information related to the recent reactivation of Volcán de Colima (Mexico) during the period March to August, 2002.
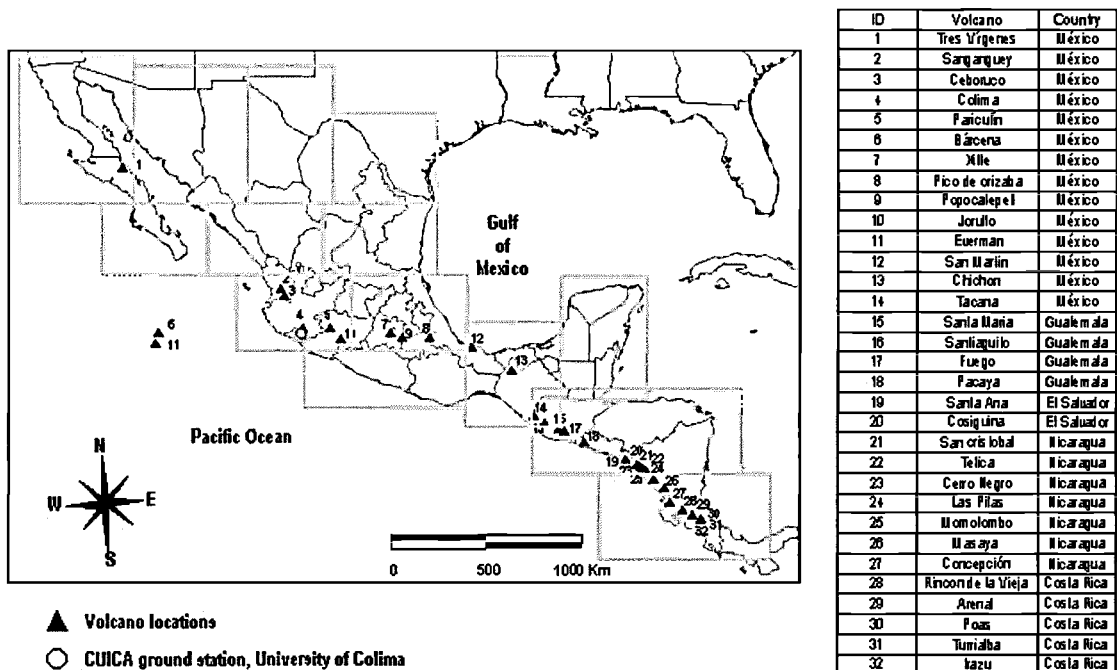
ID	Volcano	Country
1	Tres Vírgenes	México
2	Sanguanguey	México
3	Ceboruco	México
4	Colima	México
5	Paricutín	México
6	Bárcena	México
7	Xitle	México
8	Pico de orizaba	México
9	Popocalepel	México
10	Jorullo	México
11	Everman	México
12	San Martín	México
13	Chichon	México
14	Tacana	México
15	Santa María	Guatemala
16	Santiaguito	Guatemala
17	Fuego	Guatemala
18	Pacaya	Guatemala
19	Santa Ana	El Salvador
20	Cosiguina	El Salvador
21	San cristóbal	Nicaragua
22	Telica	Nicaragua
23	Cerro Negro	Nicaragua
24	Las Pilas	Nicaragua
25	Momolombo	Nicaragua
26	Masaya	Nicaragua
27	Concepción	Nicaragua
28	Rincon de la Vieja	Costa Rica
29	Arenal	Costa Rica
30	Poas	Costa Rica
31	Turrialba	Costa Rica
32	Irazu	Costa Rica

Figure 1. Mexican and Central American active volcanoes that are monitored in real-time using AVHRR by CUICA-Universidad de Colima, Mexico.

1.1. Colima Volcano

Volcán de Colima (19.51°N, 103.61°W, 3,855 m, Figure 2) is one of the most active volcanoes in Mexico [De la Cruz-Reyna, 1993; Luhr and Carmichael, 1990; Medina, 1983]. Colima Volcano is the youngest and the only currently active andesitic stratovolcano of a large Quaternary volcanic complex located in the western portion of the Trans-Mexican Volcanic Belt. Historical activity has been documented since 1560 [De la Cruz-Reyna, 1993], where more than 25 eruptions have been reported in the last 420 years. These have included a wide spectrum of eruption styles, from small phreatic explosions to catastrophic St. Helens type debris avalanches; major eruptions occurred in 1585, 1606, 1622, 1818, 1890, and 1913. The most recent Plinian eruption of 1913 produced a crater approximately 500 m deep which was subsequently filled with volcanic products.

The recent activity of Colima volcano can be traced back to the end of 1997, when AVHRR observations of the summit region showed a gradual thermal re-activation during which peaks in the thermal time series were concurrent with seismic increases, ash emissions and seismotectonic deformation [Galindo and Dominguez, 2002; Galindo et al. 1999; Navarro-Ochoa et al. 2002; Zobin et al. 2002b]. This

culminated in an explosive event and the onset of effusive activity during November 19, 1998. Due to cloud cover NOAA satellite monitoring showed neither thermal anomalies nor ash emission on November 18 and 19, 1998. However, a hot spot was observed in GOES data, on November 19 [Harris et al. 2000]. On November 20, a new dome appeared and subsequently filled the crater in about 24 hours [Navarro-Ochoa et al. 2002]. Within the first 9 hours of lava effusion, the strong thermal anomalies were apparent in AVHRR data, revealing brightness temperatures of 42.3 °C against an ambient temperature of 5.2 °C [Galindo and Dominguez, 2002].

Ash emissions from the summit and from the lava flow continued until June, 1999. This was then followed by a second phase of activity during the period November 1999 to June 2000. For this episode, GOES imagery was also applied for observation of the eruption process [Harris et al. 2000], where we found a close agreement between trends apparent in GOES imagery, the AVHRR thermal data and variations in activity.

On February 10, 1999, all stations of the seismic network recorded an explosion at the summit. The explosion formed a crater of approximately 140 m in diameter and 50 m in depth [Smithsonian Institution, 1999]. Two hours after the explosion, the largest ash emission of the eruption was
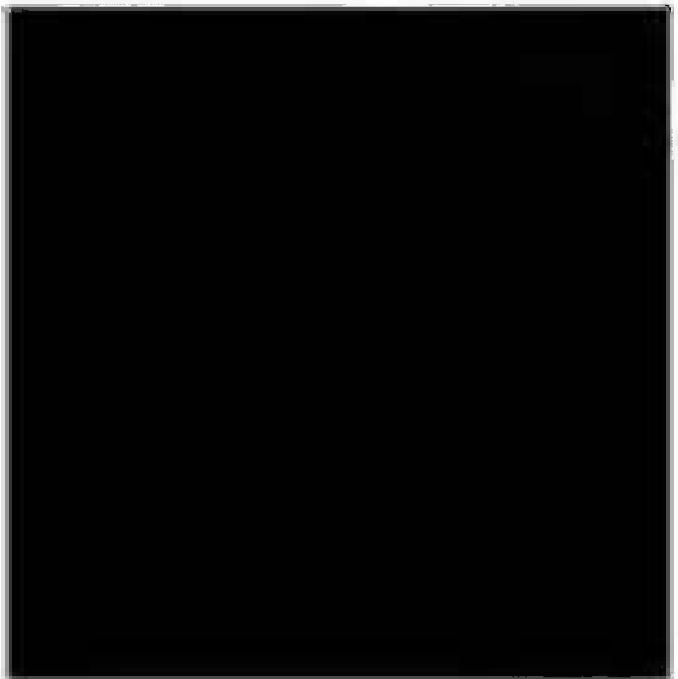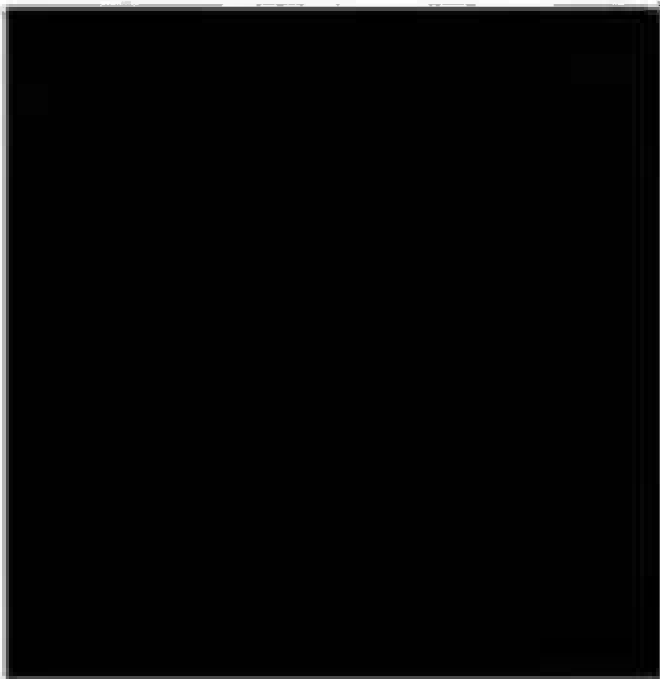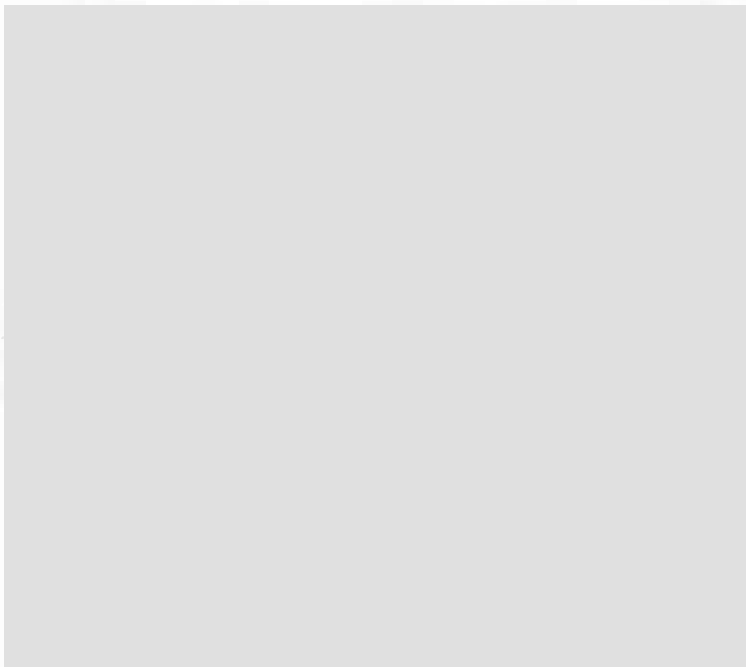
ods of continuous tremor ranged from a few minutes to ten hours in duration. Low-magnitude explosions began on 25 April and in many cases these were accompanied by intervals of volcanic tremor. The numerous, but very small-amplitude tremor and explosive events occurred simultaneously and accompanied continuous records of rockfalls and pyroclastic flows [*Smithsonian Institution*, 2002b]. On 21 June 2002, three lava flows proceeding down the SW flank were first noted; the mean rate of lava emission was very low ≈ 0.1 m^3/s [*Smithsonian Institution*, 2002c].

On 6 March 2002 real-time volcano satellite monitoring was reinitiated when a new HRPT station was installed. In what follows, we shall concentrate on the main findings obtained particularly from March to August 2002.

2. DATA AND METHODS

2.1 Data

2.1.1. AVHRR multispectral images.
The total number of nocturnal (18:00 to 8:00 hours local time) NOAA satellite AVHRR images received between March to August 2002 at our HRPT ground station was 1,052. These images were distributed as follows: 28% useful (cloudless), 23% overcast, 41% oblique view and 8% noisy. Therefore, 296 cloudless passes from the NOAA -12, -14, -15, and -16 satellites were used for volcano thermal monitoring and ash plume detection. The NOAA-14 transmitter was turned off in mid-August 2002 (NOAA, web page) In 17% of the 296 cloudless passes ash clouds were detected from the dome and also occasionally from the lava flows on the flanks of the volcano. Ash emission was detected in 14, 32, and 10 satellite passes during March, April, and May, respectively. In June, July and August, ash emission was detected only once each month.

Between March and August two well-defined climatic seasons occur in the region, namely the dry season (March, April and the first three weeks of May) and the wet season (June to August). During March and April (the driest months of the year) air transparency is good and cloudless skies are experienced most of the time. Cloudy skies begin to occur during May, reaching a maximum cloud cover in June. Therefore, the best satellite determinations are obtained during the dry season. March and April have 84 and 85% of nocturnal images with cloud free skies whereas June, July and August have an average of 30% cloud free images (Figure 3).

2.1.2. Seismic records.
The Colima seismic network (RESCO) has been monitoring seismic activity at the volcano since 1989 and consists of 13 telemetered seismic stations. Twelve of these stations consist of one short period
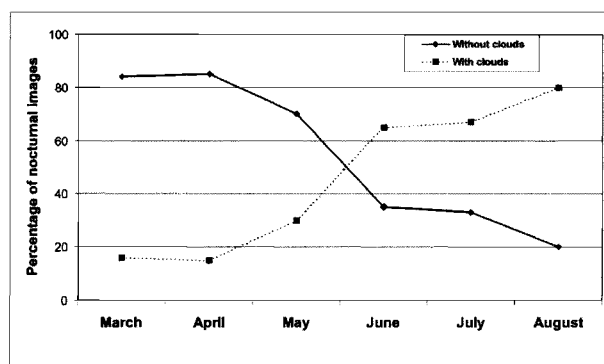

Figure 3. Number of satellite passes showing the proportion of cloudless/ clouds from March to August, 2002.

(1 sec) vertical seismometer, and one consists of a broadband sensor located 6.5 km south from the summit (EBMG). Four 1-sec stations are located on and around the volcano. One station (Soma, EZV4) is located within the caldera of the paleo-Fuego volcano and three are located around the main volcanic edifice (Yerbabuena, EZV6; Fresnal, EZV5; and Nevado, EZV3; Figure 2). The rest of the RESCO stations are deployed in different parts of the State of Colima.

For this study we used the seismic data to extract the locations of volcanic earthquakes, as well as to count the seismic events caused by small explosions and rockfalls. In addition we tracked the number of hours of continuous tremor using the broadband seismic data.

2.2. Methods

Our thermal monitoring method is based on previous work by, for example *Harris* et al. (1995a,b), *Higgins and Harris* (1997), and *Holasek and Rose* (1991), where real-time volcano monitoring uses all of the AVHRR channels 1 (0.58–0.68 μm), 2 (0.725–1.10 μm), 3 (3.55–3.93 μm), 4 (10.3–11.3 μm) and 5 (11.5–12.5 μm). Channels -1 and -2 are located in the visible and near-infrared spectral regions, as such they are used only by day for identification of plumes and topographical features. Thermal monitoring uses data from channels -3 and -4, and ash detection uses channels -4 and -5 [*Galindo and Dominguez*, 2002; *Dehn* et al., 2000; *Harris* et al. (1995 a,b), *Higgins and Harris*, 1997; *Holasek and Rose*, 1991; *Rothery*, 1992; *Langaas*, 1993; *Pereira and Setzer* 1993; *Prata* 1989; *Roach* et al., 2001; *Schneider* et al., 1995].

2.2.1. Calibration.
For AVHRR thermal channels there is a linear relationship between pixel digital numbers (DN) and satellite radiance [*Kidwell*, 1995].

$$R_i = S_i DN + I_i \qquad (1)$$

Where R_i, S_i and I_i, are radiance, slope and intercept in channel i.

Because the Planck radiation distribution law $B(\nu,T)$ is a function of two variables, namely the frequency (ν) and temperature (T), radiance can be expressed as

$$R_i = c_1 \nu^3 / [\exp(c_2 \nu / T_i) - 1] \qquad (2)$$

Inverting equation (2) allows us to obtain brightness temperature at channel-i from:

$$T_i = c_2 \nu / \ln (1 + c_1 \nu^3 / R_i) \qquad (3)$$

In which c_1 and c_2 are universal constants; 1.1910659×10^{-5} mWm^{-2} sr cm^{-4} and 1.4838833 cm K, respectively. Here ν is taken as the central wavenumber of the channel filter where the central wavenumbers for the AVHRR thermal channels differ from instrument to instrument and are given by *Kidwell* (1995) and *Wooster, Richards and Kidwell* (1995). After the geometrical rectification is applied, two data sets are generated, namely radiance and temperature images (Figure 3).

Due to the fact that the instrumental responses of the photoconductive detectors of AVHRR channels 4 and 5 are not linear, errors as large as 2 °C can be produced [Weinreb et al., 1990; Brown et al., 1993]. The National Environmental Satellite, Data and Information Service (NESDIS) supplies an alternate method of handling the non-linearity, which can be applied to radiances instead of brightness temperatures. Then to compute the corrected radiance the following quadratic equation can be used:

$$R_C = A + B R_L + C R_L^2, \qquad (4)$$

Where A,B and C are experimental coefficients given for each satellite after NOAA-13 [Kidwell, 1995].

2.2.2. Sectorization of Mexico and Central America.

A general inspection of the full image permits the operator to visualize the main synoptic features of the region and to identify cloudy regions. Then to minimize processing, the whole image is divided into 15 sectors in a UTM projection. Next, radiance and brightness temperature images are generated for each sector using the split window two-band technique.

2.2.3. Dynamic temperature thresholds.

Hot pixel detection methods either for fire or volcanic heated surfaces are based on dynamic temperature thresholds: *Kaufman* et al

(1990) proposed temperature threshold conditions to determine if a pixel is classified as a fire or not. For volcanoes, *Harris* et al (1995b) proposed an automated algorithm capable of distinguishing between solar heated and volcanic thermal anomalies. The algorithm is based in the fact that channel 3 coincides with the peak spectral exitance from blackbodies at ≈ 500 °C and channel 4 with that of blackbodies at ≈ 0 °C. The above statement means that while channel 3 has greater sensitivity for sub-pixel hotspots, channel 4 sensitivity is closer to ambient temperature. Using the thermal difference $T_3 - T_4 = \Delta T_{34}$, for the case of Etna, *Harris* et al (1995) found $\Delta T_{34} > 10$ °C for unsaturated pixels containing active lava. We have made a linear correlation between the thermal difference between the highest point at the dome, $\Delta T_{34} = T_3 - T_4$ with the thermal difference $(T_3 - T_{3r})$, T_{3r} is channel-3 temperature at Volcancito which is located at the northeast flank, 350 m below the crater. This reference point was chosen because it is not subject to magmatic heat flow and thus is representative of ambient temperature. There is a strong correlation with a regression coefficient $r^2 = 0.8908$ (see Figure 6). Therefore, in agreement with *Harris* et al, (1995b), the thermal difference ΔT_{34} is a more stable signal rather than to choose a reference point such as Volcancito, furthermore it is comparable with thermal determinations performed on other volcanoes. In any case, this comparison shows the validity of taking T_4 as the ambient temperature.

Actually there are more sophisticated and robust algorithms to detect and extract the pixel volcanic integrated signal [*Dehn* et al., 2000; *Harris and Thornber,* 1999; *Harris* et al., 2001; *Wright* et al., 2002b] however, as it is shown here, our method closely follows the dynamic temperature threshold method given by *Harris* et al. (1995b).

In what follows all results will use the AVHRR thermal difference $T_{3i} - T_{4i} = \Delta T_{3-4}$, where i stands for either the dome or the flanks of the volcano (W, NW, N, NE, E, SE, S, SW), ΔT_{3-4} represents the integrated brightness temperatures for each of the volcano sections. For each satellite pass a data base is constructed, which contains date, satellite identification, measured temperatures T_{3i}, T_{4i}, effective brightness temperatures ΔT_{34}, and notes (thin clouds veil, dubious, etc.). The detection limits of the thermal difference ΔT_{34} is defined by the point at which the pixels are saturated, i.e., when $T_3 \geq 50$ °C for data from NOAA-14 and NOAA-15 and $T_3 \geq 60$ °C for data from NOAA-16 satellites. Saturation noisy pixels are sometimes observed for certain types of cloud covers.

2.2.4. Ash clouds detection – thermal band difference method.

Weather satellite data have been used by many

investigators to observe ash clouds [*Hanstrum and Watson,* 1983; *Robock and Matson,* 1983; *Matson,* 1984; *Sawada,* 1987; *Prata* 1989; *Holasek and Rose,* 1991; *Schneider and Rose,* 1995; *Galindo,* 1996; *Galindo and Dominguez,* 2002]. Ash cloud detection methods using thermal infrared sensors are based on the fact that all minerals have characteristic molecular vibration bands (reststrahlen bands) in both reflection and emission spectra in the infrared from about 4 to 25 μm [*Lyon,* 1963; *Hovis and Callahan,* 1966; *Hunt and Salisbury,* 1974]. The AVHRR has two channels in the vicinity of the SiO2 reststrahlen bands. Channels 4 and 5 cover the broad 8.5 to 12 μm peak for fresh basalt and other volcanic rocks [*Holasek and Rose,* 1991]. Following *Hanstrum and Watson,* (1983) *Robock and Matson* (1983), *Matson* (1984), *Sawada* (1987), *Prata* (1989), *Holasek and Rose* (1991), *Schneider and Rose* (1995), *Galindo* (1996), *Galindo and Dominguez* (2002), the split window two-band technique is based on the brightness temperature difference of channels 4 and 5. The difference of brightness temperatures $\Delta T_{4-5} < 0$ °C identifies ash emission and/or ash clouds [*Prata,* 1989], while meteorological clouds generally have $\Delta T_{4-5} > 0$ °C [*Yamanouchi,* et al. 1987]. This technique has been used for routine, near-real-time, operational monitoring at the Alaska Volcano Observatory for at least 10 years [*Dean et al.,* 1998; 2002]. We started in March 1996 [*Galindo,* 1996] to use of the split window two-band technique in near-real-time, when lava extrusion began during the first phase of the reactivation of Popocatépetl volcano [*Wright et al.* 2002a].

To estimate the altitude of the ash cloud we use the following method [*Sawada,* 1994]: the method uses radiosonde data from the Manzanillo Meteorological Observatory which is located about 100 km from the volcano. We use this approach whenever radiosonde data acquisition times coincide with satellite passes (± 1.5 h). This method assumes that the top of an ash cloud under the tropopause exhibits the coldest temperature and the surface temperature at high altitude (the summit) coincides with the ambient temperature. Therefore, the height of the top of an ash cloud can be estimated using the air temperature profile from radiosonde data. Once the height of the ash cloud has been estimated, we determine the wind field for the same altitude and use this to predict the drift direction of the ash cloud [*Galindo,* 1996]. The main restrictions to these methods are as that cloud cover and cloud veils often obscure our view. Occasionally we detect also plumes from forest fires on the flanks of the volcano.

Dense haze is also a severe limiting factor which presents itself particularly during winter months in the early morning under cloudless conditions when the difference between the

bands 4 and 5 of brightness temperatures ΔT_{4-5} often drops below zero over large areas of land surface. A plausible physical explanation is that nocturnal air, containing large amounts of surface minerals and water vapor forming aerosol particles whose radius is proportional to the wavelength of the emitted infrared thermal radiance. This produces scattering and absorption. In later satellite passes, when solar heating dissipates air condensation, ash detection is unequivocal.

A simplified flow diagram based on the previous work of *Higgins and Harris* (1997) (Figure 4), summarizes our semi-automated method. At present we are in the process of incorporating atmospheric corrections (reflectivity and emissivity) into the program.

The method described here is operated in a real-time manner. The time between the pass reception and report generation takes no more than 30 minutes. Twice a day, AVHRR-based volcanic reports are sent via email to the Civil Protection and Aviation Authorities, and to the Volcano Ash Advisory Center (VAAC) in Washington, D.C., USA. In case of emergency situations (volcanic eruptions, explosions, etc) extra reports are sent immediately.

2.2.5. Seismic analysis. Seismic activity was analyzed in three different ways:

a) First we obtained a measure of the seismic energy release by making the Real-time Seismic Amplitude Measurements (RSAM) [*Murray and Endo,* 1989] from the continuous records of station EZV4, the closest station to the summit.

b) Second we obtained a measure of the seismic activity in terms of number of events per-day recorded at EZV4.
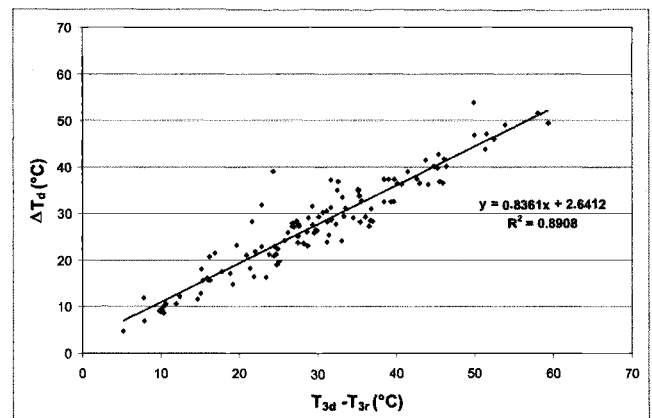

Figure 4. Linear correlation between integrated brightness temperature $\Delta T = T_{3d}-T_{4d}$ and (T_3-T_{3r}). T_{3r} is the channel-3 brightness integrated temperature at a reference point (Volcancito, 3,500 m).
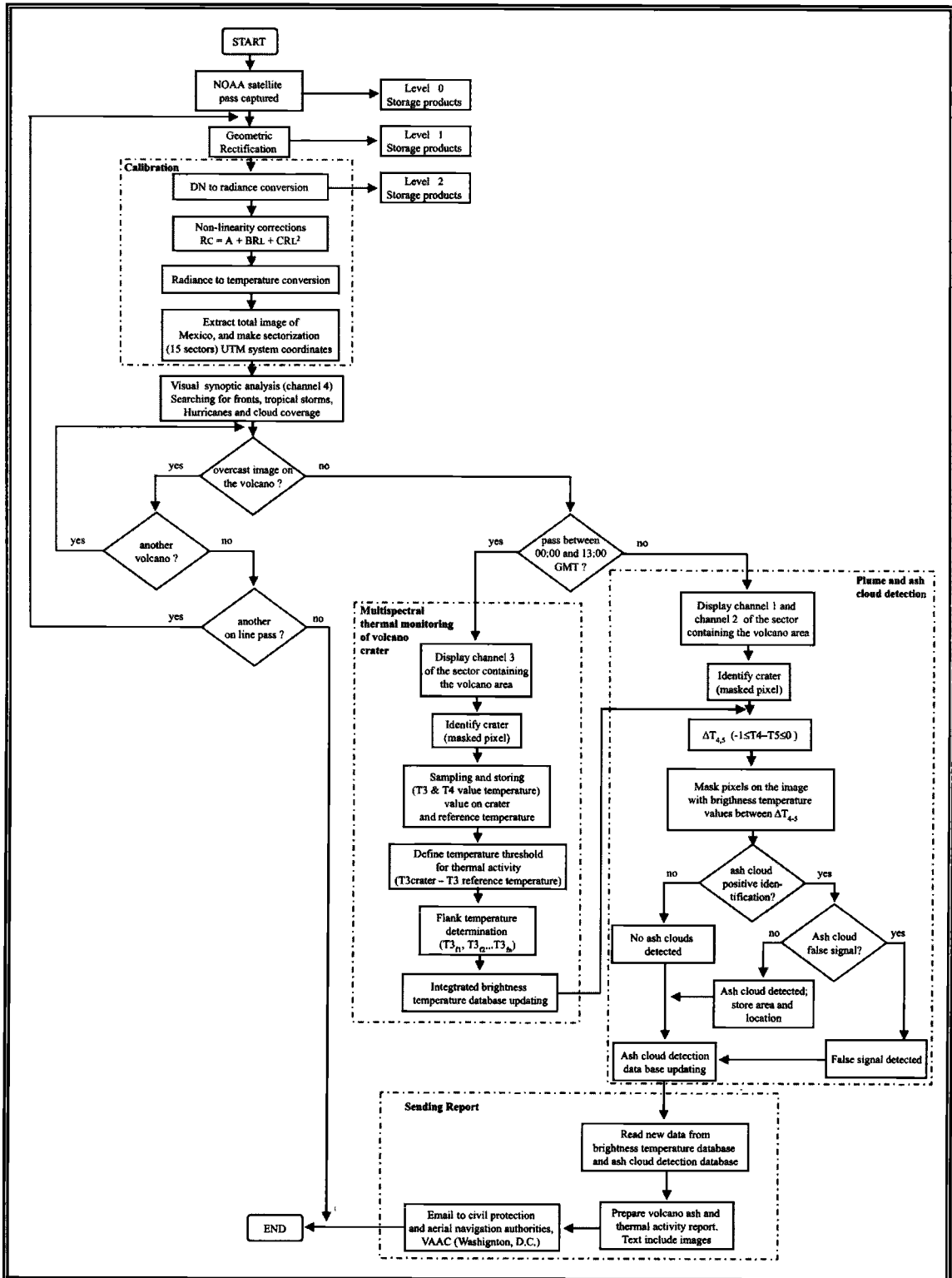
START

NOAA satellite pass captured

Level 0 Storage products

Geometric Rectification

Level 1 Storage products

Calibration

DN to radiance conversion

Level 2 Storage products

Non-linearity corrections $RC = A + BRL + CRL^2$

Radiance to temperature conversion

Extract total image of Mexico, and make sectorization (15 sectors) UTM system coordinates

Visual synoptic analysis (channel 4) Searching for fronts, tropical storms, Hurricanes and cloud coverage

overcast image on the volcano ? — yes / no

another volcano ? — yes / no

another on line pass ? — yes / no

pass between 00:00 and 13:00 GMT ? — yes / no

Multispectral thermal monitoring of volcano crater

Display channel 3 of the sector containing the volcano area

Identify crater (masked pixel)

Sampling and storing (T3 & T4 value temperature) value on crater and reference temperature

Define temperature threshold for thermal activity (T3crater – T3 reference temperature)

Flank temperature determination $(T3_n, T3_o...T3_h)$

Integrated brightness temperature database updating

Plume and ash cloud detection

Display channel 1 and channel 2 of the sector containing the volcano area

Identify crater (masked pixel)

$\Delta T_{4,5}$ ($-1 \le T4 - T5 \le 0$)

Mask pixels on the image with brightness temperature values between ΔT_{4-5}

ash cloud positive identification? — no / yes

Ash cloud false signal? — no / yes

No ash clouds detected

Ash cloud detected; store area and location

False signal detected

Ash cloud detection data base updating

Sending Report

Read new data from brightness temperature database and ash cloud detection database

Prepare volcano ash and thermal activity report. Text include images

Email to civil protection and aerial navigation authorities, VAAC (Washington, D.C.)

END

Figure 5. Simplified flow diagram of the real-time CUICA AVHRR volcano thermal monitoring and ash detection.

During April-May 2002 a series of large amplitude tremor periods were also recorded in all the stations around the volcano.

c) Finally, in order to locate the source of tremor, we used the three component records from station EBMG and perform particle motion analysis. With the aid of the Fourier transform, it was observed that tremor energy was centered on three frequencies: 1 Hz, 1.5 Hz and 2 Hz.

The azimuth of the source of the tremor was estimated by means of "odograms" (particle movement plot in 2D) using the two horizontal components filtered around the three frequencies. As the source was practically to the north from the station, we used the N-S horizontal component and the vertical component to find the depth of the source as it is shown in Figures 5.

Depths were typically between 5 and 6 kilometers below the crater.

3. RESULTS

3.1. Analysis of Heat Release, Ash Emission, Explosive Activity and Tremor

Brightness temperature is used as a proxy for volcanic heat flux from the dome and the flanks. Our AVHRR integrated brightness temperature and ash emission time series together with seismic records (tremor and explosive activity) for March 6–August 31, 2002 show two defined time periods (Figure 7): The first period (March to May) is characterized by high values of ΔT, frequent ash emissions and explosive events and tremor. During the second period (June to August), ΔT, frequent ash emissions and tremor diminish. We note also that at the end of August both AVHRR brightness temperature and recorded tremor increased again. In order to make different data comparable. Figures 7 and 8 show normalized data, i.e, a given data x_i is divide by the maximum value of that time series, x_{max} and
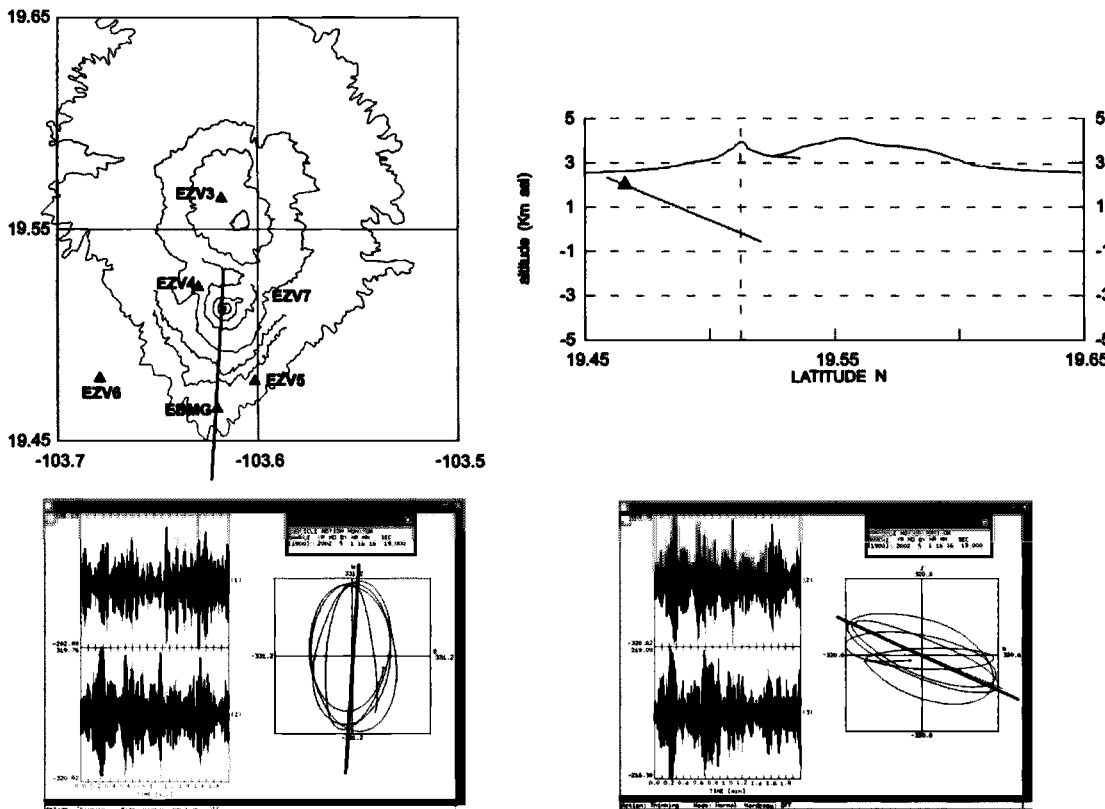
Figure 6. Odograms using both horizontal components (left) and the estimated azimuth plotted from the station EBMG (upper left) and right, the same but using the NS component against the vertical component (upper right).
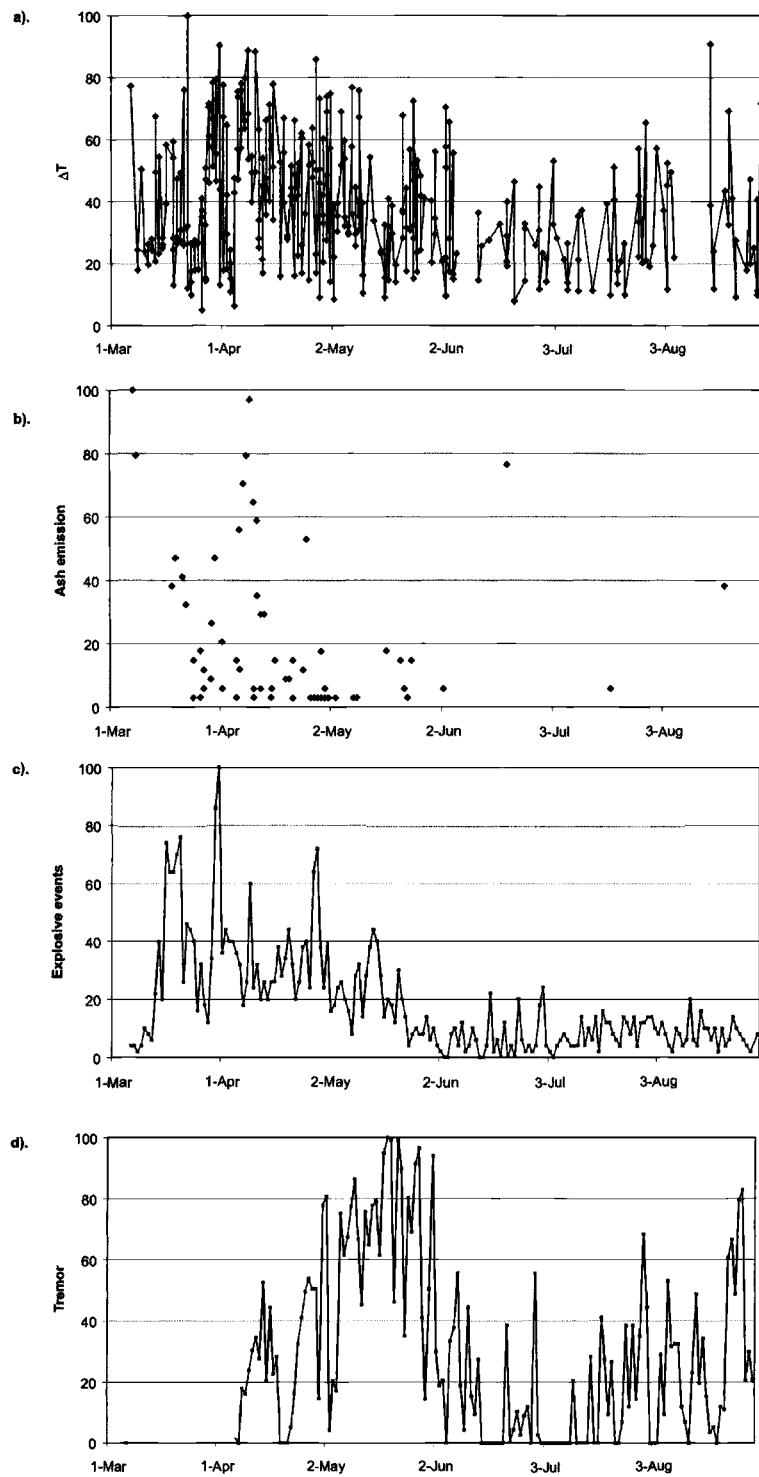
Figure 7. Normalized time series of AVHRR integrated brightness temperature, ash emission, and surface records of explosive events and tremor, March–August, 2002.
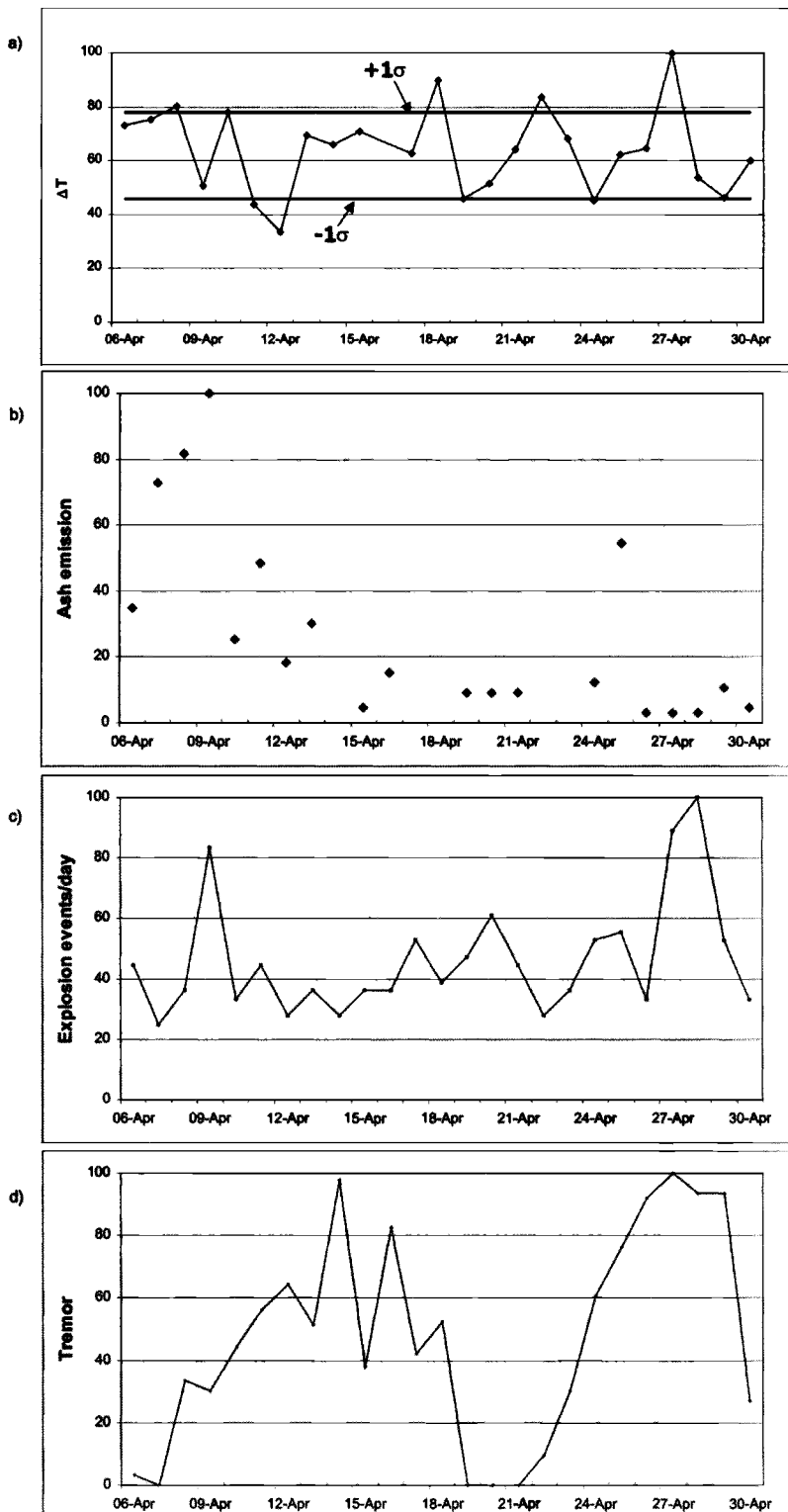
Figure 8. Normalized data for April 2002, a) dome integrated brightness temperature, b) ash emission, c) explosive events, d) tremor.

expressed as $(x_i / x_{max}) .100$. We next consider the detail during the most active period (April 2002): effective high integrated brightness temperatures at the dome within the rank $15.7 \leq \Delta T \leq 46.8\ °C$ during April tend to repeat in periods lasting between 5-7 days (Figure 8a). These thermal signals are the result of high-T_3 incandescent pyroclastic and lava flows on the flanks of the volcano. This period of intense thermal activity correlates with a period during which AVHRR-derived ash cloud areas were also large (Figure 8b). Thermal signals are not correlated with explosive events (Figure 8c, correlation coefficient 0.34) although there is no apparent correlation with tremor (Figure 8d) observed in the seismic data. However, at the end of April only events/day and tremor are well correlated.

3.2. Ash Emission Analysis

As mentioned previously, ash emissions were detected during 17% of the satellite passes. During the majority of these passes, integrated brightness temperature on the dome rose to a maximum value, observed in the image before, i.e. saturation limits just prior to the explosive event. Once the ash emission took place, the dome temperature diminished abruptly as it was seen in subsequent images. The daily mean brightness temperature at the dome during ash emission was about 30 °C, with maximum and minimum brightness temperature of 46.8 and 15.7 °C. Three relative large ash emissions covering ≈ 30–$40\ km^2$ occurred on 7 March, between 5 and 10 April, and on 20 June. As an illustration, Figure 9 shows three sequential satellite passes received on April 28. During that day, the explosion events reached its maximum value per day (36) while recorded tremor reached the third maximum value for April: 9.5 hrs.

3:44 hrs. ΔT=37.5°C   8:21 hrs. ΔT=27.2°C   19:35 hrs. ΔT=14.8°C

■ Ash cloud

8:21 hrs. One pixel

Figure 9. Hot spots and ash emission as detected in three sequential passes. April 28, 2002.

The first image at 3.44 h, showed $\Delta T = 37.5\ °C$, while in the second image, received at 8:21 h, the brightness temperature showed a maximal value of $\Delta T = 27.2\ °C$. One ash pixel 5 km north from dome can also be observed. On the third image at 19:35 h, the brightness temperature dropped to $\Delta T = 21.9\ °C$ T_4 brightness temperatures were 12.5, 12.0, and 21.9 °C, respectively.

The amount of ash ejected during the study period is analyzed in terms of its extension, the corresponding histogram shows that the most frequent ash emission (61% of all images) covers less than 7 km^2, indicating a quite low emission (Figure 10a). The most frequent height (60%) of ash columns is in the range 4–5 km above sea level, which reflects a very low-energy process (Figure 10b). Finally, the most frequent ash cloud direction (56%) is north (Figure 10c). The cloud direction strongly depends on the time of the day. The data shown here refer to the early morning passes, i.e., when the wind blows northwards in agreement with a 4-yr climatology history of the volcano (1994–1997) [*Galindo et al.*, 1998]. In none of the cases was ashfall observed in the city of Colima. Comparing these results with those obtained during the first phase (1997–1999) of the reactivation period of Colima´s volcano, one sees that during this phase the ash clouds reached 6–7 km height [*Galindo and Domínguez*, 2002]. This is an indication that the actual energy involved is less than during the activity of 1997–1999.

3.3. Analysis of Lava Flows Including Ash Emissions From the Lava Flow

New lava flows began on 14 February 2002 on the SW flank of the central crater, frequent incandescent avalanches descended along the SW, S and W slopes [*Smithsonian Institution*, 2002c]. On March 8, two days after we reinitiated our satellite monitoring, we detected ash emission E from the volcano and all the flanks were routinely thermally monitored. Daily records of detected high brightness temperatures (ΔT) and ash emission from the lava flows on the flanks of the volcano enriched our data set. Ash emission from lava flows was caused by collapse of the lava flow front and subsequent release of hot gas and ash. The main statistics of ΔT on the flanks shows that the maximum brightness temperature (51.6 °C) was reached at the S flank (data from NOAA-16 satellite pass) followed by the SE and the W flanks with maximum brightness temperature of 46.2 and 44.0 °C, respectively. These results are shown in Table 2, where also the percentage of the images involved per flank is given. Note that the northern sector of the volcano (NW to NE) has shown almost no temperature differ-
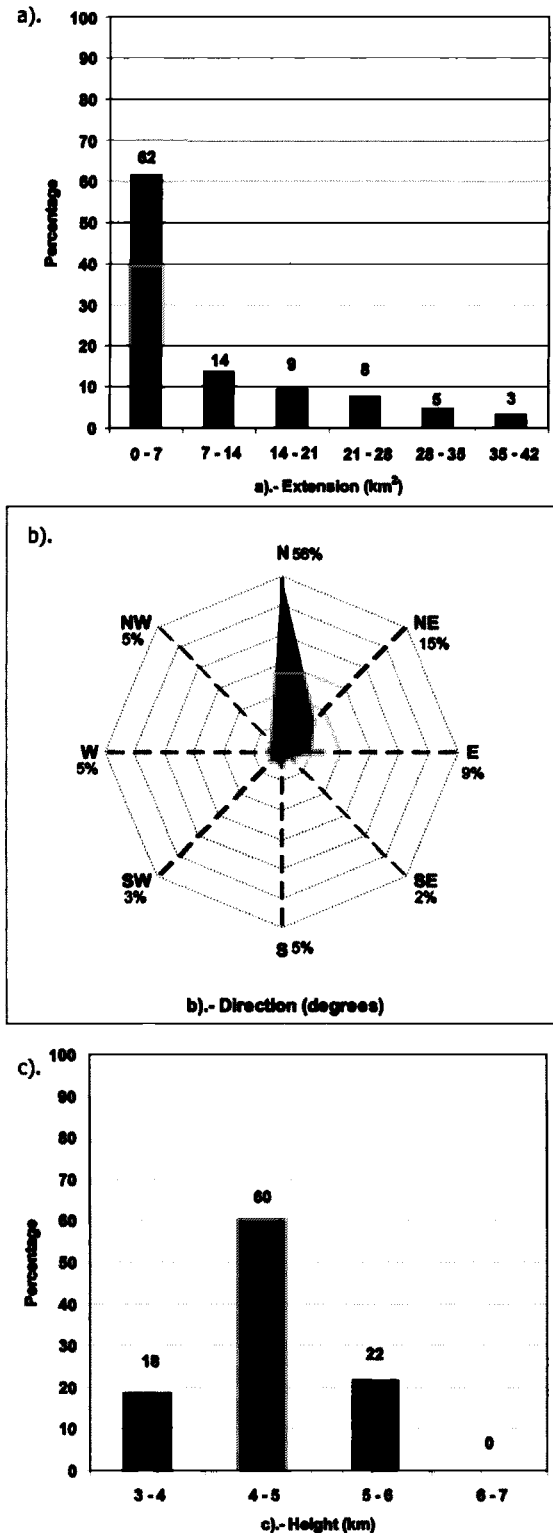
a). 100

b).

c). 100

Figure 10. Normalized relative frequency of ash emission: a) Area of ash detection (km²), b) Direction of ash propagation (degrees), c) Height (km) above sea level. March to August, 2002.

ences, i.e., no heating. This is simple due to the fact that the northern wall of the crater is the tallest and no lava flow passed it.

The normalized relative frequency in percentage of effective brightness temperature is shown in Figures 11 and 12. It is observed that temperature distribution at the dome is centered from 10 °C to 40 °C with a 68% frequency. On the affected flanks of the volcano, low-effective brightness temperatures (0–10 °C) predominate, from 57 to 80%. The overall percent distribution of temperature on the flanks follows a negative exponential decay. In this sense the southeast and eastern flanks are the coolest. We interpret the low temperature values as representative of the old lava flow, *perhaps with a still molten center*, whereas higher temperatures ($\geq$ 20 °C) belong to fresh recent effusive lava and/or the surface of pyroclastic flows.

4. CONCLUSIONS

1. Real-time satellite monitoring proved to be a very useful tool for volcano surveillance. Thermal signals provide very valuable information for the construction of possible scenarios useful for the Civil Protection Authorities. Similarly volcano ash detection on a real-time basis is extremely useful for the aerial navigation authorities.

2. The costs (USD) of an HRPT station are: initial investment $34,822, monthly operational costs $5,100. The relation costs/benefits is quite attractive if one takes into account that near-real-time satellite volcano monitoring works as an early warning system for the protection of human lives and their properties.

3. The current reactivation process of Colima's volcano is characterized by

   a) Two periods are identified: The first period (March to May) is accompanied by very high temperatures, reaching maximum temperatures in thermal pulses lasting 5 to 7 days associated with incandescent pyroclastic and lava flows at the flanks. Although during the second period (June to August), the number of cloud free images is reduced, however lower brightness temperatures were recorded and

Table 2. Frequency distribution (%) and statistics of brightness temperature ΔT_i as measured on the flanks of the volcano. March-August 2002.

	NE	NW	N	SE	E	SW	S	W
Max DT (°C)	14.4	40.4	21.4	46.2	36.8	39.9	51.6*	44.0
Avg DT (°C)	1.4	3.9	3.4	6.3	9.0	9.0	13.7	14.5
Min DT (°C)	-4.7	-8.1	-3.9	-5.9	-7.7	-4.3	-3.4	-2.3
%	1%	1%	5%	10%	12%	16%	26%	28%

* Data from NOAA-16
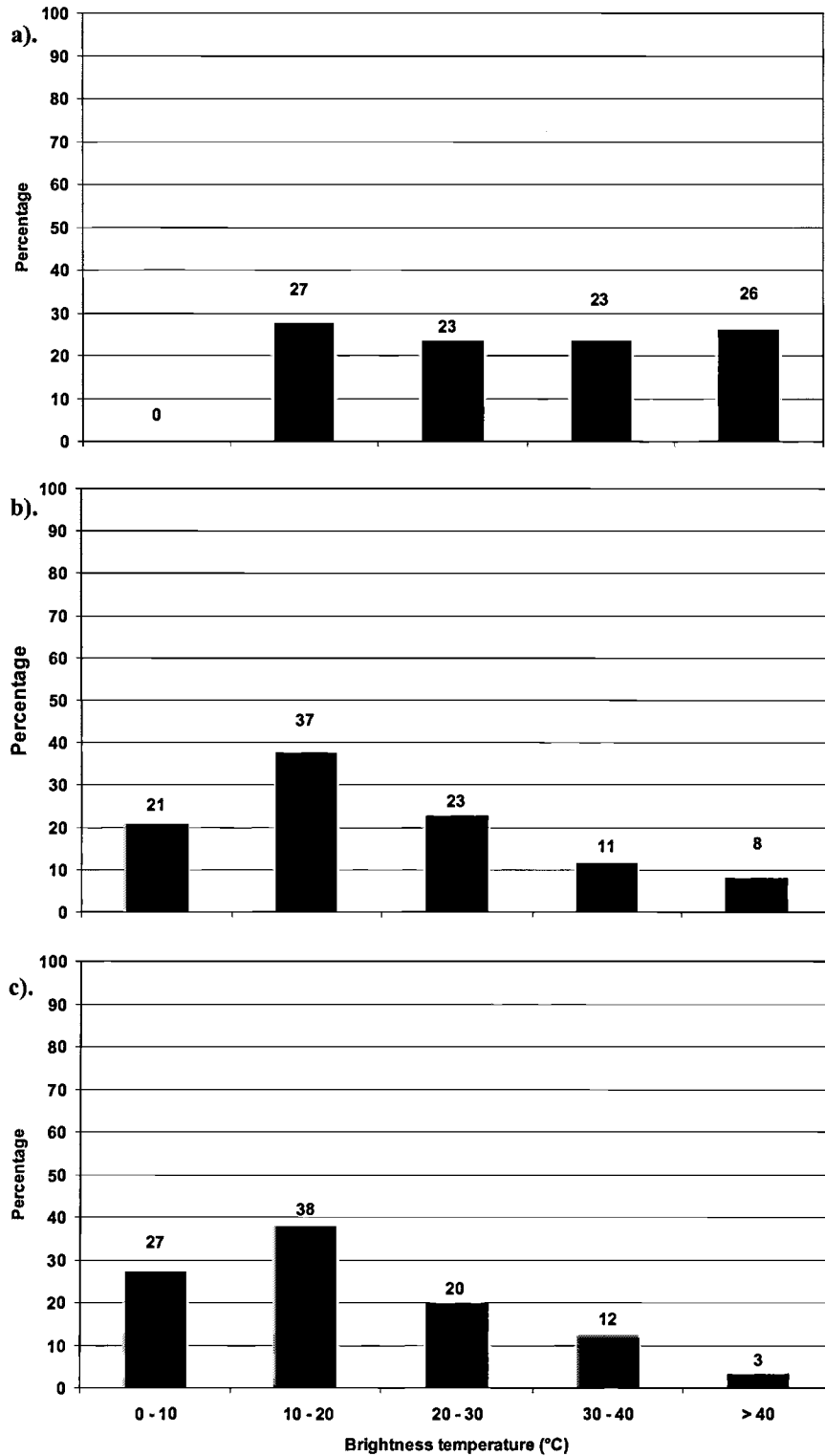
Figure 11. Normalized relative frequency of integrated brightness temperature at the dome and on the flanks: a) dome, b) west, c) southwestern.
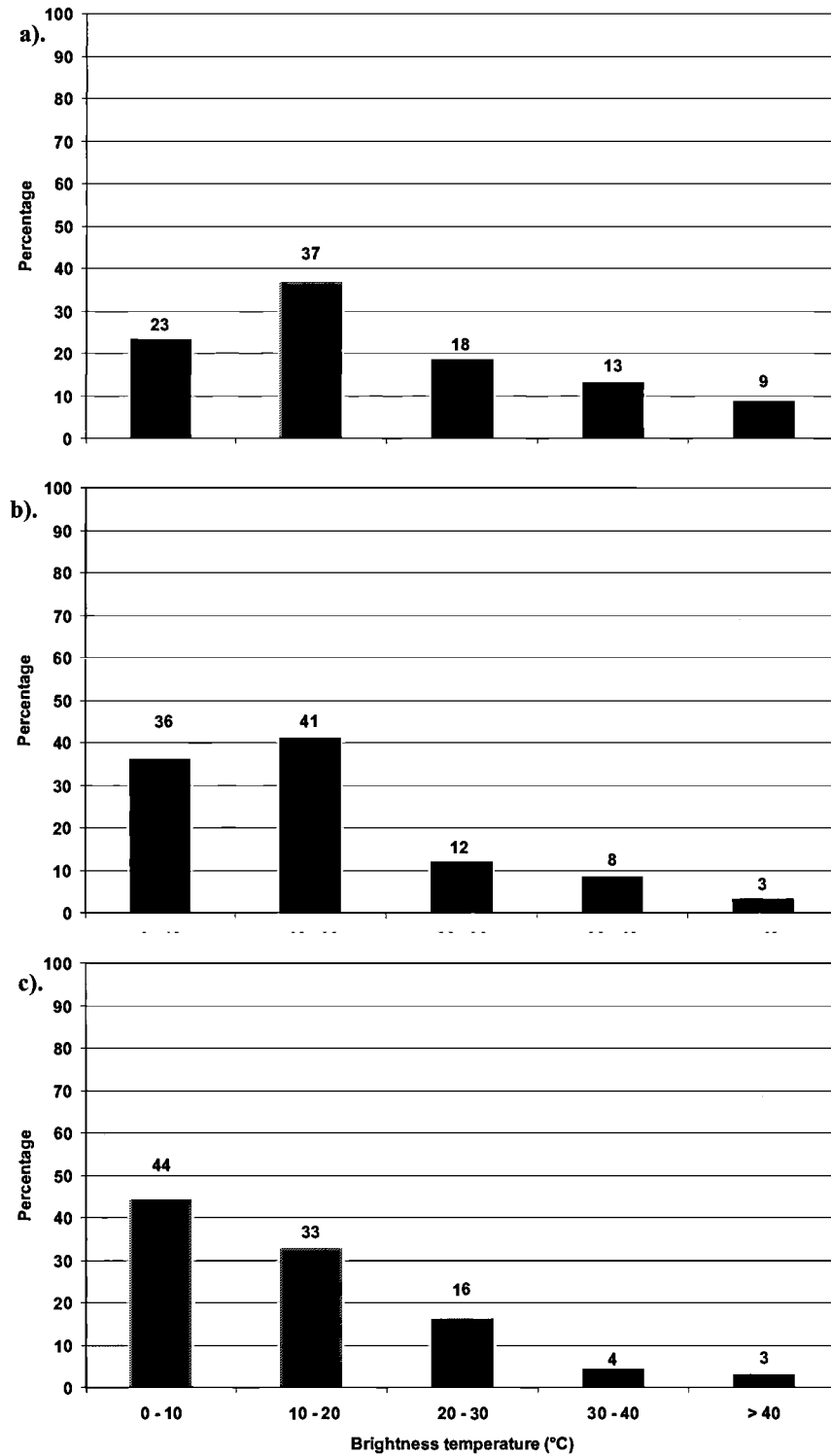
Figure 12. Normalized relative frequency of integrated brightness temperature on the flanks of the volcano: a) southern, b) southeast , c) eastern.

ash emission was observed sporadically and in quite minor amounts. It is also observed that during the middle of August there was an increase in effective temperatures but no ash emission.

b) Maximum activity was reached during April 2002 with frequent heat release accompanied by incandescent (pyroclastic and lava flows) together with ash emission measured by thermal manifestations at the surface (dome and flanks). Simultaneously seismic records show an increasing number of explosive events and tremor. There is no correlation between explosive events and integrated brightness temperature as was reported for Popocatépetl volcano [*Wright et al.*, 2002a].

c) Ash emission amounts are substantially lower than that observed during the beginning of the current reactivation process (November 1997- July 2000). Also the height of the volcanic cloud is lower indicating a much lower energy process. There have been no observations of ashfall in the city of Colima, neither damages to human health, their infrastructure nor economic activities.

REFERENCES

Brown, J.W., O.B. Brown,, and R. H. Evans, Calibration of Advanced Very High Resolution Radiometer Infrared Channels: A New Approach to Nonlinear Correction, *J. Geophys. Res.* 98, 18,257-18,268, 1993.

Dean, K.G., M. Servilla, A. Roach, B. Foster, and K. Engle, Satellite monitoring of remote volcanoes improves study efforts in Alaska, *Eos (Transactions American Geophysical Union)*, 70, p. 413, 422-423, 1998.

Dean, K.G., J. Engle, K Izbekov, P. Papp, K and Patrick, M., Operational Satellite Monitoring of Volcanoes at the Alaska Volcano Observatory in *Advances in Environmental Monitoring and Modelling*, Guest Editors: Harris, A.J.H., M.J. Wooster, and D.A. Rothery, Kings College, London, 2002.

Dehn, J., K. Dean and, K. Engle, Thermal monitoring of North Pacific volcanoes from space. *Geology*, 28, 755-758, 2000.

De la Cruz-Reyna, S., Random patterns of occurrence of explosive eruptions at Colima Volcano, Mexico. *J. Volcanol. Geotherm. Res.*, 55, 51-68, 1993.

Francis, P. W. and D. Rothery, Remote Sensing of Active Volcanoes. Ann. *Rev. Earth Planet Sci. 28*, 81-106, 2000.

Francis, P. W., G. Wadge, and P.J. Mouginis-Mark, Satellite Monitoring of Volcanoes in (R. Scarpa and R. I. Tilling, Eds.) *Monitoring and Mitigation of Volcano Hazards*, 841 pp., 1996.

Galindo, I., Volcanic clouds detection from the low energy eruption of Popocatépetl volcano (Mexico) using AVHRR bands 4 and 5. *Volcanic Ash Hazards and Aviation Workshop*, May 28-31, Anchorage, Alaska, 1996.

Galindo, I. and T. Domínguez, Near real-time monitoring during the 1997-2000 activity of Volcán de Colima (Mexico) and its relationship with seismic monitoring. *J. Volcanol. Geotherm. Res.*, 117, 91-104, 2002.

Galindo, I., A. Elizalde R. Solano y M. Cruz, 1998, *Climatología del Volcán de Fuego de Colima.* Universidad de Colima, 73 pp., Colima, México.

Galindo, I., A. Cortés, T. Domínguez, J.C. Gavilanes et M. Cruz, Note sur l'eruption actuelle du volcan Fuego de Colima (Mexique). *Bull. de la SVG*, C-1- C5, 1999.

Galindo, I., J.P. López-Pérez, and M. Evangelista-Salázar, Real-time AVHRR forest fire detection in Mexico (1998-2000), *Int. J. Remote Sensing*, 24, 9-22, 2003.

Hanstrum, B.N. and A.S. Watson, A case study of two eruptions of Mount Galunggung and an investigation of volcanic eruption cloud characteristics using remote sensing techniques. *Aust. Met. Magazine* 31, 171-177, 1983,

Harris, A. J.L., R.A. Vaughan and D. A. Rothery, Volcano detection and monitoring using AVHRR data: the Krafla eruption, 1984. *Int. J. Remote Sensing 16*, 1001-1020, 1995a.

Harris, A.J.L, S.E.J. Swabey, and J. Higgins, Automated thresholding of active lavas using AVHRR data. *Int. J. Remote Sensing, 16*, 3681-3686, 1995b.

Harris, A.J.L., A.L. Butterworth, R.W. Carlton, I. Downey, P. Miller, P. Navarro, D.A. Rothery, Low-cost volcano surveillance from space: case studies from Etna, Krafla, Cerro Negro, Fogo, Lascar and Erebus. *Bull. Volcanol. 59*, 49-64, 1997.

Harris, A.J.L., L. P. Flynn, K. Dean, E. Pilger, M. Wooster, Ch. Okubo, P.Mouginis-Mark, H. Garbeil, C. Thornber, S. De la Cruz-Reyna, D. Rothery, and R. Wright. In *Remote Sensing of Active Volcanism*, Geophys. Monograph 116, 139-159, American Geophysical Union, 2000.

Harris, A.J.L., E. Pilger, and L.P. Flynn, Web-based Hot Spot Monitoring using GOES: What it is and How it Works in *Advances in Environmental Monitoring and Modelling*, Guest Editors: Harris, A.J.L, M. J. Wooster, M.J., and D.A. Rothery, Kings College, London, 2002.

Higgins, J. and A. Harris, VAST: A Program to Locate and Analyse Volcanic Thermal Anomalies Automatically from Remotely Sensed Data. *Computer and Geosci.*, 23, 627-645, 1997.

Holasek, R.E. and W.I. Rose, Anatomy of 1986 Augustine volcano eruptions as recorded by multispectral image processing of digital AVHRR weather satellite data. *Bull. Volcanol. 53*, 420-435, 1991.

Hovis, W.A. and W.R. Callahan, Infrared reflectance of igneous rocks, tuffs, and red sandstone from 0.5 to 22 microns. *J. Opt. Soc. Amer.* 56, 639-643, 1966.

Hunt G.R. and J.W. Salisbury, Mid-infrared spectral behavior of igneous rocks. *Envir. Res. Paper* 496, pp. 1-142. US Air Force Cambridge Research Lab., Bedford, Mass., 1974.

Kaufman, Y.J., C.J. Tucker, and I. Fung, Remote sensing of biomass burning in the tropics. *J. Geophys. Res.*, 95, 9927-9939, 1990.

Kidwell, K.B., *NOAA Polar Orbiter Data Users Guide*, NOAA/NESDIS, Washington, D.C., 250 pp., 1995.

Lyon, R.J.P., Evaluation of infrared spectrophotometry for compositional analysis of lunar and planetary soils. *NASA Tech. Note TN D1871*, 1963.

Luhr, J.F., and J. Carmichael, Geology of Volcán de Colima. *Instituto de Geología, UNAM*, boletín 107. 101 pp., 1990.

Langaas, S., A parametrised bispectral model for savanna fire detection using AVHRR night images. *Int. J. Remote Sensing*, 14, 2245-2262, 1993.

Matson, M., The 1982 El Chichón volcano eruptions– a satellite perspective. *J. Volcanol. Geotherm. Res.*, 23, 1-10, 1984.

Medina, F., Analysis of the eruptive history of the Volcan Colima (Mexico) (1560-1980). *Geofis. Int.*, 22, 157-178, 1983.

Murray, T.L. and E.T. Endo, A Real-time Seismic Amplitude Measurement System (RSAM). *U.S Geological Survey Open-File Report* 89-684, 21pp., 1989.

Navarro-Ochoa, C., J.C. Gavilanes-Ruíz and A. Cortés-Cortés, Movement and emplacement of lava flows at Volcán de Colima, México: November 1998–February 1999. *J. Volcanol. Geotherm. Res.* 117, 155-167, 2002.

NOAA:http://noaasis.noaa.gov/NOAASIS/ml/status.html.

Oppenheimer, C. Volcanological applications of meteorological satellites. *Int. J. Remote Sensing*, 19, 2829-2864, 1998.

Oppenheimer, C., P.W. Francis, D.A. Rothery, and R. T. Carlton, Infrared Image Analysis of Volcanic Features: Láscar Volcano, Chile, 1984-1992. *J. Geophys. Res.* 98, 4269-4286, 1993.

Oppenheimer, C., P.W. Francis, D.A. Rothery, Infrared image-analysis of volcanic thermal features – Lascar Volcano, Chile, 1984-1992. *J. Geophys. Res.* 98, 4269-4286, 1997.

Pereira, M.C. and A. W. Setzer, Spectral characteristics of deforestation fires in NOAA/AVHRR images. *Int. J. Remote Sensing*, 14, 583-597, 1993.

Prata, A.J., Observations of volcanic ash clouds in the 10-12 mm window using AVHRR/2 data. *Int. J. Remote Sensing*, 10, 751-761, 1989.

Roach, A.L., J.P. Benoit, K. G. Dean, and S.R. McNutt, The combined use of satellite and seismic monitoring during the 1996 eruption of Pavlov volcano, Alaska. *Bull.Volcanol.*, 62, 385-399, 2001.

Robock, A. and M. Matson, Circumglobal transport of the El Chichón volcanic dust cloud. *Science*, 221, 195-197, 1983.

Rothery, D.A., Monitoring and warning of volcanic eruptions by remote sensing. In *Geohazards; Natural and Man-made*, edited by G.J.H. McCall, D.J.C. Laming, and S.C. Scott (London: Chapman & Hall) pp. 25-32, 1992.

Rothery, D.A., P.W. Francis, and C.A. Wood, Volcano monitoring using shortwave infrared data from satellites. *J. Geophys. Res.*, 93, 7993-8008, 1988.

Sawada, Y., Analysis of volcanic eruptions based on eruption cloud image obtained by the Geostationary Meteorological Satellite (GMS). *Tec. Report of the Met. Res. Inst.*, 23, 335, 1987.

Sawada, Y., Tracking of Regional Volcanic Ash Clouds by Geostationary Meteorological Satellite (GMS). Volcanic Ash and Aviation Safety Proceed. First Int. Symp. Volcanic Ash and Aviation Safety, *USGS Bull.* 2047, 397-403, 1994.

Schneider, D.J., W. I. Rose, and L. Kelly, 1995, Tracking of 1992 Eruption Clouds from Crater Peak Vent of Mount Spurr Volcano, Alaska, Using AVHRR. *USGS Bull 2139*: 27-36.

Smithsonian Institution, Colima, Mexico, *Bull. Glob. Volcan Netw*, 24, 2, 1999.

Smithsonian Institution, Colima, Mexico, *Bull. Glob. Volcan Netw*, 26, 4, 2001a.

Smithsonian Institution, Colima, Mexico, *Bull. Glob.Volcan. Netw*, 26, 5, 2001b.

Smithsonian Institution, Colima, Mexico, *Bull. Glob.Volcan. Netw*, 26, 10, 2001c.

Smithsonian Institution, Colima, Mexico, *Bull. Glob.Volcan. Netw*, 27, 2, 2002a.

Smithsonian Institution, Colima, Mexico, *Bull. Glob.Volcan. Netw*, 27, 5, 2002b.

Smithsonian Institution, Colima, Mexico, *Bull. Glob.Volcan. Netw*, 27, 11, 2002c.

Sparks, R.S. J., M. I. Bursik, S.N. Carey, J.S. Gilbert, L.S. Glaze, H. Sigurdsson, and A.W. Woods, Remote Sensing of Volcanic Plumes, Chap. 12 of *Volcanic Plumes*, John Wiley and Sons, Chichester, 307-345, 1997.

Weinreb, M. P., G. Hamilton, and S. Brown, Nonlinearity Corrections in Calibration of Advanced Very High Resolution Radiometer Infrared Channels. *J. Geophys. Res.*, 95, 7381-7388, 1990.

Wooster, M.J., Long-term infrared surveillance of Lascar volcano: contrasting activity cycles and cooling pyroclastics. *Geophys. Res. Lett*, 28, 847-850, 2001.

Wooster, M.J. and D.A, Rothery, Thermal monitoring of Lascar volcano, Chile using infrared data from the Along Track Scanning Radiometer: a 1992-1995 time series. *Bull. Volcanol.* 58, 566-579, 1997.

Wooster, M.J. and T. Kaneko, Satellite thermal analyses of lava dome effusion rates at Unzen Volcano, Japan. *J. Geophys. Res.* 103, 20935-20947, 1998.

Wooster, M. J., T.S. Richards and K. Kidwell, NOAA-11 AVHRR/2Thermal channel calibration update. *Int. J. Remote Sensing* 16, 369-363, 1995.

Wooster, M.J., T. Kaneko, S. Nakada and H. Shimizu, Discrimination of lava dome activity styles using satellite-derived th4rmal structures. *J. Volcanol. Geotherm. Res.* 102, 97-118, 2000.

Wright R., S. De La Cruz-Reyna, A. Harris, L. Flynn, and J.J. Gomez-Palacios, Infrared satellite monitoring at Popocatépetl: Explosions, exhalations, and cycles of dome growth. *J. Geophys. Res.* 107, 2153, 2002a.

Wright R., L. Flynn, H. Garbeil, A. Harris and E. Pilger, Automated volcanic eruption detection using MODIS. *Remote Sens. Environ.* 82, 135-155, 2002b.

Yamanouchi, T., K. Suzuki, and S. Kawaguchi, Detection of Clouds in Antarctica from Infrared Multispectral Data of AVHRR. *J. Met. Soc.Japan*, 66, 949-961, 1987.

Zobin, V.M., M. González-Amezcua and G.A. Reyes-Dávila, Seismotectonic deformation of the volcanic edifice prior to the 1998 lava eruption of Volcán de Colima, México. *Bull. Volcanol.* 64: 349-355, 2002a.

Zobin, V.M., J.F. Luhr, Y. A. Taran, M. Bretón, A. Cortés, S. De la Cruz Reyna, T. Domínguez, I. Galindo, J. C. Gavilanes, J.J;. Muñiz, C. Navarro, J.J. Ramírez, G.A. Reyes, M. Ursúa, J.E. Velasco, E. Alatorre, H. Santiago, Overview of the 1997-2000 activity of Volcán de Colima, México *J. Volcanol, Geotherm. Res.* 117, 1-19, 2002b.

Ignacio Galindo, Director, Centro de Ciencias del Ambiente, Universidad de Colima, Revolución 427, 28000 Colima, Col., México

Tonatiuh Domínguez, Director, Observatorio Vulcanológico, Universidad de Colima, Bernal Díaz del Castillo 340, 28045 Colima, Col. México.

High Resolution Ice Core Records of Late Holocene Volcanism: Current and Future Contributions from the Greenland PARCA Cores

Ellen Mosley-Thompson[1], Tracy A. Mashiotta, and Lonnie G. Thompson[2]

Byrd Polar Research Center, The Ohio State University, Columbus, Ohio

A suite of spatially distributed, multi-century cores collected since 1995 under NASA's Program for Arctic Regional Climate Assessment (PARCA) provides an excellent archive of volcanic emissions reaching Greenland. As records of equivalent quality from higher accumulation sites in Antarctica become available, their integration will produce a richer, better temporally constrained and more climatologically valuable history of global volcanism. The Greenland PARCA cores have been accurately dated using multiple seasonally varying indicators ($\delta^{18}O$, insoluble dust, H_2O_2, nitrate, calcium) and the ongoing chemical analyses are providing new volcanic histories that complement the limited records that exist. The first results confirm that the sulfate aerosols from an unidentified pre-Tambora eruption called Unknown: (1) were widely dispersed across the Greenland ice sheet; (2) first arrived in the 1810 A.D. snow fall; and, (3) in 1810 A.D., the first year after the eruption (1809 A.D.), produced concentrations of excess SO_4^{2-} (EXS) comparable to those deposited in 1816 A.D., the first year after the eruption of Tambora in 1815 A.D. The EXS originating from the eruption of Laki craters or Lakagígar (1783 A.D.) is confined to a single year (1783 A.D.) and varies considerably across the ice sheet, primarily as a function of the local accumulation rate. Future chemical analyses of the PARCA cores promise richly detailed histories of EXS emissions from both known and yet to be identified volcanic eruptions. The high temporal resolution of these ice core records will help resolve timing issues and their broad spatial distribution will provide a more representative estimate of the EXS flux associated with a specific eruption.

[1]Also at the Department of Geography, The Ohio State University, Columbus, Ohio
[2]Also at the Department of Geological Sciences, The Ohio State University, Columbus, Ohio

1. INTRODUCTION

The likelihood of anthropogenic climate forcing on a global scale has necessitated efforts to differentiate the contributions of natural forcing mechanisms from those attributable to human activities of the past two centuries. One natural cause of short-term climate change is the perturbation of the Earth's radiation balance by the emission of volcanic gases into the stratosphere. Here the aerosols may remain for several years, perturbing the earth-atmosphere radiation balance and hence the surface temperature distribution that modifies atmospheric and oceanic circulation

patterns. Papers in this volume review the character of both modern and ancient volcanic eruptions, their radiative effects, and efforts to measure and model the earth-system responses. The impacts of volcanism on the Earth's climate system are reviewed by *Robock* [2000] who stresses that evaluation of the causes of climatic change over the last few millennia requires a 'reliable' record of atmospheric aerosol loading from volcanic eruptions. This paper presents the first volcanic records from the Greenland PARCA cores that will eventually yield a rich and detailed history of atmospheric aerosols of volcanic origin.

No perfect archive of explosive volcanic eruptions exists as each recording system (e.g., ice cores, tree rings, documentary evidence) has its unique biases, quality of signal preservation, and dating difficulties. The low background concentration of most chemical species in polar ice cores makes them an excellent medium for identification of volcanic emissions. Holocene volcanic eruptions are rarely recorded as visible tephra layers in polar cores although a few have been reported [*Zielinski et al.*, 1997]. More generally volcanic events are identified by elevated concentrations of EXS deposited as particulate aerosols that form when gaseous compounds (mainly sulfur dioxide) are oxidized to sulfuric acid and water. If the gases are injected into the stratosphere, particularly from low to mid-latitude volcanoes, the aerosols can spread globally. Observations after the June 15, 1991 eruption of Mt. Pinatubo in the Philippines (15°8'N; 120°21'E) revealed that the aerosols rapidly spread zonally [*Bluth et al.*, 1992] and then began to disperse poleward [*Trepte et al.*, 1993].

In the last decade several authors have used ice cores to establish more firmly the history of explosive volcanism and to quantify the sulfate emissions attributable to specific eruptions for inclusion in climate models [*Robock and Free*, 1995; *Zielinski*, 1995; *Claussen et al.*, 1997; *Crowley and Kim*, 1999; *Crowley*, 2000]. This paper highlights the valuable information that the high resolution PARCA cores can provide about the history of volcanic activity and the quantity of volcanic sulfate deposited over the Greenland ice sheet. The latter allows the associated stratospheric sulfate burden to be estimated and this is critical for including the effect of volcanic eruptions in climate models. The paper does not provide a comprehensive review of the Earth's volcanic history as reconstructed from ice cores, but it attempts to provide a balanced discussion of the strengths and limitations of ice core-derived volcanic information. Here we report new analyses that complement and expand previous volcanic chronologies and emissions estimates, confirm that eruption of the pre-Tambora Unknown event occurred in 1809 A.D., and pro-

vide new evidence suggesting that the sulfate emissions from Lakagígar (henceforth Laki) arrived on the Greenland ice sheet in 1783 and not in 1784.

2. ICE CORE-DERIVED VOLCANIC HISTORIES

Since the 1960s when the first long ice cores were recovered from Greenland (1966 at Camp Century) and Antarctica (1968 at Byrd Station), polar firn and ice cores have provided unique details about the nature, timing and impacts of volcanic eruptions on regional to global scales. *Gow and Williamson* [1971] reported numerous ash and dusty layers in Byrd ice core sections from the latter part of the Last Glacial Stage (LGS, ~16–30 ka BP). This lead to renewed interest in the possible role of prolonged, explosive volcanism on the climate at the Last Glacial Maximum (~18 ka BP) [*Harvey*, 1988]. Was the volcanism responsible for the occurrence of the coldest global temperatures just prior to climate recovery or did the volcanism extend the duration of the LGS? Subsequently, most of these events were attributed to regional (Antarctic or sub-Antarctic islands) eruptions [*Kyle et al.*, 1981] that likely did not affect the transparency of the global atmosphere. Nevertheless, renewed interest in the volcano-climate connection was generated and soon thereafter Hammer and his colleagues used acidity measurements to demonstrate that concentrations of sulfuric acid (H_2SO_4) in Greenland ice cores were elevated by deposition of volcanic aerosols [*Hammer*, 1977; *Hammer et al.*, 1980].

2.1. Dating Ice Cores

For three decades volcanic signals preserved in ice cores have been exploited as stratigraphic markers for dating ice cores [*Hammer et al.*, 1978; *Hammer*, 1989] and as archives for augmenting and extending the historical record of globally significant volcanic events [*Hammer*, 1980; *Delmas et al.*, 1985; *Dai et al.*, 1991; *Cole-Dai et al.*, 1997; 2000; *Zielinski*, 2000]. Precise dating of a proxy record is critical for meaningful interpretation and robust comparisons with other histories. The use of volcanic horizons as "time stratigraphic" markers for dating ice cores has created an unintended 'chicken and egg' situation. If the ice core sulfate deposit is used as a marker horizon for dating then it can no longer be used to independently ascertain the arrival time of the aerosols to the ice sheet. Volcanic layers can only be used to determine the timing of aerosol deposition when the horizon is dated by counting multiple seasonally varying constituents from some other independently confirmed event. Moreover, due to the potential for mixing of snow between consecutive years by blowing, drifting, deflation and redepo-

sition, the timing of an event should be confirmed in more than one core from a region [*Gow*, 1965; *Mosley-Thompson et al.*, 1985, 2001; *Pomeroy and Jones*, 1996; *Zielinski*, 2000]. The chance of snow layer mixing increases as annual net accumulation of snow at the site decreases.

Many of the cores collected in the 1970s and early 1980s were analyzed continuously by cutting discrete samples over the entire length of the core, but often the analyses were limited to the oxygen and/or hydrogen isotopic ratios ($\delta^{18}O$, δD, respectively). Although these species often show a seasonal signal they are also subject to post-depositional modification by vapor diffusion within the firn as well as by melting or percolation. When vague seasonal signals hinder layer counting efforts, other methods may be employed to augment the dating effort. One approach is to construct a simple depth-age model for the core using the annual accumulation, thickness of the ice sheet, and ice flow characteristics. Of course, this includes the unrealistic assumption of a steady state accumulation regime, but does provide an approximate time scale. With the approximate time scale in hand, known volcanic events can be "sought" by analyzing selected sections of core for acidity signals using electrical conductivity measurements (ECM) or by chemically analyzing samples to isolate layers containing elevated sulfate concentrations. This can be risky for ice core sections with closely spaced events that might be confused if only one event is detected. Even when cores are continuously analyzed by ECM, less prominent (or unanticipated) volcanic events can be missed. Although great improvements have been made in the use of rapid, *in situ*, nondestructive ECM analysis [*Taylor et al.*, 1997; *Wolff et al.*, 1997], the technique remains dependent upon core quality, temperature of the ice at the time the measurement is made, and operator experience. Ion chromatographic analysis of discrete samples, cut to discern annual cycles (≈ 6 to 10 samples per accumulation year), is more time consuming and also dependent upon core quality, but can still be used when core quality is degraded and thus offers a more thorough examination of the core as well as more quantitative information about sulfate deposition. Additionally, as other non-volcanic chemical species may render the ice acidic, ion chromatographic analysis of sulfate (SO_4^{2-}) provides a more definitive indication of a volcanic emission and allows a more quantitative assessment of the amount of volcanic sulfate aerosol preserved in the ice.

2.2 Refining Volcanic Chronologies: Annual Resolution

Recent advances such as the continuous flow analysis (CFA) system [*Fuhrer et al.*, 1993; *Anklin et al.*, 1998] and improvements to ion chromatographic techniques now facilitate the analysis of smaller sample volumes. This has made it possible to use 'annual layer counting' in regions with lower annual average accumulation (100–200 mm a⁻¹ water equivalent, w.e.) and has resulted in more continuous analyses so that the entire core length is chemically and/or physically characterized with high temporal resolution. The result is that more volcanic events, some known and some unknown, are now being identified, quantified and compared among multiple cores.

Ice cores collected to 303-meters depth in 1985 at Siple Station (75°55'S; 84°15'W) and to 235-meters depth in 1989/90 on the Dyer Plateau (70°40'S; 64°52'W) were among the first Antarctic cores to be analyzed continuously (top to bottom) for major anions (including SO_4^{2-}), $\delta^{18}O$, and insoluble dust. The high annual average accumulation at these sites (Siple: 560 mm a⁻¹ w.e.; Dyer Plateau: 440 mm a⁻¹ w.e.) made it possible to date the cores very accurately using the excellently preserved seasonal variations in both $\delta^{18}O$ and SO_4^{2-} [*Mosley-Thompson et al.*, 1991; *Mosley-Thompson*, 1992; *Thompson et al.*, 1994]. The resulting volcanic chronology from 1417 to 1989 A.D. resolved a number of temporal ambiguities regarding known eruptions and revealed some previously unknown events in the 1600s [*Cole-Dai et al.*, 1997]. The three largest eruptions, in terms of the sulfate flux deposited at these coring sites (assumed to reflect input to the Southern Hemisphere stratosphere) are Tambora in Indonesia (1815 A.D.), Kuwae ($\approx$ 1453 A.D.) on Vanuatu (17°S; 71°W) in the tropical South Pacific, and a previously unknown tropical volcano (1809 A.D.) that was first identified in both Greenland and Antarctica by *Dai et al.* [1991].

As more ice core-derived volcanic histories have become available, questions have been raised regarding the quantity and timing of material delivered to the polar ice sheets and how much reliance can be placed upon a reconstruction from one core. Knowledge of transport time and the relationship between the quantity of sulfur gases emitted and the SO_4^{2-} deposited is critical if the full potential of the ice cores for volcanic reconstruction and climate modeling constraints is to be realized. For example, a 4000-year volcanic history from the Plateau Remote (PR) core drilled high on the East Antarctic Plateau [*Mosley-Thompson*, 1996] raises a question about the relative magnitude of the sulfate flux from Tambora and Kuwae [*Cole-Dai et al.*, 2000, their figure 2]. At the PR site (84°S; 43°E; 3330 masl) the measured sulfate flux from Kuwae is five times that from Tambora, but the low annual average accumulation ($\sim$ 40 mm a⁻¹ w.e.) is a complicating factor that calls for careful interpretation and more complementary histories. Undoubtedly, the PR record points to an event that may be very climatically

important, at least in the Southern Hemisphere if not globally, and it should be pursued more vigorously in other East Antarctic ice cores as well as in Greenland. Better dating and continuous analysis of multiple parameters in more cores will provide the robust volcanic sulfate flux histories necessary to place better constraints on the timing, duration and magnitude of stratospheric aerosol loads associated with specific eruptions.

3. THE GREENLAND PARCA CORES

A suite of spatially distributed cores collected since 1995 under NASA's Program for Arctic Regional Climate Assessment (PARCA) [*Thomas et al.*, 2001] now provides an unprecedented opportunity to assess local to regional variability of the various "climate" signals preserved within the Greenland ice sheet. PARCA cores are particularly valuable for their broad spatial distribution and the accurate dating of annual layers using multiple seasonally varying indicators ($\delta^{18}O$, insoluble dust, H_2O_2, nitrate, calcium). Figure 1 illustrates the locations of six multi-century cores collected as part of PARCA, as well as the Summit area where three cores (Site T, GISP2 and GRIP) discussed in the paper were collected, and the location of two older core sites (Crête, Dye 3) also mentioned in the text.

As the PARCA cores were drilled and analyzed primarily to reconstruct accumulation histories for different sites on the Greenland ice sheet [*Mosley-Thompson et al.*, 2001], their extensive analyses and careful interpretation resulted in very precise dating and determination of the thickness (mass accumulation) of each annual layer. Figures 2 and 3 illustrate the precision with which ice cores may be dated using multiple seasonally varying parameters. Figure 2A shows the section of the Site T Core 2 containing both Tambora and Unknown. The core (drilled in 1989 within 5 km of the GISP2 site) was analyzed continuously (top to bottom) for major anions (2039 samples) as well as for $\delta^{18}O$ (2075 samples) and dust concentrations (2075 samples). Due to the low annual average accumulation at Site T (~220 mm a^{-1} w.e.) the seasonal variations in $\delta^{18}O$ are smoothed by vapor diffusion in the firn [*Johnsen*, 1977]. The difficulty of using only $\delta^{18}O$ for dating cores from regions of low annual average accumulation (< ~250 mm a^{-1} w.e.) is readily apparent. Recently, physically-based models have been developed to 'back-diffuse' isotopic records [*Johnsen et al.*, 2000], making them more useful for dating at greater depths and in regions of lower accumulation. Fortunately, the seasonal variations in NO_3^- provided an important complement to the seasonal dust concentrations and allowed very accurate dating. Figure 2B illustrates the

contemporaneous section from a 120-m core drilled in 1996 at the GITS site (formerly Camp Century) in northwest Greenland (see Fig. 1). The GITS core was dated using seasonal variations in $\delta^{18}O$ (2586 samples) and dust (2586 samples) measured at Ohio State by these authors and seasonal variations in H_2O_2, nitrate, and calcium measured by colleagues M. Anklin, R. Bales and J. McConnell, all then at the U. of Arizona, using their continuous melter system. Finally, the dating of the upper ~50 years of both cores was confirmed by identification of beta radioactivity horizons associated with thermonuclear testing in the 1950s and 1960s. A full discussion of the methods used to date the cores is provided by *Mosley-Thompson et al.* [2001, their figures 2 and 3].
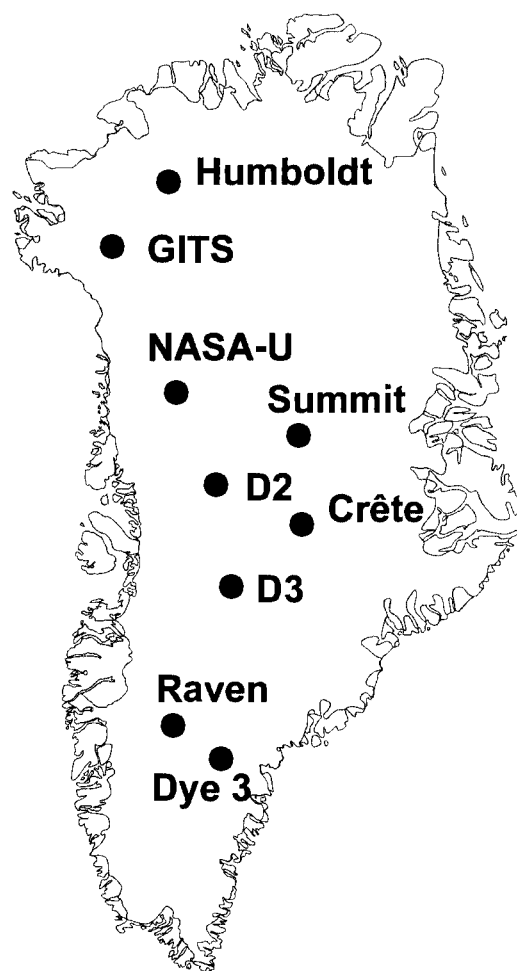

Figure 1. Shown are the locations of the six multi-century cores collected by the PARCA program, two older cores discussed in the text (Dye 3 and Crête) and the Summit Site where the GISP2, GRIP and Site T cores were drilled.

At some PARCA sites, multiple closely spaced cores demonstrate that signals of high-frequency (annual to possibly decadal scale) climate variability preserved in the ice sheet are partially masked by glaciological noise. Proxy records from the PARCA cores document that climate reconstructions, including inferences about volcanic emissions from a single core should be interpreted cautiously with application of appropriate filters to reduce local noise, and careful extrapolations from local to regional scales. The
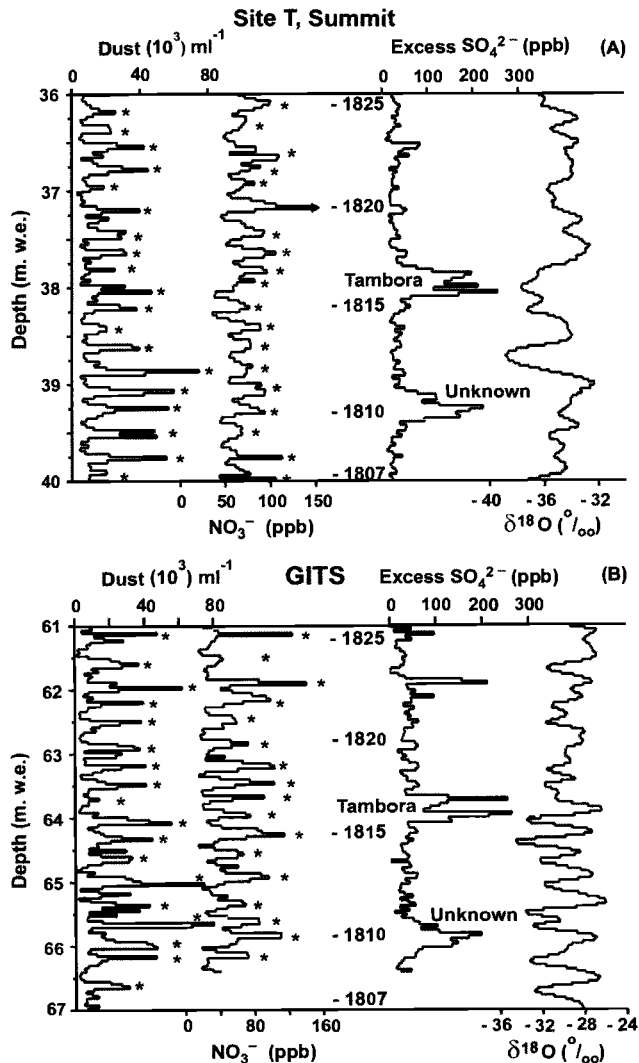
Figure 2. (A) Illustrated are the seasonal variations in dust, NO_3^-, and $\delta^{18}O$ used to date the entire Site T Core 2 and the SO_4^{2-} concentrations in the section of core containing the Tambora and Unknown eruptions; (B) The same four constituents are shown for the contemporaneous section of the GITS core that was dated using seasonal variations in dust, NO_3^-, $\delta^{18}O$, H_2O_2, and Ca^{2+}.
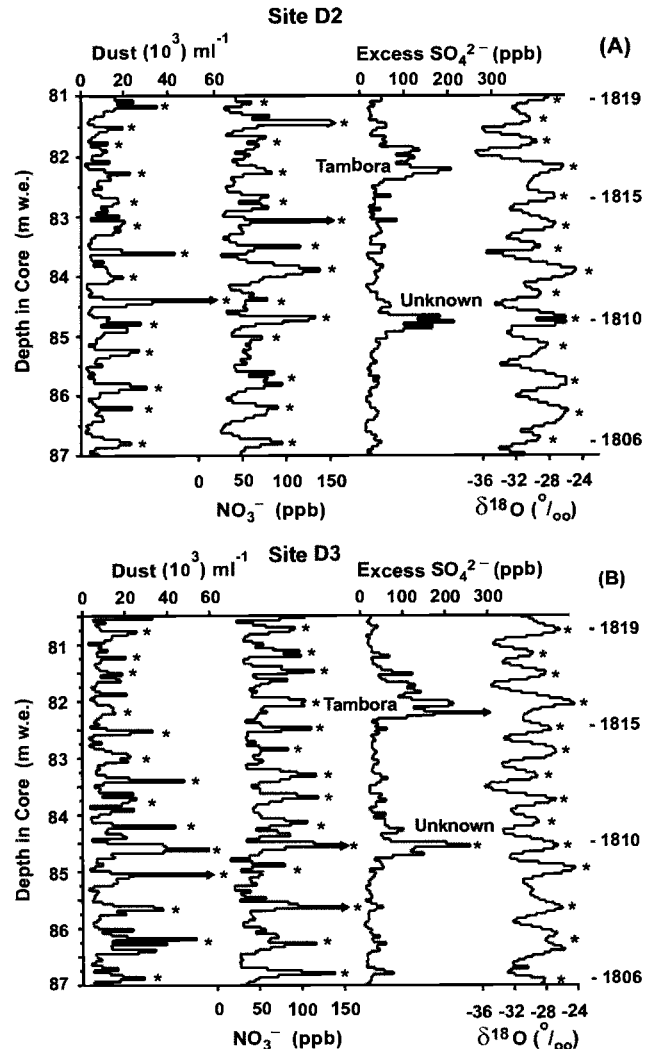
Figure 3. The seasonal variations in dust and $\delta^{18}O$ used to date both the D2 (A) and D3 (B) cores are shown along with the SO_4^{2-} and NO_3^- concentrations for the core sections containing the Tambora and Unknown eruptions.

data presented here represent our first results from an ongoing project to produce a complete (top to bottom), high resolution chemical characterization of five of the six multi-century PARCA cores, Humboldt, GITS, D3, D2 and Raven. These cores contain records extending back to 1153, 1717, 1745, 1740, and 1781 A.D., respectively. With the time scales firmly in hand, the SO_4^{2-} concentrations can be measured for sections of the cores containing known volcanic eruptions. Ultimately, the entire length of each core will be analyzed to isolate and identify all the volcanic horizons, including more modest eruptions, and to compare the timing and quantity of the volcanically derived sulfate

associated with individual events from site to site across Greenland.

3.1 Timing of the Unknown Pre-Tambora Eruption (1808 or1809?)

The PARCA cores allow the timing of the arrival of the volcanic sulfate associated with the unidentified pre-Tambora eruption (henceforth called Unknown) to be critically evaluated. The chemical analyses presented here were made by ion chromatographic analysis of samples that were cut from the core and then cleaned and melted under Class 100 clean room conditions. Details of the analytical method are described by Dai et al. [1995]. Based upon detailed chemical analysis of two cores, one from Siple Station in Antarctica and one from Site T in central Greenland, Dai et al. [1991] reported an explosive volcanic eruption in 1809 A.D. that does not appear in the historical records. As the eruption produced a sulfur rich plume that spread meridionally in the stratosphere to both polar regions the volcano is almost certainly located in the tropics. Dai et al. [1991] speculated that this event contributed to the decline in surface temperatures that preceded the eruption of Tambora in 1815 A.D. They concluded that the eruption occurred in 1809 A.D., one year prior to the 1810 A.D. arrival of the sulfate to both ice sheets, by assuming a one year delay in the arrival of sulfate at the poles similar to the delay observed for the emissions from the 1815 A.D. eruption of Tambora.

The timing of the ~1809 A.D. eruption has been questioned, primarily on the basis of the response of tropical marine air temperatures at this time [Chenoweth, 2001]. The only physical evidence for the (pre-Tambora) eruption comes from elevated sulfate layers preserved in both polar ice sheets [Dai et al., 1991; Clausen et al., 1997] and a climate response in both proxy and observed temperature records [Briffa et al., 1994, 1998; Chenoweth, 2001, respectively]. Briffa et al. [1994] used maximum late wood density as a proxy for summer temperatures across northern North America. They reported an extremely cold summer in 1810 A.D. (second or third coldest depending upon the predictor used). In their Northern Hemisphere composite (383 chronologies in 8 regions) 1810 A.D. ranks as the 15th and 49th coldest summer in their NHD2 and NHD1 chronologies, respectively [Briffa et al., 1998]. Recently, Chenoweth [2001] has suggested that the timing of the eruption is March to June of 1808 A.D., concurrent with a major cooling in two Malaysian observational land-based temperature records, and consistent with a maximum cooling of tropical marine air temperatures in 1808 A.D. Although the temperature response argument is intriguing, previously existing

ice core data point to an 1810 A.D. arrival of the excess sulfate on both Greenland and Antarctica, supporting an eruption date in 1809 A.D.

A brief review of the Greenland ice core data reveals that Clausen et al. [1997] report acidity peaks at 1816 and 1810 A.D. in the central Greenland GRIP core. They did not find the latter event in their Dye 3 core, but Langway et al. [1995] reported elevated sulfate in 1810 A.D. in their two cores from the Dye 3 area. Five Greenland cores from the southern half of the ice sheet (Crête, Dye 3-81, Dye 3-18C, see Langway et al., [1995]; GRIP, see Clausen et al., [1997], and Site T, see Figure 2A) contain sulfate deposited in 1810 A.D. However, the chicken and egg issue raised previously cannot be discounted as volcanic layers were often used to guide and adjust initial time scales based on $\delta^{18}O$ and dust in earlier cores. The reader is encouraged to review the dating details for each core.

Figure 2 (A, B) confirms that the sulfate from the Unknown event arrives at these two sites (central and northwest Greenland) in 1810 A.D., consistent with earlier results from cores in central and southern Greenland. Comparing Site T and GITS it is also evident that the peak flux of sulfate in 1810 A.D. in both cores is comparable to that arriving in 1816 A.D., one year after the eruption of Tambora. The difference is that the Tambora sulfate remains much higher in the second year (1817 A.D.) while the sulfate concentrations in 1811 A.D. return nearly to pre-eruption levels. Although providing strong support for sulfate arrival in 1810 A.D., the GITS and Summit sites are not ideal for such high resolution inspection of the depositional record. The low annual average accumulation at Summit (~ 220 mm a^{-1} w.e.) increases the potential for the mixing of consecutive layers, although that does not appear to be a problem in the Site T Core 2. The GITS site is closer to the coast and although it is much further north, it is prone to modest surface melting in summer. In some sections of the GITS core, pipes (indicating past conduits for percolating water) and sills (areas of meltwater ponding and refeezing) were recorded. This has the potential to disturb the record although Figure 2B shows no sign of disturbance and the visible stratigraphy for that section of core was free of melt signals (e.g., clear, bubble-free ice).

Two of the PARCA cores, Site D2 (71°45'N; 46°20' W) and Site D3 (69°48'N; 44°00'W), are ideally situated in a region of higher accumulation that is also very cold and dry. These cores provide the best evidence to date for the arrival of Unknown's volcanic sulfate in 1810 A.D. In fact, these data should put the issue to rest. The D2 and D3 cores (drilled in 1999, see Fig. 1 for locations) were analyzed from top to bottom for $\delta^{18}O$ and dust. The D2 core was cut

into 2542 samples each for dust and $\delta^{18}O$ while the D3 core was cut into 3027 samples for each parameter. The time scales for both cores were constructed by counting the very distinct annual layers in dust and $\delta^{18}O$ and the dating of the upper 47 years (post-1953) was confirmed by identification of beta radioactivity horizons associated with thermonuclear testing. These sites have the advantage of high annual average accumulation (D2: 424 and D3: 488 mm a^{-1} w.e.) and lie well into the cold, dry snow facies (D2: 2640 masl; D3: 2560 masl) as evidenced by the absence of melt features. Figures 3A, B leave little doubt that the sulfate associated with Unknown was deposited in 1810 A.D. snowfall over Greenland and that most of the sulfate was deposited in a single year. We conclude that it is very unlikely that the eruption occurred in March-June 1808 as suggested by Chenoweth [2001].

It is important to mention that confirmation of the arrival time of Unknown's volcanic sulfate to Antarctica rests solely on evidence from two cores from sites with sufficiently high accumulation rates to decipher and firmly date an annual event. These are the previously mentioned Siple Station and Dyer Plateau cores [Mosley-Thompson et al., 1991; Mosley-Thompson, 1992; Thompson et al., 1994]. Although emissions from Unknown have been found in other Antarctic cores, the lower accumulation rates at those sites lead to dating imprecision and enhanced likelihood of mixing with adjacent snow layers. Delmas et al. [1992] report elevated sulfate in 1810 A.D. at South Pole where the annual average accumulation today is 85 mm a^{-1} w.e. [Mosley-Thompson et al., 1999]. Langway et al. [1995] reported the same event as occurring in 1809 A.D. in their South Pole core and at 1811 A.D. in their 1989 core from Marie Byrd Land in West Antarctica (annual average accumulation reported as 100 mm a^{-1} w.e.). Clearly, low accumulation sites are not optimal for annual to sub-annual refinement of a depositional event.

3.2. Spatial Distribution of Excess Sulfate (EXS) Fluxes

Given the accurate dating of the PARCA cores discussed above, the annual flux of excess sulfate (EXS) to the ice sheet may be calculated for any volcanic event that has been chemically analyzed. As our preliminary analyses did not include cations (e.g., Na$^+$), the EXS reported here is calculated by subtracting the sea salt sulfate (SSS) determined by assuming that all of the Cl$^-$ is derived from the ocean. This is obviously not the case and sodium (Na$^+$) is generally used for that calculation. The imprecision introduced by using Cl$^-$ to calculate EXS depends upon the relative contribution of SSS to the total sulfate flux. Detailed chemical studies,

including analyses of most cationic and anionic species, are available for only a few Greenland cores, most notably GISP2 and GRIP in central Greenland. De Angelis et al. [1997] report that the bulk of the sodium measured along the GRIP core is marine in origin suggesting that Na$^+$ would be preferable to Cl$^-$ for estimating the marine contribution to the total SO$_4^{2-}$. Fortunately, use of Cl$^-$ does not introduce a large difference in the calculated EXS concentrations because sea-salt sulfate comprises only ~5% of the total sulfate flux in central Greenland snow [Legrand et al., 1997; Saltzman et al., 1997]. This was verified by analyzing a 4-meter section of both the D2 and D3 cores for both anions and cations and calculating EXS using both Na$^+$ and Cl$^-$. The differences (EXS$_{Cl}$ − EXS$_{Na}$) were 0.63 and −0.83 parts per billion (ppb) for D2 and D3, respectively and this is relative to their EXS$_{Na}$ averages of 26.4 and 24.2 ppb, respectively. The negative sign results from the SSS contribution to EXS and the small values imply that using Cl$^-$ rather than Na$^+$ makes virtually no difference (2.4% and 3.4% for D2 and D3, respectively). Thus, EXS concentrations reported here were calculated by subtracting from the total SO$_4^{2-}$ the SSS obtained by multiplying the Cl$^-$ concentration for each sample by the SO$_2^-$ / Cl$^-$ ratio in sea water (0.103). The remaining background concentration of EXS consists primarily of non-eruptive volcanic emissions and DMS emissions from marine biota [Legrand et al., 1997]. The SO$_4^{2-}$ derived from sulfur gases emitted by explosive volcanic eruptions will be superimposed as 'spikes' upon the more constant background EXS concentrations.

The annual EXS flux may be calculated by multiplying the EXS concentration in each sample by the sample's length in water equivalent and then adding all the sample fluxes for each year. The annual average background flux of non-volcanic EXS (Table 1) is calculated by averaging the non-volcanic years (excludes fluxes for 1817, 1816, 1811, and 1810 A.D. shown in Table 2). The time intervals for each background flux calculation are slightly different

Table 1. Average annual flux of background or 'non-volcanic' EXS and the average annual accumulation are shown for the time intervals indicated. Fluxes for 1817, 1816, 1811 and 1810 A.D. were removed.

Core	Time Interval	Annual Flux kg m^{-2}	Annual Accumulation mm w.e.
GITS	1825-1809	10.42	312
D2	1818-1806	12.06	424
D3	1819-1807	12.24	488
Site T	1822-1808	9.91	224
Raven	1819-1809	9.46	325

Table 2. Annual fluxes of excess sulfate in kg km^{-2} were determined at five Greenland sites for the eruptions of Tambora, Unknown and Laki. The calculations are described in the text.

Core	1817 kg m^{-2}	1816 kg m^{-2}	1811 kg m^{-2}	1810 kg m^{-2}	ratio 1810/ 1816	ratio 1811/ 1817	1784 kg m^{-2}	1783 kg m^{-2}
GITS	21.1	27.3	4.7	28.5	1.04	0.22	0.0	ua*
D2	21.4	30.9	6.0	32.0	1.04	0.28	0.0	222.0
D3	29.5	55.9	9.1	37.6	0.67	0.31	0.0	323.5
Site T	17.5	23.1	6.9	26.3	1.14	0.39	0.0	114.6
Raven	19.8	35.5	0.0	25.8	0.73	–	0.0	142.6
Average	21.9	34.5	6.7	30.0				
Humboldt	nm*	nm*	nm*	nm*			22.9	56.80
NASA-U	nm*	nm*	nm*	nm*			10.1	157.2

*nm means not measured and ua means unavailable. The section of the GITS core containing the Laki emissions was recovered in poor condition that made detailed (sub-annual) analysis impossible.

among the cores as only selected sections of the four PARCA cores have been chemically analyzed thus far. Few flux values are available for comparison as most Greenland sulfate fluxes have been calculated using either H$^+$ concentrations from ECM or acidity measurements and not SO$_4^{2-}$ analyses. As previously mentioned ECM measurements provide rapid estimates of acidity that can be compared to evaluate the relative abundance of volcanic aerosols associated with different eruptions. However, as discussed above in section 2.1 and by *Zielinski* [1995] the ECM signal also reflects other acids such as HNO$_3$, HF, and HCL so that the volcanic sulfate determined by ion chromatographic (IC) analyses provides a much better basis for estimating stratospheric sulfate loading. Therefore, the comparisons below include only sulfate fluxes based on SO$_4^{-2}$ concentrations from IC analyses.

Clausen et al. [1988] report background concentrations of H$_2$SO$_4$ (see their Table IV) associated with Laki (4 cores) that range from 6 to 11 kg km^{-2} and from 10 to 24 kg km^{-2} for Tambora at two sites. With one exception, 24 kg km^{-2}, their background fluxes (based on less than 3 years) are comparable to our SO$_4^{-2}$ fluxes (range: 9.5 to 12.24 kg km^{-2}) based on 11 to 17 years (Table 1). Plotting the average background EXS concentrations (Table 1) versus the average w.e. accumulation (for the same time interval) at each of our sites yields a linear relationship (R^2 = 0.753, significance = 94%) strongly suggesting that SO$_4^{-2}$ is deposited primarily by wet deposition (Fig. 4). A similar relationship was reported by *Legrand et al.* [1997, their figure 6] for both Antarctica and Greenland. Thus, the presence or absence of wet deposition at a site (i.e., whether it is snowing or not) contributes to the differences in EXS concentrations recorded from site to site for the same eruption.

The concentrations of background EXS for each core (Table 1) were subtracted from the annual EXS fluxes

associated with 1817, 1816, 1811, and 1810 A.D. to determine the EXS derived from Tambora and Unknown. The resulting annual fluxes (Fig. 5 and Table 2) confirm that EXS in 1816 is fairly constant among the sites except for the much higher concentration at D3. Figure 3B shows one sample with very high SO$_4^{2-}$ (344 ppb) in the Tambora horizon. The dispersion of the EXS flux among the sites is estimated by the ratio of the standard deviation (σ) to the mean (x) which is 0.33 and 0.15 for 1816 and 1810 A.D., respectively. The average EXS flux for all five cores is 34.5 kg km^{-2} a^{-1} in 1816 A.D. and 21.9 kg km^{-2} a^{-1} in 1817 A.D. The latter is ~64% of that deposited in 1816 A.D. By comparison, the average EXS flux in the second year following Unknown is much less, only ~22% of that in 1810 A.D. The average flux in 1810 (30 kg km^{-2} a^{-1}) was ~87%

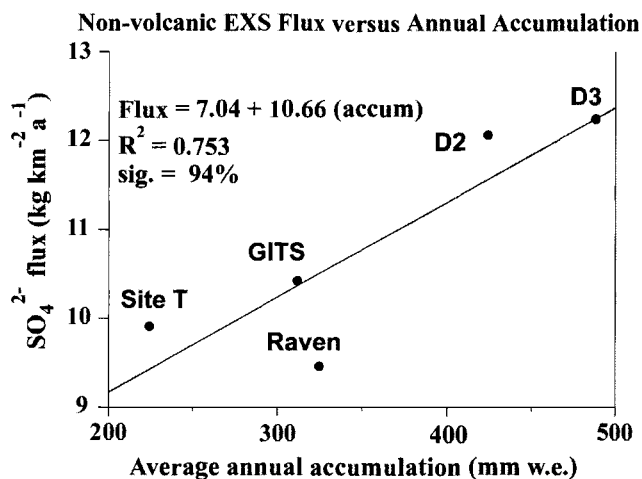**Non-volcanic EXS Flux versus Annual Accumulation**

Figure 4. A strong linear relationship exists between the annual average background (non-volcanic) EXS concentrations and the average annual net accumulation. The time interval for calculating the averages from the five different ice cores is shown in Table 1.

of that deposited in 1816, confirming that the stratospheric sulfate burden in 1810 was large and undoubtedly affected hemispheric surface temperatures [*Briffa et al.*, 1994, 1998], if not global temperatures. However, the much reduced EXS in 1811 A.D. suggests that Unknown is unlikely to have had a strong direct effect on surface temperatures in the following year.
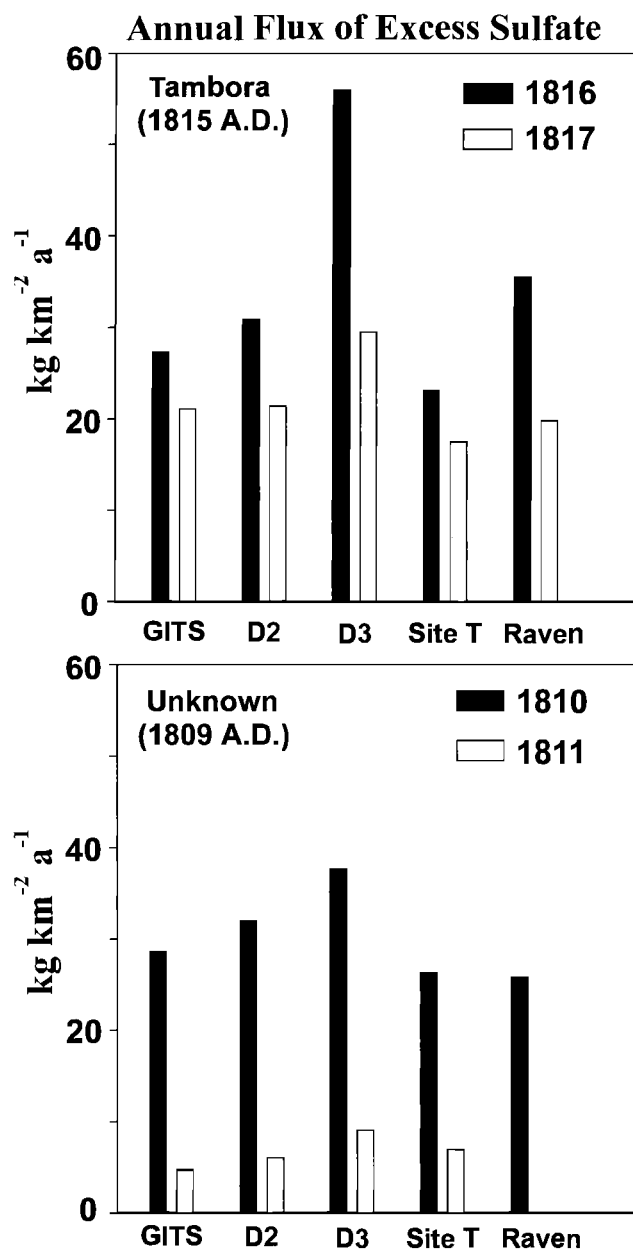

Figure 5. The annual fluxes of volcanically-derived EXS from Tambora and Unknown are compared for five Greenland ice core sites (locations shown in Fig. 1).
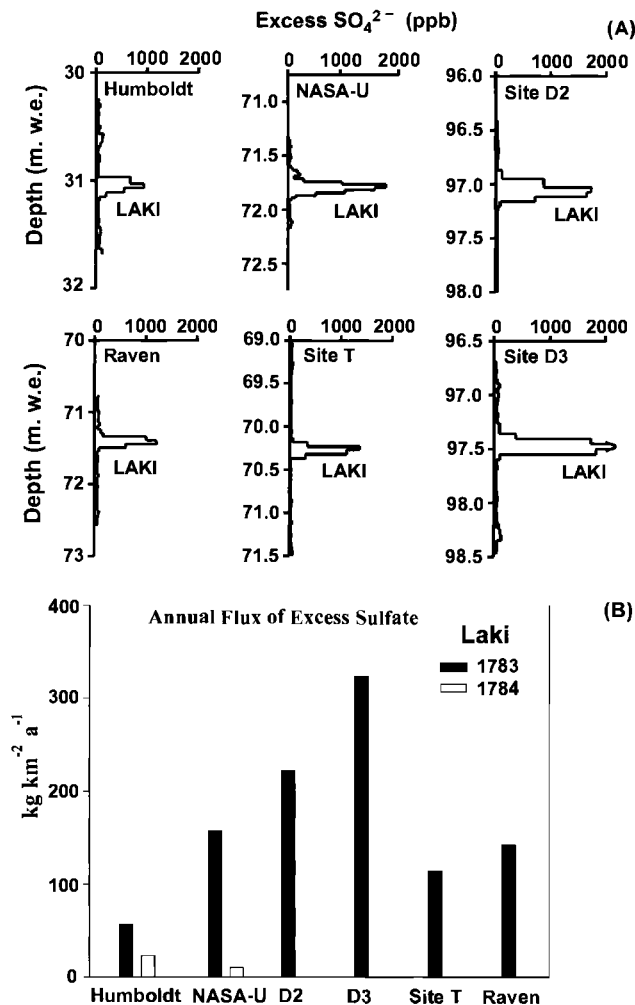
Figure 6. (A) The excess sulfate deposited at six Greenland ice core sites is shown before and after the eruption of Laki. (B) The annual flux of EXS deposited in 1783 and 1784 A.D. is compared for the six cores shown in (A).

The excess SO_4^{2-} and annual flux of EXS associated with the eruption of Laki (June 8, 1783 to February 7, 1784 A.D.) are shown in Figures 6A and 6B for four of the same cores as in Figure 5 plus the NASA-U and Humboldt cores (Fig. 1). The spatial distribution of the Laki fluxes (Fig. 6A,B) is more variable ($\sigma/x = 0.5$) than those for Tambora and Unknown ($\sigma/x = 0.33$ and 0.15, respectively). The SO_4^{2-} flux associated with Laki is similarly influenced by the rate of accumulation at the time of deposition (Fig. 7).

The EXS fluxes from Tambora and Laki can be compared for three different core sites (GRIP, GISP2 and Site T) in the Greenland Summit region. For the GRIP core *Clausen et al.* [1997] report volcanic acid deposition (principally sulfate)
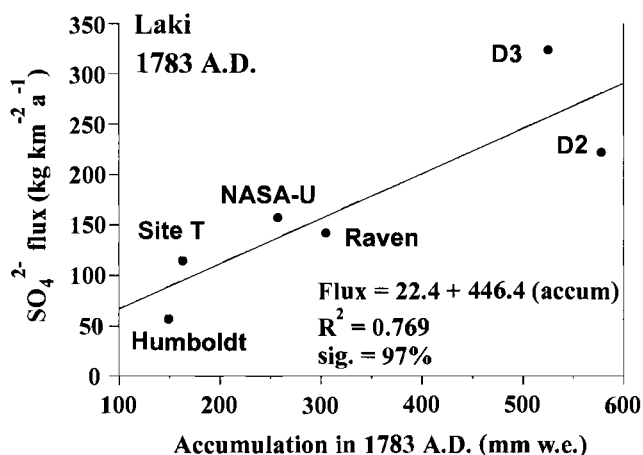
Figure 7. The strong linear dependence of the annual flux of EXS from the eruption of Laki and the annual average accumulation in that year is illustrated for six Greenland ice core sites (Fig. 1).

of 35, 25 and 147 kg km^{-2} for Tambora, Unknown and Laki, respectively. The comparable fluxes for Site T (Table 2) are 23.1 (1816), 17.5 (1817), 26.3 (1810), 6.9 (1811), and 114.6 kg m^{-2} (1783). These compare well although it is not clear whether their Tambora and Unknown fluxes are for just the first year post-eruption, or for both years post-eruption. A similar comparison is made with the *Zielinksi* [1995] fluxes from the GISP2 core from which he reports a total volcanic SO_4^{2-} flux (background removed) of 36 kg km^{-2} for the two year event. This compares well with our Site T total flux of 40.6 kg km^{-2} (Table 2, sum of 1816 and 1817 A.D.) for the Tambora eruption. Likewise, the GISP2 flux for Unknown compares well with the Site T flux (28 kg km^{-2} versus our 33.2 kg km^{-2}). The sulfate fluxes associated with Laki are much more variable among the three Summit cores. The GISP2 flux of 57 kg km^{-2} is significantly less than 114.6 kg km^{-2} deposited at Site T and both of these are less than 147 kg km^{-2} deposited at the GRIP site ~30 km east. The depositional differences in Laki sulfate could reflect a more variable (less well mixed) aerosol mass transported directly to the ice sheet via the troposphere over the 7 month duration of the eruption. As wet deposition is the primary mechanism for removal from the atmosphere, whether it is snowing at one site versus another as the aerosol mass transits the site could also affect the spatial differences. Although other explanations could be proposed it is likely that the overriding factor is the proximity of Laki to Greenland, versus the tropical locations of Tambora and Unknown that result in a much better mixed stratospheric volcanic aerosol mass.

The timing of the arrival of Laki sulfate has been assumed to be 1783 A.D., but *Fiocco et al.* [1994] have questioned this based upon their identification of glass shards from Laki that were found just below (preceding) the sulfate horizon in the GISP2 core (Summit). They suggest that the sulfate arrived in the summer and early fall of 1784, one year after the eruption. Since their result is based upon evidence from a single site where the low annual average accumulation (~220 mm a^{-1} w.e.) allows greater mixing of consecutive layers, their results must be viewed cautiously until confirmed in multiple cores at sites with higher accumulation rates.

The acidity layer associated with Laki has served as a cornerstone for nearly all Greenland ice core chronologies and has been routinely assigned to 1783 A.D.; therefore, the timing of the sulfate deposition must be independently verified as it has been for the Unknown eruption. This requires the analyses of multiple seasonally varying parameters, along with high resolution continuous anion and cation chemistry, over the entire section from 1820 A.D. down to 1780 A.D. in cores with higher accumulation and no melt disturbance. Only by such a methodical examination will the timing of the sulfate from Laki be firmly resolved. This has important implications for reconstructing the atmospheric transport pathway and sulfate distribution over the Northern Hemisphere following the eruption of Laki. The cores from PARCA sites D2 and D3 are ideal for testing the arrival of Laki sulfate and the existence of Laki ash and this investigation is now underway at Ohio State.

4. CONCLUSIONS

The anion analyses of the multi-century PARCA cores complement previous results that were more spatially restricted. These new data confirm that the sulfate aerosols from the unidentified pre-Tambora eruption called Unknown (1) were widely dispersed across the Greenland ice sheet, (2) first arrived in the 1810 A.D. snow fall, and (3) in the first year post-eruption (1810 A.D.) produced excess SO_4^{2-} concentrations comparable to those produced by Tambora in the first year post-eruption (1816 A.D.), but much less EXS in the second year post-eruption (1811 A.D.). There are more modest eruptions yet to be identified and still more for which the excess sulfate flux and its arrival time over Greenland need to be established. The annual resolution of multiple seasonally varying parameters in the PARCA multi-century cores will help resolve timing issues and their broad spatial distribution will provide a more spatially coherent estimate of the EXS flux associated with specific eruptions. These EXS estimates underpin calculations of the atmosphere's volcanic aerosol load that is a required input for modeling the climate system's range of responses to volcanic forcing. The PARCA multi-century cores will expand and refine the Northern

Hemisphere volcanic history and as similar records of equivalent temporal resolution from Antarctica become available, their combination will provide a richer, more detailed, and thus more climatologically valuable global history of explosive volcanism.

REFERENCES

Anklin, M., R. C. Bales, E. Mosley-Thompson, and K. Steffen, Annual accumulation at two sites in northwest Greenland during recent decades, *J. Geophys. Res., 103*, 28,775-28,783, 1998.

Bluth, G. J. S., S. D. Dorion, C. C. Schnetzler, and L.S. Walter, Global tracking of the SO_2 clouds from the June, 1991 Pinatubo eruptions, *Geophys. Res. Lett., 19*, 151-154, 1992.

Briffa, K. R., P. D. Jones, and F. H. Schweingruber, Summer temperatures across northern North America: Regional reconstructions from 1760 using tree-ring densities. *J. Geophys. Res., 99*, 25,835-25,844, 1994.

Briffa, K. R., P. D. Jones, F. H. Schweingruber, and T. J. Osborn, Influence of volcanic eruptions on northern hemisphere summer temperature over the past 600 years, *Nature, 393*, 450-455, 1998.

Chenoweth, M., Two major volcanic cooling episodes derived from global marine air temperature, A.D. 1807-1827, *Geophys. Res. Lett., 28*, 2963-2966, 2001.

Clausen, H. B., and C. U. Hammer, The Laki and Tambora eruptions as revealed in Greenland ice cores from 11 locations, *Ann. Glaciol., 10*, 16-22, 1988.

Clausen, H. B., C. U. Hammer, C. S. Hvidberg, D. Dahl-Jensen, J. P. Steffensen, J. Kipfstuhl, and M. Legrand, A comparison of the volcanic records over the past 4000 years from the Greenland Ice Core Project and Dye 3 Greenland ice cores, *J. Geophys. Res., 102*, 26707-26723, 1997.

Cole-Dai, J., E. Mosley-Thompson, and L. G. Thompson, Annually resolved Southern Hemisphere volcanic history from

two Antarctic ice cores, *J. Geophys. Res., 102*, 16,761-16,771, 1997.

Cole-Dai, J., E. Mosley-Thompson, S. P. Wight, and L. G. Thompson, A 4100-year record of explosive volcanism from an East Antarctica ice core, *J. Geophys. Res., 105*, 24,431-24,441, 2000.

Crowley, T. J., Causes of climate change over the past 1000 years, *Science, 289*, 270-277, 2000.

Crowley, T. J., and K.-Y. Kim, Modeling the temperature response to forced climate change over the last six centuries, *Geophys. Res. Lett., 25*, 1901-1904, 1999.

Dai, J., E. Mosley-Thompson, and L. G. Thompson, Ice core evidence for an explosive tropical volcanic eruption 6 years preceding Tambora, *J. Geophys. Res., 96*, 17361-17366, 1991.

Dai, J., L. G. Thompson, and E. Mosley-Thompson, A 485-year record of atmospheric chloride, nitrate and sulfate: results of chemical analysis of ice cores from Dyer Plateau, Antarctic Peninsula, *Ann. Glaciol., 21*,182-188, 1995.

De Angelis, M., J. P. Steffensen, M. Legrand, H. Clausen, and C. Hammer, Primary aerosol (sea salt and soil dust) deposited in Greenland ice during the last climatic cycle: Comparison with east Antarctic records, *J. Geophys. Res., 102*, 26,681-26,698, 1997.

Delmas, R. J., M. Legrand, A. J. Aristarain, and F. Zanolini, Volcanic deposits in Antarctic snow and ice, *J. Geophys. Res., 90*, 12,901-12,920, 1985.

Delmas, R. J., S. Kirchner, J. M. Palais, and J. R. Petit, 1000 years of explosive volcanism recorded at the South Pole, *Tellus, 44B*, 335-350, 1992.

Fiacco, Jr., R. J., T. Thordarsson, M. S. Germani, S. Self, J. M. Palais, S. Whitlow, and P. M. Grootes, Atmospheric aerosol loading and transport due to the 1783-84 Laki Eruption in Iceland, Interpreted from ash particle and acidity in the GISP2 ice core, *Quat. Res., 42*, 231-240, 1994.

Fuhrer, K., A. Neftel, M. Anklin, and V. Maggi, Continuous measurements of hydrogen peroxide, formaldehyde, calcium and ammonium concentrations along the new GRIP ice core from Summit, central Greenland, *Atmos. Environ., 27*, 1873-1880, 1993.

Gow, A. J., On the accumulation and seasonal stratification of snow at the South Pole, *J. Glaciol., 5*, 467-477, 1965.

Gow, A. J. and, T. Williamson, Volcanic ash in the Antarctic Ice Sheet and its possible climatic implications. *Earth Planet. Sc. Lett., 13*, 210-218, 1971.

Hammer, C. U., Past volcanism revealed by Greenland ice sheet impurities, *Nature, 270*, 482-486, 1977.

Hammer, C. U., Dating by physical and chemical seasonal variation and reference horizons, in *The Environmental Record in Glaciers and Ice Sheets*, edited by H. Oeschger and C. C. Langway, Jr., pp. 99-121, Wiley and Sons Chichester, New York, 1989.

Hammer, C. U., H. B. Clausen, W. Dansgaard, N. Gundestrup, S. J. Johnsen, and N. Reeh, Dating of Greenland ice cores by flow models, isotopes, volcanic debris and continental dust, *J. Glaciol., 20*, 3-26, 1978.

Hammer, C. U., H. B. Clausen, and W. Dansgaard, Greenland ice sheet evidence of post-glacial volcanism and its climatic impact, *Nature, 288*, 230-235, 1980.

Harvey, D. L. D., Climatic impact of ice-age aerosols, *Nature, 334*, 333-335, 1988.

Johnsen, S. J., Stable isotope homogenization of polar firn and ice, in *Isotopes and Impurities in Snow and Ice, IAHS AISH Publ., 118*, 210-219, 1977.

Johnsen, S. J., H. B. Clausen, K. M. Cuffey, G. Hoffmann, J. Schwander, and T. Creyts, Diffusion of stable isotopes in polar firn and ice; the isotope effect in firn diffusion, in *Physics of Ice Core Records*, edited by T. Hondoh, pp. 121-140, Hokkaido University Press, Sapporo, 2000.

Kyle, P. R., P. A. Jezek, E. Mosley-Thompson, and L. G. Thompson, Tephra layers in the Byrd Station ice core and the Dome-C ice core, Antarctica and their climatic importance. *J. Volcanol. Geoth. Res., 11*, 29-39, 1981.

Langway, Jr., C. C., K. Osada, H. B. Clausen, C. U. Hammer, and H. Shoji, A 10-century comparison of prominent bipolar volcanic events in ice cores, *J. Geophys. Res., 100*, 16,241-16,247, 1995.

Legrand, M., C. Hammer, M. De Angelis, J. Savarino, R. Delmas, H. Clausen, and S. J. Johnsen, Sulfur-containing species (methanesulfonate and SO_4) over the last climatic cycle in the Greenland Ice Core project (central Greenland) ice core, *J. Geophys. Res., 102*, 26,663-26,679, 1997.

Mosley-Thompson, E., Paleoenvironmental conditions in Antarctica since A.D. 1500, in *Climate Since A.D. 1500*, edited by R. A. Bradley and P. D. Jones, pp. 572-591, Routledge, London, 1992.

Mosley-Thompson, E., Holocene climate changes recorded in an East Antarctica ice core, in *Climatic Variations and Forcing Mechanisms of the Last 2000 Years*, edited by J. D. Jones, R. A. Bradley, and J. Jouzel, pp. 263-279, Springer-Verlag, Berlin, 1996.

Mosley-Thompson, E., P. D. Kruss, L. G. Thompson, M. Pourchet, and P. Grootes, Snow stratigraphic record at South Pole: Potential for paleoclimatic reconstruction, *Ann. Glaciol., 7*, 26-33, 1985.

Mosley-Thompson, E., J. Dai, L. G. Thompson, P. M. Grootes, J. K. Arbogast, and J. F. Paskievitch, Glaciological studies at Siple Station (Antarctica): potential ice-core paleoclimatic record, *J. Glaciol., 37*, 11-22, 1991.

Mosley-Thompson, E., J.F. Paskievitch, A.J. Gow, and L.G. Thompson, Late 20th Century increase in South Pole snow accumulation, *J. Geophys. Res., 104*, 3977-3886, 1999.

Mosley-Thompson, E., J. R. McConnell, R. C. Bales, Z. Li, P.-N. Lin, K. Steffen, L. G. Thompson, R. Edwards, and D. Bathke, Local to regional-scale variability of annual net accumulation on the Greenland ice sheet from PARCA cores, *J. Geophys. Res., 106*, 33,839-33,851, 2001.

Pomeroy, J. W., and H. G. Jones, Wind-blown snow: sublimation, transport and changes to polar snow, in *Chemical Exchanges between the Atmosphere and Polar Snow*, edited by E. W. Wolff and R. C. Bales, pp. 453-489, NATO ASI Series, Vol. I 43, Springer Verlag, Berlin, 1996.

Robock, A. Volcanic eruptions and climate, *Rev. Geophys., 38*, 191-219, 2000.

Robock, A., and M. P. Free, Ice cores as an index of global volcanism from 1850 to the present, *J. Geophys. Res., 100*, 11,549-11,567, 1995.

Saltzman, E. S., P.-Y. Whung, and P. A. Mayewski,Methane-sulfonate in the Greenland Ice Sheet Project 2 ice core, *J. Geophys. Res., 102*, 26,649-26,657, 1997.

Taylor, K. C., R. B. Alley, G. W. Lamorey, and P. A. Mayewski, Electrical measurements on the Greenland Ice Sheet Project 2 core, *J. Geophys. Res., 102*, 26,511-26,517, 1997.

Thomas, R. H. and PARCA Investigators, Program for Arctic Regional Climate Assessment (PARCA): Goals, key findings, and future directions, *J. Geophys. Res., 106* (D24), 33,691-33,705, 2001.

Thompson, L. G., D. A. Peel, E. Mosley-Thompson, R. Mulvaney, J. Dai, P.-N. Lin, M. E. Davis, and C. F. Raymond, Climate since AD 1510 on Dyer Plateau, Antarctic Peninsula: evidence for recent climate change, *Ann. Glaciol., 20*, 420-426, 1994.

Trepte, C. R., R. E. Veiga, and M. P. McCormick, The poleward dispersal of Mt. Pinatubo volcanic aerosol, *J. Geophys. Res., 98*, 18,563-18,573, 1993.

Wolff, E. W., J. C. Moore, H. B. Clausen, and C. U. Hammer, Climatic implications of background acidity and other chemistry derived from the electrical studies of the Greenland Ice Core Project ice core, *J. Geophys. Res., 102*, (C12), 26,325-26,332, 1997.

Zielinski, G., Stratospheric loading and optical depth estimates of explosive volcanism over the last 2100 years derived from the GISP2 Greenland ice core, *J. Geophys. Res., 100*, 20,937-20,955, 1995.

Zielinski, G., Use of paleo-records in determining variability within the volcanism-climate system, *Quat. Sci. Rev., 19*, 417-438, 2000.

Zielinksi, G., P. A. Mayewski, L. D. Meeker, K. Grönvold, M. S. Germani, S. Whitlow, M. S. Twickler, and K. Taylor, Volcanic aerosol records and tephrochronology of the Summit, Greenland, ice cores, *J. Geophys. Res., 102*, 26,625-26,640, 1997.

Tracy A. Mashiotta, Byrd Polar Research Center, 108 Scott Hall, 1090 Carmack Road, The Ohio State University, Columbus, OH 43210.

Ellen Mosley-Thompson, Byrd Polar Research Center, 108 Scott Hall, 1090 Carmack Road, The Ohio State University, Columbus, OH 43210.

Lonnie G. Thompson, Byrd Polar Research Center, 108 Scott Hall, 1090 Carmack Road, The Ohio State University, Columbus, OH 43210.

The Number and Magnitude of Large Explosive Volcanic Eruptions Between 904 and 1865 A.D.: Quantitative Evidence From a New South Pole Ice Core

Drew Budner and Jihong Cole-Dai

Department of Chemistry and Biochemistry, South Dakota State University, Brookings, South Dakota

A new volcanic record covering the period of 904 to 1865 A.D. was produced from continuous chemical analysis of a 2001 South Pole ice core. This new record is consistent with previous records in the number and dates of large volcanic events. The relative magnitudes of several prominent events in this new record were compared to the same events in previous records from South Pole and Plateau Remote (East Antarctica) ice cores. The comparison demonstrates that the discrepancies in reported magnitudes of these events are probably a result of the glaciological complications at Plateau Remote, and that volcanic deposit or flux measurements from South Pole ice cores are therefore more reliable parameters of the atmospheric mass loadings of volcanic aerosols. The new record also confirms the previous finding that five large or moderately large volcanic eruptions occurred in the 13th century. The total atmospheric aerosol mass loadings, inferred from volcanic sulfate flux in this new ice core, from these five eruptions appear to be 3 to 20 times those in other centuries during the last millennium, suggesting a significant role by explosive volcanism in the climatic transition from the Medieval Warm Period to the Little Ice Age.

1. INTRODUCTION

Explosive volcanic eruptions inject large amounts of dust and gaseous materials into the atmosphere. The major component of the injected gas is sulfur dioxide which is rapidly oxidized in the atmosphere to sulfuric acid. The resulting aerosol particles of sulfuric acid and water can reside for months to several years in the stratosphere where they are distributed throughout a hemisphere or globally by atmospheric circulation. Generally, aerosols from large explosive volcanic eruptions at the low latitudes (between 0° and 20°) of either hemisphere are capable of global distribution via the stratosphere. Elevated aerosol concentrations in the stratosphere increase the atmospheric aerosol optical depth, thereby altering the atmospheric albedo and reducing the radiation receipt at the Earth's surface. Therefore, atmospheric perturbation from large volcanic eruptions can have a significant impact on the climate and the magnitude of the impact is believed to be related to the volcanic aerosol mass loadings [*Robock*, 2000; *Zielinski*, 1995; 2000]. This climatic impact can be viewed within two timeframes: short term (up to five years after the initial perturbation) and long term. The short-term, immediate effects of explosive eruptions on climate have been well studied and well documented [*Rampino and Self*, 1982; *Robock*, 2000; *Robock and Mao*, 1995; *White et al.*, 1997]. The long term, cumulative impact of sustained explosive volcanic activities with frequent injections of large amounts of fresh sulfur aerosols during a period of a few decades has not been explored, although it has been speculated [*Briffa et al.*,

1998; *Zielinski*, 2000]. Recent observations [*Barnes and Hoffmann*, 2001; *Hervig and Deshler*, 2002] show that global stratospheric aerosols have declined continuously since 1991 when the Pinatubo eruption introduced massive amounts of volcanic aerosols into the stratosphere, indicating that volcanic aerosols linger in the stratosphere long past the period of the short-term and apparent climatic impact. This suggests that stratospheric residence times of volcanic aerosols are probably longer than previously thought and frequent injection of volcanic aerosols within a few decades could have a greater impact on climate than the short-term effects of individual volcanic eruptions.

Sulfuric acid or sulfate aerosols of volcanic origin, along with other trace atmospheric species, are deposited in the Antarctic continent with snowfall. The continuous snow accumulation creates and preserves records of variations in atmospheric composition and sources of atmospheric components, including those from explosive volcanic eruptions [*Delmas et al.*, 1985; *Legrand et al.*, 1984]. Chemical analysis for acidity or sulfate concentration of ice cores drilled in Antarctica can therefore provide chronological and continuous records of explosive volcanic eruptions dating back thousands of years. Several volcanic records from Antarctic ice cores are available [*Cole-Dai et al.*, 2000; *Delmas et al.*, 1992; *Langway et al.*, 1995; *Legrand and Delmas*, 1987; *Palmer et al.*, 2001]. These records document in detail the chronological history of explosive volcanism over the last several millennia that may have had a significant impact on atmospheric chemical composition and the climatic system. Due to the atmospheric circulation patterns, the volcanic aerosols deposited in Antarctica originate either from high southern latitude (Antarctic continent and subantarctic islands) and mid southern latitude (South America and the South Pacific) eruptions or from large eruptions in low latitudes of either hemisphere. As a result, volcanic records from Antarctic ice cores in general cover volcanoes in the Southern Hemisphere and the low latitudes.

Antarctic ice core volcanic records may differ in a number of aspects: length of time covered, temporal resolution, method of analysis, definition of nonvolcanic background and volcanic detection threshold. Therefore, climatic interpretation of ice core volcanic records may depend on specific records used. In presenting a 4100 year ice core record (PR86) from a location (Plateau Remote, 84°S, 43°E) in East Antarctica, *Cole-Dai et al.* [2000] recently compared that record with several other existing records and summarized the similarities and differences among the records. In particular, the PR86 record was compared with the 1000 year record (SP84) compiled from two South Pole cores

[*Delmas et al.*, 1992]. These two records have several similarities: (1) the cores are from locations in central East Antarctica where snow accumulation rates are low, (2) both are based on continuous examination of the core and detailed sulfate analysis, and (3) a similar definition of the volcanic threshold is used. *Cole-Dai et al.* [2000] concluded from the comparison that in terms of the number and dates of large eruptions in the last 1000 years, the two records are consistent with each other. However, significant discrepancies among the records were found in relative magnitudes of volcanic signals. For example, volcanic sulfate deposit of the 1259 A.D. Unknown eruption in SP84 is significantly larger than that of a large eruption in the 1450s (assumed to be a massive eruption of Kuwae in the South Pacific), whereas in the PR86 record the Kuwae eruption has the largest volcanic sulfate deposit and sulfate concentration during the last 1000 years. Another significant difference between SP84 and PR86 is the number of eruptions in the 13th century: *Delmas et al.* [1992] found only three volcanic eruptions, while *Cole-Dai et al.* [2000] reported five eruptions during the same time period.

Cole-Dai et al. [2000] speculated that the discrepancies between SP84 and PR86 may be due to the extremely low snow accumulation rate at Plateau Remote and significant surface snow redistribution after deposition may have affected the preservation of the volcanic chronology at that location. The mean annual accumulation at the Plateau Remote site is approximately 10 cm snow per year, while the average height of sastrugi (surface undulations) is up to 40 cm. Snow deposition at a given spot (e.g., at a sastrugi peak) could be lost to valleys on the snow surface for up to 4 or 5 years [*Cole-Dai et al.*, 2000]. The magnitude of surface snow redistribution at South Pole is considered much less, where the snow accumulation rate is higher (averaging 20 cm snow per year) [*van der Veen et al.*, 1999] and the snow surface is smoother. Another possible cause of the discrepancies may be the somewhat different analytical approaches used to reconstruct the SP84 and PR86 records. *Cole-Dai et al.* [2000] suggested that the discrepancies may be resolved by a study of additional ice cores from South Pole, using an approach similar to that used in the Plateau Remote study.

A pair of recent, intermediate-depth ice cores from South Pole offered an opportunity to produce a new volcanic record that can be compared with the previous volcanic records in an attempt to resolve these discrepancies. Using a methodology similar to those in our previous studies [*Cole-Dai et al.*, 1997a; 2000], we have constructed and hereby present a new ice core volcanic record covering the last 1000 years.

2. ICE CORE SAMPLING AND ANALYSIS

In the austral summer of 2000/2001 two ice cores were drilled to a depth of 123 m at the Amundsen-Scott South Pole Station, Antarctica. For this study one of the cores (Core 1) was sampled continuously from the depth of 25 m to the bottom. This portion of the core was chosen to focus on the older part of the ice cores, as there have been numerous studies [*Cole-Dai and Mosley-Thompson*, 1999; *Cole-Dai et al.*, 1997b; *Delmas et al.*, 1992; *Dibb and Whitlow*, 1996] from previous South Pole ice cores covering the most recent 200 years (to depth of approximately 40 m). Core sampling was performed at the US National Ice Core Laboratory in Denver, Colorado, using stringent contamination control procedures [*Cole-Dai et al.*, 1995]. A total of 3966 samples were produced for the 25–123 m part of Core 1, resulting in an average of 2.5 cm per sample. The samples were melted in sealed containers on a clean-air bench, and analyzed in the Ice Core and Environmental Chemistry Laboratory of South Dakota State University. Two Dionex DX600 ion chromatographs were used for anion and cation measurements. The cations (Na^+, NH_4^+, K^+, Mg^{2+}, and Ca^{2+}) were separated on a Dionex IonPac CS12A column with an isocratic 15 mM sulfuric acid eluent. The anions (F^-, CH_3COO^-, $HCOO^-$, MSA^-, Cl^-, NO_3^-, and SO_4^{2-}) were separated using a gradient elution of 0.75 mM to 9 mM NaOH on an IonPac AS11 column.

3. RESULTS

3.1. Sulfate Profile

Sulfate concentrations in the 3966 samples were plotted as a function of core depth in Figure 1. Although it was possible to calculate and remove non-sea-salt sulfate concentrations, we chose to make no distinction between total sulfate and non-sea-salt sulfate in this study, as previous work at South Pole has shown that greater than 95% of the sulfate in snow originates from sources other than sea salt [*Cole-Dai and Mosley-Thompson*, 1999; *Cole-Dai et al.*, 1997b]. Large concentration spikes in the depth profile were likely from volcanic eruptions and are therefore removed from the dataset when the average and standard deviation of the non-volcanic background (discussed later) sulfate concentration were calculated.

3.2. Core Dating and Error Estimates

Snow accumulation at South Pole is approximately 20 cm per year [*Cole-Dai and Mosley-Thomspon*, 1999; *van der*
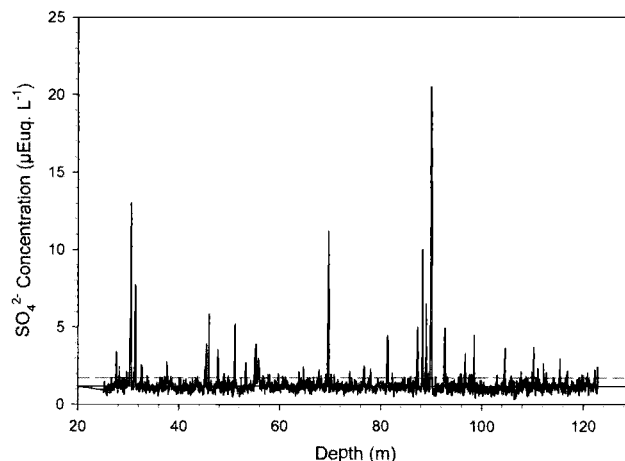
Figure 1. Continuous profile of sulfate concentration (μEqu. kg^{-1}) in the South Pole core (SP2001) as a function of depth. The solid line indicates the nonvolcanic background (1.13 μEqu. kg^{-1}) and the dashed line represents the volcanic detection threshold (1.67 μEqu. kg^{-1}).

Veen et al., 1999]. Annual layer thickness decreases with depth, as density increases, to around 10 cm at the bottom of the 123 m core. At 2.5 cm per sample, a temporal resolution of 8 (top of core) to 4 (bottom) samples per year was achieved for chemical analysis. No visible stratigraphy was observed or recorded in this study; however, the sampling resolution permits dating by annual layer counting using chemical species with seasonal variations. Detailed snow chemical analysis in previous work [*Cole-Dai and Mosley-Thompson*, 1999; *Dibb and Whitlow*, 1996; *Legrand et al.*, 1984] has shown that concentrations of several species exhibit annual or seasonal cycles. For example, Na^+, Cl^- and Mg^{2+} (all major components of sea salts) reach a maximum in winter snow at South Pole and a minimum in summer [*Cole-Dai and Mosley-Thompson*, 1999]. Aerosol studies at coastal Antarctic locations [*Wagenbach et al.*, 1998] also indicate that sea salts in air are most abundant during winter, rather than in the summer/fall season. Figure 2 demonstrates that Na^+ annual cycles are easily identified in this new South Pole core and these cycles are therefore used to date the core. An annual layer or a year is approximated as from Na^+ minimum to minimum (Figure 2), corresponding to a calendar year, for the Na^+ minimum occurs in summer (December–January).

Since the analysis did not begin at the top of the core, an alternative starting point with a known age was needed for counting annual layers. Two large volcanic signals in the sulfate record were found at 30.4 and 31.3 m (Figure 2) and were presumed to correspond to the Tambora eruption of
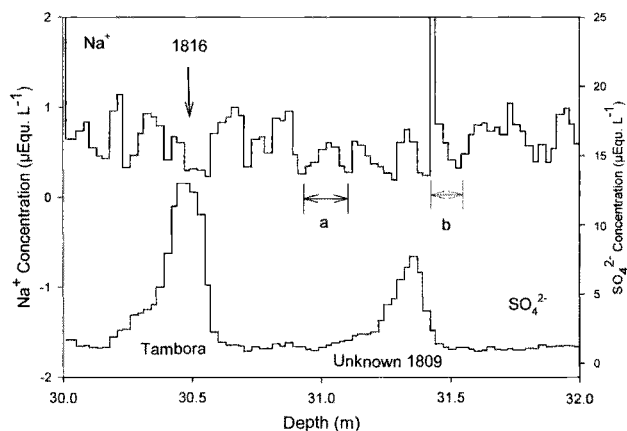
Figure 2. Sodium concentration (top profile) and sulfate concentration (bottom profile) as a function of depth for part of Core 1. The Na^+ profile was used to date the ice core. Ranges *a* and *b* are examples of single annual cycles. The peak of the 1816 Tambora sulfate at 30.44 m was used as the starting point of dating by layer counting.

1815 and the unknown eruption of 1809. This doublet has been well documented and dated in all previous ice cores from Antarctica [*Cole-Dai et al.*, 1997a; *Cole-Dai et al.*, 2000; *Cole-Dai et al.*, 1995; *Delmas et al.*, 1992; *Langway et al.*, 1995; *Legrand and Delmas*, 1987; *Palmer et al.*, 2001]. The peak deposition of the Tambora volcanic aerosols in Antarctic ice cores is most commonly dated at 1816. Therefore, the depth at the peak of the Tambora sulfate signal is assigned the year of 1816. The depth corresponding to this maximum is then the starting point for counting Na^+ annual cycles (Figure 2) in either direction. This dating was reinforced by a concurrent examination of the annual Mg^{2+} cycles (not shown) and by the dates of several well-known, and well-dated volcanic events (e.g., the 1600 Huaynaputina eruption, the Kuwae eruption in the 1450's and the 1259 Unknown eruption) in Antarctic ice cores. Through this portion of the core the dating error is ±4 years, which is attributed to the number of ambiguous annual cycles. The top of this portion (25 m) was dated at 1865 A.D. and the bottom of the core was dated at 904 A.D.

3.3. Criteria for Detection of Volcanic Signals

Volcanism is only one of several sources of sulfur species in Antarctic snow. Sulfate from non-volcanic sources constitutes background concentrations on which the sulfate from volcanic eruptions is superimposed. Therefore, to detect the presence of volcanic sulfate, the background must be quantified and a detection threshold for volcanic signals established. The background is usual-

ly established by computing the average sulfate concentration for long periods when no volcanic inputs are expected. Calculations using all available sulfate concentration data yielded an average nonvolcanic background of 1.13 µEqu. kg⁻¹ (solid line in Figure 1) and a standard deviation of 0.27 µEqu. kg⁻¹. These values are consistent with previously reported average and variations of background sulfate in South Pole snow (e.g., 1.12±0.26 µEqu. kg⁻¹ by *Cole-Dai and Mosley-Thompson* [1999]; 1.14±0.24 µEqu. kg⁻¹ by *Delmas et al.* [1992]). For this work the volcanic threshold will be as defined by *Cole-Dai et al.* [2000], i.e., the average nonvolcanic sulfate concentration plus two standard deviations (dashed line in Figure 1). This definition, with the assumption of a Gaussian distribution of the variable nonvolcanic, background sulfate concentrations, still leaves a 4.5% probability that a spurious, high background concentration may be detected as a volcanic signal. To reduce this possibility of false positive detection from a single sample with high background sulfate concentration, a second criterion was used by *Cole-Dai et al.* [2000], namely that the sulfate concentration must be elevated above this threshold for at least two consecutive samples. This second criterion is also adopted in this work. Using these criteria, we found 33 events within this portion (25–123 m) of the core. A complete list of the events is shown in Table 1. The events are numbered in order of their appearance in the core and will be referred to by these numbers in the following discussions. The date and duration of each event in Table 1 have been determined following the procedures developed and discussed by *Cole-Dai et al.* [1997a; 2000].

3.4. Volcanic Flux

The volcanic sulfate flux is defined as the total amount (in mass unit per unit area) of volcanic sulfate from an eruption deposited in Antarctic snow. The length of time associated with the volcanic flux is the duration (in number of years) in which the deposition took place (Table 1). Following the procedures used by *Cole-Dai et al.* [1997a; 2000], the volcanic flux for each event detected in this new South Pole core has been calculated and is presented in Table 1.

In general, the ice core volcanic flux of an eruption reflects the magnitude or atmospheric aerosol (sulfur dioxide or sulfuric acid) mass loading by that eruption, i.e., the larger the volcanic flux, the greater the atmospheric mass loading [*Zielinski*, 1995]. However, it is important to recognize that the volcanic flux of an eruption in polar snow is also related to the latitude of the source volcano [*Dai et al.*, 1991; *Delmas et al.*, 1985; *Langway et al.*, 1995]. For exam-

Table 1. Volcanic events found between 25 m and 123 m of a 2001 ice core from South Pole, Antarctica. Identification of volcanic eruptions is based on dates of events in core and magnitude (volcanic flux) of the signals and on comparison with previous ice core records. Determination of date/year and duration follows procedures by *Cole-Dai et al.* [2000]. The f/f$_T$ is defined as the flux of the event divided by the flux of the Tambora event.

Volcanic Eruption	Event	Year A.D.	Duration, years	Depth in core, m	Peak Sulfate, μg kg^{-1}	Volcanic Flux f, kg km^{-2}	f/f$_T$
Coseguina	SP2001-1	1842	2.8	27.61	164	9.72	0.15
	SP2001-2	1837	2.1	28.20	115	3.53	0.06
Tambora	SP2001-3	1816	3.8	30.44	626	64.01	1.00
Unknown 1809	SP2001-4	1809	2.4	31.37	371	28.04	0.44
	SP2001-5	1800	1.2	32.78	114	2.38	0.04
	SP2001-6	1759	2.6	37.65	130	5.89	0.09
	SP2001-7	1694	2.3	45.07	106	2.21	0.03
	SP2001-8	1691	3.6	45.45	293	22.17	0.35
	SP2001-9	1668	2.3	47.65	135	9.02	0.14
Parker & Deception Island	SP2001-10	1636	3.5	51.06	249	19.88	0.31
	SP2001-11	1618	2.3	53.27	130	6.54	0.10
Huaynaputina	SP2001-12	1600	3.5	55.28	185	22.98	0.36
	SP2001-13	1596	3.4	55.87	135	14.80	0.23
	SP2001-14	1508	1.6	64.67	115	0.85	0.01
Kuwae	SP2001-15	1458	4.5	69.58	537	65.55	1.02
	SP2001-16	1422	1.1	73.86	101	1.96	0.03
	SP2001-17	1396	2.3	76.70	119	5.80	0.09
	SP2001-18	1383	2.7	78.02	110	4.06	0.06
	SP2001-19	1347	3.1	81.37	214	25.46	0.40
	SP2001-20	1287	3.5	87.27	240	24.31	0.38
	SP2001-21	1276	3.3	88.23	481	45.37	0.71
	SP2001-22	1270	2.1	88.94	310	19.93	0.31
Unknown/ 1259	SP2001-23	1260	4.7	89.96	985	179.45	2.80
	SP2001-24	1236	2.8	92.66	236	26.60	0.420
	SP2001-25	1195	3.1	96.72	158	13.22	0.21
	SP2001-26	1174	1.8	98.48	215	15.69	0.25
	SP2001-27	1113	2.1	104.57	175	11.45	0.18
	SP2001-28	1094	1.0	110.21	178	8.94	0.14
	SP2001-29	1083	1.0	111.09	111	3.53	0.06
	SP2001-30	983	1.1	115.43	142	6.71	0.10
	SP2001-31	966	1.2	116.89	104	6.24	0.10
	SP2001-32	911	1.1	122.30	108	5.02	0.08
	SP2001-33	905	1.5	122.86	116	4.33	0.07

ple, an eruption in the Antarctic or subantarctic region will have a larger flux than an equivalent event originating from a low latitude location due to the loss of volcanic aerosols during transport from the low latitudes. Therefore, direct comparison and discussion of the magnitudes or mass loadings of explosive eruptions based on ice core data are only applicable to eruptions originating from the same latitude region (e.g., low latitude eruptions).

On the other hand, the volcanic flux of a particular eruption varies from location to location where the ice core is obtained, as the depositional flux is highly dependent on such parameters as scavenging efficiency and snow accu-

mulation rates which have significant spatial variations across the Antarctic continent. In general, the unique high latitude circulation pattern (i.e., the polar vortex) helps distribute stratospheric volcanic aerosols all over Antarctica. As a result, a non-Antarctica eruption can be found in ice cores across the continent. For example, the Pinatubo signal has been found in snow and ice cores from more than 5 East Antarctica locations, although the signal is too weak, in comparison to fluctuations of the nonvolcanic background, to be detected at a few West Antarctica sites (*Cole-Dai*, unpublished data). To compare volcanic flux data between ice cores of different locations, *Cole-Dai et al.* [1997a] pro-

posed a relative scale to measure the signal magnitude of volcanic eruptions in ice cores, based on the assumption that location-specific effects are minimized when the volcanic flux (f) of an event is normalized against that of a well-known event, i.e., the 1815 Tambora eruption (f_T). Consequently, the normalized volcanic flux (f/f_T) of all detected events in the new South Pole core has been calculated and is also included in Table 1.

In essence, Table 1 summarizes the volcanic record from this study, which will be henceforth referred to as the SP2001 record.

4. DISCUSSION

In addition to the mass loading of an eruption and the latitude location of the erupting volcano, several other factors also influence the magnitude (i.e., volcanic flux) of the volcanic signal in ice cores. An important atmospheric factor is the distribution and transport process that brings volcanic aerosols from the latitude of eruption to the Antarctic continent. Atmospheric observations of a number of recent volcanic eruptions (i.e., the 1963 Agung and 1982 El Chichon eruptions) demonstrate that distribution of volcanic aerosols between the two hemispheres can be highly variable and uneven, as it is subject to the inter-annual and intraannual variations of the atmospheric circulation patterns [Hitchman et al., 1994; Legrand and Wagenbach, 1999; McCormick et al., 1995; Trepte and Hitchman, 1992; Trepte et al., 1993]. Our understanding of this variability in distribution is rather poor at the present and an examination of this variability is beyond the scope of this study. However, observations of the 1991 Pinatubo eruption [Hitchman et al., 1994; McCormick et al., 1995; Trepte et al., 1993] indicate that for very large low latitude eruptions, the volcanic aerosol layers in the stratosphere eventually blanket the globe; and long residence times (more than 1 year) tend to favor equal hemispheric distribution. This suggests that exceptionally large low latitude eruptions that enhance the stratospheric sulfur reservoir for several years may have somewhat equal hemispheric distribution and similar transport efficiency to polar regions. For this study, the same atmospheric distribution and transport efficiency to Antarctica is assumed for all eruptions discussed herein. This assumption makes it possible to compare the normalized volcanic flux of volcanic events found in different ice cores.

4.1. Uncertainty of Normalized Volcanic Flux

Quantitative evaluation of eruption magnitude using the normalized volcanic flux requires the estimate of its uncertainty. Here we have elected to evaluate the uncertainty of the normalized volcanic flux by examining the uncertainty in the volcanic flux of individual events found in South Pole ice cores. The Tambora and the Unknown 1809 events have been extensively studied in numerous ice core records [Clausen and Hammer, 1988; Cole-Dai et al., 2000; Dai et al., 1991; Delmas et al., 1992; Langway et al., 1995; Legrand and Delmas, 1987], and volcanic flux data on these two events are available from several South Pole cores. The Unknown 1809 event is chosen to represent a typical low latitude event and the uncertainty of its normalized flux will be assumed to reflect the variability of normalized flux of low latitude events in South Pole ice cores. The uncertainty of the volcanic flux is assumed to be the standard deviation of these events reported from ice cores recovered near the South Pole. The values from the two 1984 South Pole ice cores by Delmas et al. [1992] (67.6 and 72.3 kg km^{-2} for Tambora, 32.0 and 29.8 kg km^{-2} for Unknown 1809) and the new SP2001 Core 1 (64.0 and 28.0 kg km^{-2}, respectively) are used to calculate the average and standard deviation of the total volcanic flux for each of these events. These values are then used to calculate the relative uncertainty of the normalized flux. The relative uncertainty of the normalized flux (%$e_{f/fT}$) is propagated as the square root of the sum of the squared relative uncertainties for the two events:

$$\%e_{f/fT} = [(\%e_{\text{Unknown 1809}})^2 + (\%e_{\text{Tambora}})^2]^{1/2}$$

Calculations with this method result in an error of 9%. Consequently, the normalized flux values of events in the SP2001 and other South Pole cores will be considered significantly different if their differences are greater than 9%.

4.2. Comparison With Previous Records

4.2.1. Number of Volcanic Events. The SP2001 record is initially compared with SP84 and PR86, in an attempt to resolve discrepancies between these two previous records. All large and moderate events (normalized volcanic flux greater than 0.20 in SP2001) in these three records between 904 A.D. and 1865 A.D., the time period covered by the SP2001 record, are listed in Table 2. An event is assigned to the same volcanic eruption when its dates are within the reported dating uncertainties and its volcanic flux values are similar in the SP2001 and SP84 records. Similar assignments were made by Cole-Dai et al. [2000] when comparing the SP84 and PR86 records.

It appears that the three Antarctic records are consistent in terms of the number and dates of large and moderate volcanic events in the last millennium. The 1691 event (SP2001-8) does not have a corresponding event in SP84, but an event similar in date and signal magnitude has been

Table 2. Comparison of large and moderate ($f/f_T > 0.20$ in SP2001) volcanic events between 904 A.D. and 1865 A.D. in several Antarctic ice cores. Correlation between records is based on date and magnitude (volcanic flux).

Volcanic Eruption	South Pole, SP2001 This work			South Pole, SP84 Delmas et al. [1992]			Plateau Remote, PR86 Cole-Dai et al. [2000]		
	Event Number	Year A.D.	f/f_T	Event Number	Year A.D.	f/f_T	Event Number	Year A.D.	f/f_T
Tambora	SP2001-3	1816	1.00	SP84-7	1816	1.00	PR-4	1816	1.00
	SP2001-4	1809	0.44	SP84-8	1809	0.47	PR-5	1810	0.37
	SP2001-8	1691	0.35				PR-6	1694	0.48
Parker & Deception Island	SP2001-10	1636	0.31	SP84-10	1641	0.29	PR-9	1639	0.32
Huaynaputina	SP2001-12	1600	0.36	SP84-12	1601	0.33	PR-10	1600	0.22
	SP2001-13	1596	0.23	SP84-13	1596	0.32	PR-11	1595	0.33
Kuwae	SP2001-15	1458	1.02	SP84-14	1450	1.10	PR-12	1454	5.96
	SP2001-19	1347	0.40	SP84-15	1340	0.28	PR-13	1343	0.66
	SP2001-20	1287	0.38				PR-14	1285	0.94
	SP2001-21	1276	0.71	SP84-16	1279	1.29	PR-15	1277	2.47
	SP2001-22	1270	0.31	SP84-17	1269	0.16	PR-16	1269	0.53
	SP2001-23	1260	2.80	SP84-18	1259	2.01	PR-17	1260	2.07
	SP2001-24	1236	0.42				PR-18	1234	1.39
	SP2001-25	1195	0.21	SP84-19	1191	0.18	PR-19	1197	0.47
	SP2001-26	1174	0.25	SP84-20	1177	0.29			
	SP2001-27	1113	0.18	SP84-21	1118	0.15			

found in a number of other Antarctic ice core records [Cole-Dai et al., 2000]. The absence of this event, and two events in the 13th century (SP2001-20 and SP2001-24), in SP84 could be due to a number of technical reasons. For example, the initial analysis of the 1984 South Pole ice core was performed using the ECM technique, rather than a continuous sulfate analysis [Delmas et al., 1992]. Very small or moderate volcanic events may not have been detected by ECM and consequently samples containing these events would not have been analyzed for sulfate concentration. The absence of events in PR86 corresponding to SP84-20 (1177 A.D.) and SP84-21 (1118 A.D.) has been discussed by Cole-Dai et al. [2000]. The SP2001 record confirms the findings in SP84 by Delmas et al. [1992] that there are indeed two moderate volcanic eruptions events in the 12th century.

Of the 17 small SP2001 events, 3 (Events 2 (1837 A.D.), 7 (1694) and 9 (1668) were also seen in PR86 (PR Events 3, 6 and 7, respectively), and one (SP2001-3 (966 A.D.) is close in time to a small event in SP84 (Event 23 (970)). Thirteen SP2001 events are not seen in either PR86 or SP84; all are small events with a volcanic flux less than 9.0 kg km^{-2} (normalized flux < 0.15). As discussed previously, detection of small events in Antarctic ice cores is subject to a number of variables: surface glaciology at the core site, analytical methodology, definition of background and detection threshold and level of background noise in the data. The absence of the 1174 and 1113 A.D. events in PR86 is an example of failure to detect minor or moderate events

in a core from a site of complicated local glaciology [Cole-Dai et al., 2000]. The fact that these 13 minor SP2001 events were not found in either SP84 or PR86 may be due to any one or a combination of these variables. However, it is more likely that some or most of them are false positive detections, due to the somewhat noisier background in the SP2001 core sulfate concentrations. In any case, small eruptions contribute little volcanic aerosols to the atmosphere and therefore can have only minimal impact on the climate system.

4.2.2. Magnitude of Signals of Several Events. As previously stated, significant differences exist between SP84 and PR86 in the signal magnitude (i.e., volcanic flux) of several large and well-known eruptions (Table 3): Huaynaputina (1600 A.D.), Kuwae (1450's), Unknown Eruption at 1347, and a number of eruptions in the 13th century. Even under the relative scale, i.e., the normalized flux, the differences persist (Table 3). Cole-Dai et al. [2000] suggested that the differences are likely caused by significant post-depositional processes (i.e., snow redistribution) at the Plateau Remote location and/or, to a lesser extent, by the different analytical methodologies used for the two previous studies. Below we discuss those differences in light of the uncertainty of the normalized volcanic flux and the new volcanic flux data in the SP2001 record produced with the same analytical methodology as that used by Cole-Dai et al. [2000]. Note that the Tambora flux in SP2001 (64.0 kg km^{-2}) is very close to that in SP84 (67.6 kg km^{-2}). Therefore, differences in nor-

Table 3. Total volcanic flux (f in kg km^{-2}) and normalized flux (f/f$_T$) values for events in the SP2001 that show discrepancies in the SP84, and the PR86 records. Uncertainties for normalized flux of SP2001 events are calculated for 9% relative error (see text). The events in the 13th century are numbered in order of occurrence. ND: not detected; N/A not available.

Event Number	Eruption/Year	South Pole, SP2001 this work		South Pole, SP84 [*Delmas et al.*, 1992]		Plateau Remote, PR86 [*Cole-Dai et al.*, 2000]	
		f	f/f$_T$	f	f/f$_T$	f	f/f$_T$
SP2001-3	Tambora/1815	64.01	1.00±0.09	67.6	1.00	22.39	1.00
SP2001-12	Huaynaputina/1600	22.98	0.36±0.03	22.5	0.33	4.91	0.22
SP2001-15	Kuwae/1454	65.55	1.02±0.09	74.4	1.10	133.37	5.96
SP2001-19	Unknown/1347	25.46	0.40±0.04	19.0	0.28	14.88	0.66
SP2001-20	Unknown/1287	24.31	0.38±0.03	ND	N/A	21.05	0.94
SP2001-21	Unknown/1276	45.37	0.71±0.06	87.3	1.29	55.39	2.47
SP2001-22	Unknown/1270	19.93	0.31±0.03	10.5	0.16	11.85	0.53
SP2001-23	Unknown/1260	179.45	2.80±0.25	135.7	2.01	46.30	2.07
SP2001-24	Unknown/1236	26.60	0.42±0.04	ND	N/A	31.21	1.39
SP2001-25	Unknown/1195	13.22	0.21±0.02	12.1	0.18	10.62	0.47

malized flux between SP2001 and SP84 are mainly due to the volcanic flux difference of the event of interest.

4.2.2.1. Huaynaputina and Kuwae. The normalized fluxes of Huaynaputina and Kuwae in PR86 are significantly different from those of the same events in SP84, given the estimated uncertainty (9%) of the normalized flux for South Pole ice cores. In fact, Kuwae is the largest event in the PR86 record [*Cole-Dai et al.*, 2000] with a very large normalized flux (5.96). The normalized flux for Kuwae in SP2001 is 1.02, about 20% of that in the PR86 record, but in agreement with that (1.10) in the SP84 record. Similarly, the SP2001 Huaynaputina normalized flux (0.36) is virtually the same as that (0.33) in SP84, and thus significantly larger than that (0.22) in PR86. These data suggest that South Pole records are more reliable in estimating volcanic flux and consequently in the normalized flux, while large variations and perhaps distortions in volcanic flux exist in the PR86 record, presumably due to the strong post-depositional snow redistribution effects at the Plateau Remote location [*Cole-Dai et al.*, 2000]. Further evidence of significant rearrangement of annual snow layers at Plateau Remote is suggested by the long duration of the Kuwae event in the PR86 record (7.2 years), almost twice as long as in either the SP84 (3.9 years) or SP2001 (4.5 years) records.

4.2.2.2. Unknown 1347. An unknown event in the mid-14th century (1347 in SP2001, 1340 in SP84 and 1343 in PR86) is considered the same event, as the age differences are within dating errors and no other volcanic events are found during this time period. The normalized flux from the three cores is significantly different from each other at 0.40, 0.28, and 0.66, respectively. The high value for PR86 could

be the result of increased snow layer thickness from redistribution. The difference between SP2001 and SP84 is more difficult to explain. Possible causes may include minor loss of volcanic sulfate in the SP84 or enrichment in the SP2001 record due to slight redistribution of snow, or the differences in analytical methodology and in the calculation of volcanic flux.

4.2.2.3. Events in the 13th Century. Delmas et al. [1992] reported three large volcanic events in SP84 dated at 1279 A.D. (SP2001-21), 1269 A.D. (SP2001-22), and 1259 A.D. (SP2001-23). *Cole-Dai et al.* [2000] found corresponding events in PR86, but the 1279 A.D. and 1269 A.D. events had significantly different normalized fluxes when compared to SP84 (Table 3). Previous discussion on the Kuwae signal suggests that the SP84 results are more reliable. However, the SP2001 results do not seem to agree with SP84, although the differences between SP84 and SP2001, in the case of the 1279 and 1269 events, are smaller than those between South Pole cores and PR86 cores. For the 1259 event, possibly the largest low latitude eruption in the last 1000 years, the normalized flux differs slightly between SP2001-23 (2.80) and SP84 (2.01). This difference is larger than the estimated uncertainty (0.25=2.80×9%) and therefore suggests that the 9% relative uncertainty derived from the 1809 Unknown Eruption may underestimate the variability of normalized flux in South Pole cores.

4.2.2.4. Unknown 1195. An unknown event at the end of the 12th century is found in all 3 records: SP2001-25 (1195 A.D.), SP84-19 (1191) and PR86-19 (1197). This event has similar normalized flux in SP2001 (0.21) and SP84 (0.18),

while its normalized flux in PR86 is significantly different (0.47). This again suggests that normalized volcanic flux for South Pole ice cores is more reproducible and therefore more reliable than that from Plateau Remote.

4.2.3. The 13th Century

4.2.3.1. Number of Events. In addition to the three events (1259, 1269 and 1279) discussed above, *Cole-Dai et al.* [2000] found in the Plateau Remote core two other moderate volcanic events (1234 and 1285, with a normalized flux of 0.21 and 0.38, respectively) in the 13th century (Figure 3a) and noted that five large and moderate volcanic events make this century an exceptional one during the last several millennia. These five events have also been reported in other Antarctic records [e.g., *Langway et al.*, 1995] that cover the last 1000 years, but the SP84 record is notably different in that the earliest (ca. 1234) and latest (ca. 1285) events are absent. The absence could be due to the fact that the initial ECM analysis may not have indicated possible volcanic events and, as a consequence, no detailed sulfate analysis was carried out at the appropriate depths.

The SP2001 results (Figure 3b) confirm the findings from other Antarctic ice cores that a total of five large and moderate volcanic eruptions occurred in the 13th century. All five eruptions (SP2001-20 to 24), produced significant amounts of volcanic aerosols, as indicated by the volcanic flux data in Table 3. Volcanic events have been found in Greenland ice cores [*Clausen et al.*, 1997; *Langway et al.*, 1995; *Zielinski.*, 1995] that are contemporaneous with three

of the five events, Events 24 (ca. 1234), 23 (1259) and 20 (ca. 1285), while no events have been reported in Greenland cores corresponding to the other two events. Recent evidence [*Dunbar et al.*, 2003] from Siple Dome and Taylor Dome (Antarctica) ice core tephra analysis indicates that the source of the 1276/1279 volcanic sulfate may well be an Antarctic volcano. Therefore, of the five events, three are likely, and one is possible, low latitude eruptions capable of impacting the global climate.

4.2.3.2. Climatic Significance of the 13th Century Events. The climatic impact of explosive volcanism has been extensively studied and reviewed recently [*Robock*, 2000; *Zielinski*, 2000]. Reduced radiative forcing by stratospheric volcanic aerosols is the recognized mechanism of volcanic forcing on climate. Therefore, volcanic impact on climate is in general short-lived (up to 5 years after the introduction of volcanic aerosols), due to the relatively short (up to a few years) of stratospheric residence time of volcanic aerosols. Such short term climatic impact has been well documented. For example, *White et al.* [1997] found that cooling of the atmosphere, as represented by δD decreases in Greenland snow, lasts no more than 5 years after an eruption. Therefore, the atmospheric impact of explosive volcanic eruptions, including unusually large eruptions such as Tambora and Kuwae, is expected to disappear several years after an eruption.

There has been some speculation that there may be long term impact on the climate by volcanic eruptions: cumulative cooling by eruptions a number of years or a few
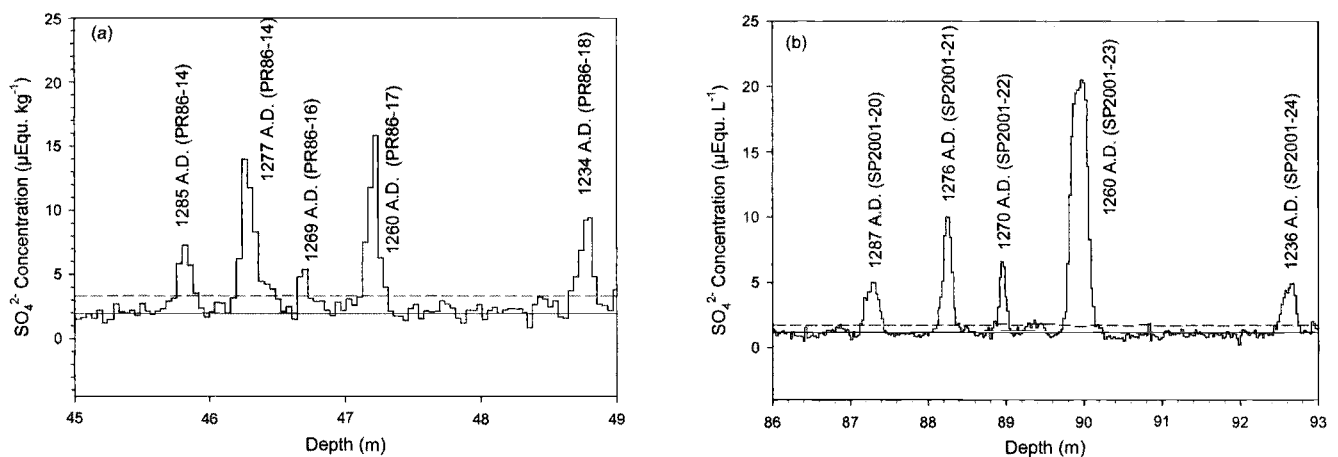
Figure 3. Five volcanic events in the 13th Century detected in the Plateau Remote core (a) and 2001 South Pole core (b). All dates indicated are the years of the event peak within the timescale of the core. Events are numbered in order of occurrence.

decades apart [*Briffa et al.*, 1998; *Zielinski*, 2000]; feedbacks via ice cover and oceanic circulation could transform short-term volcanic forcing into a longer-term effect [*Robock*, 2000]. Perhaps the strongest argument for a longer climatic impact is that stratospheric residence times of volcanic aerosols may be longer than previously thought, as indicated by the continued decline of stratospheric aerosols more than a decade after the 1991 Pinatubo eruption [*Barnes and Hoffman*, 2001; *Hervig and Deshler*, 2002]. This suggests that background stratospheric aerosol levels may have been overestimated.

The five large and moderate eruptions in the 13th century occurred within a 50 year span (Figure 3). Some cumulative climatic effect could be expected during this century and possibly in the early 14th century. Figure 4 illustrates that the 13th century has the largest total volcanic flux (larger by a factor of 3 to 20 than in other centuries), implying the highest atmospheric aerosol mass loading by volcanic eruptions during the last millennium. Even when the contribution of Event 21 (ca. 1276), a possible high latitude eruption that may not have impacted the climate system, is excluded, the cumulative volcanic sulfate flux (250 kg km^{-2}) for the 13th century is still 6 times the average century volcanic flux (~40 kg km^{-2}) for the rest of the 904–1865 A.D. period. This century of frequent large volcanic eruptions coincides with the period of transition from the Medieval Warm Period to the Little Ice Age. Model calculations [*Robock*, 2000] have shown that volcanic forcing, probably due to this series of eruptions in the 13th century, in conjunction with variations in solar and other forcings was an important cause for the onset of the Little Ice Age. It is possible and indeed proba-

ble that the cumulative effect of repeated injection of large amounts of volcanic aerosols into the stratosphere by frequent large eruptions within a few decades or a century can initiate, enhance or reverse a climatic trend. Furthermore, continuous volcanic forcing on a longer (decadal to century) timescale may be amplified by the combined ocean-atmosphere system. As already suggested by other researchers [*Robock*, 2000; *Zielinski*, 2000], these aspects of the volcano-climate system need to be further investigated in future research.
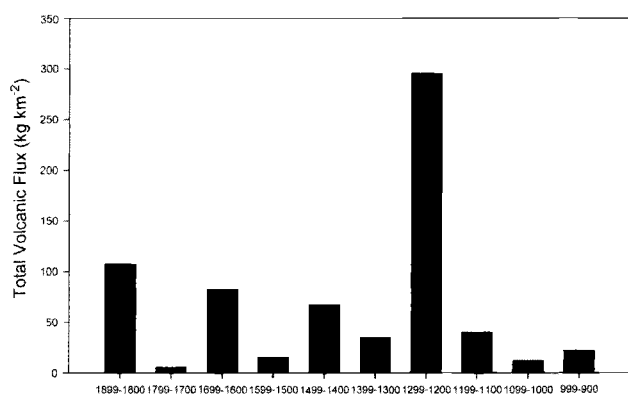
5. CONCLUSIONS

Analysis of a new South Pole ice core has produced a continuous volcanic record covering the period of 904 to 1865 A.D. In terms of the number and dates of moderate and large volcanic eruptions in this period, the new record is consistent with records from previous Antarctic ice cores. About 13 additional events in the sulfate profile slightly exceed the volcanic detection threshold value and have not been previously reported. While these may represent small volcanic signals (small volcanic flux), they are more susceptible to variations in the detection threshold definition and in flux calculation and most are considered to be false positives from the noisier background of the SP2001. These possible small events are not considered important with respect to potential climatic impact of volcanic eruptions, due to their small amounts of volcanic aerosols.

Comparison with a previous South Pole ice core volcanic record by *Delmas et al.* [1992] and a recent record from a Plateau Remote ice core by *Cole-Dai et al.* [2000] indicates that discrepancies in volcanic flux between these two previous records are probably due to glaciological complications at Plateau Remote. We conclude that volcanic flux estimates using South Pole ice cores are more reproducible and therefore more reliable and representative of atmospheric volcanic aerosol mass loadings than those from an ice core location where snow accumulation rates are extremely low and post-depositional alterations of deposition records may be significant.

The new South Pole record supports the findings in previous Antarctic ice cores (except the SP84 record) that five large and moderately large volcanic eruptions occurred in the 13th century. At least three of the five are probably large, low-latitude eruptions capable of impacting the global climate. Total volcanic flux for this century is the largest in the last millennium. We suggest that the frequent injection of large amounts of volcanic aerosols into the atmosphere dur-

Figure 4. Total volcanic flux in a century interval. The period between 1299 and 1200 has the largest amount of volcanic activity in record. The last 1899-1800 period contains only 66 years (1866-1800) as the SP2001 record covers 904–1866 A.D.

ing the 13th century may have contributed to the climatic transition from the Medieval Warm Period to the Little Ice Age. This suggestion supports previous model results [*Robock*, 2000].

REFERENCES

Barnes, J.E., and D.J. Hoffmann, Variability in the stratospheric background aerosol over Mauna Loa observatory, *Geophys. Res. Lett.*, 28, 2895-2898, 2001.

Briffa, H.P., P.D. Jones, F.H. Schweingruber, and T.J. Osburn, Influence of volcanic eruptions on Northern Hemisphere summer temperature over the past 600 years, *Nature*, 393, 450-454, 1998.

Clausen, H.B., and C.U. Hammer, The Laki and Tambora eruptions as revealed in Greenland ice cores from 11 locations, *Ann. Glaciol.*, 10, 16-22, 1988.

Clausen, H.B., C. U. Hammer, C. S. Hvidberg, D. Dahl-Jensen, J. P. Steffensen, J. Kipfstuhl, and M. Legrand, A Comparison of the volcanic records over the past 4000 years from the Greenland Ice Core Project and Dye 3 Greenland ice cores, *J. Geophys. Res.*, 102(26), 707-726, 1997.

Cole-Dai, J., and E. Mosley-Thompson, The Pinatubo eruption in South Pole snow and its potential value to ice-core paleovolcanic records, *Ann. Glaciol.*, 29, 99-105, 1999.

Cole-Dai, J., L.G. Thompson, and E. Mosley-Thompson, A 485 year record of atmospheric chloride, nitrate and sulfate: results of chemical analysis of ice cores from Dyer Plateau, Antarctica Peninsula, *Ann. Glaciol.*, 21, 182-188, 1995.

Cole-Dai, J., E. Mosley-Thompson, and L.G. Thompson, Annually resolved southern hemisphere volcanic history from two Antarctic ice cores, *J. Geophys. Res.*, 102(D14), 16761-16771, 1997a.

Cole-Dai, J., E. Mosley-Thompson, and L.G. Thompson, Quantifying the Pinatubo volcanic signal in south polar snow, *Geophys. Res. Lett.*, 24(21), 2679-2682, 1997b.

Cole-Dai, J., E. Mosley-Thompson, S.P. Wight, and L.G. Thompson, A 4100-year record of explosive volcanism from an East Antarctica ice core, *J. Geophys. Res.*, 105(D19), 2431-24441, 2000.

Dai, J., E. Mosley-Thompson, and L.G. Thompson, Ice core evidence for an explosive tropical volcanic eruption 6 Years preceding Tambora, *J. Geophys. Res.*, 96(D9), 17361-17366, 1991.

Delmas, R.J., M. Legrand, A.J. Aristarain, and F. Zanolini, volcanic deposits in Antarctic snow and ice, *J. Geophys. Res.*, 90(D7), 12901-12920, 1985.

Delmas, R.J., S. Kirchner, J.M. Palais, and J.-R. Petit, 1000 years of explosive volcanism recorded at the South Pole, *Tellus*, 44B(4), 335-350, 1992.

Dibb, J.E., and S. Whitlow, Recent climatic anomalies and their impact on snow chemistry at South Pole, 1987-1994, *Geophys. Res. Lett.*, 23(10), 1115-1118, 1996.

Dunbar, N.W., G.A. Zielinski, and D.T. Voisins, Tephra layers in the Siple Dome and Taylor Dome ice cores, Antarctica: sources and correlations, *J. Geophys. Res.*, in press, 2003.

Hervig, M., and T. Deshler, Evaluation of aerosol measurements from SAGE II, HALOE, and balloonborne optical particle counters, *J. Geophys. Res.*, 107(D3), 3-1-3-12, 2002.

Hitchman, M.H., M. McKay, and C.R. Trepte, A climatology of stratospheric aerosol, *J. Geophys. Res.*, 99, 20689-20700, 1994.

Langway, C.C.J., K. Osada, H.B. Clausen, C.U. Hammer, and H. Shoji, A 10-century comparison of prominent bipolar volcanic events in ice cores, *J. Geophys. Res.*, 100(D8), 16241-16247, 1995.

Legrand, M., and R.J. Delmas, A 220-year continuous record of volcanic H_2SO_4 in the Antarctic ice sheet, *Nature*, 327, 671-676, 1987.

Legrand, M., and D. Wagenbach, Impact of the Cerro Hudson and Pinatubo volcanic eruptions on the Antarctic air and snow chemistry, *J. Geophys. Res.*, 104(D1), 1581-1596, 1999

Legrand, M., M. De Angelis, and R.J. Delmas, Ion chromatographic determination of common ions at ultratrace levels in Antarctic snow and ice, *Anal. Chim. Acta*, 156, 181-192, 1984.

McCormick, M.P., L.W. Thomason, and C.R. Trepte, Atmospheric effects of the Mt. Pinatubo eruption, *Nature*, 373, 399-403, 1995.

Palmer, A.S., T.D. van Ommen, M.A.J. Curran, V. Morgan, J.M. Souney, and P.A. Mayewski, High-precision dating of volcanic events (A.D. 1301-1995) using ice cores from Law Dome, Antarctica, *J. Geophys. Res.*, 106(D22), 28089-28095, 2001.

Rampino, M.R., and S. Self, Historical eruptions of Tambora (1815), Krakatau (1883), and Agung (1963), their stratospheric aerosols and climatic impact, *Quat. Res.*, 18, 127-143, 1982.

Robock, A., Volcanic eruptions and climate, *Rev. Geophys.*, 38(2), 191-219, 2000.

Robock, A., and J. Mao, The volcanic signal in surface temperature observations, *J. Climat.*, 8, 1086-1103, 1995.

Trepte, C.R., and M.H. Hitchman, Tropical stratospheric circulation deduced from satellite aerosol data, *Nature*, 355, 626-628, 1992.

Trepte, C.R., R.E. Veiga, and M.P. McCormick, The poleward dispersal of Mt. Pinatubo volcanic aerosol, *J. Geophys. Res.*, 98, 18563-18573, 1993.

Wagenbach, D., F. Ducroz, R. Mulvaney, L. Keck, A. Minikin, M. Legrand, J.S. Hall, and E.W. Wolff, Sea-salt aerosol in coastal Antarctic regions, *J. Geophys. Res.*, 103(D9), 10961-10974, 1998.

White, D.E., J.W.C. White, E.J. Steig, and L.K. Barlow, Reconstruction of annual and seasonal climatic responses from volcanic events since A.D. 1270 as recorded in the deuterium signal from Greenland Ice Sheet Project 2 ice cores, *J. Geophys. Res.*, 102(D6), 19683-19694, 1997.

Zielinski, G.A., Stratospheric loading and optical depth estimates of explosive volcanism over the last 2100 years derived from the Greenland Ice Sheet Project 2 ice core, *J. Geophys. Res.*, 100(D10), 20937-20955, 1995.

Zielinski, G.A., Use of paleo-records in determining variability within the volcanism-climate system, *Quat. Sci. Rev.*, 19, 417-438, 2000.

D. Budner and J. Cole-Dai, Department of Chemistry and Biochemistry, South Dakota State University, Box 2202, Brookings, SD 57007

An Automatic Statistical Methodology to Extract Pulse-Like Forcing Factors in Climatic Time Series: Application to Volcanic Events

Philippe Naveau[1], Caspar M. Ammann[2], Hee-Seok Oh[3], and Wensheng Guo[4]

To understand the full range of natural climate variability, it is important to attribute past climate variations to particular forcing factors. In this paper, our main focus is to introduce an automatic procedure to estimate the impact of strong but short-lived perturbations from large explosive volcanic eruptions on climate. An extraction method to simultaneously model the slowly changing background climate component and the superposed volcanic pulse-like events is presented and applied to a variety of data sets (tree-ring data and a multi-proxy temperature reconstruction over the last 4 centuries and output from a coupled ocean-atmosphere general circulation model). This approach based on a statistical multi-state space model provides an accurate estimator of the timing and duration of the climate response to an eruption. It not only allows for a more objective estimation of its associated peak amplitude and the subsequent time evolution of the signal, but at the same time it provides a measure of confidence through the posterior probability for each cooling event. Because the background noise changes in time, this technique uses the local characteristics of the volcanic signal to associate a probability that is not necessarily linked to the absolute intensity of the event. This flexibility is not included in direct thresholding techniques.

1. INTRODUCTION

Large explosive volcanic eruptions can play an important role in climate over the range of a few years [*McCormick et al.*, 1995]. Their signature has been found in numerous long climatic time series, instrumental and proxy alike [*Lamb,*

[1]Department of Applied Mathematics, University of Colorado, Boulder, Colorado.
[2]Advanced Study Program & Climate and Global Dynamics Division, National Center of Atmospheric Research, Boulder, Colorado.
[3]Department of Mathematical and Statistical Sciences, University of Alberta, Edmonton, Canada.
[4]Department of Biostatistics and Epidemiology, University of Pennsylvania School of Medicine, Philadelphia, Pennsylvania.

1970; *Kelly et al.,* 1984; *LaMarche and Hirschboeck,* 1984; *Bradley,* 1988; *Robock and Mao,* 1995; *Briffa et al.,* 1998]. Statistically, they can be viewed as pulse-like events, i.e. short and intense deviations from the noise, a slowly changing trend and/or possible periodic variations. Because of their sharp features (due to very abrupt injection of large volcanic particle clouds), classical statistical tools based on averages, projections or variances are not well adapted to capture the characteristics of such rapid events. Consequently, our objective is to present a statistical methodology capable of accurately identifying the timing of such pulse-like events and to quantify their amplitudes over time. To reach this goal, we first recall the two most used techniques to solve this extraction problem.

Using prior knowledge of the volcanic activity during the last 400 years [*Lamb,* 1970; *Newhall and Self,* 1982; *Simkin and Siebert,* 1994], one can *visually* associate a number of cooling events in any given climatic time series to known volcanic events [*Briffa et al.,* 1998]. Although this identification procedure is often successful, a number of drawbacks

om

This is ideal for the illustration purposes since all attention can be focused on the individual pulses. Although other more recent reconstructions exist (e.g., *Mann et al.*, [2000]; *Esper et al.*, [2002]), we restrict the analysis here to two well-known and widely discussed series. At this point, it is not the goal to find the real world volcanic signals as this discussion would go beyond the space available, but to introduce a flexible technique ideally tailored to the detection problem of pulse like events. This also allows us to ignore the fact that additionally to the large scale cooling, volcanic aerosol also causes dynamically induced warming over the northern hemisphere continents in the winter season [see summary by *Robock*, 2000]. The selected time series here are essentially insensitive to this. A more in-depth study of the volcanic signals will be presented elsewhere.

Here, we assume that any pulse-like cooling episode is due to a large volcanic eruption. This assumption may not always be satisfied. For these cases, expressions such as "large eruptions" should be regarded as "pulse-like cooling episodes." Only at the end will this issue be addressed through cross-evaluation with other, more volcanologically rather than climatically oriented volcanic indices such as the large eruption catalogue published by the Smithsonian Institution [*Simkin and Siebert*, 1994].

3. THE EXTRACTION PROCEDURE

The main objective of this section is to translate the scientific question of how to calculate the impact of large volcanic eruptions on climatic time series into a statistical one, how to extract the intensity and the timing of a pulse-like event from a given signal. To reach this goal, the following statistical model, which has enough flexibility to represent long term trends, cycles and pulse-like events is defined

$$y(t)=v(t)+f(t)+c(t)+\varepsilon(t), \qquad (1)$$

where $y(t)$ is the annually resolved time series, $v(t)$ corresponds to the volcanic signal (pulse), $c(t)$ represents possible cycles such as the 11-year sun spot cycle, and $f(t)$ is the smooth trend due to human influence or other long term trends. Because some background noise will be present in our time series, a Gaussian white noise $\varepsilon(t)$ with standard deviation σ_ε is also incorporated in Equation (1). All the different components of (1) are assumed to be independent.

To model $v(t)$ in Equation (1), we recall that large volcanic eruptions can inject significant amounts of sulfur into the stratosphere where small sulfuric acid droplets form [*Castleman et al.*, 1974]. These small aerosol particles are more efficient in reflecting sunlight back to space than to prevent upwelling heat from escaping the system [*Lacis et al.*, 1992]. This generally causes cooling of the climate for a period from several months up to a few years. To model this signal, at least three components have to be incorporated in $v(t)$: a binary random variable to represent volcanic occurrences [*De la Cruz-Reyna*, 1991], a random input variable to model the strength of the eruption and an exponential decay to show the temporal effect of the eruption [*Dutton and Bodhaine*, 2001]. The auto-regressive model defined by

$$v(t)=a\,v(t-1)+i(t), \qquad (2)$$

where $|a| < 1$ is a constant, allows us to combine these three elements in a simple way if the volcanic input $i(t)$ is assumed to follow a *mixture* of distributions:

$$i(t)=\begin{cases} N(\mu_v,\sigma_v^2) & \text{if } o(t)=1, \\ 0 & \text{if } o(t)=0. \end{cases} \qquad (3)$$

Here, $o(t)$ is a Bernouilli variable whose parameter $\pi = P[o(t) = 1]$ denotes the probability of observing an eruption. If $o(t) = 1$, the volcanic input $i(t)$ is equal to a random normal variable with mean μ_v and standard deviation σ_v^2.

The second step in our procedure is to model the trend $f(t)$ in (1). A smoothing spline is a natural choice for the changing baseline because of its flexibility. *Wahba* [1978] showed that a smoothing spline can be obtained through a signal extraction approach by introducing a stochastic smoothing spline model. More recently, *Wecker and Ansley* [1983] expressed this smoothing spline model in a state space form. Following their formulation, we express the trend $f(t)$ in function of its derivatives $\mathbf{F}(t) = (f(t), f^{(1)}(t), f^{(2)}(t),...,f^{(m-1)}(t))'$ by writing

$$\mathbf{F}(t) = \mathbf{B}\,\mathbf{F}(t\text{-}1) + \mathbf{E}_f(t), \qquad (4)$$

where $\mathbf{B}[i,j] = 1/(j\text{-}i)!$ for $j \geq i$ or 0 otherwise and $\mathbf{E}_f(t)$ is a m-dimensional Gaussian vector with zero mean and covariance elements

$$\lambda\sigma_v^2 /[i+j-1)(i-1)!(j-1)!].$$

A cubic spline corresponds to $m = 2$ and will be used in this work.

To illustrate how to represent cycles in the model, our mathematical formulation will focus on the 11-year sunspot cycle. Other periodicities or combinations of cycles could be integrated in the same way. The component $c(t)$ in (1) is modeled by $c(t) = c(t-11) + \varepsilon_c(t)$ with $\varepsilon_c(t)$ is a Gaussian

noise with standard deviation σ_c [*Kitagawa and Gersch*, 1984]. For consistency with (4), the cyclic component is rewritten with a vectorial notation as $C(t) = D \ C(t\text{-}1) + E_c(t)$, where $C(t) = (c(t),...,c(t\text{-}10))'$, $E_c(t) = (\varepsilon_c(t),0,...,0)'$ and

$$D = \begin{bmatrix} 0 & 0 & ... & 0 & 1 \\ 1 & 0 & ... & 0 & 0 \\ 0 & 1 & ... & 0 & 0 \\ . & . & ... & . & . \\ 0 & 0 & ... & 1 & 0 \end{bmatrix}$$

A spectral analysis of the two time series under study did not show any particular decadal cycle. But to emphasize the full potential of the multi-state model we decided to keep a cycle component in the general model described in the next section. In the sections dedicated to simulations and applications, $c(t)$ will be set to 0.

3.1. MULTI-PROCESS STATE SPACE MODELS

The kind of model that combines all components, $v(t)$, $f(t)$, $c(t)$ and the associated noise belongs to a large class called *Multi-Process State Space Models*. This class has been widely used in various applications [*Guo et al.*, 1999; *West and Harrison*, 1997; *Shepard*, 1994; *Shumway and Stoffer*, 1991; *Harrison and Stevens*, 1971, 1976]. The basic idea of the state space model is that the observations $y(t)$ are generated by two equations, the *observational* and *system* equations. The former describes how the different forcings influence the observations and the latter models the temporal dynamics of the forcings. More precisely, the observational equation defines the observed signal as a linear combination of a *state* vector $X(t)$: $y(t) = H \ X(t) + \varepsilon(t)$. To link all the components, the state vector has to be defined as $X(t) = (i(t),v(t), F'(t), C'(t))'$ with $H = (0,1, (1,0,...,0),(1,0,...,0))'$. The state vector represents forcing processes and its behavior in time is described by the following *system equation* $X(t) = \Phi \ X(t\text{-}1) + E^*(t)$, where $E^*(t) = (i(t), E'_f(t), E'_c(t))'$ and

$$\Phi = \begin{bmatrix} 0 & 0 & 0 & 0 \\ 0 & a & 0 & 0 \\ 0 & 0 & B & 0 \\ 0 & 0 & 0 & D \end{bmatrix}$$

Hence, the multi-process state space model has the advantage of providing a global formulation of our problem (combination of pulse-like events with long-term trend and cycles). In addition, there exists an extensive literature

about the estimation of the parameters for such models. In particular, the Kalman filter provides an optimal way to estimate the model parameters if the assumption of normality holds. Unfortunately, the nature of pulse-like events (mixture of distribution, see Equation (3)) implies that the overall assumption of normality can not be satisfied. Another issue in terms of estimation is that we are also interested in the the posterior probability of $o(t)=j$ given $Y(t)$ in order to estimate pulse location. Following the work by *Guo at al.* [1999], the estimation of the parameters is carried out by sequentially updating the system and observations equation, i.e. a multiprocess Kalman filter. The details of such a sequential procedure can be found in the Appendix.

3.2. TESTING THE EXTRACTION PROCEDURE

To assess the quality of the extraction process, two simulated data sets are analyzed.

First, in an idealized statistical framework, a randomly generated set based on Equation (1) was successfully tested. Because this data was constructed on the assumption that background noise is white, we then evaluated if our technique (based on this assumption) would also work with data containing a red noise spectrum, as is the case for climate data [Hasselmann, 1976]. In Figure 2 panel A, we show a time series such as one based on Equation (1) but the white noise was replaced with red noise derived from a General Circulation Model control run (unforced, see also below). By comparing the true (dotted) and estimated signals (solid lines) in Figure 2, one can deduce that the estimation procedure is successful at finding the long-term trend (panel A) and at capturing the intensity and occurrence of almost all simulated volcanic events (panel B). In addition, panel C indicates that the large majority of eruptions (black dots) are detected with a posterior probability close to 1. Only very few events were either missed by the procedure—mostly because their magnitude was very small—and only few false positives were estimated that have a large posterior probability. Figure 3 summarizes this successful extraction of the peak pulses by the state space procedure. Most importantly, the estimated and expected pulse intensities essentially follow a linear relationship with a slope very close to 1.

The second simulated data set (top panel of Figure 4) is output from a 20th century experiment presented by *Ammann et al.* [2003] employing the National Center for Atmospheric Research—Climate System Model [*Boville and Gent*, 1998], a state-of-the-art coupled Ocean Atmosphere General Circulation Model. It provides a more realistic time series to test our method. Because in the mod-
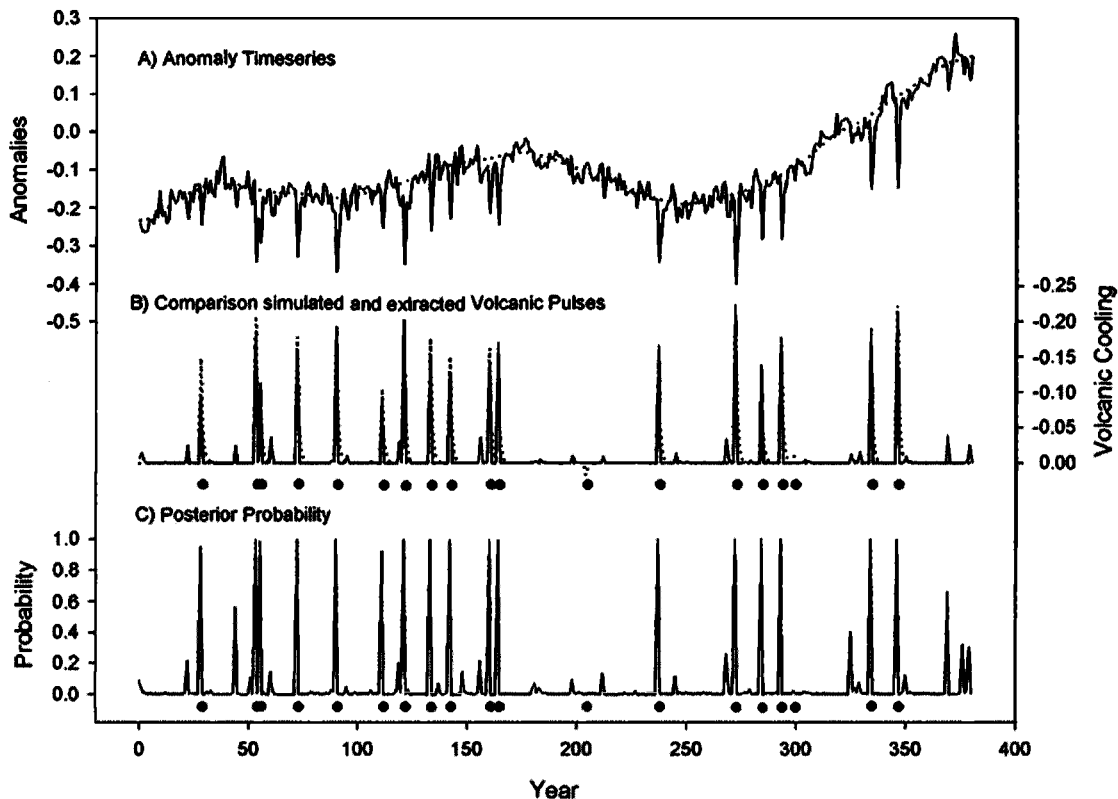
Figure 2. Panel A shows a statistically simulated time series containing volcanic signals $v(t)$ following equations (2) and (3). To verify the flexibility of the extraction procedure, white noise was replaced with red noise derived from a General Circulation Model control run. Panel B compares the simulated (dotted line) and estimated volcanic pulses (solid line) with the black dots denoting timing of events. Panel C shows the associated posterior probabilities with the detected events. A clear separation of highly probable from only marginally probable background noise is ideal.

eling framework all the forcings, including greenhouse gases and solar irradiance changes, as well as tropospheric and volcanic aerosol evolution had to be specified, it provides, consequently, a test to determine how much of the initial volcanic forcing can be detected by the extraction procedure. This direct comparison can be seen in the lower panels of Figure 4. From this graph we can conclude that most of the original forcing has been successfully extracted in terms of timing and intensity. As can be expected, the detected signals appear slightly delayed compared to the prescribed forcing because the climate response to the radiative imbalance needs to build up over time and the internal climate noise additionally masks the early signal, when the magnitude is still small. As the forcing decreases over several years, at some point the signal can no longer be clearly detected against the background noise. Thus, the extracted volcanic cooling ends before the last the volcanic aerosol has left the atmosphere. After the recent eruption of Mount Pinatubo in 1991, a climate signal was detected for

about two years until the end of 1993, while the aerosol did not reach background conditions until roughly 1996.

4. RESULTS AND DISCUSSION

Figure 5 shows the result of the extraction procedure applied to the two summer season reconstructions by *Briffa et al.* (Figure 5A) and *Jones et al.* (Figure 5B).

One of the most interesting results of the extraction procedure can be found in the lower panels of Figure 5A as well as B. They represent the estimated posterior probability of the volcanic occurrences. This measure of confidence allows to focus on events that have been detected with a large probability and to regard variations with values smaller than 50% (dotted lines) as part of the background noise. Briffa's data set provides a clearer dichotomy (separation) where strong cooling events are clearly associated with both a strong probability and a large $v(t)$. It is natural to wonder if cooling events found in both time series are related. Table 1
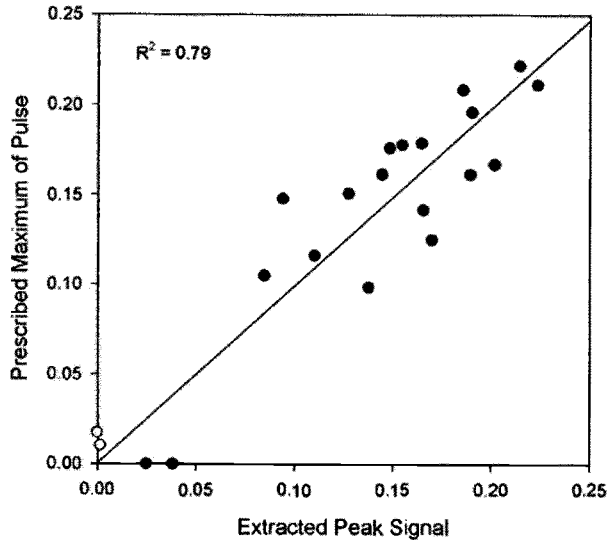
Figure 3. Verification of the extraction results focusing on the peak signals. All events from Figure 2 with posterior probability of at least 0.5 are included. Two events are false positives (prescribed peak pulse = 0.0). For comparison, the two false negatives (probability < 0.5) are also included as open circles. The linear correlation between the simulated and estimated signals (all positives with probabilities > 0.5) has a slope essentially equal to 1. Thus the results are unbiased.

provides an overview by including the 8 largest common cooling events (years in bold) with a posterior probability greater than 0.5 present in both time series. In addition, the 5 largest events not included in the 8 common list are also presented for both time series. Solely as verification, but fully independent from the extraction procedure, Table 1 contains the names of possible volcanoes whenever identification with their associated VEI (Volcanic Explosivity Index) was possible in the Smithsonian Catalogue [*Simkin and Siebert*, 1994, updated, L. Siebert, pers. communication, 2002]. In agreement with discussions in *Jones et al.* [1995] and *Briffa et al.* [1998], this list shows that both time series capture most of the really large volcanic events. Nevertheless, there exist a number of large eruptions that have their clear signature in only one of the two data sets. Also, not all cooling episodes can be associated with a volcanic eruption, which can be caused by either a lack of records or by other sources for cooling than a volcanic eruption [*Jones et al.*, 1995].

The selection threshold of 0.5 was based on three observations: (1) it represents the best separation of spikes from the background noise in the posterior probability of both the *Briffa et al.* and *Jones et al.* extraction results (see Figure 5). (2) It also holds up in the idealized scenario represented by the simulated data (Figure 2 and 3). For smaller thresholds

the false positives would increase strongly. (3) Finally, for events detected below the 0.5 posterior probability, it gets difficult to identify corresponding entries in the fully independent VEI index.

To finalize our statistical analysis of these reconstructions, the properties of the residuals are investigated in order to check if the assumptions of model (1) are satisfied. The residuals were found to be normally distributed, and the correlation function shows a short temporal dependence of up to 4 years in the residuals. This could be linked to internal climatic variations such as El Niño or others.

To conclude, five main points need to be emphasized: (1) A multi-process state space model can efficiently and globally extract the timing, intensity and a posterior probability
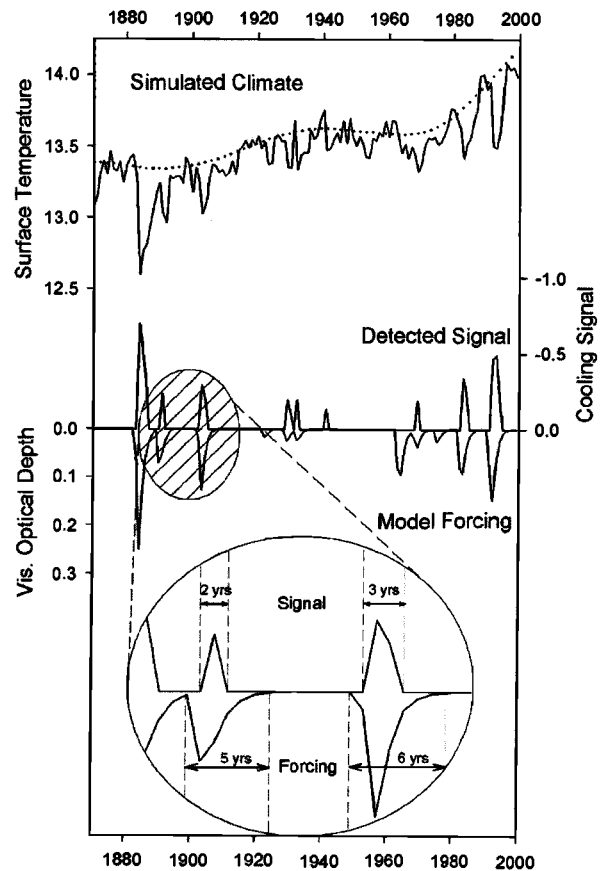
Figure 4. Extraction of cooling episodes in global average surface temperature from a run with the fully coupled NCAR-CSM. The detected signals are directly compared to prescribed volcanic forcing which was entered in the GCM simulation as aerosol optical depth. In the enlarged section at the bottom, one can clearly see that in good agreement with observations the forcing starts earlier and last longer than the detectable climate signal. See text for explanation.
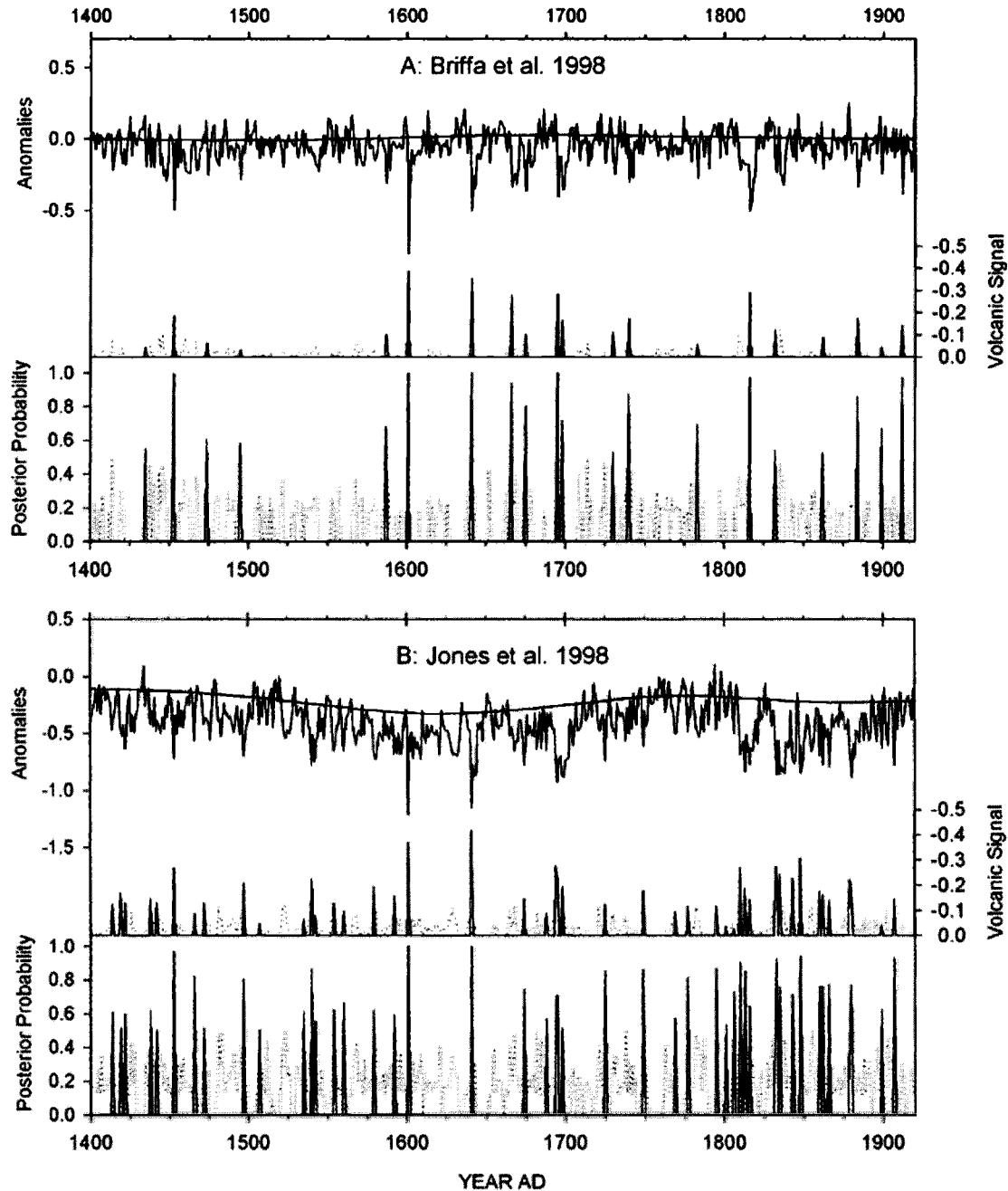
Figure 5. Comparison of volcanic pulse detection in (A) Briffa's and (B) Jones's hemispheric climate reconstructions. The top panels show the original timeseries with the estimated trends. The middle panels contain the detected volcanic pulses $v(t)$ with their associated posterior probability in each of the bottom panels. Events with a posterior probability larger then 0.5 are shown as solid lines, the others are dotted. This separation of the signals from the noise is on average cleaner in Briffa (A), independent from the detected magnitude of the events. See also Table 1.

Table 1. Comparison between the largest estimated volcanic signals ($\hat{v}(t)$) and associated posterior probability ($\hat{\pi}$) computed from *Briffa et al.* [1998] and *Jones et al.* [1998] time series. See also *Briffa et al.* [1998] and *Jones et al.* [1995] for discussion of the associations to possible source volcanoes.

Results $f(v)$ of the extraction procedure					Known Volcanic Eruptions possibly associated with detected events		
Year	Briffa et al. [1998]		Jones et al. [1998]		Year	Volcano	VEI[a]
	$\hat{v}(t)$	$\hat{\pi}$	$\hat{v}(t)$	$\hat{\pi}$			
1453	0.18	1.00	0.27	0.97	1452/3	Kuwae, Vanuatu	6
1497	–	–	0.21	0.81		?	?
1540	–	–	0.22	0.87		? series highlat. eruptions	?
1601	0.39	1.00	0.37	1.00	1600	Huaynaputina, Peru	6
1641	0.35	1.00	0.42	1.00	1641	Parker, Philippines	5
1666	0.28	0.94	-	-		? Long Island, New Guinea	6
1695	0.29	1.00	0.23[1]	0.71	1693	? Serua, Banda	4
1698	0.16	0.72	0.20	0.51		?	?
1730	0.11	0.53	–	–		?	?
1740	0.17	0.87	–	–	1739	Shikotsu, Japan	5
1810	–	–	0.27	0.90	1809	Unknown, tropical	(6)
1816	0.29	0.97	0.14	0.65	1815	Tambora, Indonesia	7
1832	0.12	0.54	0.17[2]	0.50	1831	Babuyan, Philippines	4
1835	–	–	0.24	0.76	1835	Coseguina, Nicaragua	5
1843	–	–	0.23	0.71		?	?
1848	–	–	0.31	0.94		?	?
1862	0.09	0.53	0.16	0.76	1861	Makian, Indonesia	4
1879	–	–	0.22	0.56		?	?
1884	0.17	0.86	–	–	1883	Krakatau, Indonesia	6
1912	0.14	0.97	–	–	1912	Novarupta/Katmai, Alaska	6

[a]Volcanic Explosivity Index [*Simkin and Siebert* 1994, updated in 2002, L. Siebert, pers. communication]
[1]Even higher value in *Jones et al.* [1998] for year 1694: 0.28 with 0.68 probability.
[2]Higher value in *Jones et al.* [1998] for 1833: 0.27 cooling with 0.92 probability.

of volcanic cooling events. (2) The extraction procedure is automatic and all parameters are globally estimated. In comparison to past techniques, no threshold has to be arbitrary chosen in our approach. (3) The probability of detecting an event not only depends on the intensity of the cooling signal but trend and noise are also taken into account. (4) To our knowledge, the presented method is the only statistical approach that not only extracts the maximum amplitude of volcanic signals but also estimates their cumulative impact in time (see Figures 1 and 4). (5) Interestingly, only a relatively small number of large eruptions appear to impact climate variability in a clearly detectable way against the background noise. This result is consistent with a climate model response to realistic volcanic forcing (see Figure 4).

APPENDIX : KALMAN FILTERING

The essential difference between Kalman filtering and a conventional linear model is that the state vector $X(t)$ is not assumed to be constant but may change in time. The temporal dynamic structure is incorporated via the system equation. All the unknown parameters are denoted by the vector θ. The term "Kalman filter" refers to a sequential procedure for the estimation of the state $X(t)$ based on maximization of the likelihood function

$$l(\theta, X(0)) = p(y(0)|\theta, X(0)) \cdot$$

$$\prod_{t=1}^{T} p(y(t)|Y(t-1), \theta),$$

with $Y(t) = (y(1),...,y(t))$, and $X(0)$ the initial state. To maximize such a function, a sequential forward estimation procedure [*Meinhold et al.*, 1983; *Shumway et al.*, 1991] is performed in the following manner: (1) Use the system equation to compute $p(X(t)|Y(t-1))$, (2) apply the observational equation to compute $p(y(t), X|Y(t-1))$, (3) integrate on X to get $p(y(t)|Y(t-1))$ and upgrade the likelihood, (4) calculate $p(X(t)|Y(t))$, (5) return to step (1). To implement such a procedure, we follow the temporal evolution of the first and second order statistics $\mu(t|t) = E(X(t)|Y(t))$ and $\Sigma(t|t) = \text{cov}[X(t)|Y(t)]$ from time t-1 to t. Consequently, we suppose that the moments are available up to time t-1. Our objective

is to update these quantities to time t. To reach this goal, we first derive the moments of $x(t)$ given $\{Y(t\text{-}1), o(t) = j\}$: $\mu(t|t\text{-}1, j) = \Phi\mu(t\text{-}1|t\text{-}1) + (\mu_j, \mu_j, 0)'$ and $\Sigma(t|t\text{-}1, j) = \Phi\Sigma(t\text{-}1|t\text{-}1)\Phi' + M(\sigma_j, \sigma_\varepsilon, \lambda)$, where M_j is a matrix equal to

$$M_j = \begin{bmatrix} \sigma_j^2 & \sigma_j^2 & 0 \\ \sigma_j^2 & \sigma_j^2 & 0 \\ 0 & 0 & \lambda\sigma_\varepsilon^2\Sigma_f \end{bmatrix},$$

for $j=0,1$ with $\sigma_0=0$, $\sigma_1=\sigma_v$ and $\Sigma f_{ij}=1//[(i+j\text{-}1)(i\text{-}1)!(j\text{-}1)!]$. Given $\{Y(t\text{-}1), o(t) = j\}$, the moments of $y(t)$ are: $E(y(t)|t\text{-}1, j) = H\,\mu(t\text{-}1|t\text{-}1, j)$ and $\Sigma(y(t)|t\text{-}1, j) = H\,\Sigma(t|t\text{-}1, j)\,H' + \sigma_\varepsilon$. The distribution of $(y(t)|Y(t\text{-}1))$ is a mixture of normal distributions: $\Sigma\pi_j(t)\,N(E(y(t)|t\text{-}1, j), \Sigma(y(t)|t\text{-}1, j))$. The posterior probability of $o(t) = j$ given $Y(t)$ is $q_j(t) = \pi_j(t)p(y(t)|Y(t\text{-}1), j)/p(y(t)|Y(t\text{-}1))$. Given $Y(t)$, we update the moments of $X(t)$ conditioned on $o(t)$: $\mu(t|t, j) = \mu(t|t\text{-}1, j) + K(t, j)[y(t)\text{-}E(y(t)|t\text{-}1, j)]$ and $\Sigma(t|t, j) =[I\text{-}K(t, j)H]\Sigma(t|t\text{-}1, j)$, where $K(t, j)$ is the Kalman gain matrix conditioned on $o(t) = j$. The classical assumption of the statistical Kalman Filter is that all variables are normally distributed. This explains why the second statistics, mean and variance, are the only moments to be sequentially computed. But in our case, the probability distribution function of the cooling events is a mixture, either 0 (no cooling event) or normal (see Equation (3)). To keep working with a normal distribution but not a mixture, we choose to approximate our mixture by a normal distribution with the same moments: $\mu(t|t) = \Sigma\,q_j(t)\,\mu(t|t, j)$ and $\Sigma(t|t) = \Sigma\,q_j(t)\,\Sigma(t|t, j)$. This step allows us to complete the updating of $\mu(t|t)$ and $\Sigma(t|t)$.

REFERENCES

Ammann C.M., J.T. Kiehl, C.S. Zender, B.L. Otto-Bliesner, and R.S. Bradley, Coupled simulations of the 20th-century including external forcing, *J. of Climate*, accepted pending revision, 2003.

Boville B.A. and P.R. Gent, The NCAR climate system model, version one, *J. of Climate, 11(6)*, 1115-1130, 1998.

Bradley R.S., The explosive volcanic eruption signal in northern hemisphere continental temperature records, *Climatic Change, 12*, 221-243, 1988.

Briffa K.R., P.D. Jones, F.H. Schweingruber, and T.J. Osborn, Influence of volcanic eruptions on northern hemisphere summer temperature over the past 600 years, *Nature, 393*, 450-455, 1998.

Briffa K.R., T.J. Osborn, F.H. Schweingruber, I.C. Harris, P.D. Jones, S.G. Shiyatov, and E.A. Vaganov, Low-frequency temperature variations from a northern tree ring density network, *J. Geophys. Res., 106(D3)*, 2929-2941, 2001.

Castleman A.W., H.R. Munkelwitz, and B. Manowitz, Isotopic studies of the sulfur component of the stratospheric aerosol layer, *Tellus, 26*, 222-234, 1974.

Crowley T.J., T.A. Criste, and N.R. Smith, Reassessment of Crete (Greenland) ice core acidity/volcanism link to climate change, *Geophys. Res. Lett., 20*, 209-212, 1993.

De la Cruz-Reyna~S., Poisson-distributed patterns of explosive eruptive activity, *Bull. of Volc., 54*, 57-67, 1991.

Dutton E.G. and B.A. Bodhaine, Solar irradiance anomalies caused by clear-sky transmission variations above Mauna Loa: 1958-99, *J. of Climate, 14*, 3255-3262, 2001.

Esper J., E.R. Cook, and F.H. Schweingruber, Low-frequency signals in long tree-ring chronologies for reconstructing past temperature variability, *Science, 295*, 2250-2253, 2002.

Guo W., Y. Wang, and M. B. Brown, A signal extraction approach to modeling hormone time series with pulses and a changing baseline, *J. of Am. Stat. Ass., 94*, 746-756, 1999.

Harrison P.J. and C.F. Stevens, A Bayesian approach to short-term forecasting, *Op. Res. Quart., 22*, 341-362, 1971.

Harrison P.J. and C.F. Stevens, Bayesian forecasting, *J. of the Royal Stat. Soc., Ser B, 38*, 205-247, 1976.

Hasselmann K., Stochastic climate models. Part I. Theory, *Tellus, 28*, 473-485, 1976.

Jones P.D., K.R. Briffa, and F.H. Schweingruber, Tree-ring evidence of widespread effects of explosive volcanic eruptions, *Geophys. Res. Lett., 22*, 1333-1336, 1995.

Jones P.D., K.R. Briffa, T.P. Barnett, and S.F.B. Tett, High-resolution paleoclimatic records for the last millennium: interpretation, integration and comparison with general circulation model control-run temperatures, *The Holocene, 8*, 455-471, 1998.

Kelly P.M. and C.B. Sear, Climatic impact of explosive volcanic eruptions, *Nature, 311*, 740-743, 1984.

Kitagawa G. and W. Gersch, A smoothness priors state-space modeling of time series with trend and seasonality, *J. of Am. Stat. Assoc., 79*, 378-389, 1984.

Lacis A.E., J.E. Hansen, and M. Sato, Climate forcing by stratospheric aerosol, *Geophys. Res. Lett., 19(15)*, 1607-1610, 1992.

LaMarche, V.C., Jr., and K.K. Hirschboeck, Frost rings in trees as records of major volcanic eruptions, *Nature, 307*, 121-126, 1984.

Lamb H.H., Volcanic dust in the atmosphere; with a chronology and assessment of its meteorological significance, *Trans. Roy. Phil. Soc. London, A266*, 425-533, 1970.

M.E. Mann, E. Gille, R.S. Bradley, M.K. Hughes, J. Overpeck, F.T. Keimig, and W. Gross, Global temperature patterns in past

centuries: A interactive presentation, *Earth Interactions, 4,* 29pp., 2000.

McCormick M.P., L.W. Thomason, and C.R. Trepte, Atmospheric effects of the Mount Pinatubo eruption, *Nature, 373,* 399-404, 1995.

Newhall C.G. and S. Self, The volcanic explosivity index (VEI): An estimate of explosive magnitude for historical volcanism, *J. of Geophys. Res., 87(C2),* 1231-1238, 1982.

Robock A. and M.P. Free, Ice cores as an index of global volcanism from 1850 to the present, *J. of Geophys. Res., 100(D6),* 11549-11567, 1995.

Robock A. and J. Mao, The volcanic signal in surface temperature observations, *J. of Climate, 8,* 1086-1103, 1995.

Robock A., Volcanic eruptions and climate, *Rev. Geophys., 38,* 191-219, 2000.

Shepard, N., Partially non-Gaussian state-space models, *Biometrika, 81,* 115-131, 1994.

Shumway R.H. and D.S. Stoffer, Dynamic linear with switching, *J. of Am. Stat. Assoc., 86,* 763-769, 1991.

Simkin T. and L. Siebert, *Volcanoes of the world,* Geoscience Press, Inc. and Smithsonian Institution, Tucson, AR, 2nd edition, 1994.

Wahba G., Improper priors, spline smoothing and the problem of guarding against model errors in regression, *J. of the Royal Stat. Soc., Ser. B, 40,* 364-372, 1978.

Wecker H.L. and C.F. Ansley, The signal extraction approach to nonlinear regression and spline smoothing, *J. of the Amer. Stat. Ass., 78,* 81-89, 1983.

West M. and J. Harrison, *Bayesian forecasting and dynamics models,* New-York, Springer-Verlag, 1997.

Zielinski G.A., P.A. Mayewski, L.D. Meeker, S. Whitlow, M.S. Twickler, M. Morrison, D.A. Meese, A.J. Gow, and R.B. Alley, Record of volcanism since 7000 B.C. from the GISP2 Greenland ice core and implications for the volcano-climate system, *Science, 264,* 948-952, 1994.

Caspar M. Ammann (corresponding author), Advanced Study Program & Climate and Global Dynamics Division, National Center of Atmospheric Research, 1850 Table Mesa Drive, Boulder, CO 80307-3000, USA (ammann@ucar.edu).

Wensheng Guo, Department of Biostatistics and Epidemiology, University of Pennsylvania School of Medicine, Philadelphia, PA 19104, USA (wguo@cceb.upenn.edu).

Philippe Naveau, Department of Applied Mathematics, University of Colorado, ECOT 231, Boulder, CO 80309-0526, USA (Philippe.Naveau@colorado.edu).

Hee-Seok Oh, Department of Mathematical and Statistical Sciences, University of Alberta, Edmonton, Alberta T6G 2G1, Canada (heeseok@stat.ualberta.ca).

Tropospheric Volcanic Aerosol

T. A. Mather and D. M. Pyle

Department of Earth Sciences, University of Cambridge, Downing Street, Cambridge, United Kingdom

C. Oppenheimer

Department of Geography, University of Cambridge, Downing Place, Cambridge, United Kingdom

Volcanic emissions represent an important source of aerosol to the global troposphere, and have important implications for the Earth's radiation budget at various temporal and spatial scales. Volcanogenic aerosol can also transport trace metals and other pollutants, with impacts on terrestrial ecosystems and human health. We provide here a primer on the current understanding of the origins and transformations of volcanogenic particles in the troposphere, covering their fluxes, size distribution, composition and morphology, and focusing on sulfur, halogen, and trace metal compounds. Such an understanding is essential to investigations of the atmospheric, environmental and human health impacts of volcanic volatile emissions.

1. INTRODUCTION

Volcanoes represent one of the most important natural sources of pollutants to the atmosphere, both during and between eruptions (Tables 1a and 1b; *Oppenheimer et al.* [2003]). A good understanding of volcanic volatile emissions in space and time, and of their atmospheric chemistry, and physical and radiative effects, is essential for various branches of atmospheric science. Eruptions of El Chichón (Mexico) in 1982 [e.g. *Pollack et al.*, 1983; *Hofmann*, 1987] and Mt Pinatubo in 1991 [e.g. *McCormick et al.*, 1995; *Fiocco et al.*, 1996; *Robock*, 2002] highlighted the radiative and chemical significance of *stratospheric* aerosol veils associated with large explosive volcanic eruptions, and contributed to understanding of the composition and evolution of volcanic clouds, and their wider impacts [see recent reviews by *Solomon*, 1999; *Robock*, 2000, 2002]. In con-

trast, the atmospheric and environmental impacts of volatile emissions into the *troposphere* by smaller eruptions and sustained magmatic and hydrothermal degassing are poorly understood, even though the time-averaged magnitude of such emissions exceeds that due to the rare, large events (Table 1b).

Tropospheric volcanic aerosol plays an important role in atmospheric radiation, both directly by backscattering and absorbing short-wave radiation, and modifying cloud cover and cloud radiative properties [e.g. *Hobbs et al.*, 1982; *Albrecht*, 1989, and references therein and *Kaufman et al.*, 2002]. Despite the lower source strength of volcanic emissions compared with anthropogenic sources (e.g. SO_2 in Table 1a), volcanogenic sulfur species may have at least as large an effect on the Earth's radiative budget as anthropogenic sulfur [*Graf et al.*, 1998]. This is due primarily to the comparative altitude of these sources: many volcanoes degas into the free troposphere, whereas anthropogenic emissions are generally entrained in the planetary boundary layer where species lifetimes are reduced [*Graf et al.*, 1998; *Stevenson et al.*, 2003].

Tropospheric volcanic aerosol can also affect terrestrial ecosystems and human health on local to regional scales

Table 1a. Estimates of some tropospheric aerosol and gas emission rates from volcanoes and other sources.

Material	Mean annual emission rate (Tg/yr)	Range	Reference
Primary Particle Emissions			
Sea salt	3340	1000–6000	a, b
Soil dust	2150	1000–5000	a, b
Carbonaceous aerosols	150	66–220	b
Fine ash production from small volcanic eruptions	20		c
Time-averaged volcanic sulfate return flux to the upper troposphere from the stratosphere	0.5–2	0–25	d, e
Emissions available for gas-particle conversion (Tg S/yr)			
Biogenic sulfides	25	12–42	b
Anthropogenic SO_2	79	60–110	b
Volcanoes (SO_2), troposphere only.	5–10	3–25	e, f

a – *Raes et al.* [2000]; b – *Penner et al.* [2001]; c – this work; d – *Pyle et al.* [1996]; e - *Halmer et al.* [2002]; f – see also Table 1b.

Table 1b. Recent estimates of volcanic SO_2 release to the atmosphere.

Source of estimate	Total volcanic emission (Tg S/yr)	Sporadic[#] volcanic emissions (Tg S/yr)	All continuous volcanic emissions (Tg S/yr)		
			Total	Continuously erupting	Non-erupting
Stoiber et al. [1987]	9.4	4.8	4.6	1.2	3.4
Andres and Kasgnoc [1998]	6.7	2.0	4.7		
Halmer et al. [2002]	7.5–10.5	4.5–6.3	3.0–4.2		

[#]– includes both 'small' eruptions that release SO_2 only to the troposphere, and 'large' eruptions that release SO_2 to the stratosphere. The time-averaged sulfur flux to the stratosphere from large eruptions is ~ 0.5–2 Tg S/yr [*Pyle et al.*, 1996; *Halmer et al.*, 2002].

[e.g. *Baxter et al.*, 1982; *Mannino et al.*, 1996; *Allen et al.*, 2000; *Delmelle et al.*, 2001; *Grattan et al.*, 2003]. Coarse particles (2.5–10 µm) are primarily associated with the aggravation of respiratory conditions, such as asthma, in humans. Fine particles (<2.5 µm) are implicated in increased heart, lung and respiratory disease, and symptoms such as asthma, decreased lung function, and premature death.

While volcanic emissions have contributed to atmospheric evolution throughout the history of the Earth [e.g. *Holland*, 1984; *Oppenheimer*, 2003], the increases in anthropogenic emissions since the Industrial Revolution mean that the environmental impacts of natural emissions may now be modified. It is important to understand the character and chemistry of natural tropospheric emissions in order to identify and interpret the possible effects of their interactions with anthropogenic pollutants. Air pollution studies in Mexico City, for example, have demonstrated

how anthropogenic SO_2 emission mitigation strategies may be compromised by the adsorption of volcanic SO_2 from Popocatépetl on to existing anthropogenic particulates, leading to increased sulfate production [*Raga et al.*, 1999].

In addition to their impacts on the Earth's climate and global chemical cycles [*Phelan et al.*, 1982], there are more directly volcanological motives for studying volcanic particle emissions. Studies of volcanic gas, aerosol and condensates may provide valuable information about sub-surface magmatic conditions [e.g. *Symonds et al.*, 1992, 1994]. Monitoring of particle emissions can support volcano monitoring efforts [*Rose et al.*, 1982, *Woods et al.*, 1983, *Ammann et al.*, 1992], tracking of volcanic plumes [e.g. *Chuan et al.*, 1981], and evaluation of their potential health impacts [e.g. *Moore et al.*, 2002].

The aim of this review is to report on the state of the art of the characterization of 'near-source' non-silicate volcanic particles, our understanding of their possible origins, emission

rates and impacts, and the limitations of our current knowledge. The generation and dispersal of volcanic ash in violent eruptions has been comprehensively reviewed elsewhere [e.g. *Sparks et al.*, 1997] and is referred to only in passing here.

2. CHARACTERIZING PARTICLE EMISSIONS

Aerosol is defined as a suspension of fine solid or liquid particles in a gas. Particles are collections of atoms or molecules large enough to display a structure similar to that of the equivalent bulk material; smaller entities are referred to as 'clusters' and can be up to 10^5 atoms in size, depending on composition [*Waychunas*, 2001]. Individual atmospheric aerosols typically range from a few nanometers (nm) to tens of microns (μm) in diameter, and comprise 'primary' components, emitted directly as particles (e.g. sea spray) and 'secondary aerosol', formed in the atmosphere by gas-to-particle conversion processes. (Sometimes care must be taken with this distinction. In the case of particles formed at high temperatures in volcanic vents, or during combustion, there is confusion over whether to classify them as primary or secondary. The term 'primary sulfate' has been used to describe particles formed from SO_2 by combustion sources in power plants and smelters and then emitted to the atmosphere [*Holt et al.*, 1982]. These particles are however not emitted directly as particles from the fuel source.)

Four key parameters influence the nature and impact of volcanic particulate emissions:

1. Particle emission rates, and their distribution in space and time
2. Particle size distributions
3. Size-resolved chemical compositions
4. Particle morphologies

2.1. Particle Emission Rates, and Their Distribution in Space and Time

Volcanic volatile emissions into the troposphere vary in space and time, and are strongly influenced by the style of volcanic activity. There are significant differences between the large, short-lived perturbations that accompany major explosive eruptions, and the sustained outputs from persistently active volcanoes that contribute to the tropospheric 'background', and it is essential to distinguish between these. We can broadly divide primary sources of volcanic particulate emissions into three types:

(i) *Emissions from ephemeral, major eruptions.* Large explosive (tephra-producing) and effusive (lava-produc-

ing) eruptions release considerable quantities of volatiles in a relatively short time period (hours–days). While the largest explosive events inject a substantial proportion of their volatiles into the stratosphere, some will remain within the troposphere [*Textor et al.*, 2003b].

(ii) *Emissions sustained over years and decades from persistently active, or erupting, volcanoes.* Mount Etna and Stromboli (Italy) and Masaya (Nicaragua) provide examples of long-lived 'passive' or 'quiescent' degassing directly from a lava pond or lake. Such 'open vent' volcanoes discharge considerable quantities of volatiles into the troposphere. This background degassing may be punctuated by explosive eruptions that recur on timescales ranging from tens of minutes (Stromboli) to weeks and months (Etna). Long-term lava dome eruptions of Merapi (Indonesia; 18th Century–present), and Soufrière Hills (Montserrat; 1995–present); and the lava-flow eruptions of Kilauea (Hawaii; 1983–present) can also be included in this class of activity.

(iii) *Non-eruptive 'fumarolic' discharges, usually dominated by steam, from inactive volcanoes, or between periods of magmatic activity.* Examples include White Island (New Zealand), Solfatara and Vulcano (Italy).

In addition to these primary emission sources, a fourth can also be identified: the return of particulates (fine volcanic ash, sulfate particles) and gases from the stratosphere into the upper troposphere, following large explosive eruptions. Note that this source re-enters the troposphere by crossing the tropopause, while the others are entrained at varying heights within the troposphere.

While the division between classes (i) and (ii) is arbitrary, it is important to distinguish the individual volcanoes that perturb the atmospheric aerosol budget to such an extent that they constitute a radiative forcing, from those that collectively contribute to background aerosol levels over long timescales.

As well as the temporal variability of emissions from individual volcanoes, there are also significant spatial variations in emissions, both in terms of source elevation and latitude. Uncertainties in these parameters contribute substantially to the differences between global models of the fate and impacts of volcanic sulfur emission [*Graf et al.*, 1998; *Stevenson et al.*, 2003]. In the troposphere, modeled lifetimes of volcanic sulfate aerosol vary from 2–5 days at low altitudes (< 2 km) to > 10 days (at 4 km and outside the tropics) [*Stevenson et al.*, 2003].

Due to their very nature, volcanoes tend to be located at high elevations, thereby contributing to the extended life-

times of their emissions. Seventy-five percent of volcanoes active between 1990 and 1999 have a summit elevation > 1 km and 20% exceed 3 km (Figure 1). The latitude of emission also influences aerosol lifetime. Sixty percent of recently active volcanoes lie between 30°S and 30°N (Figure 1). In this region, gas and aerosol lifetimes remain short (< 5–10 days) to considerable elevation, due to the strong convective activity in the equatorial troposphere [Graf et al., 1998].

The structure and circulation of the atmosphere varies temporally and spatially on a range of scales, and influences interactions between volcanic particles and the atmosphere. On a seasonal timescale, the tropical tropopause is higher (~ 100 hPa, ~ 16 km) and colder (~ −76°C) in the Northern Hemisphere (NH) winter, and lower (~ 115 hPa) and warmer (−70°C) during the NH summer [e.g. Highwood and Hoskins, 1998]. The extra-tropical winter tropopause tends to be lower than the summer tropopause, with the

Figure 1. Latitude and summit elevation of the 160 volcanoes active between 1990 and 1999, as recorded by the Smithsonian Institution Global Volcanism Project [Simkin and Siebert, 1994] (including 18 submarine volcanoes). 60% of these volcanoes lie in the Northern Hemisphere; more than 75% have summit elevations of over 1 km. 1 km is the approximate height of the boundary between the planetary boundary layer and the free troposphere.

minimum pressure (peak altitude) in September (NH), or January–March in the Southern Hemisphere (SH) [e.g. Wong and Wang, 2000]. Thus, one might expect a higher proportion of volcanic eruptions during (local) winter months to reach the stratosphere. The transport of material from the stratosphere into the troposphere is asymmetric (stronger in the NH), and varies seasonally [e.g. Holton et al., 1995]. Over the period 1979–1998, the peak downward flux of volcanic aerosol from the stratosphere into the upper troposphere was in local spring in each hemisphere, and concentrated at latitudes of >70°S, and >50°N [Kent et al., 1998]. The tropopause also shows short timescale variability associated, for example, with atmospheric waves [e.g. Holton et al., 1995], and interannual variability associated with features such as the El Niño-Southern Oscillation [e.g. Kiladis et al., 2001].

More specific geographical considerations, such as local topography, surface properties and meteorology, have important implications for particle emissions, especially in terms of plume transport, dilution and atmospheric lifetime. The background atmospheric chemical composition of the atmosphere will further determine what reactions the volcanic emissions may undergo during transport. Neither aspect has been evaluated in detail, other than at a handful of volcanoes [Delmelle, 2003].

2.2. Particle Size Distributions

The size characteristics of a particle population may be described by a particle number distribution. Assuming spherical particles, the number distribution can be used to calculate particle surface area, volume and mass (assuming a density) distributions with respect to particle size. Because of the r^2 and r^3 dependences, the larger particles in the distribution become more important in the surface area distribution, and even more so in the volume distribution (Figure 2).

The particle size spectrum is fundamental to many of an aerosol's properties and to the fate of particles in the atmosphere, not least because of its control on atmospheric lifetimes. Considering sedimentation alone, 1 μm diameter spheres at 5 km elevation with a density of 2000 kg m⁻³ have an atmospheric residence time of 220 days, compared to just 4 days for 20 μm particles [Junge, 1963]. However, sedimentation velocities do not present the complete picture. Particle deposition occurs both in the absence of precipitation (dry deposition) and through scavenging by atmospheric hydrometeors (wet deposition). Both pathways require the collection of particles by a surface (e.g. a plant, the sea, or soil for dry deposition; a hydrometeor surface for wet deposition). Small particles

(< 0.05 μm) act much like gases, and are efficiently transported to surfaces by Brownian diffusion. Larger particles (2–20 μm) tend to impact on surfaces due to their inertia, while the very largest particles (> 20 μm) settle out under gravity.

Collection mechanisms for particles in the 0.1–2 μm diameter range (known as the accumulation mode) are inefficient. These particles experience extended atmospheric lifetimes, unless they act as nucleation sites for cloud particles, or undergo a change in size that takes them out of the accumulation mode. Particles in this size range can have prolonged and wide reaching atmospheric effects [e.g. *Seinfeld and Pandis*, 1998; *Hobbs*, 2000].

Figure 2. Alternative descriptions of particle size distributions according to particle concentration (upper plot), surface area (center plot) and volume (lower plot), shown here for the same dataset.

Whitby [1978] summarized the different particle sizes observed in the atmosphere as follows:

(i) < 0.1 μm: the "nucleation" mode, generated primarily by gas-particle conversion processes associated with high temperature processes (e.g. combustion),

(ii) 0.1 μm - 2 μm: the "accumulation" mode, resulting from the condensation of low volatility vapors and agglomeration and growth of particles in the nucleation mode,

(iii) > 2 μm: the "coarse particle" mode, largely consisting of mechanically generated particles (e.g. wind-blown dusts).

Since particles < 2.5 μm diameter can penetrate deep into human lungs, monitoring of the accumulation mode is particularly important in terms of health impacts. The radiative effects of particles depend strongly on size, with smaller particles tending to backscatter incoming short-wave solar radiation, and larger particles tending to absorb outgoing terrestrial radiation. In the stratosphere, the transition radius between these two regimes is around 2 μm [*Lacis et al.*, 1992]. The particle size distribution as well as particle composition, determines the potential for particles to act as cloud condensation nuclei (CCN). For a given atmospheric supersaturation and composition, there will be a minimum particle diameter above which it can act as a CCN, thereby influencing the particle's atmospheric lifetime and indirect radiative effects.

The particle surface area distribution yields information concerning the area available for surface reactions. Particle growth by coagulation can increase as the particle surface area increases [*Pruppacher and Klett*, 1980].

2.2.1. Volcanic particle size distributions. Particle size distributions of volcanic aerosol have been characterized for several volcanoes (Table 2). Volcanic particle emissions tend to be multimodal, suggesting multiple processes of formation. Following Whitby, we expect fragmented magma and erosion of particles from the vent walls to be in the coarse fraction (> 2 μm), and the finer particles resulting from the condensation of volatiles and gas phase reaction products to be in the accumulation mode.

Size distributions evolve as the aerosol is advected from the vent (the larger fractions tend to settle out more rapidly) and during different stages of volcanic activity. Large explosive eruptions tend to have elevated particle concentrations, especially in the larger modes due to silicate fragments, while plumes from the waning stages of explosive activity
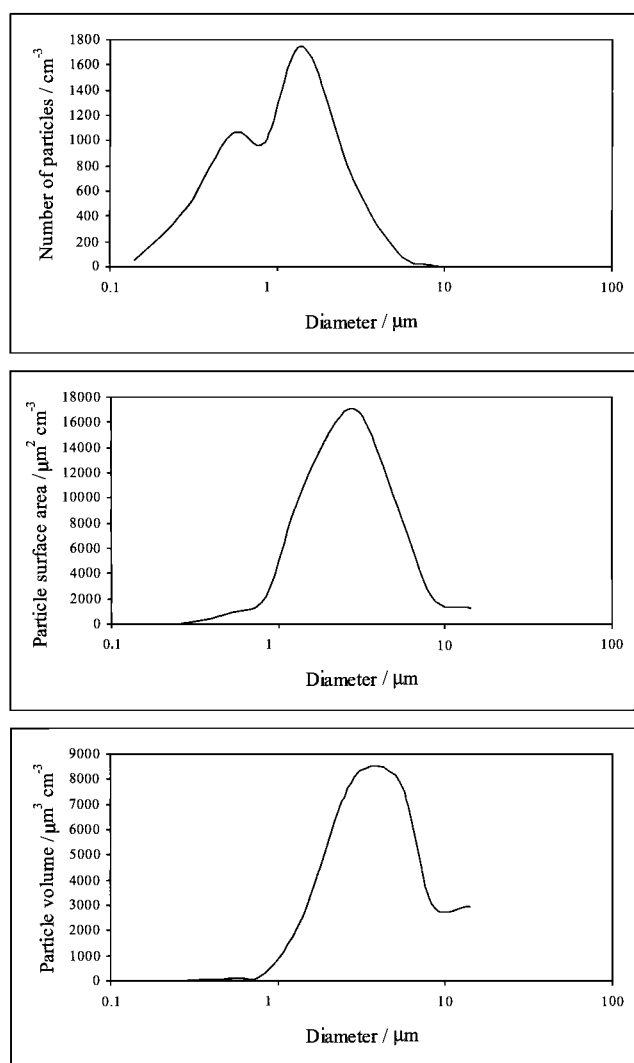
Table 2. Techniques used for the determination of particle size distributions in volcanic emissions. Adapted from *Watson and Oppenheimer* [2001].

Volcano	Basis of Data[a]	Plume height (km)	Method[b]	Particle diameter modes (μm)	Reference
Mt St. Helens,	A, D	15–20	QCM	0.2 – 1, > 10	*Chuan et al.* [1981]
USA	A, D	12–19	APS	1 – 2	*Farlow et al.* [1981]
	A, D	2.4–3.8	EAA, AC, CI	< 0.2, 1, >10	*Hobbs et al.* [1982]
	A, D	< 6	QCM	< 0.2, 3, 10	*Rose et al.* [1982]
Erebus,	A, D	4–5	OPC	< 0.2, 0.2–1	*Radke* [1982]
Antarctica	A, D	4.5–6	QCM	0.2, 2–6, > 20	*Chuan et al.* [1986]
Various (Central America)	A, D	2.5–5	QCM	0.2–0.8, 2–10	*Rose et al.* [1980]
	A, D	2–5	QCM	0.1–0.2	*Casadevall et al.* [1984]
El Chichon,	A, D	16.8–19.2	LSS/LII	4–10, > 20	*Gooding et al.* [1983]
Mexico	A, D	12.5–21.4	AC	0.8, 2.4	*Knollenberg and Huffman* [1983]
	A, D	18–21	PWI	0.2, ~ 2.0	*Oberbeck et al.* [1983]
	G, R	> 10	SP	0.6	*Asano et al.* [1985]
Etna, Italy	G, D	3–3.3	PCP	0.2–2.0	*Burtscher et al.* [1987]
	G, D	3–3.3	PCP / TEM	< 0.004	*Ammann and Burtscher* [1990]
	G, D	3–3.3	PCP / XPS	< 0.1	*Ammann et al.* [1992]
	G, D	3–3.3	PCP	< 0.1	*Ammann and Burtscher* [1993]
	G, R	3.5	SP	0.2–2.0, > 10	*Watson and Oppenheimer* [2000, 2001]
Etna + Kilauea	G, D	3–3.3	PCP / TEM	< 0.004	*Ammann et al.* [1990]
	G, D	3–3.3	PCP / TEM	0.02	*Ammann et al.* [1993]
Kilauea	A, D	3–4	OPC, DMA	0.4	*Porter and Clarke* [1997]
White Island, New Zealand	A/G, D	0.2–2	QCM	0.2, > 20	*Rose et al.* [1986]
Redoubt, Alaska	A, D	2.6–3.8	EAA, AC, CI	< 0.2, 1, > 10	*Hobbs et al.* [1991]
Pinatubo,	B, D	0–40	OPC	~ 0.2	*Deschler et al.* [1992]
Philippines	G, R	> 10	SP	1.2	*Asano et al.* [1993]
	G, R	> 10	SP	0.5	*Schmid et al.* [1997]

[a] Instrument Platform: A = Airborne, B = Balloon-borne, G = Ground based. Sampling method: D = Direct, R = Remote sensing.
[b] AC = Aerosol Counter, APS = Airborne Particle Sampler, CI = Cascade Impactor, DMA = Differential Mobility Analyser EAA = Electrical Aerosol Analyser, LII = Lucite Inertial Impactor, LSS = Laser-based Size Spectrometer, OPC = Optical Particle Counter, PCP = Photoelectron Charging (also called Aerosol Photoemission, APE), PWI = Palladium Wire Impactor, QCM = quartz crystal microbalance cascade impactor, SP = Sun-Photometer, TEM = Transmission Electron Microscopy, XPS = X-ray Photoelectron Spectroscopy.

are dominated by smaller particle modes [e.g. *Hobbs et al.*, 1982; *Rose et al.*, 1982]. Particle size distributions also change significantly with distance from the vent, as the coarser mode is deposited [e.g. *Hobbs et al.*, 1982].

2.3. Size-Resolved Chemical Compositions

The size-resolved chemical distribution can convey valuable information about the sources and evolution of particles. For example, a chemical component that corre-lates with the area distribution of particles may have been incorporated by surface adsorption; whereas a component following the volume distribution may comprise part of the bulk of the particulate matter. Given limitations in measurement techniques, it may, in practice, be difficult to differentiate between the two possibilities [*Hobbs et al.*, 1982].

The size-resolved chemical composition is important in terms of a range of aerosol properties. Particle composition influences density, and thus settling velocity, inertia,

and particle lifetime. Knowledge of the composition of fine particles is also important when evaluating potential health effects. For example, acidic particles < 2.5 μm can be particularly damaging to lung tissue. Information on the soluble and insoluble mass components of particles of various sizes can be used to estimate CCN emissions. Figure 3 shows an example of the size-resolved chemical composition of particles from the plume of Masaya volcano in Nicaragua. The species SO_4^{2-}, H^+, Na^+, K^+ and NH_4^+ are all concentrated in the accumulation modes in particles of about 0.5 μm in diameter, thus these species will experience extended atmospheric lifetimes. These fine acidic aerosols may also pose a health risk to people in the local area.
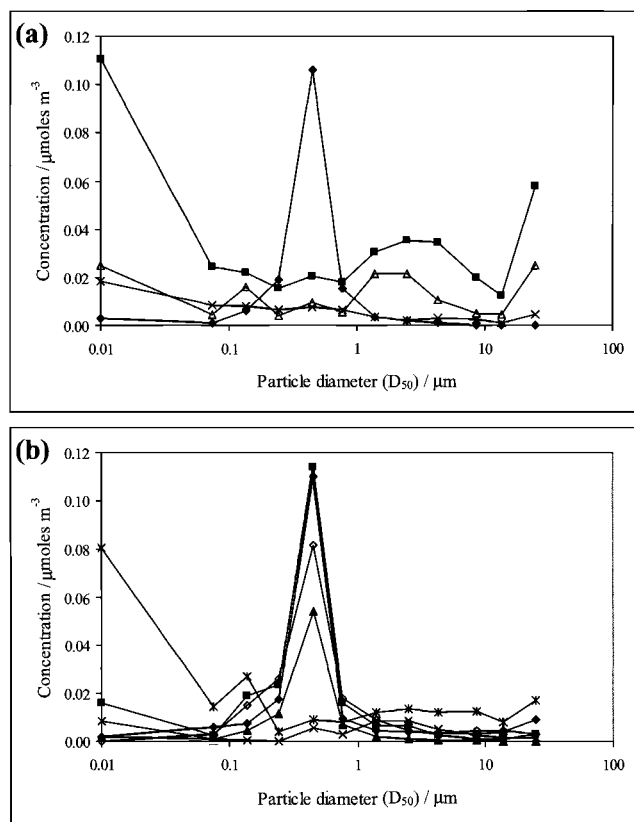
Figure 3. An example of the size resolved particle composition (of soluble ions) from the plume of Masaya volcano, Nicaragua. Measurements were made using a 10-stage micro-orifice uniform deposit impactor and species concentrations were determined using ion-chromatography. (a) Anions: diamonds = $SO_4^{2-}/10$; squares = Cl^-; triangles = F^-; crosses = NO_3^-; and (b) cations: diamonds = $H^+/10$; squares = $Na^+/10$; triangles = $K^+/10$; open diamonds = NH_4^+; crosses = Mg^{2+}; stars = Ca^{2+}. Data taken from *Mather et al.*, 2003.

2.4. Particle Morphologies

Particle morphology offers further valuable information on the formation and history of a particle, and, when coupled with chemical information, may indicate whether a particle is the product of a single nucleation event, or whether coagulation, overgrowth (growth of another substance over the surface of a particle) or surface deposition have played a role in its formation [e.g. *Obenholzner et al.*, 2003]. Particle shape and the formation of aggregates affect particle lifetimes [e.g. *Gooding et al.* 1983; *Oberbeck et al.*, 1983]. Fine ash from the Mt. St. Helen's plume was removed rapidly by aggregation, a process that was particularly successful at removing glass shards with high surface area-to-mass ratios [*Rose et al.*, 1983]. The influence of size, shape, and other factors, on the fall velocities of small ash particles has been extensively considered elsewhere [*Sparks et al.*, 1997; *Bonadonna et al.*, 1998].

2.5. Measurement Techniques

A variety of remote-sensing and direct sampling techniques has been employed in the measurement of volcanic aerosol and the characterization of volcanic plumes (Table 3). Lidar techniques can be used to give more detailed information on plume structure and location [*Hobbs et al.*, 1991]. Weather radar is useful for studies of more ash-rich clouds [*Harris et al.*, 1983].

While remote sensing techniques are widely applicable, and safe, there are as yet no satisfactory techniques for inferring the composition or shape of volcanic particles from such data. Direct sampling of volcanic plumes, either from the ground or from aircraft or other airborne platforms, remains a necessity. Currently available techniques for particle characterisation are limited to particles and clusters larger than ~ 100 nm (Figure 4). With the development of suitable substrates [e.g. Cu grids, *Pfeffer et al.*, 2001], transmission electron microscopy (TEM) techniques could be more widely used. For further discussion of the study of nanoparticles in the environment see *Banfield and Navrotsky* [2001].

3. ORIGINS AND CHARACTERISTICS

The aerosol measured in volcanic plumes may originate in any of four ways:

(i) *Pyroclastic material (tephra)*
  - juvenile fragments from the magma, including glass and crystals
  - lithic fragments eroded from the vent walls

Table 3. Techniques previously used for volcanic particle measurements. For a general review of atmospheric aerosol measurements see *McMurry* [2000].

Technique	Information given on: Size distribution	Chemical composition	Particle shapes	Example reference
Ground based Remote Sensing				
Sun Photometry (SP)	Aerosol optical depth, size, surface area and volume spectra	–	–	*Watson and Oppenheimer* [2000]
Passive infra-red (IR) Spectroscopy	Some information of aerosol sizes by comparison with models. Particle size distribution is poorly constrained.	Can distinguish for example silicates and carbonates from water / ice	Some information on shape by comparison with models.	*Lynch* [1996]
Direct sampling Single filters (e.g. Teflon, polycarbonate, cellulose, Lucite inertial impactor, LII)	Total mass can be used in size distribution models. Sizes of individual particles from imaging.	Total chemical compositions can be determined by techniques such as ion chromatography, for soluble ions, and ICP-MS*, SEM*/FESEM*/TEM* in conjunction with, for example XPS* can also give compositional data for individual particles.	If suitable substrates are used SEM/FESEM/TEM imaging techniques can be used. Short exposure times may also be necessary to ensure the integrity of individual particles.	*Hobbs et al.* [1991]; *Gooding et al.* [1983]
Filters in series	Can separate particles into 2 size fractions	As for single filters	As for single filters	*Allen et al.* [2000]
Cascade impactor (CI)	Separates particles into different size fractions by impacting them onto a series of plates.	As for single filters	As for single filters	*Hobbs et al.* [1991]
Quartz crystal microbalance impactor (QCM)	Can give real-time mass by size readings.	Can be used in SEM/FESEM/TEM	SEM/FESEM/TEM	*Chuan et al.* [1981]
Laser-based size spectrometer (LSS)	Size spectrum for particles > 2 μm - by re-suspension of particles after collection.	–	–	*Gooding et al.* [1983]
Electrical aerosol analyzer (EAA) and aerosol counter (AC)	Size spectra (0.01 μm – 4.9 μm by electrical mobility forward and 90° light scattering particle imaging by lasers.	–	–	*Hobbs et al.* [1982]
Differential mobility analyzer (DMA)	Real-time size spectrum of particles	Hygroscopic Tandem Differential Mobility Analyser can give information on hygroscopicity.	–	*Porter and Clarke* [1997]
Optical Particle Counters (OPC)	Real-time size spectrum of particles although there can be limitations on the size range.	–	Some new models can distinguish particle non-sphericity.	*Hobbs et al.* [1991]

Table 3. (continued)

Technique	Information given on: Size distribution	Chemical composition	Particle shapes	Example reference
Photoelectric Charging of Particles (PCP)	The diffusion charge is proportional to the total surface area and may be used as an estimate for the particle concentration for a given size distribution. This can study particles below 100 nm missed by impactors.	Allows extremely sensitive and selective detection of monovalent copper in alkali chloride and sulfate aerosols containing different metal traces.	—	*Ammann et al.* [1992]
Airborne Particle sampler (APS)	Particles collected on wires and size distribution recovered using SEM and statistical methods.	SEM and XPS	SEM	*Farlow et al.* [1981]
Palladium wire impactor (PWI)	Size distribution recovered using SEM and statistical methods.	SEM and XPS	SEM	*Oberbeck et al.* [1983]

* ICP-MS = Inductively Coupled Plasma Mass Spectroscopy, SEM = Scanning Electron Microscope, FESEM = Field Emission Gun SEM, TEM = Transmission Electron Microscope, XPS = X-ray Photoelectron Spectroscopy.
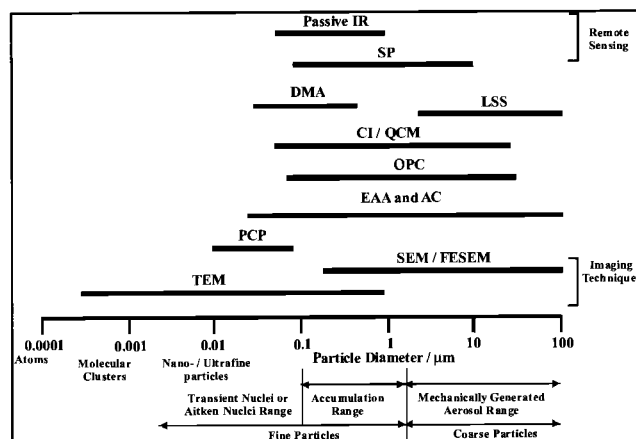
Figure 4. Size ranges covered by different particle measurement techniques. Refer to Tables 2 and 3 for explanation of abbreviations.

(ii) *Condensation of volcanic gases (originating from the following possible sources) as they cool*
- volatile species (including trace metals) released directly from the magma
- high-temperature gas-phase reaction products (involving volcanic and perhaps atmospheric components)
- boiling of hydrothermal fluids
- wall rock interactions (by condensed acid liquids and other plume components)

(iii) *Transformations of existing particles*
- adsorption of species on to the surfaces of other particles (with possible subsequent reaction or leaching of material from the host particle)
- dissolution of species into the aqueous phase

(iv) *Low temperature reactions (gas-to-particle reactions at ambient temperature and aqueous phase reactions)*

The different processes of particle formation are shown schematically in Figure 5. Many of these processes are complex, and temperature-dependent. The upper limit for condensation of magmatic volatiles is determined by the thermodynamic properties of the salt, or compound, and the temperature at which the vapors reach supersaturation. These processes have been explored by equilibrium thermodynamic modeling of gas mixtures [e.g. *Symonds et al.,* 1992, 2001; *Symonds and Reed,* 1993]. One of the key species in plumes is sulfuric acid, which has a boiling point of 330 °C. However thermodynamic modeling of the temperature of formation of $H_2SO_4.H_2O_{(aq)}$ suggests that, amongst other things, it is strongly dependent on the S content of the gas. At 10% S, $H_2SO_4.H_2O$ forms below 261 °C; while at 0.1% S, the satu-
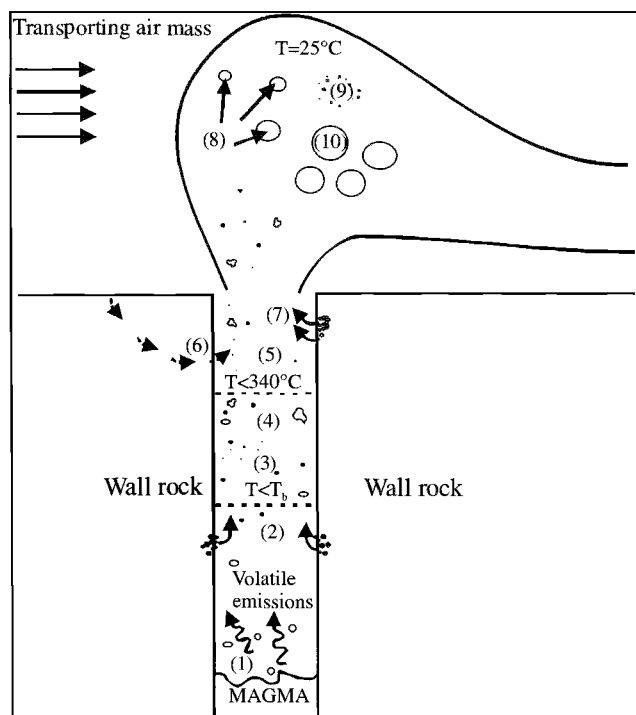
Figure 5. Cartoon illustrating processes that contribute to particle formation in volcanic plumes. The relative importance of different processes will vary between different volcanic systems (e.g., in fumarolic systems there will be few if any particles from magma fragmentation): (1) fragmented magma; (2) erosion of rock particles from the vent walls; (3) condensation of volatile species (including trace metals) released directly from the magma; (4) adsorption of species onto the surfaces of other particles and possible subsequent leaching of material from the host particle; (5) condensation of high temperature gas phase products; (6) boiling of meteoric water or water from another source that has leached the surrounding country rock into the gas; (7) interactions with the wall rock by condensed acid liquids and other plume components; (8) dissolution of species into the aqueous phase; (9) gas to particle reactions at ambient temperature; (10) aqueous phase reactions. T_b represents the boiling temperature of the different volatiles in the plume. Adapted from *Symonds et al.* [1992] and *Smith et al.* [1982].

ration temperature drops to 202 °C [*Symonds et al.*, 1992]. If such low temperatures are not achieved before the gas exits the vent, then trace element scavenging from wall rock by condensed acid droplets will not contribute significantly to the particles formed. At temperatures between those for salt crystallization and H_2SO_4 formation, adsorption of HCl and HF gas on to the surface of solidified silicates may become important [*Óskarsson*, 1980].

The presence of an aqueous phase is important for the dissolution of soluble species, and for chemical reaction path-

ways. Since H_2SO_4 is hygroscopic, condensation will take water into the particulate phase at T < 202 °C. The initial high acidity of these small droplets will dictate what else they can dissolve, and which reactions can take place within them. Later in the development of a plume, aqueous droplets may form independently of H_2SO_4, a process that will be greatly influenced by the meteorological conditions of the transporting air mass.

3.1. Pyroclastic Material

Volcanic ash particles have characteristic morphologies and compositions [e.g. *Heiken and Wohletz*, 1985] and usually remain recognizable even when alteration by acid leaching, surface adsorption, or the formation of overgrowths occurs in the plume during transport. When present, rock fragments usually account for most of the larger mode in the size distribution (> 2 μm). The coarse fraction of ash-poor emissions may contain materials ranging from amorphous and crystalline elemental sulfur particles [e.g. Mt. Erebus, Antarctica; *Chuan et al.*, 1986; Popocatépetl, Mexico, *Obenholzner et al.*, 2003] to water droplets [e.g. fumarolic emissions at White Island, New Zealand; *Rose et al.*, 1986].

Rock fragments are not always limited to the larger size fractions. The 1986 plume of Mt. St. Augustine (Alaska) contained silicates in all fractions down to 0.1 mm [*Rose et al.*, 1988]. Crystals and crystal fragments often comprise a significant proportion of the silicate fraction of the smaller size fractions [e.g. *Rose et al.*, 1980; *Cadle et al.*, 1979]. Since the scale of inhomogeneities in the melt influences tephra particle size, more-crystalline magmas are likely to be a source of larger amounts of finer particles. Dome-forming eruptions of highly crystalline magma, such as that at the Soufrière Hills Volcano (Montserrat), release considerable quantities of fine ash. Typical ash emissions on Montserrat contain 10–30 wt% of < 10 μm particles [*Baxter et al.*, 1999; *Bonadonna et al.*, 2002; *Moore et al.*, 2002].

The flux of volcanic ash into the troposphere is very poorly constrained. Previous estimates dating from the 1970s [compiled in *Warneck*, 2000] range from 4–150 Tg yr, with a 'best estimate' of 33 Tg yr [*Andreae*, 1995] based on such disparate arguments as the rate of accumulation of clays in the ocean, and the abundance of volcanogenic particles in the stratosphere. The largest mass fluxes tend to be from explosive eruptive events, which will be dominated by larger particle sizes (> 50 μm) with short atmospheric lifetimes. Large explosive 'magmatic' eruptions also have proportionally lower small particle emissions than the typical 'smaller' events [*Hobbs et al.*, 1982; *Baxter et al.*, 1999]. Since quiescent plumes account for most of the global volcanic flux of sulfur and other gases to the atmosphere [e.g.

Berresheim and Jaeschke 1983; *Stoiber et al.* 1987 and see Table 1b], the same is likely to be true for particles. There are so few data on volcanic ash emission rates from quiescently degassing and weakly active volcanoes that it is not possible to make any meaningful estimate of the ash flux from these sources. However, the emission rate of ash to the troposphere from small explosive volcanic eruptions may be constrained from the records of historical eruptions. Small explosive eruptions (involving $< 10^{11}$ kg of erupted magma) occur at a rate of about 24 per yr, and release 6500 kg s^{-1} of tephra to the troposphere [*Pyle*, 1995, 2000]. Of this mass, typically $<10\%$ comprises particles smaller than 10 μm [e.g. *Carey and Sigurdsson*, 1982; *Wilson and Walker*, 1985], giving a 'typical' flux of fine ash from small explosive eruptions of < 20 Tg yr (Table 1a). Perturbations following the very largest explosive events ($> 10^{15}$ kg of erupted magma), may briefly increase the tropospheric fine ash load to $\sim 10^5 - 10^6$ Tg.

Large explosive eruptions transport particles higher into the atmosphere, leading to an extended lifetime compared to equivalent lower level emissions. For reasons discussed earlier, a bulk global value for particle emission may not be the most useful value for the purposes of modeling the radiative effects of volcanic aerosol. An appreciation of the particle size distribution and altitude and latitude of emission will be essential to a proper assessment of volcanic dust source strengths and impacts; at the present time, however, such data are almost non-existent.

3.2. Condensation of Volcanic Gases as They Cool

3.2.1 Volatile species released directly from the magma.

Many elements have been identified in volcanic emissions (e.g. Figure 6). *Vie le Sage* [1983] documented forty. By the time of sampling, however, many of these elements are combined into distinct phases, whose formation is not well understood. Furthermore, analyses often yield information only on individual elements or ions, such that the actual compounds present must be inferred (e.g. the data presented in Figure 3). Many of these elements are trace metals. Some may have been incorporated via acid leaching of wall rock and rock fragments but they also occur independently of acid, and are thus supposed to have been directly emitted from the magma. General trends can be observed between different volcanoes. In the non-eruptive plume of Mount St. Helens, Cu-Zn oxide and Al-salts (mostly sulfate) were the dominant solid, non-silicate particles [*Rose et al.*, 1982]. At Fuego (Guatemala) and Cerro Negro (Nicaragua), CaSO$_4$ and NaCl were more prevalent [*Rose et al.*, 1973], while in emissions from Mt. Erebus, Al-salts are common [*Keys and Williams*, 1981; *Rosenberg*, 1988].

Volatile solubility is controlled by the temperature, pressure, oxidation state and composition of the melt [e.g., *Carroll and Holloway*, 1994; *Wallace and Anderson*, 2000; *Scaillet et al., this volume*]. As the major volatile constituents (CO$_2$ and H$_2$O) exsolve from the magma forming bubbles, trace species also partition into the gas phase. *Vie le Sage* [1983] invoked the degree of covalency to explain differing trace metal volatilities and abundance in volcanic emissions. However, the prevalence of metals, such as K, Ca and Al, that tend to form predominantly ionic compounds in volcanic aerosol suggests limitations to this approach. Most information concerning the speciation of volatile constituents comes from inference, or thermodynamic calculations. Modeling approaches that assume equilibrium between gas and magma have emphasized the importance of halogens, in particular, in influencing the transport of trace species in magmatic gases [e.g. *Symonds et al.*, 1987]. This is supported by limited direct observations using spectroscopic methods [*Murata*, 1960] and the correlation of trace constituent concentrations with halogen levels [*Zoller et al.*, 1983]. Oxidation state is also an important control on speciation and solubility of species such as S [e.g. *Carroll and Webster*, 1994; *Scaillet and Pichavant*, 2003], and other trace constituents [e.g. *Mizutani* 1970; *Rose et al.*, 1982].
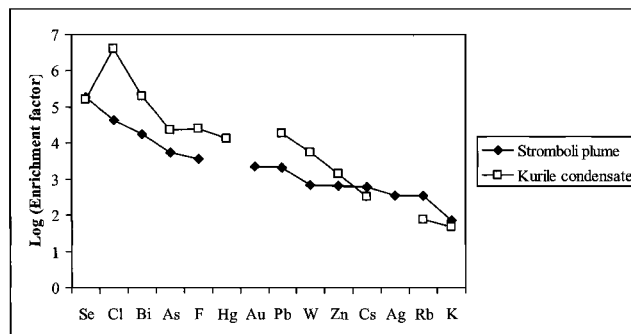
Figure 6. Abundances (relative to Mg) of selected volatile species in magmatic gas emissions from Stromboli [*Allard et al.*, 2000], and high-temperature fumarolic condensates at Kudryavy volcano, Kurile islands [*Taran et al.*, 1995]). The 'enrichment factor' [E.F.] for each element X compares the relative concentration of element X in the aerosol over that in the reference material, normalized to a reference element, R:

E.F. $(X) = (X/R)_{\text{aerosol}} / (X/R)_{\text{initial material}}$.

In this case, R is Mg, and the reference material is magma. For volcanic particles, the magma composition is usually taken as the reference material, and Al, Mg, Br and Sc have all been used as reference elements [*Vie le Sage*, 1983; *Varekamp et al.*, 1986; *Allard et al.*, 2000]. The most volatile species (Se, Cl, Br) may be enriched in the plume by five or six orders of magnitude compared to non-volatile Mg; alkali metals show 100-fold enrichment relative to Mg.

As volcanic gases cool in the atmosphere, they condense to form particles whose sizes will depend on the temperature gradient and the quantity of condensable volatiles available. Condensation products display a variety of morphologies, from the droplets and spheroids suggestive of liquid phase products, to regular, faceted structures suggestive of solid particles [e.g. *Varekamp et al.*, 1986; *Obenholzner et al.*, 2003]. Information about particle formation can be gleaned from chemical and textural particle analysis. Plumes often contain not only particles inferred to have precipitated as a single homogeneous phase at high temperatures, but also particles with multiphase histories, showing chemical zoning, concentric overgrowths, or intergrowths [e.g. *Stoiber and Rose*, 1974; *Meeker et al.*, 1993; *Obenholzner et al.*, 2003]. Thus far, most published investigations are of particles of ≥ 1 μm size. Refinements in sampling techniques [e.g. *Pfeffer et al.*, 2001] and high-resolution imaging hold much promise for extending analysis to smaller particles.

An important issue regarding trace metals is the role of gas phase transport after the magmatic vapors have left the vent. *Hinkley et al.*, [1991] showed that, within metres of an open vent on Kilauea, negligible Cd, In, Pb, Ti or Bi remained in the gaseous phase. This observation, and the high boiling points of many trace metal species, suggests that the atmospheric transport of many trace metals is predominantly in the solid phase. There are however, exceptions: appreciable quantities of Hg, Se and As *are* thought to be transported as gases [e.g. *Lambert et al.*, 1988; *Le Cloarec and Marty*, 1991].

3.2.2. High-temperature gas phase reaction products.
Although halogens may be a key species in trace metal transport, trace metals may not be preserved as halogen compounds if they undergo reaction during transport. For example, hydrolysis of $AlCl_3$ by atmospheric water may be responsible for the formation of Al_2O_3 near Vulcano's fumaroles [*Vie le Sage*, 1983].

Other than trace metals, the major gas phase reaction product of interest is sulfuric acid, which is generally considered an oxidation product of SO_2 or H_2S. The atmospheric sulfate production routes (discussed later) require oxidizing agents to mix from the ambient air. The existence of sulfate particles in the near-vent, and undiluted, emissions of some volcanoes systems may suggest a different oxidation pathway occurring in volcanic vents [e.g. *Allen et al.*, 2002]. The potential mechanism is as yet unclear, but it has been suggested that nucleation on ultrafine metal chlorides may play a role, with the metallic cations enhancing the reaction rate [*Berresheim and Jaeschke*, 1986]. Once formed, this sulfuric acid may modify

trace metal speciation by revolatilisation of HCl and the formation of metal sulfates:

$$2XCl_{(s)} + H_2SO_{4\,(l)} \Leftrightarrow X_2SO_{4\,(s/aq)} + 2HCl_{(g)}.$$
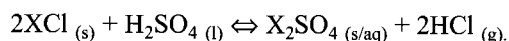
Etna volcano frequently shows distinctive differences between the emissions from lava flows, degassed at low pressures, and the summit plumes [e.g. *Gauthier and Le Cloarec*, 1998; *Burton et al.*, 2003]. The former tend to be halogen-rich, with very small particles (< 1 μm) dominated by Na and K sulfates and chlorides [e.g. *Toutain et al.*, 1995], in contrast to the 'stacked-platelet' morphology of S-Na-K bearing particles in the Cl-poor summit plumes. This may reflect reduced formation of ultrafine chloride particles in the summit plume leading to reduced S oxidation.

Other suggestions have been put forward for the absence of SO_4^{2-} in volcanic emissions. *Ammann et al.* [1992] suggested that where magmatic gases cool completely before emission, such as above lava flows and at fumaroles, no acid droplets are observed. They conclude that when gases cool under S-depleted or completely reduced conditions, initial acid formation may be suppressed because, at near ambient temperatures, SO_2 conversion rates are low. No elevated sulfate levels were observed in the Mount St. Helens eruption cloud, perhaps because opaque plumes limit photolysis, and/or because the kinetics were too slow compared with the risetime of the plume [*Hobbs et al.*, 1982]. Similar conclusions were drawn from airborne measurements of fumarole emissions from White Island [*Rose et al.*, 1986]. Since the mechanisms of sulfate production in plumes remain unclear, it is hard to say what conditions will lead to the observation of near-source sulfuric acid.

3.2.3. Wall rock interactions.
Interactions of wall rock materials with acidic and reactive gases in volcanic plumes are likely to be important, but have been little studied. Extraction of fluorine from volcanic gases by reaction with the wall rock has been invoked to explain variations of F with time and temperature in fumaroles [e.g. *Stoiber and Rose*, 1970], and suggested as the basis of a geothermometer [e.g., *Francis et al.*, 1996]. Studies of HCl-rich fumaroles at Augustine, Alaska, showed that wall rock leaching is important in the case of cooler emissions, where acids are likely to be more stable, and may also mobilize less volatile species such as Al, Ba, Sr and Mg [e.g. *Symonds et al.*, 1990].

Obenholzner et al. [2003] used high resolution scanning electron microscopy (FESEM) techniques to show the signature of a variety of contact metamorphic and related minerals in the particulate emissions from Popocatépetl. This

indicates the interaction of magma and magmatic fluids with carbonate-bearing rocks and other sediments beneath the volcano, as well as interactions at higher levels such as wall rock-magma interactions during ascent.

3.3. Transformations of Existing Particles

3.3.1. Adsorption of species on to the surfaces of other particles. The nucleation of acids on to ultrafine chloride particles can cause modification of particle morphology, resulting in acid-etched particle surfaces and overgrowths. Processes operating on larger scales are similar. Scavenging of volatiles by silicates can occur directly on to the surface, or be water-mediated. In some cases, all silicate particles are coated with a thin acidic film [e.g. *Casadevall et al.,* 1984]; in others, acidic coatings are absent [e.g. *Hobbs et al.,* 1991]. These observations are ascribed to differences in SO_2 oxidation rate under different conditions. Scavenging by ash can be an important sink for volcanic volatiles during eruptions [e.g. *Rose,* 1977; *Stith et al.,* 1978]. During explosive eruptions of Fuego, up to 33% of S and 17% of Cl were rapidly deposited to the ground by adsorption on ash [*Rose,* 1977]. For this process to occur, acidic particles must have formed, and the ash and acid particle densities must be sufficient to promote particle collisions. *Rose* [1977] observed a maximum in the soluble material on ash particles at intermediate distances from the vent, where acid droplets had had time to form but the plume was not yet dilute enough to impede particle interactions. As with smaller particles, the acids scavenged on to the ash can leach out soluble elements from the ash. Estimates can be made of the origin of any element found on the surface of an ash particle by comparing its surface enrichment with its relative concentration within the particle.

3.3.2. Dissolution of species into the aqueous phase. Once the plume exits the vent it will mix with ambient air. This background air may already contain an aqueous droplet phase, or else the cooling might cause more of the water vapor in the volcanic plume itself to condense, with the potential for small particles in the plume to seed aqueous droplets. Once formed, these aqueous droplets may be modified as they scavenge soluble species from the gas phase. The physical solubility of an arbitrary gas HA is described by the Henry coefficient H_e:

$$H_e = [HA]_{aq} / [HA]_g$$

where $[HA]_{aq}$ and $[HA]_g$ are the concentrations in the aqueous and gaseous phase, respectively. Acidic gases undergo acid-base reactions, such as:

$$HA_{(aq)} \Leftrightarrow A{-}_{(aq)} + H+_{(aq)}$$
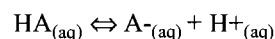
and these reactions enhance gas uptake. To take this into account, acid gas solubility is described by an effective Henry coefficient, H_e^*. This is also a function of pH and temperature. At room temperature and a pH of 2, H_e^* for HCl and SO_2 are 1.9×10^4 and 3.0 mol l⁻¹ atm⁻¹, respectively [taken from *Sander,* 1994 cited in *Textor et al.,* 2003b], hence HCl is preferentially scavenged into the aqueous phase. Enhancement of Cl over S in the particulate phase has been recognized, for example, in the plume of Augustine volcano [*Rose et al.,* 1988] and in studies of wet deposition rates for the two gases, and plume-affected rainwater analysis [e.g. *Johnson and Parnell,* 1986; *Kawaratani and Fujita,* 1990; *Aiuppa et al.,* 2001; *Edmonds et al.,* 2003].

Once SO_2 is oxidized to sulfate, the product is extremely hygroscopic, and the resulting increased acidity can decrease the H_e^* of HCl and effectively re-volatilise it. *Allen et al.* [2000] observed such an effect in the plume from Soufrière Hills, Montserrat where NaCl reacted with acid in the fine particle mode, resulting in the volatilisation of HCl from fine particles (showing high [Na⁺]:[Cl⁻] ratios), and followed by scavenging by coarser particles (showing low [Na⁺]:[Cl⁻] ratios).

3.4. Low Temperature Reactions

During atmospheric transport in the plume, the most important reactions are likely to be SO_2 oxidation and acid neutralization by background ammonia. SO_2 oxidation is thought to account for a number of observations in volcanic plumes. For example, *Farlow et al.* [1981] observed that ash collected only a day after a 1981 eruption of Mount St Helens was completely dry, whereas after that it was acid coated. SO_2 can undergo three classes of reactions in the atmosphere that may lead to the formation of particulate sulfate: gas-phase homogeneous reactions, aqueous-phase reactions, and heterogeneous reactions on the surface of solids [*Eatough et al.,* 1994].

The hydroxyl radical (OH) is considered the main agent for gas phase oxidation. OH forms in the troposphere by the reaction of photochemically generated oxygen radicals with water, and has a short lifetime. In the absence of clouds or fog, SO_2 conversion to particulate sulfate proceeds more rapidly during the day than at night, and more rapidly in summer than in winter. Studies of industrial plumes suggest that the OH reaction with SO_2 does not become important until the plume is dispersed and mixed with ambient air.

An increased conversion rate of SO_2 to sulfate is observed when water droplets are present, due to aqueous phase sul-

fur chemistry. The main oxidants are hydrogen peroxide (H_2O_2) and ozone (O_3) entrained from the surrounding atmosphere. Dissolved molecular oxygen is only a strong enough oxidizing agent in the presence of iron, manganese or other transition metal catalysts. The effectiveness of O_3 as an oxidant decreases with decreasing pH, whereas that of H_2O_2 shows little pH dependence. At the low pH associated with volcanic water droplets, H_2O_2 is the dominant oxidant. Although both O_3 and H_2O_2 are photochemically produced, their longer lifetimes in the atmosphere mean that the aqueous phase oxidation of SO_2 is much less photo-dependent than its gaseous phase equivalent. Couple this with expected lower nocturnal temperatures leading to a higher proportion of the water being in the liquid phase, and it seems likely that this oxidation pathway will be dominant at nighttime.

SO_2 can be oxidized on a variety of particle surfaces such as soot or dust. The rate of conversion depends on the nature of the surface, the presence of co-pollutants and the relative humidity. The oxidation rate can be enhanced when a film of water covers the particles, although this suggests that aqueous phase oxidation is in fact occurring. These types of reactions are thought to be important only in plumes of high particle density (> 100 μgm^{-3}).

In summary, slower gas phase reactions dominate in conditions of low humidity and daylight, with 5–10% h^{-1} of SO_2 reacted in summer and 0.3-1% h^{-1} of SO_2 reacted in winter; faster aqueous phase reactions dominate at higher humidity and at night (20–100% h^{-1} of SO_2 reacted). If the plume has a high dust/ash density then heterogeneous surface reactions may play a part too.

SO_2 loss rates, assumed to be primarily due to sulfate formation, have been calculated for several volcanic plumes. As might be expected, background atmospheric conditions strongly influence these rates. Studies of plumes in the cold Antarctic and Arctic atmospheres have shown little or no oxidation of SO_2 [e.g. Erebus, *Chuan et al.,* 1986; Mt. Redoubt, *Hobbs et al.,* 1991]. Elsewhere, *Hobbs et al.* [1982] observed oxidation rates in the Mt. St. Helens plume that were comparable to those observed in power-plant plumes (0.1% h^{-1}). If the loss rate is modeled in terms of first order kinetics, apparent rate constants range from 1.9 x 10^{-7} to 5.4 x 10^{-3} s^{-1} [*Oppenheimer et al.,* 1998].

The other major process that may occur as the plume ages is neutralization of aqueous acidic species by background ammonia. Variation is again observed in the degree of neutralization of acidic volcanic species by ammonia: *Allen et al.* [2000] documented unambiguous ammonia neutralization in the Soufrière Hills plume, but *Clarke* [cited in *Porter et al.,* 2002] observed very little in Kilauea's plume. Enhanced neutralization may help to mitigate the potential-ly detrimental environmental and health impacts of volcanic acid particles.

4. EMISSION RATES OF TRACE METAL AEROSOLS TO THE TROPOSPHERE FROM VOLCANOES

Degassing and erupting volcanoes release prodigious quantities of volatile heavy metals to the troposphere, predominantly in the particle phase (see section 3.2.1). This particle flux is not well constrained but is thought to constitute an important natural source of pollution, whose effects may be detected globally, for example in polar ice cores [e.g. *Ferrari et al.,* 2000; *Matsumoto and Hinkley,* 2001]. For some species (e.g. As, Bi, Cd, Cu, Pb, Se) volcanoes may be the largest natural emission source [e.g. *Nriagu,* 1989].

Two methods have been adopted to estimate volcanic metal fluxes. The first approach is to estimate the metal/sulfur ratio of volcanic emissions, and then use the known emission rates of sulfur to estimate the metal flux. This has been used to constrain individual metal fluxes from a few volcanoes [e.g. Erebus, *Zreda-Gostynska et al.,* 1997; Etna, *Gauthier and Le Cloarec,* 1998 and Stromboli, *Allard et al.,* 2000], as well as to estimate global emission rates [e.g. *Nriagu,* 1989; *Hinkley et al.,* 1999]. The difficulties with this approach are obvious: metal:sulfur ratios vary not only from volcano to volcano, but also temporally and spatially at any site. In part this reflects decoupling of the metal-rich particulate phase from the S-rich gas phase, but also, as is clear from Figure 7, this will also be influenced by the nature of degassing. For example, fumarolic emissions are considerably enriched in heavy metals, compared to sulfur, in contrast to the emissions from high-temperature magma degassing (Figure 7). At Etna, post-eruptive emissions from flank lava flows are also significantly enriched in heavy metals, compared to the emissions from the central craters [e.g. *Gauthier and Le Cloarec,* 1998].

In addition to uncertainties in the metal:sulfur ratio, there is significant uncertainty in the global tropospheric source strength of volcanic sulfur, which receives contributions from fumarolic activity and quiescent degassing as well as eruptions (Table 1b). While flux estimates for 'continuous' volcanic emissions of SO_2 to the troposphere agree fairly closely (3.0-4.7 Tg yr, Table 1b), there is more uncertainty (as well as spatial and temporal variability) over the proportion of sulfur (as SO_2) from small explosive eruptions emitted to the troposphere alone (2.0-6.3 Tg yr, see Table 1b). The flux of other sulfur species, such as H_2S, is so poorly known as to be unconstrained (ranging, for example, from < 0.2 Tg yr, *Stoiber et al.* [1987] to 1.5–37 Tg yr, *Halmer et al.* [2002]).
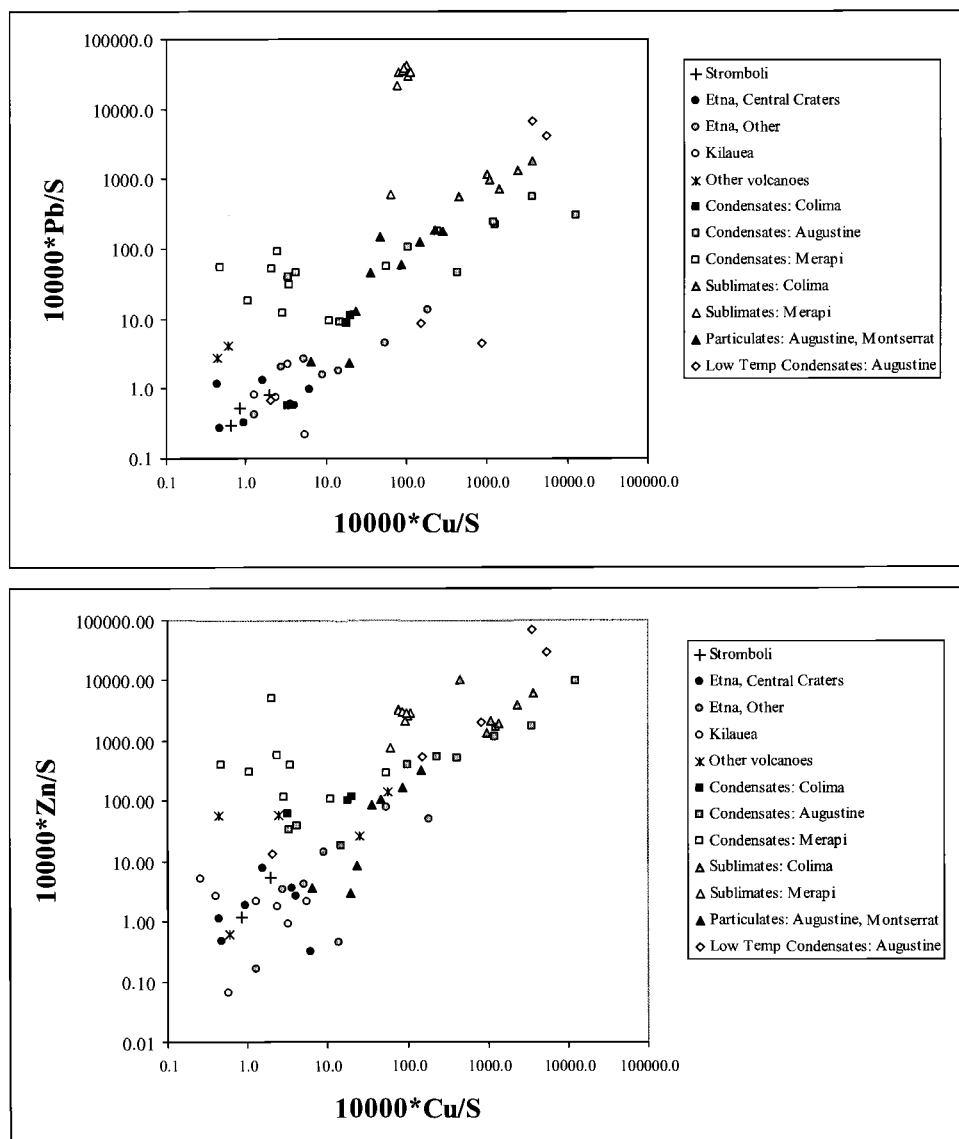
Figure 7. Covariation plots to show the metal/sulfur mass ratios in a variety of volcanic emissions and for three moderately volatile metals, Cu, Zn and Pb. Data represent determinations of: 'bulk plume' compositions (metals and sulfate collected on filters, SO_2 on base-treated filters; Stromboli, Etna, Kilauea and 'Other Volcanoes'); condensates (direct samples of condensed gas from high-temperature fumaroles); sublimates (precipitates collected in sampling tubes from high-temperature fumaroles); and particulates (filter samples of the volcanic plume). Both plots show strong correlation between metal/sulphur ratios, suggesting that the variability in metal: metal ratios in volcanic emissions is considerably less than the variability in metal/sulfur ratios. Data sources: *Allen et al.* [2000]; *Allard et al.* [2000]; *Crowe et al.* [1987]; *Hinkley et al.* [1999]; *Gauthier and Le Cloarec* [1998]; *Lepel at al.* [1978]; *Symonds et al.* [1990, 1992]; *Taran et al.* [2001]; *Zreda-Gostynska et al.* [1997].

Despite these difficulties, estimates of the *total* metal flux from degassing volcanoes agree fairly well, even if there are wide disparities for certain metals (e.g., Cu, Table 4). After correcting for a systematic error of a factor of 2 in *Nriagu's*

[1989] quoted volcanic S flux, there is a close correspondence between his estimate of 14 Gg yr^{-1} of Cu, Pb, Cd, Zn, As, Se released, and the estimate of *Hinkley et al.* [1999] of 10 Gg yr. This reflects the relatively similar 'global'

Table 4. Comparison of volcanic, natural and anthropogenic fluxes to the atmosphere of selected species.

Element	Volcanic (Gg/yr)	Natural (Gg/yr)	Anthropogenic (Gg/yr)
S	6700–10500[a]	27200[b]	77 000[b]
Al	13 280[c]	48 900[d]	7 200[d]
Co	0.96[e]	6.1[e]	4.4[d]
Cu	1.0[f], 4.7[e], 15[g], 22[h]	28[e]	35[e]
Zn	4.8[e], 7.2[f], 8.5[h]	45[e]	132[e]
Pb	0.9[f], 1.7[e], 2.5[g], 4.1[h]	12[e]	332[e]
As	1.9[e]	12[e]	19[e]
Se	0.3[h], 0.5[e]	9.3[e]	6.3[e]
Mo	0.2[e]	3.0[e]	3.3[e]
Cd	0.4[e]	1.3[e]	7.6[e]

Data sources: [a] See Table 1b; [b] *Bates et al.* [1992]; [c] *Symonds et al.* [1988]; [d] *Lantzy and Mackenzie* [1979]; [e] *Nriagu* [1989]; [f] *Hinkley et al.* [1999]; [g] *Lambert et al.* 1988; [h] *Le Cloarec and Marty* [1991];

Note: *Nriagu's* [1989] published volcanic metal emission rates were based on a range of S fluxes that were 50% too high (he quoted 15 – 50 Tg yr of S, when this value was actually 15–50 Tg yr of SO_2). The values quoted here have been corrected for this factor alone.

metal/sulfur ratios these authors adopt for degassing from purely 'magmatic' sources (for which there are relatively few data, e.g. Figure 8). Such 'global' estimates take no account of heavy metal emissions during explosive eruptions, which account for a significant but sporadic component of the annual global volcanic sulfur flux (30–70%, Table 1b), and for which the metal/sulfur ratios are essentially completely unconstrained. The estimates also neglect the fumarolic emis-

sions (both bulk fluid condensates, and the sublimates that precipitate from them) that may be considerably enriched in metals over sulfur (compare Figures 7, 8).

The second approach is to use the flux of a radioactive volatile metal (^{210}Po) as the normalizing factor [e.g. Lambert *et al.*, 1988]. While there are still relatively few $^{210}Po/S$ ratios measured on volcanic emanations, the metal/sulfur ratios estimated using this technique [e.g. Lambert *et al.*, 1988; *Le Cloarec and Marty*, 1991] are nonetheless consistent with the estimates derived by *Nriagu* [1989] and *Hinkley et al.* [1999] using the previous method (see Figure 8). Early estimates of the global volcanic S flux derived from this method (25 Tg yr^{-1}) are however somewhat higher than other estimates (see Table 1b) leading to higher metal flux estimates.

Both approaches have obvious limitations when attempting to assess the global fluxes of material to the troposphere from volcanic eruptions. First of all, many of the metals are thought to be transported as particulate halides; yet the flux measurements depend on establishing a 'typical' particulate metal to gas-phase sulfur ratio. Clearly the point of meas-
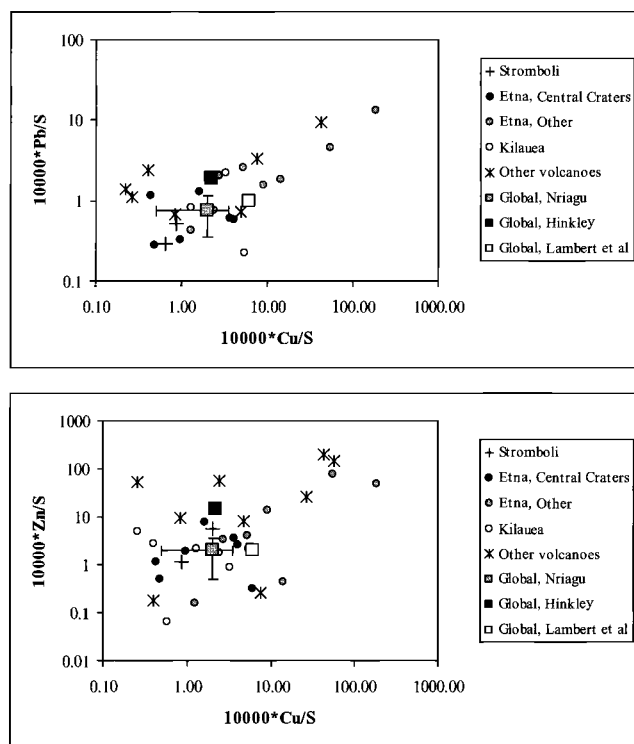
Figure 8. Estimates of metal/sulfur mass ratios (for Cu, Zn and Pb) in the 'magmatic' plumes emitted from erupting and degassing volcanoes, with three estimates for the 'Global' mean volcanic metal/sulfur value [*Nriagu*, 1989; *Hinkley et al.*, 1999; *Lambert et al.*, 1988]. Data sources as in Figure 7. 'Other volcanoes' includes data from Erebus (Cu, Zn; *Zreda-Gostynska et al.* [1997]), the Merapi Dome and Papandayan, Indonesia [*Nho et al.*, 1996]. *Nriagu's* global estimate includes error bars based on his published range of values. Note that metal/sulfur ratios from different vents at a single volcano [e.g. Etna, *Gauthier and Le Cloarec*, 1998] may vary by three orders of magnitude.

urement, and the amount of gas—particle separation that may have occurred by that point, will strongly influence the measurement [c.f. *Hinkley,* 1991]. Attempts to normalize to halogen flux might prove useful, but would be hindered by the currently poorly constrained volcanic emission rates of halogen species [e.g. *Symonds et al.,* 1988]. Finally, it is clear that even small variations in the contribution of fumarolic gases to volcanic plumes could give rise to considerable variations in the metal/sulfur ratios, and consequently flux estimates.

5. CONCLUDING REMARKS

Volcanic plume geochemical studies in the past have tended to focus on the measurement of composition and emission rates of gases. The benchmark work on *particle* composition of tropospheric volcanic plumes dates back to a number of pioneering (and courageous!) airborne campaigns carried out in the 1970s and 1980s [e.g., *Hobbs et al., 1982; Rose et al., 1986*]. Although there are exceptions [e.g., *Casadevall et al.,* 1984], most of these investigations concerned measurements of dilute eruption clouds rather than passive plumes (which typify many sustained volcanic emissions worldwide), and provided information on total particle fluxes (i.e., sulphate, ash) rather than detailed analyses of particle:gas phase ratios for individual species, and as a function of aerosol size.

There remains considerable scope, therefore, to design future field experiments on tropospheric volcanic plumes aimed at characterizing the size-resolved chemistry of aerosol, gas-particle interactions between plume constituents and the ambient atmosphere (including rural and urban atmospheres), and transport and deposition of both gaseous and particulate volcanogenic components. *Delmelle et al.* [2001] have begun work on dry deposition rates of SO_2 and HCl for the plume from Masaya volcano but indicate that considerable efforts are required to make meaningful characterizations. Physical and chemical characterization of both the gases and particles emitted by volcanoes will also feed directly into the adaptation of numerical models describing the transport and chemical evolution of plumes. Such efforts would support assessments of volcanogenic pollution scenarios, as well as contributing to understanding of the scavenging of volatiles from explosive eruption plumes bound for the stratosphere [*Textor et al.,* 2003a].

The observed variations in volcanic particle type and composition can reflect magmatic conditions, magmatic-hydrothermal processes [*Oppenheimer,* 1996], and wall rock contributions and reactions prior to emission. Once in the atmosphere, plume components undergo further modification during transport and dilution, with background meteorological conditions playing an important role. The result of all these interactions (Figure 9) is that particles may convey only limited information on mag-
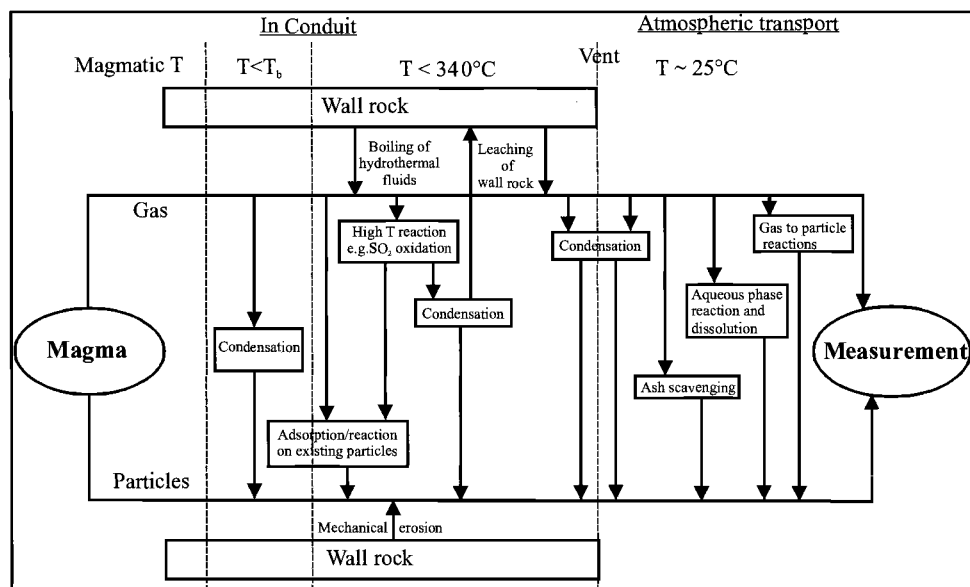
Figure 9. Flow chart to show the different processes that may contribute to particle development, between the point of emission from the magma and measurement. The pathways that are dominant will depend upon the nature of the volcanic system and the type of eruption. (T_b represents the boiling temperature of the different species in the plume).

matic processes. As *Ammann et al.* [1992] indicated, new tools and programmes for continuous, real-time volcanic particle monitoring are needed to identify potential indicators for magmagenesis and volcanic activity that could aid hazard assessment. Figure 9 also indicates that the point of measurement, i.e., the age and environment of the sample, influences the observed composition and size spectrum of any aerosol.

Table 5 summarizes particle flux estimates for individual volcanoes. This reveals orders of magnitude of variation, even for the same volcano in the same phase of activity, implying that large datasets are required to obtain meaningful averages. Due to transformation processes within the

plume and deposition, particle fluxes will also vary with plume age, further complicating these measurements. Again, future field experiments will certainly improve the emission estimates. In particular, more detailed studies of fumarolic and open-vent plumes, which are inherently more accessible and commonplace, should lead to a better understanding of emission characteristics under different conditions. Lessons from such studies could be generally applicable to larger-scale, rarer, explosive plumes, though non-linearities in scaling up are likely, especially where ash particle densities are high. Further measurements will also help to improve the global source strength estimates (Tables 1a and 4).

Table 5. Summary of published estimates of volcanic particle fluxes.

Volcano	Activity	Total Particle Mass Flux (kg s⁻¹)	Sulfate Flux (kg s⁻¹)	SO₂ Flux (kg s⁻¹)	Reference
Erebus, Antarctica	Lava lake degassing	–	6.0×10^{-2}	0.4	a
	Lava lake degassing	0.24	–	3.36	b
Kilauea, Hawaii	Lava effusion	0.6*	0.6*	16.8	c
Etna, Italy	Strombolian explosions	4.6–8	0.5–0.8	~ 10	d
Redoubt, Alaska	Intraeruptive	1–6	0.1–2	1–140	e
	Post-eruptive	0.06–0.08	–	> 2–5	e
Mt St Helens, USA	Paroxysmal	1×10^{-2}–6×10^4	2×10^{-3}–8	0.03–90	f
	Post-eruptive	0.1–0.02	0.05	0.3–0.05	f
Augustine, Alaska	Paroxysmal	3–6×10^5	–	100	g
	Intra-eruptive	1–2×10^3		2–300	g
	Post-eruptive	0.03–0.9		2–100	g
Ukinrek Maars, Alaska	Post-eruptive	0.01–5×10^{-4}	–	0.05–2×10^{-5}	g
White Island, New Zealand	Fumarolic	0.15	–	142	h
Mount Martin, Alaska	Fumarolic	0.03	–	0.01	g

a - *Radke* [1982]; b - *Chuan et al.* [1986]; c - *Porter et al.* [2002]; d - *Watson and Oppenheimer* [2000]; e - *Hobbs et al.* [1991]; f - *Hobbs et al.* [1982]; g - *Stith et al.* [1978]; h - *Rose et al.* [1986]
* Dry mass flux rate

Descriptions of activity follow *Stith et al.,* [1978]: *paroxysmal*—eruptive event occurring on a timescale of minutes; *intraeruptive*: Between paroxysmal events on a timescale of days; *post-eruptive*: After an eruptive period on a timescale of days to years.

Particle fluxes (refs. a, b, e–h) based on airborne plume traverses and direct determination of mass concentrations and plume cross sectional area. Kilauea estimate (ref. c) based on below-plume traverses with a sunphotometer, with an aerosol mass scattering coefficient based on assumed particle composition. Etna estimate (ref. d) based on sunphotometry, with an assumed plume geometry, and particle densities based on assumed particle compositions. All methods required wind speed to be included in the calculation. Poorly constrained plume transport speeds are a major source of error for ground-based measurements.

Table 6. Comparison of CCN fluxes from volcanic and anthropogenic sources, adapted from *Hobbs et al.* [1982]

Source	Strength (CCN s^{-1} at 1% Supersaturation)	Reference
Mt. St. Helens, 1980 eruption	$5 \times 10^{15} - 2 \times 10^{17}$	*Hobbs et al.* [1982]
Augustine, 1976 eruption	$10^{16} - 5 \times 10^{17}$	*Stith et al.* [1978]
Large coal-fired power plant	$10^{16} - 10^{17}$	*Hobbs et al.* [1980]
Aluminium smelters	$10^{14} - 5 \times 10^{15}$	*Hobbs et al.* [1970]
City (Denver)	1.7×10^{17}	*Frisbie and Hudson* [1993]
Urban Industrial area (E seaboard, USA)	6×10^{19}	*Radke and Hobbs* [1976]
Global Anthropogenic	6×10^{21}	*Radke and Hobbs* [1976]
Global Natural	$\sim 1 \times 10^{21}$	*Radke and Hobbs* [1976]

In terms of indirect climate forcing by cloud formation, particle composition is also important. *Hobbs et al.* [1982] used *Fitzgerald*'s [1973] theory and their measurements of the composition of the particles from the Mt. St. Helens plume to estimate the number of CCN. Table 6 compares their results to those for the 1976 Augustine eruption and anthropogenic sources. Even relatively small volcanic plumes can represent significant CCN sources. Further evaluations of volcanogenic CCN would contribute to evaluation of natural background levels, which are essential when calculating the regional and global levels of anthropogenic pollution.

Finally, we recognize that environmental and human health impact assessments in areas affected by volcanic pollution will need to take account of both gaseous and particulate emissions, and the size distribution and composition of particles. For example, the potential significance of emissions of fine, very acidic aerosol from volcanoes for human health has only recently come into focus [e.g., *Allen et al.*, 2002] but may well have important implications for public health in many populated areas located downwind of degassing volcanoes. Future field-based studies to define the key parameters that determine the effects of volcanic emissions in terms of pollution and human health are to be encouraged.

REFERENCES

Aiuppa, A., P. Bonfanti, L. Brusca, W. D'Alessandro, C. Federico and F. Parello, Evaluation of the environmental impact of volcanic emissions from the chemistry of rainwater: Mount Etna area (Sicily), *Appl. Geochem., 16*, 985-1000, 2001.

Albrecht, B. A., Aerosols, cloud microphysics, and fractional cloudiness, *Science, 245*, 1227-1230, 1989.

Allard, P., A. Aiuppa, H. Loyer, F. Carrot, A. Gaudry, G. Pinte, A. Michel and G. Dongarrà, Acid gas and metal emission rates during long-lived basalt degassing at Stromboli volcano, *Geophys. Res. Lett., 27*, 1207-1210, 2000.

Allen, A. G., P. J. Baxter and C. J. Ottley, Gas and particle emissions from Soufrière Hills Volcano, Montserrat, West Indies: characterization and health hazard assessment, *Bull. Volcanol., 62*, 8-19, 2000.

Allen, A. G., C. Oppenheimer, M. Ferm, P. J. Baxter, L. A. Horrocks, B. Galle, A. J. S. McGonigle and H. J. Duffell, Primary sulphate aerosol and associated emissions from Masaya volcano, Nicaragua, *J. Geophys. Res., 107*(D23), 4682, doi.: 10.1029/2002JD002120, 2002.

Ammann, M. and H. Burtscher, Characterisation of ultrafine particles in Mt. Etna emissions, *Bull. Volcanol., 52*, 577-583, 1990.

Ammann, M. and H. Burtscher, Aerosol dynamics and light-scattering properties of a volcanic plume, *J. Geophys. Res., 98*, 19,705-19,711, 1993.

Ammann, M., H. Burtscher and H. C. Siegmann, Monitoring volcanic activity by characterization of ultrafine aerosol emissions, *J. Aerosol Sci., 21*, Suppl. 1, S275-S278, 1990.

Ammann, M., L. Scherrer, W. Mueller, H. Burtscher and H-C. Siegmann, Continuous monitoring of ultrafine aerosol emissions at Mt. Etna, *Geophys. Res. Lett., 19*, 1387-1390, 1992.

Ammann, M., R. Hauert, H. Burtscher and H-C. Siegmann, Photoelectric charging of ultrafine volcanic aerosols: detection of Cu(I) as a tracer of chloride in magmatic gases, *J. Geophys. Res., 98*, 551-556, 1993.

Andreae, M. O., Climatic effects of changing atmospheric aerosol levels, in *Future climates of the world: a modelling perspective*, edited by A. Henderson-Sellers, *World Surv. Climatol., 16*, 347-398, 1995.

Andres, R. J. and A. D. Kasgnoc, A time-averaged inventory of subaerial volcanic sulfur emissions, *J. Geophys. Res., 103*, 25,251-25,261, 1998.

Asano, S., M. Sekine, M. Kobayashi and K. Muari, Atmospheric turbidity and aerosol size distribution in winter at Tsukuba.

Effects of the El Chichón eruption, *J. Met. Soc. Japan*, *63*, 453-463, 1985.

Asano, S., A. Uchiyama and M. Shiobara, Spectral optical thickness and size distribution of the Pinatubo volcanic aerosols as estimated by ground based sunphotometry, *J. Met. Soc. Japan*, *71*, 165-173, 1993.

Banfield, J. F. and A. Navrotsky, (Eds.), *Nanoparticles and the Environment*, Rev. Mineral., *44*, 2001.

Bates, T. S., B. K. Lamb, A. Guenther, J. Dignon and R. E. Stoiber, Sulfur emissions to the atmosphere from natural sources, *J. Atmos. Chem.*, *14*, 315-337, 1992.

Baxter, P. J., R. E. Stoiber and S. N. Williams, Volcanic gases and health: Masaya Volcano, Nicaragua, *Lancet*, *2*, 150-151, 1982.

Baxter, P. J., C. Bonadonna, R. Dupree, V. L. Hards, S. C. Kohn, M. D. Murphy, A. Nichols, R. A. Nicholson, G. Norton, A. Searl, R. S. J. Sparks and B. P. Vickers, Cristobalite in volcanic ash of the Soufrière Hills volcano, Montserrat, British West Indies, *Science*, *283*, 1142-1145, 1999.

Berresheim, H. and W. Jaeschke, The contribution of volcanoes to the global atmospheric sulfur budget, *J. Geophys. Res.*, *88*, 3732-3740, 1983.

Berresheim, H. and W. Jaeschke, Study of metal aerosol systems as a sink for atmospheric SO_2, *J. Atmos. Chem.*, *4*, 311-334, 1986.

Bonadonna, C., G. G. J. Ernst and R. S. J. Sparks, Thickness variations and volume estimates of tephra fall deposits: the importance of particle Reynolds number, *J. Volcanol. Geotherm. Res.*, *81*, 173-187, 1998.

Bonadonna, C., G. C. Mayberry, E. S. Calder, R. S. J. Sparks, C. Choux, P. Jackson, A. M. Lejeune, S. C. Loughlin, G. E. Norton, W. I. Rose, G. Ryan and S. R. Young, Tephra fallout in the eruption of Soufrière Hills Volcano, Montserrat, in *The eruption of Soufrière Hills Volcano, Montserrat, from 1995 to 1998*, edited by T. H. Druitt and B. P. Kokelaar, *Geol. Soc. Lond. Memoirs 21*, 483-516, 2002.

Burton, M., P. Allard, F. Murè and C. Oppenheimer, FTIR remote sensing of fractional magma degassing at Mt. Etna, Sicily, in *Volcanic Degassing* edited by C. Oppenheimer, D. M. Pyle and J. Barclay, *Geol. Soc. Lond. Spec. Pub. 213*, 281-293, 2003.

Burtscher, H., P. Cohn, L. Scherrer, H. C. Siegmann, G. Pennisi, V. Privitera, R. Christofolini and V. Scribano, Investigation of submicron volcanic aerosol particles by photoelectric emission, *J. Volcanol. Geotherm. Res.*, *33*, 349-353, 1987.

Cadle, R. D., A. L. Lazrus, B. J. Huebert, L. E. Heidt, W. I. Rose, D. C. Woods, R. L. Chuan, R. E. Stoiber, D. B. Smith and R. A. Zielinski, Atmospheric implications of studies of Central American volcanic eruption clouds, *J. Geophys. Res.*, *84*, 6961-6968, 1979.

Carey, S. N. and H. Sigurdsson, Influence of particle aggregation on deposition of distal tephra from the May 18, 1980, eruption of Mt St Helens volcano, *J. Geophys. Res.*, *87*, 7061-7072, 1982.

Carroll, M. R. and J. R. Holloway, (Eds.), *Volatiles in Magmas*, Rev. Mineral., *30*, 1994.

Carroll, M. R. and J. D. Webster, Solubilities of sulfur, noble gases, nitrogen, chlorine and fluorine in magmas, in *Volatiles in Magmas* edited by M. R. Carroll and J. R. Holloway, *Rev. Mineral.*, *30*, 231-279, 1994.

Casadevall, T. J., W. I. Rose, W. H. Fuller, W. H. Hunt, M. A. Hart, J. L. Moyers, D. C. Woods, R. L. Chuan and J. P. Friend, Sulfur dioxide and particles in quiescent volcanic plumes from Poas, Arenal, and Colima volcanoes, Costa Rica and Mexico, *J. Geophys. Res.*, *89*, 9633-9641, 1984.

Chuan, R. L., D. C. Woods and M. P. McCormick, Characterization of aerosols from eruptions of Mount St. Helens, *Science*, *211*, 830-832, 1981.

Chuan, R. L., J. Palais and W. I. Rose, Fluxes, sizes, morphology and compositions of particles in the Mt. Erebus volcanic plume, December 1983, *J. Atmos. Chem.*, *4*, 467-477, 1986.

Crowe, B. M., D. L. Finnegan, W. H. Zoller and W. V. Boynton, Trace element geochemistry of volcanic gases and particles from 1983-1984 eruptive episodes of Kilauea volcano, *J. Geophys. Res.*, *92*, 13708-13714, 1987.

Delmelle, P., Environmental impacts of tropospheric volcanic gas plumes, in *Volcanic Degassing* edited by C. Oppenheimer, D. M. Pyle and J. Barclay, *Geol. Soc. Lond. Spec. Pub. 213*, 381-399, 2003.

Delmelle, P., J. Stix, C. P-A. Bourque, P. J. Baxter, J. Garcia-Alvarez and J. Barquero, Dry deposition and heavy acid loading in the vicinity of Masaya Volcano, a major sulfur and chlorine source in Nicaragua, *Env. Sci. Tech.*, *35*, 1289-1293, 2001.

Deschler, T., D. J. Hofmann, B. J. Johnson and W. R. Rozier, Balloonborne measurements of the Pinatubo aerosol size distribution and volatility at Laramie, Wyoming during the summer of 1991, *Geophys. Res. Lett.*, *19*, 199-202, 1992.

Eatough, D. J., F. M. Caka and R. J. Farber, The conversion of SO_2 to sulfate in the atmosphere, *Israel J. Chem.*, *34*, 301-314, 1994.

Edmonds, M., C. Oppenheimer, D. M. Pyle and R. A. Herd, Rainwater and ash leachate analysis as proxies for plume chemistry at Soufrière Hills Volcano, Montserrat, in *Volcanic Degassing* edited by C. Oppenheimer, D. M. Pyle and J. Barclay, *Geol. Soc. Lond. Spec. Pub. 213*, 203-218, 2003.

Farlow, N. H., V. R. Oberbeck, K. G. Snetsinger, G. V. Ferry, G. Polkowski and D. M. Hayes, Size distributions and mineralogy of ash particles in the stratosphere from eruptions of Mt. St. Helens, *Science*, *211*, 832-834, 1981.

Ferrari, C. P., S. Hong, K. Van de Velde, C. F. Boutron, S. N. Rudniev, M. Bolshov, W. Chisholm and K. J. R. Rosman, Natural and anthropogenic bismuth in Central Greenland, *Atmos. Env.*, *34*, 941-948, 2000.

Fiocco, G., D. Fuà and G. Visconti (Eds.), *The Mount Pinatubo Eruption—Effects on the Atmosphere and Climate*, Springer-Verlag, Berlin, Heidelberg, 1996.

Fitzgerald, J. W., Dependence of the supersaturation spectrum of CCN on aerosol size distribution and composition, *J. Atmos. Sci.*, *30*, 628-634, 1973.

Francis, P., C. Chaffin, A. Maciejewski, and C. Oppenheimer, Remote determination of SiF_4 in volcanic plumes: a new tool for volcano monitoring, *Geophys. Res. Lett.*, *23*, 249-252, 1996.

Frisbie, P. R. and J. G. Hudson, Urban cloud condensation nuclei spectral flux, *J. Appl. Meteorol.*, *32*, 666-676, 1993.

Gauthier, P. J. and M-F. Le Cloarec, Variability of alkali and heavy metal fluxes released by Mt Etna volcano, Sicily, between 1991 and 1995, *J. Volcanol. Geotherm. Res., 81*, 311-326, 1998.

Gooding, J. L., U. S. Clanton, E. M. Gabel and J. L. Warren, El Chichón volcanic ash in the stratosphere: particle abundances and size distributions after the 1982 eruption, *Geophys. Res. Lett., 10*, 1033-1036, 1983.

Graf, H-F., B. Langmann and J. Feichter, The contribution of Earth degassing to the atmospheric sulfur budget, *Chem. Geol., 147*, 131-145, 1998.

Grattan, J., M. Durand, and S. Taylor, Illness and elevated human mortality in Europe coincident with the Laki Fissure eruption, in *Volcanic Degassing* edited by C. Oppenheimer, D. M. Pyle and J. Barclay, *Geol. Soc. Lond. Spec. Pub., 213*, 401-414, 2003.

Halmer, M. M., H-U. Schmincke and H. F. Graf, The annual volcanic gas input into the atmosphere, in particular into the stratosphere: a global data set for the past 100 years, *J. Volcanol. Geotherm. Res.,* 115, 511-528, 2002.

Harris, D. M. and W. I. Rose, Estimating particle sizes, concentrations, and total mass of ash in volcanic clouds using weather radar, *J. Geophys. Res., 88*, 10,969-10,983, 1983.

Heiken, G. and K. Wohletz, *Volcanic ash*, University of California Press, Berkeley, 1985.

Highwood, E. J. and B. J. Hoskins, The tropical tropopause, *Q. J. R. Met. Soc., 124*, 1579-1604, 1998.

Hinkley, T. K., Distribution of metals between particulate and gaseous forms in a volcanic plume, *Bull. Volcanol., 53*, 395-400, 1991.

Hinkley, T. K., P. J. Lamothe, S. A. Wilson, D. L. Finnegan and T. M. Gerlach, Metal emissions from Kilauea, and a suggested revision of the estimated worldwide metal output by quiescent degassing of volcanoes, *Earth Planet. Sci. Lett., 170*, 315-325, 1999.

Hobbs, P. V., *Introduction to Atmospheric Chemistry*, Cambridge University Press, Cambridge, UK, 2000.

Hobbs, P. V., L. F. Radke and S. E. Shumway, Cloud condensation nuclei from industrial sources and their apparent influence on precipitation in Washington State, *J. Atmos. Sci., 27*, 81-89, 1970.

Hobbs, P. V., J. L. Stith and L. F. Radke, Cloud-active nuclei from coal-fired electric power plants and their interactions with clouds, *J. Appl. Meteorol., 19*, 439-451, 1980.

Hobbs, P. V., J. P. Tuell, D. A. Hegg, L. F. Radke and M. K. Eltgroth, Particles and gases in the emissions from the 1980-1981 volcanic eruptions of Mt. St. Helens, *J. Geophys. Res., 87*, 11,062-11,086 1982.

Hobbs, P. V., L. F. Radke, J. H. Lyons, R. J. Ferek and D. J. Coffman, Airborne measurements of particles and gas emissions from the 1990 volcanic eruptions of Mount Redoubt, *J. Geophys. Res., 96*, 18,735-18,752, 1991.

Hoffman, D. J., Perturbations to the global atmosphere associated with the El Chichón volcanic eruption of 1982, *Rev. Geophys., 25*, 743-759, 1987.

Holland, H. D. *The Chemical Evolution of the Atmosphere and Oceans*, Princeton University Press, Princeton; Guilford, 1984.

Holt, B. D., R. Kumar and P. T. Cunningham, Primary sulfates in atmospheric sulfates—estimation by oxygen isotope ratio measurements, *Science, 217*, 51-53, 1982.

Holton, J. R., P. H. Haynes, M. E. McIntyre, A. R. Douglass, R. B. Rood and L. Pfister, Stratosphere—troposphere exchange, *Rev. Geophys., 33*, 403-439, 1995.

Johnson, N. and R. A. Parnell, Composition, distribution and neutralization of "acid rain" derived from Masaya volcano, Nicaragua, *Tellus, Ser. B, 38*, 106-117, 1986.

Junge, C., *Air Chemistry and Radioactivity*, Academic Press, New York, 1963.

Kaufman, Y. J., D. Tanra and O. Boucher, A satellite view of aerosols in the climate system, *Nature, 419*(6903), 215-223, 2002.

Kawaratani, R. K. and S-I. Fujita, Wet deposition of volcanic gases and ash in the vicinity of Mount Sakurajima, *Atmos. Environ., 24A*, 1487-1492, 1990.

Kent, G. S., C. R. Trepte and P. L. Lucker, Long-term stratospheric aerosol and gas experiment I and II measurements of upper tropospheric aerosol extinction, *J. Geophys. Res, 103*, 28,863-28,874, 1998.

Keys, J. R. and K. Williams, Origin of crystalline cold desert salts in the McMurdo Region, Antarctica, *Geochim. Cosmochim. Acta 45*, 2299-2309, 1981.

Kiladis, G. N., K. H. Straub, G. C. Reid and K. S. Gage, Aspects of interannual and intraseasonal variability of the tropopause and lower stratosphere, *Q. J. R. Met. Soc., 127*, 1961-1983, 2001.

Knollenberg, R. G. and D. Huffman, Measurements of the aerosol size distributions in the El-Chichón cloud, *Geophys. Res. Lett., 10*, 1025-1028, 1983.

Lacis, A., J. Hansen and M. Sato, Climate forcing by stratospheric aerosols, *Geophys. Res. Lett., 19*, 1607-1610, 1992.

Lambert, G., M-F. Le Cloarec and M. Pennisi, Volcanic output of SO_2 and trace metals: a new approach, *Geochim. Cosmochim. Acta, 52*, 39-42, 1988.

Lantzy, R. J. and F. T. Mackenzie, Atmospheric trace metals: global cycles and assessment of man's impact, *Geochim. Cosmochim. Acta, 43*, 511-525, 1979.

Le Cloarec, M-F. and B. Marty, Volatile fluxes from volcanoes, *Terra Nova, 3*, 17-27, 1991.

Lepel, E. A., K. M. Stefansson and W. M. Zoller, The enrichment of volatile elements in the atmosphere by volcanic activity: Augustine volcano, 1976, *J. Geophys. Res., 83*, 6213-6220, 1978.

Lynch, D. K., Multispectral remote sensing of aerosols, *Acta Astronautica, 38*, 947-953, 1996.

Mannino, D. M., S. Ruben, F. C. Holschuh, T. C. Holschuh, M. D. Wilson, and T. Holschuh Emergency department visits and hospitalizations for respiratory disease on the island of Hawaii, 1981 to 1991, *Hawaii Med. J., 55*, 3, 48-53, 1996.

Mather, T. A., A. G. Allen, C. Oppenheimer, D. M. Pyle and A. J. S. McGonigle, Size-resolved characterization of soluble ions in the particles in the tropospheric plume of Masaya volcano, Nicaragua: Origins and plume processing, *J. Atmos. Chem.,* in press, 2003.

Matsumoto, A. and T. K. Hinkley, Trace metal suites in Antarctic pre-industrial ice are consistent with emissions from quiescent

degassing of volcanoes worldwide, *Earth. Planet. Sci. Lett.*, *186*, 33-43, 2001.

McCormick, M. P., L. W. Thomason and C. R. Trepte, Atmospheric effects of the Mt-Pinatubo eruption, *Nature, 373*, 399-404, 1995.

McMurry, P. H., A review of atmospheric aerosol measurements, *Atmos. Env., 34*, 1959-1999, 2000.

Meeker, G. P. and T. K. Hinkley, The structure and composition of microspheres from the Kilauea volcano, Hawaii, *Am. Mineral., 78*, 873-876, 1993.

Mizutani, Y., Copper and zinc in fumarolic gases of Showashinzan volcano, Hokkaido, Japan, *Geochem. J., 4*, 87-91, 1970.

Moore, K. R., H. Duffell, A. Nicholl and A. Searl, Monitoring of airborne particulate matter during the eruption of Soufrière Hills volcano, Montserrat, in *The eruption of Soufrière Hills Volcano, Montserrat, from 1995 to 1998*, edited by T. H. Druitt and B. P. Kokelaar, *Geol. Soc. Lond. Memoirs, 21*, 557-566, 2002.

Murata, K., Occurrence of CuCl emission in volcanic flames, *Am. J. Sci., 258*, 769-782, 1960.

Nho, E-Y., M-F. Le Cloarec, B. Ardouin and W. S. Tjetjep, Source strength assessment of volcanic trace elements emitted from the Indonesian arc, *J. Volcanol. Geotherm. Res., 74*, 121-129, 1996.

Nriagu, J. O., A global assessment of natural sources of atmospheric trace metals, *Nature, 338*, 47-49, 1989.

Obenholzner, J. H., H. Schroettner, P. Golob and H. Delgado, Particles from the plume of Popocatepetl volcano, Mexico—the FESEM/EDS approach, in *Volcanic Degassing* edited by C. Oppenheimer, D. M. Pyle and J. Barclay, *Geol. Soc. Lond. Spec. Pub., 213*, 123-148, 2003.

Oberbeck, V. R., E. F. Danielsen, K. G. Snetsinger, G. V. Ferry, W. Fong and D. M. Hayes, Effect of the eruption of El Chichón on stratospheric aerosol size and composition, *Geophys. Res. Lett., 10*, 1021-1024, 1983.

Oppenheimer, C., On the role of hydrothermal systems in the transfer of volcanic sulfur to the atmosphere, *Geophys. Res. Lett., 23*, 2057-2060, 1996.

Oppenheimer, C., Volcanic degassing, *Treatise on Geochemistry*, Volume 3, Chapter 6, Elsevier, in press, 2003.

Oppenheimer, C., P. Francis, and J. Stix, Depletion rates of sulfur dioxide in tropospheric volcanic plumes, *Geophys. Res. Lett., 25*, 2671-2674, 1998.

Oppenheimer, C., D. M. Pyle, and J. Barclay (Eds.), *Volcanic Degassing, Geol. Soc. Lond. Spec. Pub., 213*, 2003.

Óskarsson, N., The interaction between volcanic gases and tephra: fluorine adhering to tephra of the 1970 Hekla eruption, *J. Volcanol. Geotherm. Res., 8*, 251-266, 1980.

Penner, J. E., M. Andreae, H. Annegarn, L. Barrie, J. Feichter, D. Hegg, A. Jayaraman, R. Leaitch, D. Murphy, J. Nganga and G. Pitari, Aerosols, their direct and indirect effects, in *Climate Change 2001: The Scientific Basis*, edited by J. T. Houghton, Y. Ding, D. J. Griggs, M. Noguer, P. J. van der Linden, X. Dai, K. Maskell and C. A. Johnson, pp. 289-348, Cambridge University Press, Cambridge, UK, 2001.

Pfeffer, M. A., F. Rietmeijer, A. Brearley, S. Basame and T. Fischer, Condensed volcanic aerosols collected near-source at

Poas, *Eos Trans. AGU, 82*(47), Fall Meet. Suppl., Abstract, V31B-10, 2001.

Phelan, J. M., D. L. Finnegan, D. S. Ballantine, W. H. Zoller, M. A. Hart and J. L. Moyers, Airborne aerosol measurements in the quiescent plume of Mount St. Helens: September, 1980, *Geophys. Res. Lett., 9*, 1093-1096, 1982.

Pollack, J. B., O. B. Toon, E. F. Danielsen, D. J. Hofmann and J. M. Rosen, The El Chichón volcanic cloud—an introduction, *Geophys. Res. Lett., 10*, 989-992, 1983.

Porter, J. N. and A. D. Clarke, Aerosol size distribution models based on in situ measurements, *J. Geophy. Res., 102*, 6035-6045, 1997.

Porter, J. N., K. A. Horton, P. J. Mouginis-Mark, B. Lienert, S. K. Sharma, E. Lau, A. J. Sutton and C. Oppenheimer, Sunphotometer and Lidar measurement of the plume from the Hawaii Kilauea Volcano Pu'u 'O'o vent: aerosol flux and SO_2 lifetime, *Geophys. Res. Lett., 29*(16), doi: 10.1029/2002GL014744, 2002.

Pruppacher, H. R. and J. D. Klett, *Microphysics of Clouds and Precipitation*, Reidel, Dordrecht, The Netherlands, 1980.

Pyle, D. M., Mass and energy budgets of explosive volcanic eruptions, *Geophys. Res. Lett., 22*, 563-566, 1995.

Pyle, D. M., Sizes of volcanic eruptions, in *Encyclopedia of Volcanoes*, edited by H. Sigurdsson et al., pp. 263-269, Academic Press, 2000.

Pyle, D. M., P. D. Beattie and G. J. S. Bluth, Sulphur emissions to the stratosphere from explosive volcanic eruptions, *Bull. Volcanol., 57*, 663-671, 1996.

Radke, L. F., Sulphur and sulphate from Mt Erebus, *Nature, 299*, 710-712, 1982.

Radke, L. F. and P. V. Hobbs, Cloud condensation nuclei on the Atlantic seaboard of the United States, *Science, 193*, 999-1002, 1976.

Raes, F., R. Van Dingenen, E. Vignati, J. Wilson, J-P. Putaud, J. H. Seinfeld and P. Adams, Formation and cycling of aerosols in the global troposphere, *Atmos. Environ., 34*, 4215-4240, 2000.

Raga, G. B., G. L. Kok, D. Baumgardner, A. Baez and I. Rosas, Evidence for volcanic influence on Mexico City aerosols, *Geophys. Res. Lett., 26*, 1149-1152, 1999.

Robock, A., Volcanic eruptions and climate, *Rev. Geophys., 38*, 191-219, 2000.

Robock, A., Pinatubo eruption - The climatic aftermath, *Science, 295*, 1242-1244, 2002.

Rose, W. I., Scavenging of volcanic aerosol by ash: Atmosperic and volcanologic implications, *Geology, 5*, 621-624, 1977.

Rose, W. I., S. Bonis, R. E. Stoiber, M. Keller and T. Bickford, Studies of volcanic ash from two recent Central American eruptions, *Bull. Volcanol., 37*, 338-364, 1973.

Rose, W. I., R. L. Chuan, R. D. Cadle and D. C. Woods, Small particles in volcanic eruption clouds, *Am. J. Sci, 280*, 671-696, 1980.

Rose, W. I., R. L. Chuan and D. C. Woods, Small particles in plumes of Mount St. Helens, *J. Geophys. Res., 87*, 4956-4962, 1982.

Rose, W. I., R. L. Wunderman, M. F. Hoffman and L. Gale, A volcanologist's review of atmospheric hazards of volcanic activity: Fuego and Mount St. Helens, *J. Volcanol. Geotherm. Res., 17*, 133-157, 1983.

Rose, W. I., R. L. Chuan, W. F. Giggenbach, P. R. Kyle and R. B. Symonds, Rates of sulfur dioxide and particle emissions from White Island volcano, New Zealand, and an estimate of the total flux of major gaseous species, *Bull. Volcanol., 48*, 181-188, 1986.

Rose, W. I., G. Heiken, K. Wohletz, D. Eppler, S. Barr, T. Miller, R. L. Chuan and R. B. Symonds, Direct rate measurements of eruption plumes at Augustine Volcano: A problem of scaling and uncontrolled variables, *J. Geophys. Res., 93*, 4485-4499, 1988.

Rosenberg, P. E., Aluminium fluoride hydrates, volcanogenic salts from Mount Erebus, Antarctica, *Am. Mineral., 73*, 855-860, 1988.

Sander, R., Modellierung von chemischen Vorgängen an und in Wolken, Ph.D. thesis, Johannes Gutenberg-Universität, Mainz, 1994.

Scaillet, B. and M. Pichavant, Experimental constraints on volatile abundances in arc magmas and their implications for degassing processes, in *Volcanic Degassing* edited by C. Oppenheimer, D. M. Pyle and J. Barclay, *Geol. Soc. London Spec. Pub., 213*, 23-52, 2003.

Schmid, B., C. Mätzler, A. Heimo and N. Kämpfer, Retrieval of the optical depth and particle size distribution of tropospheric and stratospheric aerosols by means of sunphotometry, *IEEE Trans. Geosci. Remote Sens., 35*, 172-182, 1997.

Seinfeld, J. H. and S. N. Pandis, *Atmospheric Chemistry and Physics*, John Wiley and Sons, New York, 1998.

Simkin, T. and L. Siebert, *Volcanoes of the World*, 2nd ed., Geoscience Press, Inc, Tucson, Arizona, 1994.

Smith, D. B., R. A. Zielinski, W. I. Rose and B. J. Huebert, Water-soluble material on aerosols collected within volcanic eruption clouds, *J. Geophys. Res., 87*, 4963-4972, 1982.

Solomon, S., Stratospheric ozone depletion: A review of concepts and history, *Rev. Geophys., 37*, 275-316, 1999.

Sparks, R. S. J., M. I. Bursik, S. N. Carey, J. S. Gilbert, L. Glaze, H. Sigurdsson and A. W. Woods, *Volcanic Plumes*, John Wiley and Sons, New York, 1997.

Stevenson, D. S., C. E. Johnson, W. J. Collins, and R. G. Derwent, The tropospheric sulphur cycle and the role of volcanic SO_2, in *Volcanic Degassing* edited by C. Oppenheimer, D. M. Pyle and J. Barclay, *Geol. Soc. Lond. Spec. Pub., 213*, 295-305, 2003.

Stith, J. L., P. V. Hobbs and L. F. Radke, Airborne particle and gas measurements in the emissions from six volcanoes, *J. Geophys. Res., 83*, 4009-4017, 1978.

Stoiber, R. E. and W. I. Rose, The geochemistry of Central American volcanic gas condensates, *Geol. Soc. Am. Bull., 81*, 2891-2912, 1970.

Stoiber, R. E. and W. I. Rose, Fumarole incrustations at active Central American volcanoes, *Geochim. Cosmochim. Acta, 38*, 495-516, 1974.

Stoiber, R. E., S. N. Williams and B. Huebert, Annual contribution of sulfur dioxide to the atmosphere by volcanoes, *J. Volcanol. Geotherm. Res., 33*, 1-8, 1987.

Symonds, R. B. and M. H. Reed, Calculation of multicomponent chemical equilibria in gas-solid-liquid systems: calculation methods, thermochemical data and applications to studies of high-temperature volcanic gases with examples from Mount St Helens, *Am. J. Sci., 293*, 758-864, 1993.

Symonds, R. B., W. I. Rose, M. H. Reed, F. E. Lichte and D. L. Finnegan, Volatilization, transport and sublimation of metallic and non-metallic elements in high temperature gases at Merapi Volcano, Indonesia, *Geochim. Cosmochim. Acta, 51*, 2083-2101, 1987.

Symonds, R. B., W. I. Rose and M. H. Reed, Contribution of Cl- and F- bearing gases to the atmosphere by volcanoes, *Nature, 334*, 415-418, 1988.

Symonds, R. B., W. I. Rose, T. M. Gerlach, P. H. Briggs and R. S. Harmon, Evaluation of gases, condensates, and SO_2 emissions from Augustine volcano Alaska: the degassing of a Cl-rich volcanic system, *Bull. Volcanol., 52*, 355-374, 1990.

Symonds, R. B., M. H. Reed and W. I. Rose, Origin, speciation, and fluxes of trace-element gases at Augustine volcano, Alaska: Insights into magma degassing and fumarolic processes, *Geochim. Cosmochim. Acta, 56*, 633-657, 1992.

Symonds, R. B., W. I. Rose, G. J. S. Bluth and T. M. Gerlach, Volcanic gas studies: methods, results and applications, *Rev. Mineral., 30*, 1-66, 1994.

Symonds, R. B., T. M. Gerlach, and M. H. Reed, Magmatic gas scrubbing: implications for volcano monitoring, *J. Volcanol. Geotherm. Res., 108*, 303-341, 2001.

Taran, Y. A., J. W. Hedenquist, M. A. Korzhinsky, S. I. Tkachenko and K. I. Shmulovich, Geochemistry of magmatic gases from Kudryavy volcano, Iturup, Kuril islands, *Geochim. Cosmochim. Acta., 59*, 1749-1761, 1995.

Taran, Y. A., A. Bernard, J-C. Gavilnes, E. Lunezheva, A. Cortes and M. A. Armienta, Chemistry and mineralogy of high-temperature gas discharges from Colima volcano, Mexico. Implications for magmatic gas-atmosphere interaction, *J. Volcanol. Geotherm. Res., 108*, 245-264, 2001.

Textor, C., P. M. Sachs, H-F. Graf, and T. Hansteen, The scavenging of sulphur and halogen gases in a plinian volcanic plume similar to the Laacher See eruption 12900 yr BP, in *Volcanic Degassing* edited by C. Oppenheimer, D. M. Pyle, and J. Barclay, *Geol. Soc. Lond. Spec. Pub., 213*, 307-338, 2003a.

Textor, C., H-F. Graf, M. Herzog and J. M. Oberhuber, Injection of gases into the stratosphere by explosive volcanic eruptions, *J. Geophys. Res.*, in press, 2003b.

Toutain, J-P., J-P. Quisefit, P. Briole, P. Aloupogiannis, P. Blanc and G. Robaye, Mineralogy and chemistry of solid aerosols emitted from Mount Etna, *Geochem. J., 29*, 163-173, 1995.

Varekamp, J. C., E. Thomas, M. Germani and P. R. Buseck, Particle Geochemistry of Volcanic Plumes of Etna and Mount St. Helens, *J. Geophys. Res., 91*, 12,233-12,248, 1986.

Vie le Sage, R., Chemistry of the volcanic aerosol in *Forecasting Volcanic Events* edited by H. Tazieff and J-C Sabroux, Elsevier, Amsterdam, New York, 1983.

Wallace, P. J. and A. T. Anderson, Volatiles in magmas, in *Encyclopedia of Volcanoes*, edited by H. Sigurdsson et al., pp. 149-170, Academic Press, 2000.

Warneck, P., *Chemistry of the Natural Atmosphere*, 2nd ed., pp. 927, Academic Press, London, 2000.

Watson, I. M. and C. Oppenheimer, Particle size distributions of Mount Etna's aerosol plume constrained by Sun photometry, *J. Geophys. Res., 105*, 9823-9829, 2000.

Watson, I. M. and C. Oppenheimer, Photometric observations of Mt. Etna's different aerosol plumes, *Atmos. Env., 35*, 3561-3572, 2001.

Waychunas, G. A., Structure, aggregation and characterization of nanoparticles, *Rev. Mineral., 44*, 105-166, 2001.

Whitby, K. T., The physical characteristics of sulfur aerosols, *Atmos. Env., 12*, 135-159, 1978.

Wilson, C. J. N. and G. P. L. Walker, The Taupo eruption, New Zealand. I. General aspects, *Philos. Trans. R. Soc. London Ser. A, 314*, 199-228, 1985.

Wong, S. and W-C. Wang, Interhemispheric asymmetry in the seasonal variation of the zonal mean tropopause, *J. Geophys. Res., 105*, 26,645-26,659, 2000.

Woods, D. C. and R. L. Chuan, Size-specific Composition of Aerosols in the El Chichon Volcanic Cloud, *Geophys. Res. Lett., 10*, 1041-1044, 1983.

Zoller, W. H., J. R. Parrington and J. M. Phelan Kotra, Iridium enrichment in airborne particles from Kilauea volcano: January 1983, *Science, 222*, 1118-1121, 1983.

Zreda-Gostynska, G., P. R. Kyle, D. L. Finnegan, and K. M. Prestbo, Volcanic gas emissions from Mount Erebus and their impact on the Antarctic environment, *J Geophys. Res., 102*, 15039-15055, 1997.

T. A. Mather and D. M. Pyle, Department of Earth Sciences, University of Cambridge, Downing Street, Cambridge, CB2 3EQ, UK. (tam21@cam.ac.uk)

C. Oppenheimer, Department of Geography, University of Cambridge, Downing Place, Cambridge, CB2 3EN, UK.

Aerosol Chemistry Interactions After the Mt. Pinatubo Eruption

Claudia Timmreck and Hans-F. Graf

Max-Planck Institut für Meteorologie, Hamburg, Germany

Benedikt Steil

Max-Planck Institut für Chemie, Mainz, Germany

A coupled chemistry climate model is used to study the 1991 eruption of Mt. Pinatubo, specifically the highly nonlinear interactions with atmospheric chemistry, radiation and dynamics. Both volcanic aerosol and O_3 are treated as prognostic variables and are coupled with the radiation scheme. With a bulk approach and a simple parameterization for the aerosol size distribution our model is able to reproduce the broad features of the atmospheric effects after the Pinatubo eruption. The simulated aerosol mode radius is overestimated during the first months after the eruption leading to strong perturbations in the modeled heating rates and enhanced downward transport. The evolution of simulated aerosol surface area density is found to agree rather well with observations from the Northern Hemisphere midlatitudes. Discrepancies appear to be related to inaccuracies in the simulated long range transport and to numerical vertical diffusion in the model. The simulated changes in the atmospheric trace gas concentration are reasonable. The modifications in the chemical concentration due to volcanic aerosol are a combined effect of changes in the heterogeneous chemistry, in the photolysis rates and in the heating rates. Column ozone decreases in the tropics by about 2%-3% in autumn 1991 which agrees with the observations. The strong ozone decrease in polar winter is also reproduced by the model. For a more realistic determination of the atmospheric effects of the Pinatubo aerosol, microphysical processes of the formation and the development of stratospheric aerosol must be considered.

1. INTRODUCTION

Atmospheric measurements and proxy data increase our knowledge of the nature of volcanic emissions as well as their possible impact on the climate system. Related climate model studies on the other hand improve our basic understanding of the processes and reduce uncertainties in the prediction of future climate.

Several general circulation model (GCM) studies for the Pinatubo episode, have addressed the climate impact of volcanic eruptions [e.g. *Hansen et al.*, 1992; *Graf et al.*, 1993; *Kirchner et al.*, 1999; *Ramachandran et al.*, 2000]. Chemistry climate models [*Al-Saadi et al.*, 2001; *Rozanov et al.*, 2002] have recently analyzed the impact of the Pinatubo eruption on the stratospheric trace gas concentra-

tion. However, in these studies the properties of the volcanic aerosol (surface area density, extinction) are derived from observations, which do not consider the influence of aerosol induced radiative forcing and ozone changes on the transport of the volcanic cloud. Both aerosols and ozone influence the radiative and dynamic balance of the stratosphere and will be affected by dynamic processes, too. [Kinne et al., 1992] pointed out that the volcanic aerosol induced ozone changes could alter the stratospheric circulation. Previous three-dimensional (3-D) transport simulations of Mt. Pinatubo aerosol demonstrated that the dynamic response to local aerosol heating has an important influence on the dispersal of the volcanic cloud [e.g. Young et al., 1994; Fairlie, 1995; Timmreck et al., 1999b].

To acquire a better understanding of the multiple interactions between aerosol microphysics, radiation, chemistry and dynamics, a global model is needed, in which both volcanic aerosol and ozone are transported (prognostic variables) and coupled with the radiation scheme (interactive treatment). Presently, global model studies which consider the various interactions that are necessary to analyze completely the climatic impact of volcanic eruption, are still missing.

We have coupled the chemistry climate model MAECHAM4/CHEM which consists of the stratospheric mesospheric version of the Hamburg climate model, the MAECHAM4 model [Manzini et al., 1997], and a comprehensive chemistry scheme CHEM [Steil et al., 2003] with a tropospheric sulfur scheme [Feichter et al., 1996]. Both volcanic aerosol and O_3 are treated as prognostic variables and are coupled with the radiation scheme. Hence we have set up a fully interactive model with respect to volcanic aerosol and ozone.

In this paper we introduce the model and present results of a two-year Post-Pinatubo simulation. We compared the results of the Pinatubo run with those of an undisturbed model run. Since the results of such sensitivity experiments are generally dependent on the weather noise, we concentrate mainly on parameters that are less affected by this [Stenchikov et al., 1998], like surface area density, radiative forcing of the aerosol layer or zonal mean values of heating rates and tropical averaged changes in chemical concentrations.

2. MODEL DESCRPTION

2.1 The Circulation Model

The MAECHAM4 extends with 39 layers from the surface to 0.01 hPa. The prognostic variables are vorticity, divergence, surface pressure, temperature, water vapor, and cloud (liquid and ice) water content. The MAECHAM4 is run with a spectral triangular truncation at wave number 30 (T30). Physical processes and nonlinear terms of dynamical fields are calculated on a Gaussian longitude-latitude grid with a nominal resolution of $3.75° \times 3.75°$. The Spitfire transport scheme [Rasch and Lawrence, 1998] is applied for the advective tracer transport in the model. The time step is 15 min for both the dynamics and the physics, while the radiation scheme is calculated every 2 hours.

2.2 The Chemistry Scheme

The chemistry scheme CHEM [Steil et al., 2003] describes stratospheric O_3 and tropospheric background $NO_x–HO_x–CH4–CO–O_3$ chemistry. 18 variables (CH_4, N_2O, H2, CO, H_2O_2, HCl, HNO_3 + NAT, CH_3O_2H, H_2O + ICE, ClNO3, F11, F12, CH_3CL, CCL_4, CH3CCL3, OX (O_3 + O (^3P) + O (^1D), ClO_X (Cl+ ClO+ HOCl + $2Cl_2O_2$ + $2Cl_2$, NO_x (N+ NO+ NO_2 + NO_3 + HNO_4 + $2N_2O_5$) are transported, while family members and radicals (like HO_x= H+OH+HO_2) are calculated analytically. 110 photochemical reactions and heterogeneous reactions on polar stratospheric clouds and sulfate aerosols are considered. Photolysis rates are calculated on line using the fast scheme of Landgraf and Crutzen [1998]. For the current study, a tropospheric sulfur scheme [Feichter et al., 1996] is coupled to the meteorological model and the chemistry scheme, which takes into account the oxidation pathways of sulfur dioxide (SO_2) and the removal processes of SO_2 and sulfate (SO_4^{2-}) in the troposphere. The sulfur scheme calculates transport, emission, chemistry and wet and dry deposition of dimethyl sulfide (DMS), SO_2 and SO_4^{2-}. Although sulfur photochemistry may have played a role shortly after the eruption of Pinatubo [Bekki et al., 1993], it is not taken into account in the present version of the model.

2.3 Treatment of Volcanic Aerosol

Information about the aerosol size distribution and the chemical composition are needed for both, radiation and chemistry calculation. In the current model version the H_2O/H_2SO_4 aerosol is considered by a bulk approach. It is therefore assumed as a first-order approximation that the volcanic aerosol size distribution is lognormal and monomodal, although observations after the Mount Pinatubo eruption [e.g., Deshler et al., 1993], as well as model simulations [e.g., Zhao et al., 1995], indicate that the volcanic aerosol size distribution is bimodal. Our approximation however, for modes that overlap, is accurate enough compared to other model uncertainties.

To keep track of the time evolution of the aerosol size distribution, we calculate the aerosol mode radius r_m from the effective radius r_e and the standard deviation of the size distribution σ. $\sigma=1.86$ is kept constant in time and space because the aerosol radiative properties are only weakly dependent on σ [Stenchikov et al., 1998]. The mode radius r_m can then be determined by:

$$r_m = r_e \exp [-5 \ln^2(\sigma/2)] \tag{1}$$

The effective radius will be derived from the aerosol volume V according to an empirical formula, which has been derived from 744 aerosol size distribution measurements made at Laramie Wyoming [Grainger et al., 1995]:

$$r_e = 0.357 \ V^{0.249} \tag{2}$$

The aerosol volume V is calculated from the aerosol mass M and the density ρ and sulphuric acid mass fraction W which are determined online in the model for every grid box at every time step. The loss of the particles due to gravitational sedimentation is also calculated at every time step and at every grid box. For the heterogeneous chemistry the aerosol surface area density A is derived from the aerosol volume V according to Grainger et al., [1995]:

$$A = 8.406 \ V^{0.75} \tag{3}$$

The volcanic aerosol number density N_V is a taken into account in the calculation of the actinic flux in the photolysis routine. In the original version of the photolysis routine a mixture between rural and maritime aerosol is assumed for the background number density N, which is then vertically interpolated. Now the simulated volcanic aerosol number density N_V is added to the background N.

To determine the aerosol optical parameters, Mie calculations are performed for 20 distinct radii between 0.01 μm and 2.0 μm and 6 sulphuric acid mass fractions (0.25, 0.38, 0.5, 0.75, 0.85 0.95) with increasing resolution in the region of sharp changes of the aerosol parameters. The calculated optical aerosol characteristics are then averaged over the broadband intervals of the MAECHAM4 radiative scheme in using the Planck function as a weighting function for a temperature of T = 6000 K for the solar and T = 300 K for the terrestrial bands. The refractive indices of sulfuric acid are taken from Palmer and Williams [1975]. These parameters are stored in a table. Optical parameters for other sizes and compositions are linearly interpolated.

The sulfate aerosol is coupled with the radiation and the chemistry scheme. In the chemistry scheme the aerosol is considered in the calculation of heterogeneous reactions on the surface of the aerosol particles and in the calculation of the actinic flux. In the radiation scheme optical parameters are calculated from the time dependent aerosol mass mixing ratio, normalized extinction and absorption coefficients, and a normalized asymmetry factor.

2.4 Initialization of the Volcanic Cloud

By analogy to our previous Pinatubo simulations [Timmreck et al., 1999a;b] we assume an initial volcanic cloud mass of 17 Mt SO_2, according to satellite observations [Read et al., 1993; Krueger et al., 1995]. In the horizontal the SO_2 cloud is initialized over 19 gridboxes (1.96 10^6 km^2) between $0°-18.55°N$ and $96°E-118°E$ in correspondence to TOMS observations of June 16,1991 [Bluth et al., 1992]. In the vertical, the initial SO_2 mass is distributed over four model layers between 47-15 hPa (21.5–29 km) with two thirds of the mass between 23-27 km. This corresponds to satellite observations, which have shown that the volcanic plume reached to a maximum height of 35–40 km with the bulk of the aerosol centered around 25 km and ranging between 20 km and 29 km [Sparks et al., 1997].

3. RESULTS

3.1 Global Mass

Figure 1 shows a comparison of the simulated global stratospheric aerosol mass with SAGE data [Thomason
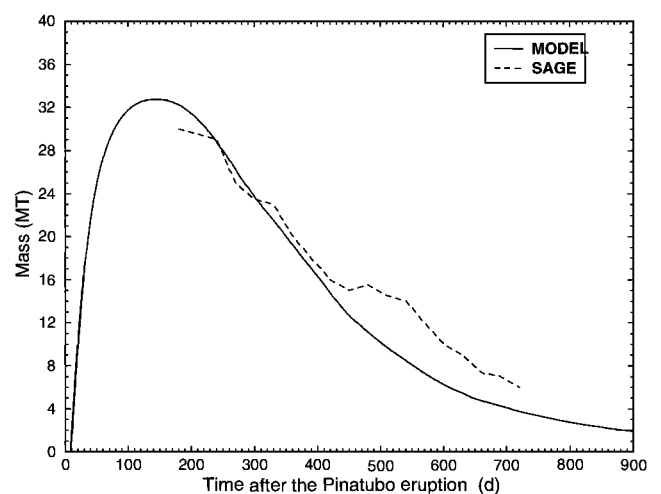
Figure 1. Comparison between model simulations (solid line) and SAGE satellite data (dashed line) of the global stratospheric aerosol mass loading (Mt) after the eruption of Mount Pinatubo.

ratio[1] at 24 km altitude is shown for the eighth day of every other month in the first year after the eruption. The simulated volcanic cloud rapidly moves westward and encircles the Earth within three weeks. This corresponds well with observations. In the first three months after the eruption the bulk of the modeled aerosol cloud is bound in a latitude band between 30°S–30°N as observed. However, in August, tongues of aerosol rich air start to develop from the tropical region. The change from summer to winter circulation in the Northern Hemisphere (NH) (and vice versa in the Southern Hemisphere (SH)), leads to an enhanced meridional poleward transport in late 1991. In February 1992 the simulated volcanic aerosol is globally spread except the NH high latitudes, where the polar vortex represents an efficient barrier for the volcanic aerosol.

3.3 Meridional Cross Sections

Figure 3 compares the simulated zonal mean aerosol surface area density latitude-height cross sections (monthly average) and surface area densities which are derived from SAGE observations [Thomason et al., 1997] for October 1991, January 1992 and April 1992. The GCM simulation and the SAGE observations differ in the persistence of the tropical maximum. In the satellite data the tropical maximum can still be observed in April 1992, while in the simulation the maximum is shifted to the high latitudes after February 1992. We observed a similar feature in previous Pinatubo simulations without stratospheric chemistry, where we failed to reproduce the tropical aerosol reservoir after December 1991 [Timmreck et al., 1999a;b]. The inclusion of stratospheric chemistry and the interactive treatment of stratospheric ozone improves our model simulations slightly, because the volcanic aerosol cloud persists one month longer in the tropics, but does not have a large effect on the stratospheric transport. The missing quasi-biennial oscillation (QBO) is a possible reason for the rapid decay of the tropical maximum in the simulations as discussed in Timmreck et al. [1999b]. Satellite observations revealed that the QBO has an important influence on the transport from the tropical stratospheric reservoir to midlatitudes [e.g. Trepte and Hitchman, 1992; Choi et al., 1998]. Mount Pinatubo erupted during the time of a descending QBO's easterly shear, where the aerosol tends to remain near the equator, whereas during the westerly shear the aerosol tends to spread poleward. In the MAECHAM4 simulations, the tropical winds are stable easterlies, similar to the observed situation in summer 1991, but the model is not capable of

properly simulating the QBO. A Pinatubo simulation with assimilated QBO wind fields is planned in the near future.

Another notable difference between model simulation and observations is the fact that the tropical maximum in the model run is located at lower altitudes. The simulated tropical maximum is located at 22 km in October 1991 and at 20 km in January 1992 while in the observations it is centered around 27 km and 25 km respectively. The pronounced vertical shift in the model simulations can be explained with the applied parameterization, which directly links the aerosol mass with the mode radius. In the first months after the eruption, when the bulk of the volcanic cloud is bound in the tropical region, large particle radii are calculated (Figure 4). This leads to fast sedimentation of the particles. Shortly after the eruption, particles not only grow due to condensation of sulfuric acid vapor, but also new particles are formed through binary homogeneous nucleation of H_2SO_4/H_2O. After the eruption of Mt. Pinatubo an increase of 1–2 orders of magnitude in the concentration of condensation nuclei in the volcanic layers was found [Deshler et al., 1992], and 98% of the observed aerosol was volatile [Deshler et al., 1992; Sheridan et al., 1992]. This indicates that homogeneous nucleation is an essential process in a volcanically disturbed atmosphere, leading to a large amount of small particles, a bimodal size distribution and an overall reduced sedimentation rate compared to our approach. Hence, Figures 3, 4 clearly show the difficulties of the applied parameterization and emphasize the importance of an explicit treatment of aerosol microphysical processes in a global model. We have therefore developed a microphysical model SAM [Timmreck et al., 2001] which we currently couple with the MAECHAM4/CHEM. This module treats binary homogeneous nucleation of H_2SO_4/H_2O, condensation and evaporation of H_2SO_4 and H_2O, Brownian coagulation and gravitational sedimentation explicitly. Figure 3 shows further that in the model the volcanic aerosol extends to higher altitudes than the observations. This difference will be discussed in more detail in the following section.

3.4 Comparison With in Situ Measurements From the NH Midlatitudes

The applied parameterization (equations 2, 3) has been derived from optical particle counter (OPC) measurements at Northern Hemisphere midlatitudes. Therefore, it may be useful to compare the model results with OPC data. Figure 5 depicts a comparison of simulated aerosol surface area density with measurements from Laramie, Wyoming (41°N) [Deshler et al., 1992a, 1993] for four different heights. Generally, the temporal development of the aerosol surface

---
[1] mass mixing ratio: mass of a substance in a given volume to the total mass in that volume

Model

SAGE

October 1991

October 1991

January 1992

January 1992

April 1992
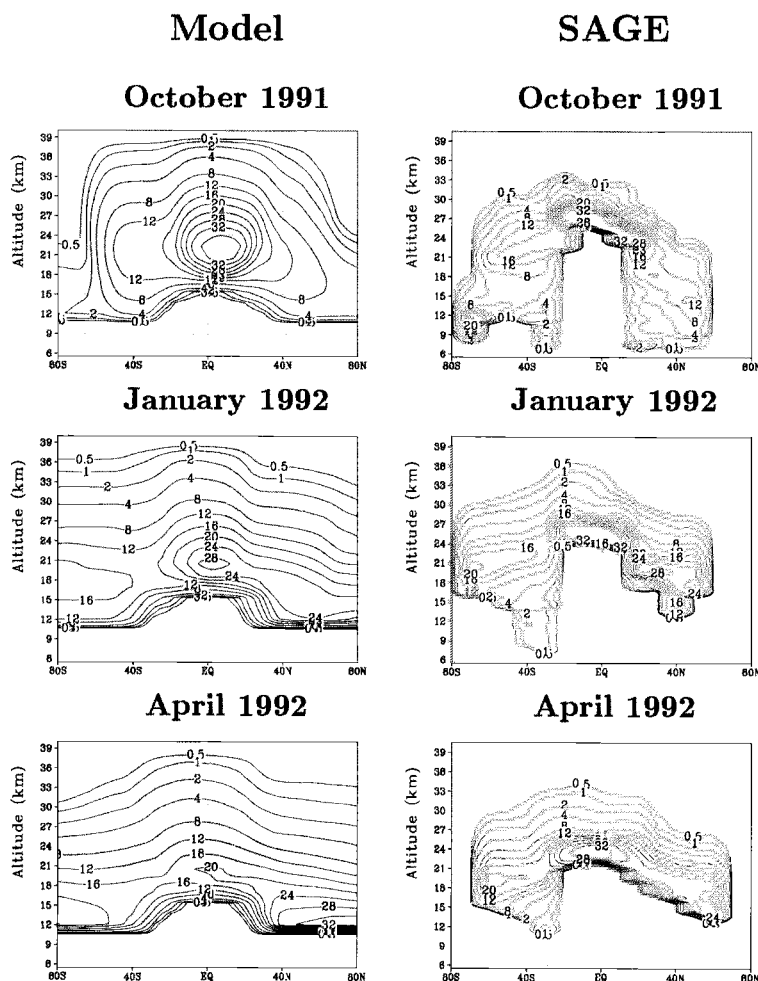
April 1992

Figure 3. Comparison of the simulated aerosol surface area density (mm^2 cm^{-3}) with SAGE II data [*Thomason et al.,* 1997] for October 1991, January 1992 and April.

area density at Laramie is well represented by the GCM simulations, in particular at 22 km and 18 km. The model however, does not reproduce the first distinct maximum three weeks after the eruption in July. This originates from a smaller eruption plume from June 12th, which injected material at lower altitudes. This eruption plume has not been considered in our simulation. In the two upper layers at 30 km and 26 km the model simulation overestimates the observation by a factor of 2–3 which can also be seen in the comparison with SAGE in Figure 3.

An explanation for this is shown in Figure 6, where observed vertical profiles of the surface area density in December 1991 and May 1992 are compared with model results for the grid box where Laramie is located. Considering, that it is in general difficult to compare in situ measurements taken at one point under specific syn-

optic conditions with climate model simulations with a nominal resolution of 320 km × 320 km, the model matches observational results quite well. The model is however not capable of reproducing the observed layered small structures. The vertical resolution in the model between 20–30 km is about 2 km, whereas the vertical resolution of the observations is 1 km. In addition to the coarse vertical resolution, numerical vertical diffusion in the model leads to artificial vertical transport and to a smoothening of the vertical profile. The observed vertically thin stable aerosol layers are known to occur not only for volcanic aerosols but also for other natural systems in the stratosphere and elsewhere. The processes leading to the stratification and layering are not resolved in the model. Furthermore, evaporation of sulfuric acid vapor from the particles is not considered in the model.

June 1991

August 1991

October 1991

December 1991

February 1992

April 1992
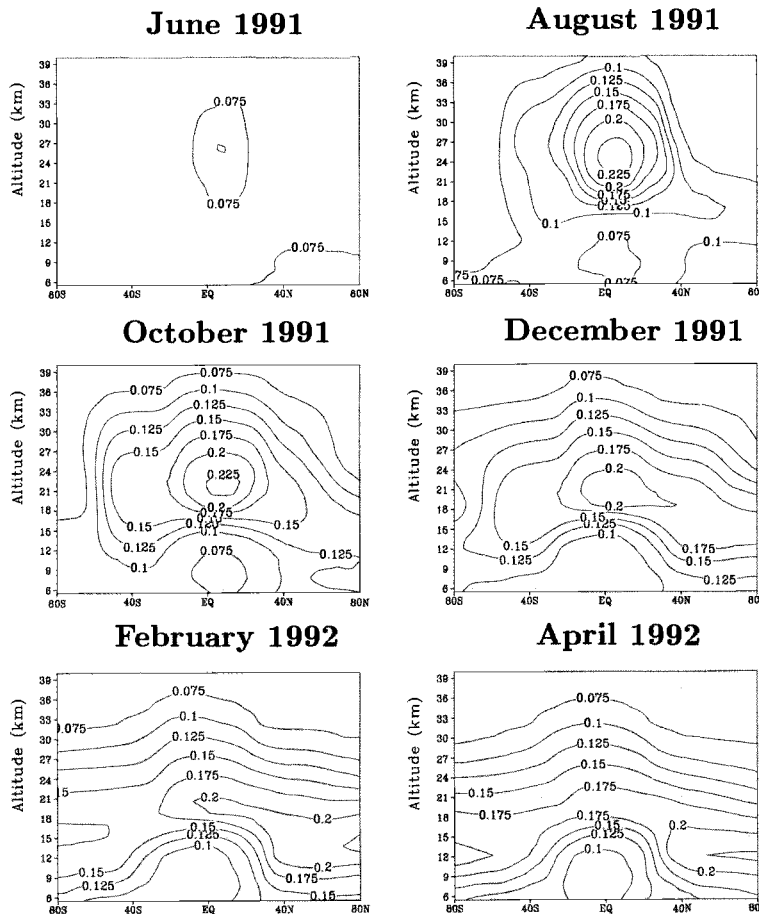
Figure 4. Latitude-altitude cross section of the monthly averaged mode radius (mm) in the first year after the eruption.

This is an important process above 26 km. To treat condensation and evaporation of H_2SO_4 gas explicitly in the model, a microphysical scheme such as the stratospheric aerosol model SAM is necessary.

3.5 Radiative Heating and Flux Anomalies

The calculation of radiative forcing is sensitive to its definition [*Stenchikov et al.*, 1998]. To obtain information about additional aerosol-induced radiative heating, the radiation code is called twice in the model simulation with Pinatubo aerosol. Radiative heating and net radiative fluxes in our model are estimated at every time step from the difference between the radiation calculations with aerosol minus the radiative calculation without aerosol. Hence, we consider the instantaneous radiative forcing. Figure 7 shows the simulated zonal mean vertical cross sections of the total aerosol radiative heating for August 1991, October 1991 and December 1991. In the first months after the eruption

aerosol induced heating rates of more than 0.3 K/day are found in the tropical region. However, the latitude of the strongest perturbations varies between the months. In August 1991 the calculated maximum heating rates are located in the SH tropics while in October 1991 and January 1992 the maximum is found in the NH tropics. In August 1991 the simulated maximum total heating rates are 0.6 K/day in the SH tropics. They are about a factor of two higher than other model results [*Stenchikov et al.*, 1998; *Ramachandran et al.*, 2000]. This can be explained with the very large mode radii which we obtain in our simulation in the first months after the eruption due to the direct correlation between mass and mode radius which was used (see Figure 4). In October1991 model results, with maxima of 0.3-0.4 K/day, agree with *Kinne et al.*, [1992], while in January 1992 our maximum heating rates, 0.2 K/day, are slightly smaller than *Stenchikov et al.*, [1998] reported.

Figure 8 shows the simulated zonal mean net radiative flux at the top of the atmosphere, the tropopause, and the surface.
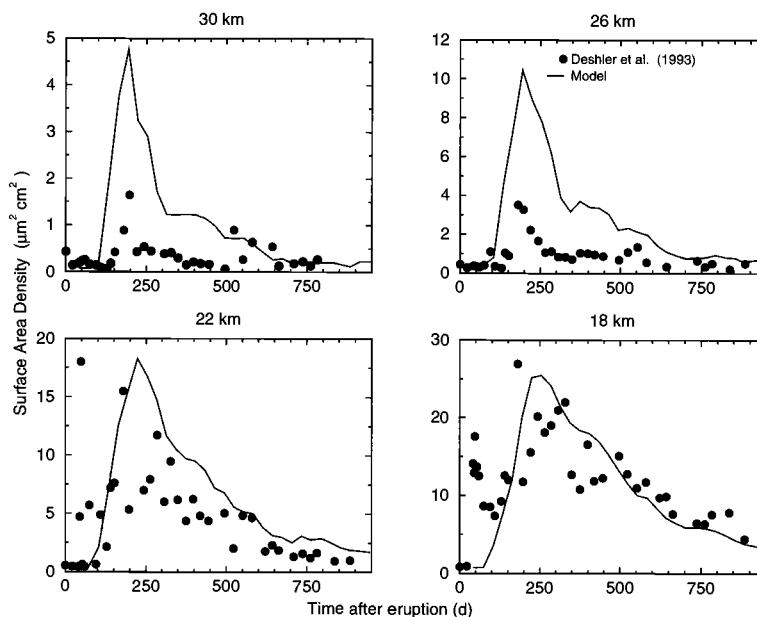
Figure 5. Temporal development of the aerosol surface area density (mm^2 cm^{-3}) at 41°N at four altitudes. The circles indicate the measurements [*Deshler et al.,* 1993] and the solid line indicates the simulated monthly mean values for the corresponding grid.

The strongest negative flux anomalies occur at the tropopause with −4 W/m^2. Compared to *Stenchikov et al.* [1998], our net radiative fluxes are slightly smaller. *Stenchikov et al.* [1998] also obtain the largest negative net flux of −5 W/m^2 at the tropopause. The calculated flux anomalies agree reasonably well with other model calculations [*Stenchikov et al.,* 1998; *Ramachandran et al.,* 2000]. The values are, however, smaller than observed by Earth Radiation Budget Experiment (ERBE) satellite data [*Minnis et al.,* 1993], which give a net radiative cooling of −8 W/m^2 in the 5°S–5°N latitude band for August 1991. This can partially be explained by the fact that we consider here only the instantaneous radiative forcing and do not take into account changes in the radiative fluxes due to the model's dynamic response. A detailed discussion of the difficulties of model-observation comparisons of radiative flux changes after the Pinatubo eruption can be found in *Ramachandran et al.* [2000].

3.6 Trace Gas Changes

Figure 9 shows an altitude-height cross section of the average simulated tropical (30°S–30°N) changes in chemical concentrations between the disturbed and the undisturbed run. Aerosol induced heating leads to an uplifting of the trace gases which can clearly be seen in the upper stratospheric increase in the CH_4 concentration of more than 10% during the first year after the eruption. Similar CH_4

increases in the upper stratosphere are found in other model studies [*Al-Saadi et al.,* 2001]. Enhanced upward transport due to additional heating is also the reason for the increase in NO_x above 40 km, while the strong loss of more than 50% in the lower stratosphere is mainly a result of heterogeneous chemistry. Heterogeneous reactions on the surface of the aerosol particles lead to a conversion of NO_x to HNO_3 and to chlorine activation (increase of ClO_x). The concentration of ClO_x increases by more than 100% in the aerosol containing layers in the first one and a half years after the eruption, with maximum values of up to 250% in January 1991. The tropical averaged O_3 concentration decreases in our Pinatubo simulation between 20 km–30 km due to heterogeneous chemistry and upward transport, and increases above 30 km due to a decrease in NO_x. This agrees with other model studies [*Rozanov et al.,* 2002] and with measurements of tropical ozone profiles after Pinatubo [*Grant et al.,* 1994]. The observations show decreases (up to 33%) between 16–28 km and small increases from 28 to 31.5 km. Below 20 km the simulated O_3 concentration slightly increases in the first months due to changes in the photolysis rates. In the first months after the eruption, the high SO_2 concentration has also a significant impact on stratospheric OH and O_3 concentration [*Bekki,* 1995]. This effect is not taken into account in the present simulation.

Figure 10 depicts the relative changes in total ozone for the first year after the eruption. Column ozone decreases in

the tropics in particular in the NH, by about 2–3% from September 1991 on with a maximum loss of 4% in October 1991. This agrees with QBO detrended observations which estimated total ozone depletion of 2–4% in the equatorial regions [e.g. *Zerefos et al.,* 1994; *Randel et al.,* 1995; *Angell,* 1997]. Total ozone increases in the SH in polar summer by more than 25%, three times higher than the ground base observations [*Angell,* 1997]. In NH polar winter the simulated total ozone decreases of by more than 20%, which is twice as large as satellite observations of 10% [*Randel et al.,* 1995] and ground based estimates of 6.1 ±2.3% [*Angell,*
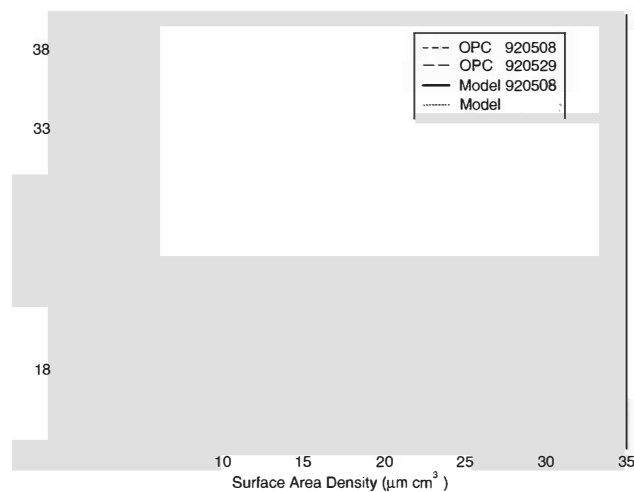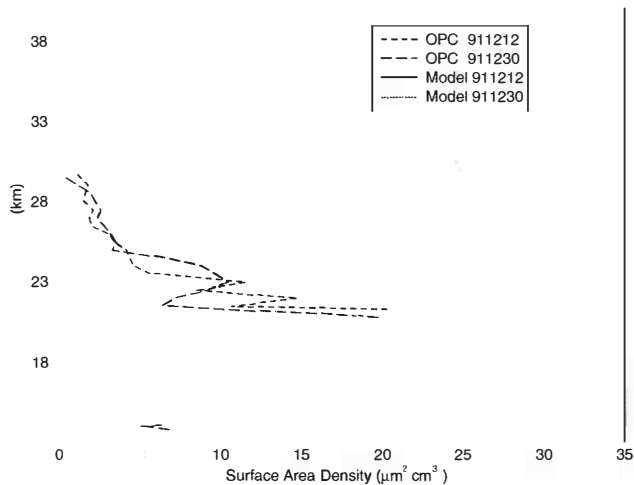
Figure 6. Comparison of the observed aerosol surface area density (mm^2 cm^{-3}) at 41°N [*Deshler et al.,* 1993] at December 1991 and May 1992 with simulated monthly mean values for the corresponding grid. The dashed lines indicate the measurements taken at two individual days (each) and the solid and the dotted lines indicates the simulated monthly mean values for the corresponding days.
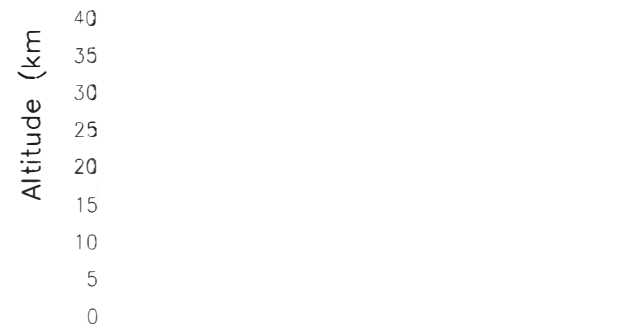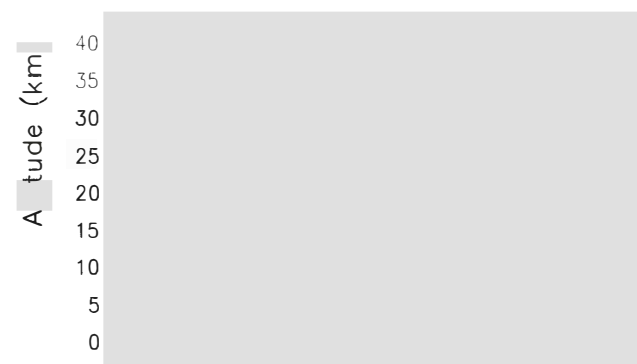
Figure 7. Simulated perturbation of the zonal and monthly mean heating rates (K/day) caused by the Pinatubo eruption for August 1991, October 1991 and January 1992.

1997]. We have considered here the difference between two model simulations: a volcanically disturbed and an undisturbed one, both of which are influenced by the meteorology of the particular years. The interannnual variability in the

Top

Tropopause
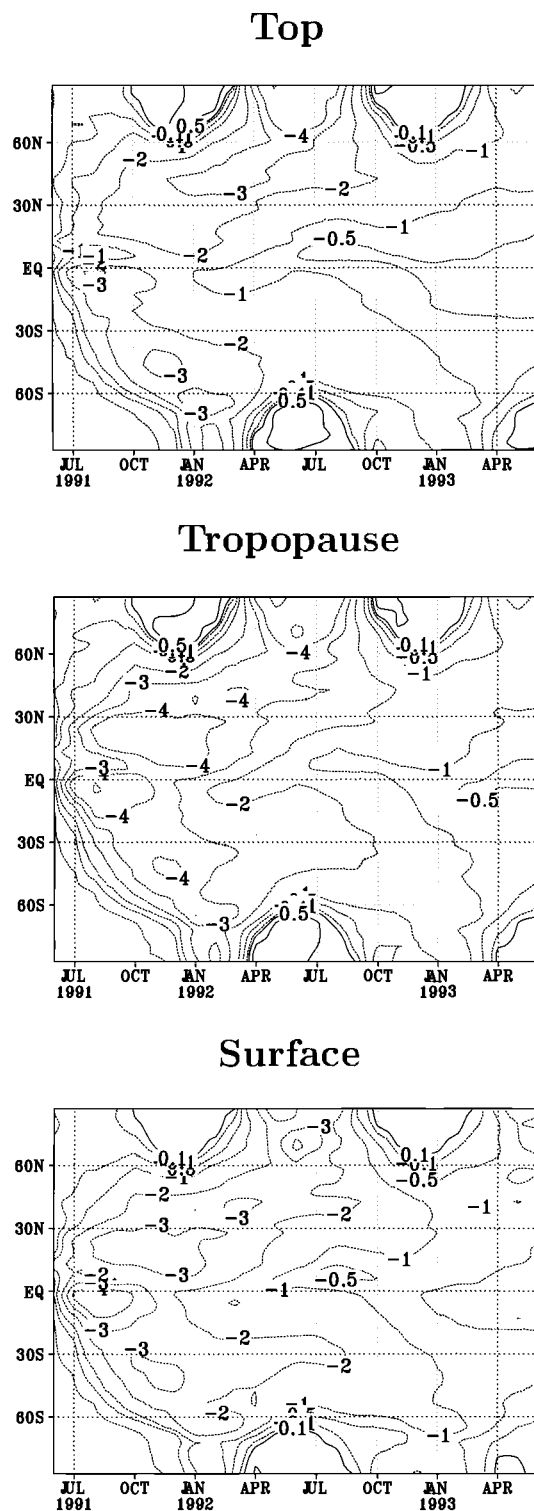
Surface

Figure 8. Simulated zonally averaged all-sky net radiative fluxes (W/m²) at the top of the atmosphere (top), the tropopause and the surface.

NH high latitudes is very high. Thus, to simulate ozone changes in high latitudes ensemble simulations are necessary, or the meridional circulation has to be forced by the assimilation of dynamical fields (wind, temperature).

Overall, the model changes in chemical concentration due to volcanic aerosol are reasonable. They are a combined effect of changes in the heterogeneous chemistry, in the photolysis rates and in the heating rates, which has to be investigated in more detail. However, for a statistically significant assessment of the chemical changes an ensemble of simulations of at least five independent runs is necessary.

4. CONCLUSIONS

We present results of a fully coupled GCM simulation of Mt. Pinatubo aerosol with respect to aerosol and ozone. The global dispersal of the simulated volcanic cloud is reasonable compared to observations. The Pinatubo cloud encircles the Earth within three weeks and remains in a latitude band between 30°S–30°N during the first three months. Enhanced meridional poleward transport takes place in October. The change from summer to winter circulation in the NH (and vice versa in the SH) is associated with an amplification of planetary scale waves in high latitudes. 'Fat air filaments' transport volcanic aerosol from the tropical region to high latitudes in the simulation. The model fails to reproduce the observed tropical aerosol maximum since January 1992. Apart from the first three months, the simulated aerosol surface area density corresponds well with observations from the NH midlatitudes. Deviations are related to difficulties in the simulated long range transport, e.g. the overestimation of the meridional northward transport. Another problem of the simulation of the NH midlatitude surface area density is the strong vertical diffusion in the model. The model does not capture the observed distinct thin aerosol layers and associated strong vertical gradients. This is mainly a problem of vertical resolution. Column ozone decreases in the tropics by about 2–3% in autumn 1991, in agreement with observations. The strong ozone decrease in polar winter is reproduced by the model. The changes in the chemical concentration due to the volcanic aerosol are a combined effect of changes in heterogeneous chemistry, in photolysis rates and in heating rates. The globally averaged O_3 concentration slightly increases below the volcanic cloud due to changes in the photolysis rate, decreases between 20–30 km due to heterogeneous chemistry and upward transport, and increases above 30 km due to a decrease in NO_x. The simulated changes in the atmospheric trace gas concentration are reasonable. The values might change with consideration of BrO_x chemistry and
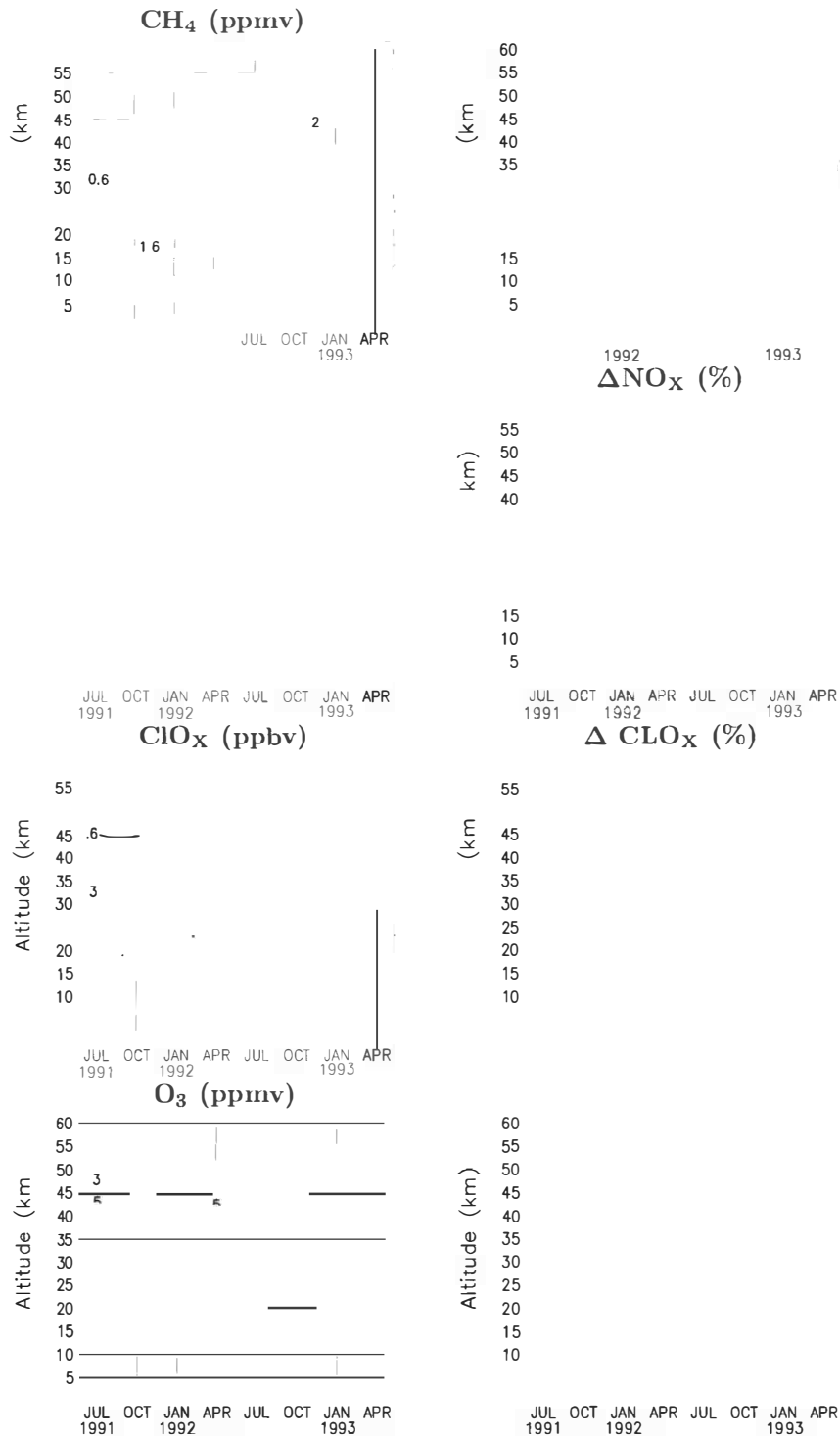
Figure 9. Altitude-height cross section of the tropical averaged (30°S–30°N) trace gas concentrations in the control run and the simulated changes between the disturbed and the undisturbed run.
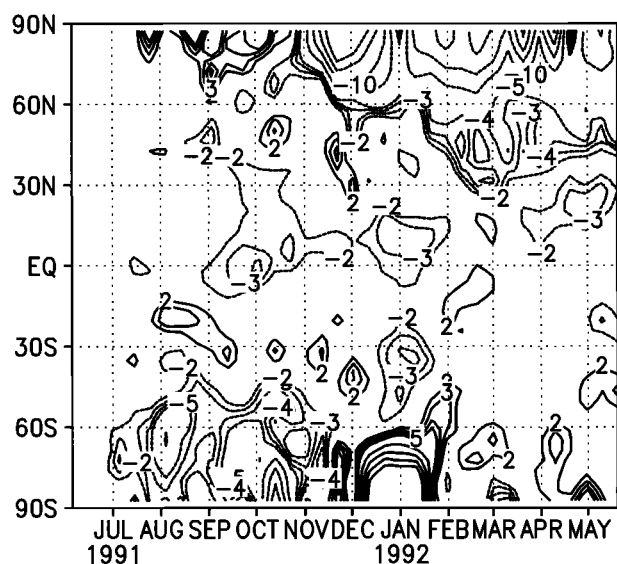
Figure 10. Total ozone changes (%) in the first year after the Pinatubo eruption.

more sophisticated sulfur chemistry, which are not included in the present model runs.

Our model results show that the treatment of the volcanic aerosol with a bulk approach and simple parameterization can reproduce some of the observed atmospheric effects after the Pinatubo eruption. However, there are differences due to the applied parameterization, which are especially evident in the first months after the eruption. Unrealistically large radii are calculated at the beginning of the simulation due to the direct relationship between mass and size. As a consequence, the sedimentation rate is too large and leads to an overestimation of the downward transport of the tropical aerosol maximum. In addition, the simple aerosol parameterization used here is largely derived from aerosol observations at NH midlatitudes following the Pinatubo eruption. It is likely that the model will not perform well for much smaller or much larger eruptions. For a realistic determination of the atmospheric effects of volcanic eruptions, microphysical processes of the formation and the development of stratospheric aerosol must be considered. This requires an explicit size resolving treatment of aerosol microphysics in the global model. We are currently developing a chemistry microphysical climate model consisting of the MAECHAM4/CHEM and the stratospheric aerosol model SAM [*Timmreck,* 2001]. Such a model will be an appropriate tool to study the atmospheric effects not only of Mt. Pinatubo, but also of other past and future volcanic eruptions.

REFERENCES

Al-Saadi, J., et al., Response of middle atmosphere chemistry and dynamics to volcanically elevated sulfate aerosol: Three-dimensional coupled model simulations, *J. of Geophys. Res.,* 106, 27,255-27,276, 2001.

Angell, J. K., Estimated impact of Agung, El Chichón and Pinatubo volcanic eruptions on global and regional total ozone after adjustment for the QBO, *Geophys. Res. Let.,* 24, 647-650, 1997.

Bekki, S., Oxidation of volcanic SO_2: A sink for stratospheric OH and H_2O, *Geophys. Res. Let.,* 22, 913-916, 1995.

Bekki, S., R. Toumi and J. A. Pyle, Role of sulphur photochemistry in tropical ozone change after the eruption of Mount Pinatubo, *Nature,* 362, 331-333, 1993.

Bluth, G., J. S., S. D. Doiron, C. C. Schnitzler, A. J. Krueger, and L. S. Walter, Global tracking of the SO_2 clouds from the June 1991 Mount Pinatubo eruptions, *Geophys. Res. Let.,* 19, 151-154, 1992.

Choi, W., W. B. Grant, J. H. Park, K.-M. Lee, H. Lee and J. M. Russel III, Role of the quasi-biennial-oscillation in the transport of aerosols from the tropical stratospheric reservoir to midlatitudes. *J. of Geophys. Res.,* 103, 60,33-6042, 1998.

Deshler, T., D. J. Hofmann, B. J. Johnson, and W. R. Rozier, Balloonborne measurements of the Pinatubo aerosol size distribution and volatility at Laramie, Wyoming during the summer of 1991, *Geophys. Res. Let.,* 19, 199-202, 1992.

Deshler, T., B. J. Johnson, and W.R. Rozier, Balloonborne measurements of Pinatubo aerosol during 1991 and 1992 at 41°N: Vertical profiles, size distribution, and volatility, *Geophys. Res. Let.,* 20, 1435-1438, 1993.

Fairlie, T. D. A., Three-dimensional transport simulations of the dispersal of volcanic aerosol from Mount Pinatubo, *Q. J. R. Meteorol. Soc.,* 121, 1943-1980, 1995.

Feichter, J., E. Kjellström, H. Rodhe, F. Dentener, J. Lelieveld, and G.-J. Roelofs, Simulation of the tropospheric sulfur cycle in a global climate model, *Atmos. Environ.,* 30, 1693-1707, 1996.

Graf, H.-F., I. Kirchner, A. Robock, and I. Schult Pinatubo eruption winter climate effects: Model versus observation, *Clim. Dyn.,* 9, 81-93, 1993.

Grainger, R. G., A. Lambert, C.D. Rodgers, F.W. Taylor, and T. Deshler, Stratospheric aerosol effective radius, surface area and volume estimated from infrared measurements, *J. of Geophys. Res.,* 100, 16507-16518, 1995.

Grant, W. B., et al., Aerosol-associated changes in the tropical stratospheric ozone following the eruption of Mt. Pinatubo, *J. of Geophys. Res.,* 99, 8197-8211, 1994.

Hansen, J., R. Ruedy, and M. Sato, Potential climate impact of Mount Pinatubo, *Geophys. Res. Let.,* 19, 215-218, 1992.

Kinne, S., O. B. Toon, and M. J. Prather, Buffering of stratospheric circulation by changing amounts of tropical ozone: A Pinatubo case study, *Geophys. Res. Let.,* 19, 1927-1930, 1992.

Kirchner, I., G. L. Stenchikov, H.-F. Graf, A. Robock and J. C. Antuna, Climate model simulation of winter warming and summer cooling following the 1991 Mount Pinatubo eruption, *J. of Geophys. Res.*, 104, 19,039-19,055, 1999.

Krueger, A. J., L. S. Walter, P. K. Bhartia, C. C. Schnetzler, N. A. Krotkov, I. Sprod, and G. J. S. Bluth, Volcanic sulfur dioxide measurements from the total ozone mapping spectrometer instruments, *J. of Geophys. Res.*, 100, 14,057-14,076, 1995.

Landgraf, J., and P. J. Crutzen, An efficient method for online calculations of photolysis and heating rates, *J. Atmos. Sci., 55*, 863-878, 1998.

Manzini, E., N. A. McFarlane, and C. McLandress, Impact of the Doppler spread parameterization on the simulation of the middle atmosphere circulation using the MA/ECHAM4 general circulation model, *J. of Geophys. Res.*102, 25,751-25,762, 1997

Minnis, P., E. F. Harrison, L. L. Stowe, G. G. Gibson, F. M. Denn, D. R. Doelling, and W. L. Smith Jr., Radiative climate forcing by the Mount Pinatubo eruption, *Science,* 259, 1411-1415, 1993.

Palmer, K. F., and D. Williams, Optical constants of sulfuric acid: Application to the clouds of Venus, *Appl. Opt.,* 14, 208-219, 1975.

Ramachandran, S, V. Ramaswamy, G. L. Stenchikov, and A. Robock, Radiative impact of the Mount Pinatubo volcanic eruption: lower stratospheric response, *J. of Geophys. Res.,* 105, 24409-24429. 2000.

Randel, W. J., F. Wu, J. M. Russell III, J. W. Waters, and L Froidevaux, Ozone and temperature changes in the stratosphere following the eruption of Mount Pinatubo, *J. of Geophys. Res.,* 100, 16,753-16,764, 1995 .

Rasch, P. J., and M. Lawrence, Recent development in transport methods at NCAR, in *MPI Workshop on Conservative Transport Schemes*, edited by B. Machenhauer et al., Rep. 265, Max—Planck-Inst. für Meteorol., Hamburg, Germany, 1998.

Read, W.G., L. Froidevaux, and J.W. Waters, Microwave limb sounder measurements of stratospheric SO_2 from the Mt. Pinatubo volcano, *Geophys. Res. Let.,* 20, 1299-1302, 1993.

Roeckner, E., K. Arpe, L. Bengtsson, M. Christoph, M. Claussen, L. Dümenil, M. Esch, M. Giorgetta, U. Schlese, and U. Schulzweida, The atmospheric general circulation model ECHAM-4: Model description and simulation of the present-day climate, Rep. 218, Max-Planck-Instit. für Meteorol., Hamburg, Germany, 1996.

Rozanov, E., M. Schlesinger, F. Yang, S. Malyshev, N. Andronova, V. Zubov, and T. Egorova Climate/Chemistry Effects of the Pinatubo volcanic eruption by the UIUC stratosphere/ troposphere GCM with interactive photochemistry, *J. of Geophys. Res.,* 107, 4594, doi:10.1029/2001JD000974, 2002.

Russell, P. B., et al., Global to microscale evolution of the Pinatubo volcanic aerosol, derived from diverse measurements and analyses, *J. of Geophys. Res.* 101,18,745-18,763, 1996.

Sparks, R. S. J., M. I. Bursik, S. N. Carey, J. S. Gilber, L. S. Glaze, H. Sigurdsson, and A. W. Woods, Volcanic Plumes, John Wiley and Sons, Chichester, 1997.

Steil, B., C. Brühl, E. Manzini, P.J. Crutzen, J. Lelieveld, P.J. Rasch, E. Roeckner, and K. Krüger, A new interactive chemistry climate model. I Present day climatology and interannual variability of the middle atmosphere using the model and 9 years of HALOE/UARS data, *J. Geophys. Res.*, (accepted), 2003.

Stenchikov, G. L., I. Kirchner, A. Robock, H.-F. Graf, J.C. Antuna, R. Grainger, A. Lambert, and L. Thomason, Radiative forcing from the 1991 Mt. Pinatubo volcanic eruption, *J. of Geophys. Res.*, 103, 13,837-13,858, 1998.

Thomason, L.W., L. R. Poole, and T. Deshler, A global climatology of stratospheric aerosol surface area density deduced from Stratospheric Aerosol and Gas Experiment II: 1984-1994, *J. of Geophys. Res.*102, 8967-8976, 1997.

Timmreck, C., H.-F. Graf, and J. Feichter, Simulation of Mt. Pinatubo aerosol with the Hamburg climate model ECHAM4, *Theor. Appl. Climatol.,* 62, 85-106, 1999a.

Timmreck, C., H.-F. Graf, and I. Kirchner, A one and a half year interactive simulation of Mt. Pinatubo aerosol, *J. of Geophys. Res.,*104, 9337-9360, 1999b.

Timmreck, C., Three-dimensional simulation of stratospheric background aerosol: First results of a multiannual GCM simulation. *J. of Geophys. Res.,* 106, 28,313- 28,332, 2001.

Trepte, C. R., and M. H. Hitchman, Tropical stratospheric circulation deduced from satellite aerosol data, *Nature,* 355, 626-628, 1992.

Young, R. E., H. Houben, and O. B. Toon, Radiatively forced dispersion of the Mt. Pinatubo volcanic cloud and induced temperature perturbations in the stratosphere during the first few months following the eruption, *Geophys. Res. Let.,* 21, 369-372, 1994.

Zerefos, C. S., K. Tourpali, and A. F. Bias, Further studies on possible volcanic signal to the ozone layer, *J. of Geophys. Res.,* 99,25741-25746, 1994.

Zhao, J., R. P. Turco, and O. B. Toon, A model simulation of Pinatubo volcanic aerosols in the stratosphere, *J. of Geophys. Res.,*100, 7315-7328, 1995.

H.-F. Graf and C. Timmreck, Max Planck Institute for Meteorology, Bundesstr. 55, D-20146 Hamburg, Germany (e-mail: graf@dkrz.de, timmreck@dkrz.de)

Benedikt Steil, Max-Planck-Institute for Chemistry, Atmospheric Chemistry Division, P.O. Box 3060, D-55020 Mainz, Germany (e-mail: steil@mpch-mainz.mpg.de).

Effects of Volcanic Eruptions on Stratospheric Ozone Recovery

Joan E. Rosenfield

Goddard Earth Science and Technology Center, University of Maryland Baltimore County, Baltimore, Maryland

The effects of the stratospheric sulfate aerosol layer associated with the eruption of the Mt. Pinatubo volcano and with future volcanic eruptions on the recovery of the ozone layer has been studied with the Goddard Space Flight Center interactive two-dimensional photochemical model. Model runs out to the year 2050 have been carried out, in which volcanoes having the characteristics of the Mt. Pinatubo volcano were erupted at ten year intervals starting in the year 2010. Compared to a control run using background aerosol loading, transient reductions of globally averaged column ozone of 1.7–2.8 % were computed as a result of each of these eruptions, with the ozone recovering to that computed for the nonvolcanic case in about five years after the eruption. Springtime Arctic column ozone losses of 9 to 17 % also recovered to the nonvolcanic case within five years. A sensitivity study with a volcano five times the magnitude of Mt. Pinatubo, as well as sensitivity studies in which the Arctic lower stratosphere was forced to be colder, resulted in recoveries to the nonvolcanic case in eight years or less. These results suggest that the long term recovery of ozone would not be strongly affected by infrequent large volcanic eruptions. Finally, in order to simulate situtations in which frequent smaller volcanic eruptions result in increasing the background sulfate loading, three runs were made in which the background aerosol was increased by reasonable amounts. This resulted in delays in ozone recovery of two to five years.

INTRODUCTION

The significant stratospheric ozone losses observed after the eruption of Mt. Pinatubo on June 15, 1991 have been shown to be caused by an enhancement in the sulfate aerosol levels [*Brasseur and Granier*, 1992; *Pitari and Rizi*, 1993; *Bekki and Pyle*, 1994; *Kinnison et al.*, 1994; *Tie et al.*, 1994; *Solomon et al.*, 1996; *Portmann et al.*, 1996; *Rosenfield et al.*, 1997; *Solomon et al.*, 1998]. Much of these ozone losses are due to heterogeneous chemistry occurring in the lower stratosphere on the surfaces of the

aerosol particles. The surface chemical reactions result in the conversion of chlorine from the reservoir species HCl and ClONO$_2$ to active chlorine (ClO$_x$ = ClO + Cl + Cl$_2$O$_2$ + HOCl) (*Brasseur and Granier*, 1992; *Solomon*, 1999). In the middle and upper stratosphere, gas phase chemical reactions cause ozone losses regardless of aerosol enhancement. In the future, as the chlorine loading of the stratosphere declines in response to controls on the release of chlorofluorocarbons, the stratospheric ozone layer is predicted to recover [*WMO*, 1999]. This paper examines the extent to which ozone recovery will be affected by future volcanic eruptions.

Tie and Brasseur [1995] studied the effect of a volcanic eruption on stratospheric ozone in an atmosphere with reduced chlorine loading. For the year 2015, they found that high northern latitude column ozone increased with a chlorine loading of 2.9 ppbv and decreased with a chlorine load-

ing of 3.7 ppbv. (The observed chlorine loading peaked at 3.7 ppbv between mid-1992 and mid-1994.) Their ozone changes were a result of the competition between increased ozone loss by the ClO_x cycle and decreased ozone loss by the NO_x (NO_x = NO + NO_2) cycle as a result of the heterogeneous conversion of nitrogen oxides into nitric acid (HNO3).

Tabazadeh et al. [2002] studied the effect of volcanic clouds on springtime Arctic ozone loss. They found that ozone loss during a cold year within the current range of natural variability could be as large as that found in the Antarctic "ozone hole". Increases in atmospheric carbon dioxide are predicted to warm the troposphere and cool the stratosphere as a result of changes in longwave cooling rates [e.g. *Ramaswamy et al.*, 2001; *Fels et al.*, 1980]. The *Tabazadeh et al.* [2002] result thus implies that a large injection of volcanic aerosols could strongly affect future ozone recovery in a stratosphere cooled by increasing greenhouse gas emissions.

The Goddard Space Flight Center (GSFC) interactive two-dimensional model of stratospheric photochemistry and transport was used to study the impact of increasing atmospheric carbon dioxide from 1980 to 2050 on the recovery of stratospheric ozone to its pre-1980 amounts [*Rosenfield et al.*, 2002]. Contemporary column ozone amounts as a function of latitude and time of year were computed to be within 10 % of observations except in the high southern latitudes, where a delay of about one month in the occurrence of the Antarctic ozone hole caused larger discrepancies. Maximum springtime column ozone depletions in 1998–2000, relative to 1980, at 75S and 75N were 42 % and 12 %, in good agreement with observations. The effect of the increases in CO_2 on ozone recovery were found to vary greatly with latitude, altitude, and time of year. Increasing CO_2 was found to speed up the recovery of globally averaged ozone by roughly ten years. This study used a stratospheric sulfate aerosol distribution appropriate for background conditions.

In this paper, the effect of future volcanic eruptions on ozone recovery is studied with the same model, taking into account the time varying chlorine loading as well as the stratospheric cooling due to increasing carbon dioxide. Volcano runs are compared to a control run which uses the same background sulfate aerosol distribution as *Rosenfield et al.*, [2002]. The focus is on annually, globally averaged ozone and on high northern latitude ozone. Relative to the control, the high northern latitudes give the greatest contributions to the annual mean ozone depletions. A short description of the model follows, after which the results computed for the Mt. Pinatubo eruption in 1991 are pre-sented. The results for future eruptions are then presented, followed by the conclusions.

MODEL DESCRIPTION

The GSFC interactive 2-D (latitude-pressure) model has been described in *Rosenfield et al.* [1997], which reported studies of the stratospheric effects of the Mt. Pinatubo eruption. Subsequent modifications were given in *Rosenfield et al.* [1998] and *Rosenfield and Douglass* [1998]. The model is interactive in the sense that computed temperatures, ozone, water vapor, and carbon dioxide are used in the calculation of the radiative heating rates. The residual circulation, which drives the transport of momentum, heat, and constituents, is determined from the computed heating rates. The model has a full chemistry scheme, with ~130 gas phase reactions. The gas phase reaction rates and photolysis cross sections use the photochemical data of *Sander et al.* [2000], together with the model computed temperatures and species concentrations.

The model includes a detailed parameterization of heterogeneous chemical reactions occurring on the surfaces of sulfate aerosols, and Type 1 and Type 2 polar stratospheric clouds (PSCs) [*Considine et al.*, 1994]. The sulfate aerosols and the two types of PSCs can coexist in the model. Type 1 PSCs, which exist above the frost point, are taken to be nitric acid trihydrate (NAT), and Type 2 PSCs are water ice. Denitrification, which plays an important role in ozone loss processes [*e.g., Solomon*, 1999], as well as dehydration are taken into account by sedimentation of the entire Type 1 and Type 2 condensed volume at a particular grid box using an average fall velocity. While it is known that Type 1 PSCs can exist in both NAT and supercooled ternary liquid solution forms, their exact composition is still under debate [*WMO*, 1999]. Recent observations taken in the Arctic winter found that a large fraction of the Type 1 cloud layers consisted of NAT particles [*Schreiner et al.*, 2003]. In addition, NAT particles are primarily responsible for denitrification [*Fahey et al.*, 2001; *Tabazadeh et al.*, 2000]. Very recently, *Drdla and Schoeberl* [2002] used a detailed microphysical model to compare chlorine activation and ozone depletion in an Arctic winter using a variety of different PSC compositions, including liquid, nitric acid dihydrate, and NAT. They found that the varying PSC compositions produced nearly identical chlorine activation and ozone loss through the end of February. After that time, the particles with NAT compositions produced greater ozone loss, aided in part by denitrification.

As discussed in *Considine et al.* [1994], the model zonal mean temperatures are not used to determine PSC amounts

and heterogeneous reaction rates, in part because of biases in the model winter polar temperatures. The chemical reaction rates use PSC surface area densities (SADs) determined by integrating over a probability distribution of observed temperatures which takes into account the longitudinal variations in temperature. The probability distribution was shifted 2 K colder, as trial and error showed that this resulted in the best agreement with observed present-day Arctic ozone losses. In addition, the center of the probability distribution was further adjusted to take into account model cooling in the stratosphere due to increasing atmospheric CO_2. The sulfate aerosol SADs were taken from the Stratospheric Aerosol and Gas Experiment II (SAGE II) instrument between 1990 and 1997 [Thomason et al., 1997] and the Stratospheric Measurement II (SAM II) instrument [McCormick et al., 1982] between 1990 and 1993. Background SADs are taken from the SAGE II and SAM II data for the year 1990, and range from ~1 $\mu m^2/cm^3$ at 100 hPa to ~0.2 $\mu m^2/cm^3$ at 30 hPa. Mass accommodation or "sticking coefficients" were taken from Sander et al. [2000].

The radiative heating rate and photolysis rate computations used sulfate aerosol number densities and single particle extinction and absorption cross sections determined from observations, as described in Considine et al. [2001]. The observations used were vertically and temporally varying size distribution balloon measurements [Deshler et al., 2003] and the SAGE II [Russell and McCormick, 1989] and SAM II [McCormick et al., 1982] 1 μm aerosol extinctions.

The size distributions and SADs used here differ from those used in our previous work on the Mt. Pinatubo eruption [Rosenfield et al., 1997]. In that work we used a single spatially and temporally independent sulfate particle size distribution in the chemistry and radiation calculations. The SADs were determined by combining SAGE II 1 μm aerosol extinctions with the size distribution, as described in Rosenfield et al. [1997]. Gas phase cross sections and reaction rates were from DeMore et al. [1987] and heterogeneous reaction "sticking coefficients" were from DeMore et al. [1994].

Transient model runs were made out to the year 2050, using WMO [1999] specifications for the source gas boundary conditions. A control run was performed in which background aerosol conditions were assumed. A volcanic run included the Mt. Pinatubo eruption in 1991, and a series of future Mt. Pinatubo-like eruptions. The sensitivity to temperature was explored with simulations in which the Arctic lower stratospheric temperatures were 4 K and 10 K colder than those given by the probability distribution discussed above. The sensitivity to aerosol loading was explored by

including a volcano five times the size of the Mt. Pinatubo eruption, and also by three different cases of increasing background aerosol concentration.

THE MOUNT PINATUBO ERUPTION

In order to demonstrate the ability of the model to predict the stratospheric effects of future eruptions, some comparisons are made here of the computed effects of the Mt. Pinatubo eruption in 1991 with observations. Plate 1 shows the 60S-60N area weighted averages of the computed and observed monthly mean, globally averaged column ozone differences from 1980. The observations are from the Total Ozone Mapping Spectrometer (TOMS) [McPeters et al., 1996; Herman et al., 1996]. The model results are generally in quite good agreement with the observations. Model computed ozone is slightly high between the years 1982 and 1986, probably due to the fact that the volcanic eruption of El Chichon in 1982 was not included in the calculations.

Figure 1 shows the computed temperature differences of the volcanic run relative to the control at 51 hPa (~21 km), averaged between 10S and 10N latitudes. The maximum computed warming of 3 K in spring 1992 agrees well with the radiosonde observed warming of 3.0±0.7 K determined by Angell [1997]. The observations were adjusted for the quasi-biennial oscillation (QBO). The QBO is the dominant mode of interannual variability in tropical lower stratospheric temperatures and ozone [Fleming et al., 2002 and references therein]. Neither the model nor the observations discussed below include the QBO. The maximum observed warming occurs two seasons after the eruption, slightly earlier than computed by the model. In a more recent analysis, Free and Angell [2002] examined the mean temperature changes for the 24 months after the Mt. Pinatubo eruption. They found a mean warming of 1.7 K for this time period, for the 30S to 30N average at 50 hPa. This can be compared to the model computed 24-month average warming of 2.1 K for the same latitude range (not shown).

In the polar regions, heterogeneous chemistry occurring on the surfaces of PSCs result in springtime ozone losses in the lower stratosphere. In the nonvolcanic control run, computed springtime 1998-2000 losses at 75N relative to 1980 were 9.9 %, compared with TOMS 70N-80N zonal mean losses of 9.4 %. In the years following the eruption of Mt. Pinatubo, the volcanic sulfate aerosol caused additional ozone loss. Figure 2 shows area-weighted averages between 60 and 90 degrees latitude of ozone mixing ratio differences from the control. There is a 10 % loss at 60–100 hPa (16–20 km) in late spring of 1992, a 20–30 % ozone loss at 70–200 hPa (12–18 km) in late spring of 1993, and 3% ozone
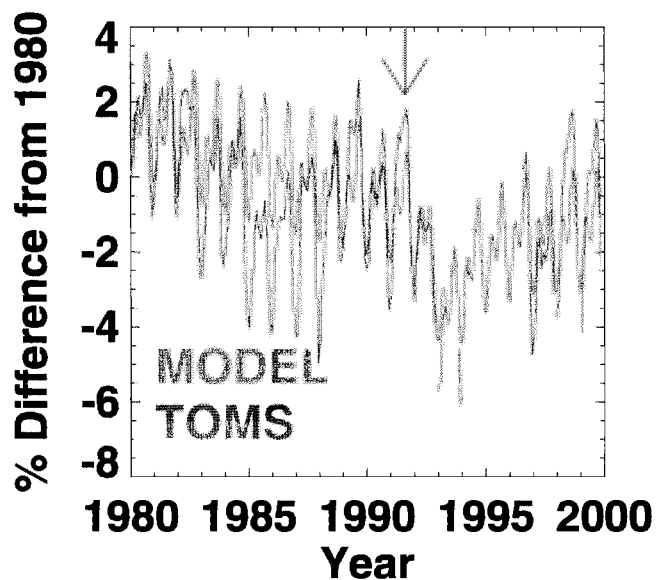
Plate 1. Differences of the monthly means of globally averaged (60S-60N) column ozone from 1980 values. The arrow indicates the eruption of Mt. Pinatubo. Some of the TOMS data is missing between 1992 and 1999. (See the color version of this plate at the back of this volume.)
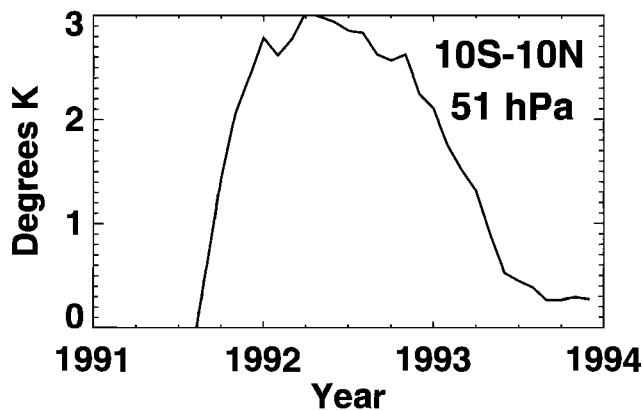
Figure 1. Change of temperature profile due to volcano (volcano minus background) at 51 hPa, averaged between 10S and 10N.

increases at ~20–35 hPa (23–28 km) in the summers of 1992 and 1993. The losses are due to heterogeneous chemistry occurring on the surface of the sulfate layer, while the increases are due to a combination of increased downwelling and decreased chemical ozone loss by the NOx catalytic cycle. The ozone losses are accompanied by moderate denitrification. During the winter of 1993 computed NO_y (N + NO + NO_2 + NO_3 + $2xN_2O_5$ + HNO_3 + HO_2NO_2 + $ClONO_2$ +...) at 75N is ~20–50 % less than that computed in a run with no heterogeneous chemistry. The computed ozone changes agree quite well with ozonesonde observed changes determined by *Angell* [1998]. He gives volcanic impacts due to the Mt. Pinatubo eruption in the North polar region of -11±3 % in the 16–24 km layer in spring of 1992,
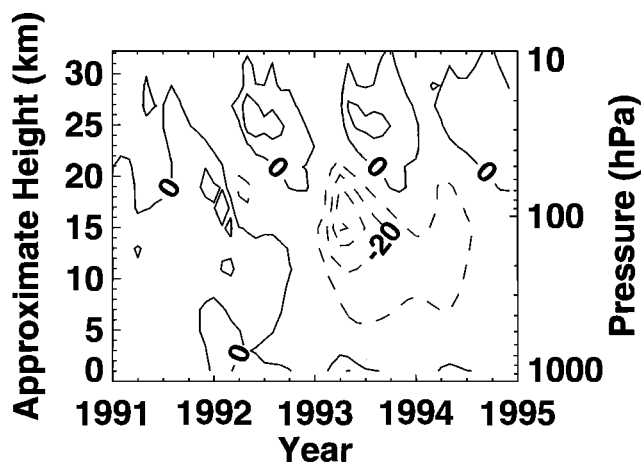
Figure 2. Percent change of ozone mixing ratios due to volcano (volcano minus background), averaged between 60N and 90N. Positive contour (solid line) is 3 percent, negative contour (dashed line) intervals are 10 percent.
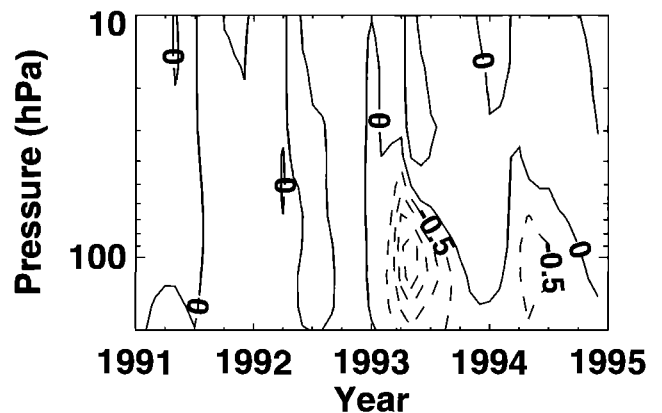
Figure 3. Temperature profile difference (volcanic minus background), averaged between 60N and 90N. The solid line is positive, the dashed lines are negative. The positive contour is 1 K and the negative contours are 0.5 K.

–20±10 % in the 8–16 km layer in spring of 1993, and +5±4 % in the 24–32 km layer in fall of 1992.

The 60N–90N area-weighted average temperature differences between the volcanic and the control run are shown in Figure 3. Cooling between 60 and 300 hPa is computed during the spring and summer of 1993, with a maximum cooling of 2 K at 100 hPa. This can be compared to the North polar radiosonde observed temperature anomalies in the 100-50 hPa layer of ~–2±1 K and in the 300-100 hPa layer of ~–3±1 K given by *Angell* [1997]. The ozone decreases shown in Figure 2 lead to a reduction in the solar heating, resulting in this cooling. A small warming of 0.5–1 K is computed above 60 hPa, due to the ozone increases shown in Figure 2.

Angell [1998] reported observed volcanic impacts on ozone in the north temperate zone (30–60N) of –17±11 % in the 8–16 km layer and –13±5 % in the 16–24 km layer, in spring of 1993. For this latitude band, the GSFC model computes a 15 % loss between 10 and 18 km in the spring of 1993 (not shown).

The ozone and temperature decreases in the Arctic lower stratosphere are smaller in magnitude in the spring of 1992 than in the spring of 1993. This is because the volcanic aerosols did not fully arrive in the North polar area until the summer of 1992, as shown in Figure 4. In *Rosenfield et al.* [1997], arctic springtime lower stratospheric ozone losses computed were greater in 1992 than in 1993. In that work, SADs were derived from SAGE II data only, with polar values determined by extrapolation. In this work, the polar SAM II data was used together with the SAGE II data, allowing a better representation of the polar regions. Another difference with the previous work is the timing of
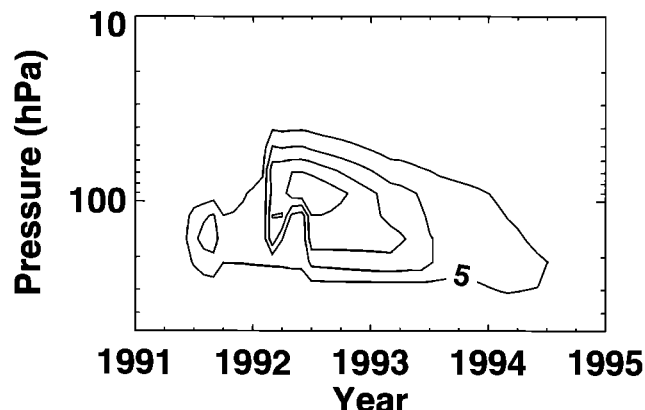
Figure 4. Aerosol surface area densities from SAGE II and SAM II data, averaged between 60N and 90N. Contours are 5 $\mu m^2/cm^3$

the volcanic temperature perturbation in the tropical lower stratosphere. In our previous work, the maximum computed temperature perturbation was delayed until the late summer of 1992. In this work it occurs in early spring, in better agreement with the observations. This can be attributed to the use of the time varying aerosol size distributions. In the previous work, a single temporally independent size distribution was used.

FUTURE VOLCANIC ERUPTIONS

In this section, the effects of future large-scale eruptions on the recovery of globally averaged column ozone and high northern latitude ozone are examined. The future eruptions were assumed to occur in mid-June of the years 2010, 2020, 2030, and 2040. The spatial and temporal characteristics of the aerosol layer were taken to be the same as that of the Mt. Pinatubo eruption. Although the Mt. Pinatubo eruption occurred in the northern hemisphere tropics in June, it has been shown that there was global dispersal of the aerosol cloud within 10 months of the eruption [*Trepte et al.,* 1993]. Trajectory computations of *Schoeberl* [private communication, 2002] show a similar rapid global dispersal of the aerosol clouds of historical large-scale eruptions located at a variety of latitudes in both hemispheres. Although a different season of eruption would probably make a difference within the first year, the long-term trend is not likely to be affected. Therefore, it is reasonable to represent the volcanic aerosol loading of future major eruptions by the Mt. Pinatubo aerosol, except perhaps for eruptions occurring inside the winter polar vortex.

The source gas boundary conditions were taken from Scenario A3 of *WMO* [1999]. Surface boundary conditions

for CO_2 and chlorine loading (CCly) are shown in Figure 5. In this scenario the CCly maximizes in ~1995, after which it eventually declines to pre-1980 values. CO_2 shows a roughly linear increase from 330 ppmv to 510 ppmv between the years 1980 and 2050. Surface N_2O increases from 302 to 370 ppbv between 1980 and 2050, resulting in the growth of NO_x. Surface CH_4 increases from 1570 to 2000 ppbv between 1980 and 2050, resulting ultimately in the growth of HO_x (OH + HO_2 + H) as a result of the oxidation of CH_4 to produce water vapor. The HO_x radicals participate in catalytic ozone destruction cycles which are important in the lower stratosphere and the upper stratosphere and mesosphere.

Figure 6 shows the computed differences of globally, annually averaged column ozone from 1980 values. Note that the latitude range here is 90S–90N, which is different from the latitude range of 60S–60N used in Plate 1. For the control run with background aerosol amounts a maximum depletion of 3.9 % was computed in 1998, after which column ozone recovered to its 1980 value in the year 2037. This is somewhat less than the maximum depletion of 4.6 % reported in *Rosenfield et al.* [2002], which used the same source gas boundary conditions. This difference is due primarily to the updated gas phase and heterogeneous reaction rates [*Sander et al.,* 2000] used in this work. In the previous work, the rates used were those given in *DeMore et al.,* [1997]. The more recent compilation reduces the rate of the NO_2 + O –> NO + O_2 gas phase reaction, resulting in less ozone loss in the middle stratosphere due to the "NO_x" catalytic cycle which dominates ozone loss in that altitude region [*Rosenfield et al.,* 2002]. The Mt. Pinatubo eruption causes a 2.9 % ozone loss relative to the control in 1993.
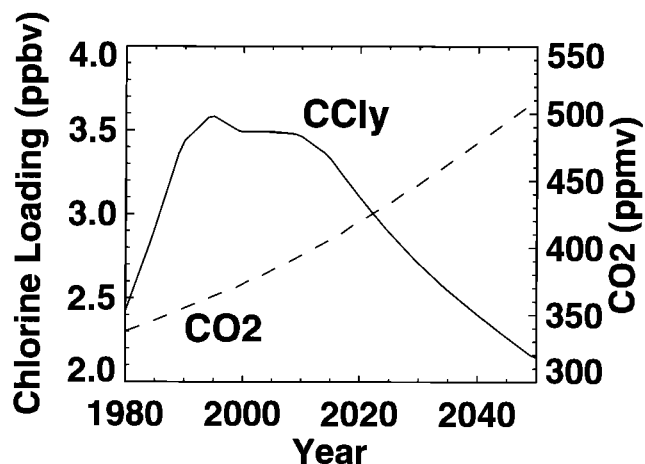
Figure 5. Surface boundary conditions for chlorine loading (CCl$_y$) and CO_2 as a function of time [*WMO,* 1999].
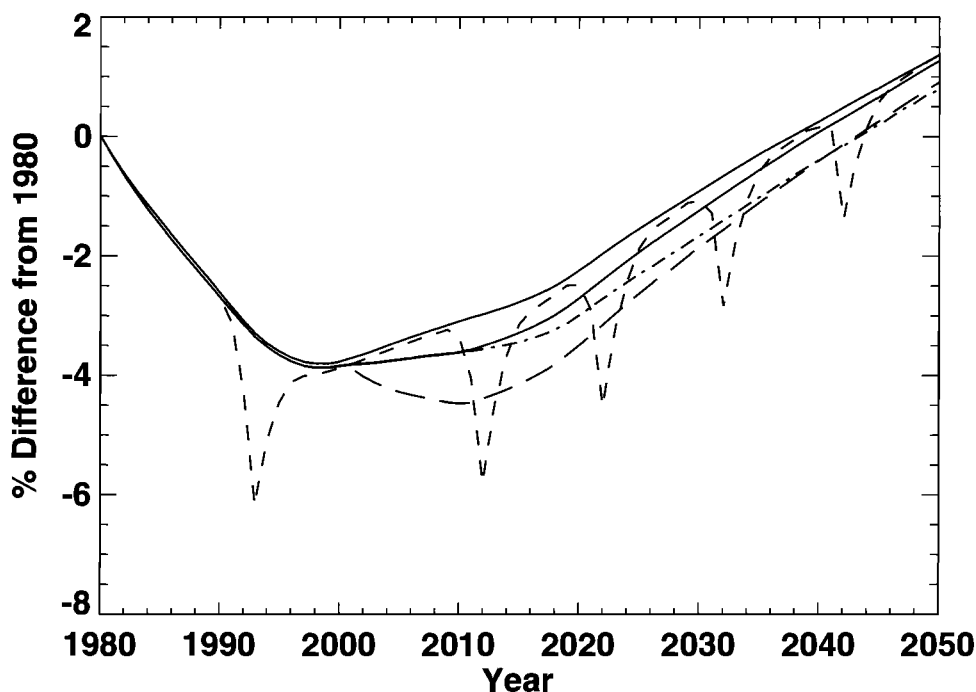
Figure 6. Globally, annually averaged column ozone differences from 1980 as a function of time (90S–90N). The solid line is the background run, the dashed line is the volcanic run, the dash-dot line is the case 1 increasing background run, the dash-dot-dot-dot line is the case 2 increasing background run, and the long dash line is the case 3 increasing background run.

This is somewhat less than the 3.2 % loss calculated in *Rosenfield et al.* [1997]. This is most likely due to the differences in the heterogeneous reaction rates used in the two studies.

The future volcanic eruptions cause transient ozone reductions which recover to the nonvolcanic control case in about five years after the eruption. Maximum depletions relative to the control are 2.8 % in 2012, reducing to 1.7 % in 2042 when the chlorine loading is lower. The high latitudes give the greatest contributions to the annual mean ozone depletions, with 2012 column ozone losses of 8 % at 75N and 4 % at 75S relative to the control (not shown). In the springtime, maximum computed Arctic column ozone losses of 9 to 17 % also recovered to the nonvolcanic case within five years. The ozone reductions are due to heterogeneous chemistry occurring on the increased sulfate aerosol layer.

In addition to the nominal volcanic run, a five times Mt. Pinatubo run was made for the 2010 volcanic eruption in order to simulate an extreme case. Surface area densities and 1 μm extinctions for this case were forced to be five times that of the Mt. Pinatubo observations. In this run, as well as the other volcano runs in this study, the aerosol sur-

face areas return to background values seven years after the eruption. The resulting maximum mid-April column ozone depletion relative to the control was 34 % at 75N in 2012 and the column ozone at that latitude took eight years to recover to the control. Globally averaged column ozone showed depletions of 7 %, with a recovery time to the control also of eight years.

COLDER ARCTIC TEMPERATURES

In addition to the above runs, two cases corresponding to a colder Arctic lower stratosphere were run. This was accomplished by shifting the temperature probability distribution used in the heterogeneous chemistry parameterization an additional 4 K and 10 K colder. These temperature decreases are much greater than the radiative cooling due to increasing CO_2. At 75N and 90 hPa, the radiative cooling is 0.6 K in the year 2012, and increases to 1.6 K in 2050. Figure 7 shows the resulting 2012 ozone mixing ratios in the springtime lower stratosphere at 75N for the background and volcanic cases. For the nominal volcanic run there is a maximum ozone depletion of 0.9 ppmv at 70 hPa (19 km). Forcing lower stratospheric temperatures to be 4 K and 10
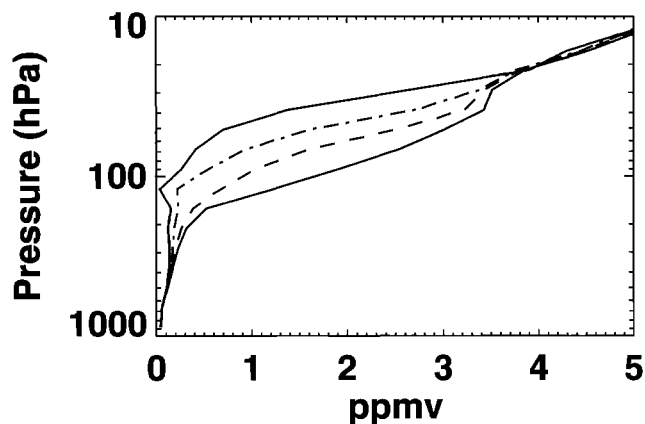
Figure 7. Ozone mixing ratios at 75N in mid-April 2012. The solid line is the background case, the dashed line is the nominal volcanic case, the dash-dot line is the 4 K colder volcanic case, and the dash-dot-dot line is the 10 K colder volcanic case.

K colder led to maximum ozone depletions of 1.6 ppmv at 70 hPa and 2.3 ppmv at 50 hPa (21 km), respectively. The additional depletion was due to the formation of increasing amounts of PSCs. In the nominal volcanic case Type 1 PSC mixing ratios ranged from 0.2 ppbv at 200 hPa to 1.2 ppbv at 30 hPa, while Type II PSC amounts were negligible. With a 4 K colder stratosphere January Type I PSC mixing ratios ranged from 0.6 ppbv at 200 hPa to 1.5 ppbv at 30 hPa, while Type II PSC amounts of ~0.4 ppmv formed at 160 hPa. With a 10 K colder stratosphere, Type II PSC formation was more favored, with mixing ratios ranging from ~2 ppmv between 212-160 hPa and ~0.5 ppmv between 120-90 hPa. For this case, Type I PSC amounts ranged from 0.3 ppbv at 200 hPa to 0.6 at 30 hPa. Relative to the control, the column ozone losses corresponding to these three volcano cases were 18 %, 34 %, and 48 %. In these cases the column depletions at 75N also reverted to the nonvolcanic case within 5 years of the eruption.

These results can be compared with the volcanic calculations of *Tabazadeh et al.* [2002]. They used a coupled chemistry-microphysics trajectory model to compute Arctic lower stratospheric ozone reductions of ~2.5 ppmv for conditions approximating a cold year with temperatures below 196 K. Their ozone loss is larger than the ~1 ppmv ozone reduction in 2012 calculated here for the nominal volcanic run. As discussed above, the heterogeneous chemistry calculations here used a temperature probability distribution derived from observations. In the nominal volcano run, the integral over the probability distribution gave 70 hPa temperatures below 196 K roughly 20–40 % of the time. In the 10 K colder run, in which temperatures were below 196 K roughly 50–75 % of the time, the computed ozone depletion

is ~2.3 ppmv. Thus most of the differences from the *Tabazadeh et al.* [2002] work are probably accounted for by the warmer temperatures used here.

Of note is the fact that no volcanically induced column ozone increases are computed for chlorine loadings as low as 2.4 ppbv, in contrast to *Tie and Brasseur* [1995] who computed column ozone increases for a chlorine loading of 2.9 ppbv in the year 2015. Although middle stratospheric ozone increases associated with the NO_x cycle are calculated here, they are not great enough to outweigh the lower stratospheric ozone decreases due to the ClO_x cycle. Both the N_2O and the CH_4 concentrations used here are very similar to those used by *Tie and Brasseur* [1995]. The difference between the present work and their work is thus most likely due to differences in the partitioning of chlorine species produced by the differing chemical schemes.

INCREASING BACKGROUND AEROSOL

In the above cases, the impact on ozone of large infrequent volcanic explosions in the future was examined. Another possibility is that the occurrence of many smaller volcanic explosions could result in an increase of background aerosol levels. To examine this possibility, three runs were made in which the background aerosol SADs and 1 μm extinctions were increased, starting in the year 2000. In case 1 these quantities were increased 10% per year, resulting in a sixfold increase of the background levels by the year 2050. In case 2 these quantities were increased 10% per year up until the year 2010, after which they were held constant at the resulting twofold increase. In case 3, as an extreme, these quantities were increased 40% per year until the year 2010, after which they were held constant at the resulting fivefold increase. Background aerosol increases greater than five or six times the present amount seem unlikely.

The resulting recovery of global average column ozone for these cases is shown in Figure 6. Both cases 1 and 2 have twice the background aerosol in year 2010, resulting in an increased ozone loss of 0.5%. In case 2 ozone recovery to 1980 values occurs in the year 2039, just two years after the background case. In case 1, in which aerosol continues to increase after 2010, ozone recovery occurs in the year 2043. In case 3 which has five times the background aerosol loading from 2010 on, there is an additional ozone loss of 1.4% in 2012, after which recovery is delayed until 2043. At 75N in the spring of 2012, cases 1, 2, and 3 give column ozone losses relative to the control of 2.1%, 1.8%, and 5.3% (not shown). At 75N in the spring of 2050, column ozone is 0.8% below 1980 values for the control case, while cases 1, 2, and 3 are 2.2%, 0.4%, and 1.8% below 1980 values.

CONCLUSIONS

This study has shown that transient reductions of globally averaged column ozone of 1.7–2.8% relative to background aerosol conditions could be expected from future volcanic eruptions having a stratospheric sulfate loading comparable to that of Mt. Pinatubo. In the springtime high northern latitudes, transient column ozone losses of 9 to 17% could be expected. However, these transient losses revert to the non-volcanic control situation within about five years after the eruption, suggesting that the long term recovery of stratospheric ozone would not be strongly affected by infrequent volcanic eruptions with the magnitude of Mt. Pinatubo.

Two sensitivity studies were carried out in which the Arctic lower stratosphere was forced to be 4 K and 10 K colder. Another sensitivity study was performed in which a volcano five times the size of Mt. Pinatubo was erupted. Transient ozone losses also occurred in these cases. For the cases with a colder Arctic, column ozone recovered to the control in five years, while for the five times Mt. Pinatubo case, column ozone recovered to the control in eight years. Sensitivity studies in which background aerosol levels were increased by reasonable amounts led to delays in the recovery of globally averaged ozone of two to five years.

REFERENCES

Angell, J. K., Stratospheric warming due to Agung, El Chichon, and Pinatubo taking into account the quasi-biennial oscillation, *J. Geophys. Res., 102*, 9479-9485, 1997.

Angell, J. K., Impact of El Chichon and Pinatubo on ozonesonde profiles in north extratropics, *Geophys. Res. Lett., 25*, 4485-4488, 1998.

Bekki, S., and J. A. Pyle, A two-dimensional modeling study of the volcanic eruption of Mount Pinatubo, *J. Geophys. Res., 99*, 18,861-18,869, 1994.

Brasseur, G., and C. Granier, Mount Pinatubo aerosols, chlorofluorocarbons, and ozone depletion, *Science, 257*, 1239-1242, 1992.

Considine, D. B., A. R. Douglass, and C. H. Jackman, Effects of a polar stratospheric cloud parameterization on ozone depletion due to stratospheric aircraft in a two-dimensional model, *J. Geophys. Res., 99*, 18,879-18,894, 1994.

Considine, D. B., J. E. Rosenfield, and E. L. Fleming, An interactive model study of the influence of the Mount Pinatubo aerosol on stratospheric methane and water trends, *J. Geophys. Res., 106*, 27,711-27,727, 2001.

DeMore, W. B., J. J. Margitan, M. J. Molina, R. T. Watson, D. M. Golden, R. F. Hampson, M. J. Kurylo, C. J. Howard, and A. R. Ravishankara, Chemical kinetics and photochemical data for use in stratospheric modeling, *Jet Propulsion Laboratory Publication 87-41*, 1987.

DeMore, W. B., D. M. Golden, R. F. Hampson, C. J. Howard, C. E. Kolb, M. J. Kurylo, M. J. Molina, A. R. Ravishankara, and S. P. Sander, Chemical kinetics and photochemical data for use in stratospheric modeling, Evaluation number 11, *Jet Propulsion Laboratory Publication 94-26*, 1994.

DeMore, W. B., S. P. Sander, D. M. Golden, R. F. Hampson, M. J. Kurylo, C. J. Howard, A. R. Ravishankara, C. E. Kolb, and M. J. Molina, Chemical kinetics and photochemical data for use in stratospheric modeling, Evaluation number 12, *Jet Propulsion Laboratory Publication 97-4*, 1997.

Deshler, T., M. E. Hervig, D. J. Hofmann, J. M. Rosen, and J. B. Liley, Thirty years of in situ stratospheric aerosol size distribution measurements from Laramie, Wyoming (41N), using balloonborne instruments, *J. Geophys. Res.*, in press, 2003.

Drdla, K., and M. R. Schoeberl, Microphysical modeling of the 1999-2000 Arctic winter 2. Chlorine activation and ozone depletion, *J. Geophys. Res.*, in press, 2003.

Fahey, D. W., et al., The detection of large HNO3-containing particles in the winter arctic stratosphere, *Science, 291*, 1026-1031, 2001.

Fels, S. B., J. D. Mahlman, M. D. Schwarzkopf, and R. W. Sinclair, Stratospheric sensitivity to perturbations in ozone and carbon dioxide: radiative and dynamical response, *J. Atmos. Sci., 37*, 2265-2297, 1980.

Fleming, E. L., C. H. Jackman, J. E. Rosenfield, and D. B. Considine, Two-dimensional model simulations of the QBO in ozone and tracrs in the tropical stratosphere, *J. Geophys. Res., 107(D23)*, 4665, doi:10.1029/2001JD001146, 2002.

Free, M., and J. K. Angell, Effect of volcanoes on the vertical temperature profile in radiosonde data, *J. Geophys. Res., 107, (D10)*, 10.1029/2001JD001128, 2002.

Herman, J. R., et al., *Meteor-3 Total Ozone Mapping Spectrometer (TOMS) Data Products User's Guide, NASA Ref. Publ. 1393*, National Aeronautics and Space Adminstration, Washington, D.C., 1996.

Kinnison, D. E., K. E. Grant, P. S. Connell, D. A. Rotman, and D. J. Wuebbles, The chemical and radiative effects of the Mount Pinatubo eruption, *J. Geophys. Res., 99*, 25,705-25,731, 1994.

McCormick, M. P., H. M. Steele, P. Hamill, W. P. Chu, and T. J. Swissler, Polar stratospheric cloud sightings by SAM II, *J. Atmos. Sci., 39*, 1387-1397, 1982.

McPeters, R. D., et al., *Nimbus-7 Total Ozone Mapping Spectrometer (TOMS) Data Products User's Guide, NASA Ref. Publ. 1384*, National Aeronautics and Space Adminstration, Washington, D.C., 1996.

Pitari, G., and V. Rizi, An estimate of the chemical and radiative perturbation of stratospheric ozone following the eruption of Mt. Pinatubo, *J. Atmos. Sci., 50*, 3260-3276, 1993.

Portmann, R. W., S. Solomon, R. R. Garcia, L. W. Thomason, L. R. Poole, and M. P. McCormick, Role of aerosol variations in anthropogenic ozone depletion in the polar regions, *J. Geophys. Res., 101(D17)*, 22,991-23,006, 1996.

Ramaswamy, V., et al., Stratospheric temperature trends: observations and model simulations, *Rev. Geophys., 39,* 71-122, 2001.

Rosenfield, J. E., A. R. Douglass, and D. B. Considine, The impact of increasing carbon dioxide on ozone recovery, *J. Geophys. Res., 107, (D6),* doi:10.1029/2001JD000824, 2002.

Rosenfield, J. E., D. B. Considine, P. E. Meade, J. T. Bacmeister, C. H. Jackman, and M. R. Schoeberl, Stratospheric effects of Mount Pinatubo aerosol studied with a coupled two-dimensional model, *J. Geophys. Res., 102,* 3649-3670, 1997.

Rosenfield, J. E., D. B. Considine, M. R. Schoeberl, and E. V. Browell, The impact of subvisible cirrus clouds near the tropical tropopause on stratospheric water vapor, *Geophys. Res. Lett., 25,* 1883-1886, 1998.

Rosenfield, J. E., and A. R. Douglass, Doubled CO2 effects on NOy in a coupled 2D model, *Geophys. Res. Lett., 25,* 4381-4384, 1998.

Russell, P. B., and M. P. McCormick, SAGE II aerosol data validation and initial data use: An introduction and overview, *J. Geophys. Res., 94,* 9335-8338, 1989.

Sander, S. P., R. R. Friedl, W. B. DeMore, D. M. Golden, M. J. Kurylo, R. F. Hampson, R. E. Huie, G. K. Moortgat, A. R. Ravishankara, C. E. Kolb, M. J. Molina, Chemical kinetics and photochemical data for use in stratospheric modeling, Evaluation number 13, *Jet Propulsion Laboratory Publication 00-3,* 74 pp., 2000.

Schreiner, J., et al., Chemical, microphysical, and optical properties of polar stratospheric clouds, *J. Geophys. Res., 108(D5),* 8313, doi:10.1029/2001JD000825, 2003.

Solomon, S., R. W. Portmann, R. R. Garcia, L. W. Thomason, L. R. Poole, and M. P. McCormick, The rold of aerosol variations in anthropogenic ozone depletion at northern midlatitudes, *J. Geophys. Res., 101(D3),* 6713-6727, 1996.

Solomon, S., R. W. Portmann, R. R. Garcia, W. Randel, F. Wu, R. Nagatani, J. Gleason, L. Thomason, L. R. Poole, M. P. McCormick, Ozone depletion at mid-latitudes: coupling of volcanic aerosols and temperature variability to anthropogenic chlorine, *Geophys. Res. Lett., 25,* 1871-1874, 1998.

Solomon, S., Stratospheric ozone depletion: a review of concepts and history, *Rev. Geophys., 37 (3),* 275-316, 1999.

Tabazadeh, A., K. Drdla, M. R. Schoeberl, P. Hamill, and O. B. Toon, Arctic "ozone hole" in a cold volcanic stratosphere, *Proc. Natl. Acad. Sci. USA, 99,* 2609-2612, 2002.

Tabazadeh, A., M. L. Santee, M. Y. Danilin, H. C. Pumphrey, P. A. Newman, P. J. Hamill, and J. L. Mergenthaler, *Science, 288,* 1407-1411, 2000.

Thomason, L.W., L.R. Poole, and T. Deshler, A global climatology of stratospheric aerosol surface area density deduced from Stratospheric Aerosol and Gas Experiment II measurements: 1984-1994, *J. Geophys. Res., 102,* 8967-8976, 1997.

Tie, X. X., G. P. Brasseur, B. Briegleb, and C. Granier, 2-Dimensional simulation of Pinatubo aerosol and its effect on stratospheric ozone, *J. Geophys. Res., 99,* 20,545-20,562, 1994.

Tie, X., and G. Brasseur, The response of stratospheric ozone to volcanic eruptions: Sensitivity to atmospheric chlorine loading, *Geophys. Res. Lett., 22,* 3035-3038, 1995.

Trepte, C. R., R. E. Veiga, M. P. McCormick, The poleward dispersal of Mount Pinatubo volcanic aerosol, *J. Geophys. Res. 98,* 18,563-18,573, 1993.

World Meteorological Organization (WMO), *Scientific assessment of ozone depletion: 1998, Rep. 44,* Geneva, 1999.

J. Rosenfield, Code 916, NASA/Goddard Space Flight Center, Greenbelt, MD 20771 (rose@euterpe.gsfc.nasa.gov).

Surface Climate Responses to Explosive Volcanic Eruptions Seen in Long European Temperature Records and Mid-to-High Latitude Tree-Ring Density Around the Northern Hemisphere

P. D. Jones, A. Moberg, T. J. Osborn, and K. R. Briffa

Climatic Research Unit, School of Environmental Sciences, University of East Anglia, Norwich, United Kingdom

Explosive volcanic eruptions are known to have an impact on surface temperatures in the two to three years after the eruption, but our ability to determine the impact is impeded by the paucity of eruptions (3–5 large events each century). We examine the response to large eruptions in instrumental temperature records for the whole Northern Hemisphere (NH) and longer European records using superposed epoch analysis. Despite the limited number of eruptions we separate the volcanoes into two groups: tropical and mid-to-high northern latitude (>40°N). The clearest response is after tropical eruptions, where the NH land temperature average cools significantly in the summer months up to three years after the eruptions, although the timing of the response differs markedly from eruption to eruption. Extending the analysis to three European regions (Fennoscandia, Central England and Central Europe) with longer temperature records shows weakly significant summer cooling after tropical eruptions over Fennoscandia, but no discernible impacts in the other two regions. The Fennoscandian series also indicates slight warming in the first, second and fourth winters (but not the third) following the eruptions, but the significance level is not reached. The lack of statistical significance (in the regional series for both summer and winter) is principally due to the greater variability of the regional series compared to the NH land temperature average, with the small number of eruptions being a contributory factor. After higher latitude eruptions significant cooling is restricted to the late summer in the NH during the eruption year, with little of significance in the longer European regional series. We also assess longer records of tree-ring density from the mid-to-high latitude regions of the NH. This analysis further highlights the dearth of major eruptions (about 20 in the last 600 years) and the differences in the spatial patterns of cooling after the eruptions. The response in the NH average of the exactly-dated tree-ring density series, however, is of such a unique character, that extremely anomalous negative values can be used to determine when major eruptions occurred in the past, even though the location of the eruption remains unknown for some dates.

1. INTRODUCTION

Ever since a link between volcanism and weather in the few years after major volcanic eruptions was first suggested by Benjamin Franklin in 1785, atmospheric scientists have

sought to determine the nature and importance of the link. The extensive literature on the subject has been reviewed by [*Lamb*, 1970] and more recently by [*Robock*, 2000]. The principal difficulties are a relative paucity of eruptions (about 20 major events in the last 600 years) and, until the last 40 years, little idea of the processes taking place in the atmosphere in response to the ash, gases and derivative aerosols emitted during eruptions. Vital observations are now beginning to be made and significant improvements to the treatment of volcanic aerosols within climate models have occurred, particularly since the 1991 eruption of Pinatubo. Other papers in this volume detail these important advances in the understanding of atmospheric chemistry and in climate modeling, but all conclude that there is still much improvement needed.

The purpose of this contribution is to reassess the surface-temperature response from instrumental records over the Northern Hemisphere (NH) and in longer records from Europe that extend back to the 17th and 18th century, and to consider the response to earlier events in exactly-dated tree-ring density records from mid-to-high latitude regions of the NH back to 1400. Much has been written on the subject [see, e.g., *Bradley*, 1988; *Bradley* and *Jones*, 1992; *Briffa et al.*, 1998; and *Robock*, 2000], but the instrumental and tree-ring data have never been considered together. The emphasis in this paper is the surface-temperature response in the most comprehensive sets of climate and tree-ring data available. We concentrate on presenting the evidence and, particularly with the instrumental records, assessing the significance of the temperature response in the immediate post-eruptive sequence of 4–5 years. Apart from considering observational links to circulation features over the North Atlantic and North European region (through the North Atlantic Oscillation, NAO) we do not discuss related work in atmospheric chemistry or climate modeling, only to note where support or lack thereof has been found.

The paper is organised as follows: Section 2 discusses the sources of instrumental temperature data and tree-ring density data. Section 3 documents the selection of explosive volcanic events and the Superposed Epoch Analysis (SEA) method used to determine the monthly instrumental temperature response, using the example of NH land areas. Section 4 details the instrumental temperature response for three European regions (Fennoscandia, Central England and Central Europe). Section 5 illustrates the response patterns in earlier extremely light tree-ring density years over mid-to-high latitudes of the NH, some of which can be clearly related to known volcanic events and others that, from their unusualness and the spatial character of the response, are likely to be. Section 6 concludes.

2. DATA SOURCES

2.1. Instrumental Temperature

Three groups have produced gridded analyses of surface temperature averages and routinely update their records on a monthly basis (Climatic Research Unit, CRU [*Jones et al.*, 1999, 2001] National Climatic Data Center, NCDC [*Peterson et al.*, 1998] and Goddard Institute for Space Studies, GISS [*Hansen et al.*, 1999; 2001]. Here, for the NH and European regions, we use the recent update of the CRU analysis [*Jones* and *Moberg*, 2003], which incorporates extensive additional data, improving both the number of station records and involving recently homogenized records for many parts of Europe and Canada. The European improvements have resulted from initiatives by both national hydrometeorological services [e.g. Fennoscandia, *Tuomenvirta et al.*, 2001] and Austria [*Böhm et al.*, 2001] and the EU-funded IMPROVE project, which has digitised and homogenized daily temperatures for seven of the longest series where records exist back to the early-to-mid 18th century [*Camuffo* and *Jones*, 2002]).

The present analysis uses four land-station-only temperature series, for the NH, Fennoscandia (55–75°N, 5–35°E), Central Europe (45–55°N, 5–30°E) and the Central England series [*Manley*, 1974; updated in *Parker et al.*, 1992]. The revised CRU analysis [*Jones* and *Moberg*, 2003] of gridded temperatures extends back to 1851, but for this study we have extended the gridding for Europe to 1781. The CRU gridding technique averages station temperature anomaly data in all 5° x 5° grid boxes where contributing stations are available. The base period for the anomalies is 1961–90. As the number of stations contributing to individual grid boxes varies with time, we use the CRUTEM2v version, that adjusts the variance to conform to infinitely sampled grid boxes [see *Jones et al.*, 2001; and *Jones* and *Moberg*, 2003, for details]. For the purposes of the present study, however, the results would be almost exactly the same with the non-variance adjusted series as regional averages are being used.

2.2. Tree-Ring Density

To assess the potential climatic impact of earlier explosive volcanic eruptions (prior to 1851 for the NH, 1781 for Fennoscandia and Central Europe and 1659 for Central England), we use nearly 400 series of maximum latewood density (MAXD) from conifers growing near the latitudinal and elevational tree lines in Eurasia and North America. The derivation of this dataset has been extensively discussed in

the literature [*Schweingruber* and *Briffa*, 1996; and *Briffa et al.*, 2001]. MAXD has been shown to explain more variance of 'summer' temperature (e.g. April–August or May–September) reconstructions than conventional ring width series from the same sites, and has also been used recently to assess the frequency and surface temperature impacts of large volcanic eruptions [*Briffa et al.*, 1998].

Many tree-ring parameters (including MAXD and ring widths) respond to climatic influences, but their expression can be confounded on longer timescales by biological factors that produce long-term trends in measured tree-ring series related to tree ageing. All series of these parameters are generally detrended or 'standardized' using a variety of techniques that remove the biological effects, but sometimes at the expense of the simultaneous removal of climatic information on longer time scales [see, e.g., *Cook* and *Briffa*, 1990; and *Cook et al.*, 1995]. Here we use a new approach to 'standardization' applied to this dataset [*Briffa et al.*, 2001] that was designed to maintain more low-frequency variations in the resulting site MAXD chronologies than has, hitherto, been achieved. This technique, known as Age-Band Decomposition (ABD), involves segregating the many measured series into discrete classes, each representing rings produced by trees within specific age ranges, e.g. 1–10 years old, 11–20 years old etc. The data within each class are then averaged to produce complete or near-complete time series. Then each of these series is normalized and averaged with all other age-band series to produce a continuous tree-ring record where the values are not biased by the average age of the source trees through time. To facilitate later analysis the ABD standardized MAXD data were gridded to the 5° x 5° grid used for the instrumental temperature data.

3. VOLCANIC ERUPTIONS AND SUPERPOSED EPOCH ANALYSIS

3.1. Volcanic Eruptions

[*Robock*, 2000] has reviewed the three common volcanic indices (Dust Veil Index, DVI; Volcanic Explosivity Index, VEI; and Ice Core Volcanic Index, IVI) and their variants. Here we select volcanic eruptions from the whole NH and the SH tropics which have a VEI ≥ 5 [*Simkin* and *Siebert*, 1994]. We omit eruptions where it is known that the ejected material did not reach the stratosphere in sufficient amounts to alter large-scale climate (e.g. Mount St. Helens in 1980) and eruptions post 1997, as our analysis technique requires 5 post-eruption years. There is considerable debate as to the VEI values of some eruptions during the last few centuries.

VEI modifications and updates have been made since 1994 and are given online on http://www.volcano.si.edu/gvp/world/index.cfm. Many are also quoted with a question mark in both [*Simkin* and *Siebert*, 1994] and on the Web site. Apart from all VEI ≥ 5(?) events we also include the Laki/Asama event in 1783 and Agung in 1963 as these events have been extensively used in the volcanic-climate link literature [see *Robock*, 2000; and references therein].

We divide the eruptions into two groups, tropical and mid-to-high NH latitudes. Many earlier studies [reviewed by *Robock*, 2000] have shown that material from tropical eruptions is generally present in ice core series from both polar regions, whereas for higher latitude (>40°) eruptions material is confined to the poleward part of the hemisphere. Table 1 lists the eight tropical and seven mid-to-high (NH) latitude eruptions considered.

3.2. Superposed Epoch Analysis (SEA)

The aim of SEA is to highlight the common responses (in series and patterns) during the years after selected eruptions. There is an extensive literature on the subject with respect to the volcano/climate link [*Kelly* and *Sear*, 1984; *Sear et al.*, 1987; *Kelly et al.*, 1996; and *Robock*, 2000]. The approach has also been used in other areas of climatology, most notably to determine the most common response regions during El Niño events [e.g. *Rasmusson* and *Carpenter*, 1982]. Its use in this area highlights the principal problem related to sampling with respect to volcano-related studies. El Niño events occur every 3–7 years, thus providing ~30 events during the period of hemispheric instrumental records. The greater frequency enables responses to be stratified by El Niño severity and compared between periods (e.g. three 50-year periods since 1851). For

Table 1. Location and Dates (Eruption Year) of the tropical and higher latitude NH eruptions[1].

Tropical		Higher latitude	
Unknown	1809	Shikotsu	1739
Tambora	1815	Laki/Asama	1783
Cosiguina	1835	St. Helens	1800
Krakatau	1883	Sheveluch	1854
Santa Maria[2]	1902	Ksudach	1907
Agung	1963	Novarupta	1912
El Chichón	1982	Bezymianny	1956
Pinatubo	1991		

[1]Full details of these eruptions are given in [*Simkin* and *Siebert*, 1994].

[2]There were also two VEI eruptions of 4 in the Caribbean in this year (Pelée and Soufriere).

volcanic applications, Table 1 indicates only 5 tropical and 4 mid-to-high latitude (NH) explosive volcanic events since 1851.

Various SEA approaches have been introduced into the literature [Kelly et al., 1996]. Here we compare four SEA methods, which all have one common feature. This is the need to consider the temperature response for the same time of year regardless of when in the year the eruptions occurred. Modeling and theoretical studies [see, e.g., Robock, 2000] clearly indicate that the greatest response tends to be during the boreal summer in the NH when the volcanic aerosols have the potential to perturb the higher radiation levels compared to the winter season. As the aerosol residence time in the stratosphere can be 1–3 years, we average the differing eruption responses with respect to the January of the eruption year (month 1). This means that the analysis will combine the same months of the year, when variability from year to year will be the same.

The basic SEA approach taken here is to consider the 120 months of temperature data centred on the January (month 1) of the eruption year. Each month (J, F, .., D) in the 120 month sequence is then expressed as a departure from the average of the five appropriate (i.e. the same month of the year) pre-eruption months. Significance levels for the 'post-eruptive' months 1 to 48 are determined using Monte Carlo procedures (generating 5000 randomly selected sets of eruption years) to estimate the 5% and 95% significance levels. We use two-sided tests to consider both summer cooling and winter warming that have been postulated in a number of earlier modeling and observational studies [see details in Robock, 2000].

The four approaches differ in the pre-treatment of the raw temperature series:

Method 1. non-normalised, non-detrended
Method 2. non-normalised, detrended
Method 3. normalised, non-detrended
Method 4. normalised, detrended

Method 1 uses the raw temperature anomaly data, while Method 2 detrends the temperature series by using the residuals from a 30–year Gaussian filter fit through all months in each temperature series. Detrending removes the influence of longer timescale warming (particularly) and cooling (rarely) that can occur and influence some of the ten-year periods. The disadvantage of both methods is that the significance levels have seasonal cycles, which makes visual interpretation slightly difficult. Methods 3 and 4 are complementary but use the normalised anomaly series, subtracting the mean and dividing by the standard deviation,

both of which have been calculated from the complete length of the respective time series. The significance levels for the normalised methods are the same for all months during the post-eruption period.

Figure 1 shows the four approaches for the five tropical eruption years that have occurred since 1851 (1883, 1902, 1963, 1982 and 1991). The vertical lines on all post-eruption months indicate the range (highest and lowest) of monthly temperatures observed within the sample of five eruption events. Although all four approaches are qualitatively very similar, Methods 3 and 4 produce the clearest results. In the later analyses with the longer European series, we use Method 4, which removes variations on 30–year timescales and longer. The significant result of the analysis is cooling during the two extended summer periods (April–September) following the year of the eruption. Cooling is also evident in the first summer but does not reach statistical significance. The results are in agreement with those found in earlier studies [Kelly and Sear, 1984; Sear et al., 1987; and Kelly et al., 1996], some of which could not use the El Chichón and Pinatubo eruptions but also included some higher latitude eruption events. There is a large inter-eruption variability, but for a few months (particularly during the April to September periods of years 2 and 3 following the December of the pre-eruption year) all 5 eruptions show cooling below the '5–event average' significance line. Cooling is also evident in the second and third winter following the eruptions but not statistically significant except for January and February in the third year after an eruption.

Figure 2 shows the responses for the five individual eruptions. Cooling is less marked for Agung (1963) and barely noticeable for El Chichón (1982). For this latter event the cooling is probably masked by the severe 1982/3 El Niño event. In this study, which concentrates later on the longer European records (where El Niño influences are negligible), we have not attempted to remove the El Niño/Southern Oscillation (ENSO) signal in the hemispheric surface temperature record. Removal is possible [see, e.g., Kelly et al., 1999], but partly dependent on the volcanic effects. [Santer et al., 2001] have pioneered an iterative process removing first one then the other influence and then repeating the process until convergence is reached, but this is beyond the scope of this study.

Finally in this section, we consider the three higher latitude eruptions that have occurred since 1851. We exclude Sheveluch (1854) as the NH temperature record only starts three years before the eruption. The results are illustrated in Figure 3. Here the response is different in character and cooling is only significant in the late summer (August and
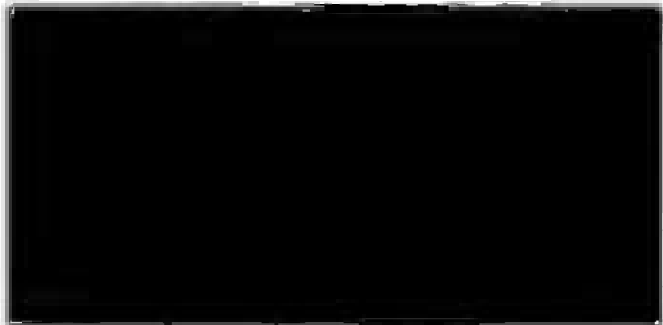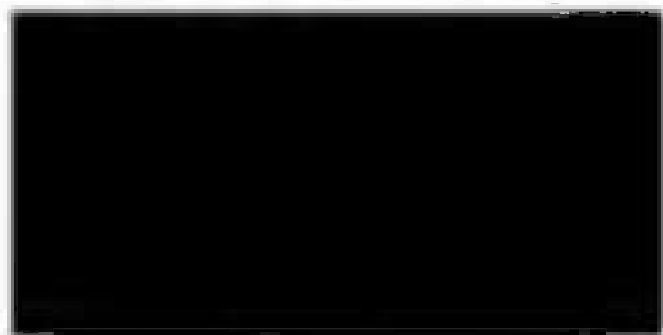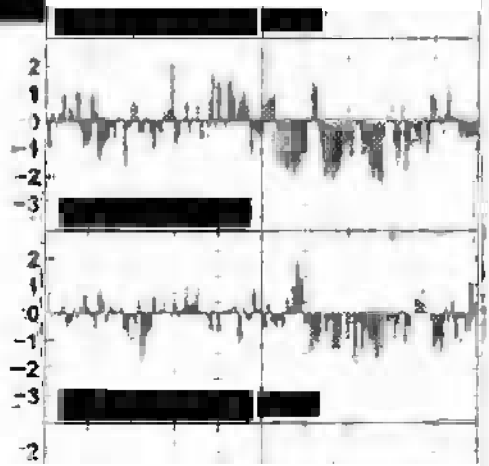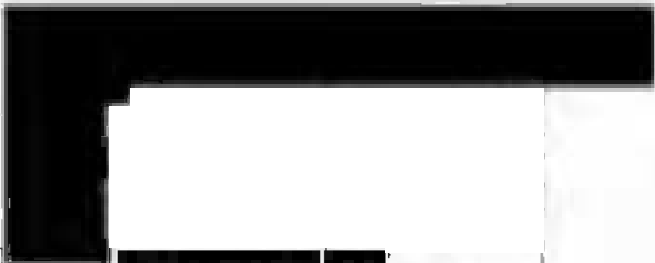
2
1
0
-1
-2
-3

7
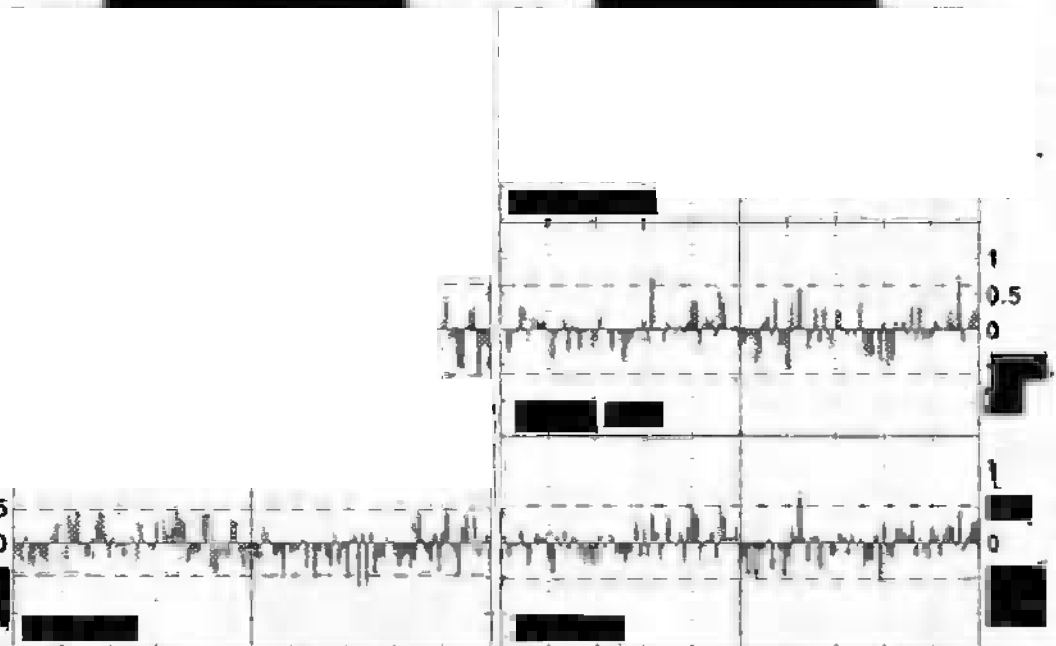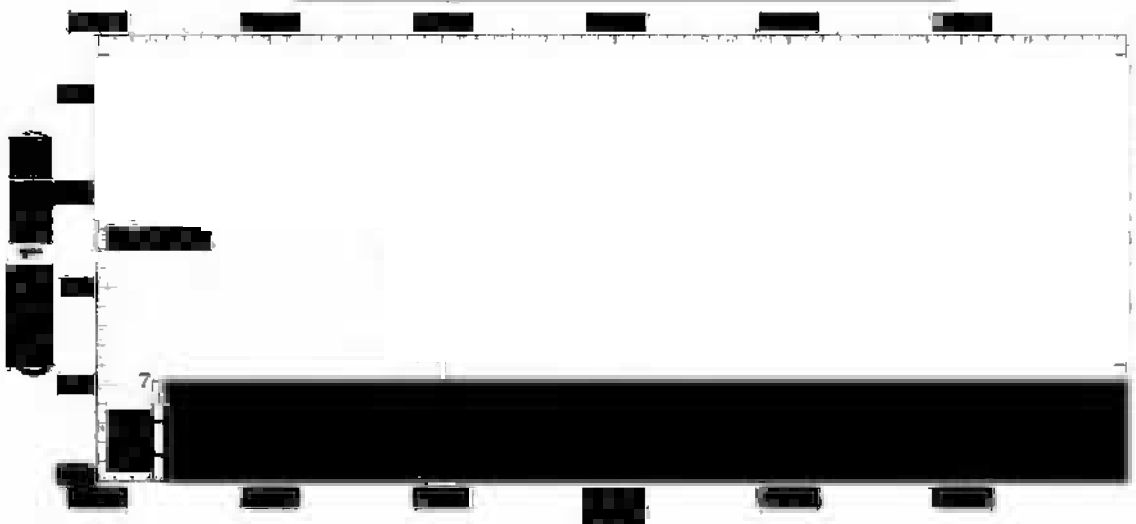
light-density years and ice cores is given by [*Jones et al.*, 1995; and *Briffa et al.*, 1998].

Plate 2 shows spatial maps of anomalous temperature (with respect to 1961–90 after calibration of the gridded density series against local gridded warm-season temperature data) for a selection of years with extremely negative hemispheric-mean tree-ring density values. We show sequences of 3 or 6 years centred on some of the key dates (1453, 1601, 1641, 1695/1698, 1740/1743, 1783 and 1816). As some of the tree-ring series do not extend back before 1700, coverage is reduced in the earliest years. The maps, therefore, also serve to illustrate the changes to the available density of coverage. Maps for all years from 1600 to 1887 are given in [*Briffa et al.*, 2002]. In the key post-eruption years light-density values (implying cold summer temperatures) are often evident over regions of northern Eurasia and eastern Canada. Large numbers of individual chronologies are involved in some of the anomalous regions, but the exact location of the centre varies from 'eruption' to 'eruption'. The maps for 1816 and 1817 possibly represents the 'classic' volcanic-cooling pattern [see the extensive discussion of this eruption by *Briffa* and *Jones*, 1992] but low temperatures were also reconstructed in northwestern Russia in 1814 and 1815. The time series in Plate 1 also clearly shows that cooling was already quite dramatic before Tambora erupted, possibly influenced by the unknown eruption of 1809.

The Laki eruption of 1783 only shows a severe impact over northwestern Russia and the northern Ural mountains. [*D'Arrigo* and *Jacoby*, 1999; and *Jacoby* and *D'Arrigo*, this volume] also document the severity of this event in central and northern Alaska, where we do not have tree-ring density data series. 1740 was the coldest year in all central European records that extend back this far (Central England, De Bilt and Berlin), yet tree-ring density reduction was modest compared to 1742. Shikotsu erupted in 1739 but the pattern of response is atypical of higher latitude eruptions. The coolest decade of the whole reconstruction (Plate 1) was the 1690s (also the coldest decade in the Central England temperature record) and possible eruptions may have caused the spikes in 1695 and 1698/9. The most extreme three-year period of the series occurred in 1641/2/3 following two major eruptions (Komagatake in Japan in 1640 and Mt Parker in the Philippines in 1641). The most extreme year of the whole record was 1601, occurring the year after the Huaynaputina eruption of 1600 which is exactly dated from historical and ice core evidence. The most severe cooling in 1601 occurred over northwestern USA and southwestern Canada, a region that doesn't appear to respond to later eruptions except for 1641. The earliest

event that can be related to a volcano was 1453, with a classic pattern like 1816. There is ice core evidence and a tentative link to the Kuwae eruption in the southwestern Pacific, which is speculated to have occurred about this time. More discussion of the extreme negative years in Plate 1 and their possible links to explosive volcanic eruptions is given in [*Briffa et al.*, 1998].

6. DISCUSSION AND CONCLUSIONS

Many volcanic eruptions over the last 600 years have been shown to have had severe climatic impacts leading to cooler summers as evidenced by instrumental temperature records and light-density tree-ring indices. Defining typical cooling amounts or characteristic patterns is difficult, however, because of the relatively few events that have occurred (about 20 major events in 600 years). Many smaller events have occurred but their impacts are impossible to determine given the levels of climatic variability that occur naturally due to a number of other factors (both internal and external to the climatic system). Just because an effect is difficult to isolate, however, does not mean it can be ignored. It is likely that volcanic eruptions contribute a major component to the negative skew evident in many temperature time series and when events tend to cluster they may cause some of the decadal-scale variability seen over the last 600 years [see, e.g., *Crowley*, 2000; *Crowley*, this volume; and *Hegerl*, this volume].

The clearest and most significant effects are seen in the land-based NH temperature average, with cooler extended summers (April–September) evident in the second and third summer following the eruption year for tropical eruptions. High latitude eruptions have a more immediate impact influencing just the late summer of the eruption year. The sample of higher latitude eruptions is small and all have occurred around the spring season. Whether the dust/aerosols would overwinter in higher latitudes from an Alaskan/Kamchatkan eruption occurring in the autumn is impossible to determine from observational evidence.

Analysis of the longer European instrumental records increases the sample of eruptions but signals are harder to isolate in the more temporally variable regional series. Also, the lack of eruptions during much of the 18th century does not allow the full extent of the longest European records to be fully utilised. The well-known dearth of explosive volcanic eruptions between 1915 and 1960 does not seem that unique in the longer eruption lists of [*Simkin* and *Siebert*, 1994], when the 18th century is considered. Of the three European regions studied, Fennoscandia shows the clearest effects after tropical eruptions, with significant summer

cooling and noticable but non-significant winter warming, results that are qualitatively in agreement with a suggestive volcanic-inducement of the NAO to more positive values. The circulation link is tenuous and has only come to be 'accepted' because of supporting evidence obtained through modeling efforts. Effects of tropical eruptions over Central England and Central Europe are highly speculative and clearly do not stand up to any degree of statistical rigor. The higher latitude eruptions produce a response in these European regions that is similar to the NH: a more rapid but less consistent signal than for the tropical set. This is likely due to the smaller eruption sample, though the addition of the eruptions in 1739, 1783 and 1800 does little to clarify the effect.

The most important conclusion from the instrumental analyses (both for the NH and Europe) is that any volcanic influence on surface temperature is highly seasonal in character, a fact that must be borne in mind when considering volcanic forcing in all climatic modeling studies. Determining the importance of volcanic forcing requires a realistic seasonal cycle within an Energy Balance Climate Model (EBM).

Longer tree-ring density records reveal about 15 additional cooling events since 1400, which are probably related to major explosive tropical eruptions. Most are evident as dust/sulphate peaks in ice cores from Greenland and the Antarctic, but only some can be specifically related to dated volcanic eruptions. The remainder are highly suggestive of a volcanic cause but the determination of the specific eruption is elusive.

REFERENCES

Böhm, R., I. Auer, M. Brunetti, M. Maugeri, T. Nanni and W. Schöner, Regional temperature variability in the European Alps: 1760-1998 from homogenized instrumental time series, *Int. J. Climatol.,* 21, 1779-1801, 2001.

Bradley, R.S., The explosive volcanic eruptions signal in Northern Hemisphere continental temperature records, *Clim. Change,* 12, 221-243, 1988.

Bradley, R.S. and P.D. Jones, Records of explosive volcanic eruptions over the last 500 years, *in Climate Since A.D. 1500,* edited

by R.S. Bradley and P.D. Jones, pp.606-622, Routledge, London, 1992.

Briffa, K.R. and P.D. Jones, The climate of Europe during the 1810s with special reference to 1816, *in The Year Without a Summer? World Climate in 1816,* edited by C.R. Harrington, pp.372-391, Can. Mus. of Nature, Ottawa, Ont., Canada, 1992.

Briffa, K.R., P.D. Jones, F.H. Schweingruber and T.J. Osborn, Influence of volcanic eruptions on Northern Hemisphere summer temperature, *Nature,* 393, 450-455, 1998.

Briffa, K.R., T.J. Osborn, F.H. Schweingruber, I.C. Harris, P.D. Jones, S.G. Shiyatov and E.A. Vaganov, Low-frequency temperature variations from a northern tree-ring density network, *J. Geophys. Res.,* 106, 2929-2941, 2001.

Briffa, K.R., T.J. Osborn, F.H. Schweingruber, P.D. Jones, S.G. Shiyatov and E.A. Vaganov, Tree-ring width and density data around the Northern Hemisphere: Part 2, spatio-temporal variability and associated climate patterns. *Holocene,* 12, 759-789, 2002.

Camuffo, D. and P.D. Jones, Improved understanding of past climatic variability from early daily European instrumental sources, *Clim. Change,* 53, 1-392, 2002.

Cook, E.R. and K.R. Briffa, A comparison of some tree-ring standardization methods, *in Methods of Dendrochronology: Applications in the Environmental Sciences,* edited by E.R. Cook and L.A. Kairiukstis, pp.153-162, Kluwer Acad., Norwell, Mass, 1990.

Cook, E.R., K.R. Briffa, D.M. Meko, D.A. Graybill and G. Funkhouser, The 'segment-length' curse in long tree-ring chronology development for palaeoclimatic studies, *Int. J. Climatol.,* 14, 379-402, 1995.

Crowley, T.J., Causes of climate change over the past 1000 years, *Science,* 289, 270-277, 2000.

Crowley, T.J., this volume.

D'Arrigo, R.D. and G.C. Jacoby, Northern North American tree-ring evidence for regional temperature changes after major volcanic events, *Clim. Change,* 41, 1-15, 1999.

Graf, H.-F., J. Perlwitz, I. Kirchner and I. Schult, On the interrelationship between recent climate trends, ozone change and increased greenhouse gas forcing, *in Atmospheric Ozone as a Climate Gas,* edited by W.C. Wang and I.S.A. Isaksen, pp.163-179, Springer-Verlag, New York, 1995.

Groisman, P.Ya., Regional climate consequences of volcanic eruptions (in Russian), *Meteorol. Hydrol.,* No. 4, 39-45, 1985.

Groisman, P.Ya., Possible climate consequences of the Pinatubo eruption: An empirical approach, *Geophys. Res. Letts.,* 19, 1603-1606, 1992.

Hansen, J., R. Ruedy, J. Glascoe and M. Sato, GISS analysis of surface temperature change, *J. Geophys. Res.,* 104, 30, 997-31,022, 1999.

Hansen, J., R. Ruedy, M. Sato, M. Imhoff, W. Lawrence, D. Easterling, T. Peterson and T. Karl, A closer look at United States and global surface temperature change, *J. Geophys. Res.,* 106, 23,947-23,963, 2001.

Hegerl, G.C., this volume.

Hurrell, J.W., Decadal trends in the North Atlantic Oscillation: Regional temperatures and precipitation, *Science*, 269, 676-679, 1995.

Jacoby, G.C. and R.D. D'Arrigo, The Laki eruption and observed dendroclimatic effects of volcanism, this volume.

Jones, P.D. and A. Moberg, Hemispheric and large-scale surface air temperature variations: An extensive revision and an update to 2001, *J. Climate*, 16, 206-223, 2003.

Jones, P.D., K.R. Briffa and F.H. Schweingruber, Tree-ring evidence of the widespread effects of volcanic explosive eruptions, *Geophys. Res. Letts.*, 22, 1333-1336, 1995.

Jones, P.D., T. Jónsson and D. Wheeler, Extension to the North Atlantic Oscillation using early instrumental pressure observations from Gibraltar and SW Iceland, *Int. J. Climatol.*, 17, 1433-1450, 1997.

Jones, P.D., M. New, D.E. Parker, S. Martin and I.G. Rigor, Surface air temperature and its changes over the past 150 years, *Rev. Geophys.*, 37, 173-199, 1999.

Jones, P.D., T.J. Osborn, K.R. Briffa, C.K. Folland, E.B. Horton, L.V. Alexander, D.E. Parker and N.A. Rayner, Adjusting for sampling density in grid box land and ocean surface temperature time series, *J. Geophys. Res.*, 106, 3371-3380, 2001.

Kelly, P.M. and C.B. Sear, Climatic impact of explosive volcanic eruptions, *Nature*, 311, 740-743, 1984.

Kelly, P.M., P.D. Jones and J. Pengqun, The spatial response of the climate system to explosive volcanic eruptions, *Int. J. Climatol.*, 16, 537-550, 1996.

Kelly, P.M., P.D. Jones and J. Pengqun, Spatial patterns of variability in the global surface temperature data set, *J. Geophys. Res.*, 104, 24,237-24,256, 1999.

Kodera, K., Influence of volcanic eruptions on the troposphere through stratospheric dynamical processes in the Northern Hemisphere winter, *J. Geophys. Res.*, 99, 1273-1282, 1994.

Kodera, K., M. Chiba, H. Koide, A. Kitoh and Y. Nikaidou, Interannual variability of the winter stratosphere and troposphere in the Northern Hemisphere, *J. Meteorol. Soc. Jpn.*, 74, 365-382, 1996.

LaMarche, V.C., Jr. and K.K. Hirschboeck, Frost rings in trees as records of major volcanic eruptions, *Nature*, 307, 121-126, 1984.

Lamb, H.H., Volcanic dust in the atmosphere, with a chronology and assessment of its meteorological significance, *Phil. Trans. R. Soc. London, Ser. A*, 266, 425-533, 1970.

LeGrand, M. and R.J. Delmas, A 220-year continuous record of volcanic H2SO4 in the Antarctic Ice Sheet, *Nature*, 327, 671-676, 1987.

Lough, J.M. and H.C. Fritts, An assessment of the possible effects of volcanic eruptions on North American climate using tree-ring data, 1602 to 1900 A.D., *Clim. Change*, 10, 219-239, 1987.

Manley, G., Central England Temperatures: monthly means 1659 to 1973, *Quart. J. Roy. Met. Soc.*, 100, 389-405, 1974.

Mosley-Thompson, E., this volume.

Osborn, T.J., K.R. Briffa, S.F.B. Tett, P.D. Jones and R.M. Trigo, The North Atlantic Oscillation as simulated by a climate model, *Climate Dynamics*, 15, 685-702, 1999.

Parker, D.E., T.P. Legg and C.K. Folland, A new daily Central England temperature series, 1772-1991, *Int. J. Climatol.*, 12, 317-342, 1992.

Perlwitz, J. and H.-F. Graf, The statistical connection between tropospheric and stratospheric circulation of the Northern Hemisphere in winter, *J. Clim.*, 8, 2281-2295, 1995.

Peterson, T.C., T.R. Karl, P.F. Jamason, R. Knight and D.R. Easterling, The first difference method: Maximising station density for the calculation of long-term temperature change, *J. Geophys. Res.*, 103, 25,967-25,974, 1998.

Rasmusson, E.M. and T.H. Carpenter, Variations in tropical sea surface temperature and surface wind fields associated with the Southern Oscillation/El Niño, *Mon. Wea. Rev.*, 110, 354-384, 1982.

Robock, A., Volcanic eruptions and climate, *Rev. Geophys.*, 38, 191-219, 2000.

Robock, A. and J. Mao, Winter warming from large volcanic eruptions, *Geophys. Res. Letts.*, 19, 2405-2408, 1992.

Santer, B.D., T.M.L. Wigley, C. Doutriaux, J.S. Boyle, J.E. Hansen, P.D. Jones, G.A. Meehl, E. Roeckner, S. Sengupta and K.E. Taylor, Accounting for the effects of volcanoes and ENSO in comparisons of modeled and observed temperature trends, *J. Geophys. Res.*, 106, 28, 033-28, 059, 2001.

Sear, C.B., P.M. Kelly, P.D. Jones and C.M. Goodess, Global surface temperature responses to major volcanic eruptions, *Nature*, 330, 365-367, 1987.

Schweingruber, F.H. and K.R. Briffa, Tree-ring density networks for climate reconstruction, in *Climatic Variations and Forcing Mechanisms of the Last 2000 Years*, edited by P.D. Jones, R.S. Bradley and J. Jouzel, pp.43–66, Springer-Verlag, New York, 1996.

Simkin, T. and L. Siebert, *Volcanoes of the World*, 2cnd ed., 349pp., *Geoscience Press*, Tucson, Ariz., 1994.

Tuomenvirta, H., A. Drebs, E. Førland, O.E. Tveito, H. Alexandersson, E. Vaarby Laursen and T. Jónsson, Nordklim Data Set 1.0—Description and illustrations, *KLIMA Report 08/01*, 26pp, Norwegian Meteorol. Institute, Oslo, Norway, 2001.

Zielinski, G.A., Stratospheric loading and optical depth estimates of explosive volcanism over the last 2100 years derived from the Greenland Ice Sheet Project 2, *J. Geophys. Res.*, 100, 20,937-20,955, 1995.

P. D. Jones, A. Moberg, T. J. Osborn and K. R. Briffa, Climatic Research Unit, School of Environmental Sciences, University of East Anglia, Norwich NR4 7TJ, U.K. (p.jones@uea.ac.uk)

Dendroclimatological Evidence for Major Volcanic Events of the Past Two Millennia

Rosanne D'Arrigo and Gordon Jacoby

Tree-Ring Laboratory, Lamont-Doherty Earth Observatory, New York

David Frank

WSL, Birmensdorf, Switzerland

Several tree ring studies have documented the spatial patterns of climatic effects following major volcanic episodes. Frost rings, micro- or narrow rings and light density latewood rings have all been used to identify severe cold periods of several years or more which are likely associated with volcanism. In northern North America, spatial variations in tree growth were found to reflect cooling influenced by atmospheric circulation patterns induced by volcanic events around AD 1640, 1783, 1815 and other years. Further back in time, historical accounts, augmented by tree ring and ice core evidence from western Europe and North America, suggest that three of the largest eruptions in the last two millennia occurred around AD 536, 934 and 1258. These events are believed to have had profound climatic and demographic repercussions over much of the globe. New tree ring chronologies from Mongolia and northern Siberia demonstrate that the climatic impact of these eruptions also extended into these remote regions.

INTRODUCTION

Instrumental records have only a limited amount of data available for evaluation of climate and circulation changes following volcanism. To supplement this information, tree rings and other proxies can be used to document climate response to major volcanic episodes in past centuries to millennia. For example, Lough and Fritts (1987) described regional variations in tree ring width data over North America, inferring spring and summer cooling in the central United States and summer warming in the western coastal United States following volcanic events. Jones et al. (1995) composited maximum latewood density tree ring records

from the North American and European continents and found a strong association between volcanic events and years of extremely negative density values.

In addition to such ring width or density changes, frost rings can signify severely cold conditions related to volcanic and other extreme cold events (*LaMarche and Hirschboeck*, 1984). Frost rings are annual growth increments that have cellular irregularities caused by freeze damage during the growing season. Cold air outbreaks or surges can cause frost rings to form, even without association with volcanic episodes. Other severe climatic or environmental events, in addition to volcanism, can also result in such tree ring anomalies.

Although climatic effects of volcanism can be more immediate, there may be a delay in manifestation of these effects by several years depending on the nature of a given volcanic eruption (e.g. *Robock and Mao*, 1995). There may also be a biological lag response in tree growth, particular-

Greenland), respectively. Additional ice core records (e.g. from Antarctica) may prove useful in resolving these ambiguities (*C. Hammer*, pers. comm.).

AD 536 was a very narrow ring in an Irish oak series; but some of the narrowest rings in this record actually occurred in AD 540–541. AD 536 was the second coldest summer in 1500 years based on a Fennoscandian tree ring record (*Briffa et al.*, 1992), and there was reduced growth from about AD 536–45 or even later in this and other European chronologies (*Baillie*, 1999). A tree-ring record from western North America shows AD 535, 536 and 541 as the second, third and fourth coldest of the past two millennia (*Scuderi*, 1990; *Scuderi*, 1993). Below average growth was found in bristlecone pine series from the western USA (*Baillie*, 1994; *Baillie*, 1999), although no frost rings were noted in the middle 500s (*LaMarche and Hirshboeck*, 1984). There is also decreased growth in a multimillennial tree ring record from Chile (*Lara and Villalba*, 1993), suggesting that this event may have also influenced conditions in the Southern Hemisphere. Several of these records show a two-stage decline separated by partial recovery in AD 537–538.

At Sol Dav, three relict wood samples cover the period around AD 536. Frost damage is observed in the latewood of this year (Figure 3) in two samples and there is light density latewood in the third. In the Sol Dav ring-width chronology, the AD 536 index value is only 0.645, relative to the long-term mean of 1.0. Standard deviation (SD) is 0.204 over the full length of record. This low growth value signals the onset of an unusually cold decade (AD 536–545) in which the mean ring width index is 0.670 (SD 0.240), with a minimum of 0.357 in AD 543. The year AD 538 shows a brief recovery with an index value of 1.223. Conditions do not return to normal values (1.0 or higher) until AD 564. As noted, this two-stage pattern is also observed in the European oak and other tree ring series and may signify a delayed climatic response to one event (as is typical for many volcanic eruptions—e.g. *Stothers*, 2000) or two separate events (*Baillie*, 1994; *Baillie*, 1999).

Our findings for Mongolia are consistent with the observations documented for northern China (i.e. frosts, and ensuing famine and deaths) in the summers of AD 536–7 (*Pang and Chou*, 1985). Additional evidence for a Eurasian response to this event comes from a cross section of wood from the Taymir Peninsula, Siberia (*Jacoby et al.*, 2000). This wood section has several hundred rings covering the middle 500s, and was dated through comparison with another Taymir tree ring series (*Naurzbaev and Vaganov*, 2000; *Briffa*, 2000). As for Mongolia, there is an abrupt growth decrease (and light density latewood) in AD 536 followed by brief recovery and subsequent decline.

The evidence for cooling in Mongolia in the middle AD 500s is consistent with the other tree ring data from the areas noted above, and with the historical observations of extreme cold, crop failure, plague and famine (*Stothers*, 1999; *Baillie*, 1999). Our results from Mongolia and Taymir indicate that the spatial impact of this episode extended further eastward into Eurasia than previously documented.

AD 934: ELDGJA, ICELAND

The massive Eldgja, Iceland volcanic event is considered one of the largest fissure eruptions of the last eleven centuries (*Stothers*, 1988). Descriptions of dry fog, famine, disease and plague from the Middle East, Iceland, and Europe were used to suggest AD 934 as the most probable date. Cold winters were chronicled in AD 934–5 and again in AD 939–40 in central Europe and the Middle East, with an intervening period of less cold conditions. Due to its long-lived stratospheric dust veil, it is estimated that Eldgja may have had impacts up to 5 to 8 years after its eruption, longer than many other events (*Zielinski et al.*, 1995; *Stothers*, 1998). Estimates from Greenland ice core acidity measurements vary, with dates given of AD 934+/–2 from the Crete ice core (*Hammer*, 1980; *Hammer*, 1984), AD 934+/–3 from Dye 3 (*Johnsen et al.*, 1992) and AD 938+/–4 from GISP2 (*Zielinski et al.*, 1995).

Tree-ring data from northern Europe and western North America did not show unusual features linked with this episode (*LaMarche and Hirschboeck*, 1984; *Scuderi*, 1990; *Zielinski et al.*, 1995). This lack of consistent findings suggests that there may not have been a major large-scale cooling following this eruption (*Zielinski et al.*, 1995), although the more recent compilation of historical accounts (*Stothers*, 1998) seems to indicate otherwise.

Stothers (1998) speculated that Eldgja's sulfuric acid aerosols almost certainly spread much farther east than northern Europe. Our tree ring samples from Taymir, Siberia (*Jacoby et al.*, 2000) do not date through this middle 900s interval. The Taymir chronology of Naurzbaev and Vaganov (2000), which does include this period (and see *Briffa*, 2000), shows decreased growth in AD 933–5 and again in 940. At Sol Dav, there are frost rings in the earlywood of AD 938 in 4/6 of the samples dating through this period. However, ring widths are only slightly below average in 935 (0.969) and in 944–51 (mean 0.853). The prevalence of these frost rings is consistent with the estimates for the timing and subsequent cooling for the Eldgja eruption. However, they could simply indicate a localized outbreak of extreme cold not linked to the Eldgja event.

AD 1258: UNKNOWN ERUPTION

Historical records from Europe and the Middle East indicate severe cold, dry fog, crop damage and pestilence in 1258–59, and a very cold winter in 1260–1261 (*Stothers*, 2000). A massive tropical volcanic event may have accounted for these conditions. Ice cores show high sulfates in both Greenland and Antarctica in or about 1259 (e.g. *Zielinski*, 1995; *Clausen et al.*, 1997). Yet the increase in sulfates actually started in 1258 (*Hammer et al.*, 1980), suggesting that this was the year that stratospheric injection began. Historical accounts note that Europe was very cold from about February–June, 1258, with one day of unusual frost reported in Russia in April 1259.

North temperate tree ring records (from Fennoscandia, Quebec and the western USA) did not show unusual cold in the late AD 1250s or early 1260s (*Zielinski*, 1995; *Stothers*, 2000), although there is decreased growth in a Sierra Nevada series in 1257 (*Scuderi*, 1990). There are no frost rings for this event in the LaMarche and Hirschboeck (1984) series.

In the Mongolia record there are 5 frost rings (out of 11 samples dating through this period): 3 in the latewood of AD 1258 and 2 in the earlywood of 1259. The Sol Dav ring width index is average in 1258 but declines in 1261, with below average growth persisting through 1268, and a growth minimum in 1262 (0.475). The frost ring evidence supports the contention that this eruption began prior to late summer in 1258. This is not inconsistent with Stothers (2000), who proposes January of 1258 as the eruption's initiation date.

Our Taymir record (*Jacoby et al.*, 2000) does not show frost rings but has decreased growth in 1258–9 (0.744 and 0.345) and 1263–4 (mean 0.556). The negative growth departures at Taymir and Sol Dav agree with the historical reports of cold for northern Europe and Russia (*Stothers*, 2000), and suggest that the greatest impact for this episode may have taken place in Eurasia.

OTHER VOLCANIC ERUPTIONS OF THE PAST TWO MILLENNIA

We have also examined the tree growth variations in Mongolia and Taymir for unusual effects following three of the other most significant eruptions of the past two millennia: in AD 626 (unknown), 1783 (Laki, Iceland) and 1815 (Tambora, Indonesia) (*Stothers*, 1999). The latter two, as mentioned above, showed pronounced cooling over regions of northern North America and elsewhere.

We do not find unusual conditions at Sol Dav around the time of the postulated AD 626 eruption (*Stothers and*

Rampino, 1983; *Stothers*, 1999). A frost ring was observed by LaMarche and Hirschboeck (1984) in AD 628 which may relate to this event. The climatic effects of Laki have been described in tree ring records for Alaska (*D'Arrigo et al.*, 1999; *Jacoby et al.*, 1999), Norway (*Jones et al.*, 1995) and other areas. Demaree *et al.* (1998) mentioned that evidence for unusual conditions east of the Altai Mountains was limited to only a few accounts for China, possibly suggesting that Laki's impact was diluted in this general area. At Sol Dav, tree growth is not especially low in 1783. However, 2/16 tree samples at this site show frost damage. For the 1815 Tambora eruption, there is below average growth in 1816 (index value 0.698); there is an even lower value in 1818 (0.567).

There is no evidence of unusual growth or frost damage at Taymir linked to either the AD 626 or 1815 eruptions. However, there is decreased growth (without frost damage) in Taymir in 1783, with an index value of 0.455. There were near normal conditions in 1784–5 and a very low index value of 0.257 in 1786, indicating a delayed climate signal in northern Siberia.

SUMMARY

We have described response to cooling and circulation changes following volcanism in temperature-sensitive tree ring records from northern latitudes. A tree ring data network from northern North America extending over the past several centuries shows pronounced cooling in 1641 in the Northwest Territories, in 1783 in Alaska and in 1816 in eastern Canada. Longer records from Eurasia (Mongolia and Taymir) reveal information regarding the spatial extent of cooling conditions following three other major events (in AD 536, 934 and 1258) further back in time. The response seen in these records includes decreased ring widths, light latewood density and frost damage.

REFERENCES

Baillie, M., Dendrochronology Raises Questions About the Nature of the AD 536 Dust-Veil Event, *The Holocene*, 4, 212- 217, 1994.

Baillie, M., *Exodus to Arthur. Catastrophic Encounters with Comets*, B. T. Batsford Ltd., London, 1999.

Briffa, K., Annual Climate Variability in the Holocene: Interpreting the Message of Ancient Trees, *Quat. Sci. Rev.*, 19, 87-105, 2000.

Briffa, K., Jones, P., Bartholin, T., Eckstein, D., Schweingruber, F., Karlen, W., Zetterberg, P. and Eronen, M., Fennoscandian Summers from AD 500: Temperature Changes on Short and Long Time Scales, *Clim. Dyn.,* 7, 111-119, 1992.

Clausen, H., Hammer, C., Hvidberg, C., Dahl-Jensen, D. and Steffensen, J., A Comparison of the Volcanic Records over the past 4000 Years from the Greenland Ice Core Project and Dye 3 Greenland Ice Cores, *J. Geophys. Res.*, 102, 26707-26723, 1997.

D'Arrigo, R., Jacoby, G., Frank, D., Pederson, N., Buckley,B., Baatarbileg, N., Mijiddorj, R. and Dugarjav, C., Mongolian tree rings, Temperature Sensitivity and Reconstructions of Northern Hemisphere Temperature, *The Holocene*, 10, 669-672, 2000.

D'Arrigo, R., Frank, D., Jacoby, G. and Pederson, N., Spatial Response to Major Volcanic Events on or about AD 536, 934 and 1258: Frost Rings and other Dendrochronological Evidence from Mongolia, *Clim. Change*, 49, 239-46, 2001a.

D'Arrigo, R., Jacoby, G., Frank, D., Pederson, N., Cook, E., Buckley, B., Baatarbileg, N., Mijiddorj, R. and Dugarjav, C., 1738 Years of Mongolian Temperature Variability Inferred from a tree ring Record of Siberian Pine, *Geophys. Res. Lett.*, 28, 543-546, 2001b.

D'Arrigo, R. and Jacoby, G., Northern North American tree ring Evidence for Regional Temperature Changes After Major Volcanic Events, *Clim. Change* 41, 1-15, 1999.

Delfin F., Newhall, C., Martinez, M., Salonga, N., Bayon, F., Trimble, D. and Solidum, R., Geological, C14 and Historical Evidence for a 17th Century Eruption of Parker Volcano, Mindanao, Philippines, *J. Geol. Soc. of Phillippines*, 52, 25-42, 1997.

Demaree, G., Ogilvie, A. and Zhang, D., Further Documentary Evidence of Northern Hemispheric Coverage of the Great Dry Fog of 1783, *Clim. Change* 39, 727-730, 1998.

Fritts, H., *Tree-Rings and Climate*, Academic Press, London, 1976.

Graf, H.-F., Kirschner, I., Robock, A. and Schult, I., Pinatubo Eruption Winter Climate Effects: Model Versus Observations, *Clim. Dyn.*, 9, 81-93, 1993.

Hammer, C., Traces of Icelandic Eruptions in the Greenland Ice Sheet, *Jokull,* 34, 51-65, 1984.

Hammer, C., Clausen, H. and Langway, C., Greenland Ice Sheet Evidence of Post-Glacial Volcanism and its Climatic Impact, *Nature*, 288, 230-235, 1980.

Jacoby, G., and D'Arrigo, R., Reconstructed Northern Hemisphere Annual Temperature Since 1671 Based on High Latitude tree ring Data from North America, *Clim. Change*, 14, 39-59, 1989.

Jacoby, G., and D'Arrigo, R., The Laki Eruption and Observed Dendroclimatic Effects of Volcanism (*this volume*).

Jacoby, G., D'Arrigo, R. and Davaajamts, Ts., Mongolian tree rings and 20th Century Warming, *Science,* 273, 771-773, 1996.

Jacoby, G., Workman, K. and D'Arrigo, R., 1783 Laki Eruption, Tree Rings and Catastrophe for Northwestern Inuit, *Quat.Sci. Rev.*, 18, 1365-1371, 1999.

Jacoby, G., Lovelius, N., Shumilov, O., Raspopov, O., Kurbainov, J. and Frank, D., Long-Term Temperature Trends and Tree Growth in the Taymir Region of Northern Siberia, *Quat. Res.* 53, 312-318, 2000.

Johnsen, S., Clausen, H., Dansgaard, W., Fuhrer, K., Gundestrup, N., Hammer, C., Iversen, P., Jouzel, J., Stauffer, B. and Steffensen, J., Irregular Glacial Interstadials Recorded in a New Greenland Ice Core, *Nature*, 359, 311-313, 1992.

Jones, P., Briffa, K. and Schweingruber, F., tree ring Evidence of the Widespread Effects of Explosive Volcanic Eruptions, *Geophys. Res. Lett.*, 22, 1333-1336, 1995.

Jones, P., Briffa, K., Barnett, T. and Tett, S., High-Resolution Palaeoclimatic Records for the Last Millennium: Interpretation, Integration and Comparison with General Circulation Model Control-Run Temperatures, *The Holocene*, 8, 455-471, 1998.

Keys, D., *Catastrophe*, Ballantine Books, NY, 1999.

LaMarche, V.C. Jr. and Hirschboeck, K., Frost Rings in Trees as Records of Major Volcanic Eruptions, *Nature*, 307, 121-126, 1984.

Lara, A. and Villalba, R., A 3620-year Temperature Record from Fitzroya cupressoides tree rings in Southern South America, *Science*, 260, 1104-1106, 1993.

Lough, J. and Fritts, H., An Assessment of the Possible Effects of Volcanic Eruptions on North American Climate Using tree ring Data, 1602-1900 AD., *Clim. Change*, 10, 219-239, 1987.

Mann, M., Bradley, R. and Hughes, M., Northern Hemisphere Temperatures During the Past Millennium: Inferences, Uncertainties, and Limitations, *Geophys. Res. Lett.,* 26, 759-762, 1999.

Naurzbaev, M. and Vaganov, E., Variations of Early Summer and Annual Temperature in the East of Taymir and Putoran (Siberia) over the last Two Millennia Inferred from tree rings, *J. Geophys. Res.*, 105, 7317-7326, 2000.

Pang, K. and Chou, H.-H., As cited in S. Weisbard, Excavating Words: A Geological Tool, *Science News*, 127, 91-94, 1985.

Robock, A. and Mao, J., Winter Warming from Large Volcanic Eruptions, *Geophys. Res. Lett.*, 12, 2405-2408, 1992.

Robock, A. and Mao, J., The Volcanic Signal in Surface Temperature Observations, *J. Climate*, 8, 1086-1103, 1995.

Scuderi, L., tree ring Evidence for Climatically-Sensitive Volcanic Eruptions, *Quat. Res.*, 34, 67-85, 1990.

Scuderi, L., A 2,000-Year tree ring Record of Annual Temperatures in the Sierra Nevada Mountains, *Science,* 259, 1433-1436, 1993.

Simkin, T. and Siebert, L., *Volcanoes of the World* (2nd ed.), Geoscience Press, Tucson, 1994.

Stothers, R., Mystery Cloud of AD 536, *Nature*, 307, 344-345, 1984.

Stothers, R., Far Reach of the Tenth Century Eldgja Eruption, Iceland, *Clim. Change* 39, 715-726, 1998.

Stothers, R., Volcanic Dry Fogs, Climate Cooling, and Plague Pandemics in Europe and the Middle East, *Clim. Change*, 42, 713-723, 1999.

Stothers, R., Climatic and Demographic Consequences of the Massive Volcanic Eruption of 1258, *Clim. Change* 45, 361-374, 2000.

Stothers, R. and Rampino, M., Volcanic Eruptions in the Mediterranean Before AD 630 from Written and Archaeological Sources, *J. Geophys.Res.*, 88, 6357-6371, 1983.

Trenberth, K., Northern Hemisphere Climate Change: Physical Processes and Observational Changes, In *Earth System Responses to Global Change. Part II: Climate Controls*, pp. 35-59, Academy Press, NY 1993.

Zielinski, G., Stratospheric Loading and Optical Depth Estimates of Explosive Volcanism over the last 2100 Years Derived from the Greenland Ice Sheet Project 2 Ice Core, *J. Geophys. Res.*, 100, 20937-20955, 1995.

Zielinski, G., Germani, M., Larsen, G., Baillie, M., Whitlow, S., Twickler, M. and Taylor, K., Evidence of the Eldgja (Iceland) Eruption in the GISP2 Greenland Ice Core: Relationship to Eruption Processes and Climatic Conditions in the Tenth Century, *The Holocene* 5, 129-140, 1995.

Rosanne D'Arrigo, tree ring Laboratory, Lamont-Doherty, Earth Observatory, 61 Route 9W, Palisades, NY 10964

David Frank, WSL, Swiss Federal Research Institute, Zuercherstrasse 111, CH-8903 Birmensdorf, Switzerland

Gordon Jacoby, tree ring Laboratory, Lamont-Doherty Earth Observatory, 61 Route 9W, Palisades, NY 10964

The Laki Eruption and Observed Dendroclimatic Effects of Volcanism

Gordon Jacoby and Rosanne D'Arrigo

Lamont-Doherty Earth Observatory, Palisades, New York

The year of the Laki eruption, 1783, is the most visibly obvious anomaly in the northwestern Alaska tree-ring record for over 400 years or more. Thicker-walled, latewood cells formed late in the growing season are virtually absent. Quantitatively the latewood density is over 4 standard deviations below the mean latewood density of white spruce (*Picea glauca*) trees from northwest Alaska; indication of extreme cold during the summer season in this region. The tree-ring response to the event weakens toward the east, indicating that extreme cold did not extend much beyond the Mackenzie River in western Canada or very far south of the Alaska Range in central Alaska. To understand the tree-ring effects due to the Laki eruption, it is helpful to also consider three other similar events in 1641, 1816–17, and 1836. In each case there is evidence of extreme cold causing very low density latewood in the rings of white spruce near the latitudinal treeline. The effects in the tree-ring record are spatially variable. Evidence of extreme cold typically extends for about 60°–70° of longitude; 1641 in north western-and-central Canada, 1783 in Alaska, 1816–17 in eastern Canada, and 1836 in north-central Canada. One interpretation of this spatial and temporal pattern is that in addition to general cooling, the thermal effects of volcanic events can lead to outbreaks of extremely cold polar air on a regional basis. This interpretation is compatible with air mass trajectories driven by Rossby wave circulation. Such extreme regional cooling can have great impact on human conditions.

INTRODUCTION

The volcanic influence on climate has been long recognized (e. g. *Franklin*, 1784; *Lamb*, 1970; 1977) although the actual mechanism was not understood until recent decades (*Sigurdsson* and *Laj*, 1992). The general concept of cooling is valid but the structure and spatial distribution of cooling and complementary warming (*Robock* and *Mao*, 1995; 1992) is complex. Understanding of the overall climate system will be aided by examining the spatial variation and cooling/warming response to individual volcanic events. One should not try to understand the climatic effects of the Laki eruption as an isolated or unique event. This event was only one of several volcanic events that had similar effects on climate. For example, there is tree-ring evidence of at least four severely cold summers over the past 500 years in tree-ring samples from the northern boreal forests of North America. In each case there was regional extreme cold and other regions with little evidence of unusual temperature change (*Jacoby* and *D'Arrigo*, 1992; *D'Arrigo* and *Jacoby*, 1999). The impacted regions change with each event but have similar areal and longitudinal extent. This paper will examine 4 events with most attention on the Laki-Grimsvotn eruption of 1783, termed locally the *Lakagigar* (Laki fissures) event (*Demaree* et al., 1998). This study pri-

marily focuses on northern treeline density data but some comparisons are made with more southerly region trees and other information.

Many of the studies showing cooling in recorded temperatures corresponding with major volcanic events used temperatures averaged over hemispheric areas (e. g. Mitchell, 1971; Schneider and Mass, 1975). Other studies examine the hemispheric extreme events and their effect on a composited record of proxy (tree-ring density) summer temperatures (Jones et al., 1995, Briffa et al., 1998). Recently studies have separated spatial variations using both recorded temperature and proxy temperature data (Robock and Mao, 1992; 1995; D'Arrigo and Jacoby, 1999). These types of studies provide greater insight into the volcanic impacts and response of the climate system. Analyses of recorded, historical, and proxy information are revealing possible mechanisms for distribution of thermal effects from volcanoes. This paper will use primarily tree-ring information to describe certain effects from one extreme event, Laki, and relate it to similar events in North America.

The Laki-Grimsvotn eruption of 1783 actually continued as a series of eruptions into the year 1785 (Thordarson and Self, 1993) but the greatest eruption was at the beginning of this period (Simkin and Siebert, 1994). It is considered the largest volume of lava flow in historical times and the volume of sulphurous gases is estimated at 77–280 million tons based on ice core data and estimated optical effects (Hammer, 1977; 1984; Stothers, 1996). Historical reports track the circulation of the aerosols from Iceland to western Europe and across Asia. There are also observations from Labrador that indicate possible westward flow of aerosols across Greenland to North America (Demaree, et al. 1998). There are contemporary reports of dimming and weakening of the solar radiation at ground level (e. g. Franklin, 1784).

TREE-RING DATA, METHODS AND RESULTS:

The trees at the northern treeline are particularly sensitive to advection of cooler polar air because they are already at the thermal limit of survival. A volcanic-related cooling superposed on the ebb and flow of air masses across the treeline, which roughly coincides with the mean position of the polar front in summer (Bryson, 1966), should be reflected in tree growth along this region. We examined data from 13 sites along the treeline of North America to see the spatial variation in response to volcanic events. White spruce (Picea glauca) is the only species used in this study. It is a dominant treeline species across northern North America. All the sampling sites are near latitudinal treeline or alpine treeline in the northern boreal forest. There is no evidence

of fire or other disturbance at the sites. They are all mesic sites and the dominant limiting factor to growth is temperature. Standard methodologies (Cook and Kairiukstis, 1990) were used in dating and data quality evaluations. All tree-ring series are well replicated over the length of record used for this study (Jacoby and D'Arrigo, 1989; Jacoby et al., 1999). The density records are the residual chronologies following standardization (Cook, 1985). These residual series emphasize high-frequency fluctuations, which are of the most interest to this paper.

The parameter of growth used in this study is maximum latewood density. Conifers grow lower density cells with larger lumen and thinner cell walls early in the growing season, termed earlywood. Higher density, flatter (in the radial direction) cells with thicker walls (including secondary walls) and smaller lumen are formed later in the growing season and are termed latewood. These cells are formed and cell walls lignified towards the end of the growing season but may correlate with monthly temperatures from May through September (Schweingruber et al., 1979; D'Arrigo et al., 1992).

Each series was normalized over the length of the common period from 1720–1977 (subtracting the mean and dividing by the standard deviation). Five chronologies begin by 1600, nine by 1640, eleven by 1699 and thirteen by 1720. Figure 1 and Table 1 show the site locations for the thirteen chronologies. Table 2 lists the twenty most extreme low density values for each series. In order to include as much data as possible the chronologies begin at different dates, since not every chronology is long enough to include earlier events. As a result the rankings are not directly comparable from site to site due to the different time spans ranked. However the departure values are directly comparable, because they are calculated as departures from the mean of the same common period. The density departures were mapped to show the spatial variations. Figures 2, 3, 4 & 5 show the spatial distributions of density departures for the four years studied. The maps indicate that in each case there is not a spatially uniform cooling and the regions of greatest cooling change for each event.

DISCUSSION

No attempt was made here to objectively evaluate all volcanic events. Rather, the four years discussed in detail (1641, 1783, 1816 and 1836) were purposely selected for their association with major known volcanic episodes and extreme density departures for subregions over the interval since 1640 for which we have nine chronologies. Two years, 1641 and 1783, have such distinctive rings over a limited

Table 2. Twenty lowest normalized growth departures for thirteen density chronologies, from west to east across northern treeline of North America. Underlined years correspond to events discussed in text. The beginning year of each chronology (Yr1) is also indicated.

#	412 1570		ARR 1630		TWM 1640		PAX 1510		TT 1570		EF 1570		FM* 1660		CR 1610		PET 1630		HRN 1520		CHU* 1710		CRI* 1720		OK* 1670	
1	1783	4.22	1783	5.12	1783	4.88	1807	3.24	1959	4.39	1641	5.45	1677	5.04	1641	3.55	1836	5.13	1641	3.73	1817	3.74	1817	2.86	1816	4.34
2	1601	3.65	1765	3.65	1670	3.90	1864	3.15	1711	4.29	1770	3.91	1699	3.97	1947	3.38	1641	4.58	1836	3.37	1836	3.25	1726	2.86	1680	2.94
3	1807	3.19	1896	3.35	1695	3.57	1815	2.90	1699	4.08	1871	3.86	1871	3.37	1871	2.79	1888	3.36	1679	3.20	1899	2.60	1816	2.48	1836	2.64
4	1652	2.78	1646	3.31	1677	3.53	1643	2.84	1670	4.01	1690	3.73	1841	3.26	1884	2.65	1778	2.76	1671	3.02	1958	2.58	1969	2.32	1800	2.59
5	1896	2.73	1670	2.97	1864	2.78	1783	2.81	1620	3.92	1827	3.40	1959	3.08	1888	2.45	1643	2.44	1619	2.74	1832	2.55	1956	2.01	1685	2.54
6	1922	2.46	1735	2.93	1685	2.64	1831	2.71	1695	3.89	1699	3.37	1813	2.93	1959	2.42	1699	2.33	1812	2.72	1870	2.06	1912	2.01	1956	2.47
7	1588	2.46	1868	2.80	1675	2.64	1677	2.65	1611	3.64	1884	3.20	1888	2.79	1699	2.41	1887	2.21	1591	2.71	1750	2.04	1853	1.99	1835	2.37
8	1656	2.46	1834	2.64	1711	2.56	1580	2.62	1641	3.61	1677	3.17	1770	2.48	1677	2.35	1959	2.18	1532	2.69	1811	1.94	1965	1.92	1855	2.29
9	1711	2.46	1780	2.53	1856	2.47	1596	2.62	1646	3.27	1959	3.02	1836	2.39	1836	2.32	1865	2.13	1870	2.64	1945	1.92	1934	1.90	1921	2.27
10	1861	2.46	1807	2.47	1646	2.44	1531	2.59	1643	3.08	1712	2.95	1947	2.35	1712	2.17	1711	2.07	1863	2.62	1755	1.92	1963	1.84	1679	2.17
11	1623	2.39	1677	2.40	1959	2.35	1601	2.56	1831	2.93	1778	2.91	1790	2.30	1848	2.09	1918	2.07	1600	2.55	1855	1.92	1845	1.69	1692	2.14
12	1742	2.37	1711	2.40	1643	2.35	1567	2.53	1717	2.90	1585	2.53	1711	2.26	1817	2.07	1811	2.04	1888	2.55	1917	1.92	1800	1.64	1832	2.02
13	1756	2.35	1717	2.26	1834	2.31	1695	2.40	1689	2.84	1592	2.51	1982	2.17	1833	1.97	1844	1.96	1816	2.49	1959	1.85	1929	1.62	1714	2.02
14	1890	2.10	1697	2.26	1678	2.25	1684	2.34	1783	2.71	1836	2.47	1881	2.15	1685	1.87	1653	1.87	1556	2.49	1888	1.85	1918	1.61	1689	1.97
15	1981	2.03	1856	2.11	1790	2.16	1561	2.31	1815	2.65	1605	2.45	1854	2.13	1813	1.84	1870	1.87	1549	2.48	1815	1.76	1843	1.56	1682	1.89
16	1646	1.96	1742	2.07	1645	2.16	1678	2.28	1752	2.53	1870	2.40	1831	2.01	1778	1.81	1968	1.84	1884	2.37	1884	1.76	1946	1.55	1791	1.87
17	1780	1.94	1861	2.07	1780	2.15	1970	2.25	1604	2.34	1978	2.12	1663	1.86	1827	1.78	1758	1.81	1735	2.32	1885	1.62	1757	1.54	1748	1.82
18	1695	1.87	1712	2.04	1765	2.13	1623	2.22	1856	2.31	1947	2.11	1695	1.86	1729	1.77	1947	1.78	1653	2.28	1956	1.60	1957	1.54	1912	1.82
19	1764	1.87	1695	2.00	1935	2.11	1809	2.18	1677	2.28	1620	2.09	1870	1.81	1877	1.74	1769	1.78	1677	2.28	1812	1.60	1740	1.54	1765	1.77
20	1675	1.78	1730	1.92	1868	2.07	1646	2.15	1830	2.28	1817	2.03	1749	1.70	1701	1.67	1831	1.76	1832	2.23	1724	1.57	1923	1.52	1672	1.77

\# See Table 1 for full names.

* These sites do not extend to 1640.
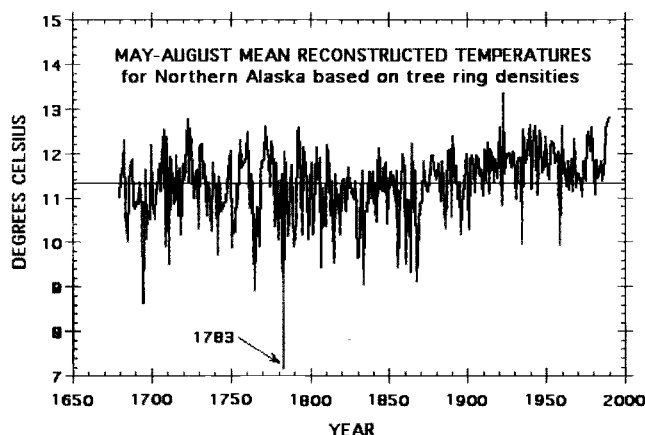
Figure 6. Reconstruction of May-August mean temperatures for northern Alaska based on tree-ring densities. Note extreme low value in 1783, associated with the Laki eruption.

The low density value for 1836 is the most unusual on record at Pet, NWT (-5.13), the second most extreme at Hornby, NWT (-3.37) and at Churchill, Manitoba (-3.25), the ninth lowest at Coppermine NWT (-2.32), and the third most extreme at Okak, Labrador (-2.64) (Figure 2d, Table 1). Extreme conditions in 1836 follow the 1835 eruption of Coseguina, Nicaragua.

The spatial distribution of low density values conforms to distances, wavelengths and regional patterns similar to typical large-scale upper-air wave configurations (e.g. *Riehl*, 1972; *Rizzoli*, 1992; *Trenberth*, 1993). They thus appear to indicate steering of colder air masses and polar frontal positions by this circulation mechanism. The mean position of the polar front delineates the regions of predominantly (50% or more) polar (northern) vs. temperate (southern) air masses (*Bryson*, 1966). In central Canada, the treeline approximately occupies the mean position of the front between Arctic and Pacific air; towards eastern Canada, air masses from the Atlantic and Hudson's Bay play a role (*Bryson*, 1966). Therefore, trees at the sites studied may be expected to record outbreaks of Arctic air masses, frontal shifts and circulation changes, which would influence temperature at the sites. Similarly, historical ice data were used to postulate that enhanced meridional flow of Arctic air masses resulted in the extreme cold in eastern Canada following the 1815 Tambora eruption (*Catchpole*, 1992; *Catchpole* and *Faurer*, 1983).

Three of the four events studied herein using northern treeline trees also appear to be related to frost rings at lower latitudes (*LaMarche* and *Hirschboeck*, 1984). These three were also of tropical origin, two with an associated (in time) higher latitude event. No notable mid-latitude frost rings were found associated with the Laki eruption, a high-latitude event. This suggests wider-scale effects from lower-latitude events.

CONCLUSION

The spatial extent of cooling from these four events is similar to the extent of waveforms of the prevailing planetary atmospheric circulation, Rossby waves. This is not a new dynamic concept. It is just evidence that the recognized existing dynamic plays a role in influencing distribution of the cooler air masses developed as a result of volcanic cooling. To preserve dynamic equilibrium there will be compensating northward flow in response to the southerly flow. In extreme cases the effect of this flow is the severe cold in some regions alternating with regions in between that show near normal or even warmer temperatures. (Figures 2-5). Thus major volcanic events may have extreme regional effects even if they are not among the greatest hemispheric events. These regional extremes of cold can have great effects on human activities (*Jacoby* et al ,1999).

REFERENCES

Briffa, K.R., P.D. Jones, and F.H. Schweingruber, 1994. Summer temperatures across North America: Regional reconstructions from 1760 using tree-ring densities, *Jour. Geophys. Res.* 99 (12) 25,835-25,844.

Briffa, K.R., P.D. Jones, F.H. Schweingruber, and T.J. Osborn, 1998. Influence of volcanic eruptions on Northern Hemisphere summer temperature over the past 600 years. *Nature* 393, 450-455.

Bryson, R. A., 1966. Air Masses, Streamlines, and the Boreal Forest, *Geogr. Bull.* 8, 228-69.

Catchpole, A. J. W., 1992. River Ice and Sea Ice in the Hudson Bay Region During the Second Decade of the Nineteenth Century, in: *The Year Without a Summer? World Climate in 1816*, Harington, C.R., (ed.), Natl. Museum of Science, Ottawa, Canada. pp. 233-44.

Catchpole, A. J. W. and M.A. Faurer, 1983. Summer Sea-Ice Severity in Hudson Strait, 1751-1870, *Climatic Change* 5, 115-39.

Cleaveland, M.K., 1992. Volcanic effects on the Colorado Plateau Douglas-Fir tree rings, 115-123, in *The Year Without a Summer?: World Climate in 1816*, Harington, C.R., (ed.), Natl. Museum of Science, Ottawa, Canada, pp. 225-65.

Cook, E. R., 1985. *A Time Series Analysis Approach to Tree-Ring Standardization*, Ph.D. thesis, University of Arizona, Tucson.

Cook, E.R. and L.A. Kairiukstis (eds.), 1990. *Methods of Dendrochronology*, Kluwer, Boston, 394 pp.

D'Arrigo, R.D. and G.C. Jacoby, 1999. Northern North American tree-ring evidence for regional temperature changes after major volcanic events. *Climate Change* 41, 1-15.

D'Arrigo, R. D., G.C. Jacoby, and R.M. Free, 1992. Tree-ring Width and Maximum Latewood Density at the North American Treeline: Parameters of Climatic Change, *Can. J. For. Res.* 22, 1290-6.

D'Arrigo, R. D., E.R. Cook, and G.C. Jacoby, 1996. Annual to Decadal-Scale Variations in Northwest Atlantic Sector Temperatures Estimated from Tree Rings, *Can. J. For. Res.* 26, 143-8.

Demaree, G., A. Ogilvie, and D. Zhang, 1998. Further documentary evidence of Northern Hemisphere coverage of the Great Dry Fog of 1783, *Climate Change* 39, 727-730.

Fiacco, R. J. Jr., T. Thordarson, M.S. Germani, S. Self, J.M. Palais, S. Whitlow, and P. Grootes, 1994. Atmospheric aerosol loading and transport due to the 1783-84 Laki Eruption in Iceland, interpreted from ash particles and acidity in the GISP2 Ice Core, *Quat. Res.* 42, 231-240.

Filion, L., S. Payette, L. Gauthier, and Y. Boutin, 1986. Light Rings in Subarctic Conifers as a Dendrochronological Tool, *Quat. Res.* 26, 272-279.

Franklin, B., 1784. Volcanoes and Climate, in: T. Simkin and R. S. Fiske. 1983. *Krakatau 1883*. Smithsonian Inst. Press, Wash., D.C. pp. 419-20.

Giddings, J. L.: 1941, *Bull. Univ. Ariz. Lab. Tree-Ring Res.* (Tree-Ring Bull.). 1, 72.

Glerum, C. and J.L. Farrar, 1966. Frost ring formation in the stems of some coniferous species, *Canadian Journal of Botany* 44, 879-886.

Hammer, C. U. 1977. Past volcanism revealed by Greenland ice sheet impurities. *Nature* 270: 482-486.

Hammer, C. U. 1984. Traces of Icelandic eruptions in the Greenland ice sheet. *Jokull* 34: 51-65.

Horstmeyer, Steven H., 1989. In search of Cincinnati's weather, *Weatherwise*, 42, 320-327.

Jacoby, G. C., I.S. Ivanciu, and L.D. Ulan, 1988. A 263-Year Record of Summer Temperature for Northern Quebec Reconstructed from Tree-ring Data and Evidence of a Major Climatic Shift in the Early 1800s, *Palaeogeography, Palaeoclimatology, Palaeoecology* 64, 69-78.

Jacoby, G.C., R.D. D'Arrigo, and G. Juday, 1999. Tree-ring indicators of climatic change at northern latitudes, *World Resources Review* 11 (1) 21-29.

Jacoby, G. C. and R.D. D'Arrigo, 1989. Reconstructed Northern Hemisphere Annual Temperatures Since 1671 Based on High Latitude Tree-ring Data for North America, *Climatic Change* 14, 39-59.

Jacoby, G. C. and R.D. D'Arrigo, 1992. Spatial Patterns of Tree Growth Anomalies from the North American Boreal Treeline in the Early 1800s, Including the Year 1816, in *The Year Without a Summer? World Climate in 1816,* Harington, C.R., (ed.), Natl. Museum of Science, Ottawa, Canada, pp. 225-65.

Jones, P. D., K. Briffa, and F. Schweingruber, 1995. Tree-ring evidence of the widespread effects of explosive volcanic eruptions, *Geophys. Res. Lett.,* 22, 1333-1336.

LaMarche, V. C. Jr. and K.K. Hirschboeck, 1984. Frost Rings in Trees as Records of Major Volcanic Eruptions, *Nature* 307, 121-6.

Lamb, H.H., 1970. Volcanic dust in the atmosphere with a chronology and assessment of its meteorological significance, *Philosophical Trans. Royal Society of London*, A266, 425-533.

Lamb, H. H. 1977. *Climate: Present, Past and Future*, Methuen, London.

Lough, J. M. 1992. Climate in 1816 and 1811-20 as Reconstructed from Western North American Tree-ring Chronologies, in *The Year Without a Summer? World Climate in 1816,* Harington, C. R., (ed.), Natl. Museum of Science, Ottawa, Canada, pp. 97-114.

Mikami, T. and Y. Tsukamura, 1992. The Climate of Japan in 1816 as Compared with an Extremely Cool Summer Climate in 1783, in *The Year Without a Summer? World Climate in 1816*, Harington, C.R., (ed.), Natl. Museum of Science, Ottawa, Canada, pp. 462-76.

Mitchell, J.M., 1971. The effect of atmospheric aerosols on climate with special references to temperature near the earth's surface. *Jour. of Applied meteorology* 10, 703-714.

Newell, J. P.: 1992. The Climate of the Labrador Sea in the Spring and Summer of 1816, and Comparisons with Modern Analogue, in *The Year Without a Summer? World Climate in 1816*, Harington, C.R., (ed.), Natl. Museum of Science, Ottawa, Canada, pp. 245-54.

phivols.dost.gov.ph/vmepd/qrn/parker.htm (website Jan. 2003)

Oquilluk, W. A., 1973. *People of Kauwerak: Legends of the Northern Eskimo*. Chapter Five: The Third Disaster, recorded by Laurel Bland, Alaska Methodist Univ., Anchorage.

Oswalt, W. H., 1957. Volcanic Activity and Alaskan Spruce Growth in A.D. 1783, *Science* 126, 928-9.

Riehl H., 1972. *Introduction to the Atmosphere*. McGraw-Hill, NY.

Rizzoli, P. M., 1992. Planetary Waves in the Ocean and Atmosphere, in *Encyclopedia of Earth System Science*, Vol. 3. Academic Press, NY, pp 609-16.

Robock, A. and M.P. Free, 1995. Ice cores as an index of global volcanism from 1850 to the present, *J. Geophys. Res.* 100, 11549-11567.

Robock, A. and J. Mao, 1992. Winter Warming from Large Volcanic Eruptions, *Geophys. Res. Lett.* 12, 2405-8.

Robock, A. and J. Mao, 1995. The Volcanic Signal in Surface Temperature Observations, *J. of Climate* 8, 1086-1103.

Schneider, S. H. and C. Mass, 1975. Volcanic dust, sunspots, and temperature trends, *Science* 190 (4216), 741-746.

Schweingruber, F.H. O.U. Braeker, E. Schaer, 1979. Dendroclimatic studies on conifers from central Europe and Great Britain. *Boreas* 8, 427-452.

Scuderi, L.A., 1990. Tree-ring evidence for climatically effective volcanic eruptions, *Quat. Res.* 34, 67-85.

Sigurdsson, H. and P. Laj, 1992. Atmospheric Effects of Volcanic Eruptions, in *Encyclopedia of Earth System Science* 1, pp. 183-99.

Simkin, T. P., L. Siebert, L. McCelland, D. Bridge, C. Newhall, and J.H. Latter, 1981, *Volcanoes of the World*, Hutchinson-Ross, Stroudsberg.

Simkin, T.P. and L. Siebert, 1994. *Volcanoes of the World. 2nd ed.* Geoscience Press, Tucson, Arizona 349 pp.

Stommel, H. and E. Stommel, 1983. *Volcano Weather: The Story of the Year Without a Summer: 1816*, Seven Seas Press, Newport, RI.

Stothers, R. B., 1996. The Great Dry Fog of 1783, *Climatic Change* 32, 79-89.

Thordarson, T. and S. Self, 1993. The Laki (Skaftar Fires) and Grimsvotn eruptions in 1783-1785. *Bull. Volcanol.* 55: 125-159.

Trenberth, K. E. 1993, Northern Hemisphere Climate Change: Physical Processes and Observed Changes , in *Earth System Responses to Global Change. Part II: Climate Controls*, Academic Press, N.Y, pp. 35-59.

Wilson, C.: 1992, Climate in Canada, 1809-20: Three Approaches to the Hudsons Bay Company Archives as an Historical Database, in *The Year Without a Summer? World Climate in 1816*, Harington, C. R., (ed.), Natl. Museum of Science, Ottawa, Canada, pp. 162-84.

Zielenski, G. A., P.A. Mayewski, L.D. Meeker, S. Whitlow, M.S. Twickler, M. Morrison, D.A. Meese, A.J. Gow, and R.B. Alley, 1994a, Record of Volcanism since 7000 B. C. from the GISP2 Greenland Ice Core and Implications for the Volcano-Climate System, *Science* 264, 948-52.

Zielenski, G. A., R.J. Fiacco, P.A. Mayewski, L.D. Meeker, S. Whitlow, and M.S. Twickler, 1994b, Climatic Impact of the A.D. 1783 Asama (Japan) Eruption was Minimal: Evidence from the GISP2 Ice Core, *Geophys. Res. Lett.* 21, 2365-8.

Rosanne D'Arrigo, Tree-Ring Laboratory, Lamont-Doherty Earth Observatory, 61 Route 9 W, Palisades, New York 10964

Gordon Jacoby, Tree-Ring Laboratory, Lamont-Doherty Earth Observatory, 61 Route 9 W, Palisades, New York 10964

Surface Atmospheric Circulation Over Europe Following Major Tropical Volcanic Eruptions, 1780–1995

M. J. Prohom, P. Esteban and J. Martín-Vide

Group of Climatology, Department of Physical Geography and RGA, University of Barcelona, Barcelona, Catalonia, Spain

P. D. Jones

Climatic Research Unit, School of Environmental Sciences, University of East Anglia, Norwich, England

We identify monthly circulation patterns of variability over the European continent within the first year after eight large tropical volcanic eruptions since the early 19th century. For this purpose, we apply an empirical orthogonal function (EOF) technique to a gridded sea level pressure data set covering the period 1780-1995. The post-eruption months with above-normal variance represented by the leading two EOFs are retained. Afterwards, we mapped their rotated equivalents to simplify physical interpretation of the results. Following the eight tropical eruptions, four months are identified during the first year fulfilling the criterion of exceptional values of variance in EOF1: January, June, July and September. January shows an anomalously dominant zonal pattern responsible for warmer temperatures over continental Europe. The summer months tend to show a more persistent south-westerly or westerly circulation over the continent, indicating a likely reduction in the strength of the Azores high. The results showing modification of the atmospheric circulation following large volcanic eruptions are consistent with previous studies based on instrumental records for more recent periods. This underscores the robustness of the circulation changes as a response to volcanic forcing. The analysis also demonstrates that empirical orthogonal functions provide a useful tool to detect these dynamical features.

1. INTRODUCTION

The definition of the temporal and spatial nature of climate change is an important issue to help understand the main causes of climatic variations. External forcing factors, such as changes in solar irradiance output and volcanic eruptions are among the natural causes of variability, while

atmosphere-ocean interactions (e.g. the El Niño-Southern Oscillation phenomenon) are well known internal factors [*Parker and Folland*, 1988; *Lean et al.*, 1995]. Jointly with natural external forcing, human activities are a continuously increasing source of variability, i.e. the anthropogenic climate forcing factor, altering the radiative balance of the Earth's atmosphere and surface. It is essential to understand how such factors affect the climate system, identifying, if possible, the temporal and spatial responses, and the magnitude of the signal of each.

In this paper we focus on the effects of one of these sources of natural variability: volcanic eruptions. Aerosols injected into the lower stratosphere by explosive eruptions
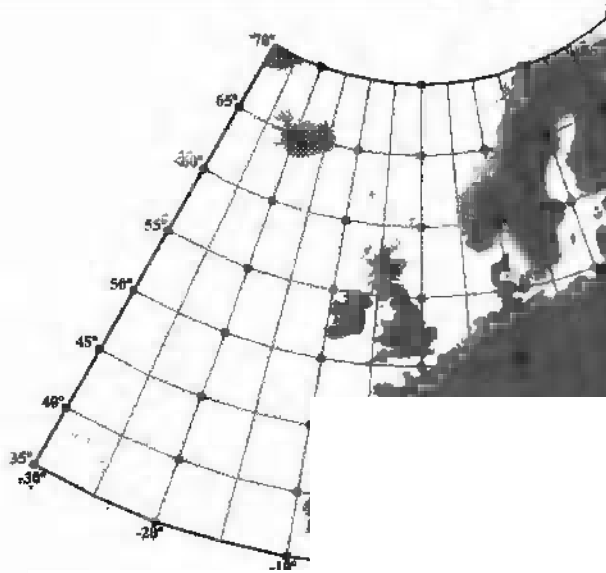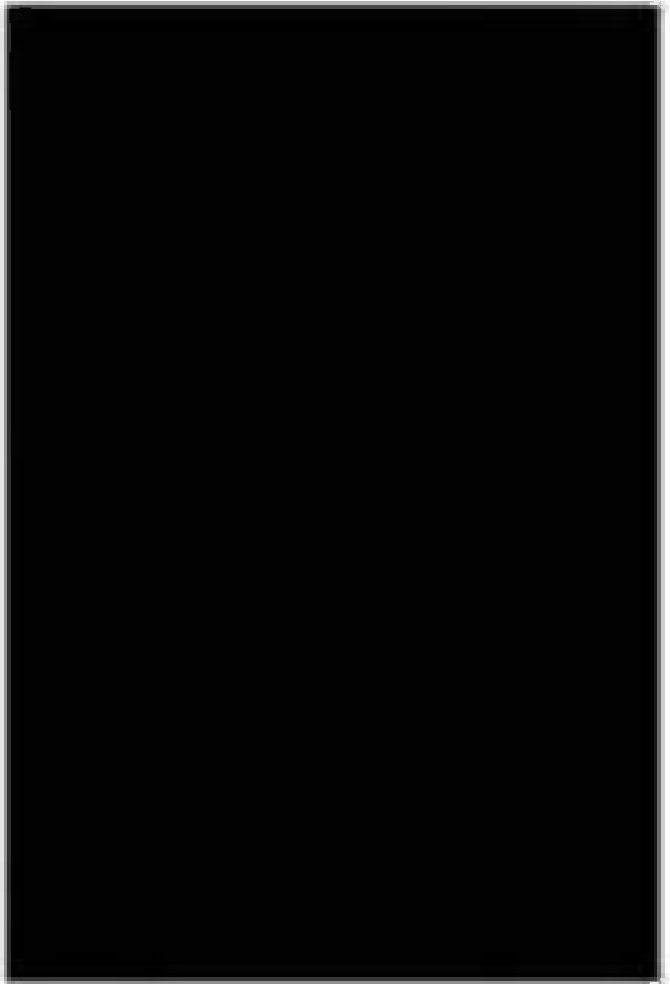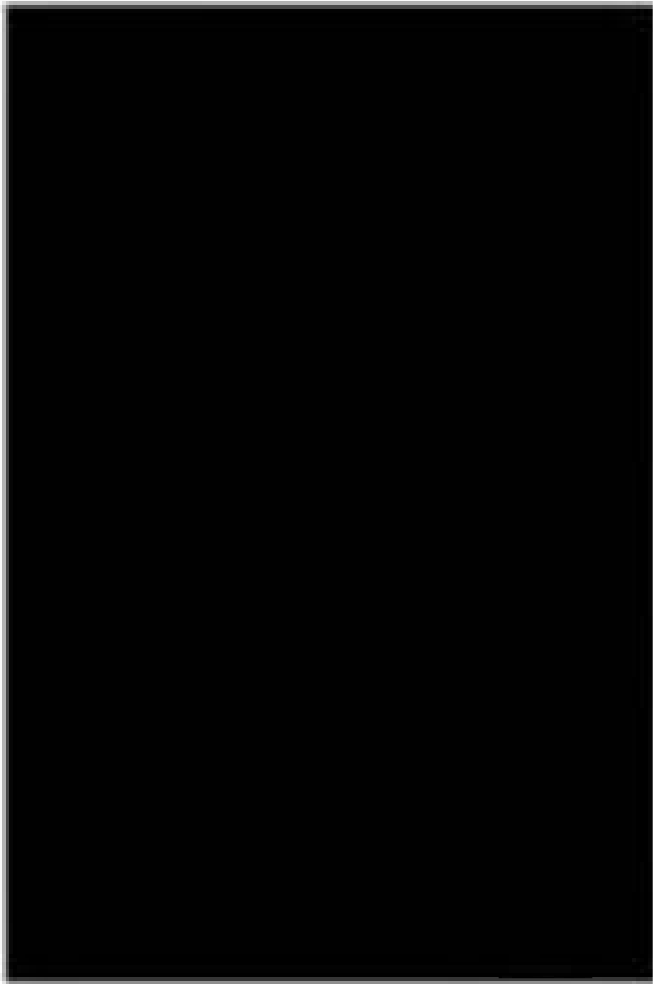
Table 1. Tropical Volcanic Eruptions Considered in this Study.

Volcano	Latitude	Longitude	Eruption date	DVI	VEI	IVI
unknown	tropical	?	?, 1808	1500	6	5.6
Tambora	8°S	118°E	April, 1815	3000	7	15.0
Coseguina	13°N	87.5°W	January, 1835	4000	5	3.2
Cotopaxi	1°S	78°W	?, 1856	700	5	na
Krakatau	6°S	105.5°E	August, 1883	1000	6	3.7
Santa María	14.5°N	92°W	October, 1902	900	6	1.6
El Chichón	17°N	93°E	April, 1982	800	5	1.9
Mt. Pinatubo	15°N	120°E	June, 1991	>1000	6	4.0

DVI (Dust Volcanic Index), VEI (Volcanic Explosivity Index), IVI (Ice core Volcanic Index).
na, not available

The tropical event of 1808 was revealed from high-resolution analyses of ice cores from Antarctica and Greenland [*Dai et al.*, 1991], although originally assigned to 1809. Documentary [*Chenoweth*, 2001] and coral [*Crowley et al.*, 1997] data suggested the previous year as the most probable eruption year, so 1808 was used in this study. In contrast, the Agung (1963) eruption was not considered because at least two thirds of the aerosol cloud had spread to the Southern Hemisphere [*Volz*, 1970; *Sato et al.*, 1993]. Extra-tropical eruptions were also excluded.

2.3. Methodology

Once the key dates of the eruptions were selected, an Empirical Orthogonal Function (EOF) analysis was performed for the post-eruptive months. EOF analysis is a recognized multivariate technique used to derive the dominant patterns of variability on an original data set of N observations and M variables, in other words, to simplify this data set (i.e. obtain a new set of variables) for purposes of interpretation and understanding [*Yarnal*, 1993; *Barry and Carleton*, 2001]. It has been widely used in climatology, especially to identify characteristic spatial patterns of variability in temperature and rainfall [*Kelly et al.*, 1982; *Folland et al.*, 1991], and also to identify the volcanic signal in global surface temperature records [*Jia and Kelly*, 1996]. We used the explained variance of every new variable or component of the EOF analysis (i.e. eigenvalues) as a criterion to detect changes in the persistence of the circulation patterns following large tropical volcanic events. Firstly, the non-rotated EOFs were calculated using the S-mode data matrix of 60 variables (grid points of SLP data) and 8 observations (post-volcanic years, on a monthly basis), via correlations of the standardized variables, looking at the resulting amount of variance represented by the first and the second components (EOF1 and EOF2). The second step involved a random selection of 100 sets of eight years each, from the whole data set used (1780–1995),

again obtaining (via S-mode data matrix and correlations) the non-rotated EOFs for each set (on a monthly basis), and retaining the percentage of variance of EOF1 and EOF2. The reason for paying attention to the percentage variance of both principal components is based on the principle that the higher amount of variance represented by the first component is related to the most persistent spatial pattern of variability for a certain month. In the same way, the second highest amount of variance (EOF2) is related to the second most persistent spatial pattern, being uncorrelated (orthogonal) to EOF1. By comparing the values of explained variance of EOF1 and EOF2 for the post-eruptive months with the corresponding EOF1 and EOF2 values taken from the 100 random-year sample, we evaluate changes in the persistence of the spatial patterns. By the calculation of the mean and the thresholds determined by the 90th and 10th percentile from the 100 random-year sample, we can detect those months with anomalous persistence of a given pattern above and below the normal values.

Finally, a VARIMAX rotation of EOFs was performed to obtain more coherent and uncorrelated spatial patterns [*Richman*, 1986]. Nevertheless, the opinion in the community is divided on the subject of rotation. While some scientists argue that rotation produces more stable and compact patterns that can be used for 'regionalization,' others criticize drawbacks like the arbitrary choice of rotation criterion or the sensitivity of the result to the normalization [*Von Storch and Zwiers*, 1999]. In the present study, the non-rotated and the VARIMAX-rotated EOFs were computed separately from the correlation matrix and represented physically (not shown). Although the rotation did not greatly simplify the spatial patterns obtained, the rotated patterns were used for the physical interpretation of the results.

3. RESULTS

We started the analysis in the first winter following major volcanic eruptions, as most of the events occurred in the

first half of the year. Four post-eruptive months were detected showing high levels of anomalous variance represented by EOF1, January (+1), June (+1), July (+1), and September (+1), while December (+1) was the only month showing extremely low levels of anomalous variance (table 2). In order to evaluate whether most of the change affects only EOF1, we also looked for possible anomalies in the variance in EOF2, detecting just two months with high values of variance: May (+1) and June (+1) (table 3). As our research is concerned with identifying those months showing a more persistent pattern, and since most of the changes affect the corresponding first post-eruptive components, we have only plotted the maps for those months exceeding the 90th percentile threshold in EOF1 (figures 2 to 5). Extremely high and low amounts of variance in EOF1 and EOF2 were not found in the second year following the events.

The strongest signal is detected in January (+1) (see Figure 2). The first EOF for this month, accounting for 64% of the variability in the pressure field of the domain, represents a mode with a dipole structure, with strong weights in the extreme northeast of opposite sign to those in the southwestern half. The positive phase of this spatial pattern is associated with strong westerly/northwesterly flow across Europe, while the negative phase represents a reduction of the zonal component of the circulation. This kind of circulation, typical of the mid-latitudes and well-established in winter, might be linked to the NAO [*Walker and Bliss*,

1932; *Barnston and Livezey*, 1987; *Hurrell*, 1995; *Slonosky et al.*, 2000], and to the AO [*Thompson and Wallace*, 1998]. Nevertheless, in the post-eruptive Januaries this pattern seems to be more persistent, showing a detectable strengthening of the Azores high, as there are no negative values to the south and, as a result, increased tropospheric westerlies at 60°N. This is consistent with previous studies of NH tropospheric mid-latitude circulation after violent volcanic eruptions that reported a strengthening of the polar stratospheric vortex and geopotential height anomalies of the 500 hPa layer [*Graf et al.*, 1994; *Kodera*, 1994]. This mechanism is explained by the heating of the tropical lower stratosphere by absorption of terrestrial and near-IR radiation, resulting in an enhanced pole-to-equator temperature gradient and in a more gentle surface temperature gradient [*Robock*, 2000; *Stenchikov et al.*, 2002]. The stationary NAO or AO pattern dominates the winter circulation, creating the winter warming shown by observations [*Groisman*, 1992; *Robock and Mao*, 1992, 1995; *Jones and Kelly*, 1996] and modeling [*Graf et al.*, 1993; *Mao and Robock*, 1998], over NH continental areas.

Two summer months were detected with anomalous persistent patterns represented by the first eigenvectors: June (+1) (Figure 3) and July (+1) (Figure 4). In June, the pattern seems to show a strong southwesterly circulation over the British Isles that has been identified as the 'European monsoon' by *Kelly et al.* [1997]. This pattern is established in mid-June and consists of the southwards displacement of

Table 2. Results of the EOF1 Analysis.

Months	Variance represented by EOF1 and for the post-volcanic months, %	Average variance represented by EOF1 obtained from 100 sets of 8 years randomly selected, %	90th percentile threshold fixed by EOF1 obtained from 100 sets of 8 years randomly selected, %	10th percentile threshold fixed by EOF1 obtained from 100 sets of 8 years randomly selected, %
DEC (0)	40.9	43.8	50.8	37.6
JAN (+1)	**63.6**	**48.8**	**58.0**	**39.8**
FEB (+1)	49.6	50.0	58.3	40.6
MAR (+1)	50.7	47.4	55.4	38.6
APR (+1)	40.8	43.0	51.4	36.0
MAY (+1)	41.9	41.5	48.2	35.3
JUN (+1)	**52.7**	**42.1**	**49.4**	**33.3**
JUL (+1)	**48.5**	**40.4**	**46.0**	**34.4**
AUG (+1)	40.3	42.4	50.2	35.2
SEP (+1)	**51.7**	**41.6**	**49.4**	**35.1**
OCT (+1)	45.7	42.0	47.8	36.1
NOV (+1)	45.6	44.3	51.4	38.2
DEC (+1)	*37.4*	*43.8*	*50.8*	*37.6*

First column shows post-eruptive months, where 0 indicates the year of the eruption and +1 the first year following the eruption. In bold, those months exceeding the 90th percentile threshold from the EOF1, and in italics those months below the 10th percentile threshold (see text for additional information).

Barry, R. G., and A. M. Carleton, *Synoptic and Dynamic Climatology*, Rouledge, London, 2001.

Briffa, K. R., T. S. Bartholin, D. Eckstein, P. D. Jones, W. Karlén, F. H. Schweingruber, and P. Zetterberg, A 1,400-year tree-ring record of summer temperatures in Fennoscandia, *Nature, 346*, 434-439, 1990.

Briffa, K. R., P. D. Jones, and F. H. Schweingruber, Influence of volcanic eruptions on Northern Hemisphere summer temperatures over the past 600 years, *Nature, 393*, 450-454, 1998.

Chenoweth, M., Two major volcanic cooling episodes derived from global marine air temperature, AD 1807-1827. *Geoph. Res. Lett., 28*, 2963-2966, 2001.

Crowley, T. J., T. M. Quinn, F. W. Taylor, C. Henin, and P. Joannot, Evidence for a volcanic cooling signal in a 335-year coral record from New Caledonia, *Paleoceanography, 12*, 633-639, 1997.

Dai, J., E. Mosley-Thompson, and L. G. Thompson, Ice core evidence for an explosive tropical volcanic eruption 6 years preceding Tambora, *J. Geophys. Res., 96* (D9), 17,361-17366, 1991.

Folland, C. K., J. A. Owen, M. N. Ward, and A. W. Colman, Prediction of seasonal rainfall in the Sahel region using empirical and dynamical methods, *J. Forecasting, 10*, 21-56, 1991.

Graf, H.-F., I. Kirchner, A. Robock, and I. Schult, Pinatubo eruption winter climate effects: Model versus observations, *Clim. Dyn., 9*, 81-93, 1993.

Graf, H.-F., J. Perlwitz, and I. Kirchner, Northern Hemisphere tropospheric mid-latitude circulation after violent volcanic eruptions, *Beitr. Phys. Atmosph., 67*, 3-13, 1994.

Groisman, P. Y., Possible regional climate consequences of the Pinatubo eruption: An empirical approach, *Geophys. Res. Lett., 19*, 1603-1606, 1992.

Hammer, C.U., H.B. Clausen and W. Dansgaard, Greenland ice sheet evidence of post-glacial volcanism and its climatic impact, *Nature, 288*, 230-235, 1980.

Hurrell, J. W., Decadal trends in the North Atlantic Oscillation: Regional temperatures and precipitation, *Science, 269*, 676-679, 1995.

Jia, P. Q., and Kelly, P. M., The identification of the volcanic signal in global surface temperature records, *Acta Meteor. Sin., 10* (2), 222-232, 1996.

Jones, P.D., and P.M. Kelly, The effect of tropical explosive volcanic eruptions on surface air temperature, in *The Mount Pinatubo Eruption Effects on the Atmosphere and Climate*, edited by G. Fiocco, D. Fuà, and G. Visconti, pp. 95-111, NATO ASI Series, Vol. I 42, Springer-Verlag, Berlin, 1996.

Jones, P.D., K. R. Briffa and F. H. Schweingruber, Tree-ring evidence of the widespread effects of explosive volcanic eruptions, *Geophys. Res. Lett., 22*, 1333-1336, 1995.

Jones, P. D., T. D. Davies, D. H. Lister, V. Slonosky, T. Jönsson, L. Bärring, P. Jönsson, P. Maheras, F. Kolyva-Machera, M. Barriendos, J. Martín-Vide, M. J. Alcoforado, H. Wanner, C. Pfister, E. Schuepbach, E. Kaas, T. Schmith, J. Jacobeit, and C. Beck, Monthly mean reconstructions for Europe, *Int. J. Climatol., 19*, 347-364, 1999.

Kelly, P. M., P. D. Jones, C. B. Sear, B. S. G. Cherry, and R. K. Tavakol, Variations in surface air temperatures, 2, Arctic regions, 1881-1980, *Mon. Weather Rev., 110*, 71-83, 1982.

Kelly, P. M., Jones, P. D., and Briffa, K., Classifying the winds and weather, in *Climates of the British Isles. Present, past and future*, edited by M. Hulme and E. Barrow, pp. 153-172, Routledge, London, 1997.

Kirchner, I., G. L. Stenchikov, H.-F. Graf, A. Robock, and J. C. Antuña, *J. Geophys. Res., 104*, 19,039-19,055, 1999.

Kodera, K., Influence of volcanic eruptions on the troposphere through stratospheric dynamical processes in the Northern Hemisphere winter, *J. Gephys. Res., 99* (D1), 1273-1282, 1994.

Lamb, H. H., Volcanic dust in the atmosphere; with a chronology and assessment of its meteorological significance, *Philos. Trans. R. Soc. London, A Math. Phys. Sci., 266*, 425-533, 1970.

Lamb, H. H., Suplementary volcanic dust veil index assessments, *Clim. Monit., 6*, 57-67, 1977.

Lamb, H. H., Update of the chronology of assessments of the volcanic dust veil index, *Clim. Monit., 12*, 79-90, 1983.

Lean, J., J. Beer, and R. S. Bradley, Reconstruction of solar irradiance since 1610: implications for climate change, *Geophys. Res. Lett., 22*, 3195-3198, 1995.

Mao, J., and A. Robock, Surface air temperature simulations by AMIP general circulation models: Volcanic and ENSO signals and systematic errors, *J. Clim., 11*, 1538-1552, 1998.

Newhall, C. G., and S. Self, The volcanic explosivity index (VEI): An estimate of explosive magnitude for historical volcanism, *J. Geophys. Res., 87*, 1231-1238, 1982.

Parker, D. E., and C. K. Folland, The nature of climatic variability, *Meteorol. Mag., 117*, 201-210, 1988.

Pinto, J. P., R. P. Turco, and O. B. Toon, Self-limiting physical and chemical effects in volcanic eruption clouds, *J. Geophys. Res., 94* (D8), 11,165-11,174, 1989.

Prohom, M. J., and R. S. Bradley, Winter precipitation anomalies over the Iberian Peninsula and Balearic Islands following large tropical volcanic eruptions, 1901-1996 (in Spanish), in *El agua en el clima—Publicaciones de la Asociación Española de Climatología*, edited by the Spanish Association of Climatology, vol. 3, pp. 511-520, 2002.

Rampino, M. R., and S. Self, Sulphur-rich volcanic eruptions and stratospheric aerosols, *Nature, 310*, 677-679, 1984.

Richman, M. B., Rotation of Principal Components, *J. Climatol., 6*, 293-335, 1986.

Robock, A., Volcanic eruptions and climate. *Rev. Geophys., 38*, 191-219, 2000.

Robock, A. and M. P. Free, Ice cores as an index of global volcanism from 1850 to the present, *J. Geophys. Res., 100*, 11,549-11,567, 1995.

Robock, A. and M. P. Free, The volcanic record in ice cores for the past 2000 years, in *Climatic Variations and Forcing Mechanisms of the Last 2000 years*, edited by P. D. Jones, R. S. Bradley, and J. Jouzel, pp. 533-546, Springer, Berlin, 1996.

Robock, A., and J. Mao, Winter warming from large volcanic eruptions, *Geophys. Res. Lett., 12*, 2406-2408, 1992.

Robock, A., and J. Mao, The volcanic signal in surface temperature observations, *J. Clim., 8*, 1086-1103, 1995. .

Sato, M., J. E. Hansen, M. P. McCormick, and J. B. Pollack, Stratospheric aerosol optical depths, 1850-1990, *J. Geophys. Res., 98*, 22987-22994, 1993.

Sear, C. B., P.M. Kelly, P.D. Jones, and C. M. Goodess, Global surface-temperature responses to major volcanic eruptions, *Nature, 330,* 365-367, 1987.

Slonosky, V. C., P. D. Jones and T. D. Davies, Variability of the surface atmospheric circulation over Europe, 1774-1995, *Int. J. Climatol., 20,* 1875-1897, 2000.

Stenchikov, G., A. Robock, V. Ramaswamy, M. D. Schwarzkoft, K. Hamilton, and S. Ramachandran, Arctic Oscillation response to the 1991 Mount Pinatubo eruption, in *The American Geophysical Union Chapman Conference on Volcanism and the Earth's atmosphere.* Santorini, Greece, p. 36. 2002

Thompson, D. W. J., and J. M. Wallace, The Arctic Oscillation signature in the wintertime geopotential height and temperature fields, *Geophys. Res. Lett., 25,* 1297-1300, 1998.

Volz, F. E., Atmospheric turbidity after the Agung eruption of 1963 and size distribution of the volcanic aerosol, *J Geophys. Res., 75* (27), 5185-5193, 1970.

Von Storch, H., and F. W. Zwiers, *Statistical Analysis in Climate Research,* Cambridge Univ. Press, 1999.

Walker, G. T., and E. M. Bliss, World Weather V, *Mem. R. Met. Soc., 44,* 53-84, 1932.

Yarnal, B., *Synoptic Climatology in Environmental Analysis—A primer,* Belhaven Press, London and Florida, 1993.

Zielinski, G. A., Stratospheric loading and optical depth estimates of explosive volcanism over the last 2100 years derived from Greenland Ice Sheet Project 2 ice core, *J. Geophys. Res., 100* (D10), 20,937-20,955, 1995.

Zielinski, G. A., P. A. Mayewski, L. D. Meeker, S. Whitlow, M. S. Twickler, M. Morrison, D. A. Meese, A. J. Gow and R. B. Alley, Record of volcanism since 7000 B.C. from the GISP2 Greenland ice core and implications for the volcano-climate system, *Science, 264,* 948-952, 1994.

M. J. Prohom, P. Esteban and J. Martin-Vide, Group of Climatology, Barcelona Science Park, Baldiri Reixac, 4-6—Tower D, 08028 Barcelona, Catalonia, Spain. (mprohom@pcb.ub.es)

P. D. Jones, Climatic Research Unit, School of Environmental Sciences, University of East Anglia, Norwich NR4 7TJ, England.

Predictions of Climate Following Volcanic Eruptions

Matthew Collins

Centre for Global Atmospheric Modelling, Department of Meteorology, University of Reading, Reading, United Kingdom

Predictions of climate for seasons and years into the future can be of considerable benefit to society. While large explosive volcanic eruptions may not be predictable with any confidence on these timescales, once the eruption has occurred the climate impact may be exploited to provide a climate forecast. In this paper, retrospective forecasts of the climate impacts of the 1982 eruption of El Chichón and the 1991 eruption of Pinatubo are examined to quantify the potential accuracy of such forecasts. Recognizing that there is no single pre-determined climate path following an eruption, and that all climate forecasts are essentially probabilistic in nature, it is shown that volcanoes of the size of El Chichón and Pinatubo can significantly bias the probability of occurrence of anomalies in climate variables such as surface air temperature and mean sea level pressure. However, the volcanic signal is only robust on the spatial scale of continents and, moreover, the signal can easily be contaminated or completely obscured by climate variability which is independent of the volcanic perturbation. It is not simply enough to issue a forecast of the form "winter will be warmer and summer will be cooler" following an eruption. Care must be taken and forecasts should explicitly quote probability levels. However, it is recommended that forecasting centers develop the capacity to forecast climate following the next big eruption.

1. INTRODUCTION

The chaotic nature of atmospheric motions means that it is impossible to make weather forecasts for many months into the future [e.g. *Lorenz*, 1982]. Weather forecasts exhibit "sensitive dependence on initial conditions" which means that two weather forecasts that start from indistinguishable atmospheric states, while remaining close for perhaps several days, eventually diverge from each other and result in two very different future weather patterns. This sensitive dependence on initial conditions means that even if one could make perfect observations of the current state of the atmosphere and introduce them perfectly into a perfect weather forecast model, it is impossible to predict the exact weather e.g. a week ahead. By defining "climate" as the aggregated effects of weather (in both space and time) it is easy to see that climate forecasts will also exhibit sensitive dependence on initial conditions: Given an initial estimate of the state of the climate system (atmosphere, ocean, biosphere, cryosphere etc.) today, it is not possible to predict e.g. the precise winter mean temperature for next year.

Climate forecasts are thus inherently probabilistic. A typical climate forecast might be of the form "there is a 75% chance of cooler than average temperatures in Western Europe next summer." An important concept in climate forecasting is that for each climate variable, such as Western European summer temperature, there is a climatological probability density function (PDF—Figure 1) from which the observed temperature will be drawn. The chaotic nature of the system means that there is no way of

2. METHODS

2.1. Modelling

The model used is version three of the Hadley Centre for Climate Prediction and Research coupled atmosphere ocean model—HadCM3 [*Gordon et al.,* 2000; *Collins et al.,* 2001]. The ocean component of the model has a horizontal resolution of 1.25° in longitude by 1.25° in latitude and has 20 levels in the vertical from the surface to the bottom of the ocean. The atmospheric component of the model has a horizontal resolution of 3.75°x2.5° in longitude and latitude with 19 unequally spaced vertical levels from the surface up to approximately 40km, with 6 levels representing the Stratosphere. The two components are coupled without the use of artificial flux corrections and the model has a stable surface climate.

Aerosol distributions associated with both El Chichón and Pinatubo are taken from an updated version of the *Sato et al.* [1993] dataset and are introduced into the model in four uniform latitudinal bands from 90°S–45°S, 45°S–equator, equator–45°N and 45°N–90°N. The representation of the volcanic forcing by such broad spatial scales in part reflects the uncertainty there would be in the transport of aerosol particles by chaotic stratospheric dynamics following an eruption. A potential improvement to this study, and a component of any operational forecasting system, would be the inclusion/prediction of a more realistic pattern of aerosol loading, with careful account taken of the phase of the quasi-biennial oscillation, season and degree of penetration into the stratosphere. Given the chaotic nature of atmospheric dynamics and the large-scale pattern of the response, quite how accurate this forcing needs to be to result in useful climate forecasts is still an open question requiring much further research.

The net radiative forcing (i.e. the change in the radiative balance of the model) resulting from the inclusion of the *Sato et al.* [1993] aerosol optical depths are shown in Figure 2. The net forcing is composed of two components, a negative (i.e. surface/troposphere cooling) shortwave component resulting from the direct reduction of incoming solar radiation by the aerosol particles, and a positive (i.e. surface/troposphere warming) longwave component resulting from the enhanced greenhouse effect of the aerosol particles. In each case, the former of these effects dominates and the general pattern of forcing is negative, although there is some small positive forcing in the polar night regions at times when there is no incident solar radiation hence no shortwave effect. *Stenchikov et al.* [1998] and *Andronova et al.* [1999] present a much more extensive study of the radiative effects of volcanic eruptions.

The radiative forcing associated with the Pinatubo eruption is larger and more long-lived than that associated with El Chichón simply because of the greater amount of SO_2 released into the stratosphere during that eruption (20 Mt in comparison with 7 Mt [*Bluth et al.,* 1992]). In addition, the forcing pattern for Pinatubo is more global in extent, where-
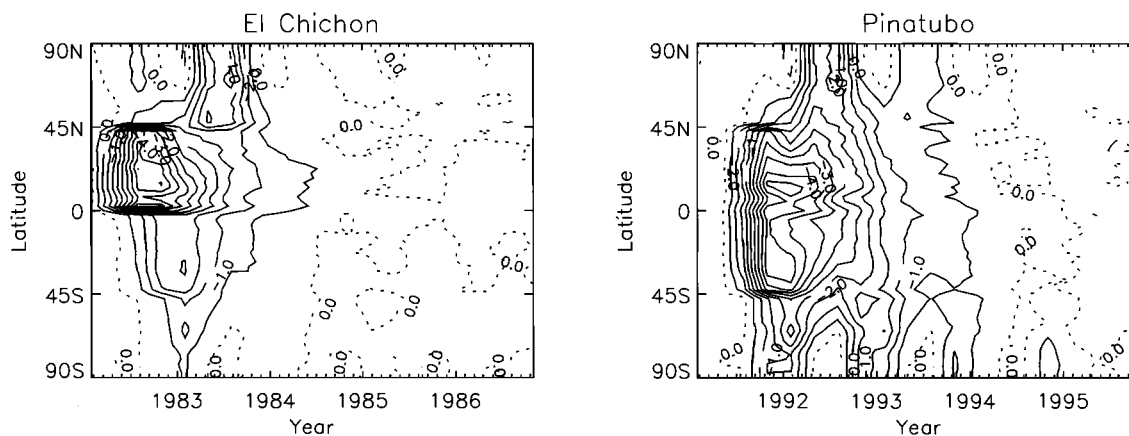
Figure 2. The latitude-time distribution (averaged over longitude) of the net tropopause radiative forcing resulting from the introduction of stratospheric aerosol into the HadCM3 coupled atmosphere-ocean model following the eruption of El Chichón (left panel) and Pinatubo (right panel). Aerosol optical depths are taken from an updated version of *Sato et al.* [1993] and are introduced uniformly in longitude in four latitude bands each with a width of 45° latitude. The contour interval is 0.5 Wm^{-2} and negative contours (indicating a cooling influence) are drawn as solid lines and the zero contour is drawn as the dotted line.

as the El Chichón forcing pattern is more confined to the northern hemisphere. The magnitude of the forcing is of the order of several Wm^{-2}, which is similar to that associated with a doubling of CO_2, but because of the relatively short lifetime of the aerosol particles in the atmosphere, the impact of the eruption on global climate is correspondingly short (see figs 3 and 4).

The effects of increasing greenhouse gases, solar variability and athropogenic aerosols are also included in the simulations [Stott et al., 2001]. The timescales for climate perturbations associated with these forcings are decadal and longer, hence we may assume that their effects are unimportant for the seasonal to interannual timescales examined here. Long-term trends (in both the observations and the model experiments) must however be taken into account when defining the base period from which to compute climate and forcing anomalies. In each case, the five years prior to the year of the eruption are used to define the climatology from which anomalies are computed.

An ensemble of 20 simulations is performed for both eruptions in order to assess probabilities. The simulations use four different oceanic initial states and 20 different atmospheric initial states [Collins et al., 2002] in order to sample uncertainty in both components of the climate system. The ocean initial state is the crucial one for the first kind or initial value prediction problem, but here no attempt is made to produce an initial state that is consistent with the observed ocean state prior to either eruption (a non-trivial task due to the paucity of sub-surface ocean observations and because of the technical requirements of assimilating the data into the model). In addition, simulations are initiated 5–6 years prior to the eruptions in order to minimize any "memory" of the ocean initial conditions. Practically this means that the initial states are essentially random, and there is a relatively clean separation of the effects of initial and boundary conditions (e.g. decadal ocean "modes" will have random phases in the simulations and their impact will be averaged out). Thus the predictability assessed here is that due to the volcanic boundary forcing only. In any operational forecasting system, account should be taken of both the current initial conditions and the boundary forcing [Collins and Allen, 2002] in order to maximize the potential for predictability.

2.2. Data Processing

The focus here is on the prediction of two climate variables. Surface air temperature (SAT) is of direct relevance to society and is directly affected by the radiative perturbation introduced by a volcanic eruption and hence is likely to be significantly perturbed with respect to climatology. Mean Sea Level Pressure (MSLP) is a good indicator of wind strength and direction (in midlatitudes) and of phenomena such as the North Atlantic Oscillation (NAO—*Hurrell* [1995]). It is not directly influenced by the radiative forcing, but can be influenced indirectly via changes in atmospheric dynamics associated with atmospheric temperature changes. Both SAT and MSLP are known to be reasonably well simulated by global circulation models (GCMs), whereas variables such as precipitation and extreme storms are less reliably simulated. One of the challenges for making all types of climate forecasts, from seasonal to centennial timescales, is the improvement of GCMs to more accurately simulate variables which are of direct impact on society

Observations of land surface air temperature (ocean temperatures are not considered as they are less relevant to society) are taken from *Jones* [1994]. Data coverage is incomplete and this may influence the comparison with the model fields. The model simulated surface air temperatures at 1.5m are thus first interpolated from the 3.75°x2.5° model grid to the 5°x5° observational grid using bilinear interpolation and model grid-boxes for which there are no observed data are also flagged as missing. This allows direct comparison between the model prediction and the observed data. Because of anthropogenic trends in both the model simulations and in the observations, seasonal mean anomalies are computed with respect to the average conditions for five years prior to the eruption. For the quantitative comparisons performed here and elsewhere, care should always be taken to compute climate anomalies in a consistent manner.

Observations of MSLP are taken from the Global Mean Sea Level Pressure (GMSLP) data set of *Basnett and Parker* [1997]. Again, data coverage is incomplete and the model MSLP is interpolated onto the 5°x5° observational grid and grid boxes are flagged as missing if there are no observations of MSLP during that particular year and season. MSLP is examined over ocean basins as, in midlatitudes, these are the main locations of the storm tracks.

In the case of many climate variables, data sets that offer complete global coverage do exist, although regions of missing data are either in-filled using statistical techniques or by taking the so-called re-analysis products of weather forecasting centers, where regions of missing data are in-filled in a more physically consistent way. For this study it is more appropriate to use the raw gridded datasets as, when using the in-filled products, there is the potential for the mis-verification of the predictions in regions where there are no observations.

Temperature Anomaly (K)
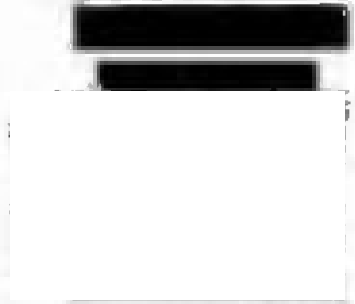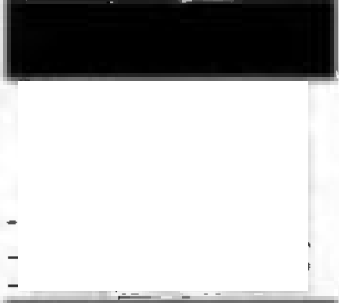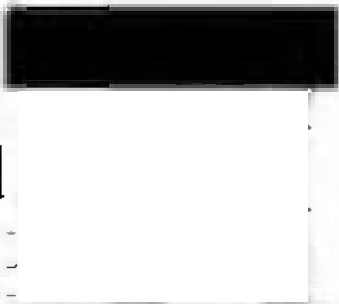
Temperature Anomaly (K)

Temperature Anomaly (K)

Temperature Anomaly (K)
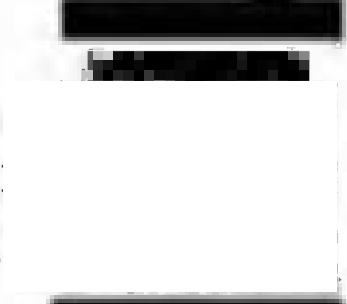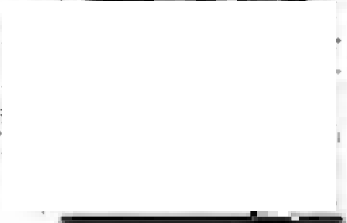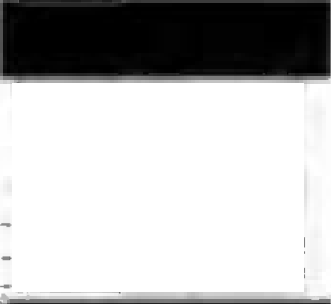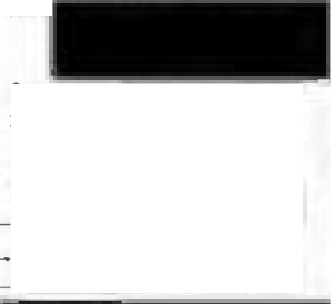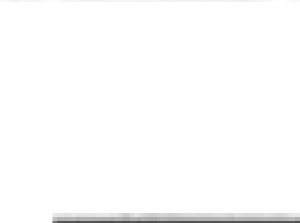
induced climate change over the next few decades [*Houghton et al.*, 2001].

The model predicts near-global patterns of cooler than average temperatures in the summer seasons following both eruptions, with somewhat stronger anomalies following Pinatubo due to the greater radiative forcing (Figure 2). Small regions of slight warming in the ensemble mean in the summer following El Chichón are simply due to chance and reflect the smaller radiative forcing. For example, the southern hemisphere forcing is only of the order of 1-2 Wm^{-2} and hence not large enough to significantly cool the Australian region which is predicted to be slightly warmer than average. (Because of the complex non-linear nature of the climate system, it is not entirely appropriate to relate radiative forcing directly to changes in surface air temperature. However, for global and large-scale patterns, an approximate relationship holds [*Stott et al.*, 2000].) In the winters following the eruptions, the patterns of mean temperature anomalies are more complex. The general pattern of cooling associated with the decrease in net radiative forcing is disrupted by a broad pattern of warming in northern Europe in both cases and over the whole of the northern Eurasian continent in the case of the 1982–3 DJF winter season following El Chichón. This "winter warming" was first pointed out by *Groisman* [1992] and later elucidated by *Robock and Mao* [1992] and *Graf et al.* [1993] and is thought to be associated with an indirect change in atmospheric circulation that is common following volcanic eruptions (see section 4.3).

Comparison of the ensemble mean model response with the observed climate anomalies (plates 1 and 2—middle panels) gives some idea of the accuracy of the model in simulating climate anomalies associated with volcanic eruptions, as well as giving some assessment of the potential for making predictions of climate. However, it should be reiterated that the observations are composed of the response to the volcanic radiative perturbation together with anomalies associated with chance climate fluctuations, and hence when the former are of a similar or lesser order of magnitude than the latter, the agreement will often be far from perfect. However, there are some qualitative agreement between the model ensemble mean predictions and the observations. The broad pattern of winter warming in northern Eurasia following El Chichón is captured qualitatively together with a tropic-wide pattern of cooling. The warmer than average temperatures in North America are not predicted by the model and are more likely due to the large El Niño event which occurred concurrently with the volcanic eruption. This is a clear example of how climate noise may obscure the volcanic signal. The model prediction of near

global scale cooling in the summer following El Chichón appears to verify less well with large-scale patterns of warmer than average temperatures observed at that time – again random climate fluctuations can spoil a simple-minded forecast based on the ensemble mean. For Pinatubo, the model predicts a more geographically confined pattern of Eurasian winter warming than actually occurred, although this could also be down to chance. Again, the ensemble mean prediction does not verify well over North America which is warmer than average in the observations. The summer temperatures following Pinatubo show near global cooler than average temperatures (with the exception of North Western Europe) as indicated by the model ensemble mean. The greater radiative forcing associated with Pinatubo results in a more robust pattern of cooling than was the case for El Chichón.

Performing an ensemble of simulations allows the examination of the PDFs of climate variables following a volcanic eruption. There are many ways to cut the PDF (e.g. into three equal probability terciles or by examining the tails of the distribution for extreme events) but all are dependent on the particular sensitivities of the individual user of the climate forecast. One of the simplest methods of examining the PDF is to look for anomalies which are either greater or less than the climatological mean (in this case the seasonal mean for the 5 years prior to the eruption). The probability of cooler than average temperatures in the winter and summer seasons following El Chichón and Pinatubo are shown in plates 1–2 (lower panels). These figures reflect the pattern of response shown in the ensemble mean figures, but also give some indication of the magnitude of the response with respect to the normal climatological variation of surface temperature. They are also the type of forecast map that might be issued following an explosive volcanic eruption. For this type of probability measure, there is a climatological probability of 0.5 and hence the greater the difference between the forecast probability from 0.5, the more confidence there is in the forecast and the greater the chance of the forecast user having to act upon that forecast. For the summer season following both El Chichón and Pinatubo, there is a near global pattern of a greater than average chance of cooler temperatures with probabilities reaching >0.8 in some regions. As in the ensemble mean, for the winter season the cooler than average pattern is disrupted by a reduced probability (i.e. <0.5) of cooler than average conditions (and hence an increase in the probability of warmer than average conditions) in the northern mid-high latitudes.

The verification of such probabilistic forecasts is difficult. For example, for a single event such as the prediction of cooler than average temperatures and a reality of warmer

than average temperatures, it is impossible to say if this was a bad forecast or if the forecaster was just unlucky. When the forecast and climatological PDF overlap (e.g. fig 1), even if the forecast is biased cold, there will still be a finite probability of warmer than average conditions. In weather forecasting, the usual way of verifying probabilistic forecasts is to consider many such cases and examine the average skill of a forecast system (e.g. by counting the number of 3 day forecasts for which the observations fall within the predicted range). Here only two volcanic eruptions are considered and it is difficult to make meaningful probabilistic verification scores. However, it is possible to draw some conclusions by averaging over all grid points.

Tables 1 and 2 show a simple form of probabilistic verification skill score for the model predictions of El Chichón and Pinatubo. For these measures, i.e. the verification of the sign of the predicted temperature anomaly in 5°x5° longitude-latitude grid boxes, there are only a few cases in which scores are significantly larger than the 50% score that would be obtained, on average, for a completely random forecast obtained by tossing a coin. For predictions of cooler than average temperatures, there are scores of around 60–70% in the seasons following El Chichón meaning that of all the grid boxes in which the temperature was predicted to be cooler than average, only 60–70% turned out to actually be cooler than average. Skill scores for predictions of cooler than average temperatures are larger following Pinatubo,

reaching 86% in the summer of 1992. Verifying predictions of one sign can be misleading as a prediction that stated that all grid boxes were to be cooler than average would result in a skill score of 100%. A more equitable measure is of the number of grid boxes in which the sign of the observed temperature anomaly was predicted correctly (column 5 in tables 1 and 2). These skill scores are in the region of 50% for the El Chichón eruption, and hence similar to what would be obtained by random forecasts, and rise only above the 60% level in the summer and autumn of 1992 following Pinatubo. For this measure, a random forecast would have performed just as well.

There are two potential reasons for these low verification scores. The model may be in error (i.e. the formulation of the model may be incorrect, having both systematic and random errors or there may be errors in the volcanic forcing) or chance climate fluctuations may have obscured the volcanic signal. The latter source of error may be examined by substituting one of the model ensemble members as the truth and recalculating the verification scores. In this way the potential for model error is eliminated by working in a "perfect model" environment. The range of skill scores obtained by substituting each ensemble member in turn is also shown in tables 1–2. In many cases, and in particular for the skill of the prediction of the sign of the anomaly (column 5), the verification of the observed temperature is bounded by the range of perfect model scores. This indi-

Table 1. Simple verification scores for the predictions of seasonally averaged surface air temperature following the eruption of El Chichón. Columns 1 and 2 indicate the year and season of the verification. Column 3 is the percentage of 5°x5° grid boxes in which the temperature was greater than average and the model predicted that this would be the case. Column 4 is the percentage of 5°x5° grid boxes in which the temperature was less than average and the model predicted that this would be the case. Column 5 is the combined skill score for anomalies of both sign i.e. the percentage of grid boxes in which the correct sign of temperature anomaly was predicted (an entirely random forecast would have an average skill of 50% in columns 3–5). A low verification score may either indicate errors in the model, or "bad luck" if the volcanic signal is obscured by some random climate fluctuation. These different error types may be separated by substituting each member of the ensemble in turn as the truth and recalculating the verification score (figures in brackets). Where the verification score for the observations lies within the "perfect model" bounds, it is more likely that the low score is simply due to "bad luck". Where the verification score is lower than indicated by the perfect model bounds, there is likely to be model error.

Year	Season	Skill of predictions of > average SAT	Skill of predictions of < average SAT	Skill of prediction of sign of SAT anomalies
1982	SON	20% (24%–38%)	67% (73%–85%)	44% (46%–66%)
1982–3	DJF	49% (43%–65%)	62% (49%–68%)	53% (46%–66%)
1983	MAM	39% (29%–48%)	66% (52%–77%)	50% (42%–59%)
1983	JJA	19% (20%–35%)	73% (75%–88%)	44% (46%–68%)
1983	SON	16% (16%–34%)	62% (67%–81%)	32% (37%–63%)
1983–4	DJF	42% (31%–56%)	63% (50%–73%)	52% (41%–64%)
1984	MAM	33% (32%–50%)	53% (54%–73%)	44% (45%–61%)
1984	JJA	24% (30%–41%)	58% (62%–77%)	42% (47%–60%)
1984	SON	41% (46%–60%)	52% (49%–70%)	48% (41%–61%)
1984–5	DJ	52% (63%–75%)	22% (27%–41%)	34% (42%–59%)

Table 2. As in table 1 but for the Pinatubo eruption.

Year	Season	Skill of predictions of > average SAT	Skill of predictions of < average SAT	Skill of prediction of sign of SAT anomalies
1991	SON	49% (38%–68%)	60% (50%–70%)	55% (43%–67%)
1991–2	DJF	35% (25%–53%)	65% (59%–80%)	48% (45%–67%)
1992	MAM	13% (15%–35%)	66% (74%–84%)	41% (45%–66%)
1992	JJA	9% (10%–20%)	86% (87%–96%)	62% (56%–76%)
1992	SON	14% (15%–28%)	77% (79%–88%)	64% (48%–68%)
1992–3	DJF	22% (26%–48%)	55% (62%–82%)	38% (47%–65%)
1993	MAM	19% (21%–33%)	69% (72%–81%)	45% (43%–64%)
1993	JJA	15% (22%–38%)	64% (71%–80%)	41% (46%–67%)
1993	SON	25% (29%–54%)	58% (58%–77%)	47% (46%–67%)
1993–4	DJF	45% (44%–65%)	46% (42%–65%)	46% (43%–59%)

cates that the latter source of error ("bad luck") dominates: The forecast of the sign of temperature anomalies in 5°x5° grid boxes is more often spoilt by chance climate fluctuations that mask the volcanic signal than by systematic model errors. However, there is some indication from tables 1–2, that there is still the potential for model improvement.

Because large-scale climate perturbations such as volcanic eruptions produce large-scale patterns of climate anomalies, and because economies are now often organized across many countries, it is perhaps better to examine the skill of the predictions averaged over larger geographical regions. It is also the case that, because of the numerical formulation of the fluid dynamical solvers incorporated in GCMs, the model should better represent scales representative of a number of grid-boxes. Time series of a selection of global and large-scale averages of temperature are shown in Figures 3-4 for the ensemble simulations and the observations. Again, the spread of the individual ensemble members highlight the range of potential trajectories that the climate system might follow after the eruption of a volcano—there is no single pre-determined path. Indeed, this is clearly highlighted in the case of global mean land surface temperatures following El Chichón (fig 3 upper panel). The ensemble mean of the model simulations suggest a global cooling for 2–3 years following the eruption (as would be expected), whereas the real world produced a global warming. This warming is, in part due to the large El Niño event that occurred at this time (El Niños are associated with warmer than average years globally), but is also due to the large Eurasian warming (plate 1).

Following El Chichón (Figure 3), there are modest, yet significant, displacements of the PDF of surface air temperature in the summer season for all the large-scale regions shown. For Eurasian land SAT, the mean of the PDF is displaced to −0.3°C which is approximately one standard deviation of the climatological PDF. This results in, for example, a 20% prob-

ability of a temperature anomaly of less than −0.5°C and a less than 1% probability of a temperature anomaly of greater than 0.5°C (in comparison with the 4% climatological chance of either). In reality, the mean temperature of the Eurasian continent was about normal, despite the increased probability of cooler than average conditions. This was then a perfectly valid forecast as the observations lie well within the bounds of the forecast PDF—again this highlights the problem of verifying probabilistic forecasts. In the winter season, there are generally smaller shifts of the PDFs with only that for Asian land SAT statistically significant. For Eurasian land SAT there is a small shift toward warmer conditions, but nothing that would suggest a significant increase in the probability of warmer than average conditions. As shown in plate 1, Eurasian land SATs were significantly warmer than normal but these ensemble simulations suggest that this could easily be just a chance fluctuation in climate. Winter warming is discussed further below.

Biases in forecast PDFs are larger for the Pinatubo case (Figure 4). For the summer season, the probability of Eurasian land SAT anomalies of less than −0.5°C is 42% and the probability of temperature anomalies of greater than 0.5°C is less than 1%. In this case, the observed temperature anomaly was −0.6°C, significantly cooler than climatology. The same is true for the other indices shown, although it is worth noting that this apparently good forecast verification (i.e. negative anomalies when negative anomalies are predicted) could equally be explained by chance fluctuations in climate, as was the poor forecast of winter warming following El Chichón. The key message from Figures 3–4 is that, in order for a definitive forecast such as "a cooler summer will follow a large volcanic eruption" the forecast PDF must be significantly displaced with respect to the climatological PDF. When the forecast PDF and climatological PDF overlap, which is the case for both El Chichón and Pinatubo, even the forecasting of relatively large regional averages

such as the Eurasian continent, can be affected by random climate fluctuations which can mask the volcanic signal.

It seems then that the model predictions verify better when looking at large-scale averages of temperature. Recomputing the verification skill scores of tables 1 and 2 for overlapping regions of size 25°x25° longitude-latitude, leads to better predictions of the sign of temperature anomalies with as much as 82% of such regions having the correct sign of anomalies predicted for the summer season following Pinatubo. Model predictions can be much more skillful at these spatial scales, both because models are generally more believable at scales of many grid-boxes and because the volcanic signal is less likely to be obscured by the noise of natural climate fluctuations.

It is clear from the analysis of these experiments that care should be taken in making and interpreting climate forecasts following volcanic eruptions. Even for large eruptions such as Pinatubo, which brought about significant global cooling, the predictions that would have been made with the climate model used here of surface air temperatures at the regional scale (i.e. scales of a few hundreds of kilometers) would have been of little use for those interested even in the sign of the temperature anomaly. For larger regions (e.g. continental scale) the situation as more promising as the signal is less likely to be obscured by the noise of natural climate fluctuations. However, for the smaller eruption of El Chichón, this indeed was the case showing that even forecasts of near global scale temperatures can go wrong.

3.2. Mean Sea Level Pressure

As was stated above, MSLP is not directly affected by changes in radiative forcing following a volcanic eruption but may, due to dynamical effects, be indirectly influenced by changes in atmospheric temperature [*Robock and Mao*, 1992; *Graf et al.*, 1993; *Robock and Mao*, 1995]. Changes atmospheric flow patterns induced by changes in temperature (and revealing themselves in changes in MSLP) may further enhance or dampen the volcanic temperature signal. The ensemble-mean MSLP anomaly response in the northern hemisphere winters following El Chichón and Pinatubo is shown in plate 3, together with the observed MSLP anomalies and the ensemble probabilities of lower than average MSLP. The patterns of MSLP are more complicated than the surface temperature patterns, reflecting the indirect nature of the forcing of the pattern. There are, however, some features that are predicted by the model. Following El Chichón, the model predicts a positive NAO-like pattern of MSLP in the North Atlantic region with lower pressure in the polar-regions and higher pressure further south. This pattern is approximately what happened in reality and is, in part, responsible for the pattern of warming predicted by the model (plate 2). However, the amplitude of the pattern is significantly larger in reality and results in a stronger observed winter warming than was predicted by the model. In the Pacific basin, the model predicts lower than average pressure in a pattern that is similar to the Pacific North American (PNA) pattern more generally associated with an El Niño event. This is indeed what happened in reality, although separating the component of the observed signal which is a result of El Niño from that resulting from El Chichón is difficult.

Despite the greater radiative forcing following Pinatubo, the model predicted MSLP response is paradoxically weaker than in the case of El Chichón. In reality, there was higher than average pressure over western Europe in the winter

Table 3. Verification skill scores for the predicted sign of temperature anomalies in overlapping regions of size 25°x25° longitude-latitude (as in tables 1–2), i.e. the percentage of 25°x25° regions in which the sign of the observed temperature was correctly predicted by the model. The figures in brackets show the range of scores obtained by substituting each ensemble member for the observations.

Year	Season	Skill of prediction of sign of SAT anomalies	Year	Season	Skill of prediction of sign of SAT anomalies
1982	SON	43% (34%–81%)	1991	SON	65%(43%–75%)
1982–3	DJF	58% (41%–74%)	1991–2	DJF	34% (32%–83%)
1983	MAM	60% (41%–70%)	1992	MAM	42% (35%–83%)
1983	JJA	45% (45%–77%)	1992	JJA	82% (55%–97%)
1983	SON	28% (38%–70%)	1992	SON	78% (44%–89%)
1983–4	DJF	69% (40%–68%)	1992–3	DJF	27% (39%–75%)
1984	MAM	55% (42%–72%)	1993	MAM	50% (33%–83%)
1984	JJA	45% (39%–77%)	1993	JJA	55% (40%–83%)
1984	SON	55% (24%–70%)	1993	SON	52% (37%–69%)
1984–5	DJF	18% (27%–72%)	1993–4	DJF	64% (32%–73%)

0.1 0.2 0.3 0.4 0.5 0.6 0.7 0.8 0.9

MSLP Anomaly (hPa)

0

MSLP Anomaly (hPa)
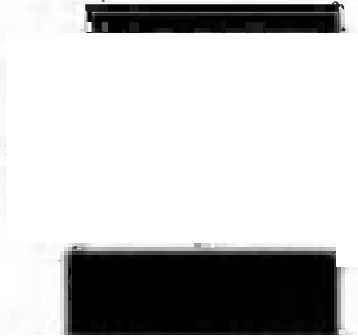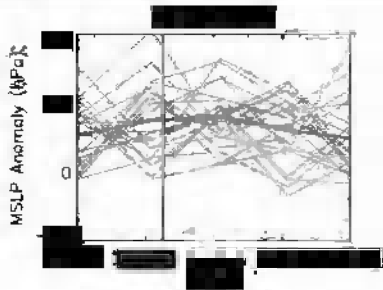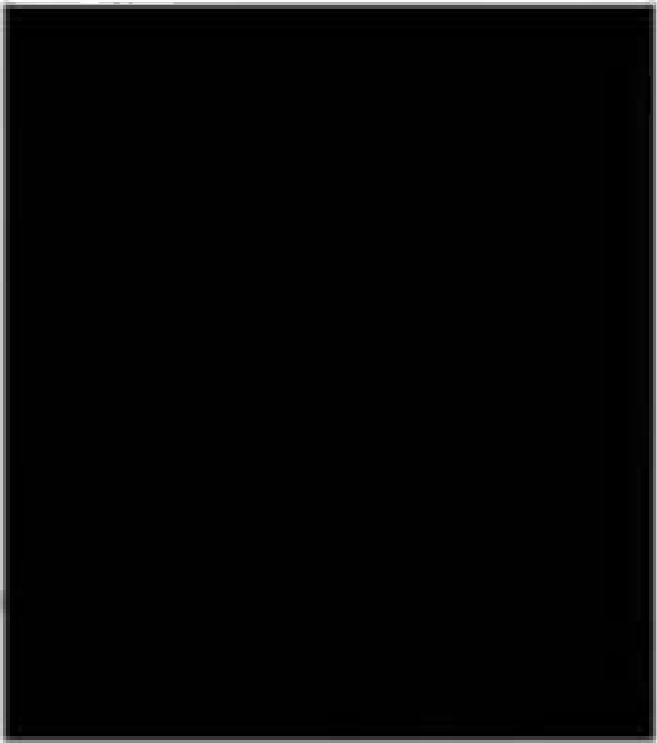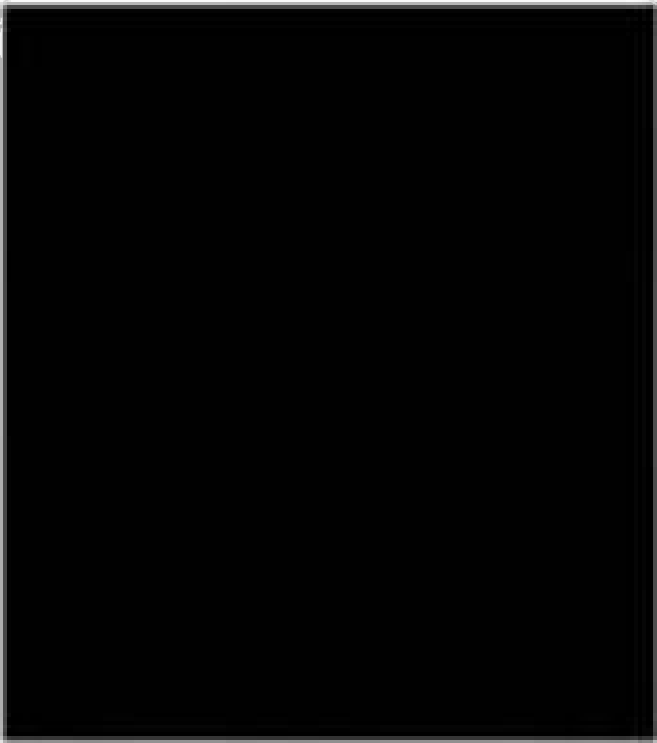
of benefit to society. In this paper, the potential for such forecasts has been quantified by examining retrospective predictions of climate following the eruptions of El Chichón (1982) and Pinatubo (1991).

Because climate forecast are inherently probabilistic, climate predictability only arises when a phenomena can significantly modify the probability density function (PDF) of some climate variable. Eruptions of the size of El Chichón and Pinatubo can significantly shift the PDFs of climate variables such as surface air temperature and mean sea level pressure, and the shifts are more robust for large continental scale seasonal averages. Care should however be taken in utilizing such climate forecasts as the volcanic signal can easily be contaminated or even completely obscured by the "noise" of natural climate fluctuations which occur regardless of the eruption.

It is clear however, that even for the simple verification presented here, there is some utility in making a forecast following the next big eruption. Also, the skill scores used in this study are rather crude and there is a danger that they may mask some aspect of the predictions that, in fact, has very high skill e.g. the prediction of extreme low temperatures. Forecast verification should always be a user driven exercise as users are often interested in different climate variables, different seasons and may also be accepting of different levels of accuracy. Only the end-user of the forecasts can really judge how useful a forecast was or might be in the future.

It is also worth putting the prediction of the climatic impacts of a volcanic eruption in the context of other climate forecasting efforts. As was stated in the introduction, the main predictable climate phenomena is the El Niño Southern Oscillation (ENSO), which only weakly affects regions such as Europe during large ENSO events [Mathieu et al., 2002]. Two key advantages of volcanic forecasts in comparison with ENSO forecasts are that volcanic forecasts may be of use in geographical regions remote from ENSO influence, and that ENSO is only predictable (on average) for a few seasons into the future [Collins et al., 2002] whereas the volcanic aerosol cloud may persist for a few years providing useful predictability. In addition, forecasts of other climate phenomena such as the North Atlantic Oscillation (NAO) are in their infancy and may, perhaps, never even be realized [Collins, 2002]. Volcanoes may yet prove to be a useful addition to the armory of the seasonal climate forecaster.

What is clear is that there should be continued effort in observing, modelling and understanding the climate impacts of volcanic eruptions. In addition, it may perhaps be wise for forecasting centers to develop the capacity to operationally forecast the impact of the next big eruption. This should include developing the ability to adequately simulate stratospheric dynamics and to transport sulphate aerosol from the source region. Because of the potential contamination of the volcanic signal by natural climate fluctuations, it is also be important to start forecasts from initial conditions appropriate to the current observed state of the climate system (principally the ocean).

REFERENCES

Andrononva, N. G., E. V. Rozanov, F. Yang, M. E. Schlesinger and G. L. Stenchikov, Radiative forcing by volcanic aerosols from 1850 to 1994. *J. Geophys. Res.*, 104, 16,807-16,826, 1999.

Basnett, T. and D. E. Parker, Development of the global mean sea level pressure data set, *Hadley Centre Technical Note*, 79, p61, 1997.

Bluth, G. J. S., S. D. Doiron, S. C. Schnetzer, A. J. Kruger and L. S. Walter, Global tracking of the SO2 clouds from the June 1991 Mount Pinatubo eruptions, *Geophys. Res. Lett.*, 19, 151-154, 1992.

Collins, M., Understanding Uncertainties in the response of ENSO to Greenhouse Warming, *Geophys. Res. Letts.*, 27, 3509-3513, 2000.

Collins, M., D. Frame, B. Sinha, and C. Wilson, C., How far ahead could we predict El Niño? *Geophys. Res. Letts.*, 29, 10.1029/2001GL013919, 2002.

Collins, M. and M. R. Allen, On assessing the relative roles of initial and boundary conditions in interannual to decadal climate predictability, *J. Climate*, 15, 3104-2109, 2002.

Collins, M., S. F. B. Tett, and C. Cooper, The internal climate variability of HadCM3, a version of the Hadley Centre coupled model without flux adjustments, *Clim. Dyn.*, 17, 61-81, 2001.

Gordon, C., C. Cooper, C. A. Senior, H. Banks, J. M. Gregory, T. C. Johns, J. F. B. Mitchell, and R. A. Wood, The simulation of SST, sea ice extents and ocean heat transport in a version of the Hadley Centre coupled model without flux adjustments. *Clim. Dyn.*, 16, 147-168, 2000.

Graf, H.-F., I. Kirchner, A. Robock, and I. Schult, Pinatubo eruption winter climate effects: Model versus observations, *Clim. Dyn.*, 9, 83-91, 1993.

Groisman, P. Y., Possible regional climate consequences of the Pinatubo eruption: An empirical approach, *Geophys. Res. Lett.*, 19, 1603-1606, 1992.

Hirono, M., On the trigger of El Niño-Southern Oscillation by the forcing of early El Chichón volcanic aerosols, *J. Geophys. Res.,* 93, 5364-5384, 1988.

Houghton, J. T., Y. Ding, D. J. Griggs, M. Noguer, P. J. van der Linden, X. Dai, K. Maskell, and C. A. Johnson (Eds.), Climate Change 2001: The Scientific Basis. *Contribution of Working Group I to the Third Assessment Report of the Intergovernmental Panel on Climate Change,* Cambridge University Press, 2001.

Hurrell, J. W., Decadal trends in the North Atlantic Oscillation: Regional temperatures and precipitation, *Science,* 268, 676-679, 1997.

Jones, P. D., Hemispheric surface air temperature variations: A reanalysis and update to 1993, *J. Clim.,* 7, 1794-1802, 1994.

Kirchner, I., G. L. Stenchikov, H.-F. Graf, A. Robock, and J. C. Antuna, Climate model simulations of winter warming and summer cooling following the 1991 Mount Pinatubo volcanic eruption, *J. Geophys. Res.,* 104, 19,039-19,055, 1999.

Lorenz, E. N., The physical basis of climate and climate modelling, in Climate Predictability, *GARP Publication Series,* 132-136, 1975.

Lorenz, E. N., Atmospheric predictability experiments with a large numerical model, *Tellus,* 34, 505-513, 1982.

Mao, J. and A. Robock, Surface air temperature simulations by AMIP general circulation models: Volcanic and ENSO signals and systematic errors. *J. Clim.,* 11, 1538-1552, 1998.

Mathieu, P-P., R. T. Sutton, B. Dong, and M. Collins, M., Predictability of winter climate over the North Atlantic European region during ENSO events. Submitted to *J. Clim.*

Robock, A. and M. P. Free, Ice cores as an index of global volcanism from 1850 to the present, *J. Geophys. Res.,* 100, 11,549-11,567, 1995.

Robock, A. and Y. Liu, The volcanic signal in the Goddard Institute for Space Studies three-dimensional model simulations, *J. Clim.,* 7, 44-55, 1994.

Robock, A. and J. Mao, Winter warming from large volcanic eruptions, *Geophys. Res. Lett.,* 19, 2405-2408, 1992.

Robock, A. and J. Mao, The volcanic signal in surface temperature observations, *J. Clim.,* 8, 1086-1103, 1995.

Robock, A. and M. Matson, Circumglobal transport of the El Chichón volcanic dust cloud, *Science,* 221, 195-197, 1983.

Robock, A., K. E. Taylor, G. L. Stenchikov, and Y. Liu, GCM evaluation of a mechanism for El Niño triggering by the El Chichón ash cloud, *Geophys. Res. Lett.,* 22, 2369-2372, 1995.

Robock, A., Volcanic Eruption and Climate, *Rev. in Geophys.,* 38, 191-219.

Robock, A., Stratospheric Forcing Needed for Dynamical Seasonal Prediction, *Bull. Amer. Met. Soc.,* 82, 2189-2191, 2001.

Sato, M., J. E. Hansen, M. P. McCormick, and J. B. Pollack, Stratospheric aerosol optical depths, 1850-1990, *J. Geophys. Res.,* 98, 22,987-22,994, 1993.

Self, S., M. R. Rampino, J. Zhao, and M. G. Katz, Volcanic aerosol perturbations and strond El Niño events: No general correlation, *Geophys. Res. Lett.,* 24, 1247-1250, 1997.

Stott, P. A., S. F. B. Tett, G. S. Jones, M. R. Allen, J. F. B. Mitchell and G. J. Jenkins, External control of 20th century temperature by natural and anthropogenic factors, *Science,* 290, 2133-2137, 2000.

Stott, P. A. and J. A. Kettleborough, Origins and estimates of uncertainty in predictions of twenty-first century temperature rise, *Nature,* 416, 723-726, 2002.

Stenchikov, G. L., I. Kirchner, A. Robock, H.-F. Graf, J. C. Antuna, R. G. Grainger, A. Lambert and L. Thomason, Radiative forcing from the 1991 Mount Pinatubo volcanic eruption. *J. Geophys. Res.,* 103, 13,837-13,857, 1998.

Stowe, L. L., R. M. Carey, and P. P. Pellegrino, Monitoring the Mount Pinatubo aerosol layer with NOAA 11 AVHRR data, *Geophys. Res. Lett.,* 19, 159-162, 1992.

Strong, A. E., Monitoring El Chichón aerosol distribution using NOAA-7 satellite AVHRR sea surface temperature observations, *Geofis. Int.,* 23, 129-141, 1984.

Matthew Collins, Centre for Global Atmospheric Modelling, Department of Meteorology, University of Reading, Earley Gate, Reading, UK, RG6 6BB.

The Campanian Ignimbrite Eruption, Heinrich Event 4, and Palaeolithic Change in Europe: a High-Resolution Investigation

Francesco G. Fedele

Sezione e Museo di Antropologia, Università di Napoli Federico II, Naples, Italy

Biagio Giaccio

Istituto di Geologia Ambientale e Geoingegneria, CNR, Rome, Italy

Roberto Isaia and Giovanni Orsi

Osservatorio Vesuviano, INGV, Naples, Italy

The Campanian Ignimbrite (CI) eruption from the Phlegraean Fields Caldera, southern Italy, represents one of the largest late Quaternary volcanic event. Its recent dating at 39,280±110 yr BP draws attention to the occurrence of this volcanic catastrophe during a time interval characterized by biocultural modifications in western Eurasia. These included the Middle to Upper Palaeolithic transition and the supposed change from Neandertal to "modern" *Homo sapiens* anatomy, a subject of continuing investigation and controversy. The paper aims to clarify the position and relevance of the CI event in this context. At several archaeological sites of southeastern Europe, the CI ash separates the cultural layers containing Middle Palaeolithic and/or "Earliest Upper Palaeolithic" assemblages from the layers in which Upper Palaeolithic industries occur. At the same sites the CI tephra coincides with a long interruption of occupation. The palaeclimatic records containing the CI products show that the eruption occurred just at the beginning of Heinrich Event 4 (HE4), which was characterized by extreme climatic conditions, compared to the other HEs. From the observation of this concurrence of factors, we advance the hypothesis of a positive climate-volcanism feedback triggered by the co-occurrence of the CI eruption and HE4 onset. Both the environmental and cultural data available for a c.5000-year interval on either side of the event, suggest that a reappraisal of the identity and destiny of the archaeological industries representing the so-called Middle to Upper Palaeolithic transition is in order. This might force a reassessment of the Upper Palaeolithic notion as traditionally employed.

INTRODUCTION AND CONTEXT

The climate of the Last Glacial is known to have been highly unstable and much more sensitive to feedback mech-

anisms than the Holocene one [*Ganopolski* and *Rahmstorf,* 2001]. However, our present knowledge of the volcanism-climate system sensitivity is mostly based on volcanic perturbations of modern climate alone, an obviously limited approach, in that the operation modes and the sensitivity of the Last Glacial volcanism-climate system could have been significantly different from those of the present [*Zielinski,* 2000]. A further limitation is inherent in the moderate magnitude of the Holocene eruptions compared to some very large Late Pleistocene events. This has led to controversy about how the volcanism-climate system was operating during the Last Glacial, and about its effects on human ecosystems, particularly concerning the largest volcanic events known, such as the mega-eruption of Toba (Sumatra, c.74,000–71,000 yr BP [*Rampino* and *Self,* 1992; 1993; *Zielinski,* 2000; *Oppenheimer,* 2002]).

Extensive deposits of about 40,000 yr BP formally named the Campanian Ignimbrite (CI) have been recognized as the product of the largest volcanic eruption in the Greater Mediterranean during the past 200,000 years [*Barberi et al.,* 1978]. This ultra-Plinian event connected with the Phlegraean Fields Caldera, Campania, southern Italy, ejected no less than 200 km³ of magma (dense rock equivalent; DRE), according to a recently revised but still conservative estimate (see below). An event of this magnitude is second only to the Toba eruption, admittedly much larger than the CI in terms of DRE, with a factor-of-fifteen difference, for which major effects on global climate and living systems have been advanced [*Zielinski et al.,* 1996b; *Rampino* and *Ambrose,* 2000; *Huang et al.,* 2001].

For the purpose of the present paper, the Greater Mediterranean area is taken to cover most of the regions in Figure 1, including in its eastern sector the Balkans, Anatolia, and the Pontic perimeter (Black Sea). Northeastern Africa and the Levant might have been affected by the eruption as well. Petrologically identified CI ash layers have been reported from both inland and marine sediments throughout most of these regions, from Italy to southern Russia [e.g. *Narcisi* and *Vezzoli,* 1999]. The ubiquitous Y5 tephra layer is the best defined CI deposit in marine sequences of the eastern Mediterranean Sea.

Detailed mapping of stratigraphic occurrences of the CI in both archaeological and non-cultural sequences has already shown that the facts and effects related to the CI are clearly significant for a number of problems, exceeding the sheer interest for volcanology and local archaeology [*Fedele et al.,* 2002]. A major area of significance is human settlement and ecology. In southern Italy and possibly some adjoining regions to the east (Greece and the Balkans, Bulgaria), the CI precisely coincides with a widespread

abandonment of sites and locales, as abrupt as the stratigraphic resolution of well-excavated sites permits to determine. The marked hiatus is ended by the appearance of the first unquestionable Upper Palaeolithic traditions millennia later. Previously unrecognized evidence even suggests that a detailed reconstruction of environmental and human responses to the CI crisis is likely to have implications for realistically describing and possibly understanding one of the most conspicuous transformations in Old World prehistory: the Middle to Upper Palaeolithic transition, and the origin or origins of the Upper Palaeolithic specifically.

Chronology is relevant to the problem. The recent dating of the CI eruption at 39,490–39,170 yr BP by a series of ^{40}Ar/^{39}Ar measurements, supported by calibration of available ^{14}C dates (see below), draws attention to the fact that this volcanic catastrophe precisely occurred during an interval of several millennia characterized by a series of fast-paced modifications in human societies. Such modifications concern both the cultural and the biological spheres, although with different timing and with no obligatory link between the two. This general process is apparent in the Greater Mediterranean and across temperate Europe the area we are especially dealing with here but can be recognized over several geographic areas of Eurasia, implying both a degree of complexity and a yet undefined range of regional circumstances. Any generalization is obviously premature.

At the basic level, however, the occurrence of a major volcanic event at such point in time, during a generally glacial interval and within an incipient or ongoing process of biocultural change, necessarily demands that its potential implications for humans be closely examined. The European situation c.40,000–35,000 yr BP probably comprised a fairly enlarged human biomass by comparison with an earlier part of the Late Pleistocene (this term sensu *Klein* [1999]), a hominin population more widely based both ecologically and geographically, and interacting in more complex ways with resources and landscape. Some discrete developments in adaptive systems technology, but also ideology and perhaps social organization seem now to have appeared at various times well before the c.40,000 BP "cultural divide", as convincingly summarized by *Gamble* [1999], among others. An outline is presented below, but it can be noted here that the data may hint to a rich and fairly dynamic culture and population scene at the point in time and space when the CI occurred.

In a positive effort to avoid prejudgmental terminology, the complicated suite of cultural and biological changes first apparent between about 45,000 and 35,000 yr BP (or roughly between 40,000–33,000 ^{14}C yr BP, uncalibrated) will be
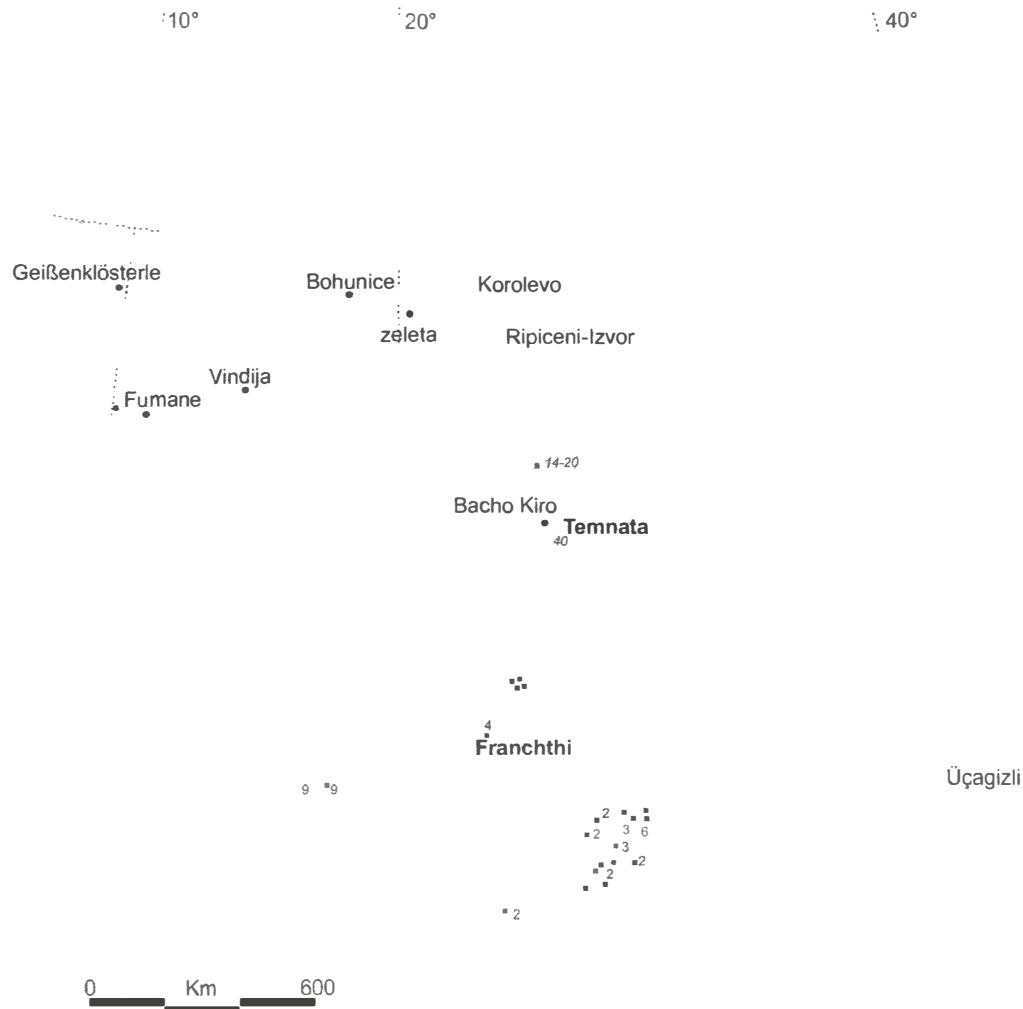
Figure 1. Geographic distribution of the Campanian Ignimbrite deposits, including archaeological and sampling sites mentioned in the paper. Solid squares: CI tephra occurrences and related thickness in cm (in italics if reworked) [modified from *Cornell et al.*, 1983; *Amirkhanov et al.*, 1993; *Cini Castagnoli et al.*, 1995; *Narcisi and Vezzoli*, 1999; *Fedele et al.*, 2002; *Upton et al.*, 2002]. Dotted area in central Italy: distribution of the CI-derived paleosol (CI-PS [*Frezzotti and Narcisi*, 1996]). Solid triangles: archaeological sites with CI ash layer. Blank triangles: archaeological sites with ash layer attributed to the CI on the basis of cultural-stratigraphic position and ^{14}C dating (*Fedele et al.*, 2002; *Giaccio and Isaia*, on file). Solid circles: selected European Palaeolithic sites within the area potentially affected by the CI air-fall.

neutrally termed the European Late Pleistocene shift [*Fedele et al.*, 2002]. In the cultural sphere, the Mousterian tool-making traditions of the so-called Middle Palaeolithic eventually changed into the industries or cultures of the Upper Palaeolithic, which many authors regard as characterized by an unprecedented explosion of artifacts reflecting ideological purposes. In broad temporal concordance, a widely accepted shift has been noted in biological populations, where the Neandertal anatomical type appears to have

been substituted by fully "modern" humans, a supposedly unrelated morphology (formal taxonomic names are avoided). The interplay of similarities and differences across the shift is a subject of intense and continuing controversy [e.g. *Carbonell* and *Vaquero*, 1996; *Clark* and *Willermet*, 1997; *Fox*, 1998; *Akazawa et al.*, 1998; *Klein*, 1999; *Zilhão* and *D'Errico*, 1999; *Bar-Yosef* and *Pilbeam*, 2000; *Straus* and *Bar-Yosef*, 2001]. No consensus yet exists as to whether the observed changes in both cultural and biological domains

should be better described as evolution or replacement, i.e. continuity or discontinuity.

Although a majority of physical anthropologists and geneticists favours discontinuity, some researchers are considering the possibility of biological continuity in human ancestry across the Late Pleistocene shift [cf *Fox*, 1998; *Omoto* and *Tobias*, 1998; *Churchill* and *Smith*, 2000; *Wolpoff et al.*, 2001]. Some authors would stress that Neandertal and modern human remains, genetics, and tool traditions all show intriguing continuities [*Gowlett*, 2001]. Not only a temporal overlap between Neandertal and modern anatomies is being demonstrated in several regions from Portugal to the Near East, but plausible instances of "hybrid" anatomies hence genetic continuum? demand explanation. At the moment, one can only point out "the apparent complexity of population relationships during the late Pleistocene, especially in the circum-Mediterranean region" [*Quam* and *Smith*, 1998, 418; cf *Smith et al.*, 1995].

Important as it is in human evolution, the biological problem of the continuity or discontinuity between Neandertals and "modern" humans is outside the scope of this paper. For the time being, in fact, it is peripheral to the project: there is no expectation that a contextual study of the CI will produce data or insights directly relevant to the solution of the biological problem; the scale and scope of problem and project are simply not comparable. On the cultural side, however, the issues involved will be touched upon briefly, as they have a more immediate bearing on the archaeological context of the CI. The inherently misleading nature of some terms and paradigms in Palaeolithic studies needs also to be addressed. Several aspects of the CI context volcanological, stratigraphic and environmental are being redefined on the basis of original evidence as so far provided by a high-resolution investigation of the CI and its impact on ecosystems.

Crucial to many fundamental aspects of the interrelationships among CI, climate, and Palaeolithic change is the precise placement of the eruption within the archaeological and environmental sequences of the regions concerned. This subject is extensively treated in the paper, with due attention for stratigraphic resolution as well as factors at the regional and super-regional scale. A specific section is devoted to the identification of the CI signal in the Greenland GISP2 volcanogenic record. This finding provides a CI age in ice core years, the eruption's precise position within the superb palaeoclimatic record of the Greenland isotope stratigraphy, and preliminary information for a quantitative estimate of the eruption's stratospheric loading.

An evaluation of the climatic impact of the CI eruption is advanced through detailed analysis of several palaeoclimatic records spanning the CI-centred interval. All rec-

ords show that the CI eruption occurred during a sensitive climatic frame and was followed by an unusually marked cooling, hypothetically triggered by positive feedback mechanisms. Furthermore, an appreciation of the anomalous behaviour of radiocarbon in the c.42,000–34,000 calibrated yr BP timespan (see also below), in conjunction with the occurrence of the CI eruption and other environmental factors, has several obvious implications for the chronology, hence the rhythms and plausible processes, involved in the European Late Pleistocene shift. What follows is a survey of results from the initial phase of the project, partly based on a critical evaluation of data and literature, and accompanied by some speculations about its attainable prospects.

AGE OF THE CAMPANIAN IGNIMBRITE

Unless stated otherwise, dates in this paper express real time in years before present (yr BP), with the exception of ^{14}C dates, which are explicitly reported as uncalibrated measurements.

The best current estimate for the CI age is $39,280\pm110$ yr BP, derived from 36 high-precision single-crystal $^{40}Ar/^{39}Ar$ measurements from 18 samples of ignimbritic deposits collected at twelve different outcrops in the dispersal area of the CI pyroclastic flows [*De Vivo et al.*, 2001]. Three previous $^{40}Ar/^{39}Ar$ measurements yielded $37,100\pm400$ yr BP [*Deino et al.*, 1994].

Two further $^{40}Ar/^{39}Ar$ dating have been performed on samples of the CI distal tephra in Tyrrhenian Sea sediments and in the Monticchio lacustrine sequence, southern Italy. In the Tyrrhenian Sea, 51 laser-heating analyses of sanidine crystals from the C-13 (= CI; = Y5) tephra layer gave ages within the $25,000\pm70,000$–$112,000\pm7000$ yr BP range, with a large subpopulation of measurements (24) defining an isochrone of $41,000\pm2100$ yr BP [*Ton-That et al.*, 2001]. At Lago Grande di Monticchio, 17 $^{40}Ar/^{39}Ar$ measurements of the CI ash layer performed on single feldspar grains yielded $36,000\pm1000$ yr BP [*Ramrath et al.*, 1999, and references therein]. However, the CI tephra layer was referred to a calendar age of 32,970 yr BP according to the varve-counting Monticchio age model [*Zolitschka* and *Negendank*, 1996].

Current radiocarbon determinations place the CI event at $35,600\pm150$ and $33,200\pm600$ ^{14}C yr BP, both dates obtained from a single carbonized branch embedded in the CI pyroclastic flow [*Deino et al.*, 1994]. Previous measurements on carbonized wood embedded in the CI gave dates scattered between c.27,000 and c.42,000 ^{14}C yr BP, with a frequency peak at c.35,000 ^{14}C yr BP [*Scandone et al.*, 1991, and references therein]. The radiocarbon age of the paleosol and carbonized wood underlying the basal pumice of the CI

layer is similarly scattered (27,000–39,000 ^{14}C yr BP), with a modal concentration between 31,000 and 34,000 ^{14}C yr BP [Scandone et al., 1991].

THE CAMPANIAN IGNIMBRITE ERUPTION

The overall size and extent of the CI eruption have been recognized long ago [Barberi et al., 1978]. Stratigraphic, grain size and compositional characteristics of proximal and distal deposits within the Campanian area, as well as flow direction detected by means of anisotropy of magnetic susceptibility studies [Rosi et al., 1987,1996; Barberi et al., 1991; Fisher et al., 1993; Orsi et al., 1996; Civetta et al., 1997; Ort et al., 1999; 2003; Pappalardo et al., 2002], show that this catastrophic eruption occurred in the Phlegraean area and was accompanied by a caldera collapse. The collapsed area was about 230 km^2 and included the present Phlegraean Fields, the city of Naples, the bay of Pozzuoli and the northwestern sector of the bay of Naples [Orsi et al., 1996].

The CI sequence includes a basal plinian fallout deposit surmounted by pyroclastic-flow units, which in proximal areas are intercalated by breccia units. The basal plinian deposit was recently investigated by Rosi et al. [1999]. It consists of a well sorted and reversely graded lower portion, followed by a well to poorly sorted and crudely stratified upper portion. Although the two portions have slight differences in dispersal axes, the whole deposit is dispersed toward the east.

The pyroclastic-flow deposits, which covered an area of about 30,000 km^2, show homogeneous sedimentological characteristics in medial and distal areas, i.e. about 10 to 80 km from the vent locality [Fisher et al., 1993]. From the base upwards, they include a very thin, discontinuous, fines-poor layer, above which lies the bulk of the ignimbrite. They are partially welded to non-welded, although they can be lithified by zeolites. The partially welded to non-welded deposits are grayish, while the zeolitised units are yellowish. The pyroclastic-flow deposits underlie much of the Campanian Plain; they also occur in isolated valleys in the Apennines, in the area of the Roccamonfina Volcano, and in the Sorrento Peninsula.

A stratigraphic and compositional study of a core—drilled north of the city of Naples—which includes four superposed pyroclastic-flow units, emplaced during the CI eruption, has given to Pappalardo et al. [2002] a unique opportunity to define the compositional features of the magma chamber, the timing of magma extraction, the withdrawal dynamics and the timing of the caldera collapse. The CI eruption was fed by a trachytic magma chamber which

included two co-genetic magmatic layers separated by a compositional gap [Civetta et al., 1997; Pappalardo et al., 2002]. The upper magma layer was more evolved and homogeneous, whereas the lower layer was less evolved and zoned.

The eruption likely began with phreatomagmatic explosions, followed by the formation of a sustained plinian eruption column, fed by simultaneous extraction of both magma layers (Figure 2a). The column reached a maximum height of about 44 km [Rosi et al., 1999]. Toward the end of this phase, due to upward migration of the fragmentation surface, reduced magma eruption rate, and/or activation of fractures, an unstable pulsating column was formed and fed only by the most evolved magma. The height of the column may have reached about 40 km maximum [Rosi et al., 1999].

This plinian phase was followed by the beginning of the caldera collapse and the generation of expanding and initially over-pressurized pyroclastic currents fed by the upper magma layer (Figure 2b). These currents moved toward the north and the south. Those moving north, surmounted the Roccamonfina Volcano (>1000 m a.s.l.) at 50 km from the vent. The southward currents reached the Sorrento Peninsula over seawater. During the following major caldera collapse, the maximum mass discharge rate was reached and both magma layers were contemporaneously tapped as an intermediate composition magma, generating further expanding pyroclastic currents which travelled radially from the vent and generated ignimbrites at distances in excess of 80 km. Toward the end of the eruption, only deeper and less differentiated magma was tapped, producing less expanded and less mobile pyroclastic currents, which travelled short distances within the Campanian Plain without crossing the Apennines or reaching the Sorrento Peninsula.

Fisher et al. [1993] and Ort et al. [2003] have suggested that the pyroclastic currents which surmounted high mountain ranges (>1500 m a.s.l.) and travelled over seawater were characterized by a transport system and a deposition system similar to those proposed for the blast-surge of Mount St.Helens [Fisher, 1990; Druitt, 1992]. Initial CI pyroclastic currents were an expanding gas-particle mixture that moved over the landscape as a dilute current. As they travelled away from the vent, they stratified continuously with respect to density, forming the deposition system in their lower part. This system was blocked by the morphological obstacles and decoupled from the transport system. It drained off ridges and down valleys in directions dictated by slope direction. The transport system moved outward from source and was thicker than the highest relief.

istics of the pyroclastic currents (deposition system decoupled by the transport system), any estimate of the volume of erupted magma faces severe difficulties at the moment. However, the volume should be no smaller than the sum of the conservative estimates for the pyroclastic-current deposits, the plinian fallout, and the Y5 ash layer, i.e. about 200 km³ DRE.

THE STRATIGRAPHIC POSITION OF THE CAMPANIAN IGNIMBRITE

Chronometric and Correlation Problems Concerning Oxygen Isotope Stage 3

Establishing the precise position of a large eruption within the best environmental and archaeological records is obviously essential for any further assessment of its effects on land and biomes. The information-rich, high-resolution environmental sequences containing the CI tephra—or its chemical signal—provide the optimal available database, insofar as they allow an examination of whatever environmental modifications occurred across the CI event. Environmental-cultural stratigraphies on land may be just slightly less useful. It must be pointed out that any stratigraphic placement of the CI on the sheer basis of chronometric dates is flawed at the moment, as it is severely limited by problems inherent in chronometric methods (radiocarbon timescale, ice core age models, and the CI age itself).

The calibration of radiocarbon beyond the present limit of c.20,000 ¹⁴C years BP [*Stuiver* and *Reimer*, 1993; *Stuiver et al.*, 1998] is still affected by substantial uncertainties [*Mazaud et al.*, 1991; *Laj et al.*, 1996; 2002; *Bard*, 1998; *Kitagawa* and *van der Plicht*, 1998; *Vogel* and *Kronfeld*, 1997; *Voelker et al.*,1998; 2000; *Schramm et al.*, 2000; *Beck et al.*, 2001]. Moreover, large variations in ¹⁴C concentration are evident during Oxygen Isotope Stage 3 (OIS 3), with a significant excursion at about 40,000 cal yr BP [*Voelker et al.*, 2000] or 44,000 cal yr BP [*Beck et al.*, 2001]. This acute flux of ¹⁴C affects the radiocarbon timescale precisely in the chronological interval of the CI, producing huge ambiguity in chronology.

Even greater are some problems in the ¹⁴C-dated marine stratigraphy. Uncertainties in marine records are further compounded by the variation of the temporal and spatial differences in oceanic ¹⁴C concentration, the so-called "ocean reservoir effect" [e.g. *Voelker et al.*, 2000; *Beck et al.*, 2001]. In the Greenland ice core chronology, although the environmental curves of the GISP2 and GRIP are significantly in agreement [e.g. *Grootes et al.*, 1993; *Johnsen*

et al., 2001], during the OIS 3 their timescales show discrepancies in the order of 3000 years, thus limiting the value of the superb stratigraphic record contained in these cores.

Establishing the CI stratigraphic position by using its age is particularly arbitrary. For instance, by employing two different datings of the CI marine tephra at c.34,000 and c.41,000 yr BP, *Zielinski et al.* [1996a] and *Ton-That et al.* [2001], respectively, indicated as possible putative CI signal two different large SO_4^{2-} peaks in GISP2, located at c.34,000 and c.40,000 yr BP. Timescale problems apart, these attempts show that assuming an age-based correlation between large volcanogenic signals and large volcanic eruptions may lead to "floating" results, unless there has been independent verification. Any age-based correlation of CI signal and climate would be similarly questionable, due to the well known, high instability of the Late Pleistocene climate [e.g. *Dansgaard et al.*, 1993].

The recent study of several southern European sequences containing the CI tephra [*Giaccio* and *Isaia*, 2002; in preparation), in conjunction with a critical examination of the Late Pleistocene high-resolution stratigraphy, allows the CI position in Greenland isotope stratigraphy to be reasonably defined. The main results are reported in the following sections.

Palaeolithic Sequences

Universally in the known archaeological sites, the CI tephra separates the cultural layers containing late Mousterian (Middle Palaeolithic), Uluzzian, and/or earliest "Upper Palaeolithic" assemblages (Proto-Aurignacian, Early Aurignacian etc.; see below), from the layers in which distinct, unquestionably defined Upper Palaeolithic industries occur, as represented by the Evolved Aurignacian of Bulgaria [*Kozlowski*, 1998], the Gravettian, and other broadly comparable industries. The stratigraphic position of the CI and these cultural units is summarized in Figures 3 and 7.

Several sites of prime importance for assessing the litho- and cultural-stratigraphic position of the CI in southern Italian Palaeolithic sequences have been identified in the regions of Campania and Apulia [*Fedele et al.*, 2002] (Figure 1). One such site is Serino, an open-air camp near Avellino, Campania, where a thick pyroclastic deposit, unambiguously representing the complete CI sequence including fall and flow units, immediately overlies a Palaeolithic occupation surface dated at 31,200±650 ¹⁴C yr BP (Figure 3). The occupation was considered Proto-Aurignacian by the excavators [*Accorsi et al.*, 1979], an industry assumed to represent the beginning of the Upper Palaeolithic in traditional terms.

(m)

librated ^{14}C age

2

3

40=48.68

4

◄CI
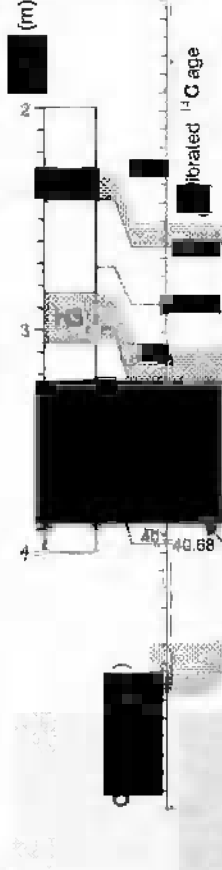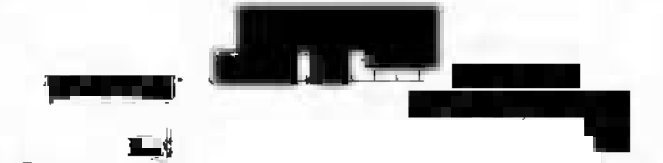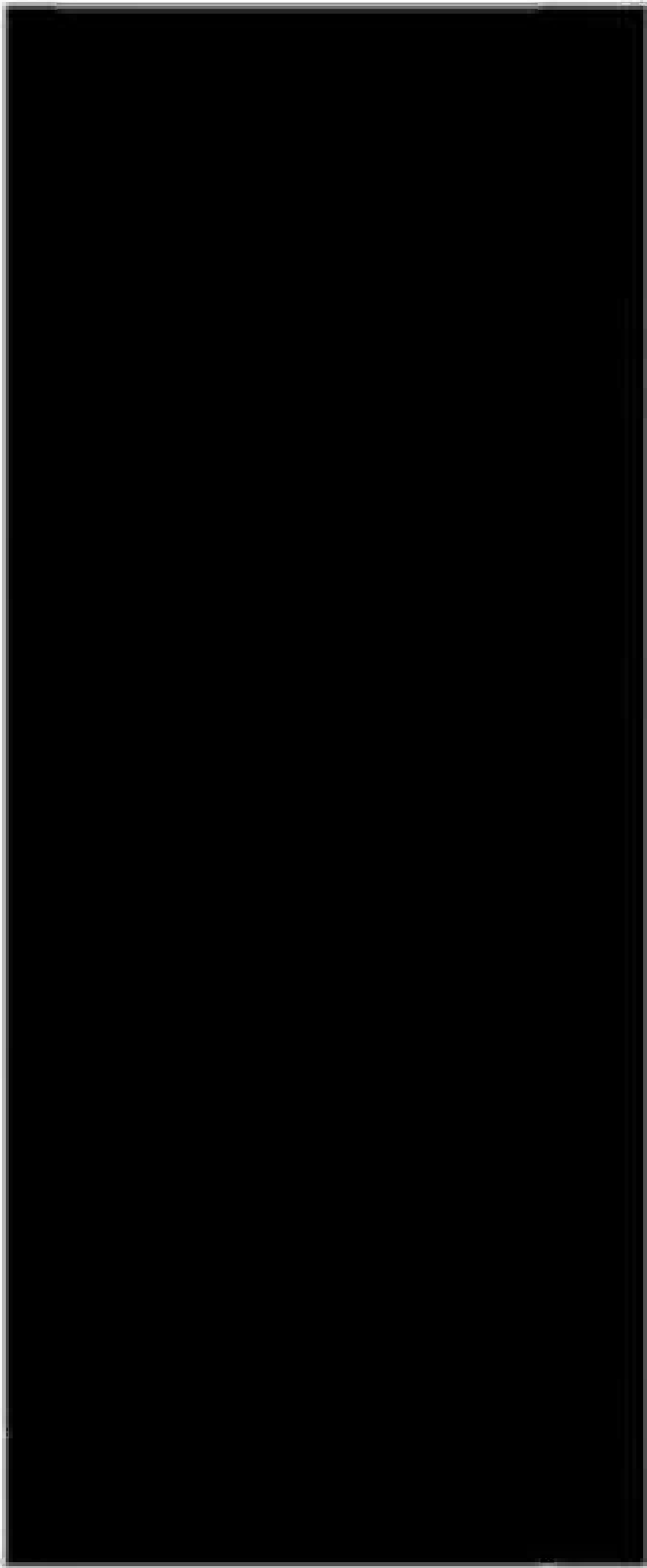
Negendank, 1996; *Allen et al.*, 1999, *Allen* and *Huntley*, 2000; *Ramrath et al.*, 1999; *Brauer et al.*, 2000] show that during the last 102,000 years the Mediterranean terrestrial environment saw rapid changes, similar to the sub-orbital climatic cycles recognized in Greenland and the North Atlantic, or Dansgaard-Oeschger (D-O) cycles [e.g. *Dansgaard et al.*, 1993; *Bond et al.*, 1993]. This allowed a good correlation between the Monticchio pollen diagram and Greenland isotope stratigraphy to be proposed (GRIP correlation from *Watts et al.* [1996; 2000]) (Figure 4).

According to this correlation the CI tephra coincides with the beginning of an arid interval equated with HE4 [*Watts et al.*, 1996]. However, this correlation is tentative because it reveals an apparent discrepancy of at least 7000 years between the records of HE4 at Monticchio and in GISP2, which could potentially conceal time transgression (Figure 4).

The Heinrich Events—sharp cooling episodes associated with collapses of the boreal ice sheet and discharges of icebergs into the North Atlantic [*Heinrich*, 1988]—have initially been regarded as typical of the high-latitude regions of the Northern Hemisphere [e.g. *Bond et al.*, 1993, *Bond* and *Lotti*, 1995; *Mayewski et al.*, 1994]. For the supposed stratigraphic relationship between the CI and HE4 to be accepted, the climatic changes in the Mediterranean should be shown to have occurred in phase with those of the northern region. This is indeed being demonstrated not only for the marine environment [e.g. *Paterne et al.*, 1999; *Cacho et al.*, 1999] but on land as well.

For instance, by comparing the pollen record and the marine palaeoclimatic proxies from the same sea-cores of the Portuguese margin and Alborán Sea, *Roucoux et al.* [2001] and *Sánchez Goñi et al.* [2002] found that the vegetation of the Iberian mainland responded synchronously to the millennial-scale climatic oscillations documented in the ice and sea-cores of the northern region. In particular, they observed an abrupt decrease in tree pollen abundance at each stadial stage of the D-O cycles and/or during the Heinrich Events. These data support the claim by *Allen et al.* [1999] that the Last Glacial variations in tree pollen abundance at Monticchio are related to North Atlantic climatic events.

Mediterranean cosmogenic nuclides and palaeomagnetic records. Late Pleistocene geomagnetic intensity is known to have been close to zero around 40,000 yr BP (the Laschamp geomagnetic excursion [*Channell et al.*, 2000; *Voelker et al.*, 2000; *Stoner et al.*, 2002]). According to recent studies [e.g. *Baumgartner et al.*, 1998; *Wagner et al.*, 2000; *Voelker et al.*, 2000; *Beer et al.*, 2002], the Laschamp Event would seem to coincide with an exceptional peak in several cosmogenic nuclides, including ^{10}Be, ^{36}Cl and ^{14}C. These

simultaneous peaks were recognized in the Arctic and Antarctic ice cores as well as in marine sediments. As the Laschamp excursion is considered synchronous on the planetary scale, the palaeomagnetic and the cosmogenic nuclide records can both be used as a global correlation tool [e.g. *Yiou et al.*, 1997; *Beer et al.*, 2002; *Channell et al.*, 2000].

In the Mediterranean, palaeomagnetic intensity [*Tric et al.*, 1992] and ^{10}Be flux data [*Cini Castagnoli et al.*, 1995] have been obtained from marine sequences containing the CI tephra. The lowest, near-zero field value, likely to be equated with the Laschamp excursion, actually roughly coincides with the CI tephra [*Tric et al.*, 1992; see also *Paterne et al.*, 1988]. Also the ^{10}Be peak, as recorded in Tyrrhenian sea-core CT 85-5, has a stratigraphic position closely connected with the CI tephra (Figure 5).

Both the Tyrrhenian Sea and Monticchio Lake records thus display good stratigraphic relationships between the CI tephra, HE4, and cosmogenic nuclides. All available data concur to show that the CI eruption neatly coincided with the onset of HE4, during a phase of enhanced ^{10}Be flux corresponding to the Laschamp Event.

GISP2 Greenland ice core. The GISP2 ice core preserves one of the most continuous and complete records of Late Pleistocene explosive volcanic history [*Zielinski et al.*, 1996a; *Zielinski*, 2000], in which eruptions are essentially indicated by acid sulfate (SO_4^{2-}) volcanogenic peaks; visible ash layers are only occasionally found and commonly derived from Icelandic eruptions [e.g. *Grönvold et al.*, 1995; *Zielinski et al.*, 1997]. Due to a lack of required chronological precision, identifying the volcanic signal of a given eruption in GISP2 is still a problem. In our case, at least 25 sulfate peaks appear to be consistent with the available age of the CI (Figure 6). However, when the above mentioned stratigraphic position of the CI in the Mediterranean records is considered (its relations to HE4 and the nuclide peak included), this number of peaks can be drastically reduced to a few, or possibly just one. Space prevents us here from a thorough discussion of this delicate topic, but the main points will be summarized.

The position of Heinrich Events in Greenland isotopic stratigraphy has been unambiguously determined by correlation with the marine records in which they had been defined [e.g. *Bond et al.*, 1993; *Bond* and *Lotti*, 1995], as well as on the basis of inference from the palaeoatmospheric curves of the GISP2 ice core itself [*Mayewski et al.*, 1994; 1997]. The onset of HE4 coincides with the Greenland Interstadial 9/Stadial 9 boundary (GI9/GS9 [*sensu Walker et al.*, 1999]). As for the position of the Laschamp Event and the related nuclide peak, both direct measurements on ice
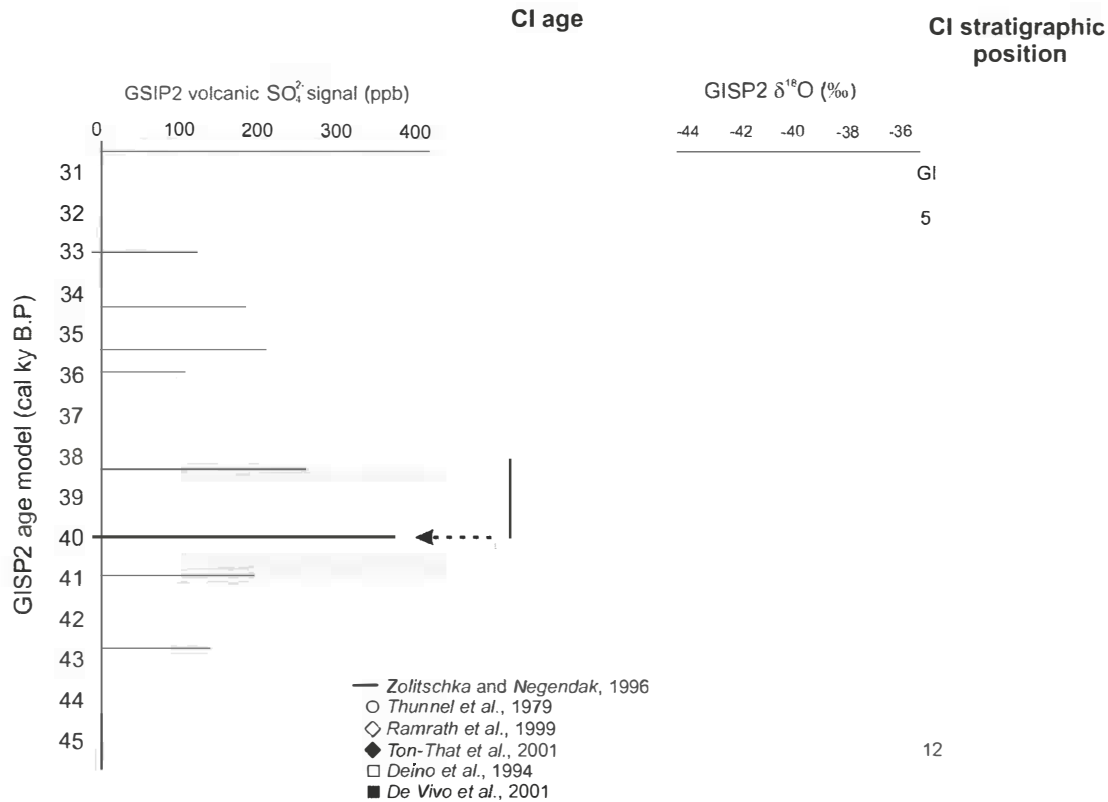
Figure 6. The Campanian Ignimbrite signal within the volcanogenic record of the GISP2 ice-core. The identification of the putative CI peak is derived from the precise placement of the CI tephra in the Mediterranean palaeoclimatic, palaeomagnetic and cosmogenic flux records (see text and Figures 4 and 5 for details). Position of HE4, the Laschamp excursion and the [10]Be peak in GISP2 according to *Bond et al.* [1993], *Voelker et al.* [2000] and *Yiou et al.* [1997], respectively.

GI11-GI7 interval provides the key to a great number of apparent chronological anomalies observed in several archaeological sequences spanning the Middle to Upper Palaeolithic "transition." Age inversions (layers older than those below) and age gaps in this crucial interval of such sequences have been until now a major source of uncertainty and controversy [e.g. *Gambassini*, 1997; *Zilhão* and *D'Errico*, 2000]. Moreover, use of the radiocarbon timescale without such caveats is inappropriate to a temporal control of the actual processes and rhythms involved in the Late Pleistocene biocultural shift. The spread of ^{14}C determinations over several millennia is entirely misleading, in the light of the ^{14}C flux; real, calendar ages in fact point to a much shorter, almost point-like timespan. Figure 7a emphasize a ^{14}C age of c.33,000 yr BP for the already observed cultural division [*Gamble*, 1999] involving several aspects of the European Palaeolithic societies.

These are very brief remarks on a major problem. The radiocarbon timescale issue is far from an easy resolution,

as the papers by *Voelker et al.* [2000] and *Beck et al.* [2001] painstakingly show, and great caution must be adopted in evaluating dates beyond 30,000 ^{14}C yr BP. Space and scope prevent us here from further pursuing the problem of the complex pattern of radiocarbon age distribution at about 33,000 ^{14}C yr BP, or about 40,000–36,000 BP in calendar years, a subject we intend to deal with elsewhere.

THE CAMPANIAN IGNIMBRITE
AND ENVIRONMENTAL CHANGE

Background: Last Glacial Climate and Super-Eruptions

To a great extent, the interactions between very large eruptions and climate instability during the last glacial period have so far been argued on the basis of the Toba mega-eruption. *Rampino* and *Self* [1992; 1993] suggested that this catastrophic event, apparently synchronous with the OIS 5a/OIS 4 boundary, triggered a series of positive feedback

a

CI eruption

...avian

Kostenki group

Later Aurignacian

Earliest Aurignacian

...urignacian

...terranian

Pré-Aurignacian

Bohunician

Mousterian

...sterian of ...aurbean Tradition

14 kyr

30
35
45

b

-42 -40 -38 -36

30

40

Cal age (ky B.P.)
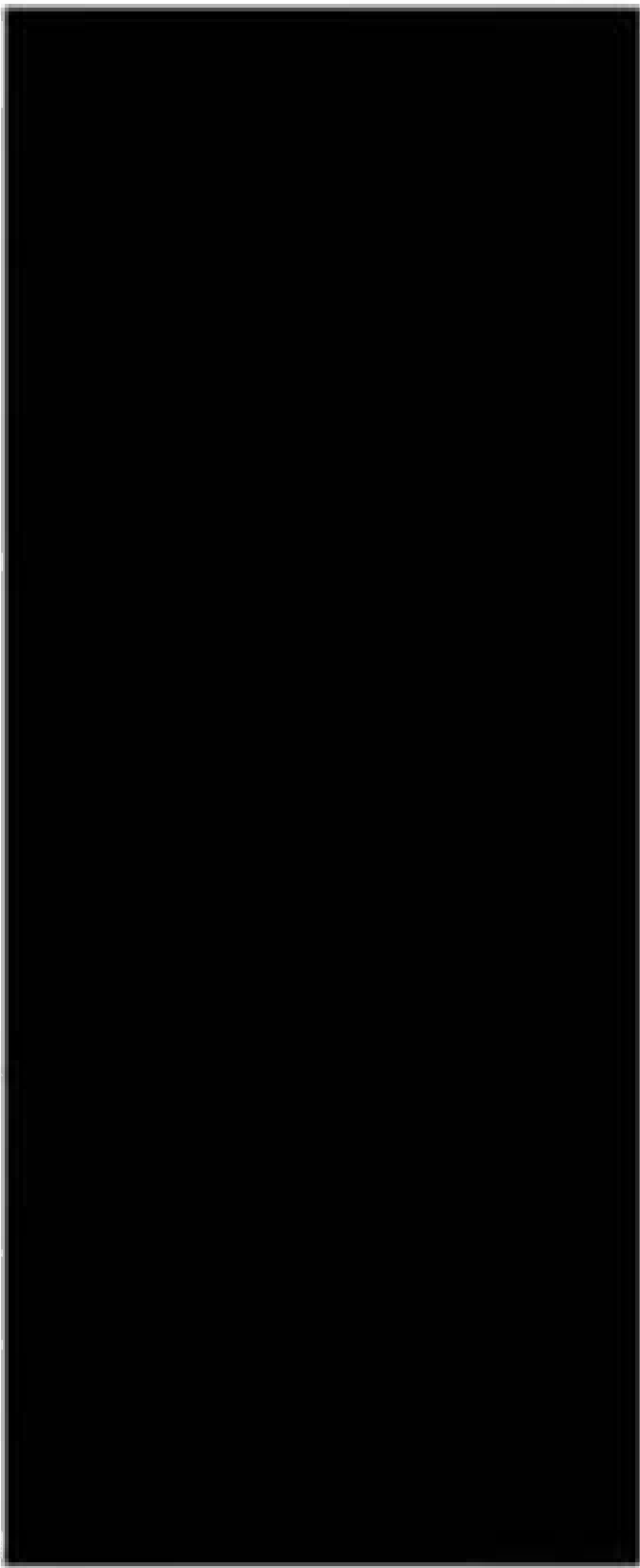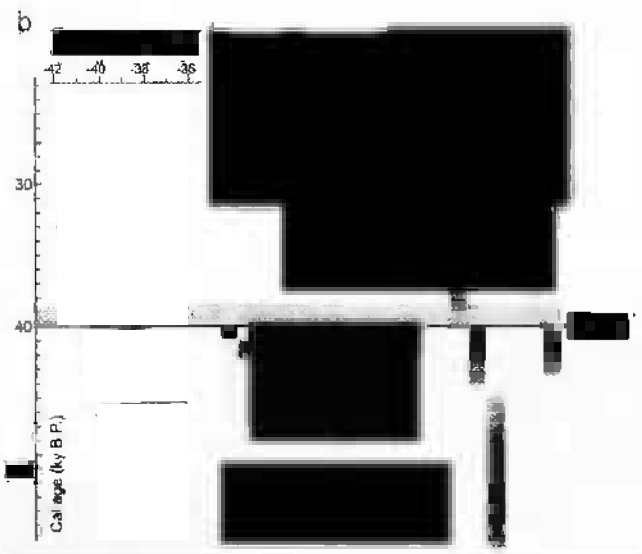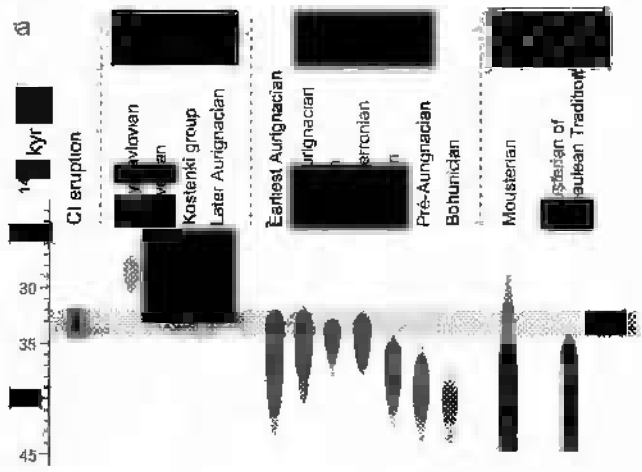
the Z2 ash layer from Iceland (557 ppb) and the Toba mega-eruption (466 pbb). However, since the large SO_4^{2-} signals of the Icelandic eruptions are amply due to tropospheric transport of aerosol [*Zielinski*, 1995], the magnitude of the CI signal can be said to be second only to Toba.

Perhaps more relevant, in the light of current concepts of climate-volcanism feedback, are the peculiar climatic conditions at the time of the CI eruption. According to *Rampino* and *Self* [1992; 1993] volcanoes and climate form a sensitive binary system, led by positive feedback during the interstadial-stadial transitions and by negative feedback during the stadial-interstadial transitions. The resulting impact of an eruption would thus depend not only on its eruptive style and the amount of sulphuric aerosol injected into the stratosphere, but also on the specific climate trend at the time of eruption. The coincidence of the CI eruption with a marked interstadial to stadial change (i.e. the onset of HE4) therefore deserves attention.

The Heinrich Events are brief but drastic cooling episodes associated with quasiperiodic discharges of European and Laurentide ice into the North Atlantic, which affected the oceanic and atmospheric circulation [*Broecker*, 1994; *Mayewski et al.*, 1994; *Cortijo et al.*, 1997; *Vidal et al.*, 1997; *Pailler* and *Bard*, 2002]. They are defined by an abundance of ice-rafted debris [*Heinrich*, 1988; *Bond et al.*, 1992] and of *Neogloboquadrina pachyderma* (sinistral) in the sediments, $\delta^{18}O$ depletion [*Bond et al.*, 1993, *Bond* and *Lotti*, 1995], and a sharp decrease in sea surface temperature, as also recorded in the Mediterranean basin [*Paterne et al.*, 1999; *Cacho et al.*, 1999]. These events mark the termination of the long-term cooling cycles known as Bond cycles [*Bond et al.*, 1993], and recent studies show that they correspond to climatic changes which significantly affected the marine and terrestrial ecosystems throughout the Northern Hemisphere [e.g. *Thouveny et al.*, 1994; *Watts et al.*, 1996; *Chen et al.*, 1997; *Schulz et al.*, 1998; *Li et al.*, 2001; *Prokopenko et al.*, 2001; see also *Voelker*, 2002 for a global database].

The quasiperiodic rhythm of the Heinrich Events could render the co-occurrence of the CI and the HE4 onset a case of simple coincidence. On the other hand, several lines of evidence suggest that the climatic conditions reflected in HE4 were extreme compared to the other Heinrich Events. Some palaeoclimatic records showing a marked and anomalous climatic signal for HE4 are shown in Figure 8 and summarized below.

According to *Cortijo et al.* [1997], HE4 is the only such event to be always recognizable in a series of 25 sequences from North Atlantic coring sites located between 40°–67°N and 60°–0°W. These cores show that during HE4 the sub-

polar front dropped to about 45°N, with its maximum southward shift of 20° located in the eastern part of the North Atlantic. The summer sea surface temperature decreased by c.2–3 °C everywhere, and up to 6 °C along the European margin. The palaeotemperature record from a sea-core near the Iberian margin (MD 95-2042) [*Pailler* and *Bard*, 2002] shows that during HE4 the sea surface temperatures were at least 2–3 °C lower than in the other Heinrich Events, with a much greater temperature excursion: 4,7 °C (10,1–14,8 °C) compared to 2–3 °C. The geochemical record from a North Atlantic core shows that the highest and indeed extreme values of the Si/Al and Zr/Al ratios, indicating loess input, coincided with HE4 [*Hinrichs et al.*, 2001] (Figure 8).

The palaeoclimatic proxies from an Alborán Sea core, in the westernmost Mediterranean, not only show that the maximum drop in sea-surface temperature occurred in the HE4 interval (4,8 °C compared to c.3,5 °C during the other Heinrich Events), but also that HE4 alone was marked by a significant abundance of *Neogloboquadrina pachyderma* (sinistral), with values above 20% (Figure 8). Palynology from the same core offers a detailed reconstruction of the terrestrial climatic conditions in southeastern Iberia at the time [*Sánchez Goñi et al.*, 2002]. During the HE4 the Iberian Peninsula experienced extremes of aridity and cooling, values of mean temperature of the coldest month between –8 and –14 °C, or 5–10 °C lower than the temperatures associated with the other stadials (Figure 8). Additional stratigraphic evidence for an unusually large palaeoclimatic imprint related to HE4 is offered by other studies [e.g. *Chapman* and *Shackleton*, 1998; *Labreiro et al.*, 1996; *Roucoux et al.*, 2001; *Thouveny et al.*, 2000; *Vidal et al.*, 1997; *Voelker et al.*, 2000]. No evidence of particularly extreme conditions during HE4 is detectable in Greenland records at the moment, but work is in progress.

Among the numerous sequences containing the CI tephra, the Tyrrhenian Sea core studied by *Paterne et al.* [1999] records that the lowest temperature of the Last Glacial immediately occurs after the CI deposition. In the Monticchio lacustrine sequence [*Allen et al.*, 1999], aridity and cooling were already in progress during the centuries before the CI eruption, but indicators display a sudden acceleration after the CI event (Figure 8); the CI deposition itself coincides with the largest minerogenic flux peak (Dray Density in Figure 8). High values of this latter parameter indicate sparse vegetation cover and enhanced erosion in the lake catchment, both consistent with cold and/or arid conditions [*Ramrath et al.*, 1999; *Brauer et al.*, 2000]. The CI event is immediately followed by a sharp decrease of arboreal pollen (from c.30% to c.10%) and a concurrent rise in Arctic-Alpine dwarf shrubs or herbs, as well as

4 to 7 [*Jacoby et al.*, 1999; *Manabe* and *Bryan*, 1985]. If the hypothesis is correct, there was ecosystem crisis on a fairly large scale.

We consider it pertinent to our argument that HE4 differs from the other Heinrich Events not only in the magnitude of cooling, but also in the timing of the marine and terrestrial responses on either side of the Iberian peninsula. By comparing the marine and terrestrial climatic proxies of the cores from the Alborán Sea and the Atlantic margin, *Sánchez Goñi et al.* [2002] demonstrate that the maximum of steppe vegetation in Mediterranean Iberia occurred immediately at the onset of HE4, earlier than the *N. pachyderma* (sinistral) peak. On the contrary, on the Atlantic margin the initial phase of HE4, like the other Heinrich Events, is characterized by relative high values of arboreal pollen; only later the steppe development occurs, alongside the maxima of ice-rafted debris and *N. pachyderma* (sinistral) [*Sánchez Goñi et al.*, 2000]. No explanation for the timing discrepancy is given.

If one accepts that the CI precisely matches the onset of HE4, the unusually sudden response of vegetation to HE4 in south-eastern Iberia could be explained as a consequence of a regional-to-continental cooling linked to the CI eruption. This cooling would have been particularly pronounced and centred on the European mainland. This hypothesis fits with the distribution of the magnitudes of cooling associated with HE4 in the North Atlantic area, which shows a significant gradient between the eastern and central part of the basin, with temperatures at least 3–4 °C lower toward the European margin [*Cortijo et al.*, 1997].

THE CAMPANIAN IGNIMBRITE AND THE MIDDLE/UPPER PALAEOLITHIC SPECTRUM: AN INTERIM FRAMEWORK

Both culturally and biologically the European Late Pleistocene shift, roughly between 45,000 and 35,000 calendar yr BP (or later), is such a focus of research and debate that the publication output has become substantial. The growing literature on the broadly similar shift in central and Northeast Asia [e.g. *Brantingham et al.*, 2001] provides additional comparative material to be taken into account. Space thus requires that references for this section are limited to a selection of relevant papers on particular topics and broader recent surveys.

As already mentioned, the CI regularly occurs within a peculiar Palaeolithic phase in Eurasia which directly follows the Mousterian industries of the Middle Palaeolithic (Figure 7). This phase is characterized by a mosaic of variously named stone-tool industries, commonly regarded as

innovative—or else "intermediate"—within the overall interval which saw the change from the Middle to the Upper Palaeolithic. In need of a vocabulary as neutral as possible, we propose to term this industrial mosaic the Middle/Upper Palaeolithic (MUP) spectrum, with the proviso that the only aim of this label is clearing the ground of preconceived partitions. Any approach to a "transition" problem is inherently flawed if the naming and taxonomy of archaeological entities are not kept free of interpretative overtones, admittedly a difficult goal. We feel that this need is especially vital for a study of the Palaeolithic industries on either side of the CI event, as well as for a successful assessment of the Late Pleistocene biocultural shift in general.

A meaningful evaluation of the CI impact implies a reappraisal of the MUP spectrum and particularly the archaeological data which bear on resource exploitation, cultural transmission and population densities. This predictably is a two-way explanation process, the MUP spectrum providing a cultural context for the CI, and the CI contributing a so far unexpected factor toward understanding the identity and evolution of the cultural spectrum. Furthermore, if one considers the centrality of the MUP spectrum to the definition of the Upper Palaeolithic as a new stage in cultural evolution, a critique of this latter definition might become unavoidable. By implication, a certain degree of taxonomic re-examination would encompass the Aurignacian, which has become commonplace to regard as the earliest, full Upper Palaeolithic "culture" and a product of anatomically modern humans. These tasks cannot—obviously—be fulfilled in this paper or at this early stage of the project; only an outline of ongoing work is reported in the rest of this section.

The MUP industrial spectrum includes such stone-tool based cultural groups of the 43,000-33,000 yr BP interval (uncalibrated) as the Bohunician and Szeletian of central Europe, the Olschewian of Croatia, the Bachokirian of the Pontic region, the Uluzzian and several "Aurignacoid" variants of Mediterranean Europe (Uluzzo-Aurignacian, Proto-Aurignacian, Earliest and Early Aurignacian etc.), and the forerunner of all, the Châtelperronian of France [cf *Hoffecker* and *Wolff*, 1988; *Palma Di Cesnola*, 1989; 2001; *Farizy*, 1990; *Knecht et al.*, 1993; *Kuhn*, 1995; *Mellars*, 1996; *Karavanic* and *Smith*, 1998; *Kozlowski*, 1998; *Broglio*, 1998; *Fox*, 1998; *Akazawa et al.*, 1998; *Mellars et al.*, 1999; *Kozlowski* and *Otte*, 2000; *Bar-Yosef* and *Pilbeam*, 2000; *Kuhn* and *Bietti*, 2000; *Allsworth-Jones*, 2000; *Mussi*, 2001; *Bolus* and *Conard*, 2001]. A simplified synopsis is given in Figure 7. To these groups one has to add the coeval—and even less understood—leaf point assemblages of the northern part of inhabited Europe (Altmühlian

etc.), as well as several "intermediate" industries of Anatolia and southern Russia. The picture gets more complicated if one considers other parts of Eurasia [e.g. *Brantingham et al.*, 2001].

Such a proliferation of archaeological entities reflects to some extent historical fact, i.e. a development of regional variants or "regionalisation", already a detectable trend in the mid-Interpleniglacial Mousterian [*Gamble*, 1999]. But inevitably it also stems in some cases from the expectation to detect Upper Palaeolithic signatures and the emergence of significant new traits, often combined with a lack of regional evidence for the evolutionary trends within the Mousterian.

Our MUP spectrum closely matches as a notion the "Earliest Upper Palaeolithic" of *Gamble* [1999, Table 6.5], or, similarly, the "Initial Upper Palaeolithic" of several current workers [cf *Bar-Yosef* and *Pilbeam*, 2000]. Such labels are in our opinion unfortunate in that they imply in advance the recognition of a Middle/Upper Palaeolithic dichotomy, which, until about 35,000 yr BP if not 25,000 BP, is not perhaps as solidly rooted in factual data as it was supposed to be. After all, the distinction between the Middle and the Upper Palaeolithic was designed over a century ago to account for what then appeared to be a clearcut artifact-type division in France, well before the cultural complexity of the Late Pleistocene came to be recognized over most of the Old World. A certain unease about these chronotypological labels, not altogether new, is perhaps gaining momentum. The labels have been stereotyped and "reified" beyond dispute and often assumed as unambiguous ethnic designations [*Clark* and *Willermet*, 1997; *Riel-Salvatore* and *Clark*, 2001, and L.G. Straus's comment therein], not unlike the Aurignacian and other industrial units, instead of being subjected to critical scrutiny. As long as the division between a Middle and an Upper Palaeolithic is emphasized as an absolute divide, even a search for revised paradigms is excluded.

This division has long been taken for granted while at the same time demanding the insertion of "intermediate", or hard to classify, industries, first of all the Châtelperronian. What needs be stressed in the present discussion is that the traditional division has survived in face of mounting evidence that the variation within both the Mousterian and the earliest "Upper Palaeolithic" is much greater than originally thought. For instance, substantial flake-based tools and Mousterian-like scrapers define most of the Proto/Early Aurignacian variants as much as the occasional bone tool or the bladelet component. In the Uluzzian industry of Italy, one can hardly perceive the advent of a major new division of the Palaeolithic when 45% to 75% of any assemblage is made of Mousterian scrapers and/or denticulates [Gioia, 1990].

Discussion about the Aurignacian as a thorough archaeological entity has just started [e.g. *Kozlowski* and *Otte*, 2000; *Stringer* and *Davies*, 2001]. The use of the Aurignacian as a reference-taxon for a growing number of "intermediate" assemblages may cast doubts on the Aurignacian being a completely valid taxon as currently employed—it may lack integrity. Within this archaeological construct which spans some 10,000 years, half a dozen groups can at least be noted in Europe alone, some of them quite different in chronology and artifactual content. If one takes away formal bone artifacts, ornaments, or "art"—an arbitrarily overemphasized behavioural component [cf *Dunbar et al.*, 1999]—it is not obvious why many early assemblages should be linked to the Aurignacian at all, rather than classified within a Mousterian-MUP spectrum *continuum*. There has been a persistent tendency to stretch the Aurignacian backwards in time in spite of any data suggesting a lack of unity, or at least requiring that new assemblages be examined neutrally in terms of their own composition.

This potential problem is compounded by a second: playing down the range and scope of temporal and regional variation within the later Mousterian, i.e. among the industries of the Interpleniglacial of Europe. Although interpretation may differ about the agents, dynamics, and timing of the Middle to Upper Palaeolithic transition, there is general agreement that a significant change did indeed occur over time, particularly after about 40,000 cal yr BP. But variation in tool making around and after the 40,000 BP timeline, now appears to be the culmination of a much longer phase of artifactual instability and innovation. Some long-term trends were perhaps set in motion as early as 55,000–60,000 years BP [*Dibble* and *Mellars*, 1992; *Stiner*, 1994; *Kuhn*, 1995; *Riel-Salvatore* and *Clark*, 2001]. *Kozlowski* [1990] has pioneered such a re-evaluation with his multiaspectual model, akin in principle to a view of Palaeolithic industries as a polythetic (variously grouped) set of artifact types [*Clarke*, 1968]. *Gamble* [1999, ch. 6], perceptively extracting information from a large body of data, is able to identify several evolutionary threads in the Interpleniglacial Mousterian and link them to social dynamics.

Artifactual "instability" is a key notion in the present discussion, cognitively and socially connected with flexibility and experiment. Particularly toward the end of the pre-40,000 cal BP interval, Mousterian technologies display an oscillating reliance on blade-based technology and/or miniaturisation of tool-kits, locally supplemented by innovations in hafting and related tool retouch and form (back-

ing or blunting etc. [cf *Kuhn*, 1995]). Prismatic cores and blades make up 30% of the lithics at several sites (e.g. Grotta Breuil, Latium, Italy [*Kuhn* and *Bietti*, 2000; *Lemorini*, 2000]), just marginally widening the role of laminar technology already successful in Late Mousterian groups [*Bar-Yosef* and *Kuhn*, 1999; *Kuhn* and *Bietti*, 2000; *Kuhn* and *Stiner*, 2001]. Such indisputable innovations have often been termed "Upper Palaeolithic" elements. We contend that these innovations are better explained in a human ecosystem perspective, and, as a point of historical method, first of all they should be appreciated against the background of the preceding traditions (i.e. the Mousterian) rather than the following ones.

As a hypothesis, these novelties might represent an expression of adaptive devices to cope with environmental alteration and stress (cf *Gibson* [1996] for a boader cognitive perspective, and *Van Andel* and *Tzedakis* [1996] for the Late Pleistocene landscapes of Europe). The appearance and success of biface technology in the form of leaf-shaped points is perhaps an additional instance, especially if these types were developed within the framework of a need for more efficient composite-tools. A common denominator to all these devices is standardization of shape, which may have acted as a cost-efficient, economizing strategy. A concurrent kind of adaptive response is the shift in raw material procurement and/or exchange networks, often noted at the Mousterian/Aurignacian interface and sometimes perceived as an abrupt change.

Change must be qualified, and it is expected that an environmental modeling of the CI will lead to a better qualification of change at least in the area of its primary impact. Useful insights could be provided by comparisons with similar industrial shifts at other times and places in the Late Pleistocene. Such developments of the advanced Interpleniglacial as those described in Europe lose most of their novelty if they are compared with similar phenomena which appeared at the onset of the Last Glacial, most notably in South Africa (the Howieson's Poort industry, c.75,000 yr BP [*Volman*, 1984; *Watts*, 1999]). Here blades, miniaturization and hafting likely formed a functional package, and there is a definite possibility that the package was a response to new demands brought about by rapidly expanding, open, cold-dry habitats. A convincing correlation with environmental deterioration has been made in that case, in spite of limited time resolution.

The archaeological pattern outlined above provides the context in which the CI eruption occurred and needs to be ecologically and culturally understood. Predictably, the interferences with human society varied widely according to the impact gradient of the CI crisis. That implies that the

interference between the CI and the Palaeolithic is better examined at two different geographic scales: regional, i.e. central and southern Italy, corresponding to the obvious range of main impact; and south-eastern European, throughout the Greater Mediterranean's core area if not beyond. At this latter scale, the CI eruption falls precisely in the middle of the European Late Pleistocene shift's age bracket: stratigraphic evidence shows that the volcanic event inserted itself, more or less dramatically, into the fluctuating spectrum of Palaeolithic developments here termed the MUP.

CONCLUSIONS

The identification of the CI volcanic event in many various stratigraphic records allows an examination of both environmental conditions and cultural configurations immediately before and after the CI eruption. The CI is here proposed as an instance of large eruption potentially capable of inducing a substantial climatic impact. The reconstructed eruptive dynamics indicate that during both the Plinian and pyroclastic flow phases a large amount of the erupted materials was injected into the stratosphere, producing the second largest volcanogenic signal recorded in the Greenland GISP2 ice core. Furthermore, the CI coincided with the onset of HE4, whose climatic signal is significantly more pronounced than the other Heinrich Events. From the observation of this exceptional concurrence of factors we advance the hypothesis of a positive climate-volcanism feedback, hence an impact of the CI on the atmosphere and consequently at the global scale. The environmental impact of this catastrophe can be explored within the framework of a human-ecosystem model.

The temporal concurrence of several categories of critical data—the CI eruption, the beginning of HE4, the abandonment of Palaeolithic sites—suggests that the overlapping of the volcanic and the climatic impacts may have induced an ecosystem crisis on a fairly large scale, human systems included and well beyond the direct-impact zone.

Over a large area in the Greater Mediterranean the CI tephra coincides with an interruption of occupation several millennia long. In extended and well-dated stratigraphic sequences of peninsular Italy, the CI deposits seal the last documented assemblages of the MUP industrial spectrum; a distinct tephra layer corresponding to the CI is regularly interbedded between the Middle Palaeolithic or the MUP occupations and the earliest appearance of well defined Upper Palaeolithic assemblages. Quite often, long series of Mousterian and MUP occupations, implying a certain persistence in regional population and circulation habits, are capped by overlying CI tephra and immediately followed by

site abandonment and long-duration human absence, particularly in southern Italy. The hiatus may have a causal relationship with the CI impact and/or the ecological disruption it generated. Conceivably, such a volcanic eruption may have impacted whole ecosystems.

At least in the direct-impact zone (defined by the areal extent where pyroclastic cover was sufficiently thick to arrest natural life cycles) the eruption may have conditioned the resident humans in three principal ways:

1) by disrupting animal populations through the collapse of the herbivore grade in the trophic chain, from suppression or deterioration of pasture;
2) by altering the species composition, growth rhythm, and/or visibility, hence the overall availability, of previously exploited staple plants;
3) by changing the pattern of water availability.

In other words, human groups may have been impacted in their capacity as upper predators in the trophic chain, not necessarily as conscious victims of a catastrophic killing or the lowering of temperature. Psychological factors are hard to assess archaeologically. However, as far as temperature is concerned, perhaps even including extreme cases of volcanic "winters," climate variation almost never conditioned humans directly. Climate only acted through variation in the land—soils, water, ice, landslides . . . —and the biome [cf Vrba et al., 1995]. This kind of reaction of sociocultural systems had been normal before the CI time, and was to remain such for several millennia afterwards.

Predictably, as stratigraphies show, a result of the environmental alteration produced by the CI was the displacement of human groups. Over an area possibly wider than southern Italy, the CI indirectly forced populations away from the traditionally inhabited and familiar territories, disrupting not only the ecological but also the cognitive balance, hence society as a whole. Cognition is a crucial component of the social fabric, and at 39,000 BP we are dealing with hunter-gatherers at a certain level of organization, with a certain degree of ability to organize culture; that was a source of both advantages and constraints, social resilience and social fragility.

Again indirectly and over a certain time interval, the environmental alteration may have pushed groups into less affected regions at the periphery of the CI impact area. This was in turn coupled with biome displacement, probably on a mosaic basis. Such processes can have been a factor of depopulation in certain regions and of crowding in others. As a hypothesis, regional crowding may have occurred in areas roughly aligned on a west-to-east, south-central

European fringe. This population shift might explain the impression of a sudden appearance of MUP spectrum groups, including the Proto/Early Aurignacian, in northern Italy [Broglio, 1998] or the Swabian corridor north of the Alps [Richter et al., 2000; Bolus and Conard, 2001; Conard and Malina, 2002].

It seems plausible to suggest that the CI interfered with active, ongoing processes in the western Eurasian Palaeolithic. The CI acted toward those processes in various possible ways, arresting, disrupting, or else re-orientating them as a catalytic agent, according to situations and regions. It possibly became a selective force, much more so than the normal environmental factor. Both catalysis and selection are keywords in this theoretical, still unquantified model, in which the CI would accelerate change by catalysing and filtering ongoing trends. As a hypothesis, it did so through the mechanisms of environmental "forcing" and population displacement.

In this paper we have presented the initial results of a detailed assessment of the CI eruption in its overall context. We have tried to show how the CI, in conjunction with other factors, already allows to reconsider the processes, rhythms, and dynamics which took place at the c.40,000 BP timeline in a comprehensive and probably more realistic way; further refinements and proper modeling are underway. The processual interplay at the base of the Middle to Upper Palaeolithic transition is certainly too complex a problem for hypotheses to be formulated in the light of the CI event alone. However, on the available evidence, one is justified to explore whether to some extent the CI was one of the contributing factors to the cultural differentiation in Western Eurasia which is called the Upper Palaeolithic.

REFERENCES

Accorsi, C.A., E. Aiello, C. Bartolini, L. Castelletti, G. Rodolfi and A. Ronchitelli, Il giacimento Paleolitico di Serino (Avellino): stratigrafia, ambienti e paletnologia, *Atti Soc. Tosc. Sci. Nat., Memorie, A, 86,* 435-487, 1979.

Akazawa, T., K. Aoki and O. Bar-Yosef, *Neandertals and modern humans in Western Asia,* New York: Plenum Press, 1998.

Allen, J.R.M., U. Brandt, A. Brauer, A.-W. Hubbertens, B. Huntley, J. Keller, M. Kraml, A. Mackensen, J. Mingram, J.F.W. Negendank, N.R. Nowaczyk, H. Oberhänsli, W.A. Watts, S. Wulf and B. Zolitschka, Rapid environmental changes in southern Europe during the last glacial period, *Nature, 400*, 740-743, 1999.

Allen, J.R.M. and B. Huntley, Weichselian palynological records from southern Europe: correlation and chronology, *Quat. Int., 73/74*, 111-125, 2000.

Allen, J.R.M., W.A. Watts and B. Huntley, Weichselian palynostratigraphy, palaeovegetation and palaeoenvironment; the Lago Grande di Monticchio, southern Italy, *Quat. Int., 73/74*, 91-110, 2000.

Allsworth-Jones, P., Dating the transition between Middle and Upper Palaeolithic in Eastern Europe, in *Neanderthals and modern humans — discussing the transition: Central and Eastern Europe from 50,000 - 30,000 B.P*, edited by J. Orschiedt and G.-C. Weniger, pp. 20-29, Neanderthal Museum, Mettmann, Germany, 2000.

Ambrose, S.H., Late Pleistocene human population bottlenecks, volcanic winter, and differentiation of modern humans, *J. Human Evol., 34*, 623-651, 1998.

Amirkhanov, H.A., M.V. Anikovitch and I.A. Borziak, Problème de la transition du Moustérien au Paléolithique Supérieur sur le territoire de la Plaine Russe et du Caucase, *L'Anthropologie, 97*, 311-330, 1993.

Barberi, F., F. Innocenti, L. Lirer, R. Munno, T.S. Pescatore and R. Santacroce, The Campanian Ignimbrite: a major prehistoric eruption in the Neapolitan area (Italy), *Bull. Volc., 41*, 10-22, 1978.

Barberi, F., E. Cassano, P. La Torre and A. Sbrana, Structural evolution of Campi Flegrei Caldera in light of volcanological and geophysical data, *J. Volc. Geotherm. Res., 48 (1/2)*, 33-49, 1991.

Bard, E., Geochemical and geophysical implications of the radiocarbon calibration, *Geochim. Cosmochim. Acta, 62*, 2025-2038, 1998.

Bar-Yosef, O. and S.L. Kuhn, The big deal about blades: laminar technologies and human evolution, *Am. Anthropol., 101*, 322-338, 1999.

Bar-Yosef, O. and D. Pilbeam, *The geography of Neandertals and modern humans in Europe and the Greater Mediterranean*, Peabody Museum of Archaeology and Ethnology, Cambridge, 2000.

Baumgartner, S., J. Beer, M. Suter, B. Dittrich-Hannen, H.-A. Synal, P.W. Kubik, C. Hammer and S. Johnsen, Chlorine 36 fallout in the Summit Greenland Ice Core Project ice core, *J. Geophys. Res., 102*, 26,659-26,662, 1997.

Baumgartner, S., J. Beer, J. Masarik, G. Wagner, L. Meynadier and H.-A. Synal, Geomagnetic modulation of 36Cl flux in the GRIP ice core, Greenland, *Science, 279*, 1330-1332, 1998.

Beck, J.W., D.A. Richards, R.L. Edwards, B.W. Silverman, P.L. Smart, D.J. Donahue, S. Hererra-Osterheld, G.S. Burr, L. Calsoyas, A.J.T. Jull and D. Biddulph, Extremely large variations of atmospheric ^{14}C concentration during the last glacial period, *Science, 292*, 2453-2458, 2001.

Beer, J., R. Muscheler, G. Wagner, C. Laj, C. Kissel, P.W. Kubik and H.-A. Synal, Cosmogenic nuclides during Isotope Stage 2 and 3, *Quat. Sci. Revi., 21*, 1129-1139, 2002.

Bolus, M. and N.J. Conard, The late Middle Paleolithic and earliest Upper Paleolithic in Central Europe and their relevance for the Out of Africa hypothesis, in *Out of Africa in the Pleistocene*, edited by L.G. Straus and O. Bar-Yosef, pp. 29-40, *Quat. Int., 75*, 2001.

Bond, G., H. Heinrich, W. Broecker, L. Labeyrie, J. McManus, J. Andrews, S. Huon, R. Jantschik, S. Clases, C. Simet, K. Tedesco, M. Klas, G. Bonani and S. Ivy, Evidence for massive discharges of icebergs into North Atlantic ocean during the last glacial period, *Nature, 360*, 245-249, 1992.

Bond, G.C. and R. Lotti, Iceberg discharges into the north Atlantic on millennial time scales during the last glaciation, *Science, 267*, 1005-1010, 1995.

Bond, G., B. Wallace, S. Johnsen, J. McManus, L. Labeyrie, J. Jouzel and G. Bonani, Correlations between climate records from North Atlantic sediments and Greenland ice, *Nature, 365*, 143-147, 1993.

Borzatti von Löwenstern, E., La Grotta di Uluzzo. Campagna di scavi 1963, *Riv. Sci. Preis., 18*, 75-89, 1963.

Borzatti von Löwenstern, E, La grotta-riparo di Uluzzo C (Campagna di scavi 1964), *Riv. Sci. Preist., 20*, 1-31, 1965.

Borzatti von Löwenstern, E., Prima campagna di scavi nella grotta "Mario Bernardini" (Nardò-Lecce), *Riv. Sci. Preist., 25*, 89-125, 1970.

Brantingham, P.J., A.I. Krivoshapkin, J. Li and Y. Tserendagva, The Initial Upper Paleolithic in Northeast Asia, *Current Anthropology, 42*, 735-747, 2001.

Brauer, A., J. Mingram, U. Frank, C. Günter, G. Scettler, S. Wulf, B. Zolitschka and J.F.W. Negendank, Abrupt environmental oscillation during the Early Weichselian recorded at Lago Grande di Monticchio, southern Italy, *Quat. Int., 73/74*, 79-90, 2000.

Broecker, W.S., Massive icebergs discharges as triggers for global climate change, *Nature, 372*, 421-424, 1994.

Broglio, A., *Introduzione al Paleolitico*, Laterza, Bari, 1998.

Cacho, I., J.O. Grimalt, C. Pelejero, M. Canales, F.J. Sierro, J. Abel Flores and M. Shackleton, Dansgaard-Oeschger and Heinrich event imprints in Alboran Sea paleotemperatures, *Paleoceanography, 14*, 698-705, 1999.

Carbonell, E. and M. Vaquero, *The last Neandertals, the first anatomically modern humans: a tale about the human diversity. Cultural change and human evolution: the crisis at 40 Ka BP*, Universitat Rovira i Virgili, Tarragona, 1996.

Channell, J.E.T., J.S. Stoner, D.A. Hodell and C.D. Charles, Geomagnetic paleointensity for the last 100 kyr from subantarctic South Atlantic: a tool for inter-hemispheric correlation, *Earth Planet. Sci. Lett.s, 176*, 145-160, 2000.

Chapman, M.R. and N.J. Shackleton, Millennial-scale fluctuation in North Atlantic heat flux during last 150,000 years, *Earth Planet. Sci. Lett., 159*, 57-70, 1998.

Chen, F.H., J. Bloemendal, J.M. Wang, J.J. Li and F. Oldfield, High-resolution multi-proxy climate from Chinese loess: evi-

dence for rapid climatic changes over the last 75 kyr, *Palaeo. Palaeo. Palaeo.*, *130*, 223-235, 1997.

Churchill, S.E. and F.H. Smith, The authors of the early Aurignacian of Europe, *Yearbook Phys. Anthropol.*, *43*, 61-115, 2000.

Cini Castagnoli, G., A. Albrecht, J. Beer, G. Bonino, Ch. Shen, E. Callegari, C. Taricco, B. Dittrich-Hannen, P. Kubik, M. Suter and G.M. Zhu, Evidence for ^{10}Be enhanced deposition in Mediterranean sediments 35 Kyr BP, *Geophys. Res. Lett.*, *22*, 707-710, 1995.

Civetta, L., G. Orsi, L. Pappalardo, R.V. Fisher, G. Heiken and M. Ort, Geochemical zoning, mingling, eruptive dynamics and depositional processes — the Campanian Ignimbrite, Campi Flegrei caldera, Italy. *J. Volc. Geotherm. Res.*, *75*, 183-219. 1997.

Clark, G.A. and C. Willermet, *Conceptual issues in modern human origins research*, Aldine de Gruyter, New York, 1997.

Clarke, D.L., *Analytical archaeology*, Methuen, London, 1968.

Clausen, H.B. and C.U. Hammer, The Laki and Tambora eruptions as revealed in Greenland ice cores from 11 locations, *Annal. Glaciol.*, *19*, 200-203, 1988.

Conard, N.J. and M. Malina, Neue Ausgrabungen in den untersten Schichten des Aurignacien und des Mittelpaläolithikums im Geißenklösterle bei Blaubeuren, Alb-Donau-Kreis, in *Archäologische Ausgrabungen in Baden-Württemberg*, pp. 16-21, Konrad Theiss Verlag, Stuttgart, 2002.

Cornell, W., S. Carey and H. Sigurdsson, Computer simulation of transport and deposition of Campanian Y-5 ash, *J. Volc. Geotherm. Res.*, *17*, 89-109, 1983.

Cortijo, E., L. Labeyrie, L. Vidal, M. Vautravers, M. Chapman, J.-C. Duplessy, M. Elliot, M. Arnold, J.-L. Turon and M. Auffret, Changes in sea surface hydrology associated with Heinrich event 4 in the North Atlantic Ocean between 40° and 60°N, *Earth Planet. Sci. Lett.*, *146*, 29-45, 1997.

Dansgaard, W., S.J. Johnsen, H.B. Clausen, D. Dahl-Jensen, N.S. Gundestrup, C.U. Hammer, C.S. Hvidberg, J.P. Steffensen, J. Jouzel and G. Bond, Evidence for general instability of past climate from 250-Kyr ice-core record, *Nature*, *364*, 218-220, 1993.

Deino, A.L., J. Southon, F. Terrasi, L. Campatola and G. Orsi, ^{14}C and ^{40}Ar/^{39}Ar dating of the Campanian Ignimbrite, Phlegrean Fields, Italy, in *Abstracts, ICOG 1994*, CA, Berkeley, 1994.

De Vivo, B., G. Rolandi, P.B. Gans, A. Calvert, W.A. Bohrson, F.J. Spera and H.E Belkin, New constraints on the pyroclastic eruptive history of the Campanian volcanic Plain (Italy), *Mineral. Petrol.*, *73*, 47-65, 2001.

Dibble, H.L. and P. Mellars, *The Middle Palaeolithic: adaptation, behaviour, and variability*, University of Pennsylvania Press (University Museum monographs, 72), Philadelphia, 1992.

Druitt, T.H., Emplacement of the 18 May 1980 lateral blast deposit ENE of Mount St. Helens, Washington. *Bull. Volc.*, *54*, 554-572, 1992.

Dunbar, R., C. Knight and C. Power, *The evolution of culture. An interdisciplinary view*, Edinburgh University Press, Edinburgh, 1999.

Farizy, C. *Paléolithique Moyen récent et Paléolithique Supérieur ancien en Europe. Ruptures et transitions: examen critique des documents archéologiques*, Actes du Colloque international de Nemours, 9-11 Mai 1988, Nemours, APRAIF (Mémoires du Musée de Préhistoire d'Ile de France, 3), 1990.

Farrand, W.R., Occurrence and age of Ischia Tephra in Franchthi Cave, Peloponnesos, Greece. *Abstracts with Programs, Geological Society of America, 9*, 971, 1977.

Fedele, F.G., B. Giaccio, R. Isaia and G. Orsi, Ecosystem impact of the Campanian Ignimbrite eruption in Late Pleistocene Europe, *Quat. Res.*, *57*, 420-424, 2002.

Fisher, R.V., Transport and deposition of a pyroclastic surge across an area of high relief: The 18 May 1980 eruption of Mount St. Helens, Washington, *Geol. Soc. Am. Bull.*, *102*, 1038-1054, 1990.

Fisher, R.V., G. Orsi, M. Ort and G. Heiken, Mobility of a large-volume pyroclastic flow — emplacement of the Campanian ignimbrite, Italy, *J. Volc. Geotherm. Res.*, *56*, 205-220, 1993.

Fox, R.G., *Current Anthropology 39, Supplement: S1-S190*, 1998.

Frezzotti, M. and B. Narcisi, Late Quaternary tephra-derived paleosols in Central Italy's carbonate Apennine range: stratigraphical and paleoclimatological implications, *Quat. Int.*, *34-36*, 147-153, 1996.

Gambassini, P., *Il Paleolitico di Castelcivita, culture e ambiente*, Electa Napoli, Naples, 1997.

Gamble, C., *The Palaeolithic societies of Europe*, Cambridge University Press, Cambridge, 1999.

Ganopolski, A. and S. Rahmstorf, Rapid changes of glacial climate simulated in a coupled climate model, *Nature*, *409*, 153-158, 2001.

Giaccio, B. and D. Coppola, Note preliminari sul contesto stratigrafico e paleoecologico del sito "Tana delle Iene" (Ceglie Messapica, Brindisi, SE Italia*)*, *Il Quaternario* — *Italian Journal of Quaternary Science*, *13*, 5-20, 2000.

Giaccio, B. and R. Isaia, The Campanian Ignimbrite position in terrestrial and marine Mediterranean successions and Greenland ice-core: implications for paleoclimatic reconstructions of the mid to high latitude OIS 3. *Geophys. Res. Abs.*, *4*, EGS02-A-04515, 2002.

Gibson, K.R., The biocultural human brain, seasonal migrations, and the emergence of the Upper Paleolithic, in *Modelling the early human mind*, edited by P. Mellars and K.R. Gibson, pp. 33-46, McDonald Institute for Archaeological Research, Cambridge, 1996.

Gioia, P., An aspect of the transition between Middle and Upper Palaeolithic in Italy: the Uluzzian, in *Paléolithique Moyen récent et Paléolithique Supérieur ancien en Europe. Ruptures et transitions: examen critique des documents archéologiques*, *Actes du Colloque international de Nemours, 9-11 Mai 1988*, directed by C. Farizy, pp. 241-250, 1990.

Gowlett, J.A.J., Out in the cold, *Nature*, *413*, 33-34, 2001.

Grönvold, K., N. Oskarsson, S.J. Johnsen, H.B. Clausen, C.U. Hammer, G. Bond and E. Bard, Ash layer from Icelandic in the Greenland GRIP ice core correlated with oceanic and land sediments, *Earth Planet. Sci. Lett.*, *135*, 149-155, 1995.

Grootes, P.M., M. Stuiver, J.W.C. White, S. Johnsen and J. Jouzel, Comparison of oxygen isotope records from the GISP2 and GRIP Greenland ice cores, *Nature*, *366*, 552-554, 1993.

Hammer, C.U., H.B. Clausen and W. Dansgaard, Greenland ice sheet evidence of post-glacial volcanism and its climatic impact, *Nature, 288,* 230-235, 1980.

Heinrich, H., Origin and consequences of cyclic ice rafting in Northeast Atlantic Ocean during the past 130,000 years, *Quat. Res., 29,* 142-152, 1988.

Hinrichs, J., B. Schnetger, H. Schale and H.-J. Brumsack, A high resolution study of NE Atlantic sediments at station Bengal: geochemistry and early diagenesis of the Heinrich layers, *Marine Geol., 117,* 79-22, 2001.

Hoffecker, J.F. and C.A. Wolff, *The early Upper Palaeolithic, evidence from Europe and the Near East,* BAR, International series, 437, Oxford, 1988.

Hoffecker, J.F., M.V. Anikovich, A.A. Sinitsyn, V.T. Holliday and S.L. Forman, Initial Upper Paleolithic in Eastern Europe: new research at Kostenki, *Abstracts for the Paleoanthropology Society Meetings, March 19-20,* Denver, 2002.

Huang, C.-Y., M. Zhao, C.-C. Wang and G. Wie, Cooling of the South China Sea by the Toba eruption and correlation with other climate proxies ~71,000 years ago, *Geophys. Res. Lett., 28,* 3915-3918, 2001.

Jacoby, G.C., W. Karen and R.D. D'Arrigo, Laki eruption of 1783, tree rings, and disaster for northwest Alaska Inuit, *Quat. Sci. Rev., 18,* 1365-1371, 1999.

Johnsen, S.J., D. Dahl-Jensen, N. Gundestrup, J.P. Steffensen, H.B. Clausen, H. Miller, V. Masson-Delmotte, A.E. Sveinbjörnsdottir and J. White, Oxygen isotope and palaeotemperature records from six Greenland ice-core stations: Camp Century, Dye-3, GRIP, GISP2, Renland and NorthGRIP, *J. Quat. Sci., 16,* 299-3017, 2001.

Kamata, H., A. Hayashida and T. Danhara, Identification of a pair of co-ignimbrite ash and underlying distal plinian ash in the Early Pleistocene widespread tephra in Japan, *J. Volc. Geotherm. Res., 78,* 51-64, 1997.

Karavaniæ, I. and F.H. Smith, The Middle/Upper Paleolithic interface and the relationship of Neanderthals and early modern humans in the Hrvatsko Zagorje, Croatia. *J. Human Evol., 34,* 223-248, 1998.

Kieffer, G., G. Vernet and J-P. Raynal, Reconnaissance de l'ignimbrite campanienne près du golfe de Policastro (Italie), jusqu'à 150 km de sa zone d'émission. Implications volcanologique et paléoenvironnementales, *Comptes Rendus de l'Academie des Sciences, Series IIA/Earth and Planetary Science, 330,* 105-110, 2000.

Kissel, C., C. Laj, L. Labeyrie, T. Dokken, A. Voelker and D. Blamart, Rapid climatic variations during marine isotope stage 3: magnetic analysis of sediments from Nordic Seas and North Atlantic, *Earth Planet. Sci. Lett., 171,* 489-502,1999.

Kitagawa, H. and J. van der Plicht, Atmospheric radiocarbon calibration to 45,000 yr B.P.: Late Glacial fluctuations and cosmogenic isotope production, *Science, 279,* 1187-1190, 1998.

Klein, R.G., *Man and culture in the Late Pleistocene. A case study,* Chandler, San Francisco, 1969.

Klein, R.G., *Ice-Age hunters of the Ukraine,* The University of Chicago Press, Chicago, 1973.

Klein, R.G., *The human career. Human biological and cultural origins,* University of Chicago Press, Chicago, 1999.

Knecht, H., A. Pike-Tay and R. White, *Before Lascaux. The complex record of the early Upper Paleolithic,* CRC Press, Boca Raton, FL, 1993.

Kozlowski, J.K., *Excavation in the Bacho Kiro cave, Bulgaria: final report,* Panstwowe Wydawnictwo Naukowe, Warsaw, 1982.

Kozlowski, J.K., A multiaspectual approach to the origins of the Upper Palaeolithic in Europe, in *The emergence of modern humans. An archaeological perspective,* edited by P. Mellars, pp. 419-438, Edinburgh University Press, Edinburgh, 1990.

Kozlowski, J.K., The Middle and the Early Upper Paleolitic around the Black Sea, in *Neandertals and modern humans in Western Asia,* edited by T. Akazawa, K. Aoki and O. Bar-Yosef pp. 461-482, Plenum Press, New York, 1998.

Kozlowski, J.K., H. Laville and B. Ginter, *Temnata Cave. Excavations in Karlukovo Karst area, Bulgaria,* Jagellonian University Press, Cracow, 1992.

Kozlowski, J.K. and M. Otte, La formation de l'Aurignacien en Europe, *L'Anthropologie, 104,* 3-15, 2000.

Kuhn, S.L., *Mousterian lithic technology. An ecological perspective,* Princeton University Press, Princeton, NJ, 1995.

Kuhn, S.L. and A. Bietti, The Late Middle and Early Upper Paleolithic in Italy, in *The geography of Neandertals and modern humans in Europe and the Greater Mediterranean,* edited by O. Bar-Yosef and D. Pilbeam, pp. 49-76, Peabody Museum of Archaeology and Ethnology, Cambridge, MA, 2000.

Kuhn, S.L. and M.C. Stiner, The antiquity of hunter-gatherers, in *Hunter-gatherers: an interdisciplinary perspective,* edited by C. Panter-Brick, R.H. Layton and P. Rowley-Conwy, Cambridge University Press, Cambridge, 99-142, 2001.

Labreiro, S.M., J.C. Moreno, I.N. McCave and P.P.E. Weaver, Evidence for Heinrich layers off Portugal (Tore Seamont: 39°N, 12°W), *Marine Geol., 131,* 47-56, 1996.

Laj, C., A. Mazaud and J.-C. Duplessy, Geomagnetic intensity and ^{14}C abundance in the atmosphere and ocean during the past 50 kyr, *Geophys. Res. Lett., 23,* 2045-2048, 1996.

Laj, C., C. Kissel, A. Mazaud, E. Michel, R. Muscheler and J. Beer, Geomagnetic field intensity, North Atlantic Deep Water circulation and atmospheric $\Delta^{14}C$ during the last 50 kyr, *Earth Planet. Sci. Lett. 200,* 177-190, 2002.

Legros, F. and K. Kelfoun, On the ability of pyroclastic flows to scale topographic obstacles, *J. Volc. Geotherm. Res., 98,* 235-241, 2000.

Lemorini, C., *Reconnaitre des tactiques d'exploitation du milieu au Paléolithique Moyen: la contribution de l'analyse fonctionnelle. Étude fonctionnelle des industries lithiques de Grotta Breuil (Latium, Italie) et de La Combette (Bonnieux, Vaucluse, France),* BAR, International series, 858, Oxford, 2000.

Li, T., Z. Liu, M.A. Hall, S. Berne, Y. Saito, S. Cang and Z. Cheng, Heinrich event imprints in the Okinawa Trough: evidence from oxygen isotope and planktonic foraminifera, *Palaeo. Palaeo. Palaeo., 176,* 133-146, 2001.

Manabe, S. and K. Bryan, Jr., CO_2-induced change in a coupled ocean atmosphere model and its paleoclimatic implications, *J. Geophys. Res., 90,* 11,689-11,707, 1985.

Mayewski, P.A., L.D. Meeker, S. Whitlow, M.S. Twickler, M.C. Morrison, P. Bloomfield, G.C. Bond, A. Alley, A.J. Gow, P.M. Grootes, D.A. Meese, M. Ram, K.C. Taylor and W. Wumkes, Changes in atmospheric circulation and ocean ice cover over the North Atlantic during the last 41,000 years, *Science, 263*, 1747-1751, 1994.

Mayewski, Q.A., L.D. Meeker, M.S. Twickler, S. Whitlow, Q. Yang, W. Berry Lyons and M. Prentice, Major features and forcing of high-latitude northern hemisphere atmospheric circulation using a 110,000-years-long glaciochemical series, *J. Geophys. Res., 102*, 26,345-26,366, 1997.

Mazaud, A., C. Laj, E. Bard, M. Arnold and E. Tric, Geomagnetic field control of ^{14}C production over the last 80 KY: implications for the radiocarbon time-scale, *Geophys. Res. Lett., 18*, 1885-1888, 1991.

McCoy, F. W. and W. Cornell, Volcaniclastic sediments in the Tyrrhenian basin, in *Proceedings of the ODP, Scientific Results 107*, edited by K.A. Kastens, J. Mascle *et al.*, pp. 291-305, 1990.

Meese, D.A., A.J. Gow, R.B. Alley, G.A. Zielinski, P.M. Grotes, M. Ram, K.C. Taylor, P.A. Mayewsky and J.F. Bolzan, The Greenland Ice Sheet Core Project 2 depth-age scale: methods and results, *J. Geophys. Res, 102*, 26,411-26,423, 1997.

Melekestsev, I.V., V.Yu. Kirianov and N.D. Praslov, Catastrophic eruption in the Phlegrean Fields region (Italy) — possible source for a volcanic ash in late Pleistocene sediments of the Eropean part of the USSR, *Vulcanologia i Seismologia, 3*, 35-44, 1984.

Mellars, P., *The Neanderthal legacy. An archaeological perspective from Western Europe*, Princeton University Press, Princeton, NJ, 1996.

Mellars, P., M. Otte, L.G. Straus, J. Zilhão and F. D'Errico, The Neanderthal problem continued, *Current Anthropology, 40*, 341-364, 1999.

Mussi, M., *Earliest Italy, An overview of the Italian Paleolithic and Mesolithic*, Kluwer Academic/Plenum, New York, 2001.

Narcisi, B., Tephrochronology of a late Quaternary lacustrine record from the Monticchio maar (Vulture volcano, southern Italy), *Quat. Sci. Rev., 15*, 115-165, 1996.

Narcisi, B. and L. Vezzoli, Quaternary stratigraphy of distal tephra layers in the Mediterranean — an overview, *Global Planet. Change, 21*, 31-50. 1999.

Omoto, K. and P.V. Tobias, *The origins and past of modern humans: toward reconciliation*, World Scientific, Singapore, 1998.

Oppenheimer, C., Limited global change due to the largest known Quaternary eruption, Toba ~74 kyr BP?, *Quat. Sci. Rev., 21*, 1593-1609, 2002.

Orsi, G., S. De Vita and M. di Vito, The restless, resurgent Campi Flegrei nested caldera (Italy): constraints on its evolution and configuration, *J. Volc. Geotherm. Res., 74*, 179-214, 1996.

Ort, M., M. Rosi and C.A. Anderson, Correlation of deposits and vent locations of the proximal Campanian Ignimbrite deposits, Campi Flegrei, Italy, based on natural remanent magnetization and anisotropy of magnetic susceptibility characteristics, *J. Volc. Geotherm. Res., 91*,167-178, 1999.

Ort, M., G. Orsi, L. Pappalardo and R. V. Fisher, Anisotropy of magnetic susceptibility studies of depositional processes in the Campanian Ignimbrite, Italy, *Bull. Volc., 65*, 55-72, 2003

Pailler, D. and E. Bard, High frequency palaeoceanographic changes during the past 140000 yr recorded by organic matter in sediments of the Iberian Margin, *Palaeo. Palaeo. Palaeo., 181*, 431-452, 2002.

Palma Di Cesnola, A., Prima campagna di scavi nella Grotta del Cavallo presso Santa Caterina (Lecce), *Riv. Sci. Preist., 18*, 41-74, 1963.

Palma Di Cesnola, A., Seconda campagna di scavi nella Grotta del Cavallo presso Santa Caterina (Lecce), *Riv. Sci. Preist., 19*, 23-39, 1964.

Palma Di Cesnola, A., L'Uluzzien: faciès italien du Leptolithique archaique, *L'Anthropologie, 93*, 783-811, 1989.

Palma Di Cesnola, A., Gli scavi a Grotta Paglicci durante il 1990, *Atti del 12° Conv. Nazionale "Preistoria-Protostoria-Storia della Daunia", San Severo 14-16 dicembre 1990*, 23-34, 1990.

Palma Di Cesnola, A., La campagna 1991 a Grotta Pagliacci, *Atti del 13° Conv. Nazionale "Preistoria-Protostoria-Storia della Daunia", San Severo 22-24 novembre 1991*, 9-13, 1993.

Palma Di Cesnola, A., *Le Paléolithique supérieur en Italie*, Editions Jérôme Million, Grenoble, 2001.

Pappalardo, L., L. Civetta, S. De Vita, M.A. Di Vito, G. Orsi, A. Carandente and R.V. Fisher, Timing of magma extraction during the Campanian Ignimbrite eruption (Campi Flegrei caldera), *J. Volc. Geotherm. Res., 114*, 479-497, 2002.

Paterne, M., Additional remarks on tephra layer from Temnata Cave, in *Temnata Cave. Excavations in Karlukovo Karst area, Bulgaria*, edited by J.K. Kozlowski, H. Laville and B. Ginter, pp. 99-100, Jagellonian University Press, Cracow, 1992.

Paterne, M., F. Guichard and J. Labeyrie, Explosive activity of the south Italian volcanoes during the past 80,000 years as determined by marine tephrochronology, *J. Volc. Geotherm. Res., 34*, 153-172, 1988.

Paterne, M., N. Kallel, L. Labeyrie, M. Vautravers, J.-C. Duplessy, M. Rossignol-Strick, E. Cortijo, M. Arnold and M. Fontugne, Hydrological relationship between the North Atlantic Ocean and the Mediterranean Sea during the past 15-75 kyr, *Paleoceanography, 14*, 626-638, 1999.

Prokopenko, A.A., D.F. Williams, E.B. Karabanov and G.K. Khursevich, Continental response to Heinrich events and Bond cycles in sedimentary record of Lake Baikal, Siberia, *Global Planet. Change., 28*, 117-126, 2001.

Quam, R.M. and F.H. Smith, A reassessment of the Tabun C2 mandible, in *Neandertals and modern humans in Western Asia*, edited by T. Akazawa, K. Aoki and O. Bar-Yosef, pp. 405-421, Plenum Press, New York, 1998.

Rampino, M.R., Supereruptions as a threat to civilizations on Earth-like planets, *Icarus, 156*, 562-569, 2002.

Rampino, M.R. and S. Ambrose, Volcanic winter in the Garden of Eden: The Toba supereruption and the late Pleistocene human population crash, in *Volcanic hazards and disasters in human antiquity*, edited by F.W. McCoy and G. Heiken, pp. 71-82, *Geological Society of America, Special Paper, 345*, 2000.

Rampino, M.R. and S. Self, Sulphur-rich volcanic eruptions and stratospheric aerosol, *Nature, 310*, 677-679, 1984.

Rampino, M.R. and S. Self, Volcanic winter and accelerated glaciation following the Toba super-eruption, *Nature, 359*, 50-52, 1992.

Rampino, M.R. and S. Self, Climate-volcanism feedback and the Toba eruption of ca. 74,000 years ago, *Quat. Res., 40*, 269-280, 1993.

Ramrath, A., B. Zolitschka, S. Wulf and J.F.W. Negendank, Late Pleistocene climatic variations as recorded in two Italian maar lakes (Lago di Mezzano, Lago Grande di Monticchio), *Quat. Sci. Rev., 18*, 977-992. 1999

Richter, D., J. Waiblinger, W.J. Rink and G.A. Wagner, Thermoluminescence, electron spin resonance and ^{14}C-dating of the late Middle and early Upper Palaeolithic site of Geißenklösterle Cave in southern Germany, *J. Archaeol. Sci., 27*, 71-89, 2000.

Riel-Salvatore, J. and G.A. Clark, Grave markers. Middle and Early Upper Paleolithic burials and the use of chronotypology in contemporary Paleolithic research, *Current Anthropology, 42*, 449-479, 2001.

Robock, A., Volcanic eruptions and climate, *Rev. Geophys., 38*, 191-219, 2000.

Rosi, M. and A. Sbrana, *The Phlegraean Fields*, CNR, Quaderni de "La ricerca Scientifica", 114, Rome, 1987.

Rosi, M., L. Vezzoli, A. Castelmenzano and G. Greco, Plinian pumice fall deposit of the Campanian Ignimbrite eruption (Phlegraean Fields, Italy), *J. Volc. Geotherm. Res., 91*, 179-198, 1999.

Roucoux, K.H., N. Shackleton, L. Abreu, J. Schönfled and P.C. Tzedakis, Combined marine proxy and pollen analyses reveal rapid vegetation response to North Atlantic millennial-scale climate oscillations, *Quat. Res., 55*, 128-132, 2001.

Sánchez Goñi, M.F., I. Cacho, J.-L. Turon, J. Guiot, F.J. Sierro, J.-P. Peypouquet, J.O. Grimalt and N.J. Shackleton, Synchroneity between marine and terrestrial responses to millennial scale climatic variability during the last glacial period in the Mediterranean region, *Clim. Dyn., 19*, 95-105, 2002.

Sánchez Goñi, M.F., J.-L. Turon, F. Eynaud and S. Gendreau, European Climatic Response to Millennial-Scale Changes in the Atmosphere–Ocean System during the Last Glacial Period, *Quat. Res., 54*, 394-403, 2000.

Scandone, R., F. Bellucci, L. Lirer and G. Rolandi, The structure of the Campanian Plain and the activity of the Neapolitan volcanoes (Italy), *J. Volc. Geotherm. Res., 48*, 1-31, 1991.

Schramm, A., M. Stein and S.L. Goldstein, Calibration of the ^{14}C time scale to >40 ka by [234]U-[230]Th dating of Lake Lisan sediments (last glacial Dead Sea), *Earth Planet. Sci. Lett., 175*, 27-40, 2000.

Schulz, H., U. von Road and H. Erlenkeuser, Correlations between Arabian sea and Greenland climate oscillations of the past 110,000 years, *Nature, 393*, 54-57, 1998.

Schulz, H., K.-C. Emeis, H. Erlenkeuser, U. von Rad and C. Rolf, The Toba Volcanic Event and Interstadial/Stadial Climates at the Marine Isotopic Stage 5 to 4 Transition in the Northern Indian Ocean, *Quat. Res., 57*, 22-31, 2002.

Seymour, K. and K. Christanis, Correlation of tephra layer in western Greece with a Late Pleistocene eruption in the Campanian province of Italy, *Quat. Res., 43*, 46-54. 1995.

Signorelli, S., G. Vaggelli, L. Francalanci and M. Rosi, Origin of magmas feeding the Plinian phase of the Campanian Ignimbrite eruption, Phlegrean Fields (Italy): constraints based on matrix-glass and glass-inclusion compositions, *J. Volc. Geotherm. Res., 91*, 199-220, 1999.

Smith, F.H., A.B. Falsetti and T. Simmons, Circum-mediterranean biological connections and the pattern of late Pleistocene human evolution, in *Man and environment in the Paleolithic*, edited by H. Ullrich, pp. 197-207, Université de Liège (ERAUL, 62), Liège, 1995.

Sparks, R.S.J., and T.C. Huang, The volcanological significance of deep-sea ash layers associated with ignimbrites, *Geol. Magaz., 117*(5), 425-436, 1980.

Stiner, M.C., *Honor among thieves. A zooarchaeological study of Neandertal ecology*, Princeton University Press, Princeton, NJ, 1994.

Stoner, J.S., C. Laj, J.E.T. Channel and C. Kissel, South Atlantic and North Atlantic geomagnetism paleointensity stacks (0-80 ka): implications for inter-hemispheric correlation, *Quat. Sci. Rev., 21*, 1141-1151, 2002.

Straus, L.G. and O. Bar-Yosef, Out of Africa in the Pleistocene, *Quat. Int., 75*, 1-124, 2001.

Stringer, C. and W. Davies, Those elusive Neanderthals, *Nature, 413*, 791-792, 2001.

Stuiver, M. and P.J. Reimer, Extended ^{14}C data base and revised CALIB 3.0 ^{14}C age calibration program, *Radiocarbon, 35*, 215-230, 1993.

Stuiver, M., P.J. Reimer, E. Bard, J.W. Beck, G.S. Burr, K.A. Hughen, B. Kromer, G. McCormac, J. van der Plicht and M. Spurk, INTCAL98 Radiocarbon Age Calibration, 24,000-0 cal BP, *Radiocarbon, 40*, 1041-1083, 1998.

Thouveny, N., J.-L. de Beaulieu, E. Bonifay, K.M. Creer, J. Guiot, M. Icole, S. Johnsen, J. Jouzel, M. Reille, T. Williams and D. Williamson, Climate variations in Europe over the past 140 kyr deduced from rock magnetism, *Nature, 371*, 503-506, 1994.

Thouveny, N., E. Moreno, D. Delanghe, L. Candon, Y. Lancelot and N.J. Shackleton, Rock magnetic detection of distal ice-rafted debris: clue for the identification of Heinrich layers on the Portuguese margin, *Earth Planet. Sci. Lett., 180*, 61-75, 2000.

Thunnel, R., A. Federman, S. Sparks and D. Williams, The origin and volcanological significance of the Y-5 ash layer in the Mediterranean, *Quat. Res., 12*, 241-253, 1979.

Ton-That, T., B. Singer and M. Paterne, 40Ar/39Ar dating of latest Pleistocene (41 ka) marine tephra in the Mediterranean Sea: implications for global climate records, *Earth Planet. Sci. Lett., 184*, 645-658, 2001

Tric, E., J.-P. Valent, P. Tucholka, M. Paterne, L. Labeyrie, F. Guichard, L. Tauxe and M. Fontugne, Paleointensity of the geomagnetic field during the last 80,000 years, *J. Geophys. Res., 97*, 9337-9351, 1992.

Upton, J., P. Cole, P. Shaw, A. Szakacs and I. Seghedi, Correlation of tephra layers found in southern Romania with the Campanian Ignimbrite (~37ka) eruption, in *The Quaternary Research*

Association and First Postgraduate Paleo-environmantal Symposium, Universiteit van Amsterdam, 36, Amsterdam, 2002.

Van Andel, T. and P. Tzedakis, Palaeolithic landscapes of Europe and environs, 150,000-25,000 years ago: an overview, *Quat. Sci. Rev., 115*, 481-500, 1996.

Vidal, L., L. Labeyrie, E. Cortijo, M. Arnold, J.C. Duplessy, E. Miche, S. Bequé and T.C.E. van Veering, Evidence for changes in the North Atlantic deep water linked to meltwater surges during Heinrich events, *Earth Planet. Sci. Lett., 146*, 13-27, 1997.

Voelker, A.H.L., M. Sarthein, P.M. Grootes, H. Erlenkeuser, C. Laj, A. Mazaud, M.-J. Nadeau and M. Schleischer, Correlation of marine ^{14}C ages from the Nordic seas with the GISP2 isotope record: implications for radiocarbon calibration beyond 25 ka, *Radiocarbon, 40*, 517-534, 1998.

Voelker, A.H.L., P.M. Grootes, M.-J. Nedeau and M. Sarnthein, Radiocarbon levels in the Iceland Sea from 25-53 kyr and their link to the earth's magnetic field intensity, *Radiocarbon, 42*, 437-452, 2000.

Voelker, A., Global distribution of centennial-scale records for Marine Isotope Stage (MIS) 3: a database, *Quat. Sci. Rev., 21*, 1185-1212, 2002.

Vogel, J.C. and J. Kronfeld, Caibration of radiocarbon dates for the late Pleistocene using U/Th dates on stalagmites, *Radiocarbon, 39*, 27-32, 1997.

Volman, T., Early prehistory of Southern Africa, in *Southern African prehistory and paleoenvironments*, edited by R.G. Klein, pp. 169-220, A.A. Balkema, Rotterdam, 1984.

Vrba E.S., G.H. Denton, T.C. Partridge and L.H. Burckle, *Paleoclimate and evolution, with emphasis on human origins*, Yale University Press, New Haven, CT, 1995.

Wagner, G., J. Beer, C. Laj, C. Kissel, J. Masarik, R. Muscheler and H.-A. Synal, Chlorine-36 evidence for Mono Lake event in the Summit GRIP ice core, *Earth Planet. Sci. Lett., 181*, 1-6, 2000.

Walker, M.J.C., S. Björck, J.J. Lowe, L.C. Cwynar, S. Johnsen, K.-L. Knudsen, B. Wohlfarth and INTIMATE group, Isotopic 'events' in the GRIP ice core: a stratotype for the Late Pleistocene, *Quat. Sci. Rev., 18*, 1143-1150, 1999.

Watts, I., The origin of symbolic culture, in *The evolution of culture. An interdisciplinary view*, edited by R. Dunbar, C. Knight and C. Power, pp. 113-146, Edinburgh University Press, Edinburgh, 1999.

Watts, W.A., J.R.M. Allen and B. Huntley, Vegetation history and palaeoclimate of the last glacial period of Lago Grande di Monticchio, southern Italy, *Quat. Sci. Rev., 15*, 133-153, 1996.

Watts, W.A., J.R.M. Allen and B. Huntley, Palaeoecology of three interstadial events during oxygen-isotope stages 3 and 4: a lacustrine record from Lago Grande di Monticchio, southern Italy, *Palaeo. Palaeo. Palaeo., 155*, 83-93, 2000.

Wolpoff, M.H., J. Hawks, D.W. Frayer and K. Hunley, Modern human ancestry at the peripheries: a test of the replacement theory, *Science, 291*, 293-297, 2001.

Woods, A.W. and K. Wohletz, Dimension and dynamics of co-ignimbrite eruption columns, *Nature, 350*, 225-227, 1991.

Yiou, F., G.M. Raisbeck, S. Baumgartner, J. Beer, C. Hammer, S. Johensen, J. Jouzel, P.W. Kubik, J. Lestringuez, M. Stévenard, M. Suter and P. Yiou, Beryllium 10 in Greenland Ice Core Project ice core at Summit, Greenland, *J. Geophys. Res., 102*, 26,783-26,794, 1997.

Zielinski, G.A., Stratosphric loading and optical depth estimates of sxplosive volcanism over the last 2100 years derived from the Greenland Ice Sheet Project 2 ice core, *J. Geophys. Res., 100*, 20,937-20,955, 1995.

Zielinski, G.A., Use of paleo-records in determining variability within the volcanism-climate system, *Quat. Sci. Rev. 19*, 417-438, 2000.

Zielinski, G.A., P.A. Mayewski, L.D. Meeker, S.I. Whitlow, M.S. Twickler, M. Morrison, A.J. Gow and R.B. Alley, Record of volcanism since 7000 B.C. from the GISP2 Greenland ice core and implications for volcano-cimate system, *Science, 264*, 948-951, 1994.

Zielinski, G.A., P.A. Mayewski, L.D. Meeker, K. Grönvold, M.S. Germani, S.I. Whitlow, M.S. Twickler and K.C. Taylor, Volcanic aerosol records and tephrochronology of the Summit, Greenland, ice cores, *J. Geophys. Res., 102*, 26,625-26,640, 1997.

Zielinski, G.A., P.A. Mayewski, L.D. Meeker, S.I. Whitlow and M.S. Twickler, A 110,000-yr record of explosive volcanism from the GISP2 (Greenland) ice core, *Quat. Res., 45*, 109-118, 1996a.

Zielinski, G.A., P.A. Mayewski, L.D. Meeker, S.I. Whitlow and M.S. Twickler, Potential atmospheric impact of the Toba mega-eruption ~71,000 years ago, *Geophys. Res. Lett., 23*, 837-840, 1996b.

Zilhão, J. and F. D'Errico, The chronology and taphonomy of the earliest Aurignacian and its implications for the understanding of Neandertal extinction, *J. World Prehist., 13*, 1-68, 1999.

Zilhão, J. and F. D'Errico, La nouvelle "bataille aurignacienne." Une révision critique de la chronologie du Châtelperronien et de l'Aurignacien ancien , *L'Anthropologie, 104*, 17-50, 2000.

Zolitschka, B. and J.F.W. Negendank, Sedimentology, dating and palaeoclimatic interpretation of a 76.3 ka record from Lago Grande di Monticchio, southern Italy, *Quat. Sci. Rev., 15*, 101-112, 1996.

F. G. Fedele, Sezione e Museo di Antropologia, Università di Napoli Federico II, via Mezzocannone 8, 80134 Naples, Italy (email: ffedele01@yahoo.it)

B. Giaccio, Istituto di Geologia Ambientale e Geoingegneria, Consiglio Nazionale delle Ricerche, via del Fosso del Cavaliere 100, 00133 Rome, Italy (email: giaccio@irtr.rm.cnr.it)

R. Isaia and G. Orsi, Osservatorio Vesuviano, Istituto Nazionale di Geofisica e Vulcanologia, via Diocleziano 328, 80124 Naples, Italy (isaia@ingv.it; orsi@ingv.it).

Color Plate Section

Winter (DJF) 1991–1992
Average Lower Troposphere Temperature Anomalies (°C)
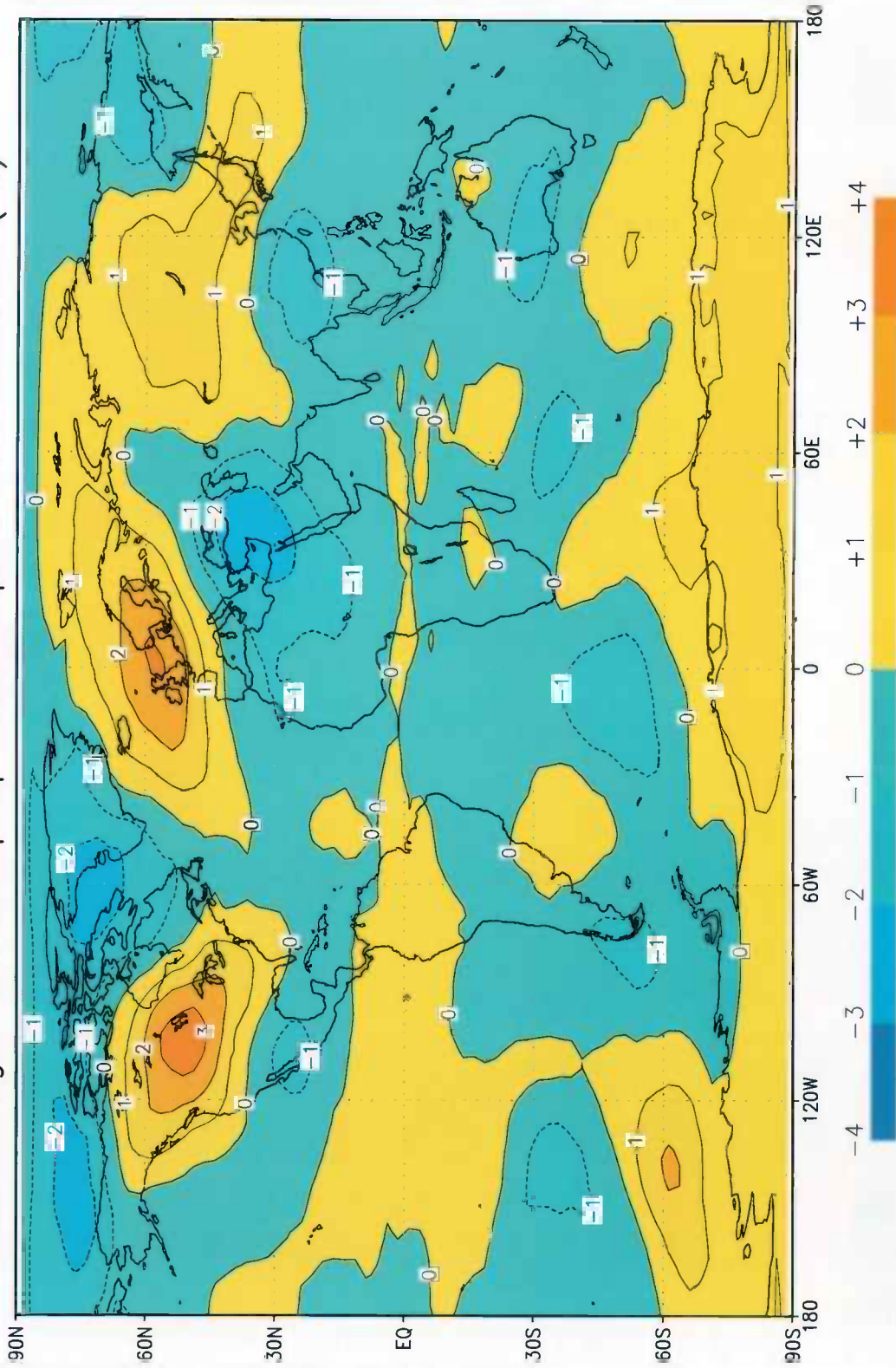
Plate 1. Winter (DJF) lower tropospheric temperature anomalies (with the non-volcanic period of 1984–1990 used to calculate the mean) for the 1991/92 Northern Hemisphere winters (DJF) following the 1991 Mt. Pinatubo eruption. This pattern is typical of that following all large tropical eruptions, with warming over North America, Europe, and Siberia, and cooling over Alaska, Greenland, the Middle East, and China. Data from Microwave Sounding Unit Channel 2R [*Spencer et al.,* 1990], updated courtesy of J. Christy and now called Channel 2LT. Anomalies greater than 1°C are shaded.

Winter (DJF) 1992–1993
Average Lower Troposphere Temperature Anomalies (°C)
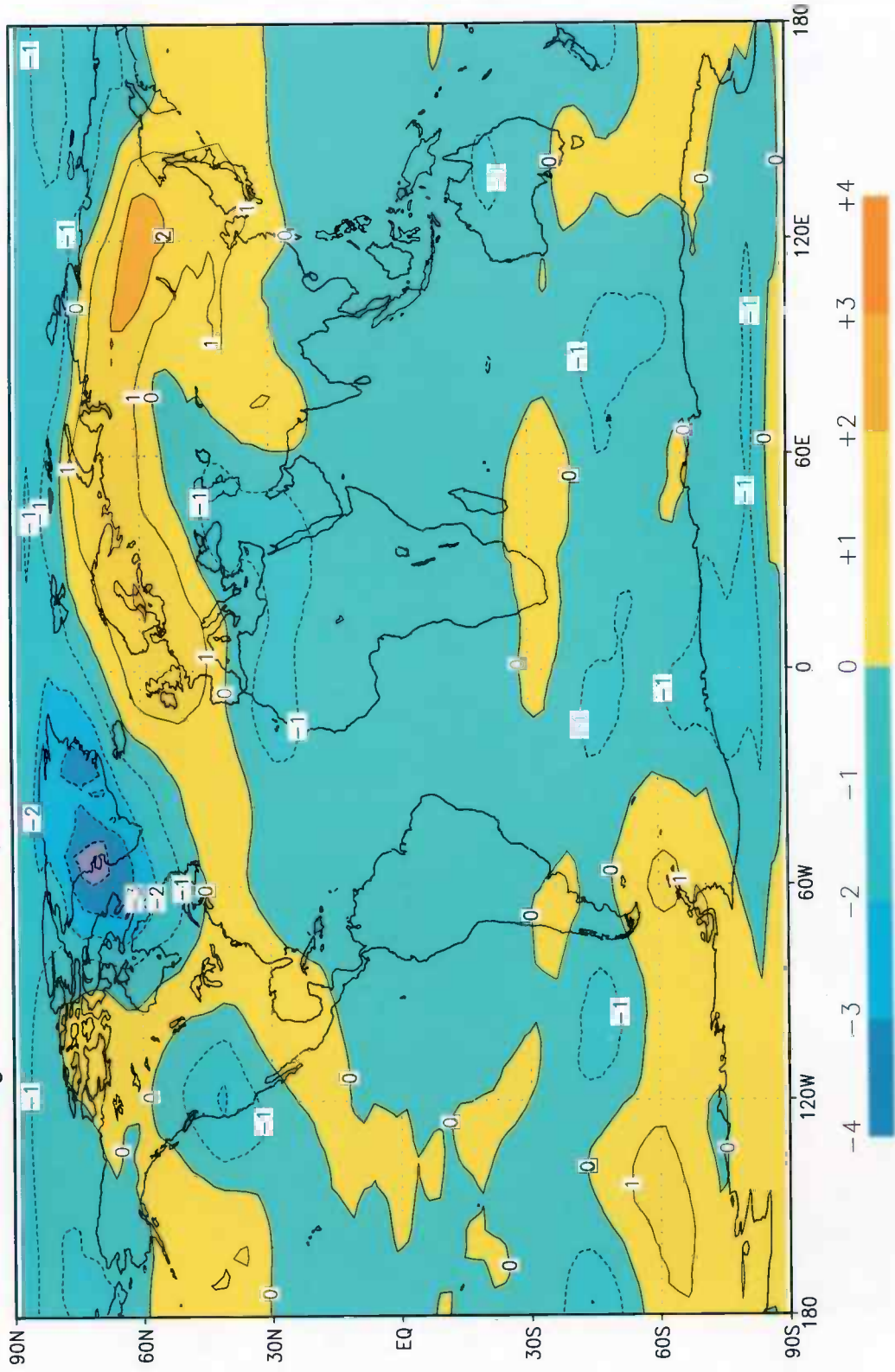
Plate 2. Same as Plate 1, but for the 1992/93 Northern Hemisphere winter.

Summer (JJA) 1992
Average Lower Troposphere Temperature Anomalies (°C)
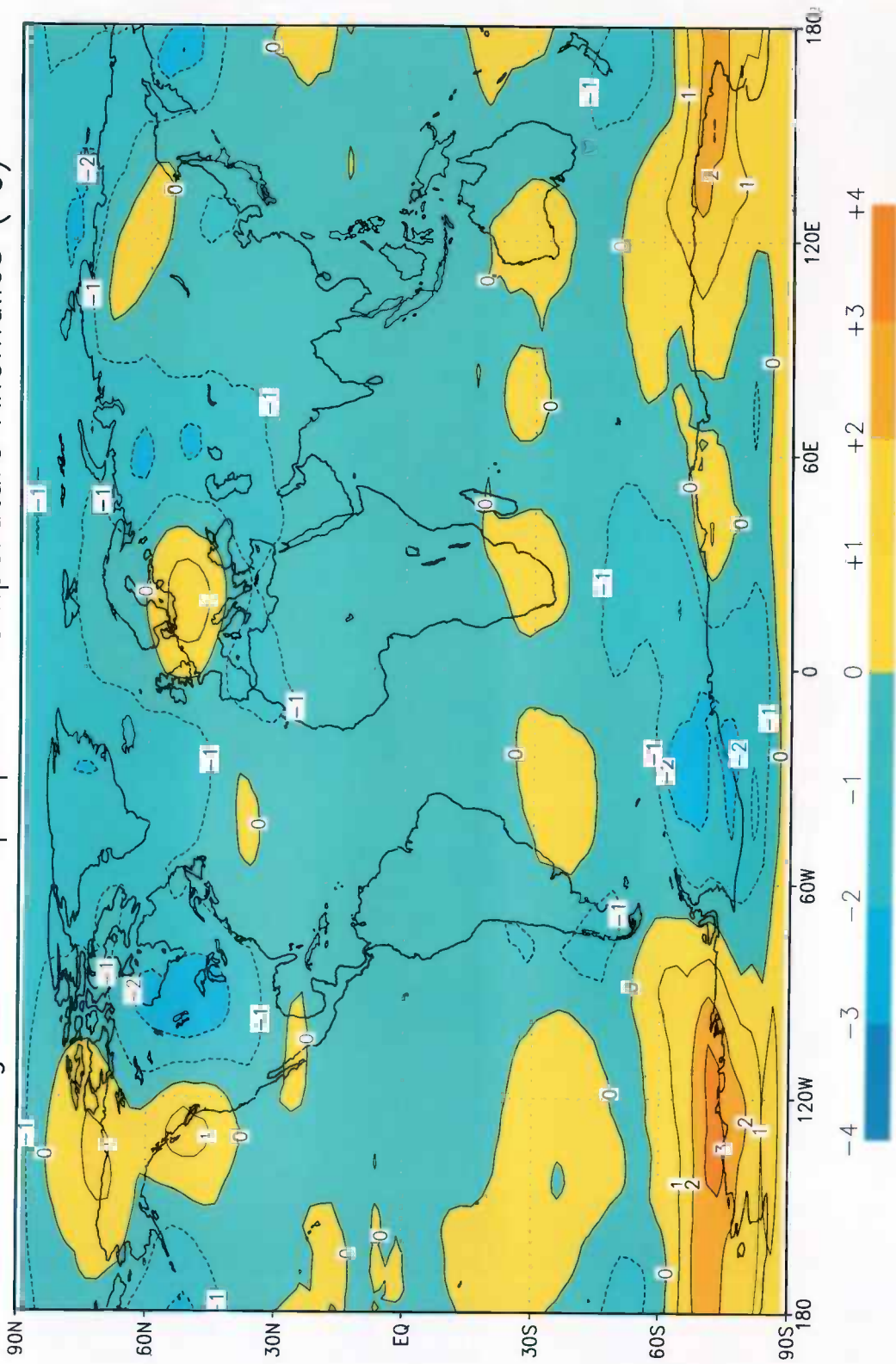
Plate 3. Summer (JJA) 1992 lower tropospheric temperature anomalies (with the non-volcanic period of 1984–1990 used to calculate the mean) following the 1991 Mt. Pinatubo eruption. Data from Microwave Sounding Unit Channel 2R [*Spencer et al.*, 1990], updated courtesy of J. Christy and now called Channel 2LT. Anomalies less than −1°C are shaded.

El Chichón   Pinatubo

Ruiz

El Chichón

Pinatubo

Ruiz

r >0.15 μm

r > 0.25 μm

Fuego

El Chichón

Pinatubo

Ruiz

Particles (cm^{-2} column)

10^7

10^6

10^5

10^4

Figure showing Solar Radiation Transmitted (%) with volcanic eruptions marked:

- Volcanic Eruptions
- Agung, 8.3 S, VEI 4
- Fuego, 14.5 N, VEI 4
- El Chichón, 17.4 N, VEI 5
- Pinatubo, 15.1 N, VEI 6

Y-axis: Solar Radiation Transmitted (%), values 70, 80, 90

SO$_2$ absorber amount (m atm-cm)

(d) NOAA-12 JUne-17 1996 16:11UT

Mass= 0.0234 Tg Area= 77825 km² Max. SO₂= 25.9 m atm-cm θ=-38.33° λ=159.75° N12-96-169 16:11UT

0   4   8

40
35
Altitude in km
30
25
20
15
10

0

-1

-2

-3

40
35
Altitude in km
30
25
20
15
10

0.4

0.3

0.2

0.1

40
35
Altitude in km
30
25
20
15
10

log$_{10}$(Number density in cm^{-3}) - September 1999

AVHRR 2/27/00 0414 UT
4-5 BTD

AVHRR 2/27/00 0554 UT
4-5 BTD

AVHRR 2/27/00 0737 UT
4-5 BTD

AVHRR 2/27/00 0923 UT
4-5 BTD

MODIS 2/27/00 1350 UT
B31 BT

MODIS 2/27/00 1350 UT
31–32 BTD

AVHRR 2/27/00 1417 UT
4–5 BTD

AVHRR 2/27/00 1557UT
4–5 BTD

AVHRR 2/27/00 1742 UT
4-5 BTD
+2 +10

MODIS 31-32 BTD
2/27/00 2015 UT
+2 +10

2/28/00 5:42 UT
NOAA 14 Band 4
+5

2/28/00 5:42 UT
NOAA 14 BTD
-1 +8

02/26/2000
21:10 UT
0   DU   200

02/27/2000
13:50 UT
10   DU   400

02/27/2000
21:55 UT
70   DU   400

02/28/2000
11:15 UT
0   DU   400

26 February 2000 21:00UTC mass=0.079 Tg

27 February 2000 13:50UTC mass=0.190 Tg

27 February 2000 21:35UTC mass=0.166 Tg

28 February 2000 11:15UTC mass=0.134 Tg

Orbit 19683
FEB 27, 2000

Milli Atm cm

30
26
22
18
14
10

Iterative SO2
EARTH PROBE TOMS
NASA / GSFC

FEB 29, 2000

Milli Atm cm

30
27
24
21
18
15

Iterative SO2
EARTH PROBE TOMS
NASA / GSFC

Orbit 19683
FEB 27, 2000

Aerosol Index

Aerosol Index
EARTH PROBE TOMS
NASA / GSFC

(°C wrt 1961-90)

1420 1453

1587

1666 1675

1641/2/3

1601

1695

1698/9

1742

1783

1816/7

1837

1884

1912

7

°C wrt 1961-90

1739 1740 1741

1742 1743 1744

1782 1783 1784

1813 1814 1815

1816 1817 1818

°C wrt 1961-90

DJF 1991–2: Observed Temperature